



# **BRAIN-COMPUTER INTERFACES FOR PERCEPTION, LEARNING, AND MOTOR CONTROL**

EDITED BY: Saugat Bhattacharyya, Amit Konar, Haider Raza and  
Anwesa Khasnobish

PUBLISHED IN: *Frontiers in Neuroscience* and *Frontiers in Human Neuroscience*



# frontiers

## Frontiers eBook Copyright Statement

The copyright in the text of individual articles in this eBook is the property of their respective authors or their respective institutions or funders. The copyright in graphics and images within each article may be subject to copyright of other parties. In both cases this is subject to a license granted to Frontiers.

The compilation of articles constituting this eBook is the property of Frontiers.

Each article within this eBook, and the eBook itself, are published under the most recent version of the Creative Commons CC-BY licence.

The version current at the date of publication of this eBook is CC-BY 4.0. If the CC-BY licence is updated, the licence granted by Frontiers is automatically updated to the new version.

When exercising any right under the CC-BY licence, Frontiers must be attributed as the original publisher of the article or eBook, as applicable.

Authors have the responsibility of ensuring that any graphics or other materials which are the property of others may be included in the CC-BY licence, but this should be checked before relying on the CC-BY licence to reproduce those materials. Any copyright notices relating to those materials must be complied with.

Copyright and source acknowledgement notices may not be removed and must be displayed in any copy, derivative work or partial copy which includes the elements in question.

All copyright, and all rights therein, are protected by national and international copyright laws. The above represents a summary only. For further information please read Frontiers' Conditions for Website Use and Copyright Statement, and the applicable CC-BY licence.

ISSN 1664-8714

ISBN 978-2-88971-851-1

DOI 10.3389/978-2-88971-851-1

## About Frontiers

Frontiers is more than just an open-access publisher of scholarly articles: it is a pioneering approach to the world of academia, radically improving the way scholarly research is managed. The grand vision of Frontiers is a world where all people have an equal opportunity to seek, share and generate knowledge. Frontiers provides immediate and permanent online open access to all its publications, but this alone is not enough to realize our grand goals.

## Frontiers Journal Series

The Frontiers Journal Series is a multi-tier and interdisciplinary set of open-access, online journals, promising a paradigm shift from the current review, selection and dissemination processes in academic publishing. All Frontiers journals are driven by researchers for researchers; therefore, they constitute a service to the scholarly community. At the same time, the Frontiers Journal Series operates on a revolutionary invention, the tiered publishing system, initially addressing specific communities of scholars, and gradually climbing up to broader public understanding, thus serving the interests of the lay society, too.

## Dedication to Quality

Each Frontiers article is a landmark of the highest quality, thanks to genuinely collaborative interactions between authors and review editors, who include some of the world's best academicians. Research must be certified by peers before entering a stream of knowledge that may eventually reach the public - and shape society; therefore, Frontiers only applies the most rigorous and unbiased reviews. Frontiers revolutionizes research publishing by freely delivering the most outstanding research, evaluated with no bias from both the academic and social point of view. By applying the most advanced information technologies, Frontiers is catapulting scholarly publishing into a new generation.

## What are Frontiers Research Topics?

Frontiers Research Topics are very popular trademarks of the Frontiers Journals Series: they are collections of at least ten articles, all centered on a particular subject. With their unique mix of varied contributions from Original Research to Review Articles, Frontiers Research Topics unify the most influential researchers, the latest key findings and historical advances in a hot research area! Find out more on how to host your own Frontiers Research Topic or contribute to one as an author by contacting the Frontiers Editorial Office: [frontiersin.org/about/contact](http://frontiersin.org/about/contact)

# BRAIN-COMPUTER INTERFACES FOR PERCEPTION, LEARNING, AND MOTOR CONTROL

Topic Editors:

**Saugat Bhattacharyya**, Ulster University, United Kingdom

**Amit Konar**, Jadavpur University, India

**Haider Raza**, University of Essex, United Kingdom

**Anwasha Khasnobish**, Tata Consultancy Services, India

**Citation:** Bhattacharyya, S., Konar, A., Raza, H., Khasnobish, A., eds. (2021).  
Brain-Computer Interfaces for Perception, Learning, and Motor Control.  
Lausanne: Frontiers Media SA. doi: 10.3389/978-2-88971-851-1

# Table of Contents

- 05 Editorial: Brain-Computer Interfaces for Perception, Learning, and Motor Control**  
Saugat Bhattacharyya, Amit Konar, Haider Raza and Anwasha Khasnobish
- 08 Deep Learning Based Inter-subject Continuous Decoding of Motor Imagery for Practical Brain-Computer Interfaces**  
Sujit Roy, Anirban Chowdhury, Karl McCreadie and Girijesh Prasad
- 24 Multiclass Classification Based on Combined Motor Imageries**  
Cecilia Lindig-León, Sébastien Rimbart and Laurent Bougrain
- 38 Hybrid EEG-fNIRS BCI Fusion Using Multi-Resolution Singular Value Decomposition (MSVD)**  
Muhammad Umer Khan and Mustafa A. H. Hasan
- 50 Parallel Spatial–Temporal Self-Attention CNN-Based Motor Imagery Classification for BCI**  
Xiuling Liu, Yonglong Shen, Jing Liu, Jianli Yang, Peng Xiong and Feng Lin
- 62 Hyperscanning EEG and Classification Based on Riemannian Geometry for Festive and Violent Mental State Discrimination**  
Cédric Simar, Ana-Maria Cebolla, Gaëlle Chartier, Mathieu Petieau, Gianluca Bontempi, Alain Berthoz and Guy Cheron
- 75 Auditory Noise Leads to Increased Visual Brain-Computer Interface Performance: A Cross-Modal Study**  
Jun Xie, Guozhi Cao, Guanghua Xu, Peng Fang, Guiling Cui, Yi Xiao, Guanglin Li, Min Li, Tao Xue, Yanjun Zhang and Xingliang Han
- 89 Modulation of Functional Connectivity and Low-Frequency Fluctuations After Brain-Computer Interface-Guided Robot Hand Training in Chronic Stroke: A 6-Month Follow-Up Study**  
Cathy C. Y. Lau, Kai Yuan, Patrick C. M. Wong, Winnie C. W. Chu, Thomas W. Leung, Wan-wa Wong and Raymond K. Y. Tong
- 99 Formulation of the Challenges in Brain-Computer Interfaces as Optimization Problems—A Review**  
Shireen Fathima and Sheela Kiran Kore
- 112 An Intracortical Implantable Brain-Computer Interface for Telemetric Real-Time Recording and Manipulation of Neuronal Circuits for Closed-Loop Intervention**  
Hamed Zaer, Ashlesha Deshmukh, Dariusz Orłowski, Wei Fan, Pierre-Hugues Prouvot, Andreas Nørgaard Glud, Morten Bjørn Jensen, Esben Schjødt Worm, Slávka Lukacova, Trine Werenberg Mikkelsen, Lise Moberg Fitting, John R. Adler Jr, M. Bret Schneider, Martin Snejbjerg Jensen, Quanhai Fu, Vinson Go, James Morizio, Jens Christian Hedemann Sørensen and Albrecht Stroh
- 126 Optimal Approach for Signal Detection in Steady-State Visual Evoked Potentials in Humans Using Single-Channel EEG and Stereoscopic Stimuli**  
Zoltan Derzsi

- 144** *Effects of Emotional Stimulations on the Online Operation of a P300-Based Brain–Computer Interface*  
Minju Kim, Jongsu Kim, Dojin Heo, Yunjoo Choi, Taejun Lee and Sung-Phil Kim
- 155** *A New Subject-Specific Discriminative and Multi-Scale Filter Bank Tangent Space Mapping Method for Recognition of Multiclass Motor Imagery*  
Fan Wu, Anmin Gong, Hongyun Li, Lei Zhao, Wei Zhang and Yunfa Fu
- 167** *Enhancement of Event-Related Desynchronization in Motor Imagery Based on Transcranial Electrical Stimulation*  
Jiaxin Xie, Maoqin Peng, Jingqing Lu, Chao Xiao, Xin Zong, Manqing Wang, Dongrui Gao, Yun Qin and Tiejun Liu
- 180** *Adaptive Filtering for Improved EEG-Based Mental Workload Assessment of Ambulant Users*  
Olivier Rosanne, Isabela Albuquerque, Raymundo Cassani, Jean-François Gagnon, Sebastien Tremblay and Tiago H. Falk
- 192** *Cross-Subject EEG Emotion Recognition With Self-Organized Graph Neural Network*  
Jingcong Li, Shuqi Li, Jiahui Pan and Fei Wang
- 202** *Changes in EEG Brain Connectivity Caused by Short-Term BCI Neurofeedback-Rehabilitation Training: A Case Study*  
Youhao Wang, Jingjing Luo, Yuzhu Guo, Qiang Du, Qiying Cheng and Hongbo Wang



# Editorial: Brain-Computer Interfaces for Perception, Learning, and Motor Control

Saugat Bhattacharyya<sup>1\*</sup>, Amit Konar<sup>2</sup>, Haider Raza<sup>3</sup> and Anwesha Khasnobish<sup>4</sup>

<sup>1</sup> School of Computing, Engineering and Intelligent Systems, Ulster University, Londonderry, United Kingdom, <sup>2</sup> Department of Computer Science and Electronic Engineering, Artificial Intelligence Laboratory, ETCE Department, Jadavpur University, Kolkata, India, <sup>3</sup> University of Essex, Colchester, United Kingdom, <sup>4</sup> TCS Innovations Laboratory, Kolkata, India

**Keywords:** perception, motor imagery, motor learning, brain-computer interfacing, brain activations

## Editorial on the Research Topic

### Brain-Computer Interfaces for Perception, Learning, and Motor Control

This special issue is aimed at offering the latest research outcomes in Brain-Computer Interfaces (BCI) with special reference to perception, learning, and motor control. Perception refers to our ability to sense and interpret the environment in form of a stimuli. Learning is a process to memorize extracts of perceived information and/or their inter-relations, to develop our ability to classify objects from their partial information (attributes) and/or to group (cluster) objects based on a certain measure of their similarity. Motor control refers to our ability to control the motion-related parameters, such as position, velocity, and acceleration of our voluntarily controllable external organs and/or muscles (Pirondini et al., 2017). Although the above terminologies apparently represent different fragments of cognition, they have a precedence relationship from the points of view of their usage. For instance, without perception, learning is impossible. Further, without learning, we cannot perform motor control (Elliott et al., 2011). It may be recalled that children develop their skill of motor control by repeated trials of executing motor actions and their successes and failures.

The motivation of this special issue is to explore the biological underpinnings of perception, learning and motor control from the brain activations captured by electroencephalography (EEG), functional Near-Infrared spectroscopy (f-NIRs), and implantable intra-cortical devices, connected with human/animal brains in the settings of a Brain-Computer Interface (BCI). The special issue includes 16 papers which are summarized below.

Xie, Peng et al. examined the scope of transcranial electrical stimulation on brain activity during motor imagery (MI) activations. The most interesting finding of this research lies in the phenomenon that transcranial current stimulation helps in regulatory brain activity and enhances valid features during non-invasive MI-BCI processing.

Wang et al. proposed a new paradigm for long-term treatment therapy for motor dysfunction caused by neurological injury in the brain. The important aspect of this paper lies in capturing the changes in the brain connectivity caused by short-term neurofeedback. This is perhaps due to the participation of new groups of neurons in the motor learning task with a tendency of rehabilitation by the participating neurons.

Zaer et al. provided a detailed design of an experimental framework for real-time recording and manipulation of neural circuits acquired from intra-cortical electrodes of freely moving animals. The signal acquisition system includes a 64-channel intra-cortical electrode array with a rechargeable battery implanted in the visual cortex to record and manipulate local field potentials. The proposed scheme gives a local signature using a wireless connection to an external network for long-term pre-clinical study of the visual neural circuit after irradiation exposure.

## OPEN ACCESS

### Edited and reviewed by:

Vince D. Calhoun,  
Georgia State University,  
United States

### \*Correspondence:

Saugat Bhattacharyya  
s.bhattacharyya@ulster.ac.uk

### Specialty section:

This article was submitted to  
Brain Imaging Methods,  
a section of the journal  
Frontiers in Neuroscience

**Received:** 13 August 2021

**Accepted:** 22 September 2021

**Published:** 20 October 2021

### Citation:

Bhattacharyya S, Konar A, Raza H  
and Khasnobish A (2021) Editorial:  
Brain-Computer Interfaces for  
Perception, Learning, and Motor  
Control. *Front. Neurosci.* 15:758104.  
doi: 10.3389/fnins.2021.758104

Kim et al. presented an experimental setup to study the effect of subjective emotional changes due to auditory stimuli on the control performance of a P300 based BCI system developed to control an electric light device. Four conditions on the auditory stimuli, such as high valence, low valence, noise, and no sound are used to influence the user to change her emotion, while the user is engaged in controlling the electric light using the P300 based BCI. The paper ultimately arrives at the conclusion that the external influence of emotional stimuli cannot influence the P300 based BCI control. The study thus emphasizes the robustness of P300 based BCI control even when the subject is disturbed by external stimuli.

Rosanne et al. proposed a novel technique of adaptive filtering to improve EEG-based mental workload assessment of ambulant users. The proposed adaptive filter relies on an accelerometer-based referential signal when the subject is engaged in multi-attribute decision-making tasks, while walking/jogging on a treadmill. In presence of the proposed adaptive filter algorithm, the authors obtained high classification accuracy of 95% using a random forest-based 2-class mental workload classification, when experimented on ambulant Users.

Li et al. proposed a self-organized graph neural network (SOGNN) for cross-subject EEG-based emotion recognition. The novelty in the proposed work lies in the dynamic construction of the graph neural network by a self-organized module. The performance analysis is undertaken by considering variations in the graph construction techniques. Visualization of the graph structure learned by the proposed model coincided with the previous neuroscience research. This implicates the effectiveness of the proposed model in the context of neuroscience.

Lau et al. examined the neuroplasticity changes in stroke survivors due to the training of hand movements by a BCI-guided robot arm. The study includes neural modulation in functional connectivity and the clinical improvements immediately after and 6 months after the training of the subjects by the assistive BCI system. The experimental results indicate that neural activity in sensory-motor and frontoparietal regions, which are highly involved in BCI-guided training, show significant changes in functional connectivity.

Derzsi examined the scope of spectral power density and phase coherency features to detect Steady-State Visual Evoked Potential (SSVEP) signals. It appears from the experiments that phase coherency features are most sensitive in the detection of weak signals such as SSVEP.

Khan and Hasan studied bimodal fusion of electroencephalography (EEG) and functional Near-Infrared spectroscopy (f-NIRs) signals to improve performance in motor-task classification. Here, the authors proposed Multi-resolution Singular Value Decomposition (MSVD) to achieve system- and feature-based fusion. Finally, the authors employed tree and k-nearest neighbors (k-NN) algorithm-based classification to determine the efficacy of the bimodal fusion.

The tangent Space Mapping (TSM) algorithm is a well-known technique to recognize multi-class motor imagery (MI). However, the EEG features induced by MI mental activities of the subjects being different, selection of subject-specific discriminative EEG frequency components has an important role

in the recognition of multi-class MI. Wu et al. extended the classical TSM algorithm by incorporating multi-scale filter banks to recognize the tangent space features in each sub-band. Finally, a Linear Support Vector Machine (LSVM) classifier is used to classify the MI. The authors claim that the classification accuracy of the extended algorithm is increased by 3.36% with respect to the traditional TSM algorithm for MI classification.

Xie, Cao et al. made an interesting and unusual claim that an introduction of moderate auditory noise enhances the BCI performance in the visual modality. This is referred to as cross-modal stochastic resonance (SR) theory. Although cross-modal SR theory has been tested in different sensory systems, its application in BCI is novel. Here, the authors employed Fast Fourier Transform (FFT) and Canonical Correlation Analysis (CCA) to evaluate the influence of noise in the periodic components of the visual response. Directed Transfer Function (DTF) was used to investigate the functional connectivity patterns, and the flow-gain value is used to measure the degree of activation of the specific brain regions in the information transmission process. The flow-gain maps demonstrated that moderate-intensity in audio noise activates the brain area to a great extent. Further analysis by weighted phase-lag index confirms that phase synchronization between visual and auditory regions in presence of auditory noise is significantly enhanced.

Simar et al. deals with an interesting problem on the detection of festive or violent intent of subjects before execution of their actions in interpersonal interactions. The authors here develop a classifier based on covariance matrix and Riemannian geometry that can effectively discriminate neutral, festive, and violent mental states on the basis of non-invasive EEG signals in both the actor and the observer participants. This research outcome may serve as an important component for the next generation of social interaction among people with portable EEG devices on their heads. The observers in such interactions may get enough time to keep themselves prepared to move away before the actual execution of the violent action by the actor.

Liu et al. proposed a novel approach to design motor imagery classifiers using Convolution Neural Network (CNN) with parallel spatial and temporal self-attention modules. The spatial self-attention module is designed to capture the spatial dependencies between channels of motor imagery EEG signals. It updates the features of each channel by considering the weighted sum of the same feature of other channels. Such updating keeps away the possibility of individual channel features being severely affected by artifacts. The temporal self-attention, on the other hand, is employed to encode the global temporal information into features over each sampling time-steps, to obtain high-level temporal features of the MI EEG signals in the time-domain. The proposed CNN model is tested in position control of drones using MI EEG signals of the experimental subject.

Roy et al. proposed an interesting solution to the long-standing inter-subject transfer learning problem in the MI-based BCI. The primary bottleneck in transfer learning under BCI settings is due to high inter-subject variability in brain signals related to MI. Here, a Convolution Neural Net (CNN)

based deep learning is proposed with provisions for inter-subject continuous decoding of MI-related EEG signals using the novel concept of Mega Blocks for adapting the network against inter-subjects' variability. The parameters of the Mega Blocks are optimized using Bayesian hyper-parameter optimization. The proposed CNN-based architecture would serve as an important module in the development of the calibration-free next-generation classifiers with the flexibility of inter-subject continuous decoding of motor imageries.

Traditional MI-based BCI systems generally employ left hand, right hand, and foot motor imageries as 3 basic commands in the BCI design. However, to develop bigger BCI systems, we may consider simultaneous activation of 2 or more basic commands, and thus generate 8 possible commands including the rest condition as well into account. The main limitation of the multi-command BCI systems is the difficulty in decoding the commands due to constraints to maintain adequate spacing among the corresponding sources, and also due to stochastic noise of the signal sources. Lindig-Leon et al. proposed a solution to the above problem by transforming the 8-class problem into a set of 3 binary problems to facilitate the use of proposed multi-label Common Spatial Patterns (CSP) algorithms. Two different realizations of multi-label CSP algorithms, called MC2CMI and MC2SMI are proposed in the paper. Both the algorithms return 3 sets of features, one for the left hand, one for the right hand,

and the rest for foot MI. Finally, the 3 sets of features are merged together into a vector to predict the user intention by employing an 8-class Linear Discriminant Analysis (LDA) classifier.

Fathima and Kore in this special issue has dealt with another interesting problem on feature selection and channel selection in EEG-BCI systems using optimization algorithms. Here, the authors demonstrate the formulation of a single objective, multi-objective, and constrained optimization objective function for different types of BCI applications, including control problem in prosthetic arms, gaming, and many others. The importance of the paper lies in the thorough review of existing works along with authors' own contributions in the choice of suitable objective functions for a given problem.

The editors strongly believe that this issue will be useful to the BCI researchers, doctoral students, and BCI-developers, who are curious to employ MI BCIs in different applications. The editors are grateful to the authors for submitting their valuable contributions to this special issue, and also to the publisher to allow them to edit this interesting volume.

## AUTHOR CONTRIBUTIONS

SB, AKo, HR, and AKh contributed in managing the review process and in drafting the editorial. All authors contributed to the article and approved the submitted version.

## REFERENCES

- Elliott, D., Grierson, L. E. M., Hayes, S. J., and Lyons, J. (2011). Action representations in perception, motor control and learning: implications for medical education. *Med. Educ.* 45, 119–131. doi: 10.1111/j.1365-2923.2010.03851.x
- Pirondini, E., Coscia, M., Minguillon, J., Millan, J., Van De Ville, D., and Micera, S. (2017). EEG topographies provide subject-specific correlates of motor control. *Sci. Rep.* 7:13229. doi: 10.1038/s41598-017-13482-1

**Conflict of Interest:** The authors declare that the research was conducted in the absence of any commercial or financial relationships that could be construed as a potential conflict of interest.

**Publisher's Note:** All claims expressed in this article are solely those of the authors and do not necessarily represent those of their affiliated organizations, or those of the publisher, the editors and the reviewers. Any product that may be evaluated in this article, or claim that may be made by its manufacturer, is not guaranteed or endorsed by the publisher.

Copyright © 2021 Bhattacharyya, Konar, Raza and Khasnobish. This is an open-access article distributed under the terms of the Creative Commons Attribution License (CC BY). The use, distribution or reproduction in other forums is permitted, provided the original author(s) and the copyright owner(s) are credited and that the original publication in this journal is cited, in accordance with accepted academic practice. No use, distribution or reproduction is permitted which does not comply with these terms.



# Deep Learning Based Inter-subject Continuous Decoding of Motor Imagery for Practical Brain-Computer Interfaces

Sujit Roy<sup>1\*</sup>, Anirban Chowdhury<sup>2</sup>, Karl McCreddie<sup>1</sup> and Girijesh Prasad<sup>1</sup>

<sup>1</sup> School of Computing, Engineering & Intelligent Systems, Ulster University, Derry-Londonderry, United Kingdom, <sup>2</sup> School of Computer Science and Electronic Engineering, University of Essex, Colchester, United Kingdom

## OPEN ACCESS

### Edited by:

Amit Konar,  
Jadavpur University, India

### Reviewed by:

Yu Zhang,  
Stanford University, United States  
Seong-Whan Lee,  
Korea University, South Korea

### \*Correspondence:

Sujit Roy  
roy-S2@ulster.ac.uk

### Specialty section:

This article was submitted to  
Brain Imaging Methods,  
a section of the journal  
Frontiers in Neuroscience

**Received:** 19 May 2020

**Accepted:** 10 August 2020

**Published:** 30 September 2020

### Citation:

Roy S, Chowdhury A, McCreddie K  
and Prasad G (2020) Deep Learning  
Based Inter-subject Continuous  
Decoding of Motor Imagery for  
Practical Brain-Computer Interfaces.  
*Front. Neurosci.* 14:918.  
doi: 10.3389/fnins.2020.00918

Inter-subject transfer learning is a long-standing problem in brain-computer interfaces (BCIs) and has not yet been fully realized due to high inter-subject variability in the brain signals related to motor imagery (MI). The recent success of deep learning-based algorithms in classifying different brain signals warrants further exploration to determine whether it is feasible for the inter-subject continuous decoding of MI signals to provide contingent neurofeedback which is important for neurorehabilitative BCI designs. In this paper, we have shown how a convolutional neural network (CNN) based deep learning framework can be used for inter-subject continuous decoding of MI related electroencephalographic (EEG) signals using the novel concept of Mega Blocks for adapting the network against inter-subject variabilities. These Mega Blocks have the capacity to repeat a specific architectural block several times such as one or more convolutional layers in a single Mega Block. The parameters of such Mega Blocks can be optimized using Bayesian hyperparameter optimization. The results, obtained on the publicly available BCI competition IV-2b dataset, yields an average inter-subject continuous decoding accuracy of 71.49% ( $\kappa = 0.42$ ) and 70.84% ( $\kappa = 0.42$ ) for two different training methods such as adaptive moment estimation (Adam) and stochastic gradient descent (SGDM), respectively, in 7 out of 9 subjects. Our results show for the first time that it is feasible to use CNN based architectures for inter-subject continuous decoding with a sufficient level of accuracy for developing calibration-free MI-BCIs for practical purposes.

**Keywords:** convolutional neural network (CNN), deep learning, motor imagery, brain-computer interface (BCI), electroencephalography (EEG), adaptive learning, SGDM, ADAM

## 1. INTRODUCTION

The practical applications of brain-computer interfaces are often hindered by the need for repeated calibration for each individual participant due to large inter-subject variability in the EEG signal. Even when different sessions on the same participant are considered, BCI systems need recalibration due to the non-stationary nature of the EEG signals leading to inter-session inconsistency (Chowdhury et al., 2018b). BCIs are often used for neurorehabilitation and for developing control and communication systems for patients suffering from various neurological disorders. Often the problem is exacerbated due to the presence of varying brain lesions among

users. Studies conducted on patient population alongside healthy individuals have shown such patterns where the variation in BCI performance was more in patient population than in healthy population (Spüler et al., 2012; Chowdhury et al., 2019). With regards to neurorehabilitation especially, the time-consuming calibration process leads to user frustration and a lack of motivation which can hinder the recovery process. This is evident from the work of Morone and colleagues who found a significant correlation between motivation and BCI performance (Morone et al., 2015) which is further found to be strongly correlated with motor recovery (Bundy et al., 2017). General sources of intra- and inter-subject variability leading to the covariate shifts in the dataset include different emotional and mental processes happening in the background of the MI (Saha and Baumert, 2020). Other sources may include the neuroanatomy of the brain for different subjects and the inter-subject difference in the cognitive style of performing a motor-task over time (Seghier and Price, 2018). The volume conduction may also play a major role in covariate shifts in the EEG data (Chowdhury et al., 2018b). Previous attempts to solve this problem involved (1) attempting to discover globally relevant EEG features and (2) the use of adaptive EEG classifiers (Lotte et al., 2018). Recent studies also utilized some BCI performance Predictors to augment the transfer learning process (Saha et al., 2018; Saha et al., 2019).

An extensive detail of transfer learning approaches for BCIs has been given in Jayaram et al. (2016). Transfer learning is often implemented by transferring stationary and/or discriminative information invariant across the subjects (Wang et al., 2015; Gaur et al., 2019a). Apart from globally relevant feature representation, other approaches to transfer learning involve ensemble learning, sparse subset of spatial filters, and classifiers (Fazli et al., 2009; Tu and Sun, 2012; Raza et al., 2019), and domain adaptation of classifiers (Vidaurre et al., 2011). A variant of the popularly used common spatial pattern (CSP) based spatial filtering, called composite CSP, proposed by Kang and colleagues, was one of the earliest efforts of inter-subject transfer learning using EEG signals (Kang et al., 2009). Regularized CSP filters derived from other subjects also gave significant performance improvement for inter-subject transfer learning (Devlamincik et al., 2011; Lotte and Guan, 2011). Another popular method of intra- and inter-subject transfer learning is covariate shift adaptation by combining the unlabeled test data with the labeled training data which corrects the covariate shifts arising from the changes of marginal distribution between different subjects/sessions (Li et al., 2010; Arvaneh et al., 2014). Some different approaches are also proposed for inter-subject transfer learning where event-related cortical sources are estimated from subject independent EEG recordings (Saha et al., 2019) which can compensate for the changes in head morphology and electrode positioning (Wronkiewicz et al., 2015). In a recent study, a Riemannian geometry-based approach is successfully applied for cross-subject and cross-session transfer learning which significantly improved BCI performance (Zanini et al., 2018; Gaur et al., 2019a). Others have also used novel filtering techniques using multivariate empirical mode decomposition (MEMD) along with CSP features for subject independent learning and have shown improved performance on BCI

Competition IV-2a dataset (Gaur et al., 2019a,b). Halme and colleagues compared several different methods for cross-subject decoding of MI and passive movements using both EEG and MEG signals. They found better cross-subject accuracy in MEG as compared to EEG for an MI task (70.6%) (Halme and Parkkonen, 2018). Transfer learning was also realized using a covariate shift adaptation technique for session-to-session transfer, although their effect on inter-subject learning is still uncertain (Chowdhury et al., 2018b). Other attempts of suppressing subject-specific calibration include Kalman filter-based decoder (Sussillo et al., 2016) and actor-critic based reinforcement learning (Pohlmeyer et al., 2014; Prins et al., 2017). So far the evidence of high performing inter-subject transfer learning models is scarce and mostly concentrates on event-related potentials (Jin et al., 2013; Kindermans et al., 2014). Of late, the use of a Sparse Group Representation Model showed promising results for inter-subject decoding which compensated reduced recording from the same subject by making use of previously recorded data from other subjects (Jiao et al., 2019).

Conventional methods of inter-subject transfer learning mentioned above are heavily dependant on feature engineering techniques which limit their capacity to be applied on a large variety of subjects. Recently, following the success of deep learning-based algorithms in image processing applications, inroads have been made in the field of biomedical engineering, especially in the classification of brain signals where reliable and stable performance is still a challenge after more than two decades of research (Roy et al., 2019).

Lu and colleagues proposed a deep belief network method using a restricted Boltzmann machine (RBM) for MI classification (Lu et al., 2017). Different architectures of deep convolutional neural networks (CNNs) have also been explored for decoding EEG signals (Schirrmeyer et al., 2017). A CNN with stacked autoencoders (SAE) has been shown to achieve better classification accuracy on BCI competition IV-2b dataset than the traditional classification approaches (Tabar and Halici, 2016; Zubarev et al., 2018; Roy et al., 2019a). Recently, Bayesian extreme learning was also proposed for improving the performance of MI-BCIs (Jin et al., 2020). However, none of these deep learning-based decoders addressed the issue of inter-subject transfer learning in BCI, except for some recent studies (Lawhern et al., 2018; Fahimi et al., 2019; Kwon et al., 2019). Even in these studies, the issue of continuous feedback was not addressed while it is of utmost importance that a BCI, especially for neurorehabilitation applications, should be capable of providing continuous neurofeedback contingent to task-dependent neural activity. The paper therefore proposes the novel concept of Mega Blocks for adapting a CNN architecture to tackle inter-subject variabilities, and validates for the first time the feasibility of such a CNN-based architecture for inter-subject continuous decoding of MI-related EEG signals. The study is important as it paves the way for calibration-free BCI designs based on CNN which can be used for vital practical purposes such as providing neurofeedback in a rehabilitative BCI setting reducing the user frustration related to the need to recalibrate. Another important aspect of this study is that it utilizes publicly available data for the validation which means that the work

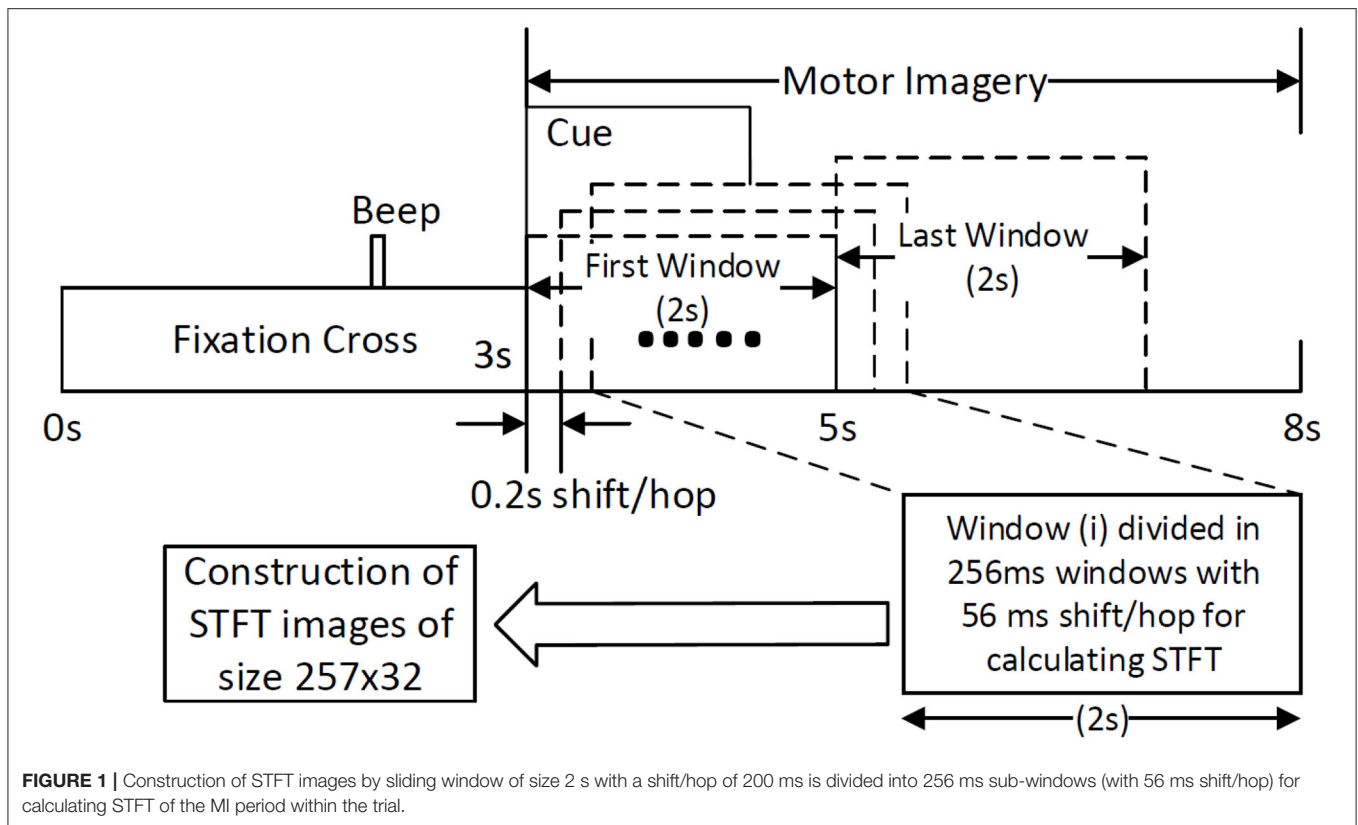


**FIGURE 1** | Construction of STFT images by sliding window of size 2 s with a shift/hop of 200 ms is divided into 256 ms sub-windows (with 56 ms shift/hop) for calculating STFT of the MI period within the trial.

can be reproducible and serve as a benchmark for further development in a similar direction. The results of intra-subject and single-trial classification accuracies using the same CNN architectures are also provided for the sake of comparability.

## 2. MATERIALS AND METHODS

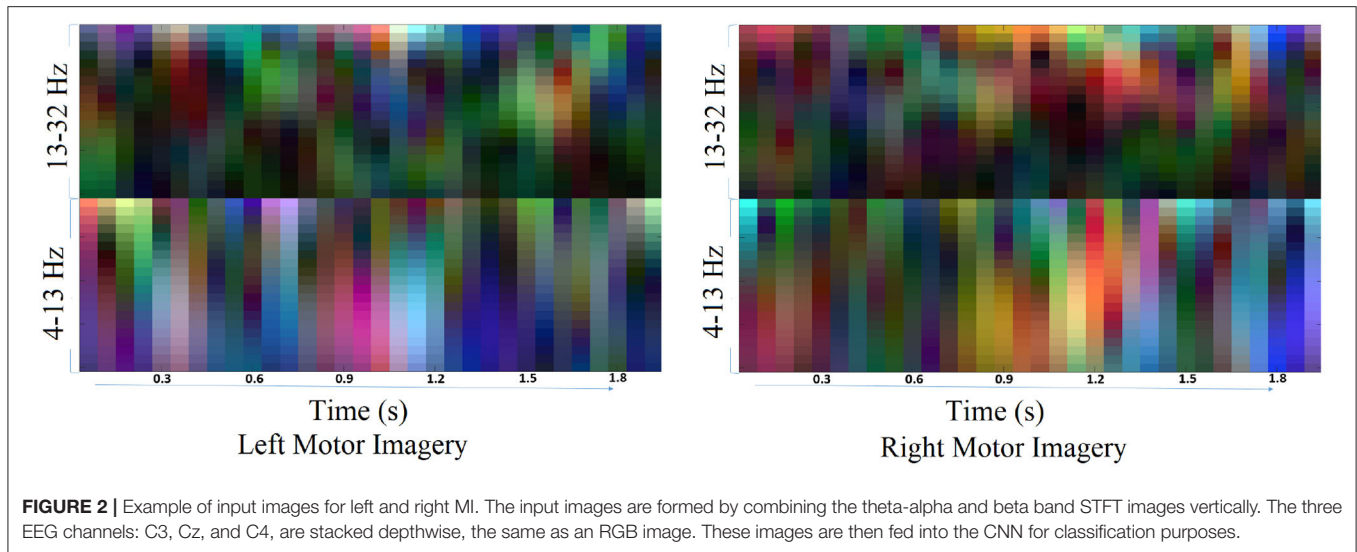
### 2.1. Dataset

BCI competition IV-2b is a well-known dataset and is used as a benchmark for testing new algorithms in the area of MI-based BCI (BCI-Competition, 2008). The dataset comprises of EEG data recorded from 9 healthy participants. The data were recorded in 5 sessions, where the first 3 sessions are for calibrating an EEG decoder and the last 2 sessions are for evaluation purposes. Three channels on the primary motor cortex, C3, Cz, and C4 were used for the bipolar recording of EEG signals at the sampling rate of 250 Hz. Signals were band-passed between 0.1 and 100 Hz with a notch filter at 50 Hz set at the time of recording using signal acquisition hardware. Each session consists of equally distributed trials of left and right hand MI classes. The timing diagram (Figure 1) shows that each trial started with a fixation cross for 3 s, after which a cue appears as an arrow for 1.5 s instructing the participant to do left or right-hand MI. After the MI period of 4 s, there was a short break of a few seconds until the start of the next trial. The only difference between the trials at the calibration and evaluation phase is that for the evaluation phase a happy or sad smiley was shown during the MI period as feedback. In our study, we have trained the CNN

classifier on the trials of the first 3 sessions' data (total 420 trials) and tested on the last 2 sessions' data (total 320 trials).

### 2.2. Input Image Construction

The traditional approach of classifying EEG signals is based on extracting time-frequency based features and training using traditional classifiers such as linear discriminant analysis (LDA), or support-vector-machine (SVM) (Chowdhury et al., 2018a). A CNN typically takes the input as an image; it is well-known that vital information is contained within the time-frequency spectrogram of EEG signals popularly known as event-related desynchronization/synchronization (ERD/ERS) in the context of MI (Chowdhury et al., 2019). Hence, a similar approach was followed for constructing input images for CNN, wherein short time Fourier transform (STFT) was used for obtaining the time-frequency spectra of the MI related changes in the EEG signal. The STFT is evaluated on a time period of 2 s within the MI period of a trial (i.e., between 3 and 7 s), which is shifted by 200 ms, thereby generating 11 input images per trial. In our previous study on the clinical effect of BCI based continuous anthropomorphic multimodal neurofeedback on stroke patients (Chowdhury et al., 2018a), the shift between the two consecutive windows was set as 500 ms which was sufficient but suffered from high latency. In order to reduce the latency by making it closer to real-time, in the present study we decreased the shift by 300 ms to set it as 200 ms. Although some studies used latencies as low as 72 ms (Foldes et al., 2015), we made a trade-off between the amount of overlap and latency



to avoid reducing it further. The choice of the time window motivated by the fact that, as we have considered frequencies as low as 4 Hz, i.e., time period of 250 ms, we kept the size of the time window sufficiently high (i.e., 2,000 ms) to allow 8 oscillations of the lowest frequency for proper bandpass filtering. Thus the combination of a 2 s time window and 200 ms shift makes 11 segments within the 5 s MI period producing 11 images in a single trial. This design would be useful when it comes to providing continuous neurofeedback in a more intuitive way and for which having low latency is an essential criterion (Foldes et al., 2015). But unlike these previous studies (Foldes et al., 2015; Chowdhury et al., 2018a) which are primarily based on within-subject learning, we have shown how continuous feedback could be incorporated into a CNN based inter-subject transfer learning setting which can then contribute to calibration-free neurorehabilitative BCI designs without compromising the richness of the neurofeedback. As the sampling frequency of the EEG signal is 250 Hz, a 2 s signal is composed of 500 samples. We have chosen a window size of 64 samples, with an overlap of 50 samples between the consecutive windows. The number of fast-Fourier-transform (FFT) points was 512. Thus the size of the spectrogram was  $257 \times 32$ , where 257 was the number of frequency components and 32 was the number of time points. Event related desynchronization (ERD) and event-related synchronization (ERS) phenomena typically occur over the frequency ranges 8–13 and 13–32 Hz, respectively (Pfurtscheller and da Silva, 1999). In one of the earlier works on CNN based MI-BCI, Tabar and Halici (2016) have used the 6–13 Hz frequency band for STFT plots with satisfactory accuracy. This shows a partial inclusion of theta band (4–7 Hz) along with the alpha (8–13 Hz) band for generating STFT plots. Hence, in our approach, we have combined the entire theta and alpha band (4–13 Hz) along with the beta band (13–32 Hz) to capture all possible neurodynamics related to the MI. From this spectrogram, we first choose the theta-alpha-spectrogram for 4–13 Hz which was of the size  $20 \times 32$ . Then we choose beta-spectrogram for 13–32 Hz, which was of size  $41 \times 32$ . To match the sizes

of these two sub-spectrograms (by sub-spectrograms we mean the theta-alpha-spectrogram and beta-spectrogram as they are the subsets of the initial spectrogram of size  $257 \times 32$  after STFT) we used cubic interpolation on the beta-spectrogram and reduced it to size  $20 \times 32$  so that the effect of both the bands remained the same on the final input to the CNN. A similar approach can also be found in Tabar and Halici (2016) where the same cubic interpolation was applied to match the sizes of the two spectrograms. The theta-alpha-spectrogram and beta-spectrogram are concatenated vertically to get a spectrogram of size  $40 \times 32$ . Thus the spectrograms of size  $40 \times 32$  are calculated for each of the three EEG channels C3, Cz, and C4. The final image is constructed by concatenating these three spectrograms on a third dimension orthogonal to the time-frequency plane. So, the size of the final image becomes  $40 \times 32 \times 3$ , where  $N_f = 40$ ,  $N_t = 32$ , and  $N_{ch} = 3$ . This construction process of the STFT images is shown in Figure 1. An example of input images formed out of the STFT images, for left and right-hand MI is shown in Figure 2. The frequency ranges stacked on top of each other are the 4–13 Hz range (combining the theta and alpha bands) and the 13–32 Hz range (the beta band). The colors in Figure 2 represents the mixed intensity of three EEG channels C3, Cz, and C4 which are stacked depthwise similar to RGB images. These input images are then decoded by the CNN for generating the neurofeedback.

### 2.3. Architecture-1 for Intra-Subject Learning

The Architecture-1 is defined with 16 filters of size  $3 \times 3$  with a stride of 1 for the first convolutional layer. An input image of  $40 \times 32 \times 3$  was used as an input to this convolutional layer. After the first convolutional layer, batch normalization and maxpooling were performed using a filter of  $3 \times 3$  and a stride of 2. Again, for the next convolutional layer, 32 filters were used of size  $3 \times 3$  and similarly, maxpooling was performed with a factor of 3 and a stride 2. After that, another convolutional layer was added with 64 filters of  $3 \times 3$  size and a stride of 1. Finally, a fully connected layer average pooling was performed with a factor of

**TABLE 1** | Parameters for Architecture-1 for intra-subject learning.

Layers	Filters	Size	Options
<b>Descriptions of the design parameters for Architecture-1</b>			
Image input layers		[40, 32, 3]	
Convolution 2D layer	16	[3, 3]	Stride = [1, 1]
Batch norm			$10^{-5}$
ReLU layer			
Maxpooling 2D layer		[3, 3]	Stride = [2, 2]
Convolution 2D layer	32	[3, 3]	Stride = [1, 1]
Batch norm			$10^{-5}$
ReLU layer			
Maxpooling 2D layer		[3, 3]	Stride = [2, 2]
Convolution 2D layer	64	[3, 3]	Stride = [1, 1]
Batch norm			$10^{-5}$
ReLU layer			
Average pooling layer		[8, 8]	Stride = [1, 1]
Fully connected layer		192	
layerlayer Softmax layer			
Classification output layer			Loss = cross entropyex

8 and a stride of 1. For learning the parameters of the CNN two different training methods used are stochastic gradient descent method (SGDM) and adaptive moment estimation (Adam).

The  $k$ -th feature map at a given layer can be represented as:

$$h_{ij}^k = f(a) = f((w^k \times x)_{ij} + b_k) \tag{1}$$

where  $x$  is the input image,  $w^k$  is the weight matrix and  $b_k$  is the bias value for  $k = (1, 2, \dots, 30)$ . The output function  $f$  is selected as rectified linear unit (*ReLU*) function and it is approximated as *softplus* function defined as,

$$f_a = ReLU(a) = \ln(1 + e^a) \tag{2}$$

The Gradient descent method attempts to minimize an objective function  $J(\theta)$  which is parameterized by a model's parameter (where  $\theta \in \mathbb{R}^d$ ) by updating the parameters in the steepest descent direction from the gradient of the objective function  $\nabla_{\theta} J(\theta)$ . The learning rate is defined by the size of steps considered to reach a local minimum. However, at each step, gradient descent requires evaluation of  $n$  derivatives, which is expensive. A popular modification is *SGD* (Johnson and Zhang, 2013), where at each iteration ( $t = 1, 2, \dots$ )  $w^t$  is defined as follows:

$$w^t = w^{(t-1)} - \eta \nabla \psi(w^{(t-1)}) \tag{3}$$

where  $\eta$  is the learning rate and  $\psi$  represents the loss function. In a simpler way, learning of the model parameters can be expressed as Equation (4), where parameters perform an update for each training example  $x^{(i)}$  and label  $y^{(i)}$ .

$$\theta = \theta - \eta \cdot \nabla_{\theta} J(\theta; x^{(i)}; y^{(i)}) \tag{4}$$

The advantage of SGDM is that computation time is  $1/n$  of standard gradient descent as every step depends upon a single derivative  $\nabla \psi_i(\cdot)$ . The Momentum (Qian, 1999) method helps SGD to accelerate in applicable direction by damping oscillations through the addition of the fraction  $\mu$  of the update vector to the current update vector. As shown in Equation (5),  $\mu$  can be considered as a momentum decay coefficient where  $\mu \in [0, 1)$ , which controls the rate at which old gradients are discarded.

$$v_{t+1} = \mu \cdot v_t - \eta \cdot \nabla l(\theta) \tag{5}$$

$$\theta_{t+1} = \theta_t + v_{t+1} \tag{6}$$

Architecture-1 has a convolutional 2D layer with  $l_2$  regularization of 0.0014 and *ReLU*-activation. The details of the parameters are shown in **Table 1**. Batch normalization was done and the model was trained for 55 epochs with a batch size of 40. For validation, 500 samples were randomly used. The learning rate for the model was  $6.7929e^{-04}$  and the initial momentum was 0.9799. The dropout rate was 0.1 and the drop period was 20. The loss function was cross-entropy which was expressed as  $Loss = \sum_{i=1}^N \sum_{j=1}^K t_{ij} \ln y_{ij}$ . The hyperparameters are chosen using Bayesian optimization. Apart from SGDM we have also used Adam as an optimizer on the same CNN architecture (Architecture-1) for tuning the hyperparameters. This is because for some participants (participants 2 and 3) the data were particularly noisy which made the convergence of SGDM very slow. Hence, the experimentation was also done using Adam as an optimizer for faster convergence using a large learning rate. It is to be noted that aside from the change in the optimizer (i.e., from SGDM to Adam) the layers of the CNN Architecture-1 were exactly the same as described in **Table 1**. The corresponding architecture diagram is shown in **Figure 3**.

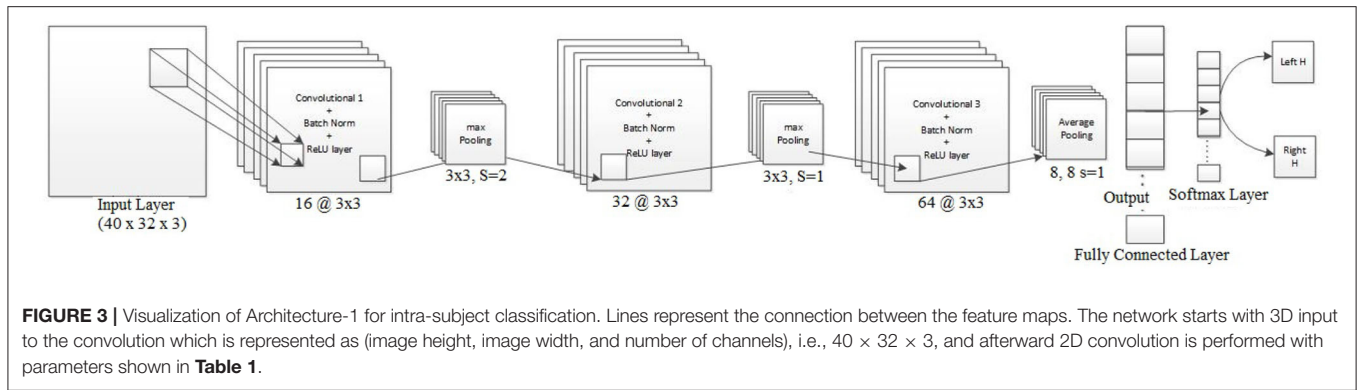
Adam can be understood as a combination of SGDM with momentum and Root Mean Square Error Propagation (*RMSprop*). It is an adaptive learning rate method, where the learning rate is computed from different parameters. Adam keeps exponentially decaying the average of past gradients  $mt$  similarly to momentum.

Adam uses an exponentially moving average which is computed on the current mini-batch gradient:

$$m_t = \beta_1 m_{t-1} + (1 - \beta_1) g_t \tag{7}$$

$$v_t = \beta_2 v_{t-1} + (1 - \beta_2) g_t^2 \tag{8}$$

where  $m_t$  and  $v_t$  are an estimation of the mean and uncentered variance of gradient ( $g$ ) and  $\beta_1$  and  $\beta_2$  are new hyperparameters.



The update rule for Adam is

$$\theta_{t+1} = \theta_t - \frac{\eta}{\sqrt{\hat{v}_t} + \epsilon} \hat{m}_t \tag{9}$$

where  $\theta$  is the model parameter,  $\theta \in \mathbb{R}^d$ , and  $\eta$  is the learning rate.

The proposed default values are 0.9 for  $\beta_1$ , 0.999 for  $\beta_2$ , and  $10^{-8}$  for  $\epsilon$  (Kingma and Ba, 2014). It was shown empirically that Adam is effective in practice and quite popular as compared to other adaptive learning-method algorithms. For Adam, the initial learning rate was 0.01 using a batch size of 50 and the model was trained for 15 epochs.

The Bayesian optimization method was used for selecting the best hyperparameters for the model. The range of parameters for the convolutional layer was set from 1 to 5, the learning rate ranged from  $e^{-06}$  to  $e^{-02}$ , the momentum in the case of SGDM was from 0.6 to 0.98, and the L2 regularization was from  $e^{-10}$  to  $e^{-02}$  for a total of 30 different objective functions to evaluate. The Bayesian optimization method tries to minimize the scalar objective function  $f(x)$  for  $x$  in a bounded set. The deterministic or stochastic function can obtain similar/different results for evaluation of the same point  $x$ . There are several steps to minimize, which include Gaussian process model of  $f(x)$ , and acquisition function  $a(x)$  based on the model of  $f(x)$  which is maximized for the next point  $x$  for evaluation. The acquisition functions evaluate the “goodness” of a point  $x$  based on the posterior distribution function  $Q$  (Gelbart et al., 2014). Bayesian optimization estimates the smallest feasible mean of posterior distribution by sampling several thousand points within variable bounds and improving them using local search.

Expected improvement ( $EI$ ) of acquisition function evaluates the acquisition function, ignoring values responsible for the increase in the objective.  $EI$  can be expressed as:

$$EI(x, Q) = E_Q[\max(0, \mu_Q(x_b) - f(x))] \tag{10}$$

where  $x_b$  is the location of the lowest posterior mean and  $\mu_Q(x_b)$  is the lowest value of posterior mean.

The Probability of improvement ( $PI$ ) optimization function calculates the probability of a better objective function value by a new point  $x$  which is modified by a margin parameter  $m$ .  $PI$  is given as,

$$PI(x, Q) = P_Q(f(x) < \mu_Q(x_b) - m) \tag{11}$$

where  $m$  is considered as the estimated noise standard deviation and the probability is evaluated as,

$$PI = \Phi(v_Q(x)) \tag{12}$$

Here  $\Phi(\cdot)$  is the unit normal Cumulative Density Function and

$$v_Q(x) = \frac{\mu_Q(x_{best}) - m - \mu_Q(x)}{\sigma_Q(x)} \tag{13}$$

where  $\sigma_Q$  is the posterior standard deviation of the Gaussian process at  $x$ .

## 2.4. Architecture-2 for Inter-subject Transfer Learning

In the case of transfer learning, the dataset was huge as the classifier needed to learn from all 8 subjects over 5 sessions. Since we have a mixed dataset it was important to account for variability over the sessions and over subjects. For performing transfer learning, huge networks are often used such as ResNet50 (He et al., 2016), AlexNet (Krizhevsky et al., 2012) in the case of image classification. But in the domain of BCI, data collection is a slow process and hence limited in size. Therefore, we needed to design an adaptive system to account for the noise and non-stationarity arising across various sessions and subjects. Thus, we designed Mega Blocks which has the capacity to repeat the specific architecture block over time. For example, in one Mega Block, we can put one or more convolution layers, the parameters of which are exactly the same as the corresponding Mega Block in the number of filters, filter size, activation function, and L2 regularization. The fixed parameters can be replicated for every convolution block inside Mega Block, which ranges from 1 to 5 in our case, and can be extended further. It is advised to add one or more Mega Blocks instead of adding more than 5 convolutional layers inside a Mega Block as the addition of more convolutional layers inside a Mega Block will increase the training parameters significantly. Also, the addition of more Mega Blocks will help in learning more micro-features. After every Mega Block, there can be maxpooling/averagepooling layer whose output is given as the input to the next Mega Block. The parameters of a Mega Block are optimized using Bayesian hyperparameter optimization, which includes, the number of

**TABLE 2** | Design Parameters for Architecture-2 for inter-subject transfer learning.

Layers	Filters	Size	Activation	Options
Image input layer		[40, 32, 3]		
Mega Block 1	9	[5,5]	relu	Stride = [1, 1] bnm = $10^{-5}$
Maxpooling layer		[3,3]		Stride = [2,2]
Mega Block 2	18	[3,3]	relu	Stride = [1, 1] bnm = $10^{-5}$
Maxpooling layer		[3,3]		Stride = [2,2]
Mega Block 3	36	[3,3]	relu	Stride = [1, 1] bnm = $10^{-5}$
Average pooling layer		[8,8]		Stride = [1, 1]
Fully connected layer		108		
Softmax layer				
Classification output layer			2	Loss = cross entropyex

convolution layers, learning rate, momentum, and regularization. Using this methodology we have observed that the trained model is less vulnerable to noisy subjects' data considering the amount of good data is significantly higher. The model can be further modified by introducing skip layers much like ResNet50 inside Mega Blocks. One Mega Block can extend itself from 1 convolution block to 5 convolution blocks with similar properties. Each convolution block has a convolutional layer connected with a batch normalization layer and a *ReLU* layer. After every Mega Block, a *maxpooling* layer was added whose output was fed to the next Mega Block input. Finally, the average pooling layer is connected with a fully connected layer, *softmax* layer and classification. The loss for training was set to cross-entropy. The design parameters of Architecture-2 are shown in **Table 2**.

It is to be noted that similar to Architecture-1, Architecture-2 was also trained using both the optimizers: SGDM and Adam. **Table 3** shows the number of convolution blocks used inside Mega Blocks 1, 2, and 3 in the case of training methods as SGDM and Adam. The number of maximum epochs for training was 50 and mini-batch size was 64. The learning rate drop rate factor was 0.1 and the drop period was 40. A general overview of the CNN architecture used here is shown in **Figure 4** which evolves into Architecture-1 (for intra-subject learning) or Architecture-2 (for inter-subject learning) depending upon the choice of parameters given in **Tables 1, 2**, respectively.

## 2.5. Training and Continuous Decoding

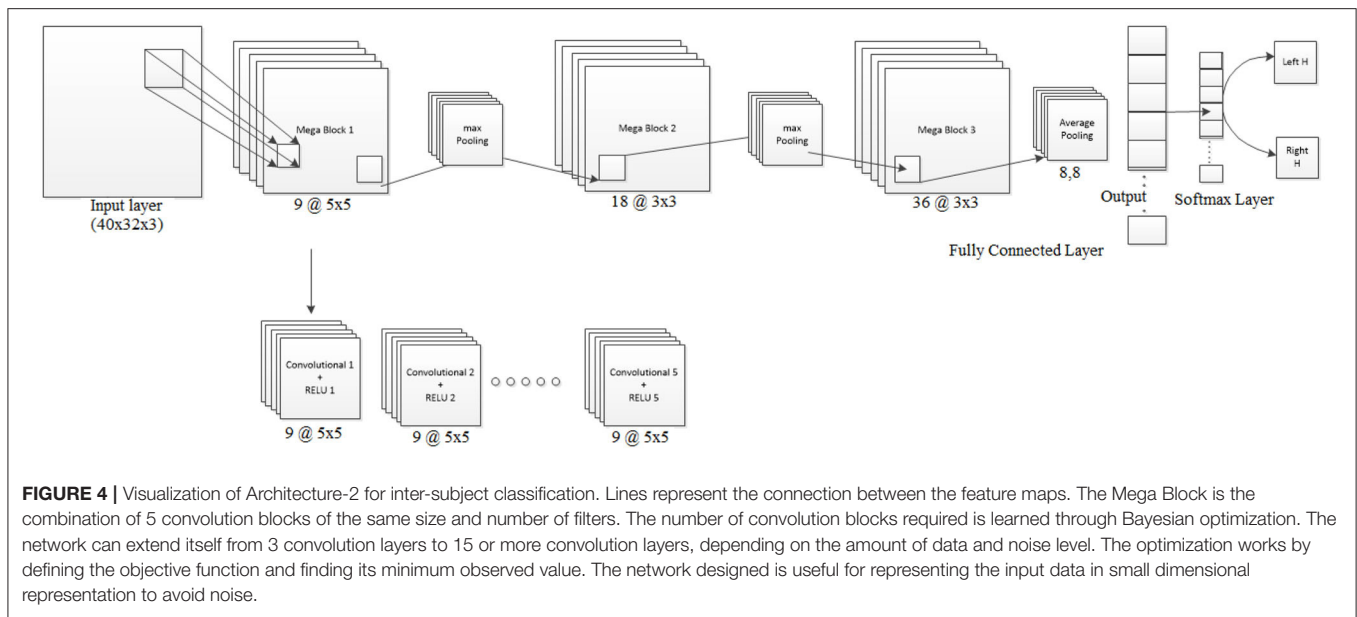
CNN was evaluated for continuous decoding of MI meaning that rather than making a decoding once within a trial, we are

**TABLE 3** | Number of convolutional layers for each subject used in Architecture-2 for inter-subject transfer learning purpose (MB = Mega Block).

Subjects	No. of conv. blocks (SGDM)			No. of conv. blocks (Adam)		
	MB 1	MB 2	MB 3	MB 1	MB 2	MB 3
S01	1	1	1	1	1	1
S02	3	3	3	1	1	1
S03	1	1	1	1	1	1
S04	3	3	3	5	5	5
S05	3	3	3	3	3	3
S06	1	1	1	1	1	1
S07	1	1	1	1	1	1
S08	2	2	2	4	4	4
S09	1	1	1	1	1	1

decoding multiple times. To facilitate this we divided the trial into multiple windows of size 2 s, which were shifted by 200 ms (i.e., 1,800 ms of overlap). Thus every trial was divided into 11 segments and the decoding was done by the CNN based classifier for each of the segments. To keep parity in the signal processing of the training and feedback stages, similar segmentation was also performed for training data also. All the 11 segments of a particular training trial were assigned the same class-label while feeding into the CNN. One advantage of such segmentation is that we can increase the training instances for CNN, as we know that the deep learning classifiers require a larger training data set. Thus rather than having 420 training examples for 420 trials, we had  $420 \times 11 = 4,620$  training examples. In this way, the CNN classifier can generate decodings every 200 ms interval within a trial and can provide continuous feedback to the participant accordingly.

The performance of the CNN architectures is evaluated by calculating the classification accuracies in three different manners, gross classification accuracy ( $CA_{gross}$ ), single-trial classification accuracy ( $CA_{ST}$ ), and optimal time-point classification accuracy ( $CA_{opt}$ ). The  $CA_{gross}$  is defined as the percentage of correctly classified feedback instances among all the available feedback instances (i.e.,  $320 \times 11 = 3,520$ , the number of all feedback instances, where 320 is the number of feedback trials across two sessions and 11 is the number of segments into which a single-trial was divided). Next,  $CA_{ST}$  is calculated as follows. To consider a single-trial to be classified correctly, we counted how many segments out of the 11 segments of a single-trial were classified correctly. If the number is 6 or more (i.e., half of the total number of segments are correct) then the feedback trial is considered to be classified correctly. Following this rule,  $CA_{ST}$  is defined as the percentage of correctly classified feedback trials among all the available feedback trials. The rationale behind the choice of such a  $CA_{ST}$  calculation lies in the fact that here we have compared the accuracies of continuous decoding ( $CA_{gross}$ ) with the single-trial decoding ( $CA_{ST}$ ) and this comparison would be inconsistent if we define two different time windows for



calculating  $CA_{gross}$  and  $CA_{ST}$ . Therefore, we needed to come up with a solution for calculating the  $CA_{ST}$  while making use of the same segmentation as in the case of continuous decoding. It is to be noted that the  $CA_{ST}$  and  $CA_{gross}$  measurements are designed in such a way so that they should not be a redundant evaluation of performance. This is because  $CA_{gross}$  deals with all the segments from all trials and does not consider an individual trial separately, which means that it is trial agnostic. On the other hand,  $CA_{ST}$  weighs how many segments (out of 11) within a trial decoded to be a particular class in majority and thereby takes the decision as to how to label that trial. So, it does not consider how many segments across all the trials are classified but how the individual trials are classified. Finally, for  $CA_{opt}$  we have considered only the time segment of maximum accuracy out of the 11-time segments. This means we calculated the accuracy taking one time-segment at a time and assigned the maximum as  $CA_{opt}$  for a particular participant. The reason we presented the performance of the inter-subject transfer learning based on three different accuracy measures  $CA_{gross}$  (for continuous neurofeedback),  $CA_{ST}$  (for single-trial neurofeedback), and  $CA_{opt}$  (for neurofeedback at optimum time point) is that we wanted to validate its feasibility across different BCI paradigms. Some BCI paradigms use continuous neurofeedback, for example in hand rehabilitation where a gradual change in grasp aperture is used (Chowdhury et al., 2018a). To the best of the authors' knowledge, an inter-subject continuous feedback approach based on CNN based transfer learning using the novel concept of Mega Blocks is presented for the first time in this paper. Moreover, it is also worth mentioning that the proposed methodology is also feasible for real-time decoding as the time required for calculation of STFT, image construction, and classification requires approximately 9.32 ms. The optimum time-point for single trial-based decoding is also calculated so that the proposed methodology can be feasible for triggered feedback (Chowdhury et al., 2018b; Chowdhury et al., 2019). The

number of trainable parameters in Architecture-1 is 23,269 and for Architecture-2 is between 7,578 and 40,914 depending on the number of convolutional layers inside a Mega Block, which are much smaller than the DeepConvNet architecture (trainable parameters = 152,219,104) (Schirrmeister et al., 2017), Subject-Independent CNN (Kwon et al., 2019) (trainable parameters = 72,264,076) and comparable to the ShallowConvNet architecture (trainable parameters = 40,644) (Schirrmeister et al., 2017). The training time for Architecture-1 (intra-subject) is 794 s which is less than (Tabar and Halici, 2016) where the training time is 1,157 s. The training time for Architecture-2 (inter-subject) is 1934 s which is also less than other inter-subject architecture such as Kwon et al. (2019) where the training time is 12 min. The single-trial decoding time in Tabar and Halici (2016) was 400 ms and in Kwon et al. (2019) it was 150 ms, whereas in the current study the single-trial decoding time is 102.52 ms which is much smaller than others. Thus, it shows that the computational complexity of the proposed CNN architectures is less or comparable to other competitive architectures given in previous studies. It is to be noted that for intra-subject classification the classifier was trained on session 1, 2, and 3 and tested on session 4 and 5 for individual subjects. Additionally, while calculating the accuracy for a particular subject in inter-subject transfer learning case, we have trained the CNN using the session 1 to 5 data from the rest of the subjects. For example, CNN for subject 1 is trained using the data from subject 2 to subject 9. The chance level of these binary classification problems is 50% as there are equal numbers of left and right hand MI trials.

### 3. RESULTS

The performance of the deep learning-based architecture for mental task decoding using EEG is evaluated by calculating the

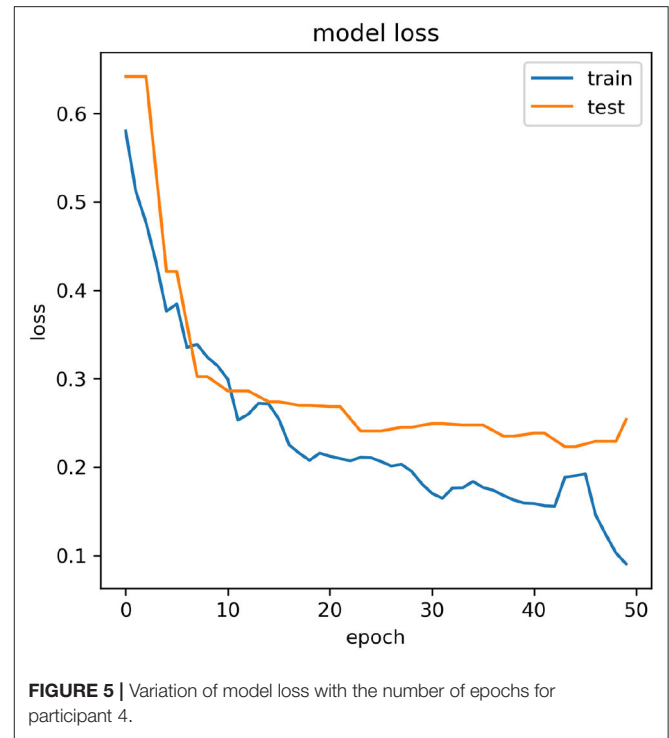
**TABLE 4** | Performance of intra-subject learning for continuous decoding.

ID	$CA_{gross}$			
	Adam		SGDM	
	Test (%)	Kappa (Test)	Test (%)	Kappa (Test)
1	67.57	0.35	68.31	0.37
2	55.83	0.12	55.10	0.10
3	51.88	0.04	54.61	0.09
4	90.82	0.82	91.14	0.82
5	80.65	0.61	80.17	0.60
6	71.78	0.44	72.23	0.44
7	68.28	0.37	67.79	0.36
8	87.77	0.76	88.65	0.77
9	79.12	0.58	80.23	0.60
Mean	72.63	0.45	73.13	0.46
Std	13.35	0.27	14.82	0.26

**TABLE 5** | Performance of inter-subject learning for continuous decoding.

ID	$CA_{gross}$			
	Adam		SGDM	
	Test (%)	Kappa (Test)	Test (%)	Kappa (Test)
1	68.23	0.36	68.02	0.36
2	55.41	0.10	54.33	0.09
3	54.20	0.08	54.15	0.08
4	81.42	0.64	80.75	0.61
5	65.40	0.28	64.62	0.29
6	71.59	0.38	68.88	0.38
7	68.53	0.37	67.98	0.36
8	72.13	0.48	72.50	0.45
9	73.13	0.47	73.14	0.46
Mean	67.78	0.35	67.15	0.34
Std	8.60	0.18	8.62	0.17

accuracy and the kappa value both for intra- and inter-subject settings. As mentioned in section 2.5, the classification accuracies are calculated in three categories  $CA_{gross}$ ,  $CA_{ST}$ , and  $CA_{opt}$ , the results are also presented separately for each one of these. The  $CA_{gross}$  for intra-subject learning is shown in **Table 4**. The average  $CA_{gross}$  across the trial for Adam was  $72.63\% \pm 13.35$ . The maximum  $CA_{gross}$  was observed for participant 4 (90.82%), while the minimum observed was 51.88% for participant 3. Indeed, 5 out of 9 participants crossed the BCI performance threshold of 70% (Blankertz and Vidaurre, 2009) in this case. The performance of SGDM for this category resulted in an average classification accuracy of  $73.13\% \pm 14.82$ , while the maximum accuracy was observed for participant 4 (91.14%) and the minimum observed for participant 3 (54.61%). There was no statistically significant difference (Wilcoxon signed-rank test) between Adam and SGDM performance ( $CA_{gross}$ ) for intra-subject learning.



The  $CA_{gross}$  for inter-subject transfer learning is shown in **Table 5**. Interestingly, although the average  $CA_{gross}$  in the case of Adam ( $67.78\% \pm 8.60$ ) is only slightly higher than average  $CA_{gross}$  in the case of SGDM ( $67.15\% \pm 8.62$ ), the difference between these two methods (Adam and SGDM) was statistically significant ( $p < 0.05$ , Wilcoxon signed-rank test). The maximum  $CA_{gross}$  for inter-subject learning was observed for participant 4 for both the methods: 81.42% for Adam and 80.75% for SGDM. The minimum  $CA_{gross}$  was 54.20% in Adam and 54.15% in SGDM; both for participant 3. It is to be noted that the number of participants crossing the BCI performance threshold (70%) for inter-subject learning is 4 in Adam and 3 in SGDM, which is less than what is observed for intra-subject learning. **Figure 5** displays the loss vs. epoch for the participant 4. To analyse number of epochs and learning rate for all the participants, data of participant 4, session 1, 2, and 3 were trained, keeping 33% of the cumulative data as validation set. The plot clearly shows that the model does not overfit or underfit as the test errors are converging. For this specific subject a divergence of validation loss be seen at nearly 50 epochs. However, the plot clearly indicates fluctuation which may be due to the low amount of data to train and validate. It is noteworthy that overfitting preventive measures such as batch normalization and dropouts are duly taken while designing the CNN architectures as described in sections 2.3 and 2.4.

The performance of the intra- and inter-subject learning for  $CA_{ST}$  is shown in **Tables 6, 7**, respectively. The average  $CA_{ST}$  and kappa in SGDM for intra-subject learning are found to be  $77.31\% \pm 14.90$  and  $0.55 \pm 0.30$ , respectively. The maximum performance using SGDM was observed in subject 4

**TABLE 6** | Performance of intra-subject learning for single-trial decoding.

ID	$CA_{ST}$			
	Adam		SGDM	
	Test (%)	Kappa (Test)	Test (%)	Kappa (Test)
1	74.92	0.50	72.73	0.45
2	57.04	0.14	54.15	0.08
3	54.42	0.09	55.83	0.11
4	94.65	0.89	95.60	0.91
5	87.50	0.75	85.94	0.72
6	76.90	0.54	77.98	0.56
7	72.84	0.46	73.80	0.48
8	93.23	0.86	92.90	0.86
9	85.63	0.71	86.88	0.74
Mean	77.46	0.55	77.31	0.55
Std	14.52	0.29	14.90	0.30

( $CA_{ST} = 95.60\%$ ,  $\kappa = 0.91$ ), while the minimum was observed in subject 2 ( $CA_{ST} = 54.15\%$ ,  $\kappa = 0.08$ ). In this case, 7 out of 9 participants qualified for the BCI literacy threshold. The average  $CA_{ST}$  and kappa for inter-subject learning with Adam was  $77.46\% \pm 14.52$  and  $0.55 \pm 0.29$ , respectively. The best and worst performance for Adam in inter-subject learning was found in participant 4 ( $CA_{ST} = 94.65\%$ ,  $\kappa = 0.89$ ) and participant 3 ( $CA_{ST} = 54.42\%$ ,  $\kappa = 0.09$ ), respectively. The BCI literacy threshold was crossed by 7 out of 9 participants in this case. Inter-subject transfer learning performance on the basis of  $CA_{ST}$  resulted in an average accuracy of  $70.94\% \pm 9.89$  with kappa  $0.42 \pm 0.20$  for Adam and the average  $70.22\% \pm 9.45$  with kappa  $0.40 \pm 0.19$  for SGDM. The maximum accuracy occurred in the case of participant 4 in both the methods with  $86.26\%$  ( $\kappa = 0.73$ ) for Adam and  $83.95\%$  ( $\kappa = 0.68$ ) for SGDM. There was no statistically significant difference (Wilcoxon signed-rank test) between Adam and SGDM on the basis of  $CA_{ST}$  and in both cases, 6 out of 9 participants qualified for the BCI literacy threshold.

**Tables 8, 9** represent the performance of intra- and inter-subject learning accordingly based on  $CA_{opt}$ . The classification accuracy of all the participants for all the 11 time instants (5 to 7 s with an interval of 0.2 s) is shown column-wise. The maximum accuracy occurring out of these 11 time instants is the  $CA_{opt}$  for individual participants. For example, in **Table 8** the first row represents accuracies achieved for participant 1 for all the 11-time instants out of which the accuracy at 5.8 s was the highest (71.16%). So, the  $CA_{opt}$  for participant 1 is 71.16% observed at 5.8 s. Thus we can see that  $CA_{opt}$  for intra-subject learning was found between 5.2 s and 5.8 s across all the participants, with an average of  $76.37\% \pm 13.91$  observed at 5.8 s. A maximum  $CA_{opt}$  of 95.91% was found in participant 4 at 5.6 s, while a minimum  $CA_{opt}$  (55.83%) was found in participant 3 at 5.6 s. Thus, on the basis of  $CA_{opt}$ , 7 out of 9 participants performed beyond the BCI literacy threshold. Again, for inter-subject learning the average  $CA_{opt}$  was found to be  $69.69\% \pm 9.23$  at 5.4 s, which was significantly ( $p < 0.05$ , Wilcoxon signed-rank test) lower than average  $CA_{opt}$  for intra-subject learning,

**TABLE 7** | Performance of inter-subject learning for single-trial decoding.

ID	$CA_{ST}$			
	Adam		SGDM	
	Test (%)	Kappa (Test)	Test (%)	Kappa (Test)
1	73.30	0.47	72.04	0.44
2	57.54	0.15	55.18	0.10
3	55.00	0.10	55.76	0.12
4	86.26	0.73	83.95	0.68
5	66.25	0.33	68.74	0.38
6	74.62	0.49	73.54	0.47
7	71.59	0.43	70.18	0.40
8	76.73	0.53	75.78	0.52
9	77.19	0.54	76.77	0.54
Mean	70.94	0.42	70.22	0.40
Std	9.89	0.20	9.45	0.19

although very close to the BCI literacy threshold. The maximum performance was found in participant 4 ( $CA_{opt} = 86.80\%$  at 5.6 s), while the minimum performance was found in participant 2 ( $CA_{opt} = 56.80\%$  at 5 s). Again, 6 out of 9 participants crossed the BCI performance threshold of 70% in this case. The accuracy of decoding throughout different time instants within the trial is also shown in **Figure 6** for intra- and inter-subject learning, which shows that the performance was significantly higher ( $p < 0.05$ , Wilcoxon signed-rank test) in the case of intra-subject than in inter-subject learning, while the  $CA_{opt}$  occurred earlier in the inter-subject case than in intra-subject. Interestingly, the accuracy curves in both the cases peaked in the middle and gradually reduced at the end of the trial. It is to be noted that the optimum time point of feedback for CNN based inter-subject transfer learning for the dataset used is 5.4 s (i.e., +2.4 s after cue), yielding an average accuracy ( $CA_{opt}$ ) close to 69.69% (**Table 9**). This observation is also according to the ERD pattern of the MI-datasets (Tangermann et al., 2012) where the bandpower of sensorimotor rhythm reaches its bottom and stabilizes until the MI is stopped. This indirectly shows the neurophysiological relevance of the features generated by the CNN.

A typical example of features generated at different layers of CNN has been shown in **Figure 7**. The features for left and right hand MI are shown one on top of the other for successive layers of convolutional and ReLU layers. Although such representations of the activations are not relatable directly with the neurophysiological interpretation due to several transformations on the original image, these are better interpretable by the trained CNN model.

## 4. DISCUSSION

This paper establishes the feasibility of CNN based architectures in inter-subject continuous decoding of MI-related EEG signals while adapting CNN architecture against inter-subject variabilities using a novel concept called Mega Blocks. So far, the

**TABLE 8** | Performance of intra-subject learning for  $CA_{opt}$  (highlighted in bold for each subject id).

ID	Accuracy (%) at different time instants within a trial										
	5s	5.2s	5.4s	5.6s	5.8s	6s	6.2s	6.4s	6.6s	6.8s	7s
1	68.03	67.71	67.40	68.65	<b>71.16</b>	68.03	67.71	68.03	68.65	68.03	68.03
2	56.68	55.96	56.32	55.60	<b>58.48</b>	53.07	51.62	57.76	51.99	52.71	55.96
3	56.54	<b>56.18</b>	56.18	55.83	56.18	55.12	53.36	53.71	51.94	50.88	54.77
4	91.19	93.40	95.28	<b>95.91</b>	95.60	94.65	92.14	88.05	88.99	85.22	82.08
5	78.13	79.69	77.50	83.75	<b>84.06</b>	82.50	81.56	79.06	79.38	77.81	78.44
6	74.01	<b>75.09</b>	73.29	74.01	73.65	71.84	72.20	71.12	70.40	69.68	69.31
7	67.73	69.01	<b>71.57</b>	71.57	70.93	64.86	66.77	70.61	64.86	66.77	61.02
8	89.03	92.26	<b>92.58</b>	92.58	92.26	91.61	88.71	87.42	84.84	81.29	82.58
9	74.69	78.44	80.31	<b>86.25</b>	85.00	84.06	80.31	80.31	78.44	77.50	77.19
Mean	72.89	74.19	74.49	76.02	<b>76.37</b>	73.97	72.71	72.90	71.05	69.99	69.93
Std	12.29	13.55	13.82	14.74	13.91	15.12	14.36	12.06	13.27	12.02	10.85

The bold values represent the maximum value in the respective rows of the table, which means at what time point the maximum accuracy is reached for a particular subject.

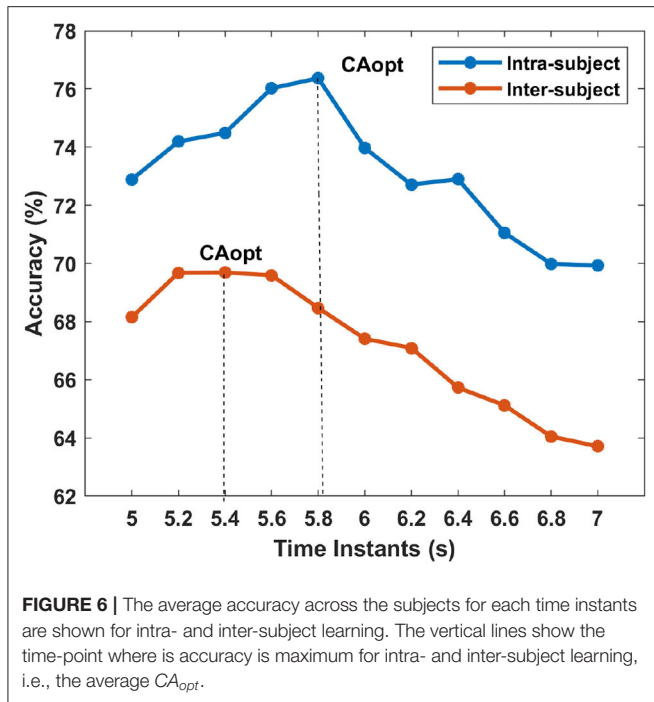
**TABLE 9** | Performance of inter-subject learning for  $CA_{opt}$  (highlighted in bold for each subject id).

ID	Accuracy (%) at different time instants within a trial										
	5s	5.2s	5.4s	5.6s	5.8s	6s	6.2s	6.4s	6.6s	6.8s	7s
1	67.04	<b>71.21</b>	69.82	70.51	68.98	67.73	67.45	65.51	66.34	67.59	66.06
2	<b>56.80</b>	54.73	55.77	53.11	55.18	54.73	53.85	51.92	54.59	52.37	54.59
3	55.30	56.21	<b>57.42</b>	55.45	55.30	53.48	54.09	52.88	52.88	51.52	51.06
4	81.63	84.76	85.31	<b>86.80</b>	84.76	83.13	78.91	78.37	75.51	74.42	74.69
5	63.76	66.11	66.11	<b>66.67</b>	66.67	65.28	66.11	64.45	61.83	61.13	62.66
6	69.08	70.77	69.08	<b>72.00</b>	69.08	68.92	68.46	66.77	67.69	68.62	67.23
7	73.00	<b>73.98</b>	72.15	71.17	68.21	66.24	67.37	65.68	64.56	63.99	61.46
8	75.10	<b>76.60</b>	75.51	75.78	73.33	73.33	73.61	72.24	69.39	66.39	66.26
9	71.63	72.74	<b>76.08</b>	74.83	74.69	73.85	73.99	73.71	73.30	70.38	69.40
Mean	68.15	69.68	<b>69.69</b>	69.59	68.47	67.41	67.09	65.73	65.12	64.05	63.71
Std	8.52	9.51	9.23	10.32	9.23	9.26	8.49	8.83	7.69	7.82	7.30

The bold values represent the maximum value in the respective rows of the table, which means at what time point the maximum accuracy is reached for a particular subject.

issue of inter-subject transfer learning has not been addressed with regards to continuous neurofeedback as the previous studies have mostly concentrated on single-trial classification. Here, we have shown inter-subject transfer learning performance of CNN based architectures for continuous decoding on the standard EEG dataset of BCI Competition-IV using two popular methods: Adam and SGDM. Earlier attempts at classifying MI signals using CNN were limited to intra-subject learning (Tabar and Halici, 2016), while our study deals with inter-subject transfer learning. The significance of designing an inter-subject transfer learning paradigm over intra-subject learning is that we can save the calibration time by making use of the data recorded in previous sessions. Some recent papers have reported inter-subject classification using CNN (Lawhern et al., 2018; Zubarev et al., 2019). Lawhern et al. (2018) in their EEGNet model argued that a single CNN can perform over multiple EEG paradigms such as P300, ERN, MRCP, and SMR, although EEGNet did not perform significantly better than conventional FBCSP approach. Additionally, DeepConvNet (Lawhern et al., 2018) is shown to have performed significantly lower than FBCSP whereas

in our case the Mega Block based deep learning architecture (Architecture-2) performed as good as FBCSP (Raza et al., 2016) and further showed validity for inter-subject learning. Moreover, the performance of EEGNet was shown based on cross-validation over the training data, whereas the performance of Architecture-2 is shown on the test data. However, the work in Zubarev et al. (2019) was focused on inter-subject learning in MEG, and showed significantly better performance than other CNN based classification techniques in BCI, although the performance was not reported on EEG. An advantage of the proposed CNN model is that it can be applied for continuous decoding within a trial, while the models in Lawhern et al. (2018) and Zubarev et al. (2019) are shown to have performed well for a single-trial decoding. Most importantly, these studies have not shown how CNN can be used for continuous decoding, an area that is vital for contingent neurofeedback for restorative BCI applications, while the proposed technique provides a complete solution for CNN based MI-BCI combining inter-subject transfer learning with continuous decoding. Another aspect of our model is automatic parameter optimization during training using the implemented



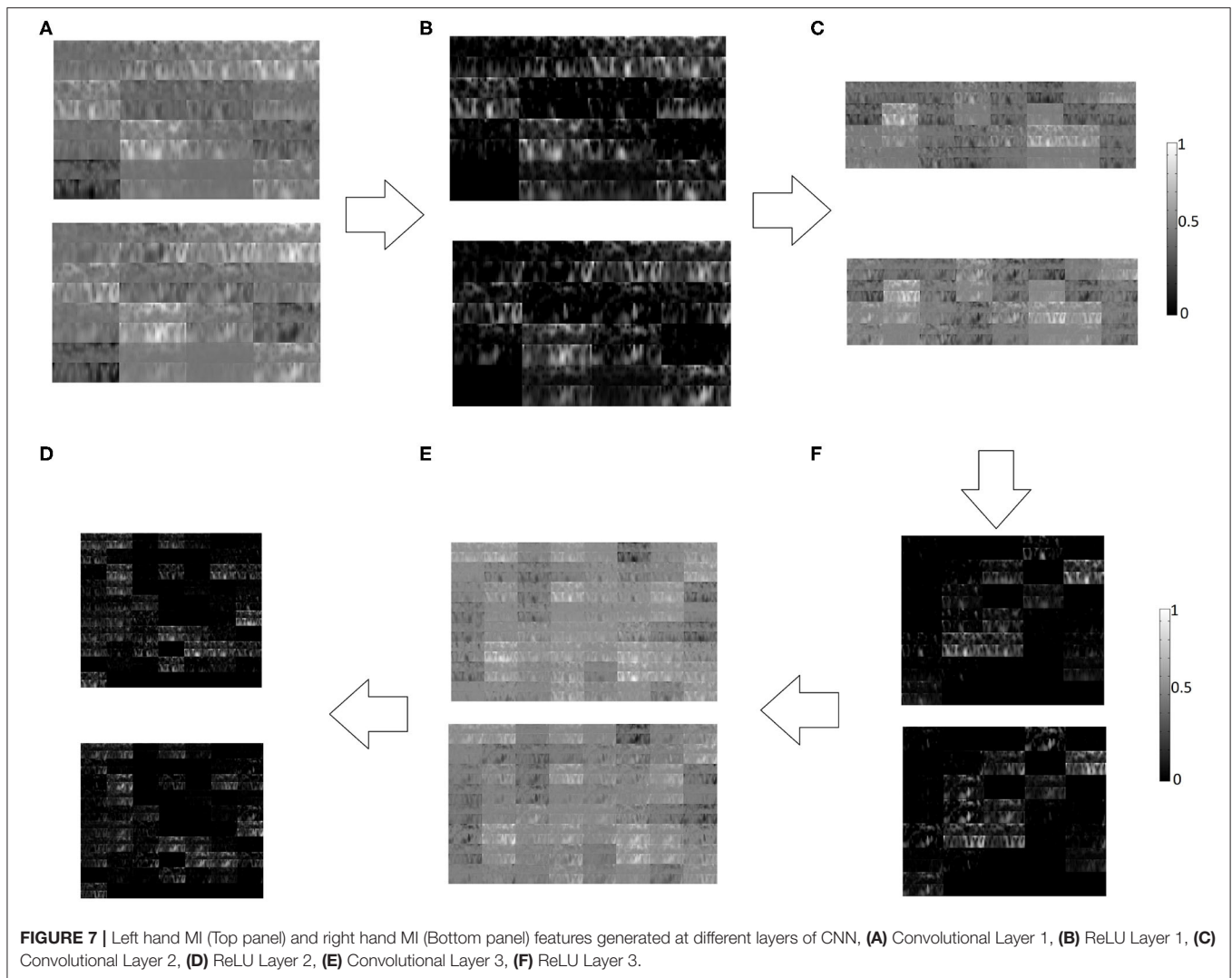
Bayesian optimization. The training time (approx. 1,796 s) of Architecture-2 is comparable to a shallowConvNet, although unlike shallowConvNet here the number of trainable parameters doesn't increase with the number of channels used. The average kappa value for intra-subject classification reported by Gandhi et al. (2015) on BCI competition IV 2b dataset was 0.54 and 0.51 on the evaluation set 04E and 05E, respectively although they used a recurrent quantum neural network (RQNN). In our case, the average kappa for intra-subject classification is 0.55 (see **Table 6**) for both Adam and SGDM. However, we know that the poor outcome in the case of subject 2 and subject 3 is mostly due to the poor quality of the data as evident by the BCI competition results (BCI-Competition, 2008), wherein these two subjects performed worst in all top 6 submissions. Hence, if we remove these two subjects from the calculation then average kappa for intra-subject classification turns out to be 0.67 for both Adam and SGDM, while the same in Gandhi et al. (2015) is 0.55 (excluding subject 2 and 3) for combined evaluation set 04E and 05E. Thus we can see that the performance of CNN for intra-subject learning is far better than RQNN and also the difference is statistically significant ( $p < 0.05$ , Wilcoxon signrank test). More importantly, it should be noted that our paper is focused on giving an acceptable solution for inter-subject transfer learning in MI task in which case the proposed method gives a satisfactory average kappa value of 0.42 (including all 9 subjects, see **Table 7**) and 0.50 (ignoring subject 2 and subject 3). It is to be noted that in Gandhi et al. (2015) there was neither evaluation for inter-subject transfer learning performance nor for continuous decoding.

The classification accuracy results highlight an important finding that it is the tuning of the hyperparameters of CNN, which is more effective than the choice of the adaptive training method. This is revealed from the fact that there were no

significant ( $p < 0.05$ ) differences between the performance of Adam and SGDM, except in the case of  $CA_{gross}$  in inter-subject learning wherein the average difference in average accuracy is only 0.62%. A probable reason for this can be found from the comments made by Wilson et al. (2017), which states that the choice of the adaptive method (such as Adam and SGDM), makes a difference in optimization-free iterative search procedures (such as GANs and Q-learning). This indicates that as we have used an optimization dependent learning architecture such as CNN, the hyperparameter tuning plays a more vital role in the performance of the classifier.

The inter-subject transfer learning performance was also compared against the intra-subject classification to determine how much compromise is needed in terms of accuracy in order to avoid subject-specific calibration and whether this compromise is worthwhile. The performance of inter-subject transfer learning is found to be significantly lower ( $p < 0.05$ ) than the intra-subject learning both in terms of continuous decoding ( $CA_{gross}$ ) and single-trial decoding ( $CA_{ST}$ ) irrespective of the adaptive training methods (Adam or SGDM) used. A possible reason for the lower performance could be the use of a large amount of pooled data from the rest of the 8 participants in the leave-one-out method while some participants (especially participant 2 and 3) had poor quality of data which may have impacted the trained models. However, the average inter-subject transfer learning accuracy for  $CA_{ST}$  was found to be higher than 70%, the BCI performance threshold. Single-trial decoding is sufficient for issuing triggered neurofeedback, which is a widely used paradigm for the rehabilitation of motor functionality (Buch et al., 2008; Ramos-Murguialday et al., 2013; Ono et al., 2014). Thus we can say that the proposed transfer learning architecture can be incorporated into motor rehabilitation paradigms without compromising on an acceptable performance criterion. Another important point to be noted is that the worst-performing subjects (subject 2 and subject 3), and the best performing subject (subject 4) are consistent across intra- or inter-subject learning conditions, which may indicate poor quality of the data and not the strength of the algorithm which negatively affected the average accuracy of inter-subject transfer learning. Hence, if we ignore subject 2 and 3, the performance of inter-subject transfer learning increases further both in terms of  $CA_{gross}$  (Adam: 70.84% and SGDM: 71.49%), and  $CA_{ST}$  (Adam: 75.13% and SGDM: 74.43%).

Previous literature on inter-subject transfer learning using CSP yielded the best average accuracy of 79% on BCI Competition III, dataset IVa, where the number of subjects was 5 (Devlaminc et al., 2011). Tangent space features drawn from the Riemannian geometry framework were used for transfer learning using BCI competition IV, dataset 2a, which achieved an average leave-one-subject-out-cross-validation accuracy of 75.52% (Gaur et al., 2019a). In a recent study, Halme and Parkkonen reported inter-subject transfer learning accuracy in EEG of 67.7% on their own experimental data using CSP with logistic regression (Halme and Parkkonen, 2018). Although a direct comparison is not possible here as the datasets used in Gaur et al. (2019a), Halme and Parkkonen (2018), and Devlaminc et al. (2011) were different but the average of 7



out of 9 subjects [ignoring subject 2 and subject 3 due to poor data quality as revealed by BCI competition results (BCI-Competition, 2008)] in our case achieved an average single-trial classification accuracy close to 75% (Adam: 75.13% and SGDM: 74.43%). It is noteworthy that previous studies on inter-subject transfer learning mentioned above did not deal with continuous decoding and used traditional approaches rather than deep learning. The work also shows that inter-subject transfer learning in MI with CNN based architecture is more sensitive to the tuning of hyperparameters rather than the choice of adaptive training methods as both Adam and SGDM performed equally well in this case.

Potential applications where the obtained results can be useful include primarily the neurorehabilitative BCI systems where continuous and meaningful neurofeedback is essential for motor recovery (Chowdhury et al., 2018a). Apart from that, the asynchronous BCI uses for activities of daily living (ADL) by the completely locked-in patients can also make use of such techniques for controlling assistive robotic

devices (Bhattacharyya et al., 2017; Tariq et al., 2018). Another important application could be the telepresence robot control by the motor-disabled patients towardz enhanced independence (Carlson et al., 2013) which needs continuous decoding with minimal calibration overhead.

One of the limitations of this study is that we combined the EEG channels depthwise similar to RGB images which could cause problems in very high dimensional datasets such as in magnetoencephalography (MEG) or very high dimensional EEG recordings. Possible future work to avoid such a problem is to use dimensionality reduction techniques such as ReliefF (RF) or Infinite Latent Feature Selection (ILFS) (Roy et al., 2019b) before input image generation. Also, to increase the number of training examples to feed into the CNN, Generalized Adversarial Networks (GAN) (Goodfellow et al., 2014) could be used rather than the segmentation of trials for creating training examples. Another limitation of using CNN based architectures is that the generated features are not relatable directly with the neurophysiology.

Therefore, we need better visualization techniques to enhance the interpretability of activations found in different layers which could have some neurophysiological significance. Other future works may involve making deep learning models more explainable to address the generalizability of inter-subject decoding. Another important challenge is to make them usable for large-scale real-world deployment for complex BCI problems (Zhang et al., 2019).

## 5. CONCLUSION

This paper presents the feasibility of inter-subject continuous decoding utilizing CNN based deep learning frameworks using a novel concept called Mega Blocks which makes it adaptive against inter-subject variabilities in the EEG data. The study addresses the long-standing issue of making an MI-BCI calibration-free as well as suitable for continuous decoding, which so far has not been addressed using a CNN-based learning approach. This could spawn the next generation of MI-BCI systems, especially in the domain of neurorehabilitation, where reducing the calibration needs and providing continuous feedback play a vital role in enhancing user-experience and thus leverage rehabilitative potential.

## REFERENCES

- Arvaneh, M., Robertson, I., and Ward, T. E. (2014). "Subject-to-subject adaptation to reduce calibration time in motor imagery-based brain-computer interface," in *2014 36th Annual International Conference of the IEEE Engineering in Medicine and Biology Society* (Chicago, IL), 6501–6504. doi: 10.1109/EMBC.2014.6945117
- BCI-Competition (2008). *BCI Competition 2008–Graz Data Set B*.
- Bhattacharyya, S., Konar, A., and Tibarewala, D. N. (2017). Motor imagery and error related potential induced position control of a robotic arm. *IEEE/CAA J. Automat. Sin.* 4, 639–650. doi: 10.1109/JAS.2017.7510616
- Blankertz, B., and Vidaurre, C. (2009). Towards a cure for BCI illiteracy: machine learning based co-adaptive learning. *BMC Neurosci.* 10:P85. doi: 10.1186/1471-2202-10-S1-P85
- Buch, E., Weber, C., Cohen, L. G., Braun, C., Dimyan, M. A., Ard, T., et al. (2008). Think to move: a neuromagnetic brain-computer interface (BCI) system for chronic stroke. *Stroke* 39, 910–917. doi: 10.1161/STROKEAHA.107.505313
- Bundy, D. T., Souders L., Baranyai, K., Leonard, L., Schalk, G., Coker, R., et al. (2017). Contralesional brain-computer interface control of a powered exoskeleton for motor recovery in chronic stroke survivors. *Stroke* 48, 1908–1915. doi: 10.1161/STROKEAHA.116.016304
- Carlson, T., Tonin, L., Perdakis, S., Leeb, R., and Millan, J. R. (2013). "A hybrid BCI for enhanced control of a telepresence robot," in *2013 35th Annual International Conference of the IEEE Engineering in Medicine and Biology Society (EMBC)* (Osaka), 3097–3100. doi: 10.1109/EMBC.2013.6610196
- Chowdhury, A., Meena, Y. K., Raza, H., Bhushan, B., Uttam, A. K., Pandey, N., et al. (2018a). Active physical practice followed by mental practice using BCI-driven hand exoskeleton: a pilot trial for clinical effectiveness and usability. *IEEE J. Biomed. Health Inform.* 22, 1786–1795. doi: 10.1109/JBHI.2018.2863212
- Chowdhury, A., Raza, H., Meena, Y. K., Dutta, A., and Prasad, G. (2018b). Online covariate shift detection-based adaptive brain-computer interface to trigger hand exoskeleton feedback for neuro-rehabilitation. *IEEE Trans. Cogn. Dev. Syst.* 10, 1070–1080. doi: 10.1109/TCDS.2017.2787040
- Chowdhury, A., Raza, H., Meena, Y. K., Dutta, A., and Prasad, G. (2019). An EEG-EMG correlation-based brain-computer interface for hand

## DATA AVAILABILITY STATEMENT

Publicly available datasets were analyzed in this study. This data can be found here: [http://www.bbci.de/competition/iv/desc\\_2b.pdf](http://www.bbci.de/competition/iv/desc_2b.pdf).

## AUTHOR CONTRIBUTIONS

SR and AC have conceptualized the idea and finalized the data processing pipeline. SR performed the data analysis and extracted results. AC and SR have written the paper. KM and GP supervised the project and performed the internal review of the paper. All authors contributed to the article and approved the submitted version.

## FUNDING

This work was supported in part by the Department of Science and Technology, India, and in part by the UK-India Education and Research Initiative (UKIERI)—Thematic Partnership Project Advancing MEG based Brain-computer Interface Supported Upper Limb Post-stroke Rehabilitation under Grant DST-UKIERI-2016-17-0128.

- orthosis supported neuro-rehabilitation. *J. Neurosci. Methods* 312, 1–11. doi: 10.1016/j.jneumeth.2018.11.010
- Devlaminck, D., Wyns, B., Grosse-Wentrup, M., Otte, G., and Santens, P. (2011). Multisubject learning for common spatial patterns in motor-imagery BCI. *Comput. Intell. Neurosci.* 2011, 1–9. doi: 10.1155/2011/217987
- Fahimi, F., Zhang, Z., Goh, W. B., Lee, T.-S., Ang, K. K., and Guan, C. (2019). Inter-subject transfer learning with an end-to-end deep convolutional neural network for EEG-based BCI. *J. Neural Eng.* 16:026007. doi: 10.1088/1741-2552/aaf3f6
- Fazli, S., Popescu, F., Danoczy, M., Blankertz, B., Muller, K.-R., and Grozea, C. (2009). Subject-independent mental state classification in single trials. *Neural Netw.* 22, 1305–1312. doi: 10.1016/j.neunet.2009.06.003
- Foldes, S. T., Weber, D. J., and Collinger, J. L. (2015). MEG-based neurofeedback for hand rehabilitation. *J. Neuroeng. Rehabil.* 12:85. doi: 10.1186/s12984-015-0076-7
- Gandhi, V., Prasad, G., Coyle, D., Behera, L., and McGinnity, T. M. (2015). Evaluating quantum neural network filtered motor imagery brain-computer interface using multiple classification techniques. *Neurocomputing* 170, 161–167. doi: 10.1016/j.neucom.2014.12.114
- Gaur, P., McCreadie, K., Pachori, R. B., Wang, H., and Prasad, G. (2019a). Tangent space features-based transfer learning classification model for two-class motor imagery brain-computer interface. *Int. J. Neural Syst.* 29:1950025. doi: 10.1142/S0129065719500254
- Gaur, P., Pachori, R. B., Wang, H., and Prasad, G. (2019b). An automatic subject specific intrinsic mode function selection for enhancing two-class EEG-based motor imagery-brain computer interface. *IEEE Sens. J.* 19, 6938–6947. doi: 10.1109/JSEN.2019.2912790
- Gelbart, M. A., Snoek, J., and Adams, R. P. (2014). Bayesian optimization with unknown constraints. *arXiv[Preprint].arXiv:1403.5607*. doi: 10.5555/3020751.3020778
- Goodfellow, I. J., Pouget-Abadie, J., Mirza, M., Xu, B., Warde-Farley, D., Ozair, S., et al. (2014). "Generative adversarial nets," in *Proceedings of the 27th International Conference on Neural Information Processing Systems*, Vol. 2 (Cambridge, MA: MIT Press), 2672–2680.
- Halme, H., and Parkkonen, L. (2018). Across-subject offline decoding of motor imagery from MEG and EEG. *Sci. Rep.* 8:10087. doi: 10.1038/s41598-018-28295-z

- He, K., Zhang, X., Ren, S., and Sun, J. (2016). "Deep residual learning for image recognition," in *2016 IEEE Conference on Computer Vision and Pattern Recognition (CVPR)*, 770–778.
- Jayaram, V., Alamgir, M., Altun, Y., Scholkopf, B., and Grosse-Wentrup, M. (2016). Transfer learning in brain-computer interfaces. *IEEE Comput. Intell. Mag.* 11, 20–31. doi: 10.1109/MCI.2015.2501545
- Jiao, Y., Zhang, Y., Chen, X., Yin, E., Jin, J., Wang, X., et al. (2019). Sparse group representation model for motor imagery EEG classification. *IEEE J. Biomed. Health Inform.* 23, 631–641. doi: 10.1109/JBHI.2018.2832538
- Jin, J., Sellers, E. W., Zhang, Y., Daly, I., Wang, X., and Cichocki, A. (2013). Whether generic model works for rapid ERP-based BCI calibration. *J. Neurosci. Methods* 212, 94–99. doi: 10.1016/j.jneumeth.2012.09.020
- Jin, Z., Gao, D., Zhou, G., and Zhang, Y. (2020). EEG classification using sparse Bayesian extreme learning machine for brain-computer interface. *Neural Comput. Appl.* 32, 6601–6609. doi: 10.1007/s00521-018-3735-3
- Johnson, R., and Zhang, T. (2013). "Accelerating stochastic gradient descent using predictive variance reduction," in *Proceedings of the 26th International Conference on Neural Information Processing Systems, NIPS'13* (Lake Tahoe: Curran Associates Inc.), 315–323.
- Kang, H., Nam, Y., and Choi, S. (2009). Composite common spatial pattern for subject-to-subject transfer. *IEEE Signal Process. Lett.* 16, 683–686. doi: 10.1109/LSP.2009.2022557
- Kindermans, P.-J., Tangemann, M., Muller, K.-R., and Schrauwen, B. (2014). Integrating dynamic stopping, transfer learning and language models in an adaptive zero-training ERP speller. *J. Neural Eng.* 11:035005. doi: 10.1088/1741-2560/11/3/035005
- Kingma, D. P., and Ba, J. (2014). ADAM: a method for stochastic optimization. *arXiv[Preprint].arXiv:1412.6980*.
- Krizhevsky, A., Sutskever, I., and Hinton, G. E. (2012). "Imagenet classification with deep convolutional neural networks," in *Advances in Neural Information Processing Systems 25*, eds F. Pereira, C. J. C. Burges, L. Bottou, and K. Q. Weinberger (Lake Tahoe: Curran Associates, Inc.), 1097–1105.
- Kwon, O., Lee, M., Guan, C., and Lee, S. (2019). Subject-independent brain-computer interfaces based on deep convolutional neural networks. *IEEE Trans. Neural Netw. Learn. Systems*. doi: 10.1109/TNNLS.2019.2946869. [Epub ahead of print].
- Lawhern, V. J., Solon, A. J., Waytowich, N. R., Gordon, S. M., Hung, C. P., and Lance, B. J. (2018). EEGNet: a compact convolutional neural network for EEG-based brain-computer interfaces. *J. Neural Eng.* 15:056013. doi: 10.1088/1741-2552/aac8c
- Li, Y., Kambara, H., Koike, Y., and Sugiyama, M. (2010). Application of covariate shift adaptation techniques in brain-computer interfaces. *IEEE Trans. Biomed. Eng.* 57, 1318–1324. doi: 10.1109/TBME.2009.2039997
- Lotte, F., Bougrain, L., Cichocki, A., Clerc, M., Congedo, M., Rakotomamonjy, A., et al. (2018). A review of classification algorithms for EEG-based brain-computer interfaces: a 10 year update. *J. Neural Eng.* 15:031005. doi: 10.1088/1741-2552/aab2f2
- Lotte, F., and Guan, C. (2011). Regularizing common spatial patterns to improve BCI designs: unified theory and new algorithms. *IEEE Trans. Biomed. Eng.* 58, 355–362. doi: 10.1109/TBME.2010.2082539
- Lu, N., Li, T., Ren, X., and Miao, H. (2017). A deep learning scheme for motor imagery classification based on restricted Boltzmann machines. *IEEE Trans. Neural Syst. Rehabil. Eng.* 25, 566–576. doi: 10.1109/TNSRE.2016.2601240
- Morone, G., Pisotta, I., Pichiorri, F., Kleih, S., Paolucci, S., Molinari, M., et al. (2015). Proof of principle of a brain-computer interface approach to support poststroke arm rehabilitation in hospitalized patients: design, acceptability, and usability. *Arch. Phys. Med. Rehabil.* 96, S71–S78. doi: 10.1016/j.apmr.2014.05.026
- Ono, T., Shindo, K., Kawashima, K., Ota, N., Ito, M., Ota, T., et al. (2014). Brain-computer interface with somatosensory feedback improves functional recovery from severe hemiplegia due to chronic stroke. *Front. Neuroeng.* 7:19. doi: 10.3389/fneng.2014.00019
- Pfurtscheller, G., and da Silva, F. L. (1999). Event-related EEG/MEG synchronization and desynchronization: basic principles. *Clin. Neurophysiol.* 110, 1842–1857. doi: 10.1016/S1388-2457(99)00141-8
- Pohlmeier, E. A., Mahmoudi, B., Geng, S., Prins, N. W., and Sanchez, J. C. (2014). Using reinforcement learning to provide stable brain-machine interface control despite neural input reorganization. *PLoS ONE* 9:e87253. doi: 10.1371/journal.pone.0087253
- Prins, N. W., Sanchez, J. C., and Prasad, A. (2017). Feedback for reinforcement learning based brain-machine interfaces using confidence metrics. *J. Neural Eng.* 14:036016. doi: 10.1088/1741-2552/aa6317
- Qian, N. (1999). On the momentum term in gradient descent learning algorithms. *Neural Netw.* 12, 145–151. doi: 10.1016/S0893-6080(98)00116-6
- Ramos-Murguialday, A., Broetz, D., Rea, M., Laer, L., Yilmaz, Z., Brasil, F. L., et al. (2013). Brain-machine interface in chronic stroke rehabilitation: a controlled study. *Ann. Neurol.* 74, 100–108. doi: 10.1002/ana.23879
- Raza, H., Cecotti, H., Li, Y., and Prasad, G. (2016). Adaptive learning with covariate shift-detection for motor imagery-based brain-computer interface. *Soft Comput.* 20, 3085–3096. doi: 10.1007/s00500-015-1937-5
- Raza, H., Rathee, D., Zhou, S.-M., Cecotti, H., and Prasad, G. (2019). Covariate shift estimation based adaptive ensemble learning for handling non-stationarity in motor imagery related EEG-based brain-computer interface. *Neurocomputing* 343, 154–166. doi: 10.1016/j.neucom.2018.04.087
- Roy, S., McCreddie, K., and Prasad, G. (2019a). "Can a single model deep learning approach enhance classification accuracy of an EEG-based brain-computer interface?" in *2019 IEEE International Conference on Systems, Man and Cybernetics (SMC)* (Bari), 1317–1321. doi: 10.1109/SMC.2019.8914623
- Roy, S., Rathee, D., McCreddie, K., and Prasad, G. (2019b). "Channel selection improves meg-based brain-computer interface," in *2019 9th International IEEE/EMBS Conference on Neural Engineering (NER)* (San Francisco, CA), 295–298. doi: 10.1109/NER.2019.8716948
- Roy, Y., Banville, H., Albuquerque, I., Gramfort, A., Falk, T. H., and Faubert, J. (2019). Deep learning-based electroencephalography analysis: a systematic review. *J. Neural Eng.* 16:051001. doi: 10.1088/1741-2552/ab260c
- Saha, S., Ahmed, K. I. U., Mostafa, R., Hadjileontiadis, L., and Khandoker, A. (2018). Evidence of variabilities in EEG dynamics during motor imagery-based multiclass brain-computer interface. *IEEE Trans. Neural Syst. Rehabil. Eng.* 26, 371–382. doi: 10.1109/TNSRE.2017.2778178
- Saha, S., and Baumert, M. (2020). Intra- and inter-subject variability in EEG-based sensorimotor brain computer interface: a review. *Front. Comput. Neurosci.* 13:87. doi: 10.3389/fncom.2019.00087
- Saha, S., Hossain, M. S., Ahmed, K., Mostafa, R., Hadjileontiadis, L., Khandoker, A., et al. (2019). Wavelet entropy-based inter-subject associative cortical source localization for sensorimotor BCI. *Front. Neuroinform.* 13:47. doi: 10.3389/fninf.2019.00047
- Schirrmester, R. T., Springenberg, J. T., Fiederer, L. D. J., Glasstetter, M., Eggensperger, K., Tangemann, M., et al. (2017). Deep learning with convolutional neural networks for EEG decoding and visualization. *Hum. Brain Mapp.* 38, 5391–5420. doi: 10.1002/hbm.23730
- Seghier, M. L., and Price, C. J. (2018). Interpreting and utilising intersubject variability in brain function. *Trends Cogn. Sci.* 22, 517–530. doi: 10.1016/j.tics.2018.03.003
- Spüler, M., Bensch, M., Kleih, S., Rosenstiel, W., Bogdan, M., and Kübler, A. (2012). Online use of error-related potentials in healthy users and people with severe motor impairment increases performance of a p300-bci. *Clin. Neurophysiol.* 123, 1328–1337. doi: 10.1016/j.clinph.2011.11.082
- Sussillo, D., Stavisky, S. D., Kao, J. C., Ryu, S. I., and Shenoy, K. V. (2016). Making brain-machine interfaces robust to future neural variability. *Nat. Commun.* 7:13749. doi: 10.1038/ncomms13749
- Tabar, Y. R., and Halici, U. (2016). A novel deep learning approach for classification of EEG motor imagery signals. *J. Neural Eng.* 14:016003. doi: 10.1088/1741-2560/14/1/016003
- Tangemann, M., Muller, K.-R., Aertsen, A., Birbaumer, N., Braun, C., Brunner, C., et al. (2012). Review of the BCI competition IV. *Front. Neurosci.* 6:55. doi: 10.3389/fnins.2012.00055
- Tariq, M., Trivailo, P. M., and Simic, M. (2018). EEG-based BCI control schemes for lower-limb assistive-robots. *Front. Hum. Neurosci.* 12:312. doi: 10.3389/fnhum.2018.00312
- Tu, W., and Sun, S. (2012). A subject transfer framework for EEG classification. *Neurocomputing* 82, 109–116. doi: 10.1016/j.neucom.2011.10.024
- Vidaurre, C., Kawanabe, M., von Bunau, P., Blankertz, B., and Muller, K. R. (2011). Toward unsupervised adaptation of LDA for brain-computer interfaces. *IEEE Trans. Biomed. Eng.* 58, 587–597. doi: 10.1109/TBME.2010.2093133

- Wang, P., Lu, J., Zhang, B., and Tang, Z. (2015). "A review on transfer learning for brain-computer interface classification," in *2015 5th International Conference on Information Science and Technology (ICIST)* (Changsha), 315–322. doi: 10.1109/ICIST.2015.7288989
- Wilson, A. C., Roelofs, R., Stern, M., Srebro, N., and Recht, B. (2017). "The marginal value of adaptive gradient methods in machine learning," in *Advances in Neural Information Processing Systems 30*, eds I. Guyon, U. V. Luxburg, S. Bengio, H. Wallach, R. Fergus, S. Vishwanathan, and R. Garnett (Long Beach, CA: Curran Associates, Inc.), 4148–4158.
- Wronkiewicz, M., Larson, E., and Lee, A. K. C. (2015). Leveraging anatomical information to improve transfer learning in brain-computer interfaces. *J. Neural Eng.* 12:046027. doi: 10.1088/1741-2560/12/4/046027
- Zanini, P., Congedo, M., Jutten, C., Said, S., and Berthoumieu, Y. (2018). Transfer learning: a Riemannian geometry framework with applications to brain-computer interfaces. *IEEE Trans. Biomed. Eng.* 65, 1107–1116. doi: 10.1109/TBME.2017.2742541
- Zhang, X., Yao, L., Wang, X., Monaghan, J., Mcalpine, D., and Zhang, Y. (2019). A survey on deep learning based brain computer interface: recent advances and new Frontiers. *arXiv*. arXiv:1905.04149.
- Zubarev, I., Zetter, R., Halme, H., and Parkkonen, L. (2018). Robust and highly adaptable brain-computer interface with convolutional net architecture based on a generative model of neuromagnetic measurements. *arXiv[Preprint].arXiv:1805.10981*.
- Zubarev, I., Zetter, R., Halme, H.-L., and Parkkonen, L. (2019). Adaptive neural network classifier for decoding MEG signals. *Neuroimage* 197, 425–434. doi: 10.1016/j.neuroimage.2019.04.068

**Conflict of Interest:** The authors declare that the research was conducted in the absence of any commercial or financial relationships that could be construed as a potential conflict of interest.

Copyright © 2020 Roy, Chowdhury, McCreddie and Prasad. This is an open-access article distributed under the terms of the Creative Commons Attribution License (CC BY). The use, distribution or reproduction in other forums is permitted, provided the original author(s) and the copyright owner(s) are credited and that the original publication in this journal is cited, in accordance with accepted academic practice. No use, distribution or reproduction is permitted which does not comply with these terms.



# Multiclass Classification Based on Combined Motor Imageries

Cecilia Lindig-León<sup>1,2\*</sup>, Sébastien Rimbart<sup>1</sup> and Laurent Bougrain<sup>1</sup>

<sup>1</sup> Université de Lorraine, CNRS, LORIA, Inria, Nancy, France, <sup>2</sup> Faculty of Engineering, Computer Science and Psychology, Institute of Neural Information Processing, Ulm University, Ulm, Germany

## OPEN ACCESS

### Edited by:

Xun Chen,  
University of Science and Technology  
of China, China

### Reviewed by:

Jun Jiang,  
Xi'an University, China  
Anubha Gupta,  
Indraprastha Institute of Information  
Technology Delhi, India

### \*Correspondence:

Cecilia Lindig-León  
cecilia.lindig-leon@uni-ulm.de

### Specialty section:

This article was submitted to  
Brain Imaging Methods,  
a section of the journal  
Frontiers in Neuroscience

**Received:** 07 May 2020

**Accepted:** 13 August 2020

**Published:** 19 November 2020

### Citation:

Lindig-León C, Rimbart S and  
Bougrain L (2020) Multiclass  
Classification Based on Combined  
Motor Imageries.  
Front. Neurosci. 14:559858.  
doi: 10.3389/fnins.2020.559858

Motor imagery (MI) allows the design of self-paced brain–computer interfaces (BCIs), which can potentially afford an intuitive and continuous interaction. However, the implementation of non-invasive MI-based BCIs with more than three commands is still a difficult task. First, the number of MIs for decoding different actions is limited by the constraint of maintaining an adequate spacing among the corresponding sources, since the electroencephalography (EEG) activity from near regions may add up. Second, EEG generates a rather noisy image of brain activity, which results in a poor classification performance. Here, we propose a solution to address the limitation of identifiable motor activities by using combined MIs (i.e., MIs involving 2 or more body parts at the same time). And we propose two new multilabel uses of the Common Spatial Pattern (CSP) algorithm to optimize the signal-to-noise ratio, namely MC2CMI and MC2SMI approaches. We recorded EEG signals from seven healthy subjects during an 8-class EEG experiment including the rest condition and all possible combinations using the left hand, right hand, and feet. The proposed multilabel approaches convert the original 8-class problem into a set of three binary problems to facilitate the use of the CSP algorithm. In the case of the MC2CMI method, each binary problem groups together in one class all the MIs engaging one of the three selected body parts, while the rest of MIs that do not engage the same body part are grouped together in the second class. In this way, for each binary problem, the CSP algorithm produces features to determine if the specific body part is engaged in the task or not. Finally, three sets of features are merged together to predict the user intention by applying an 8-class linear discriminant analysis. The MC2SMI method is quite similar, the only difference is that any of the combined MIs is considered during the training phase, which drastically accelerates the calibration time. For all subjects, both the MC2CMI and the MC2SMI approaches reached a higher accuracy than the classic pair-wise (PW) and one-vs.-all (OVA) methods. Our results show that, when brain activity is properly modulated, multilabel approaches represent a very interesting solution to increase the number of commands, and thus to provide a better interaction.

**Keywords:** brain-computer interface (BCI), combined motor imageries, multilabel classification, common spatial pattern (CSP), electroencephalography (EEG)

## 1. INTRODUCTION

Motor imagery (MI) is a mental process during which subjects imagine themselves performing a movement without executing it, specifically by activating the haptic sensations (i.e., tactile, proprioceptive, and kinesthetic) felt during a real movement (Jeannerod, 1995; Guillot et al., 2009). Considering that MI consists of evoking a motor action, such a mental process activates the primary motor cortex and the additional motor areas in the same way as a real movement (Héту et al., 2013). This activity can be analyzed by using electroencephalography (EEG) recordings, where rhythmic macroscopic oscillations with spectral peaks over the post-central somatosensory cortex around 10 Hz and over the precentral motor cortex at 20 Hz are observed (Jasper, 1936; Hari and Salmelin, 1997). These oscillations produce specific patterns of event-related desynchronization (ERD; i.e., a reduction of the oscillatory activity with respect to a resting period) and event-related synchronization (ERS; i.e., an increase in the oscillatory activity) within the mu/alpha (7–13 Hz) and beta (15–35 Hz) bands over the region associated with the body part engaged in the task (Pfurtscheller and Aranibar, 1979; Pfurtscheller and Neuper, 2001). More precisely, before and during an MI, ERD patterns appear gradually in the mu/alpha and beta bands (Pfurtscheller and Lopes da Silva (1999), whereas at the end of the MI, ERS patterns are typically observed in the beta band (Pfurtscheller, 2001), and occasionally, in the mu band (Lindig-León et al., 2015).

For discriminating MIs involving different body parts, there are two particular considerations: (i) the lateralization during the activation of the motor cortex and (ii) the focal ERD/surround ERS effect. The mentioned lateralization implies that MIs executed by one side of the body activate the opposite side of the motor cortex. Thus, an MI of the right hand induces ERD patterns in the left side of the sensorimotor cortex, while an MI of the left hand appears in the right side (Pfurtscheller and Neuper, 1997, 2001; Neuper and Pfurtscheller, 2001; Neuper et al., 2009). In this way, the recognition of an MI is based on the location over the motor cortex of the ERD patterns associated with the body part that is engaged in the task (Pfurtscheller, 2001; Blankertz et al., 2006; Blankertz et al., 2008b; Lotte et al., 2007; Müller-Putz et al., 2016). In addition, the focal ERD/surround ERS effect, which consists of the ERS patterns that are simultaneously found in the ipsilateral side of the motor cortex, also provide an insight into the body part that is engaged in the task (Suffczynski et al., 1999; Pfurtscheller, 2003; Jäncke et al., 2006). One hypothesis suggests that the focal ERD/surround ERS is a response to the selective attention given to a particular body part during a single MI (i.e., only one body part engaged in the motor task). For instance, an MI of the right hand elicits an ERD over the contralateral side (electrode C3), while inducing an ERS over the ipsilateral and central parts of the motor cortex (electrodes Cz and C4, which correspond to regions associated with the feet and left hand) (Pfurtscheller et al., 1993; Pfurtscheller, 2003). In the case of combined MIs (i.e., two or more body parts engaged at the same time), the focal ERD/surround ERS represents an interesting and still open question, considering that multiple

body parts may be simultaneously engaged in the motor task and the associated ERD patterns might cancel out the ERS elicited by other sources.

Given that no stimulation is required to produce MIs, such a paradigm allows designing self-paced brain–computer interfaces (BCIs), which provides users with the freedom to send commands on demand (Mason et al., 2006). Consequently, and in contrast to other BCI paradigms that are restricted to a predefined time frame, MI-based BCIs can potentially afford an intuitive and continuous interaction (Wolpaw and Wolpaw, 2012). Therefore, MI represents an interesting solution to control neuroprostheses. However, considering the difficulty to afford multiple commands for EEG-based BCIs, a full interaction is still a challenge. Over the past decade, impressive improvements have been made for decoding complex motor activities from intracranial electrodes (Wodlinger et al., 2014; Yin et al., 2014; Tyson et al., 2015), with which it is possible to extract multiple mental states (i.e., control commands). Yet, despite the benefits of such a framework, complex EEG-based MIs have not been extensively studied and very little is known about their suitability for this purpose. In the present study, we investigate the use of combined MIs (Royer et al., 2013; Yi et al., 2013), which in contrast to the standard paradigm considerably increases the number of classes while using the same number of body parts ( $2^n$  compared to  $n$ , where  $n$  is the number of body parts, and when all possible combinations are considered). In general, the activity sources are chosen to cover a relatively large area over the sensorimotor cortex, while maintaining an adequate spacing among them to avoid mixing up specific activity. Consequently, given the distribution of sources along the sensorimotor cortex most of the MI-based BCIs are designed to identify ERD/ERS patterns generated by the left hand, right hand, and/or feet. Under a single label approach, using the three aforementioned activity sources allows designing a BCI with only three commands for interaction, which remains limited for designing efficient systems. On the contrary, with a multilabel approach we have designed a paradigm including the single and combined use of the left hand, right hand, and both feet together which, in addition to the rest condition, provide eight different classes (rest, left hand, feet, left hand and feet, right hand, both hands, right hand and feet, and both hands and feet).

In the present work, we propose a solution to address the limited number of identifiable activity sources, and we provide two new multilabel uses of the Common Spatial Pattern (CSP) algorithm. The CSP algorithm is very convenient, since it can be applied to any MI-based BCI while favoring high classification performances, it is also easy to implement and computationally efficient. However, given its formulation, CSP is constrained to binary problems. Consequently, the most common way to extend CSP to the multiclass case consists of solving a set of binary subproblems, either in a pair-wise (PW) or a one-vs.-all (OVA) approach. The main drawback to this solution is that the number of classifiers increases significantly with the number of classes, given that for a  $k$ -class problem the PW and OVA approaches require  $k(k - 1)/2$ , and  $k$  classifiers, respectively.

Here, we address the question of whether the EEG activity elicited during combined MIs can be analyzed independently over the sources related to each one of the body parts included in the paradigm to subsequently predict the class label from the combination of the extracted information. In this way, one can transform the original 8-class problem into three binary problems (i.e., one problem associated with each body part). In other words, one can convert a  $2^n$ -problem into  $n$  binary problems, where  $n$  is the number of body parts. Importantly, this transformation allows to apply the CSP algorithm to each one of the three binary problems and to obtain signals that are optimally discriminative with respect to variance. The obtained results show that this simplification is convenient, and they confirm that characterizing a multilabel task as the superposition of the involved sources represents a plausible model. In particular, for subjects that were able to modulate their brain activity very efficiently, we could verify neurophysiological plausibility. In such cases, a multilabel approach represents a very interesting solution to control more robust systems.

The main novelty in our study is the development of an 8-class multilabel paradigm, and its simplification based on the separation of sources. In the following, we describe the experimental paradigm of an 8-class multilabel paradigm combining right hand, left hand, and feet MIs. In section 3, we first present the theoretical framework for the feature extraction based on the CSP algorithm and we introduce the two new multilabel approaches. The first one of these methods, namely MC2CMI, generates three binary problems in which all MIs engaging one of the three selected body parts are grouped together in one class, and all MIs that do not engage the same body part are grouped together in the second class. In this way, for each binary problem the CSP algorithm produces features for determining if the given body part is engaged in the task or not. The second method, namely MC2SMI, operates in a very similar way, with the only difference that any of the combined MIs is considered during the training phase, which drastically

accelerates the calibration time. In addition, we describe the classic multiclass methods named PW and OVA. In section 4, we show that both multilabel approaches outperform the classic solutions.

## 2. MATERIALS

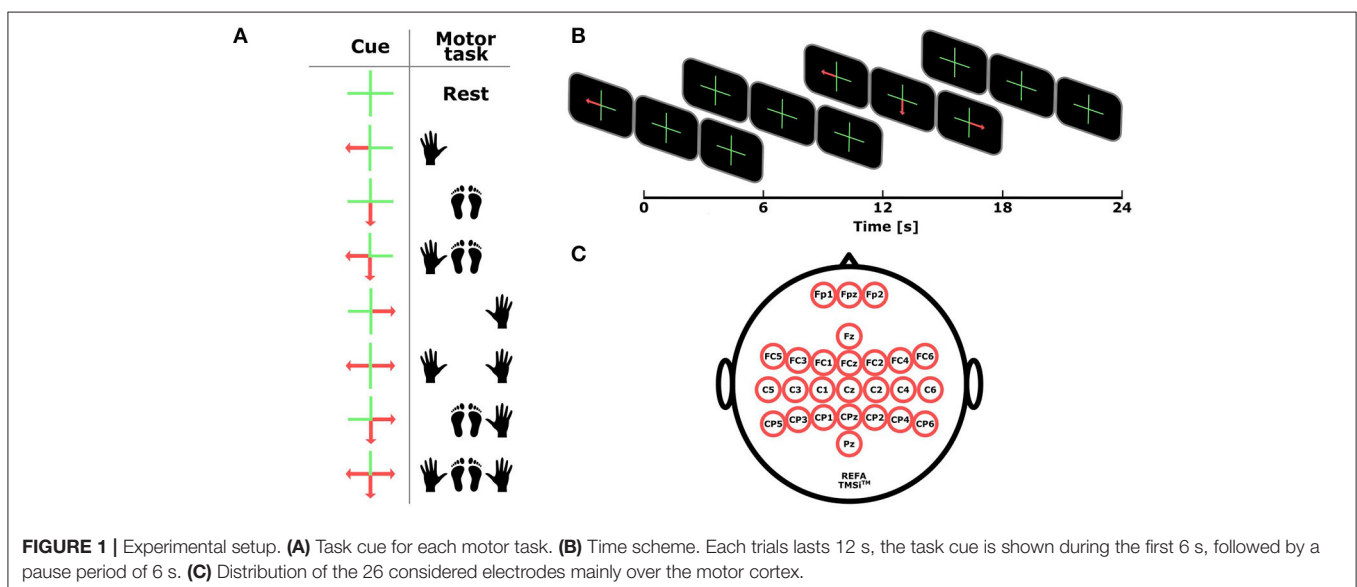
### 2.1. Participants

Seven right-handed healthy subjects (2 females, aged  $31.8 \pm 8.7$  years) were recruited for this study. Subjects had no medical history that could have influenced the task (i.e., diabetes, antidepressant treatment, or neurological disorders). The experiment followed the statements of the WMA declaration of Helsinki on ethical principles for medical research involving human subjects World Medical Association (2002) and has been approved by the local ethical committee of Inria (COERLE, approval number: 2016-011/01) as it satisfied the ethical rules and principles of the institute.

### 2.2. Experimental Paradigm

Subjects were seated in a comfortable chair with the arms at their sides in front of a screen showing the task cue to be performed, which consisted of one of the eight mental states that it is possible to generate with all the combinations including the right hand, left hand, and both feet together, i.e., rest, left hand, feet, left hand and feet, right hand, both hands, right hand and feet, and both hands and feet (see **Figure 1A**). Subjects were instructed to imagine the opening/closing of their hands (with special attention over the thumbs due to the long distance between the feet and opposite thumb motor regions), and to imagine a fast up/down movement of their feet.

The whole session consisted of four runs, containing each one 10 trials per task for a total of 40 trials per class (320 trials considering the eight classes). For stimulus presentation, we used three panels that were simultaneously displayed on the screen, each of which was associated from left to right, to the left hand,



feet, and right hand (see **Figure 1B**). Each trial was randomly presented and lasted for 12 s, starting at second “0” with a cross at the center of each panel and an overlaid arrow indicating for the next 6 s the motor task to be performed: an arrow pointing to the left side on the left panel for left hand, an arrow pointing down on the central panel for feet, an arrow pointing to the right side on the right panel for right hand, and the simultaneous presentation of these arrows for the corresponding combined MIs. The rest condition was indicated by the absence of arrows. After second 6, the task cue disappeared and the crosses were remaining for the next 6 s indicating the pause period before the next trial started.

## 2.3. EEG Recording

EEG signals were recorded at 256 Hz using a commercial amplifier Refa developed by TMS International™. Both the signal acquisition and the stimulation process were implemented on the OpenViBE platform<sup>1</sup> (Renard et al., 2010). The EEG cap was fitted with 26 electrodes, namely, Fp1, Fpz, Fp2, Fz, FC5, FC3, FC1, FCz, FC2, FC4, FC6, C5, C3, C1, Cz, C2, C4, C6, CP5, CP3, CP1, CPz, CP2, CP4, CP6, and Pz, re-referenced with respect to the common average reference across all channels and located over the extended international 10–20 system positions to cover the primary sensorimotor cortex (see **Figure 1C**). Signals were band-pass filtered within the frequency range (8–30 Hz) using a fifth-order Butterworth filter.

## 3. METHODS

In our experiment, we have focused on the activity generated by the left hand, right hand, and feet MIs. Thus, subjects activity is expected to be observed over three main regions. For the left hand, the corresponding source is located on the right hemisphere around electrode C4, whereas the right hand activates regions in the opposite side around electrode C3. In the case of the feet, both the left and right foot meet over central regions located around electrode Cz (see **Figure 1**). The following subsections present our framework for feature extraction based on the characterization of the brain activity over each one of these regions.

### 3.1. Feature Extraction

As a result of the volume conduction, EEG signals generate a rather noisy image of brain activity, which results in a poor classification performance that worsens as the number of classes increases. In consequence, spatial filters are particularly effective to recover the significant information that is dispersed over different channels, and thus to generate discriminative features. This kind of filters can be fixed beforehand considering the sensor geometry and neurophysiological insights (e.g., Laplacians, bipolar) (Wolpaw and McFarland, 2004), or they can be optimized by using subject-specific training data (Guger et al., 2000; Blankertz et al., 2007, 2008a). Such is the case of the CSP method, a very popular algorithm in BCI research (Koles et al., 1990; Blankertz et al., 2008b; Lotte, 2014).

<sup>1</sup><http://openvibe.inria.fr>

#### 3.1.1. Spatial Filtering: CSP Algorithm

The CSP algorithm is one of the most popular and efficient approaches for analyzing oscillatory activity (Koles et al., 1990; Blankertz et al., 2008b). Basically, the CSP algorithm generates a series of spatial filters that decompose multidimensional data into a set of uncorrelated components. These filters aim at extracting elements that simultaneously maximize the variance of one class, while minimizing the variance of the other one (Ramoser et al., 2001). Since the variance of band-pass filtered signals corresponds to band-power, this approach produces band power features with values that are maximally different between classes. This way the CSP algorithm achieves an efficient discrimination of mental states that are introduced by ERD/ERS activity (Pfurtscheller and Lopes da Silva, 1999).

Let us consider the mean of the normalized covariance matrices  $\bar{\Sigma}_k$  of the  $N$  successive training trials for each class  $k$  as:

$$\bar{\Sigma}_k = \frac{1}{N} \sum_{i=1}^N \frac{\mathbf{E}_{k,i} \mathbf{E}_{k,i}^\top}{\text{trace}(\mathbf{E}_{k,i} \mathbf{E}_{k,i}^\top)}, \quad (1)$$

where  $\mathbf{E}_{k,i} \in \mathbb{R}^{C \times T}$ ,  $k \in \{1, 2\}$  denotes the  $i$ th EEG trial belonging to class  $k$  recorded over  $C$  channels and  $T$  samples, with  $\top$  representing the transpose operator. The spatial filters  $\mathbf{W}$  can be obtained by solving the generalized eigenvalue decomposition problem that simultaneously diagonalize the mean covariance matrices of both classes

$$\bar{\Sigma}_1 \mathbf{W} = \Lambda \bar{\Sigma}_2 \mathbf{W}, \quad (2)$$

where  $\Lambda$  represents the diagonal matrix of eigenvalues for  $\bar{\Sigma}_1$ . The spatial filtered signal  $Y_{k,i}$  can be obtained from the EEG trials  $E_{k,i}$  as:

$$Y_{k,i} = \mathbf{W}^\top \mathbf{E}_{k,i}. \quad (3)$$

There are as many CSP filters as channels in the EEG signal, and each one of them is represented by a column vector of  $\mathbf{W}$ . These filters are paired and not all of them are relevant for discrimination. Thus, after sorting all  $\lambda$  values, only the first  $m$  and the last  $m$  columns of  $\mathbf{W}$  are selected. In the present work, for all methods and subjects  $m = 3$  pairs of filters were considered (Blankertz et al., 2008b).

#### 3.1.2. Features

The selected feature vectors  $\mathbf{v}_i$  generate the spatial filters coefficient matrix  $\tilde{\mathbf{W}}$ , from which the  $m$  pairs of CSP features of the  $i$ th trial for the band-pass filtered EEG measurements can be computed as

$$\mathbf{v}_i = \log \left( \frac{\text{diag}(\tilde{\mathbf{W}}^\top \mathbf{E}_i \mathbf{E}_i^\top \tilde{\mathbf{W}})}{\text{trace}(\tilde{\mathbf{W}}^\top \mathbf{E}_i \mathbf{E}_i^\top \tilde{\mathbf{W}})} \right). \quad (4)$$

## 3.2. Multilabel Approaches

### 3.2.1. MC2CMI

The 8-class classifier trained on multilabel CSP features obtained from combined MIs (MC2CMI) method, as illustrated in **Figure 2**, simplifies the original 8-class problem by transforming

it into a set of 3 binary problems, each one concerning one of the activity sources associated with the body parts included in the paradigm (i.e., left hand, right hand, and feet), to determine whether they are engaged in an MI or not. During the training, the band-pass filtered EEG trials of the training data set are separated by grouping together all MIs including one specific body part in one class (hereinafter referred to as class 1), and all MIs that do not include it in the second class (class 2). Thus, the 2 classes are arranged for each binary problem as follows:

- (i) Left hand:
  - Class 1: left hand, left hand and feet, both hands, and both hands and feet;
  - Class 2: rest, feet, right hand, right hand, and feet.
- (ii) Feet:
  - Class 1: feet, left hand and feet, right hand and feet, and both hands and feet;
  - Class 2: rest, left hand, right hand, both hands.
- (iii) Right hand:
  - Class 1: right hand, both hands, right hand and feet, and both hands and feet;
  - Class 2: rest, left hand, feet, left hand, and feet.

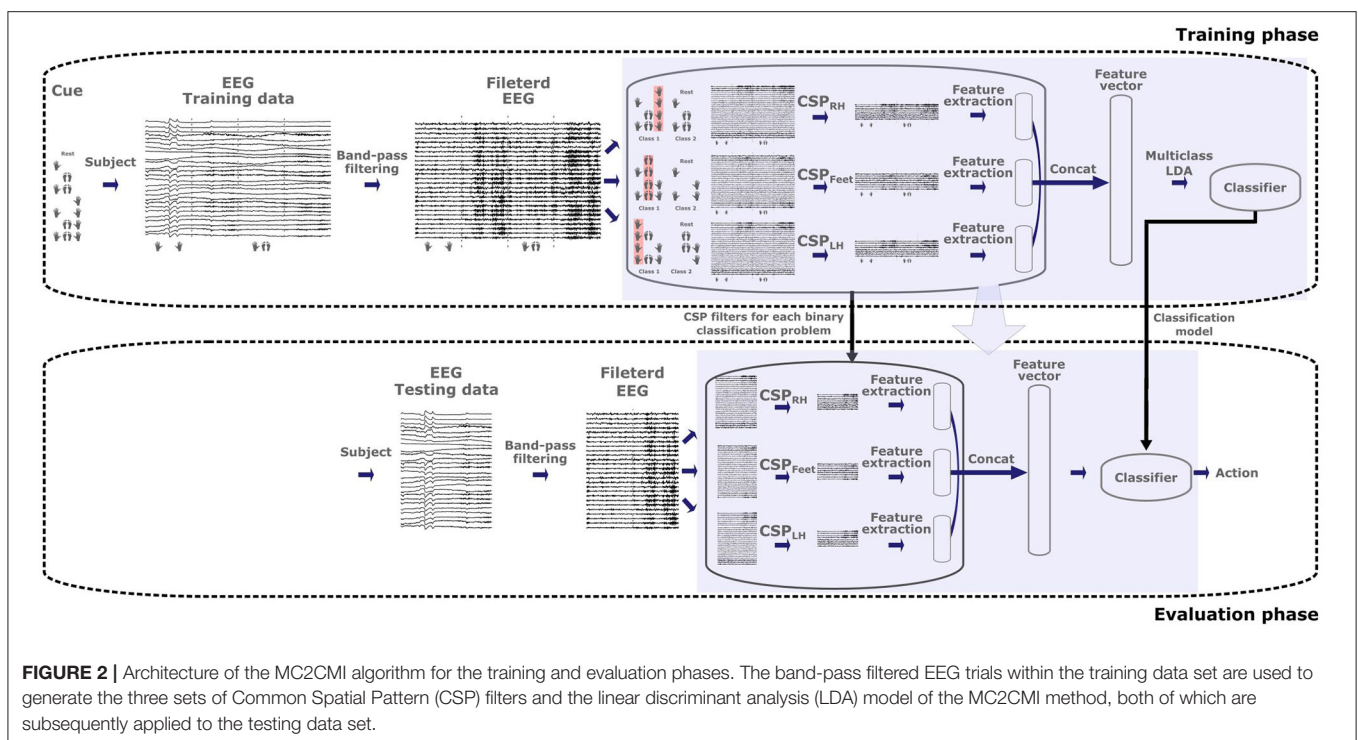
In this way, the CSP method can be applied directly to each one of the binary problems (see section 3.1.1). As mentioned, only three pairs of CSP filters are considered, and thus each binary problem generates features within a 6-dimensional space. All these features are subsequently concatenated together to generate the final feature vectors defined in an 18-dimensional space, where an 8-class linear discriminant analysis (LDA) model is

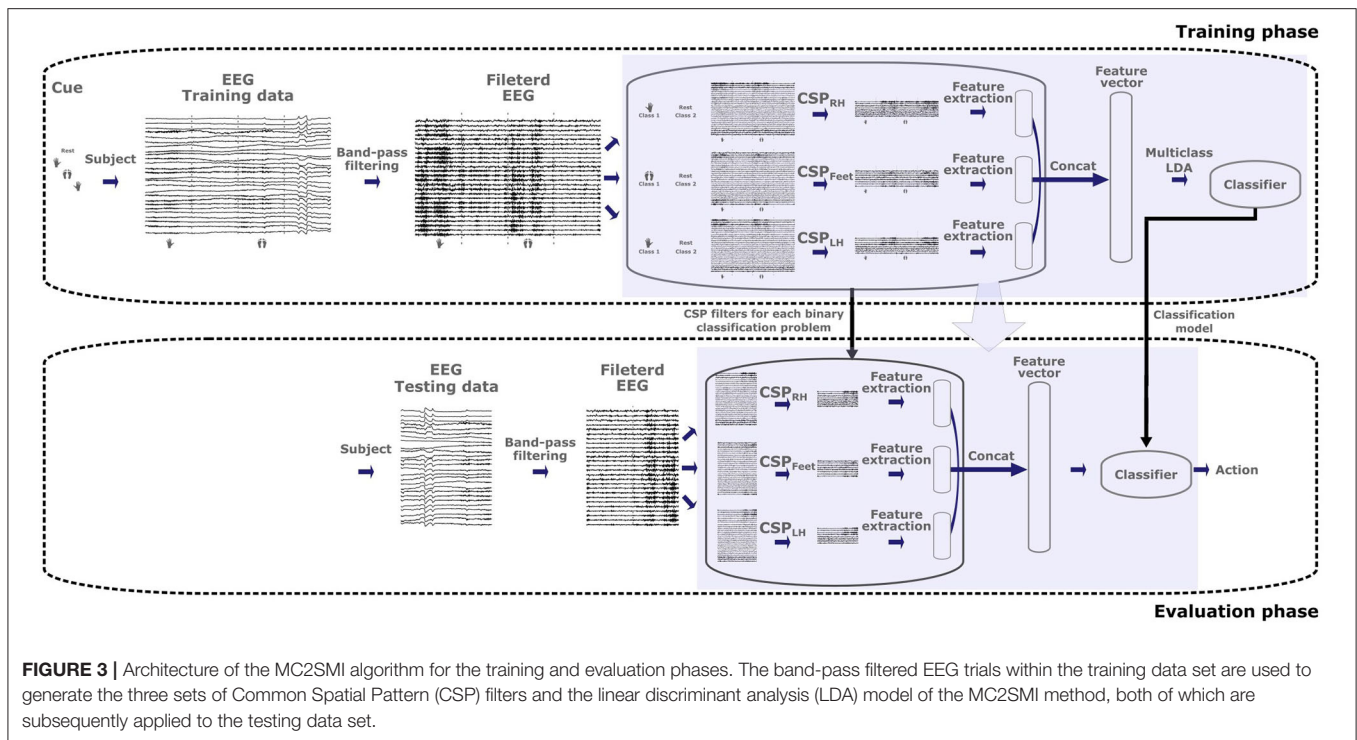
trained over the eight classes. Finally, during the validation phase, the band-pass filtered EEG trials of the testing data set are mapped into the classification space in order to predict the corresponding class labels.

### 3.2.2. MC2SMI

One simple question that we address is whether it is possible to train the classification model by using training data only from single MIs, which would considerably reduce the calibration time of the system. Contrarily to the classic multiclass extensions, the multilabel approaches allow to infer the features for combined MIs from the superposition of features extracted independently over each source during single MIs. In the case of combined MIs, the feature vectors can be generated by adding the features obtained from the rest condition over sources that are not engaged in the motor task, and by adding the features obtained from single MIs of the body part(s) that is/are engaged in the task. In this way, we have evaluated a second version in which only single MIs are considered during the training phase, namely *8-class classifier trained on multilabel CSP features obtained from single MIs* (MC2SI) approach (see Figure 3). To this end, we make the assumption that combined MIs can be modeled as the superposition of the activity generated by each one of the involved body parts. Thus, during the training phase, the two classes in each one of the three binary problems are rearranged as follows:

- (i) Left hand:
  - Class 1: left hand;
  - Class 2: rest.
- (ii) Feet:





- Class 1: feet;
- Class 2: rest.

(iii) Right hand:

- Class 1: right hand;
- Class 2: rest.

As before, we consider the three most discriminant pairs of CSP filters by applying Equation (4), which produces features over six dimensions for each one of the three binary problems. In the same way, these features are subsequently concatenated into vectors over 18 dimensions to train an 8-class LDA model. Finally, the band-pass filtered EEG trials of the testing data set are mapped into the classification space in order to predict the corresponding class labels.

### 3.3. Classical Multiclass Methods

In order to compare the performance of the MC2SMI method to classic solutions, we also include the results obtained by the PW and OVA approaches.

#### 3.3.1. PW Approach

This approach consists of training  $K(K - 1)/2$  binary classifiers for a  $K$ -multiclass problem. Each one of these binary classifiers is trained over the data points from a pair of classes in the original training set, and must learn to separate the two classes. For label prediction, all the  $K(K - 1)/2$  classifiers are applied to the unknown data point, and the label is assigned by following a voting scheme where the class that got the highest number of predictions is selected (Bishop, 2006).

Considering the eight different MIs included in the paradigm, the PW approach requires  $8*7/2 = 28$  binary classifiers, each of which is trained over features defined in a 6-dimensional space corresponding to the projection of the first three pairs of CSP filters obtained by the discrimination of two different MIs.

#### 3.3.2. OVA Approach

This strategy involves training  $K$  binary classifiers for a  $K$ -multiclass problem. Each binary classifier is trained over all data points in the original training set, with the samples of the  $K_i$  class as positive samples and all other samples as negatives. This approach requires all  $K$  binary classifiers to generate a real-valued confidence score to make a decision, rather than just a class label, considering that class labels alone can lead to ambiguities, where multiple classes are predicted for a single data point. Even though this strategy is popular, it suffers from several problems. First, the scale of the confidence values may differ between the binary classifiers. Second, even if the class distribution is balanced in the training set, the binary classification learners see unbalanced distributions because typically the set of negatives they see is much larger than the set of positives (Bishop, 2006).

Considering the eight different MIs included in the paradigm, the OVA approach requires eight binary classifiers, each of which is trained over features defined in a 6-dimensional space corresponding to the projection of the first three pairs of CSP filters obtained by the discrimination of 1 MI against all the remaining ones.

### 3.4. Classification

After feature extraction, we have applied for all methods an LDA model fitted on the feature vectors and the corresponding

training labels. The model assumes that the feature vectors present a Gaussian mixture distribution and that all classes have the same covariance matrix. The predicted label is then assigned according to the class that generates the minimum expected classification cost. We have applied a Box's M test to verify for equality of the covariance matrices, and even though it failed in some cases, we obtained better results than when using quadratic discriminant analysis (QDA), which allows the variation of the class covariance matrices. In this regard, QDA requires more parameters than LDA, i.e., the covariance matrices of all classes, which considerably increases the method variance. On the other hand, the assumption that all classes in our problem share a common covariance matrix does not cause an important bias.

The MC2CMI and MC2SMI methods concatenate the features that are generated by each one of the CSP modules, which allows using a single multiclass classification model. In contrast, the PW and OVA approaches use an LDA model for each one of the binary problems that are generated to solve the 8-class problem, i.e., 28 in the case of the PW method, and 8 for the OVA approach. In both cases, after evaluating all the binary classifications, the predicted label is assigned according to a vote scheme where the class summing the highest score is selected.

There are many classification techniques that can be applied in combination with the proposed methods. However, considering that both the MC2CMI and MC2SMI approaches consist of feature extraction methods for EEG combined MIs, we selected a simple classification model to evaluate the discriminative power of the generated features. In this way, the overall performance does not rely on the selection of multiple parameters when using more sophisticated classification techniques, which is out of the scope of this work.

## 4. RESULTS

In our study, we investigated the possibility of decoding EEG signals recorded during motor tasks combining three body parts, i.e., left hand, right hand, and feet. We recorded seven subjects in a series of trials during which they had to generate the eight possible different mental states considering the imagined movement of these three body parts, i.e., rest, left hand, feet, left hand and feet, right hand, both hands, right hand and feet, and both hands and feet (see section 2.2). The research question in our study is to determine whether the ERD patterns in the EEG signals associated with one particular region remain consistent regardless the activation of other sources. To this end, we generated three binary problems in which the EEG signals were grouped into two classes: (i) all MIs including 1 of the 3 body parts in one class, and all the MIs that do not include it in the other class, for the CM2CMI method, and (ii) a single MI in one class, and the resting state in the other class, for the CM2SMI method.

### 4.1. ERD/ERS Modulations

**Figure 4** shows a schematic view of these arrangements (on the right side) and the resulting ERD/ERS% fluctuations over the main sources associated with each body part (on the left side) (see **Supplementary Figure 1** for a complete topographic view

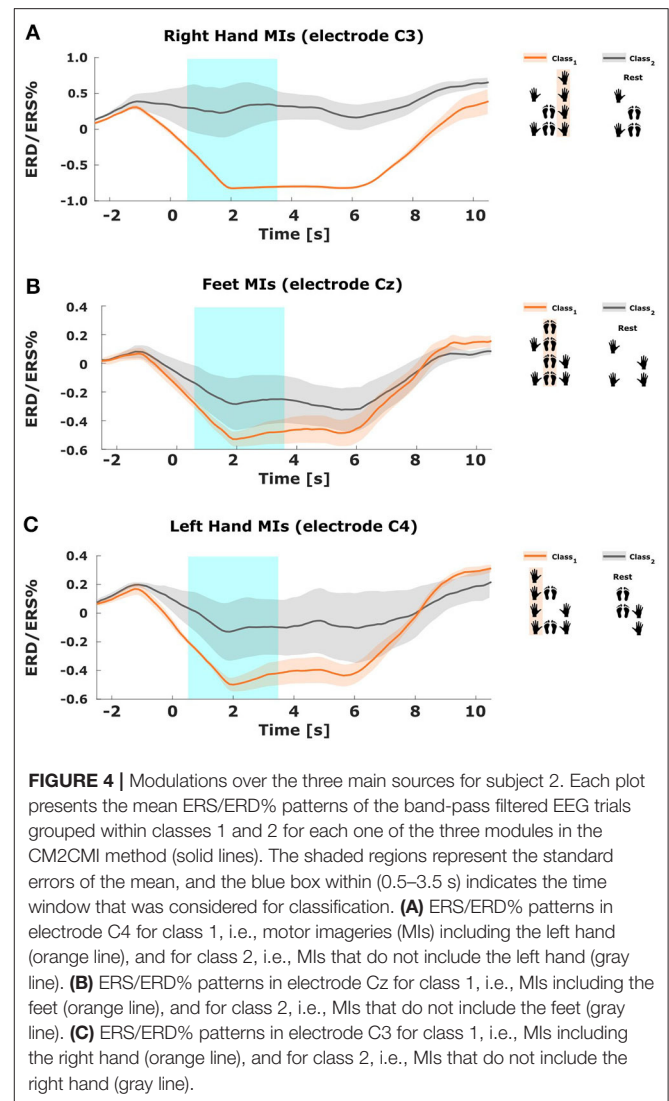


**FIGURE 4** | Modulations over the three main sources for subject 2. Each plot presents the mean ERS/ERD% patterns of the band-pass filtered EEG trials grouped within classes 1 and 2 for each one of the three modules in the CM2CMI method (solid lines). The shaded regions represent the standard errors of the mean, and the blue box within (0.5–3.5 s) indicates the time window that was considered for classification. **(A)** ERS/ERD% patterns in electrode C4 for class 1, i.e., motor imageries (MIs) including the left hand (orange line), and for class 2, i.e., MIs that do not include the left hand (gray line). **(B)** ERS/ERD% patterns in electrode Cz for class 1, i.e., MIs including the feet (orange line), and for class 2, i.e., MIs that do not include the feet (gray line). **(C)** ERS/ERD% patterns in electrode C3 for class 1, i.e., MIs including the right hand (orange line), and for class 2, i.e., MIs that do not include the right hand (gray line).

across all subjects). In all cases, we observe the well-known ERD pattern over contralateral sources during an MI of the associated body part (orange lines). Furthermore, the variation caused by the activation of other sources during combined MIs remains low. In contrast, the modulations associated with MIs excluding the same body part (gray lines) present much higher values (ERS modulation). And as expected, considering that the elements within these groups are different combinations of MIs without a consistent pattern, the variations among the mean values are also stronger (see **Supplementary Figures 2, 7** for other subjects).

From analyzing **Figure 4**, we found that a 3-s window starting 0.5 s after the cue was a convenient choice to find accentuated ERD patterns for all subjects. Therefore, we selected this period to train the CSP modules applied by the MC2CMI and the MC2SMI methods. Considering that the CSP filters generate subject-specific patterns, each method was trained independently for each subject. The mean covariance matrices  $\bar{\Sigma}_1$  and  $\bar{\Sigma}_2$  in Equation (2) are computed, respectively, by averaging the

covariance matrices of classes 1 and 2 for each one of the three CSP modules, i.e., RH (right hand), FEET (feet), and LH (left hand). **Figure 5** presents an example of the CSP analysis for each one of the three CSP modules of the MC2CMI method applied on data from subject 1. The topographic maps on top show the interpolation across all electrodes of the ERD/ERS% mean values for both classes. The smallest values shown in blue emerge again over the expected regions. Accordingly, we find correspondence of such neurophysiological insights when visualizing the CSP filter coefficients and their associated patterns (topographies below). In each case, we present two pairs of vectors ( $w_j, a_j$ ) corresponding to the largest and the smallest eigenvalues, where  $w_j$  and  $a_j$  represent the  $j$ th columns of  $W$  and  $A = W^{-1}$ , respectively (see section 3.1.1). On the other hand, the corresponding patterns show how the activity from different sources is projected onto the scalp, which can be used to verify the neurophysiological plausibility when finding strong weights over the corresponding motor cortex areas, as stated in the literature (Pfurtscheller and Neuper, 2001).

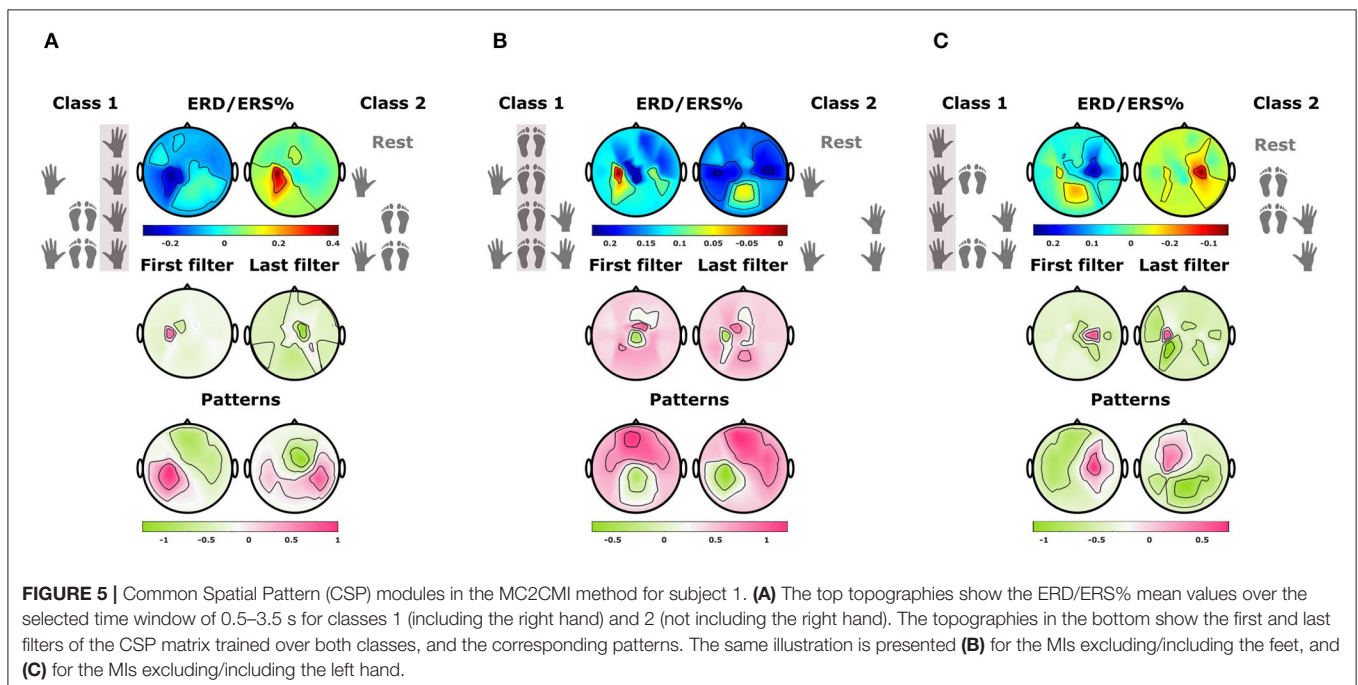
The CSP filters project the band-passed filtered EEG data in order to generate signals that are optimally discriminative with respect to their variance. The effect of the CSP filters over the band-passed filtered EEG data of subject 2 when applying the MC2CMI method is shown in **Figure 6**. Here, we can observe the CSP projections using the largest and the smallest eigenvalues generated by each one of the three CSP modules of the MC2CMI method over a segment during which the subject performed each one of the eight MIs consecutively. In each module, there is a strong contrast in the variance among segments during which the corresponding body part is engaged in the motor task, and segments during which it is not engaged. Those intervals during which the specific body part is engaged in the task are

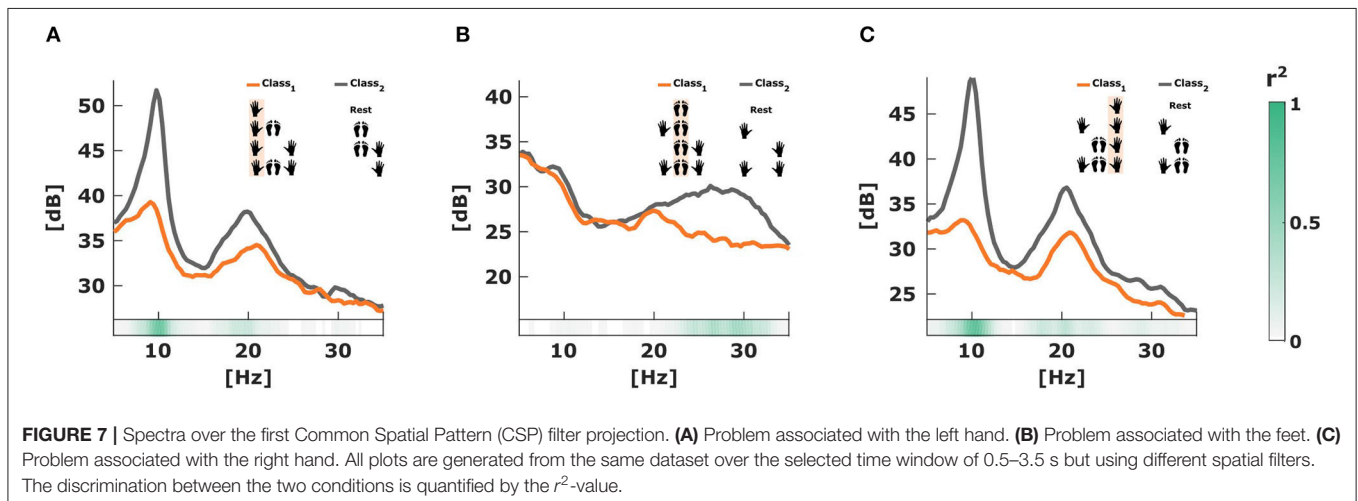
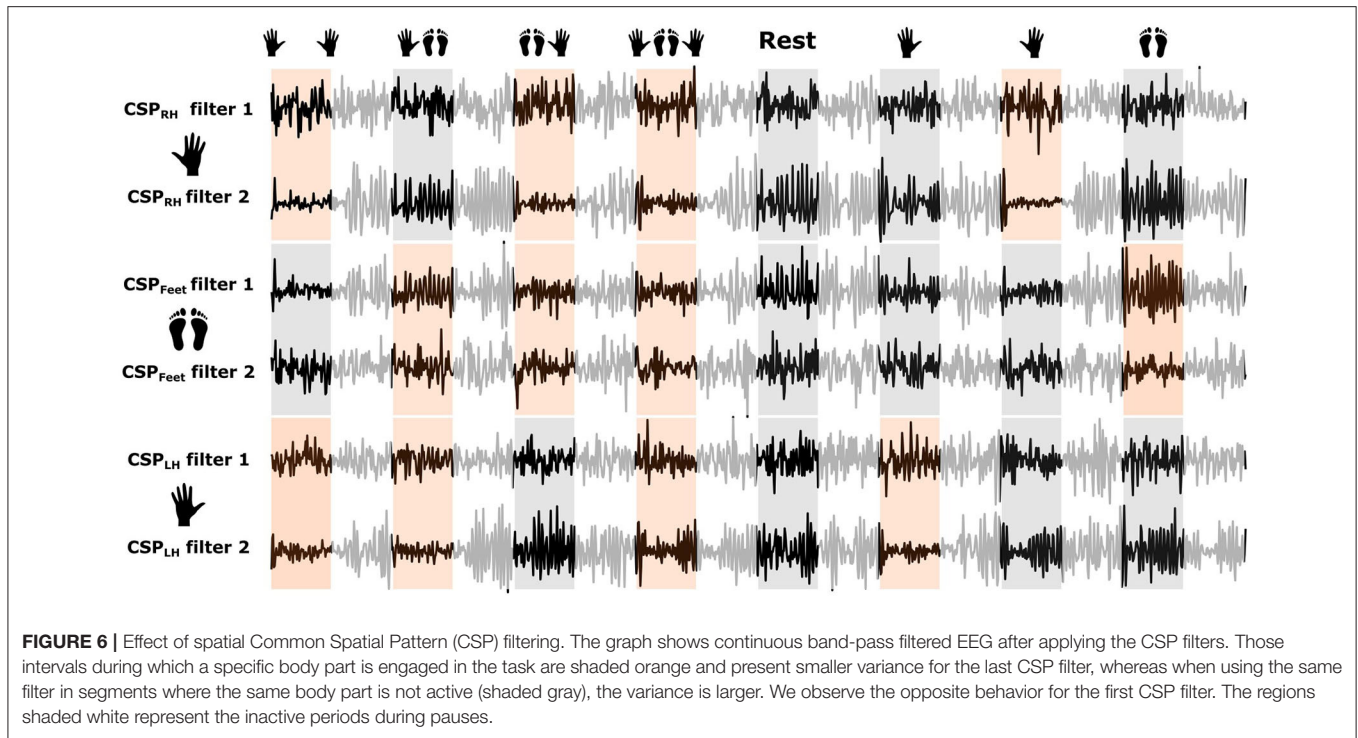
shaded orange and present smaller variance along the last filter, whereas when using the same filter in segments where the same body part is not active (shaded gray), the variance is larger. Furthermore, in projections using the first filter we observe the opposite behavior, i.e., the variance is smaller along segments during which the specific body part is not used, and larger when the same body part is engaged. These changes in variance are optimal for discriminating mental states that are introduced by ERD/ERS activity. To verify the discriminative power of these projections, we have analyzed the power spectra of both classes in the frequency domain (see **Figure 7**), where we found spectral peaks around 12 Hz revealing a strong discriminative power.

## 4.2. Spectral Analysis

The changes in variance among the two classes characterize the ERD/ERS modulation observed during motor tasks, which can be used to generate effective features for discrimination. To quantify the discriminative power of the projected signals, we can analyze the two classes in the frequency domain. In **Figure 7**, we present a comparison between the spectra of the first CSP filter projections of both classes for each one of the three CSP modules in the MC2CMI method for subject 2. The difference in amplitude showing much lower values over those signals including a specific body part (orange lines), from those that do not include it (gray lines), demonstrates the discriminative power of the CSP filtering effect, which can be measured in terms of the  $r^2$  value (green color bars shown below).

**Figure 8** shows an example of the features generated by each one of the three CSP modules in the MC2CMI method after applying Equation (4) using the first pair of CSP filters over data from subject 2. For visualization purposes, we show the results of using only the first pair of CSP filters, considering that, as





mentioned in section 3.2.1, we used three pairs of filters to extract the CSP features in each module, so that each feature vector was defined within an 18-dimensional space after concatenating all components from all three binary problems. Note that the separability between both classes in the classification space is significant, specially for the problems associated with the left hand (Figure 8A) and the right hand (Figure 8C).

We used a 10-fold cross-validation scheme to evaluate the performance of each method. During each one of the 10 evaluations, four trials per class were randomly selected (without replacement) to build the testing set (32 trials in total), whereas the 36 remaining trials were used to generate

the training set (288 trials in total). We used the same data partition to evaluate all methods to provide a fair comparison. The reached mean accuracy across subjects together with the standard error of the mean is presented in Table 1. In order to compare the performance of the MC2CMI and MC2SMI methods to the classic solutions, we also include the results obtained by the PW and OVA approaches. All methods were applied over the same band-pass filtered EEG data to provide a fair comparison. In addition to LDA, we have also applied support vector machines (SVMs) and decision trees for classification. Results using the MC2CMI method are superior than when using the classic approaches, however they do not

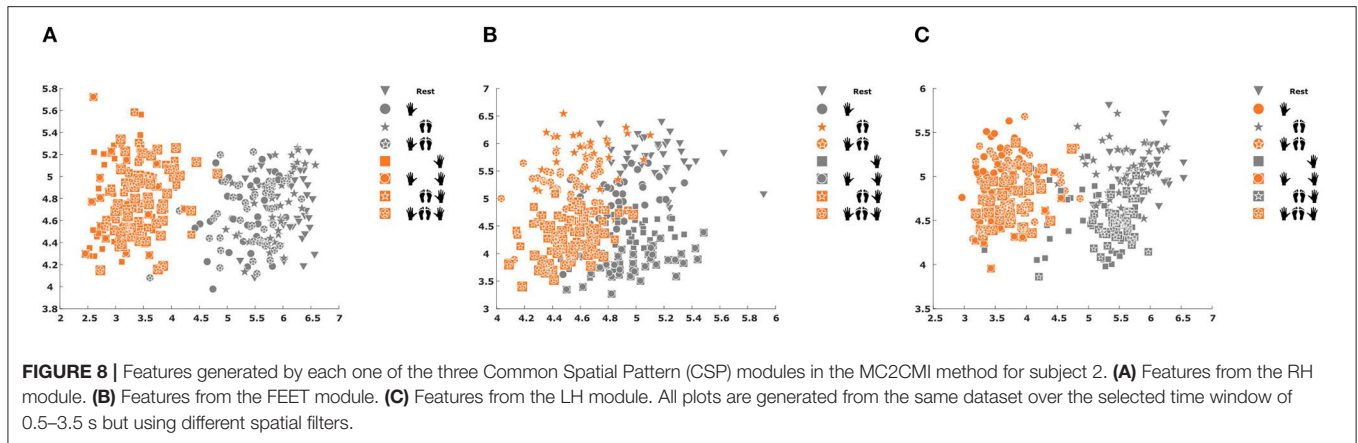


**FIGURE 8** | Features generated by each one of the three Common Spatial Pattern (CSP) modules in the MC2CMI method for subject 2. **(A)** Features from the RH module. **(B)** Features from the FEET module. **(C)** Features from the LH module. All plots are generated from the same dataset over the selected time window of 0.5–3.5 s but using different spatial filters.

**TABLE 1** | Classification accuracies.

Subject	MC2CMI	MC2SMI	PW	OVA
1	<b>51.25</b>	45.83	41.67	33.75
2	<b>82.81</b>	75.31	78.75	67.5
3	47.81	<b>51.88</b>	45.94	46.56
4	34.06	<b>39.38</b>	30.94	31.88
5	<b>47.81</b>	43.44	37.81	35.94
6	<b>55.63</b>	52.19	55.31	49.38
7	<b>65.63</b>	63.44	61.56	58.75
AVG	<b>55 ± 5.86%</b>	53.06 ± 4.72%	50.28 ± 6.14%	46.25 ± 5.09%

Performance across all subjects after applying a 10-fold cross-validation procedure to assess the MC2CMI, together with the fast training version denoted as MC2SMI that was considered to optimize calibration times by training only over single MIs. We also present the results generated by the PW and the OVA approaches. All methods were applied over the same band-pass filtered EEG data to provide a fair comparison. The mean average across subjects is presented together with the standard error of the mean. For each subject, the best result is indicated by bold characters.

outperform the accuracy reached by LDA classification, and in both cases further parameter optimization must be investigated. The results of using SVMs with linear kernel, and the results of using decision trees to evaluate all methods are shown in **Supplementary Tables 1, 2**, respectively.

**Table 2** shows the  $p$ -values generated after applying a Wilcoxon rank sum test to verify that the results generated by each one of the presented methods are significantly different. As expected, in the case of the MC2CMI and MC2SMI approaches we do not find a significant difference, considering that the MC2SMI approach is only a simplification of the MC2CMI method. On the contrary, we found a strong evidence supporting that MC2CMI method is significantly different with respect to the PW and OVA approaches. In order to confirm that this difference represents an improvement on the classification task, we present the mean receiver operating characteristic (ROC) curves across subjects for each one of the eight classes generated after applying each method (see **Figure 9**). Note that, for multiclass problems, this analysis can be performed using a pairwise comparison, i.e., one class vs. all other classes (Hand and Till, 2001). Again for

**TABLE 2** |  $p$ -Values after applying a Wilcoxon rank sum test to verify differences between independent groups.

	MC2CMI	MC2SMI	PW	OVA
MC2CMI		$p = 0.23$	$p = 0.003$	$p = 3.05e^{-8}$
MC2SMI			$p = 0.07$	$p = 1.35e^{-5}$
PW				$p = 0.011$

all classes, the MC2CMI and MC2SMI generate a larger area under the curve (AUC), which reveals a better performance in comparison to the classic approaches (see **Table 3**).

The MC2CMI method performed very efficiently and it reached an accuracy of 82.81% for subject 2. Furthermore, it outperforms both the PW and OVA methods by around 5 and 9%, respectively, achieving a higher accuracy for all subjects (see **Table 1**). In the same way, the MC2SMI method outperforms the PW and OVA methods for all subjects, which is of special interest considering that it does not require patterns of combined MIs to train the multiclass classifier.

These results are quite promising considering that most of the classifications scores are significant and higher than the chance level. According to Müller-Putz et al. (2008), Combrisson and Jerbi (2015), and Jeunet et al. (2018), and considering that we have eight different classes each comprising 40 trials, the chance level would be to 22.5%. Finally, it is worth mentioning that for our classification problem, the MC2CMI and MC2SMI approaches require only three feature extraction modules, in comparison to the 28 and eight modules required by the PW and OVA methods, respectively. In this regard, the proposed method not only outperforms the classic solutions, but also optimizes the classification process and reduces the calibration time.

## 5. DISCUSSION

In this study, we have investigated the use of combined MIs to provide EEG-based BCI interaction with an extended number of commands. Indeed, despite the benefits of such a framework, combined MIs have not been extensively studied and very little is

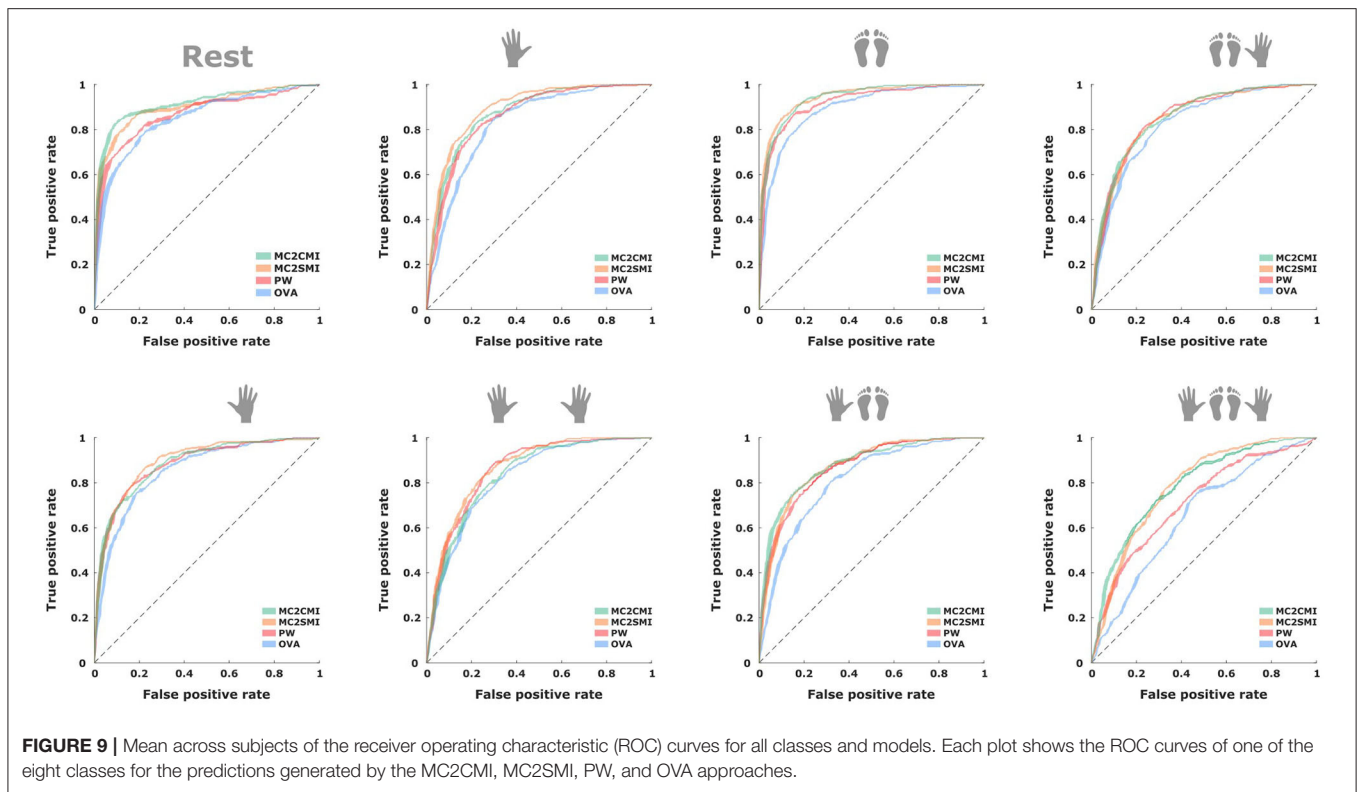


**FIGURE 9** | Mean across subjects of the receiver operating characteristic (ROC) curves for all classes and models. Each plot shows the ROC curves of one of the eight classes for the predictions generated by the MC2CMI, MC2SMI, PW, and OVA approaches.

**TABLE 3** | Area under the curve (AUC).

	MC2CMI	MC2SMI	PW	OVA
AUC	87.12 ± 2.34	<b>87.67 ± 2.28</b>	85.37 ± 2.99	81.8 ± 3.4

Average of the AUCs across the eight different classes and subjects with the corresponding error of the mean. The best result is indicated by bold characters.

known about their suitability for this purpose. To address this gap, we have designed a paradigm including of the left hand, right hand, and feet, which together with the rest condition provide eight different mental states, i.e., rest, left hand, feet, left hand and feet, right hand, both hands, right hand and feet, and all MIs. We have argued that the EEG activity elicited during combined MIs can be analyzed independently over the sources related to each one of the body parts included in the paradigm to subsequently predict the class label from the combination of the extracted information. With this idea, we have contributed with two new feature extraction approaches, namely MC2CMI and MC2SMI methods, which to our best knowledge have not been considered before.

## 5.1. Neurophysiological Specificities of Combined Motor Imageries

Analyzing the EEG activity elicited by each one of the body parts separately presents a very important advantage, considering that this simplifies the problem and reduces it into a set of binary decisions, which allows to apply the CSP algorithm for feature extraction. We have demonstrated that this approach is

plausible in a series of analyses in both the frequency and time domains. First, we have inspected the ERD/ERS modulations from the two classes considered by each one of the binary problems formulated by the MCM2CMI method (see **Figure 4**, and **Supplementary Figures 2–7** for all subjects). In all cases, there is a strong contrast between both classes given that the class grouping all mental states using one of the body parts produces oscillations with an increased desynchronization over the associated activity source. Crucially, this behavior remains relatively consistent among all MIs within each class, regardless the activity generated by other active sources during combined MIs. The topographic maps showing ERD/ERS values in **Figure 5** (top) (**Supplementary Figures 8–13** for more subjects) provide a complete view across all electrodes. Here, we can see how the brain activity is distributed over the region associated with the body part considered by each one of the three modules. This region appears in blue colors indicating small values (ERD%) for the class grouping all MIs using one of the body parts, and it appears in red colors indicating high values (ERS%) for the other class grouping all MIs that do not include the same body part. Accordingly, the CSP patterns associated with the largest eigenvalue presented below activate the same region in the brain. This provides evidence to verify neurophysiological plausibility, and it confirms that grouping all mental states within these two classes represents an effective solution. Considering that the strongest discriminative components correspond with the common source among combined MIs for one class, and a combination of the other two sources for the second class, as shown by the patterns associated with the smallest eigenvalue.

Interestingly, it was possible to train the system only with data from single MIs without a significant loss of performance. This not only reduces the calibration time and subjects' fatigue, but it also provides evidence to support our multilabel model, where the activity generated by a combined MI corresponds to the superposition of the activity generated by each one of the involved sources.

## 5.2. Difficulties to Produce (Combined) MIs

The question of whether the use of combined motor imageries is a suitable solution for EEG-based BCIs does not have a categorical answer, and this is because it totally depends on the subjects and their ability to modulate their brain waves during the different mental states. First of all, we have to consider that this task might be too complex to perform. In fact, there is evidence showing that even a single MI is generally difficult to achieve (Guillot et al., 2009; McAvinue and Robertson, 2009). Such complexity leads to highly variable MI-based BCI performances (Dickhaus et al., 2009; Vidaurre and Blankertz, 2010; Ahn et al., 2018; Thompson, 2019), and in some cases the control of this kind of systems is completely ineffective. In particular, the combination of MIs considerably increases the difficulty of the task, since it requires higher coordination and concentration (Jeunet et al., 2016). The results presented in **Table 1** show that some subjects (i.e., subject 4) had difficulties in producing suitable patterns for the different MIs. Conversely, when subjects manage to effectively modulate their brain activity (i.e., subject 4), complex solutions are highly recommended to gain control over multiple commands. In any case, multiclass paradigm represents a challenge that becomes more difficult as the number of classes increases. In this sense, it is important to design intuitive systems where the link between the mental commands and their associated label is not difficult to establish.

Interaction conditions, such as the usability of the BCI, feedback, and so on influence the performance of users, in particular by reducing their mental load (Grangeon et al., 2011; Di Rienzo et al., 2012; Talukdar et al., 2019). Subjects training becomes essential to improve the execution of combined MIs, and thus to achieve a good performance (Jeunet et al., 2016). An appropriate long-term training with efficient instruction and gradual difficulty (Lotte, 2012) is a promising way to improve multiclass BCI control. In addition, the emotional state can have a strong influence on EEG patterns. For instance, during the recording period subject 2 used to practice yoga and relaxation regularly. These activities have shown to improve BCI control (Cassady et al., 2014; Rimbart et al., 2019), which could have a greater impact on the classification performance than any other processing technique. Thus, if subjects achieve to modulate their brain oscillations and generate suitable patterns for classification, the multilabel approach represents a very appropriate solution to gain control over multiple commands.

## 5.3. Limitations and Future Work

In this study, we have validated all approaches using a database of seven healthy subjects, which represents a small sample size for rigorously evaluating the robustness of the presented methods. Moreover, even though two subjects reached an accuracy above

65%, the mean accuracy was rather poor, so it is still an open question whether this paradigm represents an effective solution to provide online control for a significant population. Therefore, a vast database of healthy subjects including a significant number of individuals that practice yoga and/or relaxation regularly must be investigated in future works.

## 6. CONCLUSION

This study contributes to enriching the limited knowledge of combined MIs to provide users with multiple commands for BCI interaction (Devlaminck et al., 2010; Meng et al., 2016). This approach has the advantage of considerably increasing the number of different brain states while using the same number of body parts (in order of  $2^k$  compared to  $k$ , where  $k$  is the number of body parts and when all possible combinations are considered). The most common approaches have focused on the left hand, right hand, and both hands (LaFleur et al., 2013; Lindig-León and Bougrain, 2015a,b). Here, we include a third source (i.e., feet), with which it is possible to obtain eight different mental states (i.e., rest, left hand, feet, left hand and feet, right hand, both hands, right hand and feet, and both hands and feet). In a similar study (Yi et al., 2013), the paradigm included the same three body parts. However, each foot was used separately together with the opposite hand during combined MIs, and the class involving all MIs (i.e., left hand, right hand, and feet) was not included.

The novelty in our study is also the analysis for feature extraction, which is carried out separately over each activity source related to the three body parts included in the paradigm. With this simplification, we have contributed with two new methods, namely MC2CMI and MC2SMI. Both approaches are multiclass uses of the CSP algorithm for multilabel problems. Both methods outperform the classic PW and OVA approaches. Moreover, in comparison to the 28 [i.e.,  $2^n(2^n - 1)/2$ , where  $n$  is the number of body parts], and 8 (i.e.,  $2^n$ ) classifiers required by the PW and OVA approaches, respectively, the multilabel methods require only 3 (i.e.,  $n$ ) feature extraction modules. Additionally, the MC2SMI is trained using data from only single MIs without a significant loss of performance, which considerably reduces the calibration time.

In general, subjects performance was low and only in a few cases results were satisfactory. In this regard, the inefficiency cannot be attributed to the feature extraction and/or classification methods. In fact, most of the subjects were not able to properly modulate their brain signals during the different motor tasks, so that features were not well-separated in the classification space. This problem requires special attention, considering that the plausibility of multilabel approaches might depend on the development of training strategies that are efficient in guiding subjects to generate suitable patterns for classification. If this modulation is appropriate and subjects generate discriminative signals, multilabel approaches represent a very interesting solution for designing systems with multiple commands to afford an intuitive and continuous interaction, such as for a full 3D control, which is of particular interest for the implementation of prosthetic devices.

## DATA AVAILABILITY STATEMENT

The raw data supporting the conclusions of this article will be made available by the authors, without undue reservation.

## ETHICS STATEMENT

The studies involving human participants were reviewed and approved by Local ethical committee of INRIA (COERLE, approval number: 2016-011/01). The patients/participants provided their written informed consent to participate in this study.

## AUTHOR CONTRIBUTIONS

CL-L and LB designed the experiment. CL-L and SR performed the experiments and analyzed the data. CL-L

designed the feature extraction methods. LB supervised the project. CL-L, SR, and LB wrote the paper. All authors contributed to the article and approved the submitted version.

## FUNDING

This research was partially funded by INRIA project-lab BCI-LIFT.

## SUPPLEMENTARY MATERIAL

The Supplementary Material for this article can be found online at: <https://www.frontiersin.org/articles/10.3389/fnins.2020.559858/full#supplementary-material>

## REFERENCES

- Ahn, M., Cho, H., Ahn, S., and Jun, C. S. (2018). User's self-prediction of performance in motor imagery brain-computer interface. *Front. Hum. Neurosci.* 12:59. doi: 10.3389/fnhum.2018.00059
- Bishop, C. M. (2006). *Pattern Recognition and Machine Learning (Information Science and Statistics)*. Berlin; Heidelberg: Springer-Verlag.
- Blankertz, B., Dornhege, G., Krauledat, M., Müller, K.-R., and Curio, G. (2007). The non-invasive berlin brain-computer interface: fast acquisition of effective performance in untrained subjects. *Neuroimage* 37, 539–550. doi: 10.1016/j.neuroimage.2007.01.051
- Blankertz, B., Losch, F., Krauledat, M., Dornhege, G., Curio, G., and Müller, K.-R. (2008a). The berlin brain-computer interface: accurate performance from first-session in bci-naive subjects. *IEEE Trans. Biomed. Eng.* 55, 2452–2462. doi: 10.1109/TBME.2008.923152
- Blankertz, B., Müller, K., Krusienski, D. J., Schalk, G., Wolpaw, J. R., Schlogl, A., et al. (2006). The BCI competition III: validating alternative approaches to actual BCI problems. *IEEE Trans. Neural Syst. Rehabil. Eng.* 14, 153–159. doi: 10.1109/TNSRE.2006.875642
- Blankertz, B., Tomioka, R., Lemm, S., Kawanabe, M., and Müller, K. (2008b). Optimizing spatial filters for robust eeg single-trial analysis. *IEEE Signal Process. Mag.* 25, 41–56. doi: 10.1109/MSP.2008.4408441
- Cassady, K., You, A., Doud, A., and He, B. (2014). The impact of mind-body awareness training on the early learning of a brain-computer interface. *Technology* 2, 254–260. doi: 10.1142/S233954781450023X
- Combrisson, E., and Jerbi, K. (2015). Exceeding chance level by chance: the caveat of theoretical chance levels in brain signal classification and statistical assessment of decoding accuracy. *J. Neurosci. Methods* 250, 126–136. doi: 10.1016/j.jneumeth.2015.01.010
- Devlamincq, D., Waegeman, W., Bauwens, B., Wyns, B., Santens, P., and Otte, G. (2010). "From circular ordinal regression to multilabel classification", in *Proceedings of the 2010 Workshop on Preference Learning, European Conference on Machine Learning*.
- Di Rienzo, F., Collet, C., Hoyek, N., and Guillot, A. (2012). Selective effect of physical fatigue on motor imagery accuracy. *PLoS ONE* 7:e47207. doi: 10.1371/journal.pone.0047207
- Dickhaus, T., Sannelli, C., Müller, K.-R., Curio, G., and Blankertz, B. (2009). Predicting BCI performance to study BCI illiteracy. *BMC Neurosci.* 10:P84. doi: 10.1186/1471-2202-10-S1-P84
- Grangeon, M., Guillot, A., and Collet, C. (2011). Postural control during visual and kinesthetic motor imagery. *Appl. Psychophysiol. Biofeedb.* 36, 47–56. doi: 10.1007/s10484-011-9145-2
- Guger, C., Ramoser, H., and Pfurtscheller, G. (2000). Real-time EEG analysis with subject-specific spatial patterns for a brain-computer interface (BCI). *IEEE Trans. Rehabil. Eng.* 8, 447–456. doi: 10.1109/86.895947
- Guillot, A., Collet, C., Nguyen, V. A., Malouin, F., Richards, C., and Doyon, J. (2009). Brain activity during visual versus kinesthetic imagery: an fMRI study. *Hum. Brain Mapp.* 30, 2157–2172. doi: 10.1002/hbm.20658
- Hand, D. J., and Till, R. J. (2001). A simple generalisation of the area under the roc curve for multiple class classification problems. *Mach. Learn.* 45, 171–186. doi: 10.1023/A:1010920819831
- Hari, R., and Salmelin, R. (1997). Human cortical oscillations: a neuromagnetic view through the skull. *Trends Neurosci.* 20, 44–49. doi: 10.1016/S0166-2236(96)10065-5
- Hétu, S., Gregoire, M., Saimpont, A., Coll, M.-P., Eugène, F., Michon, P.-E., et al. (2013). The neural network of motor imagery: an ALE meta-analysis. *Neurosci. Biobehav. Rev.* 37, 930–949. doi: 10.1016/j.neubiorev.2013.03.017
- Jäncke, L., Lutz, K., and Koeneke, S. (2006). Converging evidence of ERD/ERS and bold responses in motor control research. *Prog. Brain Res.* 159, 261–271. doi: 10.1016/S0079-6123(06)59018-1
- Jasper, H. H. (1936). Cortical excitatory state and variability in human brain rhythms. *Science* 83, 259–260. doi: 10.1126/science.83.2150.259
- Jeannerod, M. (1995). Mental imagery in the motor context. *Neuropsychologia* 33, 1419–1432. doi: 10.1016/0028-3932(95)00073-C
- Jeunet, C., Debener, S., Lotte, F., Mattout, J., Scherer, R., and Zich, C. (2018). "Mind the Traps! design guidelines for rigorous BCI experiments," in *Brain-computer Interfaces Handbook: Technological and Theoretical Advances*, eds C. S. Nam, A. Nijholt and F. Lotte (Boca Raton, FL: CRC Press Taylor & Francis Group), 613.
- Jeunet, C., Jahanpour, E., and Lotte, F. (2016). Why standard brain-computer interface (BCI) training protocols should be changed: an experimental study. *J. Neural Eng.* 13:036024. doi: 10.1088/1741-2560/13/3/036024
- Koles, Z. J., Lazaret, M. S., and Zhou, S. Z. (1990). Spatial patterns underlying population differences in the background EEG. *Brain Topogr.* 2, 275–284. doi: 10.1007/BF01129656
- LaFleur, K., Cassady, K., Doud, A., Shades, K., Rogin, E., and He, B. (2013). Quadcopter control in three-dimensional space using a noninvasive motor imagery-based brain-computer interface. *J. Neural Eng.* 10:046003. doi: 10.1088/1741-2560/10/4/046003
- Lindig-León, C., and Bougrain, L. (2015a). "Comparison of sensorimotor rhythms in EEG signals during simple and combined motor imageries over the contra and ipsilateral hemispheres," in *2015 37th Annual International Conference of the IEEE Engineering in Medicine and Biology Society (EMBC)* (Milan), 3953–3956. doi: 10.1109/EMBC.2015.7319259
- Lindig-León, C., and Bougrain, L. (2015b). "A multi-label classification method for detection of combined motor imageries," in *2015 IEEE International Conference on Systems, Man, and Cybernetics*, 3128–3133. doi: 10.1109/SMC.2015.543

- Lindig-León, C., Bougrain, L., and Rimbart, S. (2015). "Alpha rebound improves on-line detection of the end of motor imageries," in *IEEE EMBS Neural Engineering Conference* (Montpellier). doi: 10.1109/NER.2015.7146708
- Lotte, F. (2012). "On the need for alternative feedback training approaches for BCI," in *Berlin Brain-Computer Interface Workshop* (Berlin).
- Lotte, F. (2014). "A tutorial on EEG signal processing techniques for mental state recognition in brain-computer interfaces," in *Guide to Brain-Computer Music Interfacing*, eds E. R. Miranda and J. Castet (London: Springer), 5–17. doi: 10.1007/978-1-4471-6584-2\_7
- Lotte, F., Congedo, M., Lécuyer, A., and Fabrice, L. (2007). A review of classification algorithms for EEG-based brain-computer interfaces. *J. Neural Eng.* 4 R1–R13. doi: 10.1088/1741-2560/4/2/R01
- Mason, S. G., Kronegg, J., Huggins, J., Fatourech, M., and Schloegl, A. (2006). *Evaluating the Performance of Self-Paced BCI Technology*. Technical Report. Available online at: [http://www.bci-info.tugraz.at/Research\\_Info/documents/articles/self\\_paced\\_tech\\_report-2006-05-19.pdf](http://www.bci-info.tugraz.at/Research_Info/documents/articles/self_paced_tech_report-2006-05-19.pdf)
- McAvinue, L. P., and Robertson, I. H. (2009). Motor imagery: A multidimensional ability. *J. Mental Imagery* 33, 99–120.
- Meng, J., Zhang, S., Bekyo, A., Olsoe, J., Baxter, B., and He, B. (2016). Noninvasive electroencephalogram based control of a robotic arm for reach and grasp tasks. *Sci. Rep.* 6:38565. doi: 10.1038/srep38565
- Müller-Putz, G., Scherer, R., Brunner, C., Leeb, R., and Pfurtscheller, G. (2008). Better than random? A closer look on BCI results. *Int. J. Bioelektromagn.* 10, 52–55.
- Müller-Putz, G., Schwarz, A., Pereira, J., and Ofner, P. (2016). "From classic motor imagery to complex movement intention decoding: the noninvasive Graz-BCI approach," in *PBR: Brain-Computer Interfaces: Lab Experiments to Real-World Applications*, Vol. 228, ed D. Coyle (Amsterdam: Elsevier Inc.), 39–65.
- Neuper, C., and Pfurtscheller, G. (2001). Event-related dynamics of cortical rhythms: frequency-specific features and functional correlates. *Int. J. Psychophysiol.* 43, 41–58. doi: 10.1016/S0167-8760(01)00178-7
- Neuper, C., Scherer, R., Wriessnegger, S., and Pfurtscheller, G. (2009). Motor imagery and action observation: modulation of sensorimotor brain rhythms during mental control of a brain-computer interface. *Clin. Neurophysiol.* 120, 239–247. doi: 10.1016/j.clinph.2008.11.015
- Pfurtscheller, G. (2001). Functional brain imaging based on ERD/ERS. *Vision Res.* 41, 1257–1260. doi: 10.1016/S0042-6989(00)00235-2
- Pfurtscheller, G. (2003). Induced oscillations in the alpha band: functional meaning. *Epilepsia* 44, 2–8. doi: 10.1111/j.0013-9580.2003.12001.x
- Pfurtscheller, G., and Aranibar, A. (1979). Evaluation of event-related desynchronization (ERD) preceding and following voluntary self-paced movement. *Electroencephalogr. Clin. Neurophysiol.* 46, 138–146. doi: 10.1016/0013-4694(79)90063-4
- Pfurtscheller, G., and Lopes da Silva, F. H. (1999). Event-related EEG/MEG synchronization and desynchronization: basic principles. *Clin. Neurophysiol.* 110, 1842–1857. doi: 10.1016/S1388-2457(99)00141-8
- Pfurtscheller, G., and Neuper, C. (1997). Motor imagery activates primary sensorimotor area in humans. *Neurosci. Lett.* 239, 65–68. doi: 10.1016/S0304-3940(97)00889-6
- Pfurtscheller, G., and Neuper, C. (2001). Motor imagery and direct brain-computer communication. *Proc. IEEE* 89, 1123–1134. doi: 10.1109/5.939829
- Pfurtscheller, G., Neuper, C., and Kalcher, J. (1993). 40-Hz oscillations during motor behavior in man. *Neurosci. Lett.* 164, 179–182. doi: 10.1016/0304-3940(93)90886-P
- Ramoser, H., Müller-Gerking, J., and Pfurtscheller, G. (2001). Optimal spatial filtering of single trial EEG during imagined hand movement. *IEEE Trans. Rehabil. Eng.* 8, 441–446. doi: 10.1109/86.895946
- Renard, Y., Lotte, F., Gibert, G., Congedo, M., Maby, E., Delannoy, V., et al. (2010). OpenViBE: an open-source software platform to design, test and use brain-computer interfaces in real and virtual environments. *Presence Teleoper. Virtual Environ.* 19, 35–53. doi: 10.1162/pres.19.1.35
- Rimbart, S., Zaepffel, M., Riff, P., Adam, P., and Bougrain, L. (2019). Hypnotic state modulates sensorimotor beta rhythms during real movement and motor imagery. *Front. Psychol.* 10:2341. doi: 10.3389/fpsyg.2019.02341
- Royer, A. S., Doud, A. J., Rose, M., and He, B. (2013). (EEG) control of a virtual helicopter in 3-dimensiona space using intelligent control strategies. *J. Neuroeng. Rehabil.* 18, 581–589. doi: 10.1109/TNSRE.2010.2077654
- Suffczynski, P., Pjin, J., Pfurtscheller, G., and F. Lopes da Silva (1999). "Event-related dynamics of alpha band rhythms: a neuronal network model of focal ERD/surround ERS," in *Event-Related Desynchronization. Handbook of Electroencephalography and Clinical Neurophysiology*, Vol. 6, eds G. Pfurtscheller and F. Lopes da Silva (Amsterdam: Elsevier), 67–85.
- Talukdar, U., Hazarika, S. M., and Gan, J. Q. (2019). Motor imagery and mental fatigue: inter-relationship and EEG based estimation. *J. Comput. Neurosci.* 46, 55–76. doi: 10.1007/s10827-018-0701-0
- Thompson, M. C. (2019). Critiquing the concept of BCI illiteracy. *Sci. Eng. Ethics* 25, 1217–1233. doi: 10.1007/s11948-018-0061-1
- Tyson, A., Spencer, K., Christian, K., Brian, L., Ying, S., Kelsie, P., et al. (2015). Decoding motor imagery from the posterior parietal cortex of a tetraplegic human. *Science* 348, 906–910. doi: 10.1126/science.aaa5417
- Vidaurre, C., and Blankertz, B. (2010). Towards a cure for BCI illiteracy. *Brain Topogr.* 23, 194–198. doi: 10.1007/s10548-009-0121-6
- Wodlinger, B., Downey, J. E., Tyler-Kabara, E. C., Schwartz, A. B., Boninger, M. L., and Collinger, J. L. (2014). Ten-dimensional anthropomorphic arm control in a human brain-machine interface: difficulties, solutions, and limitations. *J. Neural Eng.* 12:016011. doi: 10.1088/1741-2560/12/1/016011
- Wolpaw, J., and Wolpaw, E. W. (Eds.). (2012). *Brain-Computer Interfaces: Principles and Practice*. Oxford: Oxford University Press.
- Wolpaw, J. R., and McFarland, D. J. (2004). Control of a two-dimensional movement signal by a noninvasive brain-computer interface in humans. *Proc. Natl. Acad. Sci. U.S.A.* 101, 17849–17854. doi: 10.1073/pnas.0403504101
- World Medical Association (2002). World Medical Association Declaration of Helsinki: ethical principles for medical research involving human subjects. *J. Postgrad. Med.* 48, 206–208.
- Yi, W., Qiu, S., Qi, H., Zhang, L., Wan, B., and Ming, D. (2013). EEG feature comparison and classification of simple and compound limb motor imagery. *J. Neuroeng. Rehabil.* 10:106. doi: 10.1186/1743-0003-10-106
- Yin, M., Borton, D., Komar, J., Agha, N., Lu, Y., Li, H., et al. (2014). Wireless neurosensor for full-spectrum electrophysiology recordings during free behavior. *Neuron* 84, 1170–1182. doi: 10.1016/j.neuron.2014.11.010

**Conflict of Interest:** The authors declare that the research was conducted in the absence of any commercial or financial relationships that could be construed as a potential conflict of interest.

Copyright © 2020 Lindig-León, Rimbart and Bougrain. This is an open-access article distributed under the terms of the Creative Commons Attribution License (CC BY). The use, distribution or reproduction in other forums is permitted, provided the original author(s) and the copyright owner(s) are credited and that the original publication in this journal is cited, in accordance with accepted academic practice. No use, distribution or reproduction is permitted which does not comply with these terms.



# Hybrid EEG-fNIRS BCI Fusion Using Multi-Resolution Singular Value Decomposition (MSVD)

Muhammad Umer Khan\* and Mustafa A. H. Hasan

Department of Mechatronics Engineering, Atılım University, Ankara, Turkey

Brain-computer interface (BCI) multi-modal fusion has the potential to generate multiple commands in a highly reliable manner by alleviating the drawbacks associated with single modality. In the present work, a hybrid EEG-fNIRS BCI system—achieved through a fusion of concurrently recorded electroencephalography (EEG) and functional near-infrared spectroscopy (fNIRS) signals—is used to overcome the limitations of uni-modality and to achieve higher tasks classification. Although the hybrid approach enhances the performance of the system, the improvements are still modest due to the lack of availability of computational approaches to fuse the two modalities. To overcome this, a novel approach is proposed using Multi-resolution singular value decomposition (MSVD) to achieve system- and feature-based fusion. The two approaches based up different features set are compared using the KNN and Tree classifiers. The results obtained through multiple datasets show that the proposed approach can effectively fuse both modalities with improvement in the classification accuracy.

**Keywords:** hybrid BCI, fNIRS, EEG, multi-resolution singular value decomposition, multi-modal fusion, channel selection, classification

## OPEN ACCESS

### Edited by:

Anwasha Khasnobish,  
Tata Consultancy Services, India

### Reviewed by:

Muhammad Jawad Khan,  
National University of Sciences and  
Technology (NUST), Pakistan  
M. Raheel Bhutta,  
Sejong University, South Korea

### \*Correspondence:

Muhammad Umer Khan  
umer.khan@atilim.edu.tr

### Specialty section:

This article was submitted to  
Brain-Computer Interfaces,  
a section of the journal  
Frontiers in Human Neuroscience

**Received:** 28 August 2020

**Accepted:** 12 November 2020

**Published:** 08 December 2020

### Citation:

Khan MU and Hasan MAH (2020)  
Hybrid EEG-fNIRS BCI Fusion Using  
Multi-Resolution Singular Value  
Decomposition (MSVD).  
*Front. Hum. Neurosci.* 14:599802.  
doi: 10.3389/fnhum.2020.599802

## 1. INTRODUCTION

The brain-computer interface (BCI) provides an interlink between the brain and external devices (Vidal, 1973; Wolpaw et al., 2002). The information received from the brain in the form of physiological/magnetic/metabolic signals is decoded and interpreted to determine the user intentions, and is later utilized for various purposes, such as rehabilitation (Do et al., 2013; Khan R. A. et al., 2018); control of robots (Doud et al., 2011; Bozinovski, 2016; Khan A. H. et al., 2018; Rosca et al., 2018; Duan et al., 2019) and of prosthetics (Buch et al., 2018; Yanagisawa et al., 2019); and neurogaming (Paszkiel, 2016, 2020; Vasiljevic and de Miranda, 2020). Among the existing non-invasive acquisition methods, arguably EEG (Wolpaw et al., 2002; Pfurtscheller et al., 2006; Choi, 2013; Abiri et al., 2019) and fNIRS (Ferrari et al., 1985; Delpy et al., 1988; Coyle et al., 2004, 2007; Fazli et al., 2012; Naseer and Keum-Shik, 2015; Yin et al., 2015) are considered the most explored. EEG is the physiological method, with low spatial and high temporal resolution, that measures the brain activity in the form of electrical impulses (volts) using the electrodes placed at specific positions on the scalp. On the other hand, fNIRS, based upon metabolic signals, measures the level of oxygenation and de-oxygenation in the blood with high spatial and low temporal resolution. Due to low temporal resolution, fNIRS may require several seconds to monitor the blood levels (Khan and Hong, 2017). The time involved in monitoring causes a delay in generating execution commands. For the fNIRS, this duration is almost 9 times that of EEG (Khan and Hong, 2017). Additionally, in comparison to EEG, fNIRS is considered more robust against

electromyogram artifacts and electrical noises (Blankertz et al., 2010; Ahn and Jun, 2015, 2017). The limitations of both modalities led to a multi-modal system, known as the hybrid EEG-fNIRS BCI, that has the ability to overcome the drawbacks of uni-modal systems and to improve the performance.

The hybrid EEG-fNIRS BCI has attracted the attention of many researchers due to its mobility, cost-effectiveness, and enhanced information content (compared to the uni-modal). Since the EEG obtains information from the physiological signals, and fNIRS uses metabolic signals to detect the hemodynamic, there is no significant interference between the two modalities. This further helps to obtain an enhanced BCI performance. The first notable study that concurrently recorded EEG-fNIRS data to perform motor imagery tasks was done by Fazli et al. (2012). The authors reported an improvement in the classification accuracy by 5% on average when compared to the single modality. After the promising results obtained by Fazli et al. (2012), more researchers tried to utilize the hybrid BCI, either to increase the classification accuracy and/or to generate more control commands (Khan et al., 2014; Koo et al., 2015; Aghajani et al., 2017; Ge et al., 2017; Shin et al., 2018a). The most explored areas where the hybrid BCI is utilized include mental stress (Al-Shargie et al., 2016; Aghajani et al., 2017) and gait rehabilitation (Berger et al., 2019), among many others (Putze et al., 2014; Zama et al., 2019). Though the hybrid EEG-fNIRS BCI has been able to uphold its supremacy against single modality both in terms of accuracy and stability, there are still some challenges related to the integration of both modalities.

Data-fusion in multi-modality is a challenging problem since the brain imaging data is different in nature, thus making the analysis more difficult. Most of the previous studies focused on feature-based fusion through concatenating EEG and fNIRS features (Putze et al., 2014; Hong et al., 2018; Shin et al., 2018a), and by providing them the support of other power tools. Joint independent component analysis (jICA), which was previously used for integrating EEG and fMRI (Calhoun and Adali, 2008), was used to perform the fusion of EEG and fNIRS features (Al-Shargie et al., 2016). Some researchers also used deep learning-based feature fusion approaches, such as tensor fusion and *p*th-order polynomial fusion (Chiarelli et al., 2018; Sun et al., 2020). These multi-modal fusion approaches have been able to improve the accuracy, but at the cost of increasing computational complexity and decreasing stability. In Yin et al. (2015), the authors introduced a features combination and optimization approach using joint mutual information (JMI), and the study decoded the motor imagery of the force and speed of hand clenching. The feature optimization method, JMI, was developed with the intention to remove unessential information that may reduce classification accuracy. The authors reported achieving an improved performance of up to 5% when compared to previous studies. In 2017, Al-Shargie et al. (2017) proposed a canonical correlation analysis (CCA) to perform feature-based fusion. The aim was to investigate the effects of mental stress on prefrontal cortex (PFC) based upon simultaneously recorded EEG and fNIRS signals. CCA is a statistical method that maximizes the correlation between the features of brain signals recorded by each modality EEG-fNIRS.

Though the improvements achieved by jICA, JMI, and CCA were satisfactory, the fusion was applied on the feature level, where the two modalities were processed separately. Therefore, a true system-level fusion is needed in order to capture the maximum benefits of the hybrid BCI, maximize the correlation between each modality, and reduce the computational complexity. In this study, we propose a novel hybrid BCI fusion approach using Multi-resolution singular value decomposition (MSVD) to perform a feature-based and system-based fusion for both EEG and fNIRS by employing selected channels from each hemisphere. The MSVD has previously been utilized primarily for image analysis, fusion (Kakarala and Ogunbona, 2001; Ashin et al., 2005; Naidu, 2011) and pattern recognition (Lung, 2002). To our knowledge, the present study is the first attempt to perform a hybrid EEG-fNIRS BCI fusion at the system level using MSVD. This approach not only helps to improve the classification accuracy, but also to reduce the dimensionality and the computational complexity. To evaluate the performance, the proposed approach is tested for two datasets: Buccino dataset (Buccino et al., 2016) and dataset from Technical University Berlin (TU Berlin) (Shin et al., 2018b).

## 2. MATERIALS AND METHODS

### 2.1. Datasource and Experimental Paradigm

The proposed approach has the tendency to work with datasets of different nature. To prove its effectiveness, it is tested on two simultaneously recorded EEG-fNIRS data for motor execution and cognitive tasks. Both datasets have been widely used by the research community in the recent past as they can be openly accessed (Congedo et al., 2017; Saadati et al., 2020).

#### 2.1.1. Buccino dataset

The publicly available dataset obtained from an online repository (<http://dx.doi.org/10.6084/m9.figshare.1619640> and <http://dx.doi.org/10.6084/m9.figshare.1619641>) was provided by Buccino et al. (2016). The raw data from EEG and fNIRS was concurrently recorded for four motor execution tasks—right and left arm; right and left hand—against the rest. Fifteen healthy subjects, aged between 23 and 54, were involved in the experiments that lasted an hour. A screen was installed nearly 100 cm away from the subjects on which visual instructions were displayed; the subjects were asked to follow the instructions without any intentional delay. The total duration of each experiment was segmented into rest and activity periods; each trial started with a rest for 6 s followed by another 6 s of movements.

#### 2.1.2. TU Berlin Dataset

The second open-access dataset considered in this study was from TU Berlin (Shin et al., 2018b), where 26 healthy persons participated in the experiment ranging between 17 and 33 years of age. A 24in LCD monitor was placed in front of the participants, approximately at a distance of 1.2 m. They were instructed to place their middle and index fingers on the numeric keypad attached to the armrest of the chair. The EEG and NIRS signals were recorded simultaneously for three cognitive

tasks over a period of approx. 3.5 h: n-back (0-, 2-, and 3-back), discrimination/selection response task (DSR), and word generation (WG). In this study, we considered only the n-back tasks where a series of nine tasks were performed by each participant. At the start of each series, a type of task is displayed on the screen for 2 s, followed by the actual task period of 40 s, and then 20 s rest period. The participants responded to the screen instructions by either pressing the target key (number 7) or non-target key (number 8) with their right index finger and right middle finger. More details about the dataset can be obtained from Shin et al. (2018b) and ([http://doc.ml.tu-berlin.de/simultaneous\\_EEG\\_fNIRS/](http://doc.ml.tu-berlin.de/simultaneous_EEG_fNIRS/)).

## 2.2. Data Acquisition

### 2.2.1. Buccino Dataset

The EEG system (microEEG, BioSignal Group, US) was used to record the signals through twenty-one channels, sampled at a rate of 250 Hz. The fNIRS system, NIRScout 8-16 (NIRx Medizintechnik GmbH, Berlin, Germany) equipped with 12 sources and 12 electrodes on 34 channels was used to acquire signals at a sampling frequency of 10.42 Hz. The EEG electrodes and fNIRS probes were mounted on an extended EEG cap (actiCAP 128, Brain Products GmbH, Germany) according to the international 10-20 system.

### 2.2.2. TU Berlin Dataset

A multi-channel BrainAmp EEG amplifier (Brain Products GmbH, Gilching, Germany) working at a sampling rate of 1,000 Hz was used to store the raw EEG data. The fNIRS system, NIRScout (NIRx Medizintechnik GmbH, Berlin, Germany), combined with thirty-six channels was used to record data at a sampling rate of 10.4 Hz. Thirty EEG electrodes, and sixteen pairs of NIRS sources and detectors, were mounted on a cap (EASYCAP GmbH, Herrsching am Ammersee, Germany) according to the international 10-5 system.

## 2.3. Data Pre-processing

### 2.3.1. Buccino Dataset

The initial trial was segmented out prior to the motor execution tasks. The raw fNIRS data obtained at a sampling frequency of 10.42 Hz was decomposed into Oxy-haemoglobin and Deoxy-haemoglobin concentration changes (HbO and HbR) through the Modified Beer-Lambert law (Cope et al., 1988; Baker et al., 2014). Later, the concentration signals were filtered with a 4th order IIR Butterworth filter between 0.01 and 0.2 Hz. The EEG signals were also filtered with a 4th order IIR Butterworth filter between 1 and 50 Hz to remove artifacts.

### 2.3.2. TU Berlin Dataset

The raw NIRS data were transformed to HbO and HbR using the Modified Beer-Lambert law, and down-sampled to 10 Hz. The obtained data was filtered (6th order zero-phase Butterworth) with 0.2 Hz cut-off frequency to remove systemic physiological noises. The raw EEG data were down-sampled to 200 Hz and band-pass filtered (6th order zero-phase Butterworth) between 1 and 40 Hz. Additionally, the second-order blind

identification method was applied to the filtered data to eliminate ocular artifacts.

The filtered EEG and fNIRS data were baseline-corrected by subtracting the mean and dividing by the standard deviation. For both datasets, the EEG data were downsized through an average moving window of 1 s to ascertain consistency and synchronization. Additionally, we selected HbO as the main feature for the fNIRS signal as the concentration change is more observable in HbO and can produce higher accuracy when compared to HbR and total haemoglobin (HbT) (Aihara et al., 2012; Morioka et al., 2014; Buccino et al., 2016).

## 2.4. Channel Selection

The criteria of channel selection is based upon the correlation coefficient,  $\rho$ , determined between the filtered data of each modality. Some researchers have investigated the utilization of the Pearson correlation coefficient to solve practical problems in medical industry (Yildiz and BERGIL, 2015; Akoglu, 2018). Our previous study in this context (Hasan et al., 2020) demonstrated that this approach can be effectively utilized to select optimal channels for EEG and fNIRS.

## 2.5. Feature Extraction

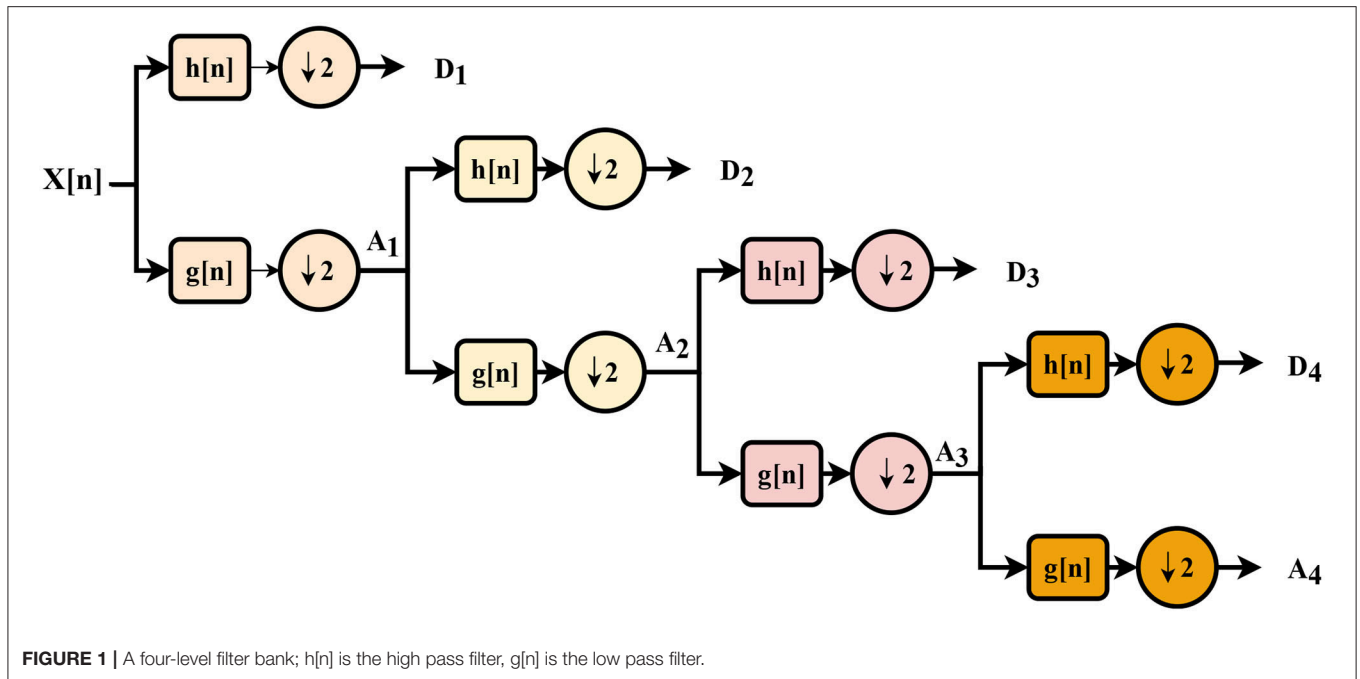
### 2.5.1. Discrete Wavelet Transform (DWT)

The DWT of a signal  $X[n]$ , as shown in **Figure 1**, is obtained through a series of low- and high-pass filter pairs, named as quadrature mirror filters. As the frequency bandwidth is reduced to half, the filtered signal can be down-sampled by two according to the Nyquist's rule. The reduced output from the low- and high-pass filter branches are regarded as approximation ( $A_i$ ) and detail ( $D_i$ ) coefficients, where  $i$  represents the level of the transform. The same procedure can be repeated multiple times to improve the frequency resolution by considering the coefficients from the previous level as an input. The tree structure is also known as a filter bank. After each decomposition, the time resolution is halved through down-sampling, whereas the frequency resolution is doubled through filtering. Based upon the work of Subasi (2007), the authors in Li et al. (2017) reported that the approximation coefficient from the output of the last DWT layer is the main carrier of the signal's power. They suggested the use of a 4-layer "Symlet" wavelet network to obtain higher classification accuracy.

#### Decomposition Level

For DWT, the mother wavelet transform directly impacts the calculation of the approximation and detail coefficients (Mallat, 1989), thereby affecting overall accuracy. The most commonly used families are biorthogonal, reverse biorthogonal, daubechies, symlets, coiflets, discrete meyer, and haar (Faust et al., 2015). In this study, from the family of symlets, sym4 is selected having a filter size of eight as a mother wavelet.

The number of decomposition levels of DWT is associated with the input signal and mother wavelet. With more depth of decomposition, a detailed description of the signal can be obtained, but it may produce features redundancy leading to the lower accuracy and higher computational cost. The highest level  $L$  of the decomposition is determined as  $\text{floor} \left( \log_2 \left( \frac{N}{F-1} \right) \right)$ ,



where  $N$  is the size of the input signal and  $F$  is the mother wavelet filter size (eight in our case) (Wu et al., 2000). Chen et al. (2017) reported that beyond a certain level, not much improvement can be observed in the accuracy. Even in some cases, the accuracy even dropped with the increase in the decomposition level. Hence, more levels of decomposition do not necessarily mean improved accuracy, but definitely adding to the computational cost. For our case, we obtained the maximum accuracy with four levels of decomposition.

### 2.5.2. Statistical Features

In addition to DWT, six different statistical features are extracted using spatial averaging of selected channels. The considered features set are: mean (M), peak (P), skewness (SK), kurtosis (KR), standard deviation (SD), and variance (VAR). The selection of these features is based upon the existing literature, where there is also a comparison between the performance of individual features and their combinations (Hong et al., 2017; Khan R. A. et al., 2018; Hasan et al., 2020). The extracted features set are re-scaled between 0 and 1, using:

$$X_{new} = \frac{X_i - \min(X_i)}{\max(X_i) - \min(X_i)} \quad (1)$$

After processing the extracted features using Equation (1), the normalized feature vectors are obtained as  $M_{new}$ ,  $P_{new}$ ,  $SK_{new}$ ,  $KR_{new}$ ,  $SD_{new}$ , and  $VAR_{new}$ . To avoid ambiguity and for the sake of easiness, the normalized features are still represented using the same variables, but without the subscript.

## 3. DATA-FUSION

### 3.1. Multi-Resolution Singular Value Decomposition (MSVD)

The motivation behind the proposed approach is to build a framework for multi-modal fusion using MSVD. Similar to DWT, an input signal is processed through high- and low-pass finite impulse response (FIR) filters at the first stage, followed by down-sampling. In the following stage, the approximation coefficient from the previous level is bifurcated to achieve decomposition (Naidu, 2011). The same procedure is repeated to obtain  $d$  level decomposition, where the FIR filters are replaced with the MSVD.

Let  $X \in \mathbb{R}^{n' \times m'}$  contains the statistical features of the input signal or the fused signal, where  $(n', m')$  are constrained as an even number due to the decomposition process.

$$X = \begin{matrix} \begin{matrix} x(1,1) & x(1,2) & x(1,3) & x(1,4) & \dots & x(1,m'-1) & x(1,m') \\ x(2,1) & x(2,2) & x(2,3) & x(2,4) & \dots & x(2,m'-1) & x(2,m') \\ x(3,1) & x(3,2) & x(3,3) & x(3,4) & \dots & x(3,m'-1) & x(3,m') \\ x(4,1) & x(4,2) & x(4,3) & x(4,4) & \dots & x(4,m'-1) & x(4,m') \\ \vdots & \vdots & \vdots & \vdots & \ddots & \vdots & \vdots \\ x(n'-1,1) & x(n'-1,2) & x(n'-1,3) & x(n'-1,4) & \dots & x(n'-1,m'-1) & x(n'-1,m') \\ x(n',1) & x(n',2) & x(n',3) & x(n',4) & \dots & x(n',m'-1) & x(n',m') \end{matrix} & \begin{matrix} v_1 \\ v_2 \\ \vdots \\ v_{n'/2} \end{matrix} \end{matrix}$$

By introducing new variables  $(n, m)$  as  $(\frac{n'}{2}, \frac{m'}{2})$ , the data matrix,  $A \in \mathbb{R}^{4 \times nm}$ , is built upon the matrix  $X$  as:

$$A = [ \mathcal{V}_1 \ \mathcal{V}_2 \ \dots \ \mathcal{V}_m ] \quad (2)$$

where each  $\mathcal{V}_i$  contains two adjacent columns of  $X$ , and is defined as follows:

$$\mathcal{V}_i = [ u_1 \ u_2 \ \dots \ u_n ] \quad (3)$$

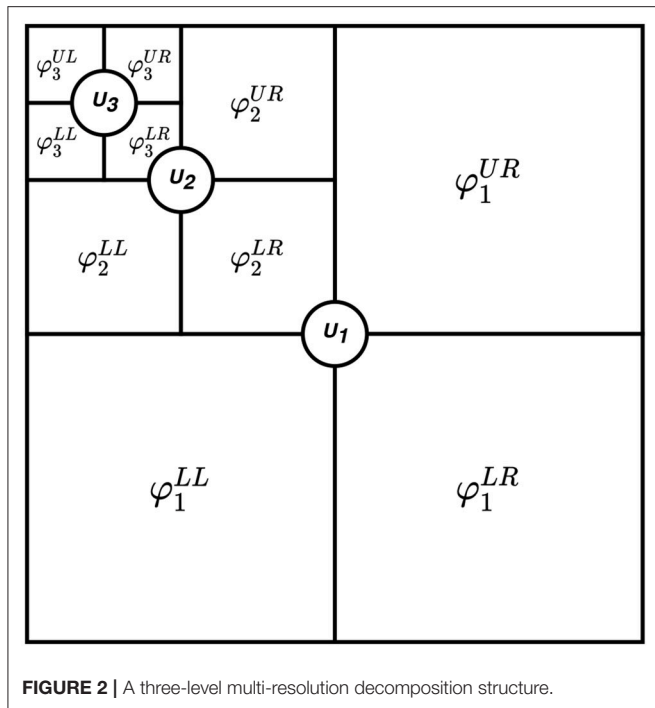


FIGURE 2 | A three-level multi-resolution decomposition structure.

Each individual vector  $v_i$  contains a feature set of four elements of  $X$ , and is formulated as:

$$v_i = [v_i^{UL} \ v_i^{UR} \ v_i^{LL} \ v_i^{LR}]^T \tag{4}$$

where  $UL$ ,  $UR$ ,  $LL$ , and  $LR$  represents upper-left, upper-right, lower-left, and lower-right elements, respectively.

Afterwards, the singular value decomposition is applied on the generated data matrix  $A$  as:

$$A = USV^T \tag{5}$$

where the columns of  $U$  contain left singular vectors,  $S$  holds singular values as diagonal entries, and rows of  $V^T$  have the right singular vectors. The singular vectors are chosen to satisfy:

$$U^T A = SV^T \tag{6}$$

A scatter matrix,  $T \in \mathbb{R}^{4 \times nm}$ , is defined using Equation (6) as:

$$T = U^T A \tag{7}$$

The vectors  $\{\vec{t}_1, \vec{t}_2, \vec{t}_3, \vec{t}_4\}$  specify the rows of  $T$ , where each  $\vec{t}_i \in \mathbb{R}^{1 \times nm}$ . These vectors are reshaped to generate corresponding matrices  $\{\Gamma_1, \Gamma_2, \Gamma_3, \Gamma_4\}$ , where each  $\Gamma_i \in \mathbb{R}^{n \times m}$ . A split matrix  $\varphi \in \mathbb{R}^{n' \times m'}$  is introduced as:

$$\varphi = \begin{bmatrix} \varphi^{UL} & \varphi^{UR} \\ \varphi^{LL} & \varphi^{LR} \end{bmatrix} = \begin{bmatrix} \Gamma_1 & \Gamma_2 \\ \Gamma_3 & \Gamma_4 \end{bmatrix} \tag{8}$$

Figure 2 shows the structure of the split matrix with three decomposition levels. In case of a multiple input signals, a split matrix using MSVD is obtained for an individual input.

For instance, two input signals  $S_1$  and  $S_2$ , having the same dimensions, are decomposed into  $L$  ( $l=1,2,\dots, L$ ) levels using MSVD (Figure 3). After the generation of the split matrix, fusion has to be performed. To do so, it is necessary to store detail component vectors  $\varphi_l^{\{UR,LL,LR\}}$  and singular-vector matrix  $U_l$  for  $l=1,2,\dots, L$ , whereas it is sufficient to store the approximation component vector only at the coarsest level  $L$  i.e.,  $\varphi_L^{\{UL\}}$ . The fusion rules mentioned in Figure 3 are used to fuse the signals from multi-sources. At each decomposition level  $l$ , the largest absolute detail component vector is selected since it assumed to carry the main power of the signals. Similarly, the average of the singular-vector matrix is computed at each level. At the coarsest level ( $l=L$ ), the average of the approximation coefficients is calculated.

It can be observed that based upon the information from the split matrix, a decision is made. Once the fusion rules are applied in order to merge all the information into a single modality, an inverse process is applied to obtain the fused matrix.

The scatter matrix  $T$  is reconstructed based upon the information from the split matrix since the steps are reversible. The sub-matrices of the split matrix  $\varphi$  are reshaped from  $\mathbb{R}^{n \times m} \rightarrow \mathbb{R}^{1 \times nm}$  to redefine scatter matrix  $T$ :

$$T = \begin{bmatrix} \vec{t}_1 \\ \vec{t}_2 \\ \vec{t}_3 \\ \vec{t}_4 \end{bmatrix} \tag{9}$$

Using Equation (9), a data matrix  $A$  is obtained as:

$$A = UT \tag{10}$$

The structure of the data matrix is defined as:

$$A = \begin{bmatrix} a(1,1) & a(1,2) & \dots & a(1,mn) \\ a(2,1) & a(2,2) & \dots & a(2,mn) \\ a(3,1) & a(3,2) & \dots & a(3,mn) \\ a(4,1) & a(4,2) & \dots & a(4,mn) \end{bmatrix}$$

$a_1 \quad a_2 \quad \dots \quad a_{mn}$

Each column vector  $a_i$  contains four elements and is used to define a fused feature matrix  $X$  as:

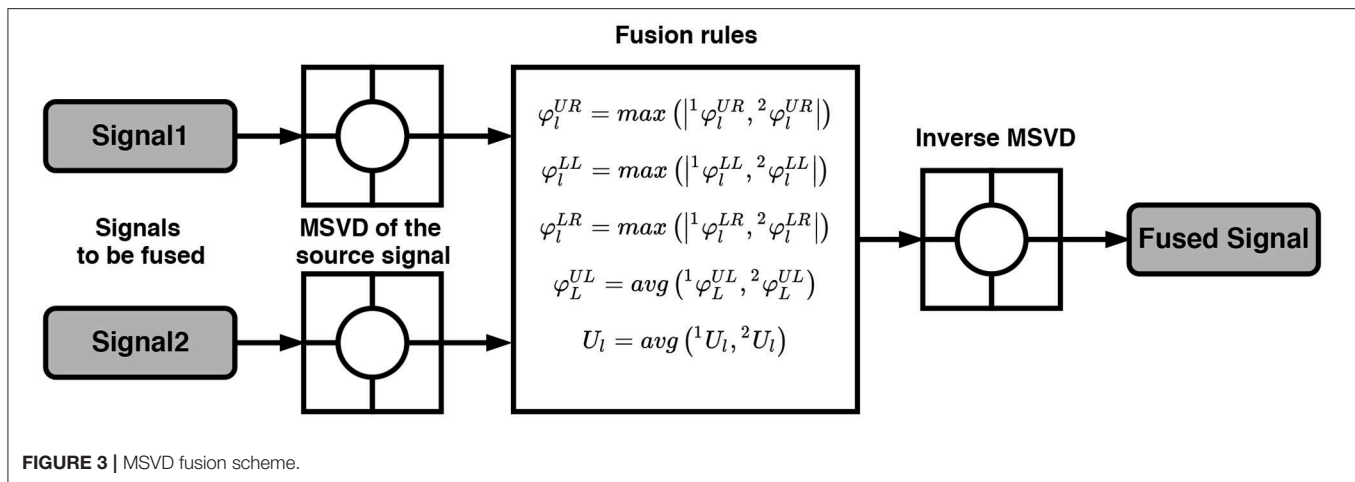
$$X = \begin{bmatrix} a_1 & a_{m+1} & \dots & a_{m(n-2)+1} & a_{m(n-1)+1} \\ a_2 & a_{m+2} & \dots & a_{m(n-2)+2} & a_{m(n-1)+2} \\ \vdots & \vdots & \ddots & \vdots & \vdots \\ a_{m-1} & a_{2m-1} & \dots & a_{m(n-1)-1} & a_{mn-1} \\ a_m & a_{2m} & \dots & a_{m(n-1)} & a_{mn} \end{bmatrix} \tag{11}$$

where

$$a_i = \begin{bmatrix} a(1,i) & a(2,i) \\ a(3,i) & a(4,i) \end{bmatrix} \tag{12}$$

### 3.2. Feature-Based Fusion

EEG-fNIRS correlation analysis helped to reveal the intrinsic relationship between both modalities. To maximize the accuracy and to increase the number of the generated commands,



statistical and optimization-based feature extraction methods are among the most commonly used. However, most of the previous studies focused on the feature-based level fusion by simply concatenating EEG and fNIRS features  $[f_{EEG} : f_{fNIRS}]$ . In this paper, we proposed the utilization of the MSVD to perform EEG-fNIRS feature-based fusion. For the given datasets, the details about the pre-processing steps, such as filtering and windowing are provided in section 2.3. Based upon the correlation coefficient, six optimal channels are selected from both modalities. Six statistical features from the fNIRS and six normalized DWT features (one from each channel) from the EEG are extracted (Figure 4A). Afterwards, MSVD decomposes the features set into sub-bands through filtering, and the output of each filter is dismantled by a factor of two to complete the first level of decomposition. Afterwards, the fusion rules mentioned in Figure 3 are applied, followed by the classification to determine the specific tasks.

### 3.3. System-Based Fusion

Figure 4B is a schematic representation of the proposed system-based fusion using MSVD for a hybrid BCI system. To our knowledge, none of the previous studies have so far applied fusion at the system-level, mainly due to the complexity and lack of computational approaches. The pre-processed signals (filtered, down-sampled) are used to extract the desirable number of channels using the correlation coefficient (Hasan et al., 2020). Six channels are selected from both modalities and processed using MSVD to perform system-based fusion. Multiple features are extracted from the fused signal: DWT, statistical, and a combination of DWT and statistical. Later, the extracted features are fed to the classifier to determine the specific tasks.

## 4. RESULTS

This section mainly evaluates the performance of the two fusion schemes, feature- and system-based fusion, by utilizing Buccino and TU Berlin datasets. To reduce the computational complexity, a reduced number of channels of both modalities are utilized for the classification. On Buccino dataset, the computational time,

recorded as the temporal distance between the filtration and feature extraction, is highlighted in Table 1 for EEG and fNIRS based upon all channels and the reduced number of channels. The analysis made is based upon the sampled data of 1 s, obtained through both modalities. The response time is reduced by 40 and 50% for EEG and fNIRS, respectively.

### 4.1. Classification

For EEG and fNIRS, the classification accuracies using the KNN and Tree classifiers are evaluated for four different motor tasks against the rest based upon Buccino dataset; whereas, hybrid EEG-fNIRS analysis is made for both Buccino and TU Berlin datasets, using the same classifiers. The KNN classifier proximate the nearest observation points from the training data into a single class. It is preferred due to its simplicity, easiness to implement and high classification performance (Bablani et al., 2018). The Tree classifier constructs the decision tree with branches and node(s) based on the extracted features. At each node, either a single feature or several features contribute to minimizing the entropy label of the class (Aydemir and Kayikcioglu, 2014). To evaluate the classifiers' performance, a 10-fold cross-validation scheme is applied to the feature vectors of EEG, fNIRS, and EEG-fNIRS.

### 4.2. EEG

The average classification accuracies in Table 2 are obtained using the KNN and Tree classifiers for the eight selected subjects based upon Buccino dataset. The four approximation coefficients obtained using four-level DWT are defined as the EEG features. It is noted that the Tree classifier, when compared to KNN, has only been able to produce moderate results. The classification accuracy of more than 80% is achieved using the last approximation coefficient  $A_4$ , when processed through KNN. This phenomenon is observed as DWT helps decompose the EEG signals into four layers, and the last approximation coefficient is assumed to hold the most effective event-related potential (ERP) of the brain activity. The DWT decomposition also helped to reduce the dimensionality of the system.

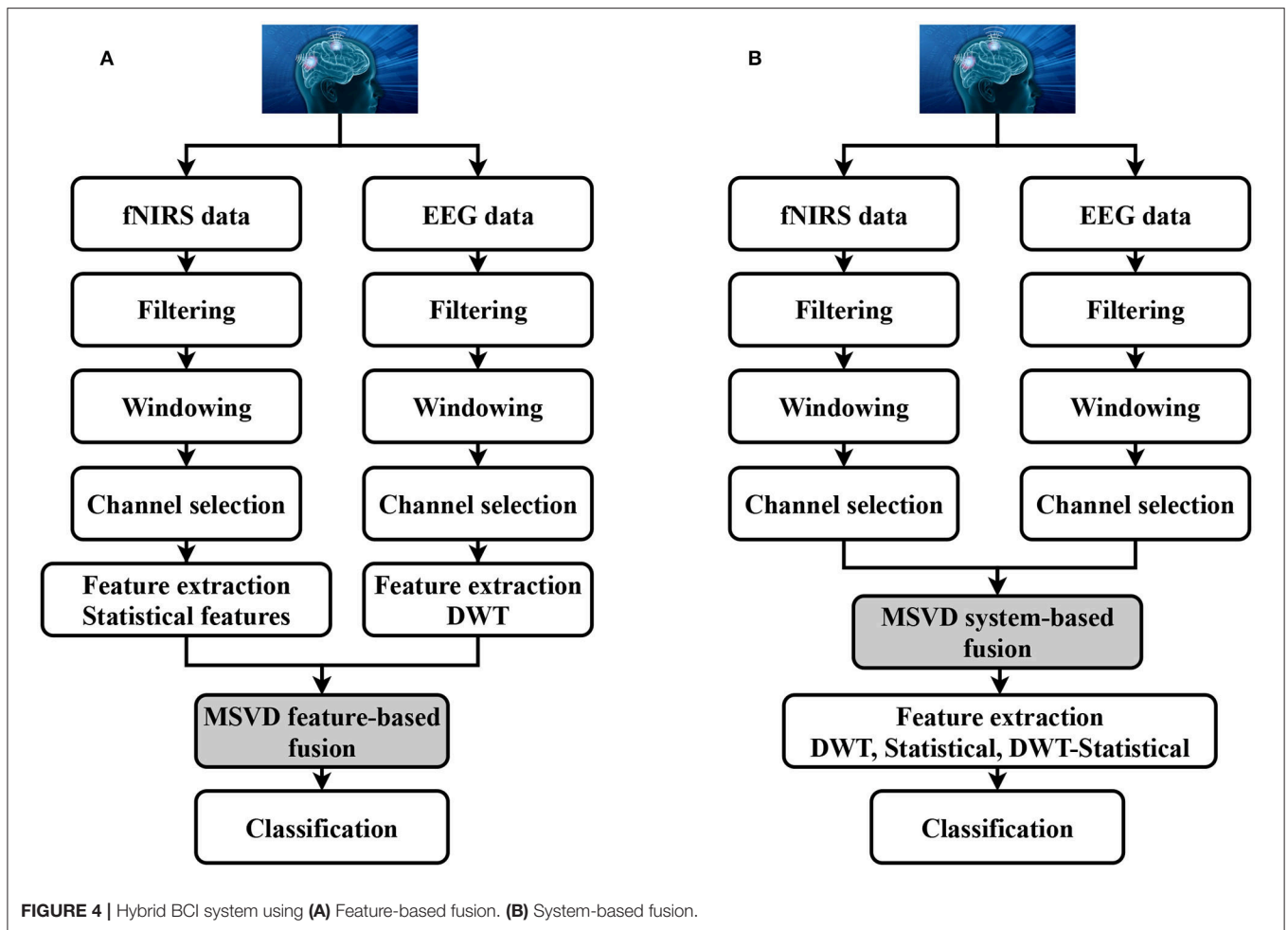


FIGURE 4 | Hybrid BCI system using (A) Feature-based fusion. (B) System-based fusion.

### 4.3. fNIRS

Table 3 shows the KNN and Tree classification results obtained for the eight subjects (Buccino dataset) using fNIRS-only features. A feature set, consisting of fifteen feature vectors, is developed from a combination of the six statistical features. In this study, it is revealed that the combination of mean and skewness produces the highest average classification accuracies for both KNN and Tree. It is concluded that, similar to EEG, fNIRS has not been able to produce any satisfactory results.

### 4.4. Hybrid EEG-fNIRS

The performance of the hybrid EEG-fNIRS based upon feature- and system-based fusion is evaluated using accuracy, specificity, and area under curve (AUC). The most commonly used performance measures, such as precision, recall, and F1-score are not useful for the multi-classification, as they produces the same results. Hence, for the purpose, AUC is employed, its value ranges between 0 and 100%. The closer the value is to 100%, the better is the classification performance of the model.

#### 4.4.1. Feature-Based Fusion

For feature-based fusion, based upon the selected channels from both modalities, the six statistical features from the fNIRS, and

TABLE 1 | Impact of channels selection on the computational time for both EEG and fNIRS.

Number of channels	EEG (s)	fNIRS (s)
All channels	0.1639	0.1405
6 channels	0.0935	0.0724

DWT's last layer approximation coefficients from the EEG are used as the main features. The number of selected channels from both modalities is kept the same. A combined feature set of EEG-fNIRS is processed through MSVD. Table 4 illustrates the classification performance measures obtained for the eight subjects using feature-based fusion.

#### Buccino Dataset

The proposed method delivered promising performance for the motor execution tasks. Table 4 shows consistent accuracy above 85% across all subjects using the KNN. Considering all the subjects, the average classification accuracies of 90.25 and 74.98% are obtained through the KNN and Tree classifiers, respectively. It can be observed that the KNN has been able to outperform the Tree classifier for feature-based fusion. It is also noticeable

**TABLE 2** | Average classification accuracies for the eight subjects using the EEG.

Features set	EEG	
	KNN (%)	Tree (%)
A <sub>1</sub>	44.45	50.62
A <sub>2</sub>	59.96	53.10
A <sub>3</sub>	70.83	60.55
A <sub>4</sub>	82.36	71.32

**TABLE 3** | Average classification accuracies for the eight subjects using the fNIRS.

Features set	fNIRS	
	KNN (%)	Tree (%)
M, P	64.80	69.82
M, SK	70.97	73.63
M, KR	68.85	71.81
M, SD	69.62	71.66
M, VAR	68.08	71.66
P, SK	70.36	73.27
P, KR	66.42	71.32
P, SD	67.58	71.13
P, VAR	67.28	71.10
SK, KR	56.66	64.52
SK, SD	65.00	69.16
SK, VAR	64.11	69.13
KR, SD	63.81	68.36
KR, VAR	62.98	68.38
SD, VAR	46.91	56.61

that there is a variation among individual subject's performance, causing a direct effect on the overall accuracy. There can be many possible reasons for this phenomenon: it could be due to the subject's experiencing such tasks first hand or loss of interest at some stage during the process. This can be corrected by properly training the subjects before performing the experiments, as well as by shortening the duration of the experiments. Regarding the individual's performance, the best performing subjects are S5 and S7, who achieved the highest accuracies of 97.0 and 95.8% through KNN.

#### TU Berlin Dataset

The n-back tasks classification results using the KNN and Tree classifiers are presented in **Table 4**. For all the subjects, highest classification accuracy is achieved by the KNN. The highest accuracies (%) attained for the eight subjects are 94.4, 72.4, 92.1, 91.0, 95.5, 76.4, 79.9, and 81.9. The average classification accuracies obtained using the KNN and Tree classifiers are 85.45 and 77.91%, respectively. It is re-observed that due to the individual's performance, there has been a significant drop in the overall accuracy, despite the fact that four subjects have been able to achieve an accuracy of 91% or above (KNN). Although, the results are reported for a single feature set (DWT-statistical), the proposed method can be further tested with other combinations to yield the highest accuracies.

#### 4.4.2. System-Based Fusion

System-based fusion presents many advantages as compared to feature-based fusion; it is less time-consuming since we are analyzing the fused signals instead of processing each signal separately, and then fusing them. It is also more robust toward cross-data set variations of the components, which can be used for generating group-level inferences in different ways. The processed EEG-fNIRS data obtained from the selected channels is fused using MSVD system-based Fusion.

#### Buccino dataset

**Table 5** summarizes the classification accuracies obtained using a combined features set (DWT, statistical, DWT-statistical) through the KNN and Tree classifiers for the eight subjects. Among three features set, DWT is able to produce the highest accuracy of 98.9% (KNN) followed by DWT-statistical which attained 94.43% (Tree) at most. Moreover, consistent best accuracies (%) were 97.0, 98.9, 98.9, 98.6, 93.6, 98.3, 98.2, 98.9 for eight subjects, respectively, as obtained using the KNN. Based upon the performance, S2, S3 and, S8 can be considered as the best-performing subjects.

#### TU Berlin Dataset

In **Table 5**, performance measures based upon the classification results are shown. The highest and the lowest accuracies of 99.7 and 40.9% are obtained using DWT and the six statistical features, respectively. The huge difference between the best-performing and worst-performing subjects causes the significant drop in the overall accuracy. Therefore, extreme caution must be taken to exclude the non-favorable features and subjects. For eight subjects, KNN in comparison to Tree has been able to produce the highest accuracies (%) of 99.5, 99.7, 99.5, 80.1, 96.6, 99.4, 99.3, and 99.3.

## 5. DISCUSSION AND CONCLUSION

A hybrid EEG-fNIRS BCI enables the assessment of brain activities from different perspectives; hence, a broader range of information is obtained. Additionally, it also compensates for the weaknesses of individual modalities. The performance of the hybrid EEG-fNIRS is compared against EEG-only and fNIRS-only for the eight subjects. The results supported the argument that the hybrid EEG-fNIRS should be preferred over the individual modalities. The obtained classification accuracy for the hybrid system is higher than EEG-only and fNIRS-only for all subjects. The reduced number of channels from both modalities are utilized to obtain the results. The selected channels are based upon the ranking of the correlation coefficient; the six highest ranked channels of both modalities are selected. As shown in **Table 1**, the response time is improved by 40% for both modalities without affecting the accuracy.

In this study, we presented an MSVD approach for bi-modalities data-fusion. The proposed approach is investigated for both feature- and system-based fusion of EEG-fNIRS, with the intention to improve the system's performance and to reduce dimensionality. The MSVD-based data-fusion works on the same principle as DWT; at each level, the signals are filtered and dismantled by a factor of two to decompose the data into their

**TABLE 4 |** Classification performance of the hybrid EEG-fNIRS for the eight subjects using the (Tree,KNN), based upon feature-based fusion.

	S1/S2/S3/S4			S5/S6/S7/S8		
	Accuracy (%)	Specificity (%)	AUC (%)	Accuracy (%)	Specificity (%)	AUC (%)
Buccino	(72.1,93.6)	(80.0,93.6)	(81.0,94.0)	(78.9,97.0)	(93.4,97.0)	(86.0,97.0)
TU Berlin	(87.4,94.4)	(88.8,94.7)	(90.0,95.0)	(83.4,95.5)	(91.7,97.0)	(93.0,98.0)
Buccino	(73.2,85.7)	(81.0,85.0)	(82.0,89.0)	(70.9,85.0)	(78.0,87.3)	(85.0,89.0)
TU Berlin	(71.0,72.4)	(77.5,74.0)	(81.0,76.0)	(68.6,76.4)	(76.1,79.0)	(80.0,83.0)
Buccino	(79.1,92.4)	(81.3,92.0)	(83.0,92.0)	(77.7,95.8)	(81.0,98.0)	(88.0,98.0)
TU Berlin	(84.8,92.1)	(86.8,93.2)	(91.0,94.0)	(72.4,79.9)	(78.4,83.5)	(87.0,86.0)
Buccino	(77.1,86.1)	(85.3,89.0)	(87.0,91.0)	(70.9,86.4)	(72.1,85.0)	(74.0,85.0)
TU Berlin	(77.0,91.0)	(81.3,91.9)	(87.0,93.0)	(78.7,81.9)	(82.5,84.7)	(91.0,90.0)

**TABLE 5 |** Classification performance of the hybrid EEG-fNIRS for the eight subjects using the (Tree,KNN), based upon system-based fusion.

	Features set	S1/S2/S3/S4			S5/S6/S7/S8		
		Accuracy (%)	Specificity (%)	AUC (%)	Accuracy (%)	Specificity (%)	AUC (%)
Buccino	Six Statistical and DWT	(81.1,65.1)	(94.1,89.6)	(93.0,80.0)	(82.1,63.5)	(92.0,69.0)	(94.0,72.0)
	Six Statistical	(50.1,41.6)	(85.7,83.7)	(57.0,52.0)	(53.0,44.3)	(58.3,52.1)	(61.0,59.0)
	DWT	(83.1,97.0)	(94.7,99.0)	(93.0,97.0)	(83.8,93.6)	(88.2,98.1)	(94.0,99.0)
TU Berlin	Six Statistical and DWT	(95.6,83.4)	(95.7,84.6)	(96.0,81.0)	(96.1,79.5)	(98.5,82.0)	(99.0,89.0)
	Six Statistical	(62.4,59.7)	(66.0,71.3)	(68.0,60.0)	(46.1,45.5)	(62.0,60.0)	(66.0,63.0)
	DWT	(96.7,99.5)	(96.7,99.9)	(97.0,100)	(96.5,96.6)	(98.7,99.0)	(99.0,100)
Buccino	Six Statistical and DWT	(93.8,90.6)	(98.0,96.9)	(95.0,92.0)	(91.7,79.6)	(96.3,81.2)	(98.0,82.0)
	Six Statistical	(59.8,53.0)	(61.0,54.2)	(71.0,65.0)	(54.5,51.7)	(62.0,59.2)	(62.0,61.0)
	DWT	(94.3,98.9)	(95.1,99.0)	(95.0,99.0)	(92.4,98.3)	(98.0,99.0)	(98.0,99.0)
TU Berlin	Six Statistical and DWT	(94.6,80.7)	(94.9,83.9)	(95.0,84.0)	(95.6,82.6)	(97.0,88.0)	(98.0,89.0)
	Six Statistical	(51.3,50.2)	(61.2,58.0)	(63.0,59.0)	(54.6,56.0)	(65.0,56.0)	(67.0,73.0)
	DWT	(95.9,99.7)	(96.9,99.8)	(97.0,100)	(95.9,99.4)	(97.7,99.8)	(98.0,100)
Buccino	Six Statistical and DWT	(94.4,87.4)	(95.9,90.9)	(94.0,84.0)	(91.8,77.1)	(93.9,79.0)	(94.0,86.0)
	Six Statistical	(73.8,71.2)	(81.5,79.8)	(58.0,54.0)	(54.9,47.4)	(60.0,55.0)	(61.0,56.0)
	DWT	(95.0,98.9)	(96.3,99.2)	(95.0,99.0)	(92.4,98.2)	(95.0,98.0)	(95.0,98.0)
TU Berlin	Six Statistical and DWT	(96.2,81.8)	(97.8,84.0)	(98.0,86.0)	(93.4,84.7)	(98.0,88.0)	(98.0,90.0)
	Six Statistical	(56.4,54.5)	(59.0,62.0)	(70.0,65.0)	(59.1,56.8)	(75.0,60.0)	(79.0,71.0)
	DWT	(96.0,99.5)	(97.0,99.0)	(98.0,100)	(96.9,99.3)	(98.8,99.9)	(99.0,100)
Buccino	Six Statistical and DWT	(89.3,85.0)	(94.9,90.0)	(94.0,91.0)	(91.2,78.1)	(94.7,79.0)	(95.0,86.0)
	Six Statistical	(56.3,52.6)	(62.0,56.0)	(63.0,57.0)	(55.2,50.7)	(62.0,55.9)	(63.0,56.0)
	DWT	(92.0,98.6)	(96.2,99.0)	(96.0,99.0)	(91.9,98.9)	(96.0,99.0)	(96.0,100)
TU Berlin	Six Statistical and DWT	(77.7,79.5)	(85.0,83.0)	(87.0,84.0)	(94.0,76.8)	(96.5,76.0)	(97.0,83.0)
	Six Statistical	(63.3,63.5)	(66.4,64.0)	(76.0,71.0)	(40.9,40.9)	(59.0,52.0)	(61.0,57.0)
	DWT	(79.6,80.1)	(85.0,81.0)	(88.0,82.0)	(95.5,99.3)	(97.0,99.6)	(98.0,100)

latent components. From the classification performance results in **Tables 4, 5**, it is apparent that the system-based fusion dominated the feature-based fusion for the all the subjects from both datasets using the Tree classifier. Contrarily, KNN has performed better for the feature-based fusion rather than the system-based fusion in most cases. Overall, the results show that MSVD is a powerful tool that naturally allows for the analysis and fusion of multiple

data sets. Being quite simple from the computational perspective, it could be well-suited for real-time applications as well.

The analysis and results are obtained from offline data, but the proposed approach is implementable for a real-time setup. Instead of processing all the channels from both modalities, only the most optimized channels using a correlation coefficient can be applied for feature extraction. It is shown in Hasan

et al. (2020) that it helps to reduce the computational burden while maintaining the classification accuracy. The selection of channels for the individual subjects can be added as an initialization step. The computation of SVD for a large matrix can be time-consuming; hence, limits the real-time application. For a rectangular matrix, instead of computing the SVD of a matrix  $A$  as in Equation (5), we can form a square matrix i.e.,  $A^T A$  for a thin matrix, and  $AA^T$  for a fat matrix to compute the SVD. The computation of SVD for these square matrices is considered efficient; therefore, suitable for online systems.

The features selection does have direct impact on the classification accuracy; thus, care must be taken in this regard. It is desirable that those features must be extracted, who truly represent the data and are as compact as possible. In **Table 5**, three different feature sets—DWT features, six statistical features, and a combination of DWT-statistical—are extracted to evaluate the performance of the system-based fusion for a hybrid EEG-fNIRS. In contrast to the feature-based fusion approach, the features are extracted from the fused EEG-fNIRS signal in the system-based fusion. Thus, for both fusion schemes, different behaviors can be expected. On Buccino dataset, the results show that the features set pertaining to the DWT-statistical, statistical, and DWT, in case of the KNN (Tree) classifiers, have 78.3% (89.4%), 51.6% (57.2%), and 97.8% (90.61%) average accuracies for all the subjects, respectively. On TU Berlin dataset, the average accuracies obtained for all the subjects, using the KNN (Tree) classifiers, for features set related to DWT-statistical, statistical, and DWT are 81.12% (92.9%), 53.38% (54.26%), and 96.67% (94.12%), respectively. These numbers reveal that by using the last layer's approximation coefficient of DWT, the highest accuracy is achieved; whereas, the lowest accuracy is obtained using the six statistical features. For DWT-statistical and statistical features, Tree classifier yielded the highest average accuracies; whereas, KNN achieved the highest accuracy for DWT features.

System-based fusion using MSVD enables the processing of fused EEG-fNIRS signals, rather than processing each modality separately for feature extraction and fusing them later. One of the concerns of this study, when it comes to system-based fusion, is the requirement of the same number of channels for both modalities, thus making channel selection compulsory. As such, future work will explore the possibility of system-based fusion when there is a mismatch between the number of channels for both modalities.

The second limitation of our study is the manual selection of features for the classification. The manual extraction of the features is a cumbersome process and has a direct impact on the classification accuracy. With the selection of optimal features, effective pre-processing, and various classification techniques, this accuracy can be improved (Khan R. A. et al., 2018; Hasan

et al., 2020). However, it is not guaranteed that the optimal feature for one task will be able to produce desirable results for the other tasks. Therefore, this process has to be repeated for individual tasks, and this consumes a lot of time. Recently, deep learning techniques, such as convolution neural network (CNN) and recurrent neural network (RNN) have been utilized for automatic feature extraction, pre-processing, and classification (Zhang et al., 2017; Yang et al., 2018; Tayeb et al., 2019). The obtained results have been promising when compared to the conventional classifiers (Trakoolwilaiwan et al., 2017; Chiarelli et al., 2018; Kumar et al., 2019; Asgher et al., 2020; Ghonchi et al., 2020). Considering the improvement in accuracy obtained using deep learning techniques, even in light of the limited amount of data and fewer pre-processing requirements, this improvement motivates us to work upon the combination of such techniques with MSVD in the future.

In conclusion, the present work proposed a novel hybrid EEG-fNIRS fusion approach for the classification. The primary goal is to improve the classification accuracy and to reduce the computational complexity of the hybrid EEG-fNIRS BCI. In order to achieve this, an MSVD approach is proposed for feature-based fusion and system-based fusion. To validate the effectiveness of the proposed approach, eight different subjects were considered and multiple trials were performed. As is evident from the results, our hybrid system significantly reduces the computational burden while achieving higher classification accuracy. The authors anticipate and hope that the proposed fusion approach will lead to more effective applications of BCI.

## DATA AVAILABILITY STATEMENT

Publicly available datasets were analyzed in this study. This data can be found here: <http://dx.doi.org/10.6084/m9.figshare.1619641>; <http://dx.doi.org/10.6084/m9.figshare.1619640>; [http://doc.ml.tu-berlin.de/simultaneous\\_EEG\\_NIRS/](http://doc.ml.tu-berlin.de/simultaneous_EEG_NIRS/).

## ETHICS STATEMENT

The studies involved were conducted according to the Helsinki declaration and were approved by the Institutional Review Board at University of Houston and by the Ethics Committee of the Institute of Psychology and Ergonomics, Berlin Institute of Technology. The patients/participants provided their written informed consent to participate in this study.

## AUTHOR CONTRIBUTIONS

MK and MH conceived of the presented idea. MH developed the theory and performed the computations. MK verified the analytical methods. All authors discussed the results and contributed to the final manuscript.

## REFERENCES

- Abiri, R., Borhani, S., Sellers, E. W., Jiang, Y., and Zhao, X. (2019). A comprehensive review of EEG-based brain-computer interface paradigms. *J. Neural Eng.* 16:011001. doi: 10.1088/1741-2552/aaf12e
- Aghajani, H., Garbey, M., and Omurtag, A. (2017). Measuring mental workload with EEG+ fNIRS. *Front. Hum. Neurosci.* 11:359. doi: 10.3389/fnhum.2017.00359
- Ahn, M., and Jun, S. C. (2015). Performance variation in motor imagery brain-computer interface: a brief review. *J.*

- Neurosci. Methods* 243, 103–110. doi: 10.1016/j.jneumeth.2015.01.033
- Ahn, S., and Jun, S. C. (2017). Multi-modal integration of EEG-fNIRS for brain-computer interfaces-current limitations and future directions. *Front. Hum. Neurosci.* 11:503. doi: 10.3389/fnhum.2017.00503
- Aihara, T., Takeda, Y., Takeda, K., Yasuda, W., Sato, T., Otaka, Y., et al. (2012). Cortical current source estimation from electroencephalography in combination with near-infrared spectroscopy as a hierarchical prior. *Neuroimage* 59, 4006–4021. doi: 10.1016/j.neuroimage.2011.09.087
- Akoglu, H. (2018). User's guide to correlation coefficients. *Turk. J. Emerg. Med.* 18, 91–93. doi: 10.1016/j.tjem.2018.08.001
- Al-Shargie, F., Kiguchi, M., Badruddin, N., Dass, S. C., Hani, A. F. M., and Tang, T. B. (2016). Mental stress assessment using simultaneous measurement of EEG and fNIRS. *Biomed. Opt. Express* 7, 3882–3898. doi: 10.1364/BOE.7.003882
- Al-Shargie, F., Tang, T. B., and Kiguchi, M. (2017). Assessment of mental stress effects on prefrontal cortical activities using canonical correlation analysis: an fNIRS-EEG study. *Biomed. Opt. Express* 8, 2583–2598. doi: 10.1364/BOE.8.002583
- Asgher, U., Khalil, K., Khan, M. J., Ahmad, R., Butt, S. I., Ayaz, Y., et al. (2020). Enhanced accuracy for multiclass mental workload detection using long short-term memory for brain-computer interface. *Front. Neurosci.* 14:584. doi: 10.3389/fnins.2020.00584
- Ashin, R., Morimoto, A., and Vaillancourt, R. (2005). Image compression with multiresolution singular value decomposition and other methods. *Math. Comput. Modell.* 41, 773–790. doi: 10.1016/j.mcm.2003.12.014
- Aydemir, O., and Kaykicioglu, T. (2014). Decision tree structure based classification of EEG signals recorded during two dimensional cursor movement imagery. *J. Neurosci. Methods* 229, 68–75. doi: 10.1016/j.jneumeth.2014.04.007
- Bablani, A., Edla, D. R., and Dodia, S. (2018). Classification of EEG data using k-nearest neighbor approach for concealed information test. *Proc. Comput. Sci.* 143, 242–249. doi: 10.1016/j.procs.2018.10.392
- Baker, W. B., Parthasarathy, A. B., Busch, D. R., Mesquita, R. C., Greenberg, J. H., and Yodh, A. (2014). Modified beer-lambert law for blood flow. *Biomed. Opt. Express* 5, 4053–4075. doi: 10.1364/BOE.5.004053
- Berger, A., Horst, F., Müller, S., Steinberg, F., and Doppelmayer, M. (2019). Current state and future prospects of EEG and fNIRS in robot-assisted gait rehabilitation: a brief review. *Front. Hum. Neurosci.* 13:172. doi: 10.3389/fnhum.2019.00172
- Blankertz, B., Tangermann, M., Vidaurre, C., Fazli, S., Sannelli, C., Haufe, S., et al. (2010). The Berlin brain-computer interface: non-medical uses of BCI technology. *Front. Neurosci.* 4:198. doi: 10.3389/fnins.2010.00198
- Bozinovski, S. (2016). "Signal processing robotics using signals generated by a human head: from pioneering works to EEG-based emulation of digital circuits," in *International Conference on Robotics in Alpe-Adria Danube Region* (Springer), 449–462. doi: 10.1007/978-3-319-49058-8\_49
- Buccino, A. P., Keles, H. O., and Omurtag, A. (2016). Hybrid EEG-fNIRS asynchronous brain-computer interface for multiple motor tasks. *PLoS ONE* 11:e0146610. doi: 10.1371/journal.pone.0146610
- Buch, V. P., Richardson, A. G., Brandon, C., Stiso, J., Khattak, M. N., Bassett, D. S., et al. (2018). Network brain-computer interface (NBCI): An alternative approach for cognitive prosthetics. *Front. Neurosci.* 12:790. doi: 10.3389/fnins.2018.00790
- Calhoun, V. D., and Adali, T. (2008). Feature-based fusion of medical imaging data. *IEEE Trans. Inform. Technol. Biomed.* 13, 711–720. doi: 10.1109/ITTB.2008.923773
- Chen, D., Wan, S., Xiang, J., and Bao, F. S. (2017). A high-performance seizure detection algorithm based on discrete wavelet transform (DWT) and EEG. *PLoS ONE* 12:e0173138. doi: 10.1371/journal.pone.0173138
- Chiarelli, A. M., Croce, P., Merla, A., and Zappasodi, F. (2018). Deep learning for hybrid EEG-fNIRS brain-computer interface: application to motor imagery classification. *J. Neural Eng.* 15:036028. doi: 10.1088/1741-2552/aaaf82
- Choi, K. (2013). Electroencephalography (EEG)-based neurofeedback training for brain-computer interface (BCI). *Exp. Brain Res.* 231, 351–365. doi: 10.1007/s00221-013-3699-6
- Congedo, M., Barachant, A., and Bhatia, R. (2017). Riemannian geometry for EEG-based brain-computer interfaces; a primer and a review. *Brain Comput. Interfaces* 4, 155–174. doi: 10.1080/2326263X.2017.1297192
- Cope, M., Delpy, D. T., Reynolds, E. O. R., Wray, S., Wyatt, J., and Van der Zee, P. (1988). "Methods of quantitating cerebral near infrared spectroscopy data," in *Oxygen Transport to Tissue X* (New York, NY: Springer), 183–189. doi: 10.1007/978-1-4615-9510-6\_21
- Coyle, S., Ward, T., Markham, C., and McDarby, G. (2004). On the suitability of near-infrared (nir) systems for next-generation brain-computer interfaces. *Physiol. Meas.* 25:815. doi: 10.1088/0967-3334/25/4/003
- Coyle, S. M., Ward, T. E., and Markham, C. M. (2007). Brain-computer interface using a simplified functional near-infrared spectroscopy system. *J. Neural Eng.* 4:219. doi: 10.1088/1741-2560/4/3/007
- Delpy, D. T., Cope, M., van der Zee, P., Arridge, S., Wray, S., and Wyatt, J. (1988). Estimation of optical pathlength through tissue from direct time of flight measurement. *Phys. Med. Biol.* 33:1433. doi: 10.1088/0031-9155/33/12/008
- Do, A. H., Wang, P. T., King, C. E., Chun, S. N., and Nenadic, Z. (2013). Brain-computer interface controlled robotic gait orthosis. *J. Neuroeng. Rehabil.* 10:111. doi: 10.1186/1743-0003-10-111
- Doud, A. J., Lucas, J. P., Pisansky, M. T., and He, B. (2011). Continuous three-dimensional control of a virtual helicopter using a motor imagery based brain-computer interface. *PLoS ONE* 6:e26322. doi: 10.1371/journal.pone.0026322
- Duan, X., Xie, S., Xie, X., Meng, Y., and Xu, Z. (2019). Quadcopter flight control using a non-invasive multi-modal brain computer interface. *Front. Neurobot.* 13:23. doi: 10.3389/fnbot.2019.00023
- Faust, O., Acharya, U. R., Adeli, H., and Adeli, A. (2015). Wavelet-based EEG processing for computer-aided seizure detection and epilepsy diagnosis. *Seizure* 26, 56–64. doi: 10.1016/j.seizure.2015.01.012
- Fazli, S., Mehnert, J., Steinbrink, J., Curio, G., Villringer, A., Müller, K. R., et al. (2012). Enhanced performance by a hybrid NIRS-EEG brain computer interface. *Neuroimage* 59, 519–529. doi: 10.1016/j.neuroimage.2011.07.084
- Ferrari, M., Giannini, I., Sideri, G., and Zanette, E. (1985). "Continuous non invasive monitoring of human brain by near infrared spectroscopy," in *Oxygen Transport to Tissue VII* (Boston, MA: Springer), 873–882. doi: 10.1007/978-1-4684-3291-6\_88
- Ge, S., Yang, Q., Wang, R., Lin, P., Gao, J., Leng, Y., et al. (2017). A brain-computer interface based on a few-channel EEG-fNIRS bimodal system. *IEEE Access* 5, 208–218. doi: 10.1109/ACCESS.2016.2637409
- Ghonchi, H., Fateh, M., Abolghasemi, V., Ferdowsi, S., and Rezvani, M. (2020). Deep recurrent-convolutional neural network for classification of simultaneous EEG-fNIRS signals. *IET Signal Process.* 14, 142–153. doi: 10.1049/iet-spr.2019.0297
- Hasan, M. A. H., Khan, M. U., and Mishra, D. (2020). A computationally efficient method for hybrid EEG-fNIRS BCI based on the Pearson correlation. *Biomed. Res. Int.* 2020:1838140. doi: 10.1155/2020/1838140
- Hong, K.-S., Bhutta, M. R., Liu, X., and Shin, Y.-I. (2017). Classification of somatosensory cortex activities using fNIRS. *Behav. Brain Res.* 333, 225–234. doi: 10.1016/j.bbr.2017.06.034
- Hong, K.-S., Khan, M. J., and Hong, M. J. (2018). Feature extraction and classification methods for hybrid fNIRS-EEG brain-computer interfaces. *Front. Hum. Neurosci.* 12:246. doi: 10.3389/fnhum.2018.00246
- Kakarala, R., and Ogunbona, P. O. (2001). Signal analysis using a multiresolution form of the singular value decomposition. *IEEE Trans. Image Process.* 10, 724–735. doi: 10.1109/83.918566
- Khan, A. H., Li, S., Zhou, X., Li, Y., Khan, M. U., Luo, X., et al. (2018). Neural & bio-inspired processing and robot control. *Front. Neurobot.* 12:72. doi: 10.3389/fnbot.2018.00072
- Khan, M. J., and Hong, K. S. (2017). Hybrid EEG-fNIRS-based eight-command decoding for BCI: application to quadcopter control. *Front. Neurobot.* 11:6. doi: 10.3389/fnbot.2017.00006
- Khan, M. J., Hong, M. J., and Hong, K.-S. (2014). Decoding of four movement directions using hybrid NIRS-EEG brain-computer interface. *Front. Hum. Neurosci.* 8:244. doi: 10.3389/fnhum.2014.00244
- Khan, R. A., Naseer, N., Qureshi, N. K., Noori, F. M., Nazeer, H., and Khan, M. U. (2018). fNIRS-based neurobotic interface for gait rehabilitation. *J. Neuroeng. Rehabil.* 15:7. doi: 10.1186/s12984-018-0346-2
- Koo, B., Lee, H.-G., Nam, Y., Kang, H., Koh, C. S., Shin, H.-C., et al. (2015). A hybrid NIRS-EEG system for self-paced brain computer interface with online motor imagery. *J. Neurosci. Methods* 244, 26–32. doi: 10.1016/j.jneumeth.2014.04.016

- Kumar, S., Sharma, A., and Tsunoda, T. (2019). Brain wave classification using long short-term memory network based optical predictor. *Sci. Rep.* 9, 1–13. doi: 10.1038/s41598-019-45605-1
- Li, R., Potter, T., Huang, W., and Zhang, Y. (2017). Enhancing performance of a hybrid EEG-fNIRS system using channel selection and early temporal features. *Front. Hum. Neurosci.* 11:462. doi: 10.3389/fnhum.2017.00462
- Lung, S.-Y. (2002). Multi-resolution form of svd for text-independent speaker recognition. *Pattern Recogn.* 35, 1637–1639. doi: 10.1016/S0031-3203(02)00015-8
- Mallat, S. G. (1989). A theory for multiresolution signal decomposition: the wavelet representation. *IEEE Trans. Pattern Anal. Mach. Intell.* 11, 674–693. doi: 10.1109/34.192463
- Morioka, H., Kanemura, A., Morimoto, S., Yoshioka, T., Oba, S., Kawanabe, M., et al. (2014). Decoding spatial attention by using cortical currents estimated from electroencephalography with near-infrared spectroscopy prior information. *Neuroimage* 90, 128–139. doi: 10.1016/j.neuroimage.2013.12.035
- Naidu, V. (2011). Image fusion technique using multi-resolution singular value decomposition. *Defence Sci. J.* 61, 479–484. doi: 10.14429/dsj.61.705
- Naseer, N., and Keum-Shik, H. (2015). fNIRS-based brain-computer interfaces: a review. *Frontiers in human neuroscience*, 9(3). doi: 10.3389/fnhum.2015.00003
- Paszkiel, S. (2016). Control based on brain-computer interface technology for video-gaming with virtual reality techniques. *J. Automat. Mobile Robot. Intell. Syst.* 10, 3–7. doi: 10.14313/JAMRIS\_4-2016/26
- Paszkiel, S. (2020). “Using BCI and VR technology in neurogaming,” in *Analysis and Classification of EEG Signals for Brain-Computer Interfaces* (Cham: Springer), 93–99. doi: 10.1007/978-3-030-30581-9\_11
- Pfurtscheller, G., Scherer, R., and Neuper, C. (2006). “EEG-based brain-computer interface,” in *The Brain at Work*, ed R. Parasuraman (Oxford University Press, Inc.), 315–328. doi: 10.1002/9780471740360.ebs1309
- Putze, F., Hesslinger, S., Tse, C.-Y., Huang, Y., Herff, C., Guan, C., et al. (2014). Hybrid fNIRS-EEG based classification of auditory and visual perception processes. *Front. Neurosci.* 8:373. doi: 10.3389/fnins.2014.00373
- Rosca, S., Leba, M., Ionica, A., and Gamulescu, O. (2018). “Quadcopter control using a BCI,” in *IOP Conference Series: Materials Science and Engineering* (Hunedoara: IOP Publishing), 012048. doi: 10.1088/1757-899X/294/1/012048
- Saadati, M., Nelson, J., and Ayaz, H. (2020). “Convolutional neural network for hybrid fNIRS-EEG mental workload classification,” in *Advances in Neuroergonomics and Cognitive Engineering. AHFE 2019. Advances in Intelligent Systems and Computing*, ed H. Ayaz, Vol. 953 (Cham: Springer), 221–232. doi: 10.1007/978-3-030-20473-0\_22
- Shin, J., Kwon, J., and Im, C.-H. (2018a). A ternary hybrid EEG-NIRS brain-computer interface for the classification of brain activation patterns during mental arithmetic, motor imagery, and idle state. *Front. Neuroinform.* 12:5. doi: 10.3389/fninf.2018.00005
- Shin, J., Von Lüthmann, A., Kim, D.-W., Mehnert, J., Hwang, H.-J., and Müller, K.-R. (2018b). Simultaneous acquisition of EEG and nirs during cognitive tasks for an open access dataset. *Sci. Data* 5:180003. doi: 10.1038/sdata.2018.3
- Subasi, A. (2007). EEG signal classification using wavelet feature extraction. *Expert Syst.* 32, 1084–1093. doi: 10.1016/j.eswa.2006.02.005
- Sun, Z., Huang, Z., Duan, F., and Liu, Y. (2020). A novel multimodal approach for hybrid brain-computer interface. *IEEE Access* 8, 89909–89918. doi: 10.1109/ACCESS.2020.2994226
- Tayeb, Z., Fedjaev, J., Ghaboosi, N., Richter, C., Everding, L., Qu, X., et al. (2019). Validating deep neural networks for online decoding of motor imagery movements from EEG signals. *Sensors* 19:210. doi: 10.3390/s19010210
- Trakoolwilaiwan, T., Behboodi, B., Lee, J., Kim, K., and Choi, J.-W. (2017). Convolutional neural network for high-accuracy functional near-infrared spectroscopy in a brain-computer interface: three-class classification of rest, right-, and left-hand motor execution. *Neurophotonics* 5:011008. doi: 10.1117/1.NPh.5.1.011008
- Vasiljevic, G. A. M., and de Miranda, L. C. (2020). Brain-computer interface games based on consumer-grade EEG devices: a systematic literature review. *Int. J. Hum. Comput. Int.* 36, 105–142. doi: 10.1080/10447318.2019.1612213
- Vidal, J. J. (1973). Toward direct brain-computer communication. *Annu. Rev. Biophys. Bioeng.* 2, 157–180. doi: 10.1146/annurev.bb.02.060173.001105
- Wolpaw, J. R., Birbaumer, N., McFarland, D. J., Pfurtscheller, G., and Vaughan, T. M. (2002). Brain-computer interfaces for communication and control. *Clin. Neurophysiol.* 113, 767–791. doi: 10.1016/S1388-2457(02)00057-3
- Wu, Y.-L., Agrawal, D., and El Abbadi, A. (2000). “A comparison of DFT and DWT based similarity search in time-series databases,” in *Proceedings of the Ninth International Conference on Information and Knowledge Management (ACM)*, 488–495. doi: 10.1145/354756.354857
- Yanagisawa, T., Fukuma, R., Seymour, B., Hosomi, K., Kishima, H., Shimizu, T., et al. (2019). “Using a BCI prosthetic hand to control phantom limb pain,” in *Brain-Computer Interface Research*, eds C. Guger, N. Mrachacz-Kersting, and B. Allison (Cham: Springer), 43–52. doi: 10.1007/978-3-030-05668-1\_4
- Yang, J., Yao, S., and Wang, J. (2018). Deep fusion feature learning network for mi-EEG classification. *IEEE Access* 6, 79050–79059. doi: 10.1109/ACCESS.2018.2877452
- Yildiz, M., and Bergil, E. (2015). The investigation of channel selection effects on epileptic analysis of EEG signals. *Balkan J. Electric. Comput. Eng.* 3, 236–241. doi: 10.17694/bajece.22796
- Yin, X., Xu, B., Jiang, C., Fu, Y., Wang, Z., Li, H., et al. (2015). A hybrid BCI based on EEG and fNIRS signals improves the performance of decoding motor imagery of both force and speed of hand clenching. *J. Neural Eng.* 12:036004. doi: 10.1088/1741-2560/12/3/036004
- Zama, T., Takahashi, Y., and Shimada, S. (2019). Simultaneous EEG-NIRS measurement of the inferior parietal lobule during a reaching task with delayed visual feedback. *Front. Hum. Neurosci.* 13:301. doi: 10.3389/fnhum.2019.00301
- Zhang, D., Yao, L., Zhang, X., Wang, S., Chen, W., and Boots, R. (2017). EEG-based intention recognition from spatio-temporal representations via cascade and parallel convolutional recurrent neural networks. *arXiv [Preprint]*. arXiv:1708.06578.

**Conflict of Interest:** The authors declare that the research was conducted in the absence of any commercial or financial relationships that could be construed as a potential conflict of interest.

Copyright © 2020 Khan and Hasan. This is an open-access article distributed under the terms of the Creative Commons Attribution License (CC BY). The use, distribution or reproduction in other forums is permitted, provided the original author(s) and the copyright owner(s) are credited and that the original publication in this journal is cited, in accordance with accepted academic practice. No use, distribution or reproduction is permitted which does not comply with these terms.



# Parallel Spatial–Temporal Self-Attention CNN-Based Motor Imagery Classification for BCI

*Xiuling Liu*<sup>1,2</sup>, *Yonglong Shen*<sup>1,2</sup>, *Jing Liu*<sup>2,3,4\*</sup>, *Jianli Yang*<sup>1,2</sup>, *Peng Xiong*<sup>1,2</sup> and *Feng Lin*<sup>5</sup>

<sup>1</sup> College of Electronic Information Engineering, Hebei University, Baoding, China, <sup>2</sup> Key Laboratory of Digital Medical Engineering of Hebei Province, Hebei University, Baoding, China, <sup>3</sup> College of Computer and Cyber Security, Hebei Normal University, Shijiazhuang, China, <sup>4</sup> Beijing Key Laboratory of Mobile Computing and Pervasive Device, Institute of Computing Technology, Chinese Academy of Sciences, Beijing, China, <sup>5</sup> School of Computer Science and Engineering, Nanyang Technological University, Singapore, Singapore

## OPEN ACCESS

### Edited by:

Saugat Bhattacharyya,  
Ulster University, United Kingdom

### Reviewed by:

Davide Valeriani,  
Massachusetts Eye & Ear Infirmary,  
Harvard Medical School,  
United States  
Jacobo Fernandez-Vargas,  
University of Essex, United Kingdom

### \*Correspondence:

Jing Liu  
liujing01@ict.ac.cn

### Specialty section:

This article was submitted to  
Brain Imaging Methods,  
a section of the journal  
Frontiers in Neuroscience

**Received:** 26 July 2020

**Accepted:** 14 October 2020

**Published:** 11 December 2020

### Citation:

Liu X, Shen Y, Liu J, Yang J, Xiong P  
and Lin F (2020) Parallel  
Spatial–Temporal Self-Attention  
CNN-Based Motor Imagery  
Classification for BCI.  
*Front. Neurosci.* 14:587520.  
doi: 10.3389/fnins.2020.587520

Motor imagery (MI) electroencephalography (EEG) classification is an important part of the brain-computer interface (BCI), allowing people with mobility problems to communicate with the outside world via assistive devices. However, EEG decoding is a challenging task because of its complexity, dynamic nature, and low signal-to-noise ratio. Designing an end-to-end framework that fully extracts the high-level features of EEG signals remains a challenge. In this study, we present a parallel spatial–temporal self-attention-based convolutional neural network for four-class MI EEG signal classification. This study is the first to define a new spatial-temporal representation of raw EEG signals that uses the self-attention mechanism to extract distinguishable spatial–temporal features. Specifically, we use the spatial self-attention module to capture the spatial dependencies between the channels of MI EEG signals. This module updates each channel by aggregating features over all channels with a weighted summation, thus improving the classification accuracy and eliminating the artifacts caused by manual channel selection. Furthermore, the temporal self-attention module encodes the global temporal information into features for each sampling time step, so that the high-level temporal features of the MI EEG signals can be extracted in the time domain. Quantitative analysis shows that our method outperforms state-of-the-art methods for intra-subject and inter-subject classification, demonstrating its robustness and effectiveness. In terms of qualitative analysis, we perform a visual inspection of the new spatial–temporal representation estimated from the learned architecture. Finally, the proposed method is employed to realize control of drones based on EEG signal, verifying its feasibility in real-time applications.

**Keywords:** motor imagery, EEG, BCI, spatial-temporal self-attention, deep learning

## 1. INTRODUCTION

Electroencephalography (EEG) has been widely used in many noninvasive brain–computer interface (BCI) studies because it is simple, safe, and inexpensive (Kübler and Birbaumer, 2008; Lotte et al., 2018). Among the different types of EEG signals, motor imagery (MI) is most commonly used. When people imagine or execute a movement with their hands, both feet, or tongue, the

power of the mu (8–12 Hz) and beta (16–26 Hz) rhythms are suppressed or promoted in the sensorimotor region of the contralateral and ipsilateral hemispheres (Pfurtscheller et al., 1997; Pfurtscheller and Da Silva, 1999; Neuper and Pfurtscheller, 2001). Our goal is to classify these MI EEG associated brain activities accurately to allow people with mobility problems to communicate with the outside world via assistive devices.

Numerous studies have examined the classification of MI EEG signals. These studies can be divided into two categories: traditional methods and deep learning-based methods. Among the traditional methods, the common spatial pattern (CSP) algorithm (Müller-Gerking et al., 1999; Ramoser et al., 2000) and its variants are widely used to extract the spatial distribution of features from multi-channel EEG data. The fundamental principle of CSP is to find a set of optimal spatial filters through the diagonalization of a matrix, so as to maximize the difference between the variance values of the two types of signals, and thereby obtain a feature vector with higher discrimination. Filter bank common spatial pattern (FBCSP; Ang et al., 2008) is a variant of CSP that improves the classification accuracy by performing autonomous selection of the discriminative subject frequency range for bandpass filtering of the EEG measurements. Jin et al. (2019) used Pearson's correlation coefficient to manually select the channel that contained the most correlated information, and then employed the regularized common spatial pattern (RCSP) to extract effective features and a support vector machine (SVM) as a classifier. However, the feature selection is heavily reliant on handcrafted features. In addition, because MI EEG signals have limited spatial resolution, a low signal-to-noise ratio (SNR), and highly dynamic characteristics, traditional methods are unable to achieve high decoding accuracy.

Currently, deep learning (DL) exhibits excellent performance in a variety of medical applications (Kumar A. et al., 2016; De et al., 2017; Ma et al., 2017, 2018), and an increasing number of BCI researchers are investigating the use of DL models in MI classification tasks (Schirmer et al., 2017). The majority of studies use either feature-based input networks or original signal-based input networks. In the former case, the EEG signals are first transformed from 1D feature vectors into 2D manually specified feature maps by combining spatial, spectral, and temporal information using conventional feature-extraction methods (such as spectrograms and wavelets). The extracted features are then fed into a classification network (Lu et al., 2016; Tabar and Halici, 2016; Zhu et al., 2019). Kumar S. et al. (2016) used CSP to extract features, which were fed into a multilayer perceptron (MLP). Sakhavi et al. (2018) proposed a new feature representation method that combined FBCSP and the Hilbert transform to extract spatial and temporal features. Subsequently, a 5-layer convolutional neural network (CNN) architecture was used for classification. The work (Vaswani et al., 2017) is the first to propose the self-attention mechanism to draw global dependencies of inputs and applies it in machine translation, attention modules are increasingly applied in many fields (Lin et al., 2017; Shen et al., 2018; Fu et al., 2019). However, feature information about the MI signals will be lost when a manually specified feature extraction method is used, which has a negative effect on performance.

Input networks based on the original signal, i.e., the  $C$  (channel)  $\times T$  (time point) matrices, obtain high-level implicit representations from raw EEG signals without manual feature selection. In such networks, the feature extraction and classification steps are combined in a single end-to-end model with (or without) minimal preprocessing. EEGNet (Lawhern et al., 2018) is a successful network that uses relatively few parameters to achieve good performance on various EEG classification tasks. Azab et al. (2019) proposed a novel weighted transfer learning approach that improves the accuracy of MI classification in BCI systems. Song et al. (2019) improved the classification performance with limited EEG data by combining the representation module, classification module, and reconstruction module into an end-to-end framework. Sakhavi et al. (2018) introduced a new data representation using a spatial-temporal DL model architecture that is designed to learn temporal information from the original input signals. Amin et al. (2019) used a multilayer CNN model that fuses different characteristics of the raw EEG data from the spatial and temporal domains. Zhao et al. (2019) developed a new 3D representation of EEG, a multibranch 3D CNN, and a corresponding classification strategy. Their approach achieved good performance and significantly improved the classification accuracy for different subjects.

Although DL has made remarkable progress in MI classification, it still faces many challenges. First, previous methods mainly select signal channels in motor regions such as C3, Cz, and C4, but MI for different body parts may activate different functional regions of the brain (Ehrsson et al., 2003; Gong et al., 2018). All brain functional areas will have certain effects on the different MI tasks, not only the motor regions. Because the strength of the MI EEG signals varies from person to person, it is impossible to determine exactly which brain regions are most associated with MI (Ma et al., 2020). Second, MI signals are temporally continuous with low SNR and are susceptible to a variety of biological affects (e.g., eye blinks and muscle activity) or environmental artifacts (e.g., noise). Dynamic changes to the EEG signal in the time domain often contain valuable information about the raw MI EEG signals, although these are often neglected by traditional methods, making feature extraction more complicated. The combination of these factors means that previous methods have a limited ability to extract general representations and suffer from low classification accuracy.

To overcome these problems, we propose an end-to-end parallel spatial-temporal self-attention-based CNN for four-class MI EEG signal classification based on the raw MI EEG signals. The proposed method assumes that motor-dependent channels and sampling time steps should be assigned higher weight values than motor-independent channels and sampling time steps during brain activity. The weight values are calculated based on the proposed parallel spatial-temporal self-attention mechanism, which captures high-level distinguishable spatial-temporal features and defines a more accurate compact representation in the space and time domains of the raw MI EEG signal data. Our CNN is capable of modeling high-level, robust, and salient feature representations hidden in the raw EEG signal

streams, and can capture complex relationships within data via the stacking of multiple layers of information processing modules in a hierarchical architecture. The major contributions of this study can be summarized as follows:

- In the spatial domain, each channel is recorded from each electrode in various brain areas. We use the spatial self-attention module to capture the potential spatial links between any two channels of the MI EEG signals. The features in a certain channel are updated by aggregating the features over all channels with a weighted summation, where the weights are automatically learned by the feature similarities between the corresponding channels. This module defines a new learned spatial representation of the raw MI EEG data that choose the best channels by automatically assigning higher values to motor-dependent channels and lower values to motor-independent channels. This verifies our assumption that when people think about an action, any channel with similar motor-dependent characteristics can promote mutual improvement, regardless of its spatial location in the brain. As a result, this module improves the classification accuracy and eliminates the artifacts caused by the manual selection of signal channels.
- In the temporal domain, we know that MI EEG signals are continuous with low SNR, which means that there must be a correlation between each time step. Therefore, we use the temporal self-attention module to capture the temporal dependencies between any two sampling time steps, and update each sampling time step using a weighted sum of all sampling time steps. This module defines a new temporal representation of the raw MI EEG data that enhances the temporal representation by encoding the relevant continuous dynamic changes into the global temporal features of each sampling step in the time domain. This is superior to a single-valued representation. In other words, instead of a single sampling value, a new automatically learned temporal representation of the signal is used to extract high-level temporal features from the MI EEG signals in the time domain. Through this module, we assign more weight to the sampling points related to MI and reduce the weight of sampling points that are not related to MI. It is generally believed that there is little useful information in the artifacts, so the temporal self-attention module effectively reduces the interference caused by artifacts.
- The proposed model is evaluated on two challenging datasets to validate its robustness against data variations. The corresponding results demonstrate that our method outperforms several traditional methods (11.09% better on average) and DL-based methods (4.14% better on average) for four-class MI EEG classification by combining spatial and temporal features via the proposed parallel spatial-temporal self-attention architecture. To intuitively verify the rationality of the self-attention mechanism from physiological signals, we plot topographic maps of MI EEG data to illustrate that MI not only activates channels C3, C4, and Cz, but also affects different signal channels. In addition, a BCI application experiment is performed in which we train a model using the data collected in our laboratory and apply it to a drone's online

control system based on AirSim (Shah et al., 2018), which is an open source simulator developed by Microsoft.

The remainder of this paper is organized as follows. Section 2 describes the datasets and discusses the details of our method. Experimental results are then presented and use EEG MI to control a drone in section 3. In section 4, we discuss the experimental results from the EEG topographic map. Finally, section 5 presents our conclusions and provides some suggestions for future work.

## 2. MATERIALS AND METHODS

### 2.1. Overview

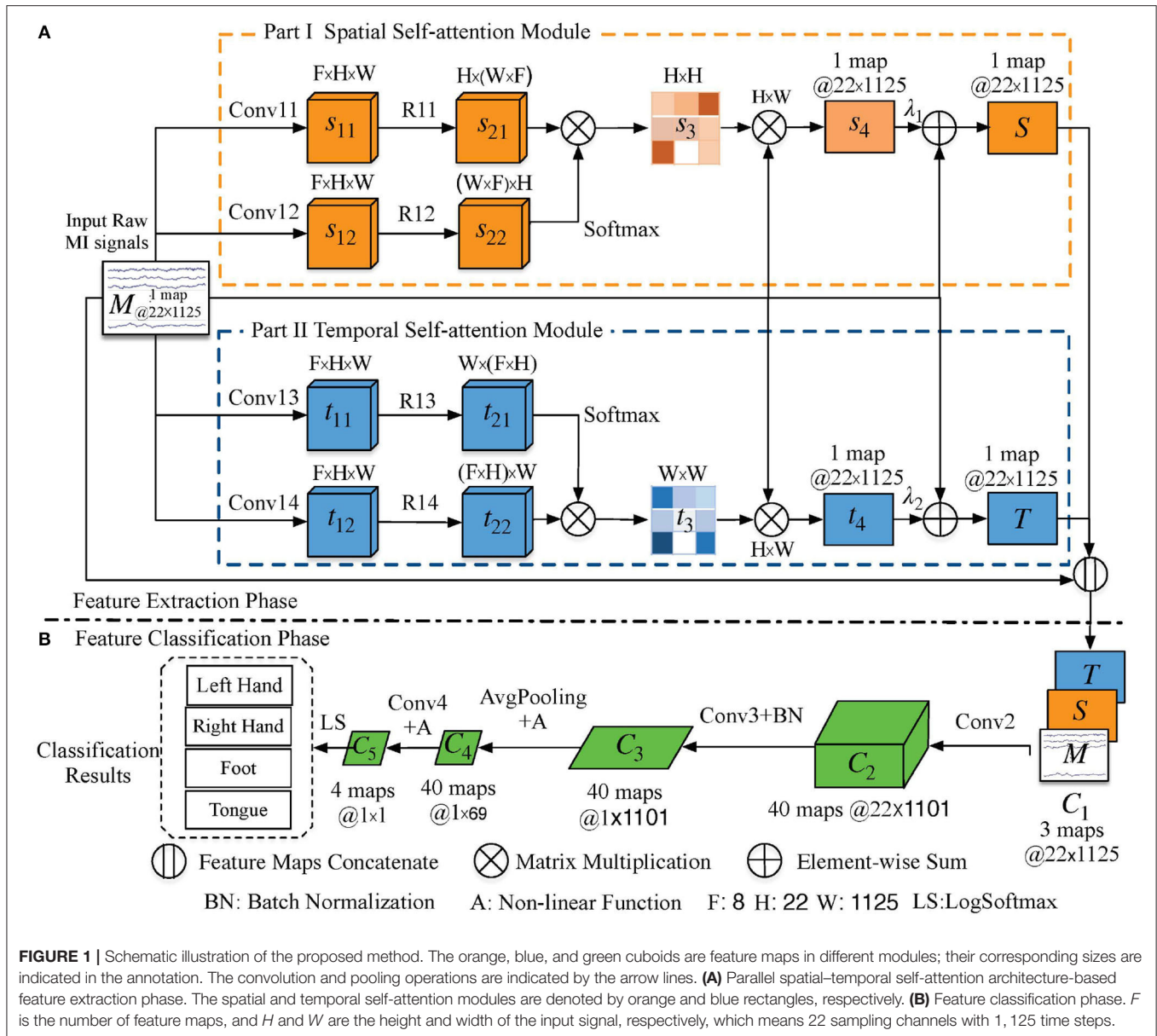
In this study, we employed two widely used public EEG MI datasets for evaluation. The main differences between them are the number of channels, trials, subjects, tasks, and sampling rates.

The first dataset is the BCI Competition IV dataset 2a (BCIIV2a) (Tangermann et al., 2012), which recorded a four-class MI task (left hand, right hand, both feet, and tongue) performed by nine subjects across 25 channels (22 EEG and 3 electrooculogram) with a 250 Hz sampling rate. Each channel was preprocessed with a bandpass filter of 0.5–100 Hz. For each subject, two sessions were recorded on different days. Each session comprised six runs separated by short breaks. One run consisted of 48 trials (12 for each of the four possible classes), yielding a total of 288 trials per session. We used one session as the training set, with the other session used to test the classifier and evaluate the performance. Thus, the training set consisted of the 288 trials from the first session and the test set consisted of the 288 trials from the second session. In addition, each trial was extracted using the same time window of  $[-0.5, 4s]$  on the MI phase of the signals over all 22 EEG channels. Hence, the input signal of our method consists of time series from 22 channels containing 1, 125 sampling points ( $22 \times 1, 125$ ).

The second dataset is the high gamma dataset (HGD) (Schirrmester et al., 2017), recorded during a four-class MI task across 44 EEG channel signals by 14 healthy subjects performing 4-s trials of certain movements, with 13 runs per subject. The four classes of movements involved the left hand, the right hand, both feet, and rest (no movement). For each subject, the training set consisted of approximately 880 trials (all runs except the last two runs), and the test set consisted of approximately 160 trials (the last two runs). The sampling rate for HGD was 500 Hz. For a fair comparison with BCIIV2a, HGD was resampled to 250 Hz and used the same 4.5-s time window, so that  $44 \times 1, 125$  data points were obtained for each trial.

We performed basic preprocessing of the MI EEG data, such as frequency filtering and normalization. A low-pass filter of 38 Hz and a high-pass filter of 0 Hz were applied to BCIIV2a, and a low-pass filter of 38 Hz and a high-pass filter of 4 Hz to HGD (Schirrmester et al., 2017). We performed exponential moving standardization to compute the exponential moving means and variances for each channel, and used these to standardize the continuous data.

The network architecture, as illustrated in **Figure 1**, consists of two phases: a feature extraction layer and a



feature classification layer. We first describe the feature extraction layer, which contains a parallel spatial-temporal self-attention architecture that extracts distinguishable features in the space and time domains. We then describe how to concatenate the extracted spatial-temporal features for the classification of the MI task and its corresponding training strategy. The code for our model is available in <https://github.com/Shenyonglong/Spatial-Temporal-attention->.

## 2.2. Construction of Self-Attention Module

### 2.2.1. Spatial Self-Attention Module

Traditional approaches usually select EEG channels manually, or assume that each channel plays an equal role. However, the active brain regions for the same MI action are different for different people, which means that the strength of the MI

signal varies from subject to subject, as well as for different trials by the same subject. This variation results in low classification accuracy. Therefore, to automatically select the most useful signal channel for extracting discriminant feature representations for subjects and eliminate the artifacts caused by manual selection of signal channels, we propose a spatial self-attention module.

Consider the orange rectangle in **Figure 1** and its network parameters in **Table 1**. Let  $M \in \mathbb{R}^{H \times W}$  be the raw data of height ( $H$ ) 22 and width ( $W$ ) 1,125. We first feed these data into two convolution layers (*Conv11* and *Conv12*) to generate feature maps  $s_{11}$  and  $s_{12}$ , where  $s_{11}$  and  $s_{12}$  belong to  $\mathbb{R}^{F \times H \times W}$  and  $F = 8$  denotes the number of feature maps. Then,  $s_{11}$  and  $s_{12}$  are reshaped (*R11* and *R12*) to  $\mathbb{R}^{H \times (F \times W)}$  and  $\mathbb{R}^{(F \times W) \times H}$ , respectively, to enable matrix multiplication between them.

**TABLE 1** | Detailed architecture of the proposed spatial self-attention module.

Spatial-attention module							
Input	$M(22, 1125)$	$M(22, 1125)$	$s_{11}(8, 22, 1125)$	$s_{12}(8, 22, 1125)$	$s_{21}, s_{22}$	$s_3, M$	$s_4, M, \lambda_1$
Layer	Conv11	Conv12	R11	R12	MMN	MM	ES
Output	$s_{11}(8, 22, 1125)$	$s_{12}(8, 22, 1125)$	$s_{21}(22, 9000)$	$s_{22}(9000, 22)$	$s_3(22, 22)$	$s_4(22, 1125)$	$S(22, 1125)$
Feature maps	8	8	1	1	1	1	1
Kernel	(1, 1)	(1, 1)	–	–	–	–	–
Stride	(1, 1)	(1, 1)	–	–	–	–	–

MMN, Matrix multiplication + Normalization + Softmax; MM, matrix multiplication; ES, element-wise sum.

Finally, a softmax function is applied to obtain the spatial self-attention weight map  $s_3 \in \mathbb{R}^{H \times H}$  as:

$$s_3^{ij} = \frac{\text{Func}(s_{21}^i, s_{22}^j)}{\sum_{j=1}^H \text{Func}(s_{21}^i, s_{22}^j)} \quad (1)$$

where *Func* is the similarity function, which uses matrix dot multiplication to calculate the similarity.  $s_3^{ij}$  denotes the similarity between the *i*th and *j*th channels, and ranges from 0 to 1 (with 0 indicating no similarity and 1 indicating complete similarity).

Matrix multiplication between  $s_3$  and  $M^{H \times W}$  is performed to obtain the spatial predicted signal  $s_4 \in \mathbb{R}^{H \times W}$ . Signal  $s_4$  is a spatial predicted signal in which each channel is a weighted sum of other channels from the raw data in the space domain. This task automatically learns similar weights between channels and updates each channel by adaptively aggregating spatial signal data across all channels with the weighted summation. In addition, we perform a residual block by multiplying a learnable parameter  $\lambda_1$  by  $s_4$  and perform an element-wise sum operation with the raw signal to obtain the final spatial feature signal ( $S \in \mathbb{R}^{H \times W}$ ) as follows:

$$S = \lambda_1 \times s_4 + M \quad (2)$$

where  $\lambda_1$  is initialized as 0 and is gradually updated to assign more appropriate weights during the training of the whole DL system (Zhang et al., 2019).  $S$  enhances the representative capability of the inter-subject classification. This means that when people think about an action, any channel with similar characteristics promotes mutual improvement, regardless of its spatial location in the brain.

### 2.2.2. Temporal Self-Attention Module

MI EEG signals are temporally continuous with a low SNR. Therefore, we constructed a temporal self-attention module (blue rectangle in **Figure 1**) to generate a temporal predicted signal that is the same size as the raw input data and model the interdependencies between time steps so as to eliminate the artifacts caused by subject and environmental artifacts. The corresponding network parameters are listed in **Table 2**.

The largest difference between this module and the spatial self-attention module is that we reshaped  $t_{11}$  and  $t_{12}$  (R13 and R14) to  $\mathbb{R}^{W \times (F \times H)}$  and  $\mathbb{R}^{(F \times H) \times W}$  to enable matrix multiplication

between them. A softmax function is applied to obtain the temporal self-attention weight map  $t_3 \in \mathbb{R}^{W \times W}$  by:

$$t_3^{pq} = \frac{\text{Func}(t_{21}^p, t_{22}^q)}{\sum_{q=1}^W \text{Func}(t_{21}^p, t_{22}^q)} \quad (3)$$

where *Func* is the similarity function, which uses matrix dot multiplication to calculate the similarity.  $t_3^{pq}$  denotes the similarity between the *p*th and *q*th sampling time steps, and ranges from 0 to 1 (with 0 indicating no similarity and 1 indicating complete similarity). Furthermore, we perform matrix multiplication between the raw signal  $M^{H \times W}$  and  $t_3$  to obtain the temporal predicted signal  $t_4 \in \mathbb{R}^{H \times W}$ , which captures the temporal dependencies between any two time steps and updates each time step with a weighted sum of all time steps in the time domain. Finally, a residual block is given by multiplying a learnable parameter  $\lambda_2$  by  $t_4$  and performing an element-wise sum operation with the raw signal  $M^{H \times W}$  to obtain the final temporal feature signal ( $T \in \mathbb{R}^{H \times W}$ ) by:

$$T = \lambda_2 \times t_4 + R \quad (4)$$

where  $T$  encodes the global temporal information into the features of each time step, thus enhancing the representative capability. Therefore, we can extract high-level temporal features of the MI signal in the time domain, thus weakening the artifacts.

## 2.3. Feature Classification

In this section, we describe the concatenation of spatial and temporal feature signals ( $S$  and  $T$ ) from the raw MI data into the spatial-temporal continuous feature ( $C_1 \in \mathbb{R}^{(3 \times 22 \times 1125)}$ ) as:

$$C_1 = \{M, S, T\} \quad (5)$$

A convolution (*Conv2*) with kernel size  $1 \times 25$  is implemented in the time domain, and then  $C_1$  is fed into the classification network (part b in **Figure 1**, **Table 3**). The shape of the output ( $C_2$ ) is transformed from (3, 22, 1125) to (40, 22, 1101). Furthermore, a convolution (*Conv3*) with kernel size  $22 \times 1$  is applied to the extracted features ( $C_2$ ) in the space domain. The corresponding shape of output  $C_3$  is (40, 1, 1101). Third, the average pooling operation (AvgPooling) with kernel size  $1 \times 75$  and stride  $1 \times 15$  is applied over  $C_3$  to generate a coarser feature representation, with the output dimension reduced to (40, 1, 69).

**TABLE 2** | Detailed architecture of the proposed temporal self-attention module.

Temporal-attention module							
Input	$M(22, 1125)$	$M(22, 1125)$	$t_{11}(8, 22, 1125)$	$t_{12}(8, 22, 1125)$	$t_{21}, t_{22}$	$M, t_3$	$t_4, M, \lambda_2$
Layer	Conv13	Conv14	R13	R14	MMN	MM	ES
Output	$t_{11}(8, 22, 1125)$	$t_{12}(8, 22, 1125)$	$t_{21}(1125, 176)$	$t_{22}(176, 1125)$	$t_3(1125, 1125)$	$t_4(22, 1125)$	$S(22, 1125)$
Feature maps	8	8	1	1	1	1	1
Kernel	(1,1)	(1,1)	–	–	–	–	–
Stride	(1,1)	(1,1)	–	–	–	–	–

MMN, Matrix multiplication + Normalization + Softmax; MM, matrix multiplication; ES, element-wise sum.

**TABLE 3** | Detailed architecture of the proposed temporal self-attention module.

Feature classification module									
Input	$M, S, T$	$C_1(3, 22, 1125)$	$C_2(40, 22, 1101)$	$C_3(40, 1, 1101)$	$C_3(40, 1, 1101)$	$C_3(40, 1, 1101)$	$C_4(40, 1, 69)$	$C_4(40, 1, 69)$	$(4, 1, 1)$
Layer	Concatenate	Conv2	Conv3	Batch normalization	Square	AvgPooling	Log	Conv4	LogSoftmax
Output	$C_1(3, 22, 1125)$	$C_2(40, 22, 1101)$	$C_3(40, 1, 1101)$	$C_3(40, 1, 1101)$	$C_3(40, 1, 1101)$	$C_4(40, 1, 69)$	$C_4(40, 1, 69)$	$(4, 1, 1)$	$(4, 1, 1)$
Feature maps	3	40	40	40	40	40	40	40	4
Kernel	–	(1,25)	(22,1)	–	–	(1,75)	–	(1,69)	–
Stride	–	(1,1)	(1,1)	–	–	(1,15)	–	(1,1)	–

Additionally, the square nonlinear activation is used before the AvgPooling operation and the log nonlinear activation is applied to the output of the AvgPooling operation. All feature maps of  $C_4$  are fed into the final convolution layer (Conv4), whose output  $C_5$  has dimensions of (4, 1, 1). Finally, the LogSoftmax function is used to perform multi-classification by converting  $C_5$  to the conditional probability of the four labels.

## 2.4. Training Strategy

For the four-class MI classification, the NLLoss function in Pytorch was defined as the loss function (Zhu et al., 2018). All parameters in the network were initialized using the Xavier algorithm (Glorot and Bengio, 2010). Adam (Sharma et al., 2017) was employed for the optimization. The learning rate was 0.0001 for the BCIIV2a dataset and 0.001 for HGD. The batch size was 32. Because BCIIV2a and HGD have clearly divided training and test datasets, the training datasets were randomly divided into training (80%) and validation (20%) sets; all test data were selected for the testing stage. This enables us to use the early stopping strategy, developed in the computer vision field, whereby the training set is split into training and validation datasets and the first phase of training stops when the validation accuracy does not improve for a predefined number of epochs. Training then continues on the combined training and validation datasets using the parameter values that led to the best accuracy on the validation dataset. Training ends when the loss function on the validation dataset drops to the same value as that on the training dataset at the end of the first training phase (Schirmermeister et al., 2017). The hyperparameter in the dropout layer and the constant and weight decay rate in the batch normalization layer were set to 0.5,  $10^{-5}$ , and 0.1, respectively. All experiments were conducted in Ubuntu 16.04 on a 64-bit system with a Core i9-9900k CPU and 128 GB RAM. Nvidia RTX 2080Ti

GPU was utilized for training and testing our model, which was coded using Pytorch and MNE-Python (Gramfort et al., 2014).

## 2.5. Evaluation Metrics

The proposed method was evaluated on two public datasets, BCIIV2a and HGD. The accuracy was used as the evaluation metrics. The accuracy was calculated as:

$$Accuracy = \frac{TP + TN}{TP + TN + FP + FN} \times 100\% \quad (6)$$

where TP is the number of true positives, TN is the number of true negatives, FP is the number of false positives, and FN is the number of false negatives.

## 3. RESULTS

To verify the performance and feasibility of our proposed model, we conducted a series of experiments for MI classification on two datasets. The intra-subject classification experiment was intended to verify the performance of the proposed network for an individual subject. The inter-subject transfer experiment was conducted to verify the transfer ability of the proposed method. In this experiment, EEG recordings from other subjects were used to train a model in advance. Next, this model was transferred as the initial weight to further train the individual model.

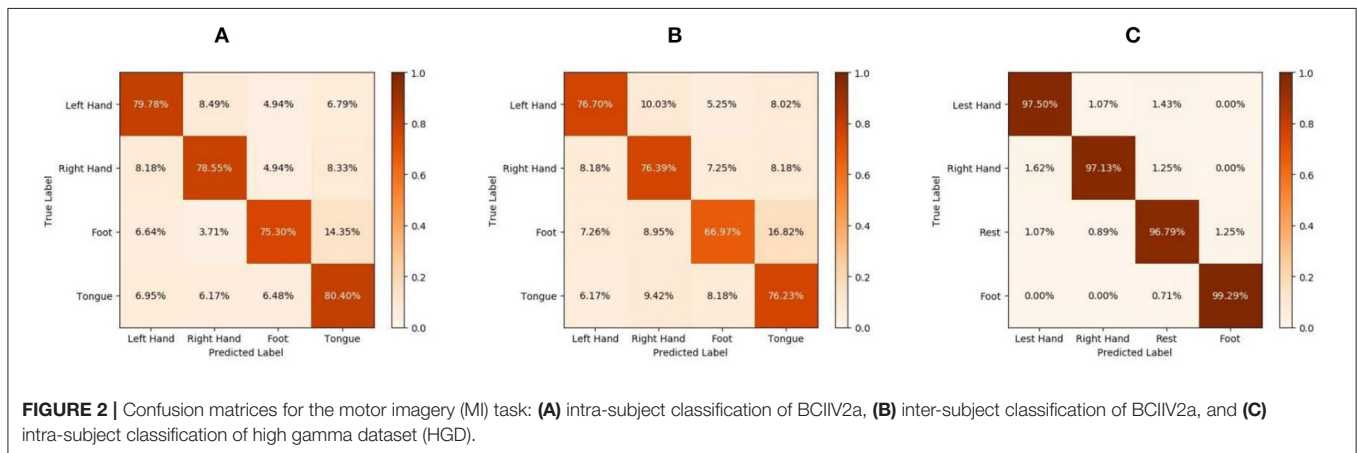
### 3.1. Quantitative Evaluation of BCIIV2a for Intra-Subject Classification

To confirm the effectiveness and accuracy of the proposed method, we first conducted intra-subject classification using BCIIV2a and compared the accuracy of our method with that given by state-of-the-art DL-based methods [EEGNet (Lawhern

**TABLE 4** | Accuracy on BCIV2a for intra-subject classification: comparison between proposed method and other state-of-the-art methods.

Subject	Accuracy (%)								
	FBCSP	DeepCNN	M3DCNN	LTICNN	DMTLCNN	MCCNN	WTL	EEGNet	Proposed
1	76.00	76.50	77.39	87.50	83.50	<b>90.21</b>	90.00	71.88	82.99
2	56.50	50.60	60.14	<b>65.28</b>	49.00	63.40	55.00	51.04	56.25
3	81.25	85.00	82.92	90.28	92.70	89.35	93.00	79.17	<b>93.06</b>
4	61.00	67.60	72.28	66.67	74.90	71.16	60.00	57.99	<b>84.03</b>
5	55.00	72.40	<b>75.83</b>	62.50	71.30	62.82	68.00	64.58	68.75
6	42.25	55.10	<b>68.98</b>	45.49	63.70	47.66	60.00	51.04	58.34
7	82.75	71.70	76.03	89.58	80.08	<b>90.86</b>	73.00	66.32	88.20
8	81.25	74.40	76.85	83.33	80.00	83.72	<b>98.00</b>	74.31	88.20
9	70.75	79.20	84.66	79.51	81.70	82.32	83.00	72.57	<b>86.81</b>
AVG	67.42	70.28	75.01	74.46	75.21	75.72	75.56	65.43	<b>78.51</b>

*Bold font indicates the best scores.*



et al., 2018), DeepCNN (Schirmer et al., 2017), M3DCNN (Zhao et al., 2019), LTICNN (Sakhavi et al., 2018), DMTLCNN (Song et al., 2019), MCCNN (Amin et al., 2019), WTL (Azab et al., 2019)]; traditional FBCSP (Ang et al., 2012) was used as a baseline method to recognize MI EEG data, and an SVM was used as the classifier.

**Table 4** lists the accuracy of the various methods for each subject and the corresponding average accuracy for the BCIV2a dataset. Our method clearly outperforms the state-of-the-art DL-based methods, obtaining an average accuracy of 78.51% for the intra-subject classification. Furthermore, confusion matrices for the MI task and the experimental results on the test sets are given in **Figure 2A**. Although FBCSP provides the best performance for MI signal classification, its average accuracy over all subjects is only 67.42%, which is nearly 11.09% lower than that of the proposed method. Thus, the proposed method yields superior results compared with the traditional machine learning method.

The DeepCNN model, which is widely used in MI classification algorithms, contains four convolution–pooling block modules. However, because this model is easily overfitted when there are few labeled data for training, the average accuracy

of DeepCNN is 70.28%, which is far lower (by 8.23%) than that of our method.

The other DL-based methods compared here are state-of-the-art techniques with excellent representation and accuracy. In this task, their average accuracy values range from 74.46 to 75.72%. LTICNN employs FBCSP as a data preparation method and uses a CNN to extract features. However, because of the need to change the parameters for different subjects, it readily becomes overfitted, and thus achieves worse performance than the proposed method, i.e., 4.05% lower on average. The M3DCNN model combines a new 3D representation of EEG, a multibranch 3D CNN, and a corresponding classification strategy to enhance its resistance to overfitting on different subjects. This model achieves the best results for two subjects (5 and 6) and demonstrates better performance than LTICNN. The greatest contribution of M3DCNN is to demonstrate that a deeper and more complex representation of EEG can help improve the performance. However, its accuracy of 75.01% is 3.50% lower than that of our method. DMTLCNN and WTL employ transfer learning techniques to yield a remarkable increase in classification accuracy, reaching 75.21 and 75.56%, respectively. Compared with this performance, our model is

**TABLE 5** | Intra-subject classification of 10-fold cross-validation results on the BCIIV2a.

Accuracy (%)										
Subjects	1	2	3	4	5	6	7	8	9	AVG
Accuracy	93.93	75.33	97.74	86.46	89.94	78.32	99.14	94.43	96.02	90.15

**TABLE 6** | Results of inter-subject transfer learning classification using the BCIIV2a dataset.

Accuracy (%)										
Subjects	1	2	3	4	5	6	7	8	9	AVG
MCCNN	62.07	42.44	63.12	52.09	49.96	37.16	62.54	59.32	69.43	55.34
DeepCNN	78.80	<b>51.80</b>	86.80	<b>71.60</b>	<b>68.70</b>	64.60	82.30	80.90	75.40	73.40
DMTLCNN	80.30	50.30	85.50	70.60	66.20	60.60	83.00	82.80	<b>78.4</b>	73.10
Proposed	<b>82.99</b>	45.84	<b>94.10</b>	67.37	54.84	<b>75.72</b>	<b>85.07</b>	<b>87.85</b>	73.27	<b>74.07</b>

*Bold font indicates the best scores.*

3.30 and 2.95% more accurate, respectively. The MCCNN model first fuses different CNN modules to prove that the spatial and temporal features can improve the classification over handcrafted features. Previously, MCCNN has achieved the highest accuracy, reaching 75.72%. However, this model focuses on the spatially invariant features of MI EEG signals, and does not consider the interrelationship between the temporal features and spatial features in depth. This interrelationship is the focus of this study. Compared with MCCNN, our average accuracy is 2.79% higher. In addition to the average accuracy, we achieved the best results for three of the nine subjects (3, 4, and 9).

The above results show that the proposed method outperforms all traditional (11.09% better on average) and DL-based methods (4.14% better on average) for four-class MI EEG classification by combining spatial and temporal features via the proposed parallel spatial-temporal self-attention architecture.

For the evaluations using 10-fold cross-validation, we combined the training and testing set of BCIIV2a, and then randomly divided into 10 equal parts. In each run, nine subsets were used as training set and 1 subset was used as the testing set. That means there are 518 trials for training, 58 trials for testing. The final accuracy was obtained by averaging the best values of the 10-fold. Compared with the 288 trials we used for training and 288 trials for testing before, the 10-fold cross-validation significantly increases the amount of the training set, so it can achieve better accuracy (90.15% on average) in Table 5.

### 3.2. Quantitative Evaluation of BCIIV2a for Inter-Subject Transfer Learning Classification

One of the main contributions of the proposed method is to improve the accuracy of inter-subject classification through the parallel spatial-temporal self-attention architecture. This is the first time the attention mechanism has been used to study the relationship between channels. Here, by using transfer learning techniques, we utilize the other subjects' EEG data to train a model on the BCIIV2a dataset, and then apply this model as the initial weight of the network and load data from a new subject for

**TABLE 7** | Intra-subject classification results using high gamma dataset (HGD).

Accuracy (%)					
FBCSP	DeepCNN	MCCNN	CPMixedNet	MSFBCNN	Proposed
90.90	91.40	95.40	93.70	94.40	<b>97.68</b>

*Bold font indicates the best scores.*

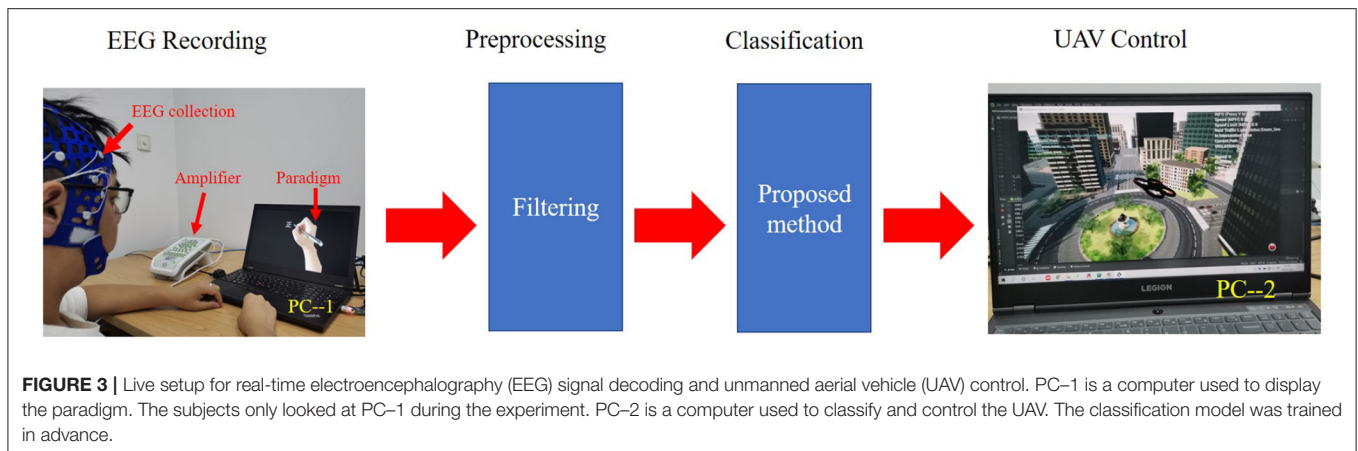
further training. In this way, we can consider the trained model to integrate the information of other subjects, thus making it more robust.

Table 6 presents the corresponding classification results for each subject. Because of the large differences between subjects, the results in Table 6 are not better than the intra-subject results (listed in Table 4). Figure 2B shows the confusion matrices for the BCIIV2a dataset inter-subject classification results. Compared with other state-of-the-art DL-based methods (MCCNN, DeepCNN, and DMTLCNN, which provided the inter-subject comparison results), the proposed method obtains the best average accuracy of 74.07%, with particularly good results for five of the nine subjects (1, 3, 6, 7, and 8). The results show that our method not only weakens the artifacts caused by manually selecting a signal channel, but also automatically provides a more robust and generic feature representation with higher classification accuracy of MI EEG signals.

### 3.3. Quantitative Evaluation of HGD for Intra-Subject Classification

To further verify the adaptability of the proposed method, we conducted intra-subject classification evaluations on another challenging dataset (HGD). In Schirmermeister et al. (2017), we set the low cut-off frequency of HGD to 4 Hz. Because some state-of-the-art methods only report average accuracy values for HGD, we only list the average accuracy in Table 7.

Recall that the tasks used to construct HGD and BCIIV2a are different. The tasks performed for BCIIV2a involve the left hand, right hand, both feet, and tongue, which are different from the four categories of HGD. Additionally, HGD contains much more data than BCIIV2a. As we know, the amount



of data is an important factor affecting the performance of DL. Thus, these data allow the proposed method to attain evaluation results that are even more encouraging, with a significant improvement over the other methods. The proposed method reaches 97.68% accuracy, while the second-best method (MSFBCNN; Wu et al., 2019) can attain 94.40% accuracy. The final classification accuracy of MSFBCNN is lower than that of our method because it focuses on multi-scale convolution in the temporal domain, and ignores the spatial relationship between channels. CPMixedNet (Li et al., 2019) also analyzes the time domain, using regular and dilated convolution to extract the temporal EEG information. The classification accuracy is 93.70% after amplitude-perturbation data augmentation. However, there is no analysis of the spatial distribution of EEG information, so the accuracy is 3.98% lower than that of our method. These experimental results demonstrate the capability of the proposed network with data augmentation for MI EEG signal classification. In **Figure 2C**, we show the accuracy for each class of HGD in the form of confusion matrices.

### 3.4. Control of the Drone Based on EEG Signal

We further tested and validated the real-time capability of the proposed model through the online decoding of MI movements from streamed EEG signals for virtual drone control. We used a Greal 32-channel EEG amplifier developed by Neuroscan to collect the MI EEG data. First, the subjects were asked to imagine writing a Chinese character with their left or right hand according to the paradigm of Qiu et al. (2017). At the beginning of a trial ( $t = 0$  s), a fixation cross appeared on the black screen. At  $t = 2$  s, the fixation cross was replaced by a picture of the forearm and a Chinese character. Each subject had 6 s to perform the MI task, in which hand movements followed the strokes of the Chinese character on the screen. Subjects then had a short break of 2 s. Second, a band-pass filter of 4–38 Hz was applied to the EEG signals. Third, the preprocessed data were sent to the trained network for classification. Finally, the AirSim-based virtual unmanned aerial vehicle (UAV or drone) was directed to

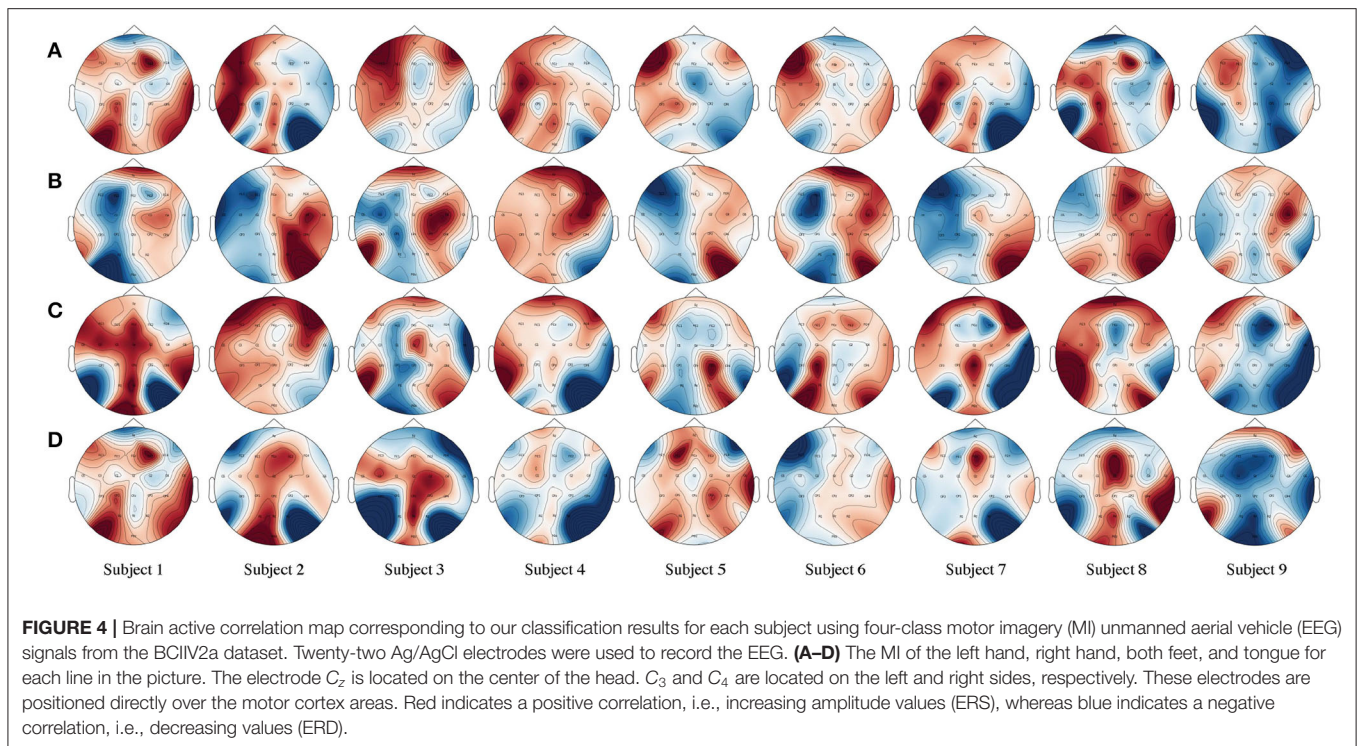
move either left or right according to the decoded movement from the EEG signals.

**Figure 3** shows the whole process of how we used the data collected in the laboratory to control the flight of the virtual UAV. When the subjects imagined writing with their left hand, the virtual UAV would fly to the left. Similarly, when the subjects imagined writing with their right hand, the UAV would fly to the right. A video of a successful live demo is available in the **Supplementary Materials**.

## 4. DISCUSSION

This study has investigated the design and training of an end-to-end neural network using raw EEG signals. This is the first time that a new spatial-temporal representation of raw EEG signals has been defined using the self-attention mechanism for extracting the distinguishable spatial-temporal features. Through intra- and inter-subject transfer learning experiments on the BCIIV2a dataset and HGD, we demonstrated that the proposed method outperforms several state-of-the-art methods in terms of the classification accuracy. At the same time, we visualized topographic maps of MI EEG data to explain the rationality of our temporal and spatial attention mechanism from the perspective of physiological EEG characteristics. Finally, as reported later in this section, we applied this method to control the flight of a UAV using MI EEG data.

In **Figure 4**, we present a brain active correlation map corresponding to our classification results for each subject using four-class MI EEG signals from the BCIIV2a dataset. As we know, when people imagine or execute movements of their left or right hand, both feet, and tongue, the power of the mu (8–12 Hz) and beta (16–26 Hz) rhythms can decrease or increase in the sensorimotor region of the contralateral and ipsilateral hemispheres. The red color indicates a positive correlation, i.e., event-related synchronization (ERS), with a deeper color denoting a stronger positive correlation. In contrast, the blue color indicates a negative correlation, i.e., event-related desynchronization (ERD), with



a deeper color denoting a stronger negative correlation. For example, the first row in **Figure 4** shows the brain activation pattern for MI data corresponding to left-hand motion. Our classification results are for the MI EEG signals of left-hand motion, and the corresponding brain active correlation map shows the ERS and ERD in the left and right hemispheres.

In addition, the evaluation results shown in **Figure 4** prove the validity of our assumption that when people think about an action, any channel with similar motor-dependent characteristics can promote mutual improvement, regardless of its spatial location in the brain. Taking the left-hand MI as an example, the traditional method often manually chooses  $C_3$ ,  $C_4$ , and  $C_z$  as inputs. However, as shown by the brain active correlation map for the left-hand MI of subject 1 in **Figure 4**, in neurophysiological terms, channels FC3, FCz, FC2, C5, Cz, CP1, and CP4 all exhibit the same ERS trend as channel  $C_3$ , which is located in the motor cortex area. Similarly, channels Fz, FC4, C2, CPz, and Pz exhibit the same ERD trend as channel  $C_4$ . This proves that our initial hypothesis is correct.

Therefore, different from the traditional method, we use the spatial self-attention module to capture the potential spatial links between any two channels of the MI EEG signals. The features within a certain channel are updated by aggregating the features across all channels with a weighted summation, where the weights are automatically learned according to the feature similarities between the corresponding channels. This module defines a new learned spatial representation of the raw MI EEG data that chooses the best channels by automatically assigning higher values to motor-dependent channels and lower values to motor-independent channels. The evaluation results show that our method effectively improves the accuracy of classification.

## 5. CONCLUSION

This paper has described a parallel spatial-temporal self-attention CNN-based architecture for four-class MI EEG classification. The self-attention mechanism is first introduced for capturing robust and generic feature dependencies in the spatial and temporal dimensions. As a result, we can extract distinguishable spatial-temporal features of MI signals. The experimental results on two public datasets show that the proposed model outperforms several state-of-the-art methods. Furthermore, successful real-time control of a virtual UAV was achieved using the trained model. In the future, we plan to explore the multi-task analysis of MI EEG signals.

## DATA AVAILABILITY STATEMENT

The original contributions presented in the study are included in the article/**Supplementary Materials**, further inquiries can be directed to the corresponding author/s.

## AUTHOR CONTRIBUTIONS

XL and YS processed and analyzed the data and wrote the manuscript. JL developed the parallel spatial-temporal self-attention CNN method. JY helped in data analysis. PX helped in manuscript editing. JL and FL supervised development of work, helped in manuscript edit, and evaluation.

## FUNDING

This work was supported in part by the National Natural Science Foundation of China under Grants (61802109,

61673158, and 61703133), in part by the Natural Science Foundation of Hebei Province under Grants (F2020205006 and F2018201070), in part by the Top Youth Talents of Science and Technology Research Project in Hebei Province under Grant (BJ2020059), in part by the Youth Talent Support Program of Hebei Province (BJ2019044), and in part by the Science Foundation of Hebei Normal University under Grant (L2018K02).

## REFERENCES

- Amin, S. U., Alsulaiman, M., Muhammad, G., Mekhtiche, M. A., and Hossain, M. S. (2019). Deep learning for EEG motor imagery classification based on multi-layer CNNs feature fusion. *Future Gener. Comput. Syst.* 101, 542–554. doi: 10.1016/j.future.2019.06.027
- Ang, K. K., Chin, Z. Y., Wang, C., Guan, C., and Zhang, H. (2012). Filter bank common spatial pattern algorithm on BCI competition IV datasets 2a and 2b. *Front. Neurosci.* (Hong Kong), 6:39. doi: 10.3389/fnins.2012.00039
- Ang, K. K., Chin, Z. Y., Zhang, H., and Guan, C. (2008). “Filter bank common spatial pattern (FBCSP) in brain-computer interface,” in *2008 IEEE International Joint Conference on Neural Networks (IEEE World Congress on Computational Intelligence)*, 2390–2397.
- Azab, A. M., Mihaylova, L., Ang, K. K., and Arvaneh, M. (2019). Weighted transfer learning for improving motor imagery-based brain-computer interface. *IEEE Trans. Neural Syst. Rehabil. Eng.* 27, 1352–1359. doi: 10.1109/TNSRE.2019.2923315
- De, J., Zhang, X., Lin, F., and Cheng, L. (2017). Transduction on directed graphs via absorbing random walks. *IEEE Trans. Pattern Anal. Mach. Intell.* 40, 1770–1784. doi: 10.1109/TPAMI.2017.2730871
- Ehrsson, H. H., Geyer, S., and Naito, E. (2003). Imagery of voluntary movement of fingers, toes, and tongue activates corresponding body-part-specific motor representations. *J. Neurophysiol.* 90, 3304–3316. doi: 10.1152/jn.01113.2002
- Fu, J., Liu, J., Tian, H., Li, Y., Bao, Y., Fang, Z., et al. (2019). “Dual attention network for scene segmentation” in *Proceedings of the IEEE Conference on Computer Vision and Pattern Recognition* (Long Beach, CA), 3146–3154. doi: 10.1109/CVPR.2019.00326
- Glorot, X., and Bengio, Y. (2010). “Understanding the difficulty of training deep feedforward neural networks,” in *Proceedings of the Thirteenth International Conference on Artificial Intelligence and Statistics* (Sardinia), 249–256.
- Gong, A., Liu, J., Chen, S., and Fu, Y. (2018). Time-frequency cross mutual information analysis of the brain functional networks underlying multiclass motor imagery. *J. Motor Behav.* 50, 254–267. doi: 10.1080/00222895.2017.1327417
- Gramfort, A., Luessi, M., Larson, E., Engemann, D. A., Strohmeier, D., Brodbeck, C., et al. (2014). MNE software for processing MEG and EEG data. *Neuroimage* 86, 446–460. doi: 10.1016/j.neuroimage.2013.10.027
- Jin, J., Miao, Y., Daly, I., Zuo, C., Hu, D., and Cichocki, A. (2019). Correlation-based channel selection and regularized feature optimization for MI-based BCI. *Neural Netw.* 118, 262–270. doi: 10.1016/j.neunet.2019.07.008
- Kübler, A., and Birbaumer, N. (2008). Brain-computer interfaces and communication in paralysis: extinction of goal directed thinking in completely paralysed patients? *Clin. Neurophysiol.* 119, 2658–2666. doi: 10.1016/j.clinph.2008.06.019
- Kumar, A., Lin, F., and Rajapakse, J. C. (2016). Mixed spectrum analysis on fMRI time-series. *IEEE Trans. Med. Imaging* 35, 1555–1564. doi: 10.1109/TMI.2016.2520024
- Kumar, S., Sharma, A., Mamun, K., and Tsunoda, T. (2016). “A deep learning approach for motor imagery EEG signal classification,” in *2016 3rd Asia-Pacific World Congress on Computer Science and Engineering (APWC on CSE)* (Nadi), 34–39. doi: 10.1109/APWC-on-CSE.2016.017
- Lawhern, V. J., Solon, A. J., Waytowich, N. R., Gordon, S. M., Hung, C. P., and Lance, B. J. (2018). EEGNet: a compact convolutional neural network for EEG-based brain-computer interfaces. *J. Neural Eng.* 15:056013. doi: 10.1088/1741-2552/aace8c

## SUPPLEMENTARY MATERIAL

The Supplementary Material for this article can be found online at: <https://www.frontiersin.org/articles/10.3389/fnins.2020.587520/full#supplementary-material>

The BCIIV2a dataset can be found at: <http://www.bbci.de/competition/iv/>, and HGD can be found at: <https://gin.g-node.org/robintibor/high-gamma-dataset/>.

- Li, Y., Zhang, X.-R., Zhang, B., Lei, M.-Y., Cui, W.-G., and Guo, Y.-Z. (2019). A channel-projection mixed-scale convolutional neural network for motor imagery EEG decoding. *IEEE Trans. Neural Syst. Rehabil. Eng.* 27, 1170–1180. doi: 10.1109/TNSRE.2019.2915621
- Lin, Z., Feng, M., Santos, C. N. d., Yu, M., Xiang, B., Zhou, B., et al. (2017). A structured self-attentive sentence embedding. *arXiv preprint arXiv:1703.03130*.
- Lotte, F., Bougrain, L., Cichocki, A., Clerc, M., Congedo, M., Rakotomamonjy, A., et al. (2018). A review of classification algorithms for EEG-based brain-computer interfaces: a 10 year update. *J. Neural Eng.* 15:031005. doi: 10.1088/1741-2552/aab2f2
- Lu, N., Li, T., Ren, X., and Miao, H. (2016). A deep learning scheme for motor imagery classification based on restricted Boltzmann machines. *IEEE Trans. Neural Syst. Rehabil. Eng.* 25, 566–576. doi: 10.1109/TNSRE.2016.2601240
- Ma, J., Lin, F., Wesarg, S., and Erdt, M. (2018). “A novel Bayesian model incorporating deep neural network and statistical shape model for pancreas segmentation,” in *International Conference on Medical Image Computing and Computer-Assisted Intervention* (Granada: Springer), 480–487. doi: 10.1007/978-3-030-00937-3\_55
- Ma, J., Wang, A., Lin, F., Wesarg, S., and Erdt, M. (2017). “Nonlinear statistical shape modeling for ankle bone segmentation using a novel Kernelized robust PCA,” in *International Conference on Medical Image Computing and Computer-Assisted Intervention* (Quebec City, QC: Springer), 136–143. doi: 10.1007/978-3-319-66182-7\_16
- Ma, X., Qiu, S., Wei, W., Wang, S., and He, H. (2020). Deep channel-correlation network for motor imagery decoding from the same limb. *IEEE Trans. Neural Syst. Rehabil. Eng.* 28, 297–306. doi: 10.1109/TNSRE.2019.2953121
- Müller-Gerking, J., Pfurtscheller, G., and Flyvbjerg, H. (1999). Designing optimal spatial filters for single-trial EEG classification in a movement task. *Clin. Neurophysiol.* 110, 787–798. doi: 10.1016/S1388-2457(98)00038-8
- Neuper, C., and Pfurtscheller, G. (2001). Evidence for distinct beta resonance frequencies in human EEG related to specific sensorimotor cortical areas. *Clin. Neurophysiol.* 112, 2084–2097. doi: 10.1016/S1388-2457(01)00661-7
- Pfurtscheller, G., and Da Silva, F. L. (1999). Event-related EEG/MEG synchronization and desynchronization: basic principles. *Clin. Neurophysiol.* 110, 1842–1857. doi: 10.1016/S1388-2457(99)00141-8
- Pfurtscheller, G., Neuper, C., Flotzinger, D., and Pergenzer, M. (1997). EEG-based discrimination between imagination of right and left hand movement. *Electroencephalogr. Clin. Neurophysiol.* 103, 642–651. doi: 10.1016/S0013-4694(97)00080-1
- Qiu, Z., Allison, B. Z., Jin, J., Zhang, Y., Wang, X., Li, W., et al. (2017). Optimized motor imagery paradigm based on imagining Chinese characters writing movement. *IEEE Trans. Neural Syst. Rehabil. Eng.* 25, 1009–1017. doi: 10.1109/TNSRE.2017.2655542
- Ramoser, H., Müller-Gerking, J., and Pfurtscheller, G. (2000). Optimal spatial filtering of single trial eeg during imagined hand movement. *IEEE Trans. Rehabil. Eng.* 8, 441–446. doi: 10.1109/86.895946
- Sakhavi, S., Guan, C., and Yan, S. (2018). Learning temporal information for brain-computer interface using convolutional neural networks. *IEEE Trans. Neural Netw. Learn. Syst.* 29, 5619–5629. doi: 10.1109/TNNLS.2018.2789927
- Schirmer, R. T., Springenberg, J. T., Fiederer, L. D. J., Glasstetter, M., Eggensperger, K., Tangermann, M., et al. (2017). Deep learning with convolutional neural networks for EEG decoding and visualization. *Hum. Brain Mapp.* 38, 5391–5420. doi: 10.1002/hbm.23730
- Shah, S., Dey, D., Lovett, C., and Kapoor, A. (2018). “AirSim: High-fidelity visual and physical simulation for autonomous vehicles,” in *Field and Service Robotics*,

- eds M. Hutter and R. Siegart (Cham: Springer International Publishing), 621–635. doi: 10.1007/978-3-319-67361-5\_40
- Sharma, M., Pachori, R., and Rajendra, A. (2017). Adam: a method for stochastic optimization. *Pattern Recogn. Lett.* 94, 172–179. doi: 10.1016/j.patrec.2017.03.023
- Shen, T., Jiang, J., Zhou, T., Pan, S., Long, G., and Zhang, C. (2018). “DiSAN: directional self-attention network for RNN/CNN-free language understanding,” in *The Thirty-Second AAAI Conference on Artificial Intelligence*, eds S. McIlraith and K. Weinberger (Association for the Advancement of Artificial Intelligence (AAAI)), 5446–5455. Available online at: <https://aaai.org/Conferences/AAAI-18/>
- Song, Y., Wang, D., Yue, K., Zheng, N., and Shen, Z.-J. M. (2019). “EEG-based motor imagery classification with deep multi-task learning,” in *2019 International Joint Conference on Neural Networks (IJCNN)* (Budapest), 1–8. doi: 10.1109/IJCNN.2019.8852362
- Tabar, Y. R., and Halici, U. (2016). A novel deep learning approach for classification of EEG motor imagery signals. *J. Neural Eng.* 14:016003. doi: 10.1088/1741-2560/14/1/016003
- Tangermann, M., Müller, K.-R., Aertsen, A., Birbaumer, N., Braun, C., Brunner, C., et al. (2012). Review of the BCI competition IV. *Front. Neurosci.* 6:55. doi: 10.3389/fnins.2012.00055
- Vaswani, A., Shazeer, N., Parmar, N., Uszkoreit, J., Jones, L., Gomez, A. N., et al. (2017). “Attention is all you need,” in *Advances in Neural Information Processing Systems* (Long Beach, CA), 5998–6008.
- Wu, H., Li, F., Li, Y., Fu, B., Shi, G., Dong, M., et al. (2019). A parallel multiscale filter bank convolutional neural networks for motor imagery EEG classification. *Front. Neurosci.* 13:1275. doi: 10.3389/fnins.2019.01275
- Zhang, H., Goodfellow, I., Metaxas, D., and Odena, A. (2019). “Self-attention generative adversarial networks,” in *International Conference on Machine Learning* (Long Beach, CA), 7354–7363.
- Zhao, X., Zhang, H., Zhu, G., You, F., Kuang, S., and Sun, L. (2019). A multi-branch 3D convolutional neural network for EEG-based motor imagery classification. *IEEE Trans. Neural Syst. Rehabil. Eng.* 27, 2164–2177. doi: 10.1109/TNSRE.2019.2938295
- Zhu, D., Yao, H., Jiang, B., and Yu, P. (2018). Negative log likelihood ratio loss for deep neural network classification. *arXiv preprint arXiv:1804.10690*. doi: 10.1007/978-3-030-32520-6\_22
- Zhu, X., Li, P., Li, C., Yao, D., Zhang, R., and Xu, P. (2019). Separated channel convolutional neural network to realize the training free motor imagery BCI systems. *Biomed. Signal Process. Control* 49, 396–403. doi: 10.1016/j.bspc.2018.12.027

**Conflict of Interest:** The authors declare that the research was conducted in the absence of any commercial or financial relationships that could be construed as a potential conflict of interest.

Copyright © 2020 Liu, Shen, Liu, Yang, Xiong and Lin. This is an open-access article distributed under the terms of the Creative Commons Attribution License (CC BY). The use, distribution or reproduction in other forums is permitted, provided the original author(s) and the copyright owner(s) are credited and that the original publication in this journal is cited, in accordance with accepted academic practice. No use, distribution or reproduction is permitted which does not comply with these terms.



# Hyperscanning EEG and Classification Based on Riemannian Geometry for Festive and Violent Mental State Discrimination

Cédric Simar<sup>1</sup>, Ana-Maria Cebolla<sup>2</sup>, Gaëlle Chartier<sup>3,4</sup>, Mathieu Petieau<sup>2</sup>, Gianluca Bontempi<sup>1</sup>, Alain Berthoz<sup>3</sup> and Guy Cheron<sup>2,5\*</sup>

<sup>1</sup> Machine Learning Group (MLG), Computer Science Department, Université libre de Bruxelles (ULB), Brussels, Belgium, <sup>2</sup> Laboratory of Neurophysiology and Movement Biomechanics, ULB Neuroscience Institute, Université libre de Bruxelles, Brussels, Belgium, <sup>3</sup> Centre Interdisciplinaire de Biologie, Collège de France-CNRS, Paris, France, <sup>4</sup> Department of Health, Medicine and Human Biology, Université Paris 13, Bobigny, France, <sup>5</sup> Laboratory of Electrophysiology, Université de Mons-Hainaut, Mons, Belgium

## OPEN ACCESS

### Edited by:

Saugat Bhattacharyya,  
Ulster University, United Kingdom

### Reviewed by:

Rodrigo Ezequiel Ramele,  
Instituto Tecnológico de Buenos  
Aires, Argentina  
Khadijeh Sadatnejad,  
Inria Bordeaux—Sud-Ouest Research  
Centre, France  
Tasos Papastylilianou,  
University of Essex, United Kingdom

### \*Correspondence:

Guy Cheron  
gcheron@ulb.ac.be

### Specialty section:

This article was submitted to  
Brain Imaging Methods,  
a section of the journal  
Frontiers in Neuroscience

Received: 28 July 2020

Accepted: 04 November 2020

Published: 16 December 2020

### Citation:

Simar C, Cebolla A-M, Chartier G, Petieau M, Bontempi G, Berthoz A and Cheron G (2020) Hyperscanning EEG and Classification Based on Riemannian Geometry for Festive and Violent Mental State Discrimination.  
*Front. Neurosci.* 14:588357.  
doi: 10.3389/fnins.2020.588357

Interactions between two brains constitute the essence of social communication. Daily movements are commonly executed during social interactions and are determined by different mental states that may express different positive or negative behavioral intent. In this context, the effective recognition of festive or violent intent before the action execution remains crucial for survival. Here, we hypothesize that the EEG signals contain the distinctive features characterizing movement intent already expressed before movement execution and that such distinctive information can be identified by state-of-the-art classification algorithms based on Riemannian geometry. We demonstrated for the first time that a classifier based on covariance matrices and Riemannian geometry can effectively discriminate between neutral, festive, and violent mental states only on the basis of non-invasive EEG signals in both the actor and observer participants. These results pave the way for new electrophysiological discrimination of mental states based on non-invasive EEG recordings and cutting-edge machine learning techniques.

**Keywords:** EEG, mental state, classification, machine learning, Riemannian geometry

## INTRODUCTION

Hyperscanning refers to the technique of simultaneous scanning, initially performed using fMRI, of participants' brains who mutually interact in a controlled setting (Montague et al., 2002). The underlying neural basis is a consistent dynamical relationship between the interacting brains, which constitutes the essence of social interaction. Despite fMRI allowing high spatial resolution, this imaging technique cannot be employed during regular movements executed during social interaction in daily life. Hyperscanning EEG offers direct access to global electrical neural activity with an excellent temporal resolution that is necessary for assessing the brain dynamics of the interacting participants (Babiloni et al., 2006; Dumas et al., 2010; Barraza et al., 2019; Balconi et al., 2020). Moreover, EEG may characterize brain functions and states (Buzsáki and Draguhn, 2004). Hyperscanning EEG has been used in four specific domains of social interactions, joint action, shared attention, decision making, and affective communication (Liu et al., 2018). Although what

is perceived as violent varies among societies and throughout human history (Elias, 1997), the effective recognition of festive or violent intent before the action execution remains advantageous for survival. When a violent intent emerges, individuals cognitively mobilize a particular mental state. In order to trace neural signals related to this mental state, we designed an experiment during which individuals perform the same kind of gesture—tossing a ball—but in a festive way and in a violent way.

Here, we present an experimental design in which two persons (one acting and the other observing) facing each other execute and observe, respectively, real movements with either festive, neutral, and violent intent. Both participants' EEG, kinematics, and electromyographic signals were simultaneously recorded. Hyperscanning EEG during an actor-observer in a real face-to-face paradigm of social interaction coupled with kinematics has been previously introduced and investigated (Ménoret et al., 2014), showing that modulation of beta EEG oscillations in brain motor areas depended on the context (interaction vs. observation) and the role assignment (actor vs. observer). Also, EEG temporal dynamics have provided preliminary evidence of the ability to distinguish between the perception of kind, hostile, and non-interactive social intent inferred through visual scenarios on TV (Decety and Cacioppo, 2012; Wang et al., 2015) supporting that intentionality is the first input to moral computations (Decety and Cacioppo, 2012). In the last decade, new classification methods have been developed and applied mostly on brain-derived signals such as EEG (Wu et al., 2017; Lotte et al., 2018) and MEG (Fatima and Kamboh, 2017). The major area of interest was related to BCI application and less often to behavioral states identification, although previous work studied mental states directly linked to emotions (Kim et al., 2013; Schindler and Bublatzky, 2020) and social interactions (Kinreich et al., 2017; Liu et al., 2018; Czeszumski et al., 2020).

In this work, we used a classification algorithm on raw EEG trials of 10 couples of participants performing a repetition of festive, neutral, and violent throws. We hypothesized that EEG signals contain the distinctive information characterizing movement intent already before movement execution and that such distinctive information can be identified by state-of-the-art classification algorithms, among them one based on Riemannian geometry. Riemannian geometry classifiers have received growing attention in the last few years (Lotte et al., 2018), particularly due to their performance in international Brain-Computer Interface (BCI) competitions.

Here, we first illustrated the face-to-face hyperscanning condition before and during the execution of movement. Then, we justified the reason why the classification pipelines were applied on EEG periods occurring 1 s before the onset of movement. Then, we introduced the preprocessing algorithms and classification pipelines as well as the advantages of using Riemannian metrics when manipulating covariance matrices. The final classification results were then illustrated using a boxplot summarizing the performances of the classification pipelines applied on the EEG data from each of the 10 couples (actors and observers separately). We demonstrated that state-of-the-art classification pipelines can effectively discriminate between neutral, festive, and violent mental states using EEG

signals from both the actors and observers. These results pave the way for new electrophysiological discrimination of mental states based on non-invasive EEG recordings.

## MATERIALS AND METHODS

### Participants

The data were collected from 20 healthy right-handed [determined by the Handedness inventory (Oldfield, 1971)] male volunteers ( $24.5 \pm 4.5$  years old). Each participant gave informed consent to the experimental procedures, all of which were in accordance with the 1964 Helsinki declaration and its later amendments or comparable ethical standards.

### Experimental Design

This study has been inspired by the paradigm of Chartier et al. (2017) concerning the performance and perception of transitions from festive to violent gestures between two persons. The experiments were performed in the Jacques Lecoq theater school in Paris (Prof. Jos Huben). The gesture that was chosen was the simulation of the throwing of a ball to a partner. In this previous study, the actor's gestures were analyzed when the throw was made in a neutral, festive, and progressively more and more violent mode. In these conditions, the main kinematic characteristics of the three categories of gestures were measured. In addition, from the recorded movie pictures of the throws, it was demonstrated that the intent behind actor's gestures can be recognized by an observer even with morphing of the face taking away any possibility to recognize the emotional valence by the face expression. It has also been well demonstrated that bodily expression of emotions are well perceived without facial expression (de Gelder, 2016).

Here, we present a modification of this initial paradigm. In this new experimental protocol, two persons (one acting, the "actor," and the other observing the "observer") facing each other execute and observe, respectively, real movements with either festive, neutral, and violent intent.

Each couple of participants stood in an upright position facing each other and being separated by a distance of 4 m. The arms were at their sides. The actor held a foam ball (7 cm diameter) with the right hand. A LED light was fixed on the forehead of the observer. The verbal instructions to the actors were given in French to perform the following four tasks: resting, festive ball throw, violent ball throw, and neutral ball throw. The turn-on of the LED light placed on the observer's forehead was the "go" signal administered in the four kinds of tasks:

- In the resting task, both participants remained standing at rest facing each other for 5 s during which the LED light on the observer's forehead was turned on. This task was repeated 10 times.
- In the festive ball throw task, the actor was asked to perform 30 festive ball throws with the right upper limb aiming the LED light when it turned on and with increasing intensity of festivity following the indications of "execute a festive ball

throw (10 times), a more festive ball throw (10 times) and an even more festive ball throw (10 times).”

- In the violent ball throw task, the actor was asked to perform 30 violent ball throws aiming the LED light when it turned on with increasing intensity of violence following the indications of “execute a violent ball throw (10 times), a more violent ball throw (10 times) and an even more violent ball throw (10 times).”
- In the neutral ball throw task, the actor was asked to perform 30 ball throws at slow (10 times), rapid (10 times), and as fast as possible (10 times) velocities and aiming the LED light when it turned on without any specific intent. This task was included in order to care about a possible velocity effect in the previous conditions.

The festive and violent increasing gradation used was inspired by Gregory Bateson’s analyses (Bateson, 1955). The actor was asked to keep the same “type” of movement during the different trials and tasks (Figure 1). He tried all the tasks for familiarization before starting recordings. The observer was asked to not react to the foam ball throws in any condition. In order to facilitate the establishment of the different mental states, blocks of a same movement type were performed instead of intermixing trials of the different conditions.

During this procedure, the mental states of both participants were modified. For each of the three tasks, an instruction was given to the actor (neutral, festive, violent gesture) but the observer could hear the instruction and was, therefore aware of the mental state of the actor. Then, the successive repetitions of the same type of action reinforced, on one hand, the actor’s mental state related to his action by a modification of the motor

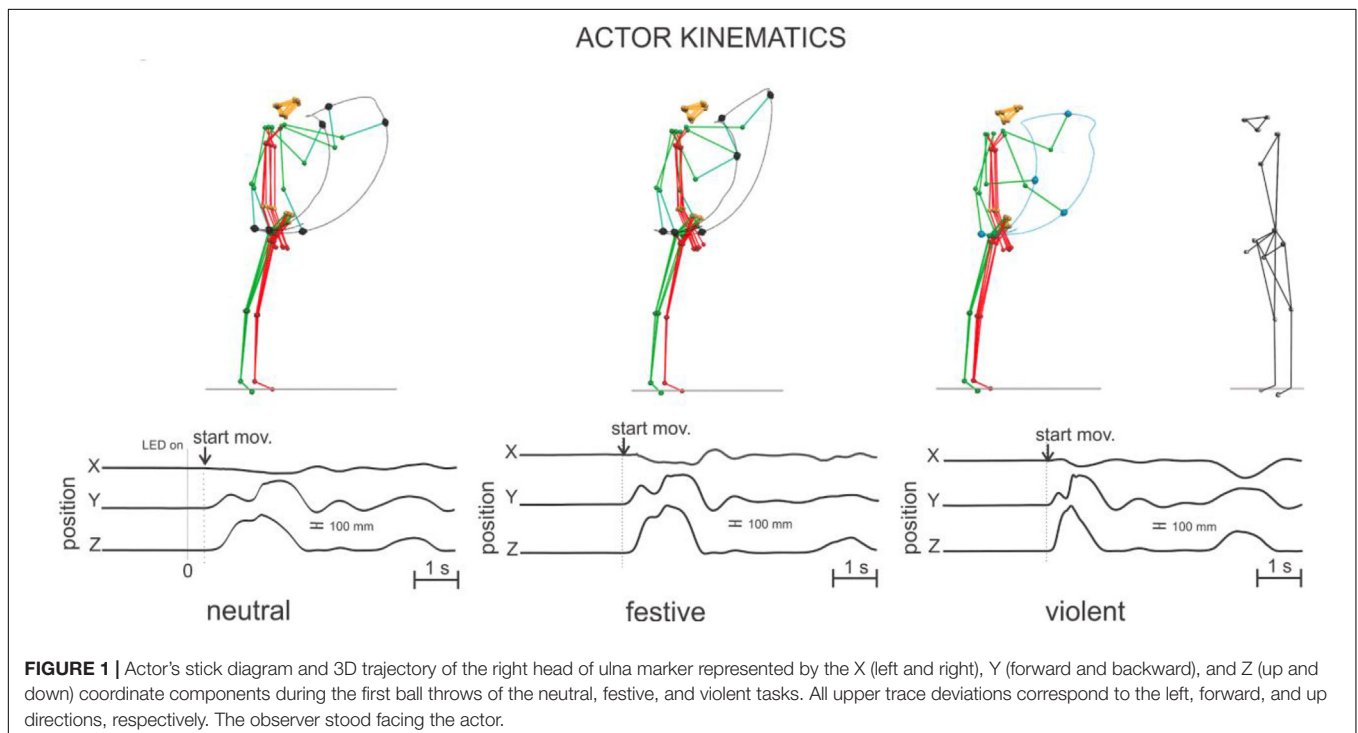
networks from frontal and prefrontal cortex to supplementary motor (Scangos et al., 2013) and sensory-motor areas and more subcortical structures involvement, and, on the other hand, by the emergence of a “perceptual resonance” (Schütz-Bosbach and Prinz, 2007). For the observer, the repetition of the actor’s gesture induced, on one hand, an activation of the motor simulation (or “motor resonance”) networks involving the “mirror system” (Rizzolatti and Sinigaglia, 2007; Rizzolatti et al., 2014) and, on the other hand, an activation of the perceptual and motor imagery networks (Thirioux et al., 2010). Furthermore, a possible fatigue effect was avoided by the introduction of pauses between the different conditions.

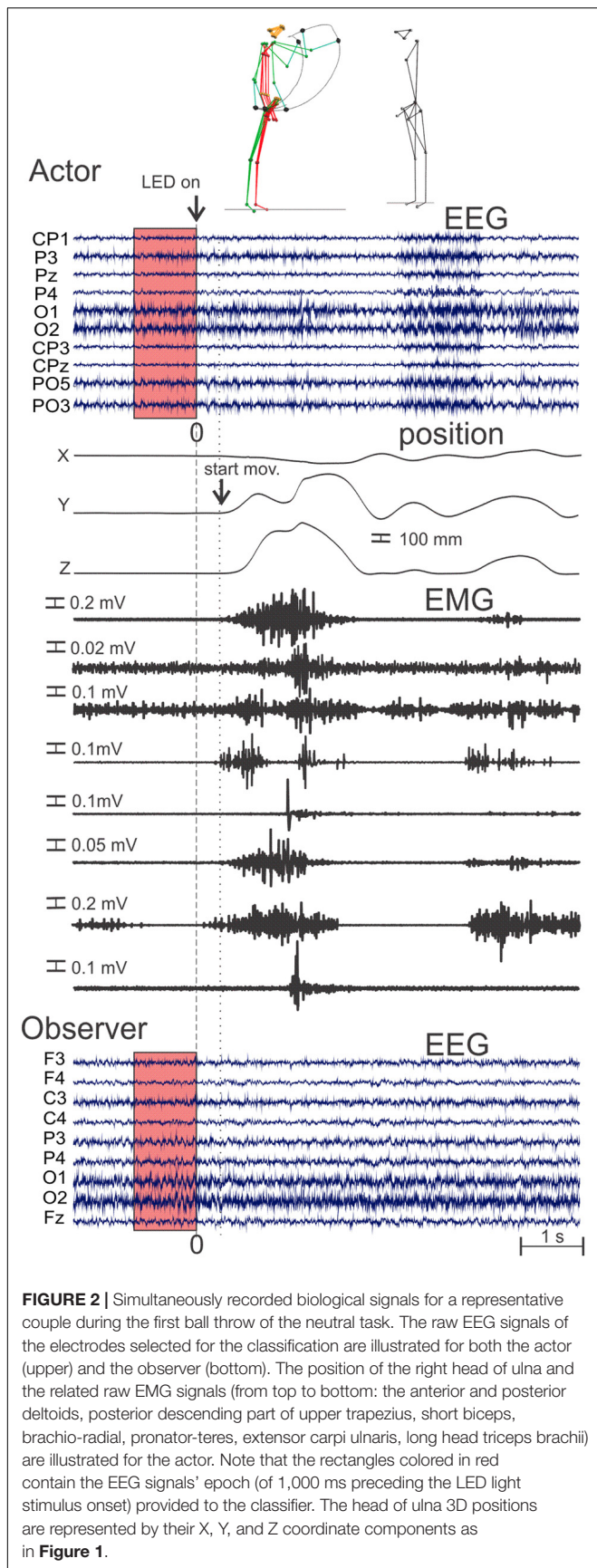
## EEG Recordings

Both participants’ EEG, kinematics, and electromyographic signals were simultaneously recorded.

EEG data of the actors were recorded with 128 channels (ANT neuro system) at a sampling frequency of 2,048 Hz and with a resolution of 71.5 nV per bit. An active-shield cap using 128 Ag/AgCl sintered ring electrodes and shielded co-axial cables (5–10 electrode system placements) was comfortably adjusted to the participant’s head. In addition, electro-oculograms (EOG) (for horizontal and vertical eye movements) were recorded. EEG data of the observers were recorded with 32 channels (Brain Products Brainamp DC with actiCAP) with a resolution of 0.1  $\mu$ V per bit at a sampling rate of 1,000 Hz. Common average reference was used for both recording systems.

Kinematics recordings were performed simultaneously (Figure 2) on both participants with VICON Motion Capture System with 10 cameras at 100 Hz sampling frequency. Passive infrared reflective markers were placed on the skin over nasion,





tragus, acromion, lateral epicondyle of the right and left elbow, along an imaginary line between acromion and epicondyle on the right and left arms, over the head of right and left ulna, along an imaginary line between epicondyle and head of ulna on the right and left forearms, over the third metacarpal head on the right and left hands, right and left anterior superior iliac spines, right and left greater trochanter, right and left lateral epicondyle of the knees, along an imaginary line between greater trochanter and epicondyle of the knee on the right and left shanks, lateral malleolus, along an imaginary line between epicondyle of the knee and lateral malleolus over right and left legs, and over the second right and left metatarsal heads.

Electromyography (EMG) was also simultaneously recorded (**Figure 2**) with a sampling frequency rate of 1,000 Hz (Delsys Trigno Wireless System) on both participants with surface electrodes over the belly of the anterior and posterior deltoids, posterior descending part of upper trapezius, short biceps, brachio-radial, pronator-teres, extensor carpi ulnaris, and long head triceps brachii.

The four recording systems (ANT neuro systems, Brain Products, Vicon Motion Capture, and Delsys Trigno Wireless system) were synchronized with a common external TTL square signal delivered by an external signal generator to each recording system. This signal presented three rising and three falling edges at 1 Hz delivered at the beginning and the end of every task.

### EEG Data Treatment

The first offline data treatment consisted in eliminating the respective data portions recorded before the corresponding system received the first rectangular pulse of the synchronization signal.

Offline EEG data treatment was performed using the EEGLAB software (Delorme and Makeig, 2004). Initially, a 200 Hz low-pass filter, a 512 Hz resampling, and a 3 Hz high-pass filter were applied. Synchronous or partially synchronous artifactual activity (mostly blinks) was detected and rejected by independent component analysis (ICA). Baseline-corrected epochs were extracted from  $-1$  to  $3$  s of the LED light turning on, i.e., the “go” signal. The signal-to-noise ratio (SNR) was computed on each electrode following Möcks et al. (1984), Turetsky et al. (1988), and Cheron et al. (2014). Formally, let  $M$  be the number of trials,  $N$  be the number of samples in a trial, and  $\bar{X}$  denote the averaged signal over all trials; the total noise power  $\sigma_{noise}^2$  and the total signal power  $\sigma_{sig}^2$  can be defined as:

$$\sigma_{noise}^2 = \frac{1}{N(M-1)} \sum_{m=1}^M \left( \sum_{n=1}^N (X_m(n) - \bar{X}(n))^2 \right) \quad (1)$$

$$\sigma_{sig}^2 = \frac{1}{N} \sum_{n=1}^N \bar{X}^2(n) - \frac{1}{M} \sigma_{noise}^2 \quad (2)$$

and the SNR can eventually be estimated by:

$$SNR = \frac{\sigma_{sig}^2}{\sigma_{noise}^2} \quad (3)$$

For the following classification methodology, from all the biological signals of the actors and the observers, we selected epochs of EEG signals from  $-1$  s to  $0$  s before the “go” indication and thus before movement preparation and execution (the selected epoch of a representative trial was represented by a red rectangle on the actor and observer’s EEG data in **Figure 2**).

### Classification Methodology

In order to verify that the classification was not based on the introduction of additional artifactual noise in one condition with respect to the others, we first built a naive classifier (Logistic Regression) solely based on SNR features.

Subsequently, in order to validate the possibility of effectively discriminating between different mental states, we applied two different state-of-the-art classification approaches. The first one used the Common Spatial Pattern algorithm (CSP) (Koles, 1991) improved with the robust estimation of covariance matrices manipulated with Riemannian geometry (Barachant et al., 2010a). For a binary classification task, the CSP algorithm optimizes spatial filters in a supervised way in order to maximize the variance of the filtered signals for one class and minimize their variance for the other class. Formally, let  $E \in \mathbb{N}$  be the number of electrodes,  $N \in \mathbb{N}$  be the number of time samples,  $J \in \mathbb{N}$  be the number of spatial filters,  $W \in \mathbb{R}^{E \times J}$  be the spatial filtering matrix used by the CSP algorithm,  $X_y \in \mathbb{R}^{E \times N}$  be the matrix representation of an epoch from class  $y$ ,  $\Sigma^{(y)} \in \mathbb{R}^{E \times E}$  be the mean covariance matrix of class  $y$ , and  $W^T X_y$  be the spatially filtered signal from class  $y$ . Given a binary classification task, the CSP algorithm first determines discriminative spatial filters  $W$  by the joint diagonalization of the two covariance matrices  $\Sigma^{(1)}$  and  $\Sigma^{(2)}$  as follows (Blankertz et al., 2008; Barachant et al., 2010a):

$$\begin{cases} W^T \Sigma^{(1)} W = D^1 \\ W^T \Sigma^{(2)} W = D^2 \\ D^1 + D^2 = I \end{cases} \quad (4)$$

Subsequently, the  $n$  most discriminative spatial filters ( $n$  being a parameter of the algorithm) determined on the training set are applied on EEG signals, and the variance of the resulting signal is then estimated. Since the variance of a signal band-pass filtered between the cutoff frequencies  $f_L$  and  $f_H$  is equal to the power of that signal in the  $[f_L - f_H]$  frequency range, the CSP algorithm actually optimizes spatial filters in order to produce maximal power difference between the two classes. The output vector of the CSP algorithm is composed of the  $n$  variance estimations and will constitute the input of a classification algorithm such as a Logistic Regression. The multiclass generalization of the CSP algorithm is given by Grosse-Wentrup and Buss (2008).

The second approach using covariance matrices manipulated with Riemannian geometry have notably received growing attention in the last few years (Lotte et al., 2018), particularly due to their first-class performance in international BCI competitions (Congedo et al., 2017). In the present study, we used Riemannian geometry to manipulate covariance matrices of the filtered EEG signal, which is hypothesized to contain a simplified but discriminative representation of a mental state. Covariance matrices are symmetric positive definite (SPD) and do not lie in

a vector space but in a convex cone (Moakher, 2005) called the Riemannian manifold. Thus, Riemannian metrics, i.e., distance and mean, should be preferred in order to manipulate these matrices accurately.

The Riemannian distance and mean are defined by Eqs (5) and (6), respectively:

$$\delta_R(\Sigma_1, \Sigma_2) = \|\log(\Sigma_1^{-1/2} \Sigma_2 \Sigma_1^{-1/2})\|_F \quad (5)$$

$$\zeta(\Sigma_1, \dots, \Sigma_I) = \underset{\Sigma \in P(n)}{\operatorname{argmin}} \sum_{i=1}^I \delta_R^2(\Sigma, \Sigma_i) \quad (6)$$

where  $\delta_R$ ,  $\Sigma \in \mathbb{R}^{E \times E}$ ,  $\|\cdot\|_F$ , and  $P(n)$  denote the Riemannian distance, a covariance matrix estimated from  $E$  electrodes, the Frobenius norm, and the variety of symmetric positive definite matrices, respectively.

Additionally, for each point of the manifold, there is an associated tangent space where a scalar product is defined, and Barachant et al. (2013) showed that the Euclidean distance in the tangent space is a good approximation of the Riemannian distance on the manifold itself. This important finding means that tools and classification algorithms based on Euclidean geometry can be directly used in the tangent space without substantial loss in performance.

The projection operator from the Riemannian manifold to the tangent space at a reference point  $\Sigma_{ref}$  is defined by Eq. (7):

$$\phi(\Sigma) = \operatorname{Log}_{\Sigma_{ref}}(\Sigma) = \Sigma_{ref}^{1/2} \operatorname{logm}\left(\Sigma_{ref}^{-1/2} \Sigma \Sigma_{ref}^{-1/2}\right) \Sigma_{ref}^{1/2} \quad (7)$$

where  $\operatorname{Log}_{\Sigma_{ref}}(\Sigma)$  denotes the logarithmic map (Barachant et al., 2013) of  $\Sigma$  with respect to  $\Sigma_{ref}$  and  $\operatorname{logm}$  denotes the logarithm of a matrix. A good choice of  $\Sigma_{ref}$  is proposed by Barachant et al. (2013) to be the geometric mean of the whole set of covariance matrices and motivated by the observation from Tuzel et al. (2008) that the geometric mean is the point where the mapping on the tangent space leads to the best local approximation of the manifold.

### Classification Pipeline

High-density EEG typically records brain activity from at least 64 electrodes. However, from our own finding, manipulating covariance matrices estimated from a large number of electrodes might induce numerical errors that break their SPD property. Moreover, by using such large covariance matrices, the dimensionality of the feature space becomes significantly higher than the number of training data and thus increases overfitting and reduces the generalization accuracy of the classification algorithm (i.e., the curse of dimensionality). In such a situation, a common practice is a features selection procedure to reduce the number of features (in this case, the number of electrodes) in order to improve classification performances. In order to avoid biasing the classification results, the electrode selection procedure was applied using separate EEG recordings performed during the training period of the first couple preceding the effective hyperscanning performance during which the subjects executed a series of 30 throws in each condition. The same subsets of

electrodes related to the actors and observers were subsequently used for the classification tasks of all 10 couples.

Firstly, we used separate data from the training period to empirically select electrodes that maximized the distance between class-conditional mean covariance matrices using a backward elimination method introduced in Barachant and Bonnet (2011). For this, we computed the average cross-validated binary classification accuracy with respect to the number of electrodes using the training data filtered with an IIR bandpass filter with cutoff frequencies at 1 and 20 Hz. This feature selection procedure resulted in a physiologically plausible choice of electrodes, namely, a common occipito-parietal subset (O1, O2, Pz, P3, and P4) for both the actors and observers and two different subsets, a centro-parietal subset (CP1, Cpz, CP3, PO3, and PO5) for the actors and a centro-frontal subset (C3, C4, F3, F4, and Fz), for the observers. Visual inspection of the selected electrode signals confirmed that no EMG contamination was present. We acknowledge that such feature selection procedure based on distances between class-conditional covariance matrices may slightly favor classification pipelines based on covariance matrices. Nevertheless, this potential bias is limited since the selected electrodes were well representative of the behavioral context linked to the task for both the actors and the observers. Moreover, such possible bias did not impact the main objective of this work, i.e., to demonstrate that state-of-the-art classification algorithm can effectively discriminate between neutral, festive, and violent mental states.

Subsequent to the electrodes selection procedure described here above, the EEG data files from the 10 couples were imported using the MNE 0.17 Python library (Gramfort et al., 2014). A zero-phase IIR bandpass filter with cutoff frequencies at 1 and 20 Hz was applied and epochs from  $-1,000$  to 0 ms (0 ms being the “go” signal indicated by the LED lighting up) were extracted. In order to verify that the throw movement was not initiated before this “go” signal, the kinematic recording of the acting arm was visually inspected. At this stage, the dataset of each couple was composed of 180 matrices (30 for each class and for each role) of shape: 10 electrodes  $\times$  512 samples. The covariance matrix from each epoch is then estimated using the well-conditioned Ledoit-Wolf estimator (Ledoit and Wolf, 2004).

The following classification pipelines were then applied using the same subsets of electrodes:

- SNR with logistic regression: the SNR with logistic regression (SNR-LR) pipeline first estimates the SNR defined by Eq. (3) on each electrode. A logistic regression (LR) classifier is subsequently trained on the SNR values.
- Power spectrum density with logistic regression: the power spectrum density with logistic regression (PSD-LR) pipeline represents a simplistic approach that does just capture a part of the problem complexity and is not expected to yield state-of-the-art results. Nevertheless, this approach will serve as a robust baseline from which to evaluate more complex models. The power spectrum density (PSD) computes the log 10 of the average power in specific frequency bands (delta, theta, alpha, beta, and low-gamma) estimated using Welch’s method (Welch,

1967) on the epoch of EEG signal. The combined binned spectrograms from each electrode are flattened into a one-dimensional array of size 5 frequency bands  $\times$  electrodes that represents an input to a LR classification algorithm.

- Common Spatial Pattern with logistic regression: the Common Spatial Pattern with logistic regression (CSP-LR) pipeline first applies the CSP algorithm on the raw EEG signals in order to optimize  $n$  spatial filters (in this work, we used  $n = 4$ ). The covariance matrices used internally by the CSP algorithm are estimated using the well-conditioned Ledoit-Wolf estimator (Ledoit and Wolf, 2004). A LR classifier is subsequently trained on the resulting features of the CSP algorithm.
- Covariance matrices with Minimum Distance to Mean: the covariance matrices with Minimum Distance to Mean (MDM) pipeline first estimates, for each epoch of EEG signal the corresponding covariance matrix using the well-conditioned Ledoit-Wolf estimator (Ledoit and Wolf, 2004). Subsequently, the Minimum Distance to Mean algorithm classifies covariance matrices directly on the Riemannian manifold.
- Geodesic filtering and covariance matrices with Minimum Distance to Mean: the geodesic filtering and covariance matrices with Minimum Distance to Mean (MDM-GF) pipeline first applies a geodesic filtering (Barachant et al., 2010b) in order to reduce the negative impact of noise on the distances between two covariance matrices. Subsequently, the MDM pipeline is applied on the output of the geodesic filtering.
- Projection on the tangent space and logistic regression: the projection on the tangent space and logistic regression (PTS-LR) pipeline first estimates, for each epoch of EEG signal, the corresponding covariance matrix using the well-conditioned Ledoit-Wolf estimator (Ledoit and Wolf, 2004). Then, each covariance matrix is projected on the tangent space of the Riemannian manifold using the projection operator defined by Eq. (7) and a LR classifier is subsequently trained on the projected covariance matrices.

The classification pipelines were implemented in the Python 3.6 programming language and use the NumPy (van der Walt et al., 2011), SciPy (Jones et al., 2001), scikit-learn (Pedregosa et al., 2012), and pyRiemann (Barachant and King, 2015) Python libraries.

## RESULTS

First and foremost, it is important to highlight the fact that the classification pipelines were only applied on EEG signals occurring 1 s before the movement onset (see the red rectangle in **Figure 2**) in order to avoid the contamination of the EEG signals by muscular artifacts that would bias the classification performances.

### SNR Analysis

As a preliminary result, we verified that any specific changes in electrical potential ( $\mu\text{V}$ ) was not obvious by simple visual

inspection in any condition. For the 10 couples of subjects, the 30 trials of every condition (neutral, festive and violent) were plotted side by side separately for actor and observer. **Figure 3** illustrates, for one representative couple, that the variation of electrical potential ( $\mu\text{V}$ ) for every single EEG trial corresponding to every single epoch (1 s before the LED light turned on) before the throws for one representative electrode (CP3) cannot be visually discriminated. This first visual impression was then confirmed by a classifier based on SNR features that was not able to discriminate between the different mental states above chance level (see **Figure 4**).

On the basis of the unsuccessful results of SNR classification, we turned to state-of-the-art classification pipelines (**Figure 5**) using CSP filtering and covariance matrices with Riemannian geometry.

### Benefits of Applying Riemannian Metrics

In order to graphically illustrate the benefits of using Riemannian metrics and the projection on the tangent space when manipulating covariance matrices (estimated from the 10 selected EEG electrodes), we applied one procedure using the EEG data of one representative participant (the actor of the first couple). This procedure, called “distance to mean,” initially

computed the mean covariance matrix of each class and subsequently represented the covariance matrix of an epoch on a graph by a single point whose coordinates corresponded to the distances between that covariance matrix and each mean covariance matrix. **Figure 6** illustrates the benefits of using the Riemannian metrics to compute the distances between covariance matrices corresponding to the violent and festive EEG data set recorded from the actor of the first couple. In the Euclidean space, the experimental points associated with the two classes are overlapping (**Figures 6A,C**). In contrast, in the Riemannian space, the violent and festive data are better separable (**Figures 6B,D**).

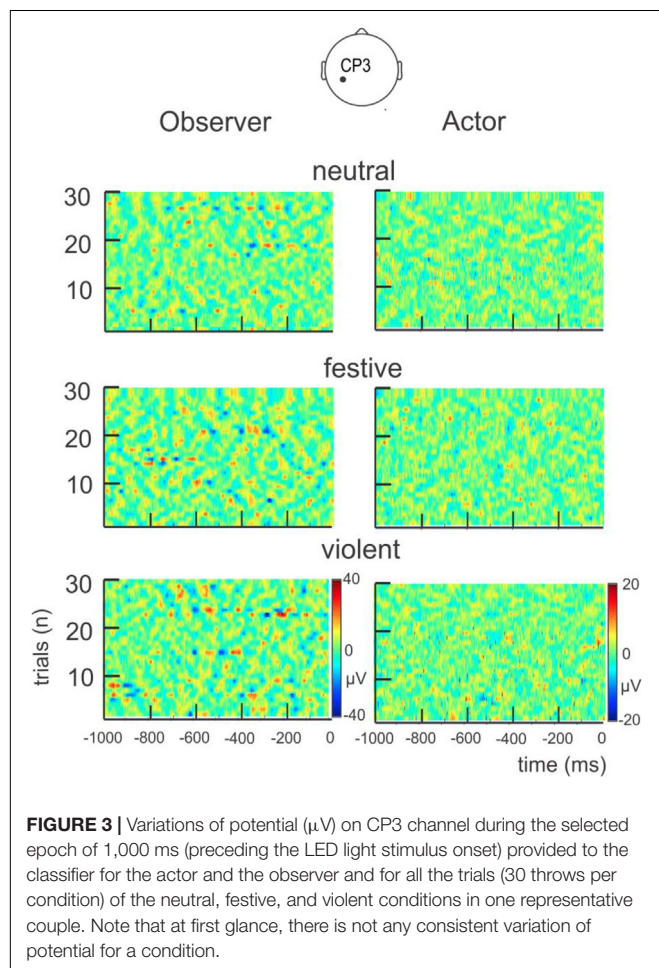
### Classification Results

The boxplots of **Figure 4** summarize the comparative analysis of all classification pipelines with respect to the mental state combinations. The datasets of all mental states and participants are perfectly balanced and the classification results for all pipelines were computed using a 10-fold cross-validation. We observed that statistically significant differences with a  $p$ -value  $< 0.05$  computed using the Wilcoxon signed-rank test were found between the SNR-LR and all the other classification pipelines, regardless of the mental states or the conditions. This result combined with the SNR-LR classification accuracy under chance level confirmed our first impression that SNR features do not contain enough information to effectively discriminate between different mental states.

The PSD-LR results were also significantly lower than all the other classification pipelines in the Actor condition regardless of the mental states. In the Observer condition, the PSD-LR results were significantly lower than all the other pipelines except for the MDM in the Festive vs. Violent mental state (**Figure 4B**) and for the MDM and the CSP-LR pipelines in the Festive vs. Neutral mental state (**Figure 4D**). Even though there are few statistically significant differences between the CSP-LR and the Riemannian classification pipelines (MDM, MDM-GE, and TS-LR), the mean accuracies of the latter are slightly higher than the ones of the CSP-LR.

### DISCUSSION

Understanding action intent of others involves matching the observed action to the internal representation of such an action built on one's own multi-sensory-motor experience (Rizzolatti and Sinigaglia, 2007). Previously, hemodynamic-based neuroimaging brain studies have shown that the activated brain areas are different when understanding and judging a negative intent, which included the right amygdala, the temporoparietal junction, and hypothalamus (Sinke et al., 2010), compared to a positive intent, which included the right temporoparietal junction and the right dorsolateral prefrontal cortex (Yoder and Decety, 2014). In addition, fMRI (Vuilleumier and Pourtois, 2007; Bachmann et al., 2018; Engelen et al., 2018; Schönfeld and Wojtecki, 2019) and TMS (Borgomaneri et al., 2015; Engelen et al., 2015, 2018) studies demonstrated the existence of dynamical interactions between the amygdala,



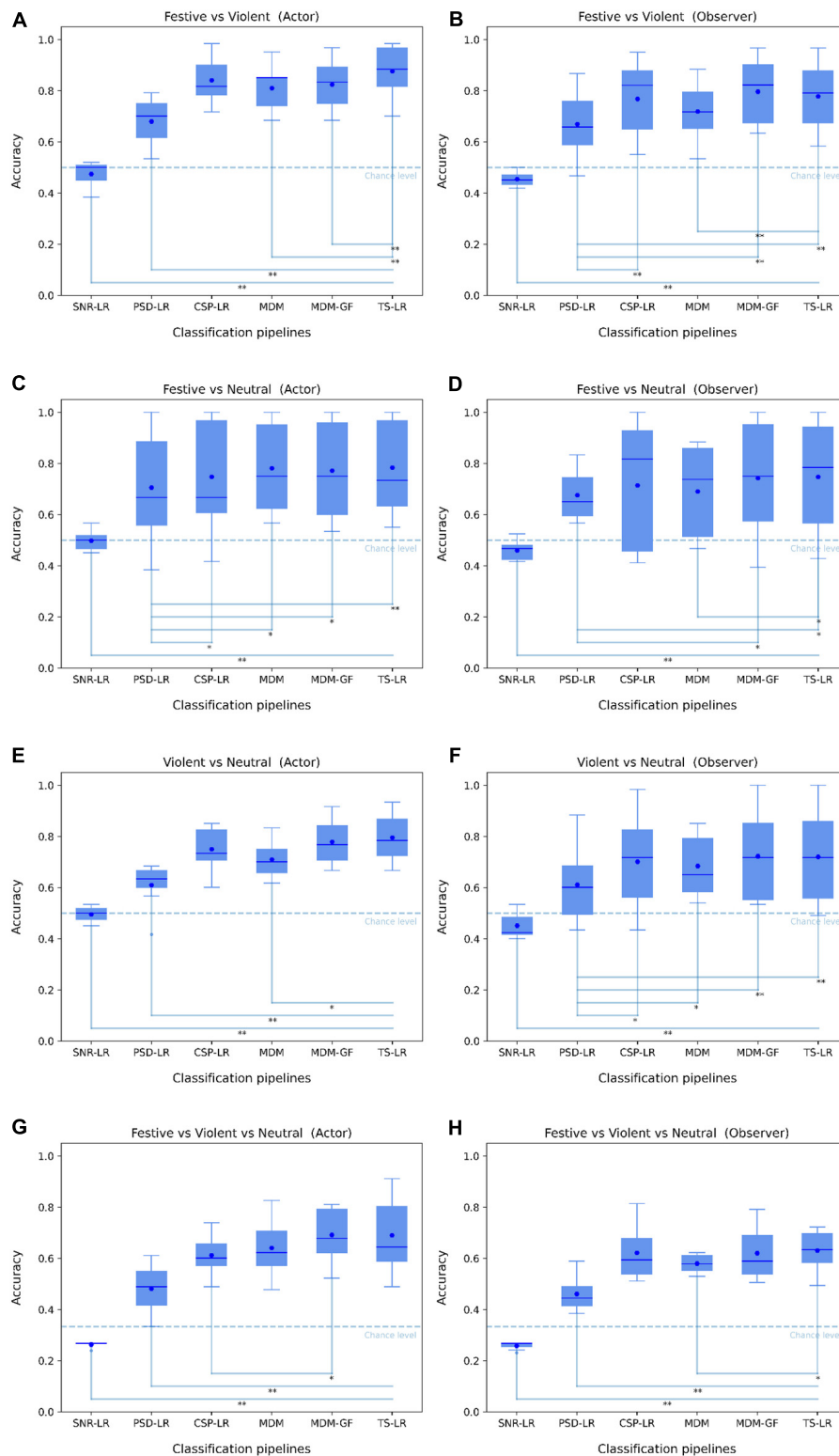
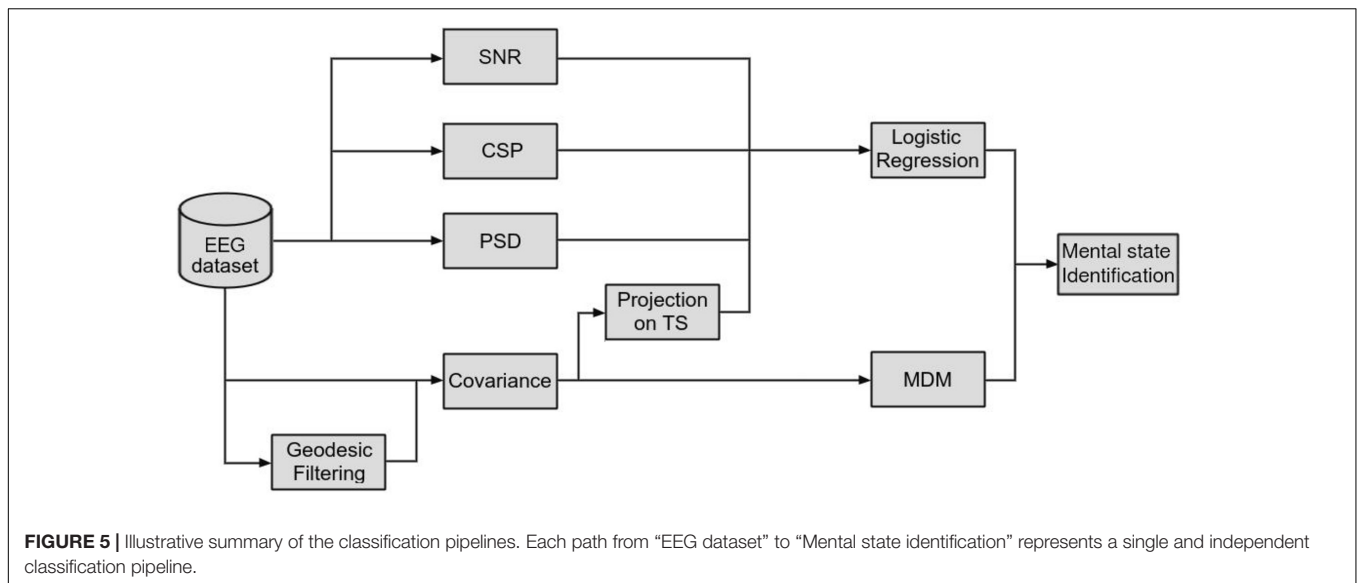


**FIGURE 4 |** Boxplots illustrating the binary/multi-class classification accuracy (True Positives vs. All) of the SNR-LR, PSD-LR, CSP-LR, MDM, MDM-GF, and TS-LR classification pipelines for the Festive vs. Violent, Festive vs. Neutral, Violent vs. Neutral, and Violent vs. Festive vs. Neutral mental states with regard to the participant conditions [Actor (**A,C,E,G**) and Observer (**B,D,F,H**)]. The horizontal dashed lines indicate the chance level. The blue hexagons indicate the mean classification accuracy values. Statistically significant differences between pairwise performances of two classification pipelines are represented using one or two asterisks when the *p*-value of the Wilcoxon signed-rank test is strictly below 0.05 or 0.01, respectively.



the inferior parietal lobule, and the ventral premotor cortex involved in the perception of emotions and the preparation of an action. The functional dynamical mechanisms underlying communication between brain areas have been approached with EEG, which, in this case, is particularly appropriate because it captures electrical brain oscillations that assess direct brain function with a millisecond precision. EEG recordings, while observing an intent inference task displayed on a screen, have shown that moral cognition processes occur as soon as at 200 ms where kind intent featured larger peak N2 amplitude component supported by left cingulate gyrus activity. Hostile intent featured later a larger peak P3 amplitude component supported by the left anterior cingulate cortex activity (Wang et al., 2015).

In this work, we propose a more realistic protocol where both the observer and the actor (of the violent, festive, and neutral ball throws) are real persons standing up and facing each other. This protocol allows access to the synchronized EEG dynamics, kinematics, and electromyographic activity of both participants. Although further investigation will be needed with a larger population to understand and characterize such EEG dynamics, kinematics, and muscular activity before, during, and after the movement, we demonstrated here that even without knowing the underlying dynamical mechanisms, classification algorithms can effectively discriminate between neutral, festive, and violent mental states. These successful classification results were obtained in both the actors’ and observers’ EEG signals of 10 couples during 1 s before the action, suggesting that festive and violent intent can be detected before the action. These results pave the way for new electrophysiological discrimination of mental states based on non-invasive EEG recordings.

## Design Considerations

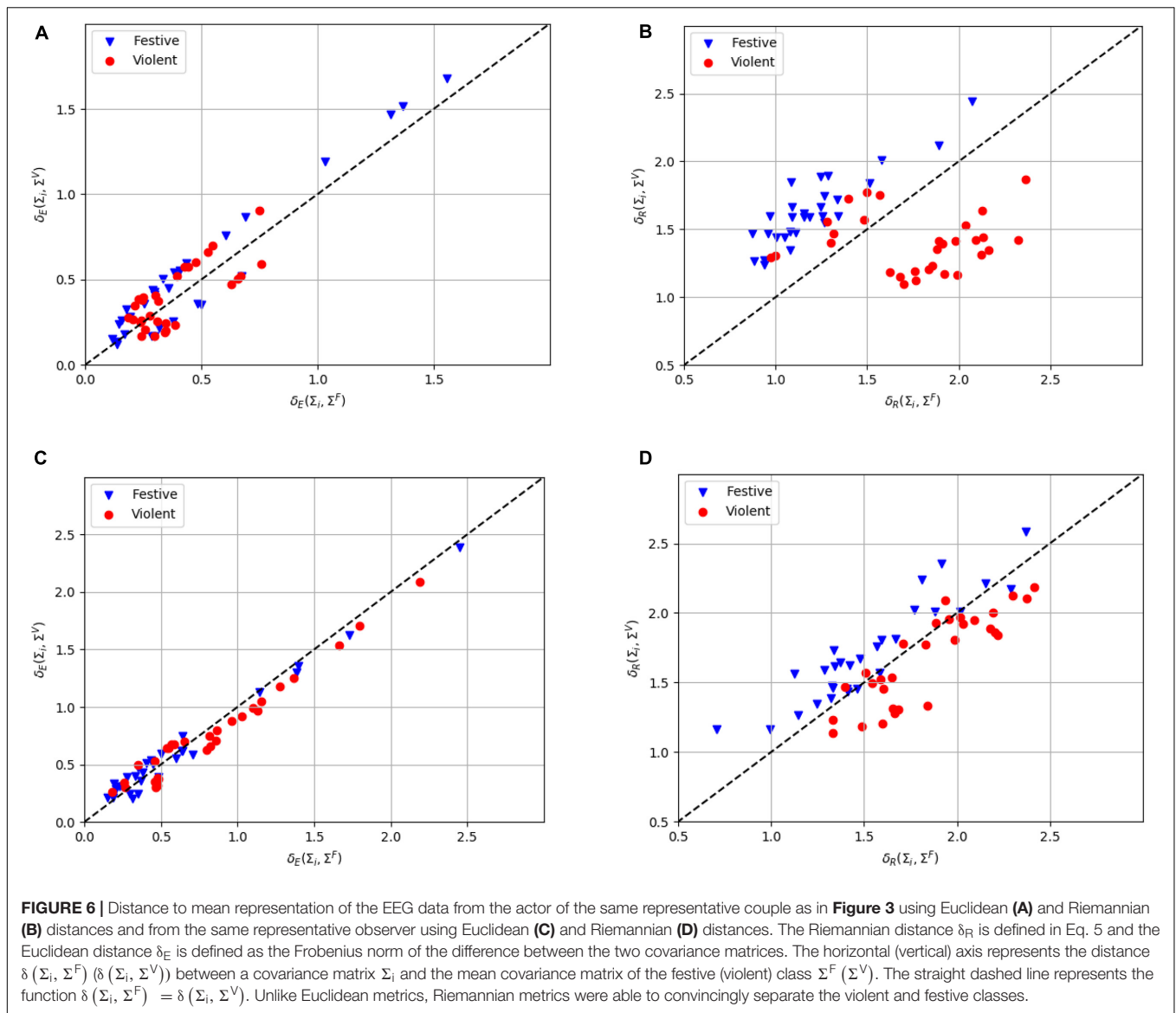
The terms “festive” and “violent” can be understood differently depending on the context and interpretational meaning. The debate on whether and how linguistic data are a part of a complex interpretational structure and how they can be implemented in

the mind of the participants remain largely unknown (Hagoort, 2020; Martin and Baggio, 2020). In this perspective, we propose a protocol inspired by Gregory Bateson’s analysis of double framing (Bateson, 1955). Bateson studied monkeys who were play-fighting and observed that this situation relied on two frames: the frame of the battle and the frame of the play. In the present design, the two participants are in the second frame of meta-communication since both the actor and the observer are aware of the general state imposed by the experimenter. This means that not only the posture and the gesture of the participant but also the imposed meta-cognitive communication may greatly contribute to the establishment of the required mental state. The fact that significant classification performances were obtained for the 10 couples of participants may indicate that the interpretational meaning of the “festive” vs. “violent” vs. “neutral” conditions were relatively well understood by all participants.

One of the major difficulties was to establish an experimental design able to provide a clear relationship between the intentional context, the mental states, and the behavioral output (Isoda, 2016). For this, we have approached the mental state by means of high-density EEG and the motor output by means of kinematics and EMG recordings. As it was reported that movement and EMG contamination of the EEG remain not satisfactorily solved (Castermans et al., 2014), we have focused the present mental state identification only during the epoch of 1 s before movement identification. During this preparatory period, the EMG artifact contaminations were not visible on the FFT spectrum and not identified with a classifier based on the SNR. In addition, no specific changes in electrical potential was detected by simple visual inspection. We may thus conclude that the present mental state classification was not based on EMG contamination.

## The Different Classification Methods and the Advantages of the Present One

The use of Riemannian geometry may at first be considered a mere mathematical sophistication. However, we here



demonstrated that it has a profound impact on class separability and thus classification accuracy. This result strengthens evidence of the Riemannian geometry efficiency already reported in different scientific fields such as radar signal processing (Arnaudon et al., 2013), image classification (Tuzel et al., 2008), thermodynamics (Mausbach et al., 2018), morphogenesis (Hu et al., 2018), graph theory (Bakker et al., 2018) and BCI (Mayaud et al., 2016; Han et al., 2019; Rodrigues et al., 2019).

In order to verify our working hypothesis that the EEG signals characterized distinctively the festive, violent, and neutral mental states, we have systematically compared different classification methods currently used in the field and appropriate to the first explorative experiment carried out on a pair of synchronized EEG recordings of 10 observers and 10 actors. Our results demonstrate that state-of-the-art classification algorithms based on Riemannian geometry (MDM, MDM-GF, and PTS-LR) or Common Spatial Pattern (CSP-LR) are able to effectively

discriminate between mental states (reaching a cross-validated classification accuracy of 0.88 for the Festive vs. Violent states) and provide significantly better performance with respect to classifiers based only on SNR or PSD. We showed that the use of the variance–covariance alone was unable to effectively discriminate between the three mental states, which indicates that the Riemannian geometry is crucial for neural signal discrimination based on covariance matrices. Although classifiers based on the CSP algorithm perform slightly worse than the Riemannian methods in international BCI competitions (Lotte et al., 2018), the CSP-based classifier has here produced comparable performances. It is also interesting to mention that, in spite of the fact that both participants are aware of the Festive or Violent required condition, EEG classification performances were better for the Actor, which may indicate that the motor-action preparatory processes propagate to the EEG signals and thus play a role in the identification of the mental state.

The assumption that the EEG signal observed prior to the action is necessarily a sign of intent must be met with some caution, as there could be other equally plausible explanations, such as the prediction of an incoming “known” stimulus, which cannot be excluded in the absence of “blinding.” Further studies could potentially provide further evidence for or against the specific mechanism proposed in this work.

Interestingly, state-of-the-art classifiers used in this study were able to achieve significant discriminability using a limited number of trials. Such desirable characteristics is paramount to avoiding side effects such as fatigue, habituation, or loss of awareness induced by too much repetition of the same behavior and related mental state induction. Nevertheless, these results are also relevant for future BCI applications where limited signal acquisition is a major constraint to train a functional classification algorithm.

## DATA AVAILABILITY STATEMENT

Requests to access the datasets should be directed to GCe, gcheron@ulb.ac.be.

## ETHICS STATEMENT

All experimental protocols were approved by the Ethic comity of Université Libre de Bruxelles, CHU Brugmann and conducted

in conformity with the European Union directive 2001/20/EC of the European Parliament. The patients/participants provided their written informed consent to participate in this study.

## AUTHOR CONTRIBUTIONS

AB and GCa conceived the original idea. CS, A-MC, and GCe designed the experiment. AB, CS, A-MC, and GCe performed the experiment. CS and GB performed the data analysis, GCe and CS wrote the manuscript. AB, GCa, A-MC, and GB contributed to the writing. All authors contributed to the article and approved the submitted version.

## ACKNOWLEDGMENTS

We would like to thank the research fund and the Leibniz fund of the Université Libre de Bruxelles and of the Université de Mons, Belgium. We would also like to thank Eric Brian and Marie Jaisson for their valuable guidance and constructive suggestions throughout this work, as well as T. D’Angelo, E. Toussaint, E. Hortmanns, and M. Dufief for their expert technical assistance and Elena Pecoraro for secretarial assistance. We thank Eric Brian and Marie Jaisson from University of Paris who are the Directors of the thesis of Gaeële Chartier who is supported by a PHD and ATER grants from University Paris 13, Department of Health, Medicine and Human Biology.

## REFERENCES

- Arnaudon, M., Barbaresco, F., and Yang, L. (2013). Riemannian medians and means with applications to radar signal processing. *IEEE J. Select. Top. Signal. Process.* 7, 595–604. doi: 10.1109/jstsp.2013.2261798
- Babiloni, F., Cincotti, F., Mattia, D., Mattiocco, M., De Vico Fallani, F., Tocci, A., et al. (2006). Hypermethods for EEG hyperscanning. *Conf. Proc. IEEE Eng. Med. Biol. Soc.* 2006, 3666–3669.
- Bachmann, J., Munzert, J., and Krüger, B. (2018). Neural underpinnings of the perception of emotional states derived from biological human motion: a review of neuroimaging research. *Front. Psychol.* 9:1763. doi: 10.3389/fpsyg.2018.01763
- Bakker, C., Halappanavar, M., and Visweswara Sathanur, A. (2018). Dynamic graphs, community detection, and Riemannian geometry. *Appl. Netw. Sci.* 3:3.
- Balconi, M., Fronza, G., and Vanutelli, M. E. (2020). When gratitude and cooperation between friends affect inter-brain connectivity for EEG. *BMC Neurosci.* 21:14. doi: 10.1186/s12868-020-00563-7
- Barachant, A., and Bonnet, S. (2011). “Channel selection procedure using riemannian distance for BCI applications,” in *Proceedings of the 5th International IEEE/EMBS Conference on Neural Engineering (NER 2011)*, Cancun.
- Barachant, A., Bonnet, S., Congedo, M., and Jutten, C. (2010a). “Common spatial pattern revisited by riemannian geometry,” in *Proceedings of the 2010 IEEE International Workshop on Multimedia Signal Processing (MMSP)*, St-Malo.
- Barachant, A., Bonnet, S., Congedo, M., and Jutten, C. (2010b). “Riemannian geometry applied to BCI classification,” in *Latent Variable Analysis and Signal Separation, Lecture Notes in Computer Science*, eds V. Vigneron, V. Zarzoso, E. Moreau, R. Gribonval, and E. Vincent (Berlin: Springer), 629–636. doi: 10.1007/978-3-642-15995-4\_78
- Barachant, A., Bonnet, S., Congedo, M., and Jutten, C. (2013). Classification of covariance matrices using a Riemannian-based kernel for BCI applications. *Neurocomput. Adv.* 112, 172–178. doi: 10.1016/j.neucom.2012.12.039
- Barachant, A., and King, J.-R. (2015). *PyRiemann*. doi: 10.5281/zenodo.593816
- Barraza, P., Dumas, G., Liu, H., Blanco-Gomez, G., Heuvel, M., van den Baart, M., et al. (2019). Implementing EEG hyperscanning setups. *MethodsX* 6, 428–436. doi: 10.1016/j.mex.2019.02.021
- Bateson, G. (1955). A theory of play and fantasy; a report on theoretical aspects of the project of study of the role of the paradoxes of abstraction in communication. *Psychiatr. Res. Rep. Am. Psychiatr. Assoc.* 2, 39–51.
- Blankertz, B., Tomioka, R., Lemm, S., Kawanabe, M., and Muller, K. (2008). Optimizing spatial filters for robust EEG single-trial analysis. *IEEE Signal. Process. Magaz.* 25, 41–56. doi: 10.1109/msp.2008.4408441
- Borgomaneri, S., Gazzola, V., and Avenanti, A. (2015). Transcranial magnetic stimulation reveals two functionally distinct stages of motor cortex involvement during perception of emotional body language. *Brain Struct. Funct.* 220, 2765–2781. doi: 10.1007/s00429-014-0825-6
- Buzsáki, G., and Draguhn, A. (2004). Neuronal oscillations in cortical networks. *Science* 304, 1926–1929. doi: 10.1126/science.1099745
- Castermans, T., Duvinage, M., Cheron, G., and Dutoit, T. (2014). About the cortical origin of the low-delta and high-gamma rhythms observed in EEG signals during treadmill walking. *Neurosci. Lett.* 561, 166–170. doi: 10.1016/j.neulet.2013.12.059
- Chartier, G., Berthoz, A., Brian, É., and Jaisson, M. (2017). Violence and uncertainty: Interactional sketches for a cognitive analysis of violent actions. *Soc. Sci. Inform.* 56, 198–219. doi: 10.1177/0539018417694772
- Cheron, G., Leroy, A., Palmero-Soler, E., De Saedeleer, C., Bengoetxea, A., Cebolla, A.-M., et al. (2014). Gravity influences top-down signals in visual processing. *PLoS One* 9:e82371. doi: 10.1371/journal.pone.0082371
- Congedo, M., Rodrigues, P. L. C., Bouchard, F., Barachant, A., and Jutten, C. (2017). “A closed-form unsupervised geometry-aware dimensionality reduction method in the riemannian manifold of SPD matrices,” in *Proceeding of the 2017 39th Annual International Conference of the IEEE Engineering in Medicine and Biology Society (EMBC)*, Seogwipo.
- Czeszumski, A., Eustergerling, S., Lang, A., Menrath, D., Gerstenberger, M., Schuberth, S., et al. (2020). Hyperscanning: a valid method to study neural

- inter-brain underpinnings of social interaction. *Front. Hum. Neurosci.* 14:39. doi: 10.3389/fnhum.2020.00039
- de Gelder, B. (2016). *Emotions and the Body*. Oxford: Oxford University Press.
- Decety, J., and Cacioppo, S. (2012). The speed of morality: a high-density electrical neuroimaging study. *J. Neurophysiol.* 108, 3068–3072. doi: 10.1152/jn.00473.2012
- Delorme, A., and Makeig, S. (2004). EEGLAB: an open source toolbox for analysis of single-trial EEG dynamics including independent component analysis. *J. Neurosci. Methods* 134, 9–21. doi: 10.1016/j.jneumeth.2003.10.009
- Dumas, G., Nadel, J., Soussignan, R., Martinerie, J., and Garnero, L. (2010). Inter-brain synchronization during social interaction. *PLoS One* 5:e12166. doi: 10.1371/journal.pone.012166
- Elias, N. (1997). *Über Den Prozess Der Zivilisation. Soziogenetische Und Psychogenetische Untersuchungen Band I: Wandlungen Des Verhaltens In Den Weltlichen Oberschichten Des Abendlandes*. Frankfurt: Suhrkamp.
- Engelen, T., de Graaf, T. A., Sack, A. T., and de Gelder, B. (2015). A causal role for inferior parietal lobule in emotion body perception. *Cortex* 73, 195–202. doi: 10.1016/j.cortex.2015.08.013
- Engelen, T., Zhan, M., Sack, A. T., and de Gelder, B. (2018). Dynamic interactions between emotion perception and action preparation for reacting to social threat: a combined cTBS-fMRI study. *eNeuro* 5:ENEURO.0408-17.2018. doi: 10.1523/ENEURO.0408-17.2018
- Fatima, S., and Kamboj, A. M. (2017). “Decoding brain cognitive activity across subjects using multimodal M/EEG neuroimaging,” in *Proceedings of the 2017 39th Annual International Conference of the IEEE Engineering in Medicine and Biology Society (EMBC)*, Seogwipo.
- Gramfort, A., Luessi, M., Larson, E., Engemann, D. A., Strohmeier, D., Brodbeck, C., et al. (2014). MNE software for processing MEG and EEG data. *Neuroimage* 86, 446–460. doi: 10.1016/j.neuroimage.2013.10.027
- Grosse-Wentrup, M., and Buss, M. (2008). Multiclass common spatial patterns and information theoretic feature extraction. *IEEE Trans. Biomed. Eng.* 55, 1991–2000. doi: 10.1109/tbme.2008.921154
- Hagoort, P. (2020). The meaning-making mechanism(s) behind the eyes and between the ears. *Philos. Trans. R. Soc. Lond. B Biol. Sci.* 375, 20190301. doi: 10.1098/rstb.2019.0301
- Han, C.-H., Kim, Y.-W., Kim, D. Y., Kim, S. H., Nenadic, Z., and Im, C.-H. (2019). Electroencephalography-based endogenous brain-computer interface for online communication with a completely locked-in patient. *J. Neuroeng. Rehabil.* 16:18.
- Hu, Z., Petoukhov, S. V., and Petukhova, E. S. (2018). On symmetries, resonances and photonic crystals in morphogenesis. *Biosystems* 173, 165–173. doi: 10.1016/j.biosystems.2018.09.004
- Isoda, M. (2016). Understanding intentional actions from observers' viewpoints: a social neuroscience perspective. *Neurosci. Res.* 112, 1–9. doi: 10.1016/j.neures.2016.06.008
- Jones, E., Oliphant, T., and Peterson, P. (2001). *SciPy: Open Source Scientific Tools for Python*. Boston, FL: ScienceOpen Inc.
- Kim, M.-K., Kim, M., Oh, E., and Kim, S.-P. (2013). A review on the computational methods for emotional state estimation from the human EEG. *Comput. Math. Methods Med.* 2013:573734.
- Kinreich, S., Djalovski, A., Kraus, L., Louzoun, Y., and Feldman, R. (2017). Brain-to-brain synchrony during naturalistic social interactions. *Sci. Rep.* 7:17060.
- Koles, Z. J. (1991). The quantitative extraction and topographic mapping of the abnormal components in the clinical EEG. *Electroencephalogr. Clin. Neurophysiol.* 79, 440–447. doi: 10.1016/0013-4694(91)90163-x
- Ledoit, O., and Wolf, M. (2004). A well-conditioned estimator for large-dimensional covariance matrices. *J. Multivar. Anal.* 88, 365–411. doi: 10.1016/s0047-259x(03)00096-4
- Liu, D., Liu, S., Liu, X., Zhang, C., Li, A., Jin, C., et al. (2018). Interactive brain activity: review and progress on EEG-based hyperscanning in social interactions. *Front. Psychol.* 9:1862. doi: 10.3389/fpsyg.2018.01862
- Lotte, F., Bougrain, L., Cichocki, A., Clerc, M., Congedo, M., Rakotomamonjy, A., et al. (2018). A review of classification algorithms for EEG-based brain-computer interfaces: a 10 year update. *J. Neural Eng.* 15:031005. doi: 10.1088/1741-2552/aab2f2
- Martin, A. E., and Baggio, G. (2020). Modelling meaning composition from formalism to mechanism. *Philos. Trans. R. Soc. Lond. B Biol. Sci.* 375:20190298. doi: 10.1098/rstb.2019.0298
- Mausbach, P., Köster, A., and Vrabec, J. (2018). Liquid state isomorphism, Rosenfeld-Tarazona temperature scaling, and Riemannian thermodynamic geometry. *Phys. Rev. E* 97:052149.
- Mayaud, L., Cabanilles, S., Langenhove, A., Congedo, M., Barachant, A., Pouplin, S., et al. (2016). Brain-computer interface for the communication of acute patients: a feasibility study and a randomized controlled trial comparing performance with healthy participants and a traditional assistive device. *Brain Comput. Interf.* 3, 197–215. doi: 10.1080/2326263x.2016.1254403
- Ménoret, M., Varnet, L., Fargier, R., Cheylus, A., Curie, A., des Portes, V., et al. (2014). Neural correlates of non-verbal social interactions: a dual-EEG study. *Neuropsychologia* 55, 85–97. doi: 10.1016/j.neuropsychologia.2013.10.001
- Moakher, M. (2005). A differential geometric approach to the geometric mean of symmetric positive-definite matrices. *SIAM J. Matrix Anal. Appl.* 26, 735–747. doi: 10.1137/s0895479803436937
- Möcks, J., Gasser, T., and Tuan, P. D. (1984). Variability of single visual evoked potentials evaluated by two new statistical tests. *Electroencephalogr. Clin. Neurophysiol.* 57, 571–580. doi: 10.1016/0013-4694(84)90093-2
- Montague, P. R., Berns, G. S., Cohen, J. D., McClure, S. M., Pagnoni, G., Dhamala, M., et al. (2002). Hyperscanning: simultaneous fMRI during linked social interactions. *Neuroimage* 16, 1159–1164. doi: 10.1006/nimg.2002.1150
- Oldfield, R. C. (1971). The assessment and analysis of handedness: the Edinburgh inventory. *Neuropsychologia* 9, 97–113. doi: 10.1016/0028-3932(71)90067-4
- Pedregosa, F., Varoquaux, G., Gramfort, A., Michel, V., Thirion, B., Grisel, O., et al. (2012). Scikit-learn: machine learning in Python. *J. Mach. Learn. Res.* 12, 2825–2830.
- Rizzolatti, G., Cattaneo, L., Fabbri-Destro, M., and Rozzi, S. (2014). Cortical mechanisms underlying the organization of goal-directed actions and mirror neuron-based action understanding. *Physiol. Rev.* 94, 655–706. doi: 10.1152/physrev.00009.2013
- Rizzolatti, G., and Sinigaglia, C. (2007). Mirror neurons and motor intentionality. *Funct. Neurol.* 22, 205–210.
- Rodrigues, P. L. C., Jutten, C., and Congedo, M. (2019). Riemannian procrustes analysis: transfer learning for brain-computer interfaces. *IEEE Trans. Biomed. Eng.* 66, 2390–2401. doi: 10.1109/tbme.2018.2889705
- Scangos, K. W., Aronberg, R., and Stuphorn, V. (2013). Performance monitoring by presupplementary and supplementary motor area during an arm movement countermanding task. *J. Neurophysiol.* 109, 1928–1939. doi: 10.1152/jn.00688.2012
- Schindler, S., and Bublitzky, F. (2020). Attention and emotion: an integrative review of emotional face processing as a function of attention. *Cortex* 130, 362–386. doi: 10.1016/j.cortex.2020.06.010
- Schönfeld, L.-M., and Wojtecki, L. (2019). Beyond emotions: oscillations of the Amygdala and their implications for electrical neuromodulation. *Front. Neurosci.* 13:366. doi: 10.3389/fnins.2019.00366
- Schütz-Bosbach, S., and Prinz, W. (2007). Perceptual resonance: action-induced modulation of perception. *Trends Cogn. Sci.* 11, 349–355. doi: 10.1016/j.tics.2007.06.005
- Sinke, C. B. A., Sorger, B., Goebel, R., and de Gelder, B. (2010). Tease or threat? Judging social interactions from bodily expressions. *Neuroimage* 49, 1717–1727. doi: 10.1016/j.neuroimage.2009.09.065
- Thirioux, B., Mercier, M. R., Jorland, G., Berthoz, A., and Blanke, O. (2010). Mental imagery of self-location during spontaneous and active self-other interactions: an electrical neuroimaging study. *J. Neurosci.* 30, 7202–7214. doi: 10.1523/jneurosci.3403-09.2010
- Turetsky, B. I., Raz, J., and Fein, G. (1988). Noise and signal power and their effects on evoked potential estimation. *Electroencephalogr. Clin. Neurophysiol.* 71, 310–318. doi: 10.1016/0168-5597(88)90032-9
- Tuzel, O., Porikli, F., and Meer, P. (2008). Pedestrian detection via classification on riemannian manifolds. *IEEE Trans. Patt. Anal. Mach. Intell.* 30, 1713–1727. doi: 10.1109/tpami.2008.75
- van der Walt, S., Colbert, S. C., and Varoquaux, G. (2011). The NumPy array: a structure for efficient numerical computation. *Comput. Sci. Eng.* 13, 22–30. doi: 10.1109/mcse.2011.37

- Vuilleumier, P., and Pourtois, G. (2007). Distributed and interactive brain mechanisms during emotion face perception: evidence from functional neuroimaging. *Neuropsychologia* 45, 174–194. doi: 10.1016/j.neuropsychologia.2006.06.003
- Wang, Y., Huang, L., Zhang, W., Zhang, Z., and Cacioppo, S. (2015). Spatio-temporal dynamics of kind versus hostile intentions in the human brain: an electrical neuroimaging study. *Soc. Neurosci.* 10, 253–267. doi: 10.1080/17470919.2014.990641
- Welch, P. (1967). The use of fast Fourier transform for the estimation of power spectra: a method based on time averaging over short, modified periodograms. *IEEE Trans. Audio Electroacoust.* 15, 70–73. doi: 10.1109/tau.1967.1161901
- Wu, D., Lance, B. J., Lawhern, V. J., Gordon, S., Jung, T.-P., and Lin, C.-T. (2017). EEG-based user reaction time estimation using riemannian geometry features. *IEEE Trans. Neural Syst. Rehabil. Eng.* 25, 2157–2168. doi: 10.1109/tnsre.2017.2699784
- Yoder, K. J., and Decety, J. (2014). The Good, the bad, and the just: justice sensitivity predicts neural response during moral evaluation of actions performed by others. *J. Neurosci.* 34, 4161–4166. doi: 10.1523/jneurosci.4648-13.2014

**Conflict of Interest:** The authors declare that the research was conducted in the absence of any commercial or financial relationships that could be construed as a potential conflict of interest.

Copyright © 2020 Simar, Cebolla, Chartier, Petieau, Bontempi, Berthoz and Cheron. This is an open-access article distributed under the terms of the Creative Commons Attribution License (CC BY). The use, distribution or reproduction in other forums is permitted, provided the original author(s) and the copyright owner(s) are credited and that the original publication in this journal is cited, in accordance with accepted academic practice. No use, distribution or reproduction is permitted which does not comply with these terms.



# Auditory Noise Leads to Increased Visual Brain-Computer Interface Performance: A Cross-Modal Study

Jun Xie<sup>1,2,3,4\*</sup>, Guozhi Cao<sup>1</sup>, Guanghua Xu<sup>1,4</sup>, Peng Fang<sup>2</sup>, Gailing Cui<sup>3\*</sup>, Yi Xiao<sup>3</sup>, Guanglin Li<sup>2</sup>, Min Li<sup>1</sup>, Tao Xue<sup>1</sup>, Yanjun Zhang<sup>1</sup> and Xingliang Han<sup>1</sup>

<sup>1</sup> School of Mechanical Engineering, Xi'an Jiaotong University, Xi'an, China, <sup>2</sup> CAS Key Laboratory of Human-Machine Intelligence-Synergy Systems, Shenzhen Institutes of Advanced Technology & Shenzhen Engineering Laboratory of Neural Rehabilitation Technology, Shenzhen, China, <sup>3</sup> National Key Laboratory of Human Factors Engineering, China Astronauts Research and Training Center, Beijing, China, <sup>4</sup> State Key Laboratory for Manufacturing Systems Engineering, Xi'an Jiaotong University, Xi'an, China

## OPEN ACCESS

### Edited by:

Haider Raza,  
University of Essex, United Kingdom

### Reviewed by:

Russell W. Chan,  
Stanford University, United States  
Rajesh Singla,  
Dr. B. R. Ambedkar National Institute  
of Technology Jalandhar, India  
Richard Gault,  
Queen's University Belfast,  
United Kingdom

### \*Correspondence:

Jun Xie  
xiejun@mail.xjtu.edu.cn  
Gailing Cui  
gege\_bj2006@sina.com

### Specialty section:

This article was submitted to  
Brain Imaging Methods,  
a section of the journal  
Frontiers in Neuroscience

**Received:** 03 August 2020

**Accepted:** 18 November 2020

**Published:** 22 December 2020

### Citation:

Xie J, Cao G, Xu G, Fang P, Cui G,  
Xiao Y, Li G, Li M, Xue T, Zhang Y and  
Han X (2020) Auditory Noise Leads  
to Increased Visual Brain-Computer  
Interface Performance:  
A Cross-Modal Study.  
*Front. Neurosci.* 14:590963.  
doi: 10.3389/fnins.2020.590963

Noise has been proven to have a beneficial role in non-linear systems, including the human brain, based on the stochastic resonance (SR) theory. Several studies have been implemented on single-modal SR. Cross-modal SR phenomenon has been confirmed in different human sensory systems. In our study, a cross-modal SR enhanced brain-computer interface (BCI) was proposed by applying auditory noise to visual stimuli. Fast Fourier transform and canonical correlation analysis methods were used to evaluate the influence of noise, results of which indicated that a moderate amount of auditory noise could enhance periodic components in visual responses. Directed transfer function was applied to investigate the functional connectivity patterns, and the flow gain value was used to measure the degree of activation of specific brain regions in the information transmission process. The results of flow gain maps showed that moderate intensity of auditory noise activated the brain area to a greater extent. Further analysis by weighted phase-lag index (wPLI) revealed that the phase synchronization between visual and auditory regions under auditory noise was significantly enhanced. Our study confirms the existence of cross-modal SR between visual and auditory regions and achieves a higher accuracy for recognition, along with shorter time window length. Such findings can be used to improve the performance of visual BCIs to a certain extent.

**Keywords:** brain-computer interface (BCI), steady-state motion visual evoked potential (SSMVEP), auditory noise, cross-modal stochastic resonance, functional connectivity, phase synchronization

## INTRODUCTION

Brain-computer interface (BCI) is a device which enables users to control a computer or a computer-connected device using brain activity and has shown prospects of broad application (Wolpaw et al., 2000). However, BCI performance has long been limited by the non-linear characteristic of human brain, as well as the weak detectability of electroencephalogram (EEG) signals. Many studies have been conducted and plenty of new paradigms and methods have been presented to solve this problem. Stochastic resonance (SR) theory (Benzi et al., 1981; Collins et al., 1996; Gammaitoni et al., 1998), is one of these methods. Stochastic resonance theory claims that random fluctuation can enhance weak signal input to improve signal transmission and sensitivity to

environmental changes in a non-linear system, leading to an improvement in system performance. Such SR effects have been also demonstrated in the neuronal systems, such as the human muscle spindle (Cordo et al., 1996), rat cutaneous mechanoreceptor (Collins et al., 1996), and human tactile sensation perception (Collins et al., 1997).

In the field of BCI, several studies investigating SR have been conducted. Srebro and Malladi (1999) applied two-dimensional spatial temporal noise to traditional visual stimuli which was used to elicit visual evoked potential (VEP). Results indicated that VEP could be enhanced by presenting visual noise. In fact, the power of the second harmonic of the VEP could increase as high as 4.2-fold under conditions of noise, peaking at 30% noise contrast. The power of the fourth VEP harmonic also increased 1.3-fold, peaking at 20% noise contrast. In our previous study, a BCI technology based on pure visual modality SR was proposed (Xie et al., 2012). In the study, subjects were exposed to visual stimuli and visual noise at the same time, which led to an enhancement of nervous system excitability. In 2019, we further evaluated the performance of visual noise imposed on two different BCI paradigms, i.e., motion-reversing simple ring and complex checkerboard (Xie et al., 2019). Additionally, Nakamura et al. (2017) applied auditory noise to auditory steady-state response (ASSR) based BCI and achieved a better performance compared to traditional paradigm, which confirms the existence of a SR effect in the human auditory system.

The studies mentioned above have mainly focused on single-modal SR, that is to say, stimulation and noise belong to the same sensory mode and enter the same sensory channel of the human brain. Besides single-modal SR, cross-modal SR in the human nervous system has also been reviewed (Krauss et al., 2018). Douglass et al. (1993) found that by applying periodic stimulation and environmental noise to the mechanical receptors of crayfish, the periodicity of spike intervals generated by neurons was enhanced. Ross et al. (2006) showed that an appropriate amount of auditory noise is conducive to understanding audiovisual speech and information detection. Kayser et al. (2005) tested changes in the blood oxygen level dependent (BOLD) response of the primate auditory cortex of monkeys to sound stimulation, tactile stimulation, as well as a combination of sound and tactile stimulation, respectively. This study further confirmed that the auditory cortex, including the primary auditory cortex, has integrates auditory and tactile information, and that such integration occurs in early sensory areas. In 2018, Krauss et al. (2018) reviewed these cross-modal enhancement phenomena and speculated that SR in one sensory modality driven by input from another modality may be a general principle, namely multisensory integration causing SR like cross-modal enhancement. However, such cross-modal SR phenomena have not been utilized in the field of BCI yet. Therefore, whether cross-modal SR phenomena can be used to promote BCI performance, like single-modal SR that used in BCI application, remains unclear.

In this study, we applied auditory noise to a steady-state motion visual evoked potential (SSMVEP) (Xie et al., 2012) based BCI paradigm with an oscillating checkerboard stimulation

to investigate whether the external auditory noise can lead to an enhancement of SSMVEP responses and improve BCI performance. Gaussian white noise with an intensity of  $-30$ ,  $-10$ ,  $10$ , and  $30$  dBW was selected as auditory noise. The effect of auditory noise on visual responses was verified by both the fast Fourier transform (FFT) spectrum and canonical correlation analysis (CCA) results. We found that BCI performance progressively improved and then decreased with the increment of noise intensities, i.e., a relationship between BCI performance and the moderate increase of noise level. Directed transfer function (DTF) method was applied to investigate the functional connectivity pattern of activated brain regions under different noise levels, which verified the theoretical research, as well as the practical application value, of the proposed BCI paradigm. Furthermore, weighted phase-lag index (wPLI) method was used to analyze the phase synchronization between visual and auditory regions which demonstrated a significant enhancement under moderate auditory noise level. Finally, the analysis on channel combinations and accuracy rate further confirmed the enhancement effect of auditory noise. Our study illustrates the existence of cross-modal SR in the human brain and the enhancement effect of auditory noise, which can be used to enhance visual BCI performance.

## MATERIALS AND METHODS

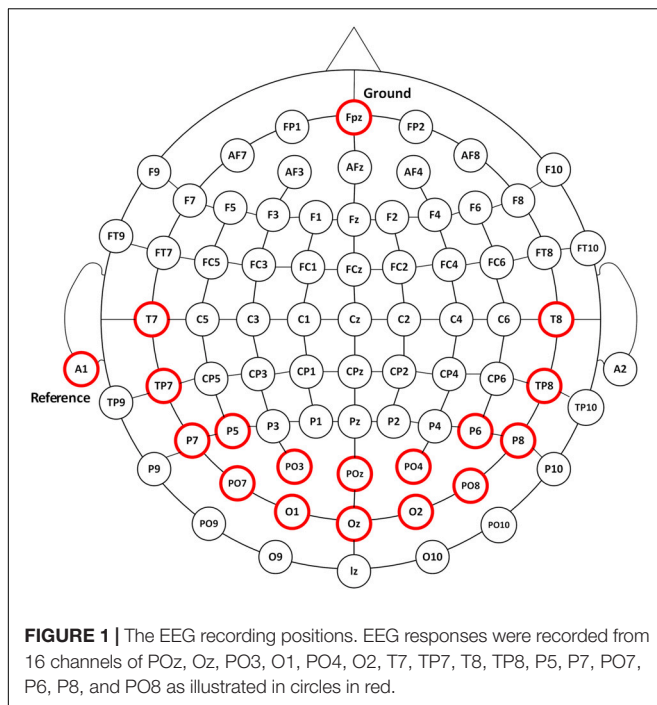
### Subjects

Ten subjects from Xi'an Jiaotong University participated in the experiment. Seven were males and three were females (aged  $25 \pm 3$  years old). All subjects had normal or corrected-to-normal hearing and eyesight and had prior experience with SSVEP-BCIs. All subjects had no history of visual or auditory disorders and were not paid for their participation. The experiment was undertaken in accordance with the recommendations of the Declaration of Helsinki. Written informed consent was obtained from each participant, which followed the guidelines approved by the institutional review board of Xi'an Jiaotong University.

### EEG Recordings

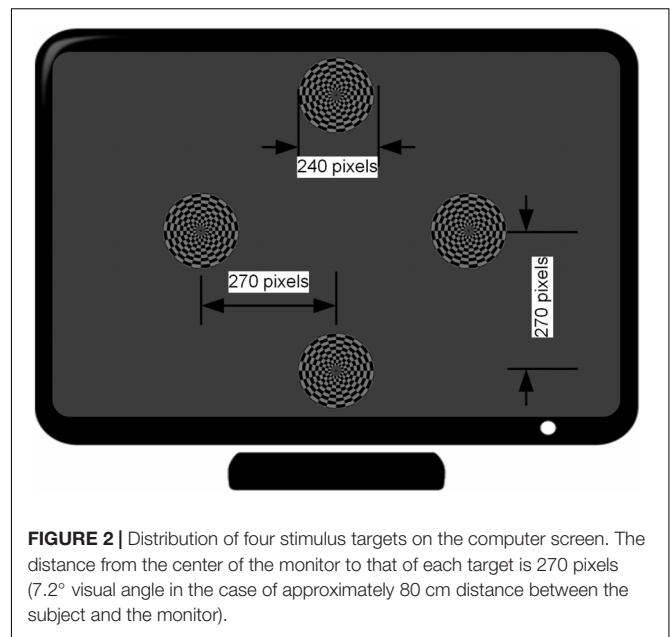
According to the International 10–20 electrodes position system, 16-channel EEG signals were recorded from the occipital, parietal, and temporal areas of POz, Oz, PO3, O1, PO4, O2, T7, TP7, T8, TP8, P5, P7, PO7, P6, P8, and PO8 sites at a sampling rate of 1200 Hz using the g.USBamp system (g.tec, Graz, Austria) (Figure 1). EEG signals were referenced to a unilateral earlobe and grounded over site Fpz. The impedance was kept below 5 K ohm. After application of the analog filter, the EEG signals were filtered between 0.1 and 100 Hz by an 8th-order Butterworth band-pass filter. A notch filter was implemented to remove the power line interference between 48 and 52 Hz with a 4th-order Butterworth band-stop filter. Further analysis was performed in Matlab environment.<sup>1</sup>

<sup>1</sup><http://www.mathworks.com>



## Stimulation Design

The motion-reversal visual stimulation, i.e., an oscillating checkerboard, programmed by Psychophysics Toolbox<sup>2</sup> (Brainard, 1997; Pelli, 1997), was introduced as a spatial selective steady-state BCI paradigm. A 27-inch ASUS liquid crystal display (LCD) monitor with a resolution of 1920 × 1080 pixels and a screen refresh rate of 144 Hz was used for the presentation of the visual stimulation. The static image of the oscillating checkerboard was made up of 10 concentric rings (Figure 2). The outer and inner diameters of the motion checkerboard were set to 120 pixels and 12 pixels, respectively. A black spot with radius of 3 pixels was set at the center to keep subjects focused on it during the experiment. Each ring was divided into 24 alternate gray and black blocks. The areas of the bright and dark regions in each ring were equal. The bright color was gray (120, 120, 120) and the dark grids was black (0, 0, 0). The width of each block was set to 10 pixels and subtended a horizontal and vertical visual angle of approximately 4.8° when viewed by the subjects from a fixed distance of approximately 80 cm, in accordance with prior studies which have shown that a stimulation size over 3.8° would saturate brain responses (Ng et al., 2012). The expansion - contraction of the checkerboard constitutes the motion process modulated by a sinusoid function. When the phase of the sinusoidal function shifts from 0 to  $\pi$ , the motion ring contracts with an amplitude of 10 pixels and then expands as the phase shifts from  $\pi$  to 0. Therefore, the direction of motion changes twice in one cycle. This motion direction changing rate is defined as motion-reversal frequency, which is two times the cycle frequency. Since SSMVEP mainly comes from brain activities which are

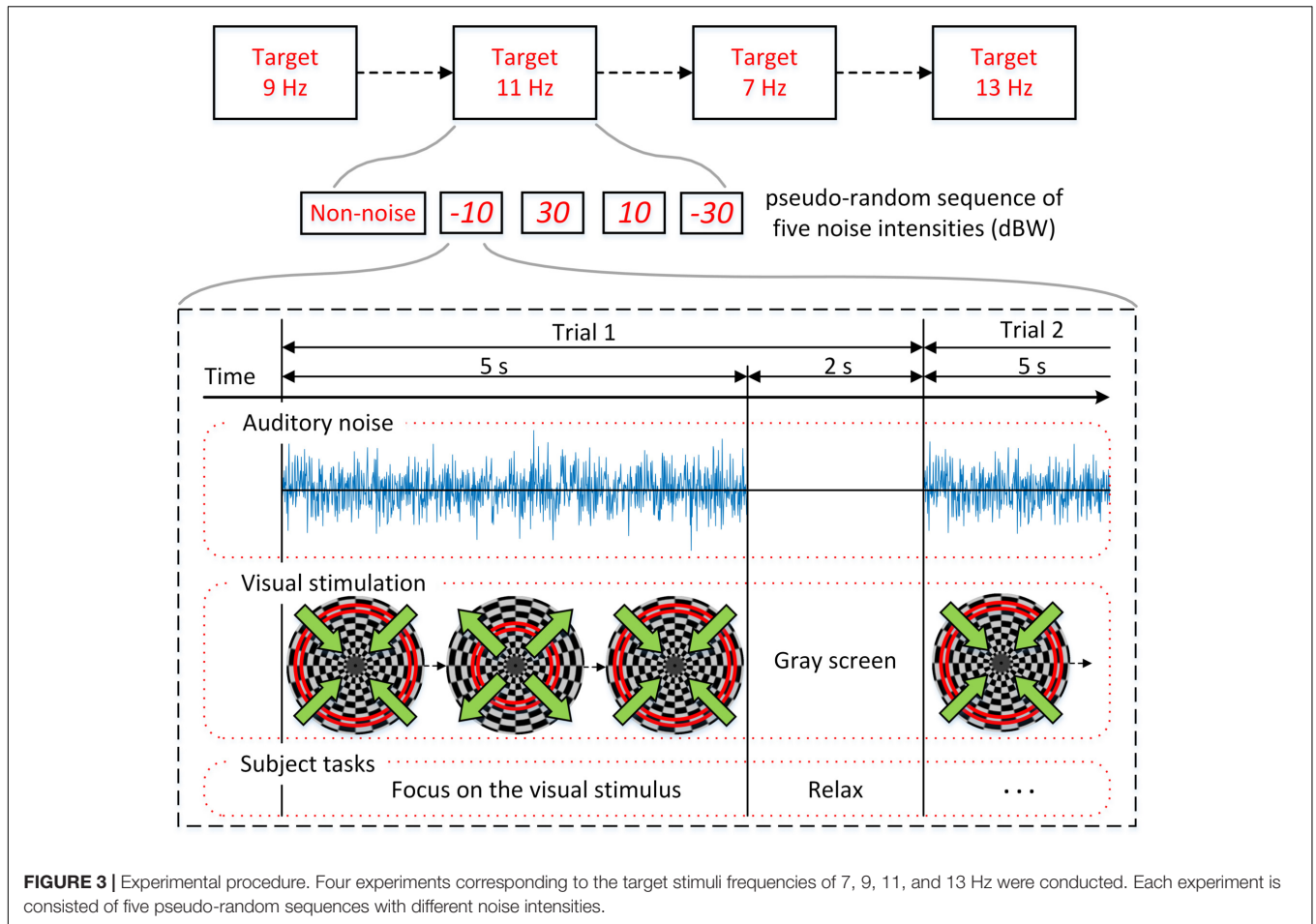


triggered by directional changes, we adopted this motion-reversal frequency as the fundamental frequency of visual stimulation.

Four stimuli were arranged in the corners of a rhombus layout. The distance from each stimulus target to that of the center of monitor is at a 7.2° visual angle (i.e., 270 pixels). Each stimulus target had distinct motion-reversal frequencies. According to a previous report, the low (4–13 Hz), medium (13–30 Hz) and high frequency range (>30 Hz) are the three main frequency ranges to elicit an SSVEP (Regan, 1989). In general, the low frequency range could elicit larger amplitude SSVEP responses than the medium and high frequency ranges. In this study, the frequencies of 7, 9, 11, and 13 Hz were assigned to the left, right, upper, and lower stimulus target, respectively. The four stimuli were simultaneously presented to subjects and the distance between each subject and LCD monitor was set to approximately 80 cm at eye level (Wu and Lakany, 2013). When the subject gazed at the stimulation, auditory noise (i.e., Gauss white noise) was played in both ears of the subject. Due to our previous test, the maximal auditory noise level our subjects can accept is around 30 dBW, and -30 dBW is barely audible. After determining the maximal and minimal level, auditory noise level was graded by equal division of the noise range into four levels by noise power of -30, -10, 10, and 30 dBW, using 1 watt as a baseline. In addition, an experiment was conducted without auditory noise, which constituted the control group. For power calculations, it is assumed that there is a load of 1 Ohm and measure for the output is in Volts. Noise was generated and played using Matlab and presented through a pair of kernel earphones (Sennheiser IE 80s, Germany).

The experimental procedure is shown in Figure 3 and the overall BCI system setup is depicted in Figure 4. For each subject, four experiments were conducted for oscillating checkerboard SSMVEP BCI, which corresponded to the target stimuli frequencies of 7, 9, 11, and 13 Hz, respectively. Each

<sup>2</sup><http://psychtoolbox.org/>



experiment contained five runs, which consisted of five pseudo-random sequences of all four auditory noise intensities as well as the non-noise condition. For different target frequencies and different noise levels, the sequences were performed randomly to avoid adaptation and habituation of long-term stimulation that could potentially affect assessment of SR effect (Bergholz et al., 2008). Each run consisted of 20 trials, with each trial lasting 5 s. Between two trials there was a 2-s inter-trial interval (ITI). Additionally, after every two runs, there was a break of 2 min. The whole experiment for each subject lasted approximately 50 min. During each trial, there were four stimuli that were simultaneously presented. The subjects were instructed to only pay attention to one stimulus designated by the operator at each single run; meanwhile auditory noise was presented in both ears. The stimulus target and noise intensity remain unchanged in each single run. During the experiment, the subjects were asked to sit on an armchair in a dim and quiet room. They were not allowed to move their bodies during the experiment and were asked to fixate on the center of screen during the ITI periods.

### DTF and Flow Gain

Directed transfer function, a method that is based on multivariable autoregressive model (MVAR), was used to estimate the brain functional connectivity driven by SSMVEP

responses under different noise levels. The EEG data  $X$  can be described in the following form:

$$X = [x_1(t), x_2(t), \dots, x_n(t)]^T \tag{1}$$

where  $t$  refers to time and  $n$  refers to the number of channels. Through the use of MVAR, EEG data set  $X$  can be expressed as the following autoregressive process (Bartels and Zeki, 2004):

$$\sum_{k=0}^p A(k) X(t-k) = U(t) \quad A(0) = 1 \tag{2}$$

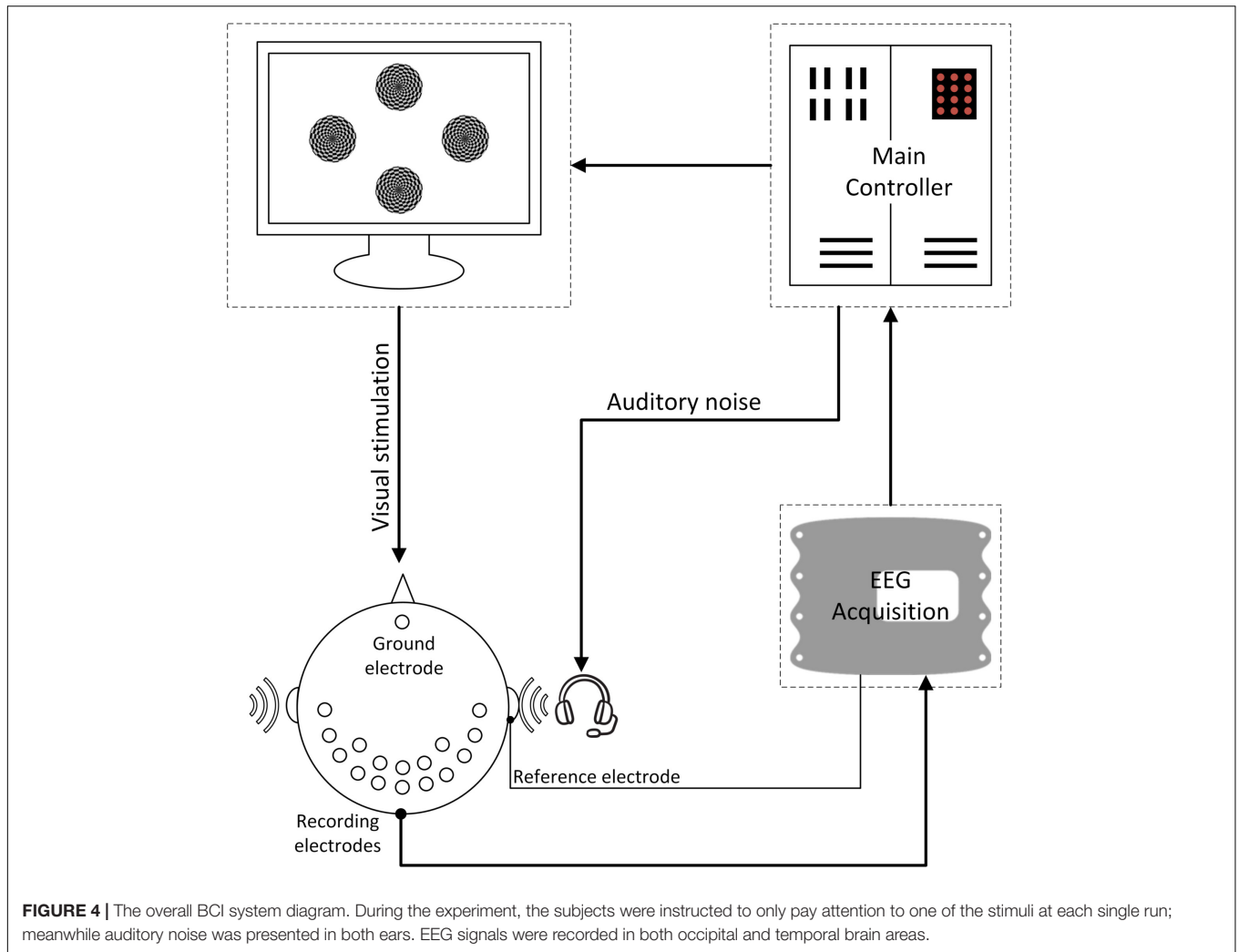
where  $p$  is the model order chosen with the Akaike information criteria (AIC; Kamiński et al., 2001), i.e., a widely used criteria for AR model order determination.  $A(k)$  represents the  $N$  by  $N$  matrix of model coefficients, and  $U(t)$  is a white noise process with zero mean and non-singular covariance matrix.

In order to investigate the spectral features of the examined process, Eq 2 is transformed to the frequency domain:

$$A(f) X(f) = U(f) \tag{3}$$

where

$$A(f) = \sum_{k=0}^p A(k) e^{-j2\pi f \Delta t k} \tag{4}$$



Hence, Eq 3 can be rewritten as

$$X(f) = A(f)^{-1} U(f) = H(f) U(f) \tag{5}$$

$H(f)$  is the transfer matrix of the system, in which the element  $H_{ij}$  represents a connection between the  $j$ th input and the  $i$ th output of the system (Bassett and Bullmore, 2006). Using these definitions, the causal influence of the cortical waveform estimated in the  $j$ th channel on that estimated in the  $i$ th channel, i.e., the DTF  $H_{ij}$ , can be defined as (Kaminski and Blinowska, 1991):

$$\theta_{ij}^2(f) = |H_{ij}(f)|^2 \tag{6}$$

The normalization of DTF matrix constructed above is as follows (He et al., 2011):

$$\gamma_{ij}^2(f) = \frac{|H_{ij}(f)|^2}{\sum_{m=1}^N |H_{im}(f)|^2} \tag{7}$$

$\gamma_{ij}(f)$  represents the ratio of influence of the cortical waveform estimated in the  $j$ th channel on the cortical waveform

estimated on the  $i$ th channel, with respect to the influence of all estimated cortical waveforms. Normalized DTF values are in the interval [0,1] when the normalization condition of

$$\sum_{n=1}^N \gamma_{in}^2(f) = 1 \tag{8}$$

is applied.

The inflow and outflow of the information transmission process in the brain can be defined as  $\sum_{j=1}^N \gamma_{mj}^2$  and  $\sum_{i=1}^N \gamma_{im}^2$ , respectively. The inflow indicates the magnitude of all the incoming links from the other channels. This information depicts each channel as the target of functional connections from the other channels. On the contrary, the outflow, depicting each channel as the source, indicates the magnitude of the considered channel linking out toward the others (Yan and Gao, 2011).

Hence, flow gain value was defined as the ratio of outflow to inflow. For channel  $m$ :

$$\rho_m = \frac{\sum_{i=1}^N \gamma_{im}^2}{\sum_{j=1}^N \gamma_{mj}^2} \tag{9}$$

The value of  $\rho_m$  represents the contribution that channel  $m$  plays during information transmission process, and a higher value represents more contribution of information output during the transmission process.

### CCA Method

Canonical correlation analysis is one of the most commonly used algorithms to measure the maximum correlation between two sets of multidimensional variables in multi-channel SSVEP-based BCIs (Lin et al., 2006; Xie et al., 2012). In this case, we used CCA algorithm to compare actual EEG signals with reference signals to identify their correlation coefficients. The reference signals are defined as a set of cosine and sine signals with the fundamental frequency and harmonics as follows:

$$Y_i = \begin{pmatrix} \cos(2\pi \cdot f_i \cdot t) \\ \sin(2\pi \cdot f_i \cdot t) \\ \cdot \\ \cdot \\ \cos(2\pi \cdot Hf_i \cdot t) \\ \sin(2\pi \cdot Hf_i \cdot t) \end{pmatrix}, t = \frac{1}{F_s}, \dots, \frac{S}{F_s} \quad (10)$$

where  $F_s$  refers to the sampling rate,  $H$  is the number of harmonics,  $f_i$  is the stimulus frequency,  $t$  is the discrete time series of predefined time-window length, and  $S$  is sampling numbers. The set of EEG signals are defined as follows:

$$X = \begin{pmatrix} x_1(t) \\ \cdot \\ \cdot \\ \cdot \\ x_n(t) \end{pmatrix}, t = \frac{1}{F_s}, \dots, \frac{S}{F_s} \quad (11)$$

where  $x$  refers to EEG signals recorded from each single channel and  $n$  refers to the channel number.

Given the multivariable matrices of  $X$  and  $Y_i$ , CCA first projects them into one dimension by the two weight vectors  $W_x$  and  $W_{y_i}$ , and then calculates their correlation coefficients in one-dimensional space. CCA seeks the weight vectors  $W_x$  and  $W_{y_i}$  to maximize their linear correlation  $\rho_{x,y_i}$ :

$$\begin{aligned} x &= X^T W_x \\ y_i &= Y_i^T W_{y_i} \\ \rho_{x,y_i} &= \frac{\text{cov}(x,y_i)}{\sqrt{D(x)}\sqrt{D(y_i)}} \end{aligned} \quad (12)$$

where  $\rho_{x,y_i}$  indicates the canonical correlation between  $X$  and  $Y_i$ , and the stimulus frequency  $f_i$  ( $i = 1, \dots, K$ ) can be recognized based on maximum of  $\rho_{f_i}$ .

With the corresponding correlation coefficient  $\rho_{f_i}$ , CCA can be performed on each stimulus frequency  $f_i$  ( $i = 1, \dots, K$ ) separately. Then the target  $f_{target}$  can be recognized as:

$$f_{target} = \max_{i=1, \dots, K} \rho_{f_i} \quad (13)$$

Here, the stimulus frequency  $f_i$  ( $i = 1, \dots, 4$ ) is set to the frequency of each oscillating checkerboard, the number of  $C$  channels was set to 16, and the harmonics of  $H$  was set to 1.

### wPLI Method

The wPLI method (Vinck et al., 2011) analyzes phase synchronization between two time series  $x(t)$  and  $y(t)$ . Weighted phase-lag index uses only the imaginary component of the cross-spectrum and is immune to both volume conductor effect and measurement noise. At the same time, wPLI exhibits increased sensitivity to phase interactions between signals (Vindiola et al., 2014). The instantaneous phase lag and magnitude is acquired through cross power density spectrums:

$$C(f) = \int_{-\infty}^{+\infty} X(f) \cdot Y(t-f) \cdot dt \quad (14)$$

where  $X(f)$  and  $Y(f)$  are finite Fourier transform of signal  $x(t)$  and  $y(t)$ .

Then wPLI index is calculated as follow:

$$wPLI = \frac{|E\{\{C\}\}|}{E\{|\{C\}|\}} \quad (15)$$

where  $\{C\}$  is the imaginary component of the cross-spectrum  $C(f)$ .

The value of wPLI index is limited between 0 and 1, with a higher value representing stronger phase synchronization.

### Statistical Analyses

The values of each individual subject across the non-noise and auditory noise integrated BCI conditions were analyzed using the one-way analysis of variance (ANOVA) statistic. The level of statistical significance was set to  $p < 0.05$ . Bonferroni correction was employed for multiple comparisons. The results were expressed as mean  $\pm$  standard deviation (SD).

## RESULTS

### The Influence of Auditory Noise on Visual Responses

In order to examine the influence of auditory noise on visual responses, EEG responses acquired from the temporal-parietal but not the occipital area were used to analyze the response amplitude changes under different auditory noise levels. Fast Fourier transform was performed on the EEG data obtained from T7, P7, TP7, T8, P8, and TP8 channels in this study. Inter-subject normalization was attained by dividing amplitude estimates by the average computed from all amplitude values of both non-noise and auditory noise integrated conditions, but separately for each subject (Xie et al., 2017). There is a resonance between normalized FFT values and the intensities of auditory noise, i.e., moderate auditory noise enhanced the FFT value while too much noise weakened it (Figure 5). For target frequency of 7 Hz, normalized SSMVEP spectral amplitudes significantly increased by 25.97% at auditory noise level of  $-10$  dBW, when compared

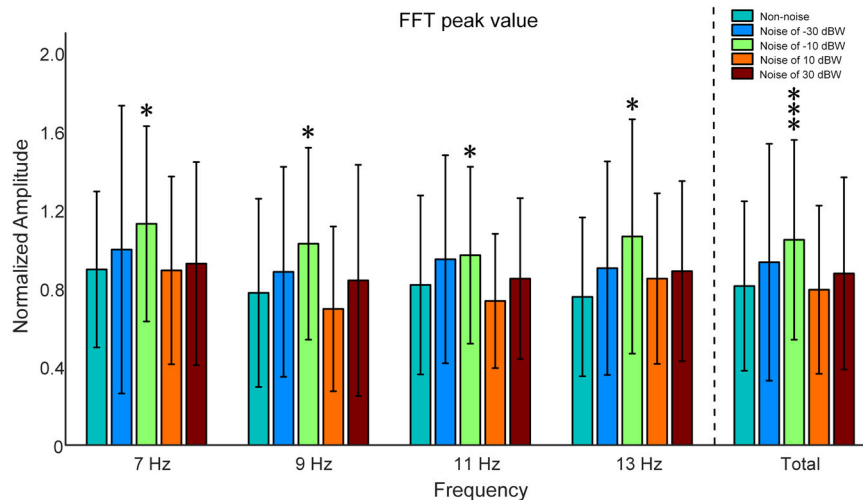


**FIGURE 5** | Comparison of normalized SSMVEP spectral amplitudes with a change of noise levels across subjects. All statistics were assessed using one-way ANOVA, \* $p < 0.05$  represent significance among non-noise and auditory noise integrated BCI tasks, \*\*\* $p < 0.001$  among non-noise and auditory noise integrated BCI tasks.

to the non-noise condition and other noise intensities ( $-10$  dBW:  $1.1277 \pm 0.4977$ , non-noise condition:  $0.8952 \pm 0.3974$ , one-way ANOVA:  $F = 2.4005$ ,  $p = 0.0498$ ). For target frequency of 9 Hz, normalized SSMVEP spectral amplitudes significantly increased by 32.30% at noise level of  $-10$  dBW in comparison to the non-noise condition and other noise intensities ( $-10$  dBW:  $1.0265 \pm 0.4890$ , non-noise condition:  $0.7759 \pm 0.4796$ ,  $F = 2.4210$ ,  $p = 0.0498$ ). For target frequency of 11 Hz, normalized SSMVEP spectral amplitudes significantly increased by 18.58% at noise level of  $-10$  dBW in comparison to the non-noise condition and other noise intensities ( $-10$  dBW:  $0.9676 \pm 0.4507$ , non-noise condition:  $0.8160 \pm 0.4561$ ,  $F = 2.8344$ ,  $p = 0.0248$ ). For target frequency of 13 Hz, normalized SSMVEP spectral amplitudes also significantly increased by 40.75% at noise level of  $-10$  dBW compared with non-noise condition and other noise intensities ( $-10$  dBW:  $1.0632 \pm 0.5971$ , non-noise condition:  $0.7554 \pm 0.4046$ ,  $F = 2.5683$ ,  $p = 0.0387$ ). The average value for all four frequencies at noise level of  $-10$  dBW is  $1.0510$  (SD =  $0.5090$ ), which is 28.16% higher than that of non-noise condition and other noise intensities ( $F = 9.0782$ ,  $p < 0.001$ ).

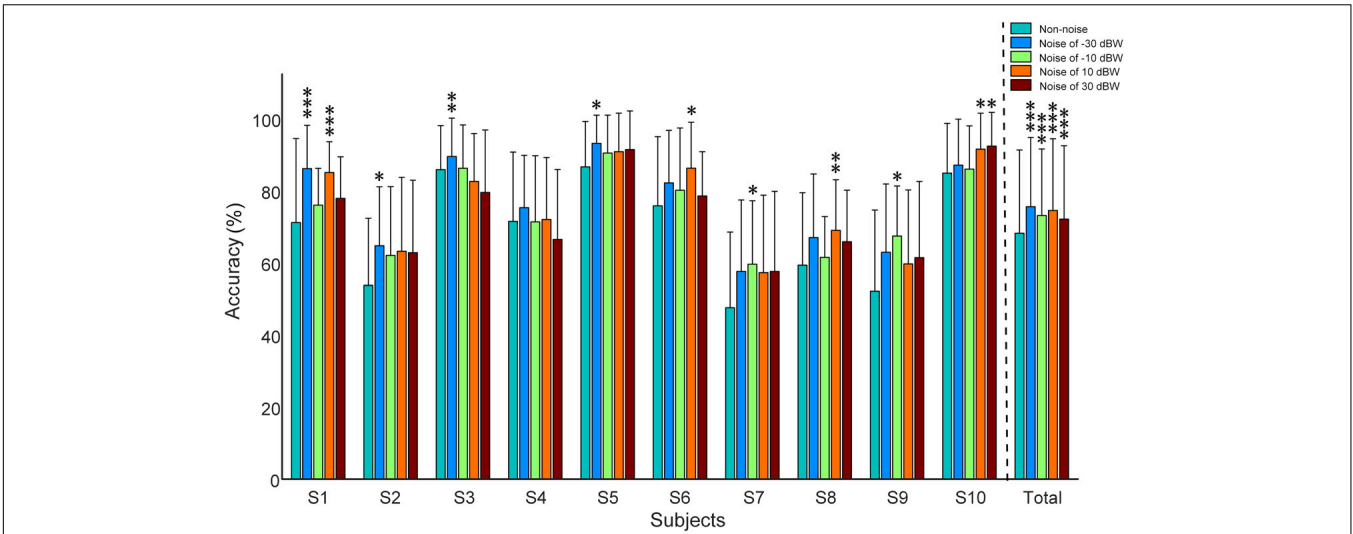
## Auditory Noise Promoted Visual BCI Recognition Accuracy

Figure 6 shows the recognition accuracy of all subjects under visual stimulus frequencies of 7, 9, 11, and 13 Hz. Recognition accuracy, obtained using the CCA recognition algorithm, is defined as the number of correct selections divided by total number of trials. All 16 channels that involve visual and auditory brain areas were selected for analysis. Considering the fact that long time window would possibly lead to high accuracy values even in multi-choice SSVEP BCI (i.e., the ceiling effect), which would make it difficult to inspect the impact of auditory noise on visual BCI performance, the 5-s single-trial data was truncated into 0.25 s and was consequently analyzed. Consistent with

the phenomena observed in the normalized SSMVEP spectra of visual responses, a resonance is reached between the BCI accuracy and the noise intensity (Figure 6). Additionally, for Subject S1, S2, S3, S5, S6, S7, S8, S9, and S10, moderate auditory noise at the resonance points significantly improved BCI accuracies ( $F = 6.3667$ ,  $p < 0.001$  for Subject S1;  $F = 2.6921$ ,  $p = 0.0316$  for Subject S2;  $F = 4.2652$ ,  $p = 0.0023$  for Subject S3;  $F = 2.6689$ ,  $p = 0.0328$  for Subject S5;  $F = 2.8481$ ,  $p = 0.0249$  for Subject S6;  $F = 3.2148$ ,  $p = 0.0132$  for Subject S7;  $F = 3.8410$ ,  $p = 0.0046$  for Subject S8;  $F = 3.2224$ ,  $p = 0.0137$  for Subject S9;  $F = 2.9871$ ,  $p = 0.0204$  for Subject S10). However, it was not significant for Subject S4 ( $F = 2.3666$ ,  $p = 0.0524$ ). For grand accuracies across subjects, the accuracy rates of all auditory noise levels (i.e.,  $-30$ ,  $-10$ , 10 dBW as well as 10 dBW) were significantly higher than that of non-noise condition ( $F = 9.8923$ ,  $p < 0.001$ ). Such results indicate that there exist optimal noise intensities that can improve the BCI performance using cross-modal SR effect.

## Auditory Noise Optimized the Trade-off Between Time-Window Length and Performance in Accuracy

In order to further investigate the effect of auditory noise on the trade-off between time-window length, performance in accuracy, and stability of auditory noise integrated BCI paradigm, EEG data was truncated to different time-window lengths within the 5-s single-trial duration. As the time window increased gradually in steps of 0.25 s from 0.75 to 2.5 s, the changes in mean accuracy rates and corresponding standard deviations obtained across all target frequencies and all subjects, using the CCA method, are shown in Figure 7. Brain-computer interface accuracies showed sustainable improvement with increasing time-window lengths for both non-noise and auditory noise integrated BCI tasks. Overall, the accuracies of auditory noise



**FIGURE 6 |** Recognition accuracy rates under different auditory noise levels when subjects gazed at a target stimulus of 7 Hz. All statistics were assessed by one-way ANOVA, \* $p < 0.05$  represent significance among non-noise and auditory noise integrated BCI tasks, \*\* $p < 0.01$  among non-noise and auditory noise integrated BCI tasks, \*\*\* $p < 0.001$  among non-noise and auditory noise integrated BCI tasks.

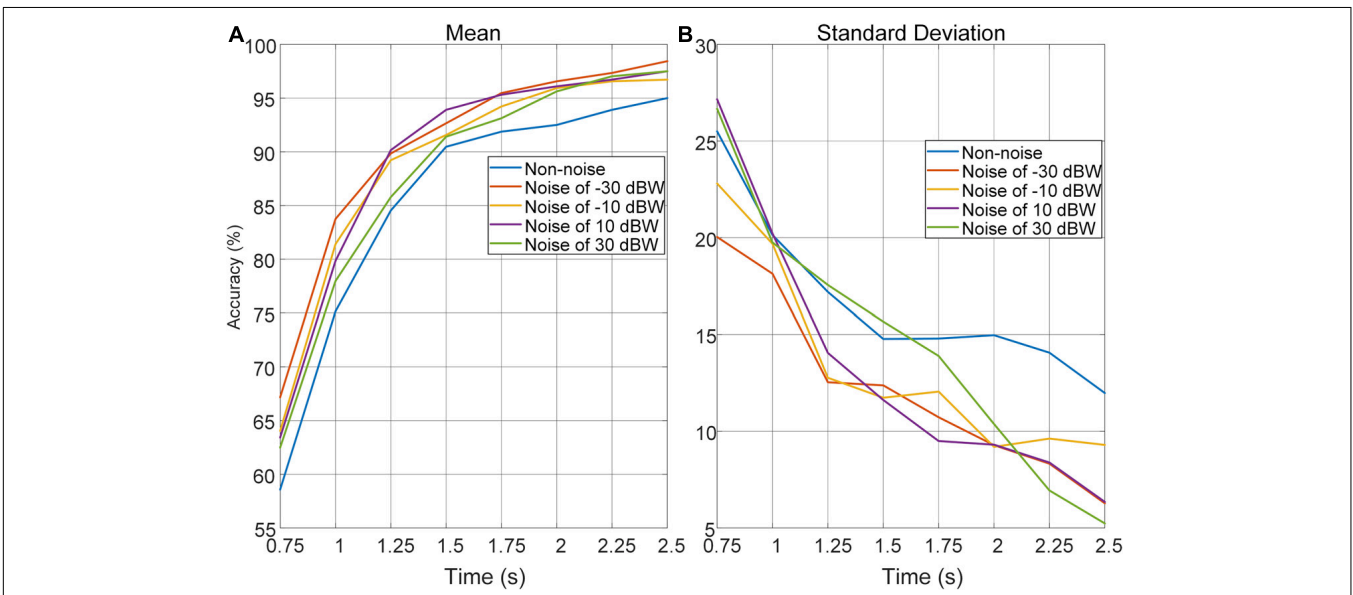


**FIGURE 7 |** Average recognition accuracies and corresponding standard deviations obtained across all target frequencies, noise levels and subjects by CCA method with different time-window lengths. **(A)** Average recognition accuracies with different time-window lengths. **(B)** Standard deviations of accuracies with different time-window lengths.

integrated tasks under noise levels of  $-30$ ,  $10$ , and  $30$  dBW were higher than that of non-noise task as time-window length increases from  $1.25$  to  $5$  s ( $F = 6.5139$ ,  $p < 0.001$ ). For auditory noise level of  $10$  dBW, the average accuracy exceeded  $90\%$  for a time window of  $1.25$  s, and  $95\%$  for a time window of  $1.5$  s, indicating that the auditory noise integrated paradigm can achieve a high performance in a short time window (**Figure 7A**). Comparisons of standard deviations between non-noise and auditory noise integrated paradigms are depicted in **Figure 7B**. Compared to the non-noise condition, the standard deviations

of accuracies of auditory noise integrated tasks under noise levels of  $-30$ ,  $10$ , and  $30$  dBW drop sharply as time-window length increases from  $1.25$  to  $5$  s ( $F = 5.6619$ ,  $p < 0.001$ ). In particular, for a time-window length of  $1.5$ – $2.5$  s, the standard deviations of accuracies of noise level  $10$  dBW were almost one-half to one-third of the standard deviations under non-noise condition. The comparatively lower standard deviations related to the auditory noise integrated tasks suggest that auditory noise integrated BCI can achieve a more stable performance in accuracy compared to the ordinary non-noise paradigm. Taken

together, the optimal auditory noise level of 10 dBW concurrently achieved both higher accuracy and lower standard deviations. This indicates that when compared with non-noise condition, it took less time to achieve a higher recognition accuracy and more stable BCI performance when adding moderate auditory noise to subjects in visual BCI application. Thus, the trade-off between time-window length and performance in accuracy, a common problem in BCI, can be optimized through the cross-modal SR effect.

### Illustration of the Functional Connectivity Under Different Auditory Noise Levels via Flow Gain Maps

Although the method of analysis in frequency domain such as FFT can analyze the influence of auditory noise on visual BCI responses, the functional connection between different regions caused by auditory noise in the brain, such as connectivity between occipital lobe and temporal lobe, remains unclear. For different auditory noise intensities, the eConnectome toolbox (He et al., 2011), based on the DTF, was applied to analyze the direct interconnections of different brain regions. Flow gain value was defined as the ratio of outflow to inflow of information in a certain channel in order to measure the contribution a channel plays in the information transmission process. As a ratio of outflow to inflow, flow gain value integrates input and output information simultaneously, so that the results shown by flow gain are more direct and clearer. A higher flow gain value indicates that the region makes more contributions to other regions. The topographic distributions of the flow gain values form the corresponding flow gain map. **Figure 8** shows the averaged flow gain maps of SSMVEP responses under different auditory noise intensities. The results were an average of all ten subjects and all four stimulus frequencies. As expected, it can be seen on the flow gain maps that under the non-noise condition, the EEG responses were mainly involved in the occipital region. Then with increments of auditory noise levels, the EEG responses started to gradually expand outward from the occipital region to bilateral temporal cortices, which represented a wider region of activation in the brain. Additionally, when the auditory noise level reached to 30 dBW, the connectivity between occipital lobe and temporal lobe lessened. In this study, the flow gain values between temporal region (T7 and T8 sites) and occipital region (O1 and O2 sites) were compared. For non-noise condition, statistical results showed that the flow gain values of temporal region are comparable with that of occipital region with no statistical significance ( $F = 0.0273$ ,  $p = 0.8694$ ). With the increase of the noise intensity, the flow gain values of temporal region are significantly higher than that of occipital region under noise level of  $-30$  and  $-10$  dBW ( $F = 4.3677$ ,  $p = 0.0407$  for  $-30$  dBW;  $F = 4.1331$ ,  $p = 0.0463$  for  $-10$  dBW). When further increasing the noise level, no statistical significant flow gain difference can be found between temporal and occipital regions ( $F = 2.7200$ ,  $p = 0.1042$  for 10 dBW;  $F = 2.1168$ ,  $p = 0.1507$  for 30 dBW). From the flow gain maps and corresponding statistical analysis, we can conclude that moderate noise can activate wider area of brain, while too much inhibits it. This result qualitatively evaluated the

functional connectivity between visual and auditory areas of the brain under different auditory noise levels.

### The Phase Synchronization Between Temporal Region and Occipital Region

For further quantitative evaluation of neural interactions between the temporal and occipital region under different noise levels, we implemented a more sophisticated analysis using wPLI to quantify the phase synchronization between these two regions. The wPLI between T7-O1 sites, as well as T8-O2 sites, of all ten subjects are calculated. The values of wPLI across all ten subjects for stimulus frequencies of 7, 9, 11, 13 Hz exhibited an enhancement by moderately increasing the noise intensity (**Figure 9**). Statistical analysis indicated that, for the total results of the four frequencies, wPLIs under  $-10$  and 10 dBW are significantly higher than that under the non-noise condition ( $F = 4.3340$ ,  $p = 0.0017$ ) (**Figure 9E**). Additionally, wPLI values increased from  $0.1172 \pm 0.0997$  (range: 0.0175–0.2169) under non-noise condition to a maximum of  $0.1258 \pm 0.1130$  (range: 0.0128–0.2388) under noise level of  $-10$  dBW condition. Specifically, at stimulus frequency of 7 Hz, wPLIs significantly increased by 12.0% from  $0.1099 \pm 0.0901$  (range: 0.0198–0.2000) under non-noise condition to a maximum of  $0.1231 \pm 0.1187$  (range: 0.0044–0.2418) under noise level of  $-10$  dBW ( $F = 3.2071$ ,  $p = 0.0122$ ) (**Figure 9A**). At stimulus frequency of 9 Hz, wPLIs significantly increased by 11.9% from  $0.1096 \pm 0.0947$  (range: 0.0149–0.2043) under non-noise condition to a maximum of  $0.1226 \pm 0.0984$  (range: 0.0242–0.2210) under noise level of 10 dBW ( $F = 5.9517$ ,  $p < 0.001$ ) (**Figure 9B**). At 11 Hz, wPLIs significantly increased by 14.2% from  $0.1147 \pm 0.0873$  (range: 0.0274–0.2020) under non-noise condition to a maximum of  $0.1310 \pm 0.1205$  (range: 0.0105–0.2515) under noise level of  $-30$  dBW ( $F = 3.4980$ ,  $p = 0.0074$ ) (**Figure 9C**). Lastly, at 13 Hz, wPLIs significantly increased by 29.3% from  $0.1168 \pm 0.0905$  (range: 0.0263–0.2073) under non-noise condition to a maximum of  $0.1510 \pm 0.1313$  (range: 0.0197–0.2823) under noise level of  $-10$  dBW ( $F = 14.85$ ,  $p < 0.001$ ) (**Figure 9D**). All these results indicate that the neural interaction between visual and auditory brain areas were quantitatively enhanced by the cross-modal SR effect with the combination of visual stimulation and auditory noise.

### Optimal Noise Activates More Channels

In order to study the resonance effect of auditory noise on activation of different EEG sites, we calculated BCI accuracy in different EEG recording channel combinations (**Figure 10**). EEG channels were divided into four different combinations. The first was the single Oz-channel condition, the second was the O1-Oz-O2 three-channel combination, the third encompassed the channels from occipital-temporal region (Oz, O1, O2, PO3, PO4, POz, T7, P7, TP7, T8, P8, TP8) condition and fourth was the all 16-channel combination. For the non-noise task, the accuracy rate decreased as more channels became involved but without any statistical significance. However, for an auditory noise integrated task, the results were surprisingly different. Under the noise level of  $-30$  dBW, the accuracy

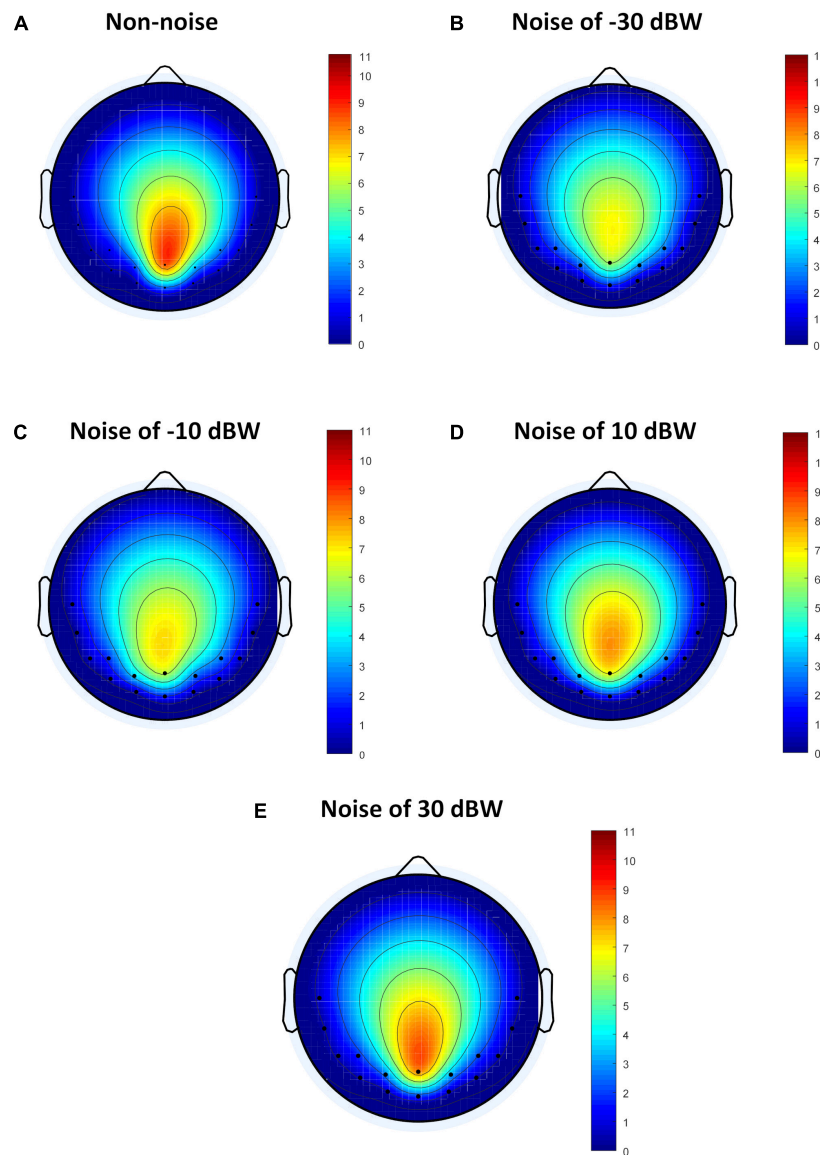


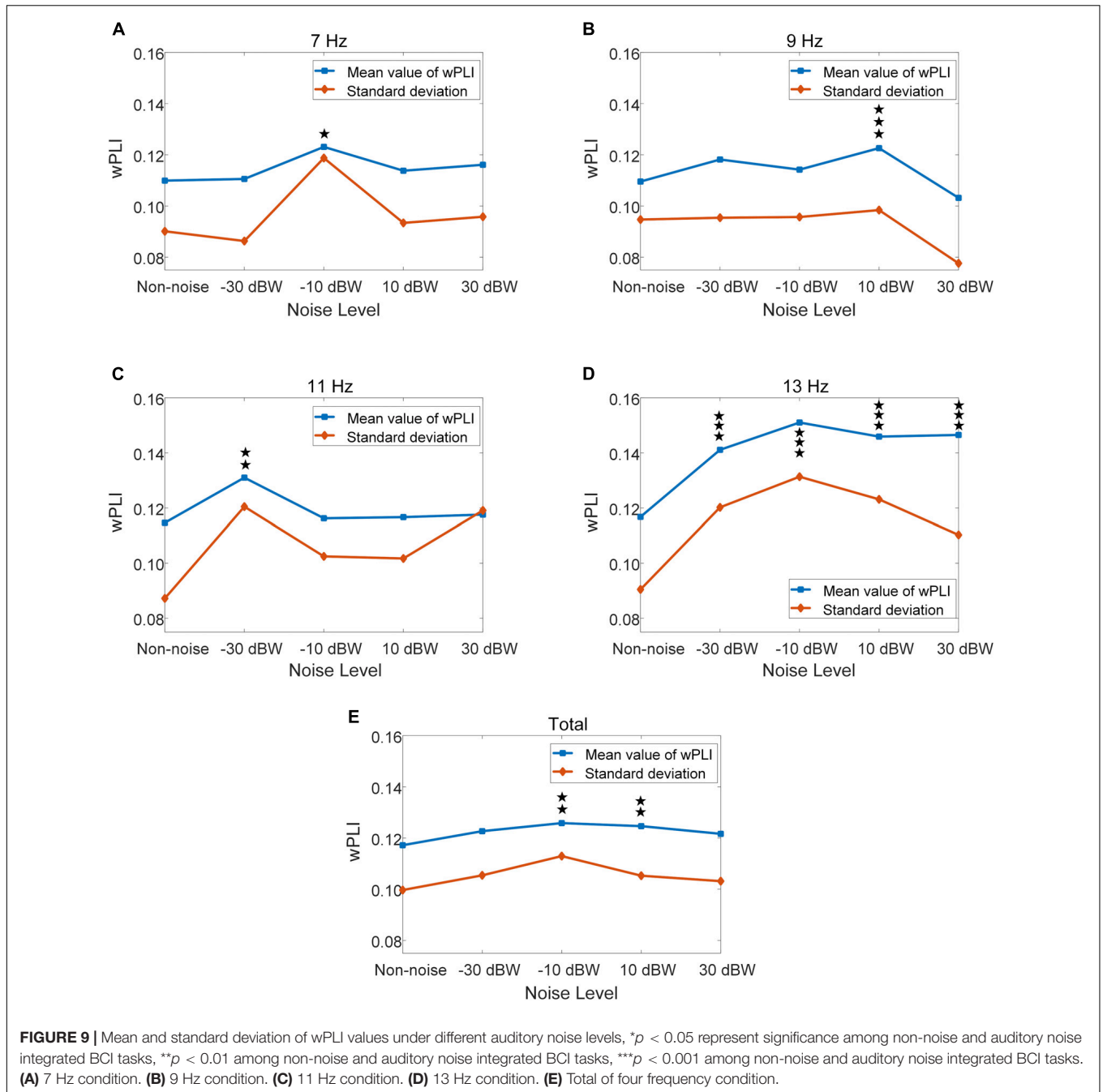
**FIGURE 8 |** The average flow gain maps under different auditory noise levels. **(A)** Non-noise condition. **(B)** Noise level of  $-30$  dBW condition. **(C)** Noise level of  $-10$  dBW condition. **(D)** Noise level of  $10$  dBW condition. **(E)** Noise level of  $30$  dBW condition.

rate at a channel combination condition of occipital-temporal region was higher compared to the single Oz condition ( $F = 3.1018$ ,  $p = 0.0301$ ). Additionally, for noise level of  $-10$  and  $10$  dBW conditions, the accuracy rates at channel combination of occipital-temporal region, as well as all 16-channel combination, were significantly higher compared to that of single Oz condition ( $F = 3.7910$ ,  $p = 0.0127$  and  $F = 4.6986$ ,  $p = 0.0040$ , respectively). However, for the  $30$  dBW noise level condition, while the trend was similar to noise level of  $-30$  dBW condition, no statistical significance was found ( $F = 1.9126$ ,  $p = 0.1324$ ). These results indicate a small amount of noise can enhance occipital EEG responses, demonstrated by the increased accuracy in the channel combination of occipital-temporal region on noise level of  $-30$  dBW. With further

increments of auditory noise intensity such as  $-10$  and  $10$  dBW, such effect spread to a wider region, including the temporal region, which is demonstrated by the increased accuracy in occipital-temporal channel combination on noise level of  $10$  dBW. Furthermore, when the noise level was too high, e.g., at  $30$  dBW, such enhancement effect would attenuate and the accuracy rate decreased.

## DISCUSSION

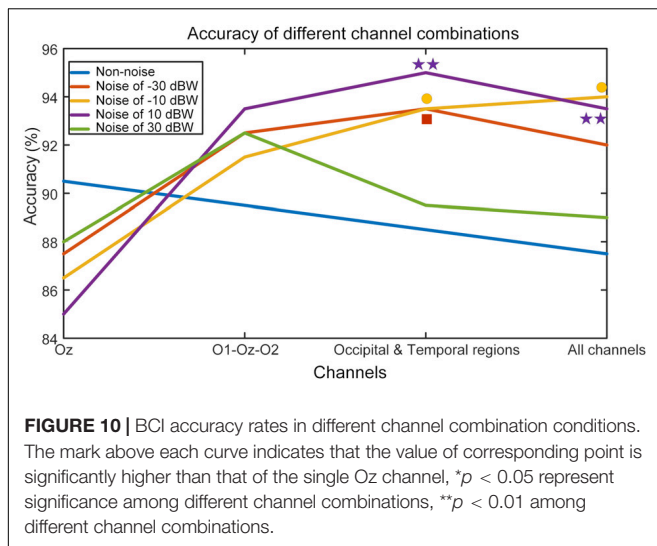
While noise can often be a harmful component, for dynamic and non-linear system such as human brain, noise can help improve system performance, as explained by the SR theory. Several



studies that have explored both single-modality SR and cross-modality SR phenomena, have proven this theory (Srebro and Malladi, 1999; Xie et al., 2012; Nakamura et al., 2017; Krauss et al., 2018). In this study, we applied Gaussian white auditory noise with intensities of  $-30$ ,  $-10$ ,  $10$ , and  $30$  dBW during SSMVEP-BCI experiment to explore the cross-modal SR effect between human visual and auditory modality.

In this study, FFT analysis revealed that, when compared to non-noise conditions, additional auditory noise did raise peak FFT value at a target frequency, proving that SSMVEP response could be enhanced using auditory noise. The BCI

accuracy rate obtained using the CCA method further revealed this phenomenon. As noise intensity moderately increases, the correct rate of BCI recognition performance first increased and then decreased. This finding is consistent with previous studies in single-modality BCIs, which demonstrate that moderate noise can enhance BCI performance (Srebro and Malladi, 1999; Xie et al., 2014; Nakamura et al., 2017). In this study, we showed that the proposed cross-modal BCI leads to a similar conclusion. However, it should be noted that the participant variability has a distinct impact on the experimental results. The optimal noise level varies with different subjects and stimulus frequencies. For



some subjects, certain noise can cause a sudden drop on peak FFT value, such as Subject S2 at noise level of  $-30$  dBW, and Subject S4 and S5 at noise level of  $10$  dBW. This may be due to high variability of sensory thresholds and internal noise sources of humans, leading to different sensitivities of neurons in the visual cortex (Srebro and Malladi, 1999). To reduce the impact of participant variability, there will be a larger participant sample in our future work.

From the perspective of time window, we found that it took less time to achieve a higher recognition accuracy when we added moderate auditory noise. In other words, under additional auditory noise, our brain tends to be more sensitive to steady-state visual stimuli, and the response time of the BCI system is shortened. This is especially true in the time-window length of  $0.75$ – $1.25$  s, in which optimal auditory noise benefits much higher accuracy rate compared to non-noise condition. Interestingly, such phenomenon is in accordance with Harper's finding (Harper, 1979) in 1979, which is much earlier than the first time the SR theory was defined (Benzi et al., 1981). Here, the accuracy rate was obtained through CCA method, which is one of the most commonly used algorithms in SSVEP-BCI recognition. Furthermore, we believe that, with more powerful algorithms, better performance can be achieved in future work. Since accuracy rate of the proposed BCI paradigm has to be improved to a larger extent, and the response speed can also be accelerated via the usage of the proposed cross-modal modality, this proposed BCI paradigm can help potentially build high speed SSVEP-BCI systems.

In this analysis, we also drew flow gain maps to further investigate the role that auditory noise plays in the interaction between different brain regions. Under noise levels of  $-30$ ,  $-10$ , and  $10$  dBW, EEG responses may spread to more brain regions compared to the non-noise condition. However, for the noise level of  $30$  dBW, this effect may attenuate. Considering the results of the FFT response and accuracy rate obtained by CCA method, such results can be anticipated.

For single-modal SR, such as in the pure visual or auditory sensory pathway, SR effect can be explained as additive noise that turns neurons from subthreshold to superthreshold (Xie et al., 2014; Tanaka et al., 2015). However, in the current study, the underlying mechanism is more complicated since auditory noise and visual stimulation belong to two different sensory pathways.

The wPLI results are helpful when it comes to understanding the underlying mechanism. As the noise intensity increases, the wPLI values first increase and then decrease, just as observed in FFT value and BCI accuracy. Although the absolute value is not high, statistical analysis indicates that this conclusion is robust. On one hand, low absolute value indicates that the normal neural interaction between auditory and visual regions is relatively weak. On the other hand, the relationship between wPLI values and auditory noise levels implies that the auditory noise enhances synchronization between temporal and occipital regions, and such enhancement is consistent with enhancement of brain responses and BCI performance, as characterized by the SR effect. At stimulus frequencies of  $11$  and  $13$  Hz, the BCI performance elevation under optimal noise condition, compared to the non-noise condition, could be as high as  $24$  and  $43\%$ , respectively. Furthermore, from the analysis of different channel combinations, we can see how such effect changes with increases in noise level. When applied to a noise intensity of  $-30$  dBW, SR effect concentrates on the visual region and combination of other channels even weakens the efficiency of target recognition. At noise level of  $-10$  and  $10$  dBW tasks, there is no significant accuracy differences between O1-Oz-O2 combination condition and the single Oz-channel condition. Once the auditory region related EEG channels were included, the BCI accuracy rate significantly increased.

Based on these findings, we can extrapolate that cross-modal SR may involve integration of different sensory processing regions. In fact, in sensory processing, cross-modal interactions are quite common and many studies have further confirmed this phenomenon. For example, it has been proven that the dorsal cochlear nucleus, the earliest processing stage in the auditory pathway, receives not only input from the cochlea, but also from the somatosensory system that process tactile information (Ryugo et al., 2003; Shore and Zhou, 2006; Dehmel et al., 2012; Zeng et al., 2012). Furthermore, Huang et al. (2017) found that electro-tactile stimulation applied to the index finger significantly improves speech perception thresholds. As for audio-visual integration, it is well-known that sometimes hearing can be misled by vision input, which is well-known as the McGurk effect (McGurk and MacDonald, 1976). Additionally, Caclin et al. (2011) found that visual perception can be enhanced by auditory stimulation, and even subthreshold visual stimuli may be perceived through spatially converging audio-visual inputs (Bolognini et al., 2005). For these cross-modal improvement phenomena, Krauss et al. (2018) speculated that SR in one sensory modality driven by input from another modality may be a general principle, namely multisensory integration, which would cause SR-like cross-modal enhancement. Our findings in this study support this speculation.

## CONCLUSION

In this study, we propose an auditory-noise-enhanced visual SSMVEP-BCI paradigm with application of cross-modal SR mechanism. The results indicate that moderate auditory noise can increase BCI recognition accuracy and reduce response time, which provides a novel method to improve BCI performance. The combination of flow gain maps and wPLI values both qualitatively and quantitatively revealed that the existence of auditory noise may spread EEG responses to a wider brain area. Furthermore, this phenomenon could be caused by enhancing neural interaction between auditory and visual pathways via the cross-modal auditory-noise-induced SR mechanism. Such findings reveal the principle of cross-modal SR of the brain and provide a potentially novel approach for designing more effective audiovisual hybrid BCI systems.

## DATA AVAILABILITY STATEMENT

The raw data supporting the conclusions of this article will be made available by the authors, without undue reservation.

## ETHICS STATEMENT

The studies involving human participants were reviewed and approved by the institutional review board of Xi'an Jiaotong University. The patients/participants provided their written informed consent to participate in this study.

## REFERENCES

- Bartels, A., and Zeki, S. (2004). Functional brain mapping during free viewing of natural scenes. *Hum. Brain Mapp.* 21, 75–85. doi: 10.1109/SMC.2013.317
- Bassett, D. S., and Bullmore, E. D. (2006). Small-world brain networks. *Neuroscientist* 12, 512–523. doi: 10.1177/1073858406293182
- Benzi, R., Sutera, A., and Vulpiani, A. (1981). The mechanism of stochastic resonance. *J. Phys. A Math. Gen.* 14:6. doi: 10.1088/0305-4470/14/11/006
- Bergholz, R., Lehmann, T. N., Fritz, G., and Rütger, K. (2008). Fourier transformed steady-state flash evoked potentials for continuous monitoring of visual pathway function. *Doc. Ophthalmol.* 116, 217–229. doi: 10.1007/s10633-007-9085-6
- Bolognini, N., Frassinetti, F., Serino, A., and Ládavas, E. (2005). “Acoustical vision” of below threshold stimuli: interaction among spatially converging audiovisual inputs. *Exp. Brain Res.* 160, 273–282. doi: 10.1007/s00221-004-2005-z
- Brainard, D. H. (1997). The psychophysics toolbox. *Spatial Vis.* 10, 433–436. doi: 10.1163/156856897x00357
- Caclin, A., Bouchet, P., Djoulah, F., Pirat, E., Pernier, J., and Giard, M. H. (2011). Auditory enhancement of visual perception at threshold depends on visual abilities. *Brain Res.* 1396, 35–44. doi: 10.1016/j.brainres.2011.04.016
- Collins, J. J., Imhoff, T. T., and Grigg, P. (1996). Noise-enhanced information transmission in rat sal cutaneous mechanoreceptors via aperiodic stochastic resonance. *J. Neurophysiol.* 76, 642–645. doi: 10.1152/jn.1996.76.1.642
- Collins, J. J., Imhoff, T. T., and Grigg, P. (1997). Noise-mediated enhancements and decrements in human tactile sensation. *Phys. Rev. E* 56:923. doi: 10.1103/PhysRevE.56.923

## AUTHOR CONTRIBUTIONS

JX conceived the study, participated in the design of the study, and carried out the experiments. GZC carried out the experiments and wrote the manuscript. GHX, GLC, YX, and PF designed the study. TX and YJZ carried out the experiments and collected the data. XLH carried out the statistical data analyses. GLL and ML corrected the language. All authors contributed to the article and approved the submitted version.

## FUNDING

This work was supported by the National Key Research & Development Program of China (2017YFA0701103), the Open Funding Project of National Key Laboratory of Human Factors Engineering (SYFD061903K and SYFD160051806), the National Natural Science Foundation of China (61503298, 61773364, and 81927804), the Foundation of the Key Laboratory for Equipment Advanced Research (6142222200209 and 6142222180204), the Foundation Project in the field of Equipment Advanced Research (61400020402), the CAS Key Laboratory of Human-Machine Intelligence-Synergy Systems, Shenzhen Institutes of Advanced Technology (2014DP173025), the CAS Youth Innovation Promotion Association (2018395), the Shenzhen Basic Research Program (JCYJ20170818163724754), and the Shenzhen Engineering Laboratory of Neural Rehabilitation Technology.

## ACKNOWLEDGMENTS

We would like to thank the subjects for participating in these experiments and the reviewers for their helpful comments.

- Cordo, P., Inglis, J. T., Verschuere, S., Collins, J. J., Merfeld, D. M., Rosenblum, et al. (1996). Noise in human muscle spindles. *Nature* 383:769. doi: 10.1038/383769a0
- Dehmel, S., Pradhan, S., Koehler, S., Bledsoe, S., and Shore, S. (2012). Noise overexposure alters long-term somatosensory-auditory processing in the dorsal cochlear nucleus—possible basis for tinnitus-related hyperactivity? *Int. J. Neurosci.* 32, 1660–1671. doi: 10.1523/JNEUROSCI.4608-11.2012
- Douglass, J. K., Wilkens, L., Pantazelou, E., and Moss, F. (1993). Noise enhancement of information transfer in crayfish mechanoreceptors by stochastic resonance. *Nature* 365, 337–340. doi: 10.1038/365337a0
- Gammaitoni, L., Hänggi, P., Jung, P., and Marchesoni, F. (1998). Stochastic resonance. *Rev. Mod. Phys.* 70:223. doi: 10.1103/RevModPhys.70.223
- Harper, D. W. (1979). Signal detection analysis of effect of white noise intensity on sensitivity to visual flicker. *Percept. Mot. Skills* 48:791. doi: 10.2466/pms.1979.48.3.791
- He, B., Dai, Y., Astolfi, L., Babiloni, F., Yuan, H., and Yang, L. (2011). eConnectome: A MATLAB toolbox for mapping and imaging of brain functional connectivity. *J. Neurosci. Meth.* 195, 261–269. doi: 10.1016/j.jneumeth.2010.11.015
- Huang, J., Sheffield, B., Lin, P., and Zeng, F. G. (2017). Electro-tactile stimulation enhances cochlear implant speech recognition in noise. *Sci. Rep.* 7:2196. doi: 10.1038/s41598-017-02429-1
- Kamiński, M. J., and Blinowska, K. J. (1991). A new method of the description of the information flow in the brain structures. *Biol. Cybern.* 65, 203–210. doi: 10.1007/BF00198091
- Kamiński, M., Ding, M., Truccolo, W. A., and Bressler, S. L. (2001). Evaluating causal relations in neural systems: Granger causality, directed transfer function

- and statistical assessment of significance. *Biol. Cybern.* 85, 145–157. doi: 10.1007/s004220000235
- Kaysers, C., Petkov, C. I., Augath, M., and Logothetis, N. K. (2005). Integration of touch and sound in auditory cortex. *Neuron* 48, 373–384. doi: 10.1016/j.neuron.2005.09.018
- Krauss, P., Tziridis, K., Schilling, A., and Schulze, H. (2018). Cross-modal stochastic resonance as a universal principle to enhance sensory processing. *Front. Neurosci.* 12:578. doi: 10.3389/fnins.2018.00578
- Lin, Z., Zhang, C., Wu, W., and Gao, X. (2006). Frequency Recognition Based on Canonical Correlation Analysis for SSVEP-Based BCIs. *IEEE Transact. Biomed. Eng.* 53, 2610–2614. doi: 10.1109/TBME.2006.886577
- McGurk, H., and MacDonald, J. (1976). Hearing lips and seeing voices. *Nature* 264:746. doi: 10.1038/264746a0
- Nakamura, H., Matsubara, A., and Nishifuji, S. (2017). “Noise-assisted auditory brain computer interface,” in *2017 IEEE 6th Global Conference on Consumer Electronics (GCCE)*, (Japan: IEEE GCCE), 1–5. doi: 10.1109/GCCE.2017.8229231
- Ng, K. B., Bradley, A. P., and Cunnington, R. (2012). Stimulus specificity of a steady-state visual-evoked potential-based brain–computer interface. *J. Neural. Eng.* 9:036008. doi: 10.1088/1741-2560/9/3/036008
- Pelli, D. G. (1997). The Video Toolbox software for visual psychophysics: Transforming numbers into movies. *Spatial Vis.* 10, 437–442. doi: 10.1163/156856897X00366
- Regan, D. (1989). *Evoked potentials and evoked magnetic fields in science and medicine. Human brain electrophysiology*. Amsterdam: Elsevier, 59–61.
- Ross, L. A., Saint-Amour, D., Leavitt, V. M., Javitt, D. C., and Foxe, J. J. (2006). Do you see what I am saying? Exploring visual enhancement of speech comprehension in noisy environments. *Cereb. Cortex* 17, 1147–1153. doi: 10.1093/cercor/bhl024
- Ryugo, D. K., Haenggeli, C. A., and Doucet, J. R. (2003). Multimodal inputs to the granule cell domain of the cochlear nucleus. *Exp. Brain Res.* 153, 477–485. doi: 10.1007/s00221-003-1605-3
- Shore, S. E., and Zhou, J. (2006). Somatosensory influence on the cochlear nucleus and beyond. *Hearing Res.* 216, 90–99. doi: 10.1016/j.heares.2006.01.006
- Srebro, R., and Malladi, P. (1999). Stochastic resonance of the visually evoked potential. *Phys. Rev. E* 59:2566. doi: 10.1103/PhysRevE.59.2566
- Tanaka, F., Matsubara, A., and Nishifuji, S. (2015). “Evidence of stochastic resonance of auditory steady-state response in electroencephalogram for brain machine interface,” in *2015 IEEE 4th Global Conference on Consumer Electronics (GCCE)*, (Japan: IEEE), 195–199. doi: 10.1109/GCCE.2015.7398638
- Vinck, M., Oostenveld, R., Van Wingerden, M., Battaglia, F., and Pennartz, C. M. (2011). An improved index of phase-synchronization for electrophysiological data in the presence of volume-conduction, noise and sample-size bias. *Neuroimage* 55, 1548–1565. doi: 10.1016/j.neuroimage.2011.01.055
- Vindiola, M. M., Vettel, J. M., Gordon, S. M., Franaszczuk, P. J., and McDowell, K. (2014). Applying EEG phase synchronization measures to non-linearly coupled neural mass models. *J. Neurosci. Meth.* 226, 1–14. doi: 10.1016/j.jneumeth.2014.01.025
- Wolpaw, J. R., Birbaumer, N., Heetderks, W. J., McFarland, D. J., Peckham, P. H., Schalk, G., et al. (2000). Brain-computer interface technology: a review of the first international meeting. *IEEE Trans. Rehabil. Eng.* 8, 164–173. doi: 10.1109/TRE.2000.847807
- Wu, C. H., and Lakany, H. (2013). “The Effect of the Viewing Distance of Stimulus on SSVEP Response for Use in Brain-Computer Interfaces,” in *Proceedings of the International IEEE Conference on Systems, Man, and Cybernetics (SMC)*, (San Antonio: IEEE), 1840–1845. doi: 10.1109/SMC.2013.317
- Xie, J., Du, G., Xu, G., Zhao, X., Fang, P., Li, M., et al. (2019). Performance Evaluation of Visual Noise Imposed Stochastic Resonance Effect on Brain-Computer Interface Application: A Comparison Between Motion-Reversing Simple Ring and Complex Checkerboard Patterns. *Front. Neurosci.* 2019:1192. doi: 10.3389/fnins.2019.01192
- Xie, J., Xu, G., Luo, A., Li, M., Zhang, S., Han, C., et al. (2017). The Role of Visual Noise in Influencing Mental Load and Fatigue in a Steady-State Motion Visual Evoked Potential-Based Brain-Computer Interface. *Sensors* 17:s17081873.
- Xie, J., Xu, G., Wang, J., Zhang, F., and Zhang, Y. (2012). Steady-state motion visual evoked potentials produced by oscillating newton’s rings: implications for brain-computer interfaces. *PLoS One* 7:e39707. doi: 10.1371/journal.pone.0039707
- Xie, J., Xu, G., Wang, J., Zhang, S., Zhang, F., Li, Y., et al. (2014). Addition of visual noise boosts evoked potential-based brain-computer interface. *Sci. Rep.* 4:4953. doi: 10.1038/srep04953
- Yan, Z., and Gao, X. (2011). Functional connectivity analysis of steady-state visual evoked potentials. *Neuroence Lett.* 499, 199–203. doi: 10.1016/j.neulet.2011.05.061
- Zeng, C., Yang, Z., Shreve, L., Bledsoe, S., and Shore, S. (2012). Somatosensory projections to cochlear nucleus are upregulated after unilateral deafness. *Int. J. Neurosci.* 32, 15791–15801. doi: 10.1523/JNEUROSCI.2598-12.2012 doi: 10.1523/jneurosci.2598-12.2012

**Conflict of Interest:** The authors declare that the research was conducted in the absence of any commercial or financial relationships that could be construed as a potential conflict of interest.

Copyright © 2020 Xie, Cao, Xu, Fang, Cui, Xiao, Li, Li, Xue, Zhang and Han. This is an open-access article distributed under the terms of the Creative Commons Attribution License (CC BY). The use, distribution or reproduction in other forums is permitted, provided the original author(s) and the copyright owner(s) are credited and that the original publication in this journal is cited, in accordance with accepted academic practice. No use, distribution or reproduction is permitted which does not comply with these terms.



# Modulation of Functional Connectivity and Low-Frequency Fluctuations After Brain-Computer Interface-Guided Robot Hand Training in Chronic Stroke: A 6-Month Follow-Up Study

## OPEN ACCESS

### Edited by:

Haider Raza,  
University of Essex, United Kingdom

### Reviewed by:

Floriana Pichiorri,  
Santa Lucia Foundation (IRCCS), Italy  
Ren Xu,  
Guger Technologies, Austria

### \*Correspondence:

Raymond K. Y. Tong  
kytong@cuhk.edu.hk

†These authors have contributed  
equally to this work

### Specialty section:

This article was submitted to  
Brain-Computer Interfaces,  
a section of the journal  
Frontiers in Human Neuroscience

**Received:** 28 September 2020

**Accepted:** 18 December 2020

**Published:** 20 January 2021

### Citation:

Lau CCY, Yuan K, Wong PCM,  
Chu WCW, Leung TW, Wong W-w  
and Tong RKY (2021) Modulation of  
Functional Connectivity and  
Low-Frequency Fluctuations After  
Brain-Computer Interface-Guided  
Robot Hand Training in Chronic  
Stroke: A 6-Month Follow-Up Study.  
*Front. Hum. Neurosci.* 14:611064.  
doi: 10.3389/fnhum.2020.611064

Cathy C. Y. Lau<sup>1†</sup>, Kai Yuan<sup>1†</sup>, Patrick C. M. Wong<sup>2</sup>, Winnie C. W. Chu<sup>3</sup>,  
Thomas W. Leung<sup>4</sup>, Wan-wa Wong<sup>5</sup> and Raymond K. Y. Tong<sup>1\*</sup>

<sup>1</sup> Department of Biomedical Engineering, The Chinese University of Hong Kong, Hong Kong, China, <sup>2</sup> Brain and Mind Institute, The Chinese University of Hong Kong, Hong Kong, China, <sup>3</sup> Department of Imaging and Interventional Radiology, Prince of Wales Hospital, The Chinese University of Hong Kong, Hong Kong, China, <sup>4</sup> Department of Medicine and Therapeutics, Prince of Wales Hospital, The Chinese University of Hong Kong, Hong Kong, China, <sup>5</sup> Department of Psychiatry and Biobehavioural Sciences, University of California, Los Angeles, Los Angeles, CA, United States

Hand function improvement in stroke survivors in the chronic stage usually plateaus by 6 months. Brain-computer interface (BCI)-guided robot-assisted training has been shown to be effective for facilitating upper-limb motor function recovery in chronic stroke. However, the underlying neuroplasticity change is not well understood. This study aimed to investigate the whole-brain neuroplasticity changes after 20-session BCI-guided robot hand training, and whether the changes could be maintained at the 6-month follow-up. Therefore, the clinical improvement and the neurological changes before, immediately after, and 6 months after training were explored in 14 chronic stroke subjects. The upper-limb motor function was assessed by Action Research Arm Test (ARAT) and Fugl-Meyer Assessment for Upper-Limb (FMA), and the neurological changes were assessed using resting-state functional magnetic resonance imaging. Repeated-measure ANOVAs indicated that long-term motor improvement was found by both FMA ( $F_{[2,26]} = 6.367, p = 0.006$ ) and ARAT ( $F_{[2,26]} = 7.230, p = 0.003$ ). Seed-based functional connectivity analysis exhibited that significantly modulated FC was observed between ipsilesional motor regions (primary motor cortex and supplementary motor area) and contralesional areas (supplementary motor area, premotor cortex, and superior parietal lobule), and the effects were sustained after 6 months. The fALFF analysis showed that local neuronal

activities significantly increased in central, frontal and parietal regions, and the effects were also sustained after 6 months. Consistent results in FC and fALFF analyses demonstrated the increase of neural activities in sensorimotor and fronto-parietal regions, which were highly involved in the BCI-guided training.

**Clinical Trial Registration:** This study has been registered at ClinicalTrials.gov with clinical trial registration number NCT02323061.

**Keywords:** stroke, rehabilitation robotics, functional magnet resonance imaging, brain-computer interface, fractional amplitude low-frequency fluctuations

## INTRODUCTION

Stroke survivors require high demand in rehabilitation and long-term care services, especially for upper extremity motor function (Norouzi-Gheidari et al., 2012). Fortunately, the existence of neuroplasticity, which characterizes the potential of modifying the size of cortical receptive field or motor output modules in response to altered synaptic input (Seitz et al., 1995), makes the development of various stroke rehabilitation methods possible.

Brain-computer interface (BCI)-guided training therapy has been promoted as a post-stroke motor rehabilitation training tool. It is designed to enhance motor recovery by modulating sensorimotor activity through repetitive practice with corresponding feedback or reward, thereby modifying the neuronal activity (Biasiucci et al., 2018; Remsik et al., 2019). In practice, BCI has been developed to translate brain activities into control signals of corresponding external execution devices such as robots, orthosis, and functional electrical stimulation (FES) (Soekadar et al., 2015; Cho et al., 2019; Mrachacz-Kersting et al., 2019; Mane et al., 2020). Therefore, combining the BCI system with a unilateral robotic hand technology makes it possible for stroke subjects to control the robotic hand with his/her brain signals, in order to restore the paretic hand function by promoting neuroplasticity and facilitating motor relearning (Frolov et al., 2017; Carino-Escobar et al., 2019). Clinical evidence showed that BCI-guided training elicits clinically significant and long-lasting motor recovery in chronic stroke survivors (Biasiucci et al., 2018; Ramos-Murguialday et al., 2019). A meta-analysis also suggested that BCI technology could be a more effective intervention for post-stroke upper-limb rehabilitation than other conventional therapies (Cervera et al., 2018). Despite the promising findings achieved, the underlying neurophysiological mechanisms induced by BCI-guided training for chronic stroke have not been thoroughly investigated. Besides, most existing BCI-guided robot-assist training studies adopted proximal joint upper limb training strategy (e.g., reaching and retrieving), such as in (Várkuti et al., 2012; Ramos-Murguialday et al., 2013), while our study applied robot hand on the distal joint of the upper-limb. Recently, studies comparing distal and proximal robot-assisted training therapies showed that distal training exhibited better performance than proximal training in the whole upper-limb (Hsieh et al., 2018; Qian et al., 2019).

The functional magnetic resonance imaging (fMRI) could be an essential tool to understand the effects of rehabilitation therapies on neuroplasticity. It is one of the most commonly

used neuroimaging tools for assessing the cortical modulations in stroke (Kimberley et al., 2008). Resting-state fMRI (rs-fMRI) measures the blood oxygen level-dependent (BOLD) signal at the resting-state, which maps the functional organization of the brain (Van Essen et al., 2012). Functional connectivity (FC) calculates the temporal dependency of neuronal activation patterns in anatomically separated brain regions, and it is the most commonly used index in rs-fMRI studies (Van Den Heuvel and Hulshoff Pol, 2010). FC gives valuable information in the network-wide effects of stroke by providing great insight into network dysfunction and functional reorganization (Carter et al., 2012). It is suitable to investigate multiple distributed networks that were damaged by stroke and how connectivity patterns may be reorganized after recovery (Grefkes and Fink, 2014). In addition to provide a way to quantify neural activities across the whole brain, the fractional amplitude of low-frequency fluctuations (fALFF) reflects a different aspect of the BOLD signal, measuring the power of low-frequency fluctuations (Zuo et al., 2010). Lower frequency fluctuations allow us to study the amplitude of regional neuronal activity, which is an indication of local metabolic changes associated with the BOLD signal across the whole brain (Chen et al., 2015). fALFF analysis has been used to study post-stroke depression (Egorova et al., 2017) and motor recovery (Wang et al., 2020). However, few studies have combined FC and fALFF in investigating neuroplasticity changes induced by motor rehabilitation after stroke. These two measurements might provide complementary information as well as further validation for each other, which would make the evaluation more comprehensive. A comprehensive exploration in the whole-brain level is needed to fill the gap.

The hemispheric changes of resting-state functional connectivity and activation pattern shift during motor task after BCI-guided robot hand training have been demonstrated by our previous studies (Khan et al., 2020; Yuan et al., 2020). In this study, we aim at exploring the whole-brain neuroplasticity changes using rs-fMRI. Motor imagery studies have consistently disclosed activity in cortical and subcortical motor areas, which substantially overlap the neural substrates of motor execution (Hanakawa et al., 2008). Besides, motor imagery also involves some distinctive regions in the frontal and parietal regions which are not involved in motor execution (Hanakawa et al., 2008; Sharma et al., 2009). Therefore, we hypothesize that BCI-guided training could boost beneficial functional activity dependent plasticity to attain clinically important outcomes, through the contingency between suitable motor-related cortical

activity and the afferent feedback. We believe that there should be functional reorganization within the sensorimotor and frontoparietal regions involved in the BCI-guided upper-limb training, which might account for the clinical improvement in the upper-limb function. We also expect the FC and the fALFF to show complementary results and to validate each other, since they represent different aspects of the fMRI data. Furthermore, we also tried to explore the neuroplasticity changes in a 6-month follow-up session to investigate whether the neuroplasticity changes could be maintained.

## MATERIALS AND METHODS

### Subjects

Fourteen chronic stroke survivors (13 males, mean age =  $54 \pm 8$  years) with right ( $n = 9$ ) or left ( $n = 5$ ) hemisphere impairment were recruited from the local community. The inclusion criteria were (1) first-ever stroke, (2) onset of stroke diagnose more than 6 months, (3) a single unilateral brain lesion, (4) sufficient cognition and comprehensive ability to understand and perform corresponding tasks assessed by Montreal Cognitive Assessment (MoCA) with a score of  $>21$ , (5) moderate to severe motor dysfunctions for the paretic upper extremity (Fugl-Meyer Assessment for upper-extremity score  $< 47$ ) (Woodbury et al., 2013) and (6) no additional rehabilitation therapies applied to the subject during the intervention. Subjects with (1) aphasia, neglect, and apraxia, history of alcohol, drug abuse, or epilepsy, (2) severe hand spasticity, (3) hand deformity and wound, (4) bilateral infarcts, uncontrolled medical problems, and (5) serious cognitive deficits were excluded. The study was approved by the Joint Chinese University of Hong Kong-New Territories East Cluster Clinical Research Ethics Committee and all subjects signed written consent before any experiments started. This study has been registered at <https://clinicaltrials.gov> with clinical trial registration number NCT02323061.

Fugl-Meyer Assessment for upper-extremity (FMA) (Fugl-Meyer et al., 1975) and Action Research Arm Test (ARAT) (Lyle, 1981) were used to assess the motor function of the paretic upper limbs for all stroke subjects before (Pre), immediately after (Post) and 6 months after the intervention (Post6month) respectively. ARAT measures the affected upper limb's ability to reach, grasp, manipulate, and release objects which are regularly encountered during activities of daily living, with a maximum score of 57. FMA measures the motor function of the whole upper limb, with a maximum score of 66. Both assessments are widely used in upper-extremity rehabilitation.

### Training System and Intervention Protocols

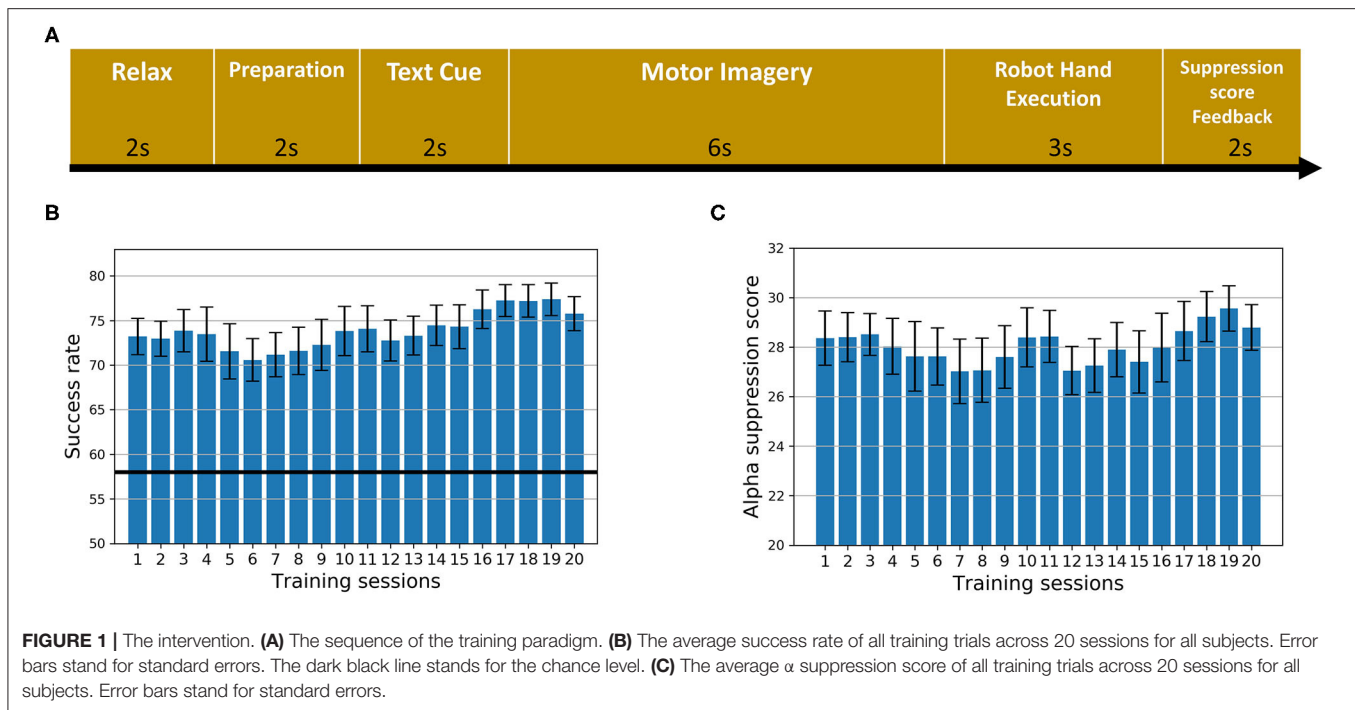
During the training, subjects were asked to imagine the action of either grasping or releasing a cup following the instruction (generated by Psychophysics Toolbox 3.0, <http://psychtoolbox.org/>) displayed on the monitor. The task of motor imagery of opening and grasping the paretic hand is frequently used in our daily life, however, it is very challenging for stroke survivors. Through this task, the alpha suppression is detectable in the motor regions, according to previous studies (Neuper et al., 2009). This task is also widely adopted in other

motor imagery studies (Neuper et al., 2009; Pichiorri et al., 2015). Each subject's electroencephalography (EEG) signals were acquired using a portable signal acquisition system (g.LADYbird, g.Tec Medical Engineering, GmbH, Austria) with 16 electrodes covering the motor-related regions in both ipsilesional and contralesional hemispheres (located at C1, C2, C3, C4, C5, C6, Cz, FC1, FC2, FC3, FC4, FCz, CP1, CP2, CP3, and CP4 according to the international 10–20 system). Impedances of electrodes were kept below 5 k $\Omega$ . EEG signals were referenced to the unilateral earlobe, the ground at Fpz, and sampled at 256 Hz. To remove artifacts and power line noise, a 2–60 Hz bandpass filter and 48–52 Hz notch filter were utilized in the real-time. All the channels were used to generate the dynamic potential topography of the whole brain for the trainer to inspect the state of each subject. An exoskeleton robot hand (Tong et al., 2013) was used to assist the paretic hand to grasp and open. From the fully extended position to the fully flexed position, the fingers assembly provided 55 degrees and 65 degrees range of motion (ROM) for the metacarpophalangeal (MCP) and proximal interphalangeal (PIP) finger joints, respectively. The robot hand assisted the subjects to open and grasp their paretic hand, which was very challenging by themselves. The biofeedback was easily sensible and functionally meaningful, resulting in providing rich sensory inputs via the natural afferent pathways in the real-time. We kept the robot hand's power assistance consistent throughout the 20-session training.

The sequence of the training paradigm is illustrated in **Figure 1A**. During each trial, the subject was asked to relax for 2 s followed by a white cross for 2 s to remind them to get ready. A text cue of “hand grasp” or “hand open” was then displayed for 2 s to instruct the subject to imagine the corresponding action as if performed by his/her affected hand. After that, a video clip with a duration of 6 s showing either the action of grasping or releasing a cup was displayed simultaneously for guidance. The trigger to the robot hand was then sent based on the  $\alpha$  suppression (8–13 Hz) of the EEG signal during the motor imagery. In the following 3 s, the robot hand assisted the subject in completing the grasping/opening task. Afterwards, the  $\alpha$  suppression score as a feedback was displayed on the screen for 2 s to motivate the subject to achieve a higher score in the subsequent trials. Finally, a 2 s rest was given to the subject before the next trial started. The text cue of “hand grasp” and “hand open” appeared alternately. To compute the  $\alpha$  suppression score, the EEG signal from either the C3 or C4 channel was chosen, according to the lesion side, and transformed to the frequency domain through fast Fourier transform with a Hanning window. The mean power was calculated in the  $\alpha$  band (8–13 Hz) and compared with the baseline before motor imagery. Specifically, the  $\alpha$  suppression score ( $\alpha_S$ ) was calculated as follows (Ono et al., 2014):

$$\alpha_S = -\frac{P_{MI} - P_{rest}}{P_{rest}} \times 100\%$$

where  $P_{MI}$  represented the mean power of  $\alpha$  band during motor imagery and  $P_{rest}$  stood for the mean  $\alpha$  power during resting



state. In our study, we predefined that the robot hand would apply a mechanical force to assist the subject in completing the hand opening or grasping tasks if the suppression score  $\alpha_S$  exceeded 20% based on the previous study (Perry and Bentin, 2009). The success rate was defined as the percentage of correctly detected trials at each session. All subjects received a 20-session BCI robot hand training with an intensity of 3–5 sessions per week and completed the whole process within 5–7 weeks. During each training session, the subject was required to perform 100 repetitive hand opening/grasping tasks and the intermittent breaks were given at every 10 repetitions to avoid fatigue.

## Data Acquisition

MRI scans were acquired for all the 14 subjects at Pre and Post sessions. Ten subjects had a Post6month session scan, while four subjects did not attend the Post6month session. A 3T Philips MR scanner (Achieva TX, Philips Medical System, Best, Netherlands) with an 8-channel head coil was used to acquire high resolution T1-weighted anatomical images (TR/TE = 7.47/3.45 ms, flip angle = 8°, 308 slices, voxel size =  $0.6 \times 1.042 \times 1.042 \text{ mm}^3$ ) using a T1-TFE sequence (ultrafast spoiled gradient echo pulse sequence), and BOLD fMRI images (TR/TE = 2,000/30 ms, flip angle = 70°, 37 slices/volume, voxel size =  $2.8 \times 2.8 \times 3.5 \text{ mm}^3$ ) using a FEEPI sequence (gradient-echo echo-planar-imaging sequence). The sequences were displayed using EPrime 2.0 (Psychology Software Tools, PA USA). During the acquisition of rs-fMRI data, subjects were presented with a white cross in a black background and instructed to rest while focusing on the fixation cross. One rs-fMRI block lasted for 8 min.

## Assessment Score and Training Performance Analysis

Repeated measure analysis of variance (ANOVA) at time level (Pre, Post, and Post6month) were applied to examine whether the FMA and ARAT scores improved after the intervention. Paired *t*-tests were used as *post-hoc* tests to examine significant changes in different combinations of three time-points for the FMA and ARAT scores. Normality of the data was checked using Kolmogorov-Smirnov tests and the results showed the data were normally distributed. Bonferroni corrections were used to adjust for multiple comparisons. Statistical analyses were performed using SPSS 25.0 (IBM SPSS Statistics, NY, US) with the significance level set at corrected  $p < 0.05$ . Moreover, the minimal clinically important difference (MCID) was also calculated to reflect the clinical significance by setting minimal changes in clinical assessments. The MCID of FMA is 4.25 (Page et al., 2012) and the MCID of ARAT is 5.7 in chronic stroke (Van Der Lee et al., 2001). Mean success rate and suppression score of training trials across 20 sessions for all the subjects were calculated, respectively.

## fMRI Analysis Preprocessing

The rs-fMRI data were preprocessed using DPARSF toolbox. The first 10 volumes were discarded to assure the remaining volumes of fMRI data were at magnetization steady state. The remaining volumes were corrected with slice timing and realigned for head motion correction. Nuisance variables were then regressed out, including white matter, cerebrospinal fluid (CSF), global mean signal, and Friston 24 head motion parameters (Friston et al., 1996). To further control for head motion, the scrubbing process was performed for the volumes with framewise displacement

(FD) value exceeding 0.3 (Power et al., 2012). If over 25% of all the volumes exceed the FD threshold, the data for this subject would be discarded, and no subject was discarded in the rs-fMRI analysis. Then the functional dataset was aligned to the anatomical dataset. Detrending and temporal band-pass filtering (0.01–0.1 Hz) (Zuo et al., 2010) were performed to remove higher frequency physiological noise and lower frequency scanner drift. Subsequently, the functional images were spatially normalized to the Montreal Neurological Institute (MNI) template, resliced to  $2 \times 2 \times 2 \text{ mm}^3$  voxels, and smoothed with a Gaussian kernel with a full-width at half-maximum (FWHM) of 6 mm. To perform group statistical analysis later, subjects with left-hemispheric lesions were flipped along the midsagittal plane using MRIcron ([www.mccauslandcenter.sc.edu/mricro/mricron](http://www.mccauslandcenter.sc.edu/mricro/mricron)), so that the lesions of all subjects were in the right hemisphere. For the preprocessing steps for the fALFF analysis, the bandpass filter was not applied.

### Seed-Based FC Analysis

We did a seed-based whole-brain analysis with the seed at the ipsilesional primary motor cortex (iM1) and supplementary motor area (iSMA), and the seed locations were (38, -22, 56) and (8, -8, 57) in MNI space, respectively. The seeds were defined as spherical balls with a radius of 5 mm in MNI standard space. The average time course of the BOLD signals within the seeds was used to calculate the FC with every other voxel in the brain, producing maps of FC with the seeds. A paired *t*-test was carried out between each pair of sessions for all the seed-based FC maps. Multiple comparisons were corrected using Gaussian random field theory at the cluster level (minimum  $z > 2.7$ ; cluster-wise significance:  $p < 0.05$ , corrected) (Chen et al., 2018). All the analyses for seed-based FC and paired *t*-test were carried out in DPARSF toolbox (Yan et al., 2016).

### fALFF Analysis

The fALFF values were computed on preprocessed data using the DPARSF software (Yan et al., 2016). DPARSF has in-built fast Fourier transform functions to convert time series data to the frequency domain and calculate the power spectrum. Briefly, on a voxel-by-voxel basis, the time course was converted into the frequency domain using a Fast Fourier Transform, the square root of the power spectrum was computed, and the average of the amplitudes in the range of 0.01–0.1 Hz was then calculated to obtain the ALFF (Zou et al., 2008; Zuo et al., 2010). Dividing each voxel's ALFF value by the amplitudes of the entire detectable frequency range (0–0.55 Hz) yields the fALFF (Zou et al., 2008). All analyses were performed at the whole-brain level. A paired *t*-test was carried out between each pair of sessions for results from fALFF analysis.

## RESULTS

### Assessment Scores and Training Performance

Subject demographic and assessment scores are shown in **Table 1**. The repeated measure ANOVA on FMA scores with time (Pre, Post, and Post6month) as within-subject factor indicated that

a significant effect of time ( $F_{[2,26]} = 6.367$ ,  $p = 0.006$ ) was observed. *Post-hoc* tests indicated that there were significant increases in FMA scores between Pre and Post ( $p = 0.017$ , Bonferroni corrected) as well as between Pre and Post6month ( $p = 0.034$ , Bonferroni corrected). No significant change was found between Post and Post6month ( $p = 1.00$ , Bonferroni corrected). The repeated measure ANOVA on ARAT scores with time (Pre, Post, and Post6month) as within-subject factor indicated that a significant effect of time ( $F_{[2,26]} = 7.230$ ,  $p = 0.003$ ) was observed. *Post-hoc* tests indicated that there were significant increases in ARAT scores between Pre and Post ( $p = 0.015$ , Bonferroni corrected), marginally significant between Pre and Post6month ( $p = 0.055$ , Bonferroni corrected). No significant change was found between Post and Post6month ( $p = 0.879$ , Bonferroni corrected). The result indicated that the BCI robot hand training was able to promote motor recovery with a long-term effect. For FMA scores, 43% of the subjects achieved the MCID at Post and 36% of the subjects achieved the MCID at Post6month. For ARAT scores, 36% of the subjects achieved the MCID at Post and 29% of the subjects achieved the MCID at Post6month. For suppression score at the ipsilesional motor area (**Figure 1C**), a slightly increasing trend from the beginning to the end of all the sessions could be observed, with the average of 28.19% for the first five sessions to 28.85% for the last five sessions. For the success rate of training trials (**Figure 1B**), an increasing trend was observed, with the average of 73.01% for the first five sessions to 76.78% for the last five sessions. The chance level was 58% (Müller-Putz et al., 2008). The results on the performances of motor imagery tasks showed that the subjects were improving with the increased number of training sessions.

### Seed-Based FC Analysis

Seed-based whole-brain FC was explored between each pair of sessions with the seed set at iM1 and iSMA. The FC map in the Pre session with the iM1 seed was shown in the left panel of **Figure 2A**. Significant increased FC was found between iM1, and the contralesional premotor cortex as well as part of SMA (**Figure 2A**), when comparing Post and Pre sessions; significant increased FC was found between iM1 and contralesional SMA (**Figure 2A**) when comparing Post6month and Pre sessions. The FC map in the Pre session with the iSMA seed was shown in the left panel of **Figure 2B**. Significant increased FC was found between iSMA with bilateral superior parietal lobe (SPL) when comparing Post and Post6month to Pre session (**Figure 2B**).

### fALFF Analysis

Significantly increased fALFF was observed in the ipsilesional precentral area and superior parietal lobule (**Figure 3A**) when comparing Post and Pre sessions; significantly increased fALFF was observed in the contralesional precentral area and ipsilesional superior frontal area (**Figure 3B**) when comparing Post6month and Pre sessions; significantly increased fALFF was observed in bilateral SMA and paracentral lobule (**Figure 3C**) when comparing Post6month and Post sessions.

**TABLE 1** | Demographic and assessment scores. Fourteen chronic stroke subjects participated in this study.

Subjects	Age range	Gender	Lesion Locations	Stroke Onset Time (years)	Stroke Type	ARAT (max. score: 57)			FMA (max. score: 66)		
						Pre	Post	Post 6month	Pre	Post	Post 6month
1#	45–49	M	R MFG, SFG, precentral supramarginal, SMA	1	I	3	21	19	19	34	28
2	65–69	M	L insula, putamen, IFG, temporal pole	8	H	10	21	15	22	27	32
3	65–69	M	R insula, ITG, IOG, putamen	1	H	8	15	26	13	16	27
4	60–64	M	R insula, putamen, IFG, rolandic operculum	3	I	4	6	8	16	14	18
5	45–49	M	R ITG, MTG, STG, MOG, angular, supramarginal	0.7	H	16	17	17	17	25	25
6	60–64	M	L PLIC, putamen, insula, postcentral, SFG	11	I	15	14	11	22	24	24
7	55–59	M	R insula, IFG, rolandic operculum	6	I	12	21	20	13	23	20
8	40–44	M	R insula, rolandic operculum, IFG, STG, putamen, temporal pole	5	H	9	14	10	15	17	16
9#	50–54	F	L insula, rolandic operculum, putamen	3	H	19	23	22	34	34	37
10	40–44	M	R insula, MTG, STG, temporal pole, putamen, rolandic operculum	3	H	11	14	13	17	20	20
11#	55–59	M	L insula, IFG, putamen	5	H	10	12	8	28	33	24
12#	50–54	M	L putamen, caudate nucleus	1	I	15	13	16	24	22	22
13	55–59	M	R putamen, temporal pole, IFG, insula, rolandic operculum	7	I	14	19	17	20	25	21
14	45–49	M	R insula, putamen	1	H	12	33	18	34	37	35
Mean ± Std						11.3 ± 4.3	<b>17.3 ± 6.2*</b>	15.7 ± 5.1	21.0 ± 6.7	<b>25.1 ± 7.0*</b>	<b>25.0 ± 6.1*</b>

# Subjects that did not have Post6month MRI scan.

\*Significant increase compared with the Pre ( $p < 0.05$ ).

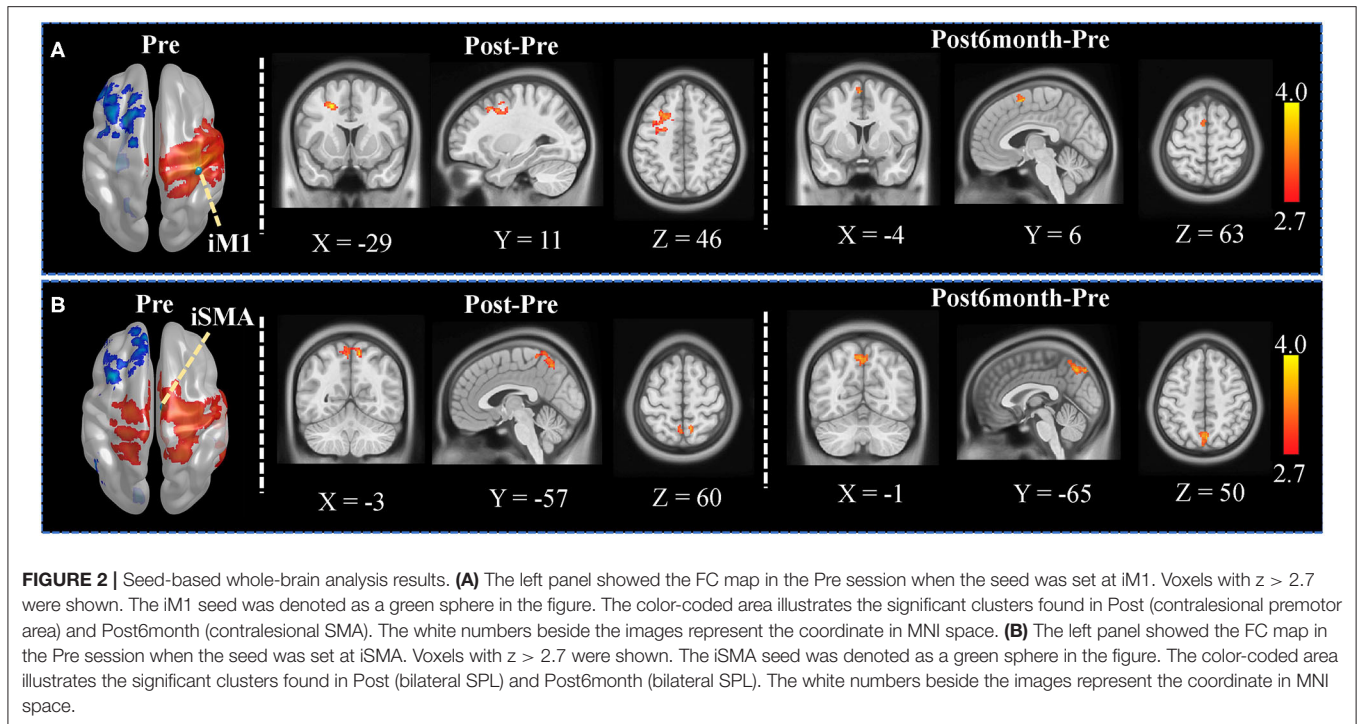
ARAT, Action Research Arm Test; F, female; FMA, Fugel-Meyer Assessment for upper limb; H, hemorrhage stroke; I, ischemic stroke; IFG, Inferior frontal gyrus; IOG, Inferior occipital gyrus; ITG, Inferior temporal gyrus; L, left; M, male; MFG, Middle frontal gyrus; MOG, Middle occipital gyrus; MTG, Middle temporal gyrus; PLIC, Posterior limb of the internal capsule; R, right; SFG, superior frontal gyrus; SMA, Supplementary motor area; STG, Superior temporal gyrus.

## DISCUSSION

This study explored the effects of BCI-guided robot hand training on the paretic hand in chronic stroke survivors by providing repetitive exercise with integrated sensorimotor feedback. The subjects showed upper-limb motor function improvement, as reflected by the FMA and the ARAT scores, after the 20-session training and these improvements were sustained 6 months after the intervention. Moreover, this study also revealed the neuroplasticity changes after the intervention. The FC between iM1 and contralesional premotor cortex and SMA significantly increased immediately after the 20-session training; The FC between iSMA and bilateral SPL also significantly increased immediately after the 20-session training. Besides, the fALFF analysis showed that local neuronal activities significantly increased in central, frontal, and parietal regions. Our study demonstrated the modulated neuroplasticity changes introduced by the BCI-guided robot hand training immediately and 6 months after the intervention.

Stroke survivors experience spontaneous recovery within the first few months after stroke onset and they then become clinically stable with hand weakness (Tombari et al., 2004;

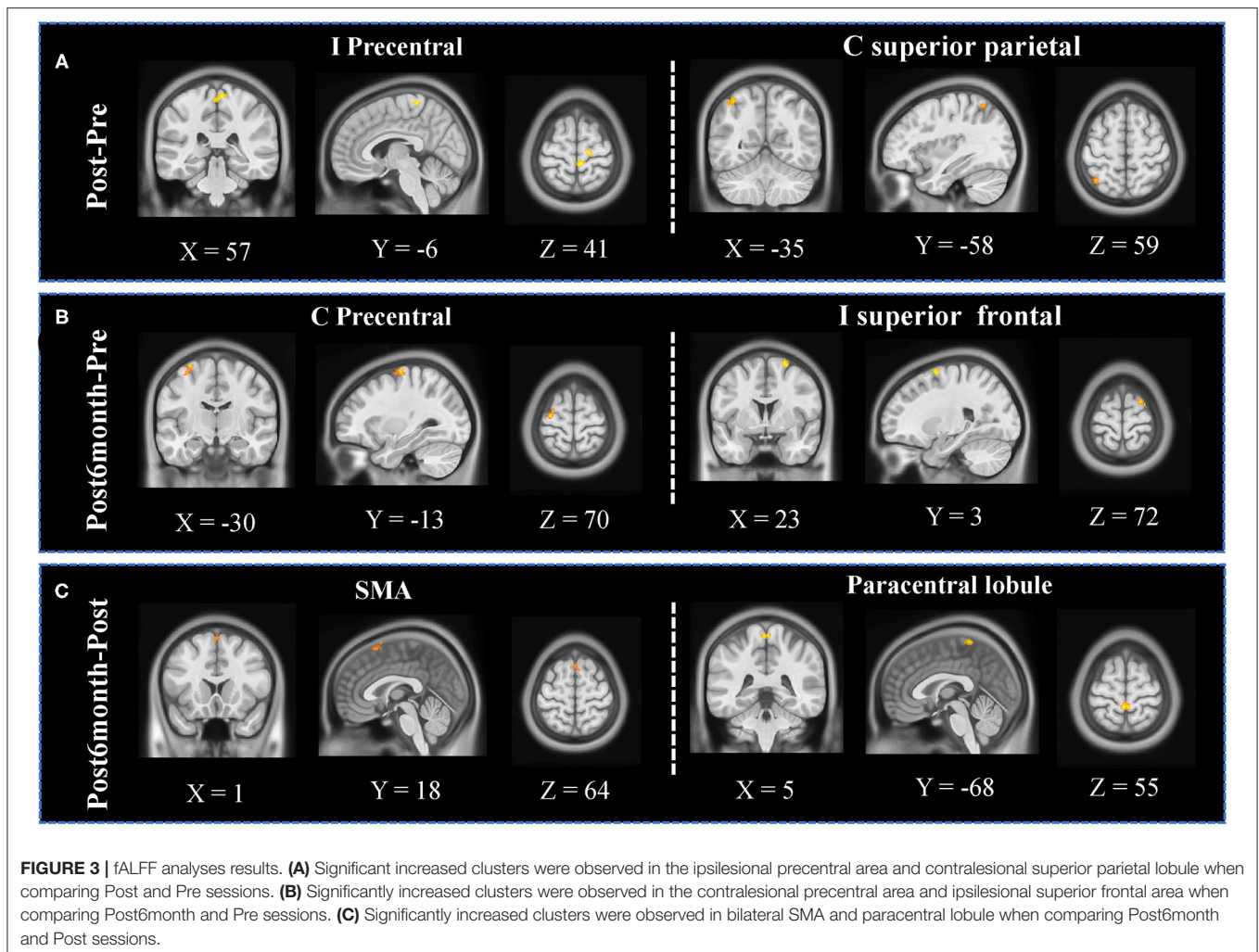
Kwakkel et al., 2006). BCI-guided robot therapy has shown the potential to restore motor function and to improve rehabilitation outcomes after stroke or spinal cord injury (Frolov et al., 2017). The feedback facilitates the appraisal of performance by enforcing the sensory aspect in the sensorimotor loop and thereby restoring the action-perception coupling (Daly and Wolpaw, 2008; Van Dokkum et al., 2015). The feedback in this study is the hand opening and grasping movement assisted by the robot hand, which is easily sensible and functionally meaningful. It provides rich sensory inputs through the natural afferent pathways in real-time. Studies have reported that BCI-guided training helps promote upper-limb motor function more than conventional therapies, as well as induces functional reorganization in the brain (Ramos-Murguialday et al., 2013; Biasiucci et al., 2018). According to these studies, no significant improvement was found in upper-limb FMA scores in the groups who received random functional electrical stimulation (FES) (Biasiucci et al., 2018) or received random robotic orthosis feedback (Ramos-Murguialday et al., 2013). Our results further validate the potential of BCI-guided intervention in promoting hand function recovery for persons with chronic stroke.



In our study, the seed-based whole-brain analysis showed that the FC between iM1 and contralateral premotor cortex and SMA was significantly increased after the 20-session training. Studies have suggested that premotor cortex and M1 play a crucial role during motor-imagery as well as during motor execution tasks (Bajaj et al., 2015). The crucial role of the SMA in motor recovery has already been demonstrated in previous fMRI studies (Loubinoux et al., 2003; Tombari et al., 2004). A longitudinal fMRI study indicated that the connectivity of the iM1 with the contralateral regions including SMA at the early stage of stroke was positively correlated with motor improvement (Park et al., 2011). A concurrent TMS-fMRI study indicated that the contralateral premotor area might support the residual motor function following stroke and have an increasing influence on the survived sensorimotor cortex in the ipsilesional hemisphere on subjects with more impairment (Bestmann et al., 2010), which may be the potential reason for the increased FC between the iM1 and premotor area after training. Besides, the FC between iSMA and bilateral SPL also increased, according to the current study. During both motor imagery and motor execution, SPL is activated (Guillot et al., 2012), although not exactly overlapping with each other. The MI-based BCI training in our study decoded the sensorimotor EEG signals to trigger the robotic hand, offering rich afferent neural feedback. The whole training process involved these modulated brain regions and hence, promoting motor relearning during the training.

Investigating different dimensions of resting-state BOLD activity is important, as differences may lie not only in the patterns of connectivity but also the power of local neuronal activity. Apart from the FC, we also investigate the changes in

fALFF. While FC measures the temporal correlation between the activations at two given regions, the fALFF measures the power of low-frequency fluctuations, which allows us to study the amplitude of regional neuronal activity. As different frequency bands originate from different neural sources, they could relate to different aspects of brain processing. With the oscillation in the range that is most closely related to gray matter signal, it shows the most extensive change after stroke (Zhu et al., 2015; Wang et al., 2020). A longitudinal study on stroke subjects showed that stroke survivors exhibited lower amplitude of oscillations in comparison to healthy controls in the subacute stage, and those same subjects showed a recovery of the oscillations, reaching near equivalence to the healthy controls (La et al., 2016). Another recent study on chronic stroke subjects suggested that motor imagery training plus conventional rehabilitation therapy-induced increased fALFF in the ipsilesional inferior parietal lobule, which is positively correlated with upper-limb motor function improvement (Wang et al., 2020). We found that the fALFF significantly increased in the ipsilesional precentral area and superior parietal lobule (SPL) immediately after the intervention, moreover, increases in the contralateral precentral area and ipsilesional superior frontal area were observed 6 months after the intervention. Interestingly, the significantly modulated regions in the fALFF analysis were quite consistent with the results from the FC analysis, which further validated each other. Other studies have also reported that brain regions in the fronto-parietal network were highly related to motor imagery BCI training (Cincotti et al., 2012), and correlated with the performance of MI-BCI (Zhang et al., 2016). Pichiorri et al. indicated that the BCI-supported MI training group showed more significantly increased connections over the MI-only group



between ipsilesional motor area and contralesional frontal and parietal areas in the beta band of resting-state EEG data, which were speculated as related to training effects (Pichiorri et al., 2015). In our study, significant modulated neural activities were observed not only in central regions but also in frontal and parietal regions, which were highly specific to BCI-guided robot hand training. These findings might suggest that the intervention could modulate the brain activities not limited to the sensorimotor network, but also in other regions associated with motor imagery and robot hand training.

This pilot study has shown the potential of the intervention for promoting hand function recovery and its long-term effect in chronic stroke survivors. fMRI might be able to provide insights into neural mechanisms underlying the recovery of motor function and reorganization of brain networks. Our findings provide some insights into the effects on neuroplasticity changes induced by the BCI-guided upper-limb training. Several limitations need to be stated in this study. First of all, the current study lacks a control condition. In order to differentiate the effects brought by volitional BCI based training and pure robot hand training, a control condition is needed. Second, the sample

size is relatively small which might limit the generalization power. More subjects should be recruited to validate and extend the findings of this study.

## DATA AVAILABILITY STATEMENT

The raw data supporting the conclusions of this article will be made available by the authors, without undue reservation.

## ETHICS STATEMENT

The studies involving human participants were reviewed and approved by The Joint Chinese University of Hong Kong-New Territories East Cluster Clinical Research Ethics Committee. The patients/participants provided their written informed consent to participate in this study.

## AUTHOR CONTRIBUTIONS

CL, KY, and RT made substantial contributions to data analysis and drafting the manuscript. CL and

W-wW contributed to experimental design and data collection. PW, WC, and TL offered their expert advice in screening the subjects and interpreting the results. All authors contributed to the article and approved the submitted version.

## REFERENCES

- Bajaj, S., Butler, A. J., Drake, D., and Dhamala, M. (2015). Brain effective connectivity during motor-imagery and execution following stroke and rehabilitation. *Neuroimage Clin.* 8, 572–582. doi: 10.1016/j.nicl.2015.06.006
- Bestmann, S., Swayne, O., Blankenburg, F., Ruff, C. C., Teo, J., Weiskopf, N., et al. (2010). The role of contralesional dorsal premotor cortex after stroke as studied with concurrent TMS-fMRI. *J. Neurosci.* 30:11926. doi: 10.1523/JNEUROSCI.5642-09.2010
- Biasiucci, A., Leeb, R., Iturrate, I., Perdakis, S., Al-Khodairy, A., Corbet, T., et al. (2018). Brain-actuated functional electrical stimulation elicits lasting arm motor recovery after stroke. *Nat. Commun.* 9:2421. doi: 10.1038/s41467-018-04673-z
- Carino-Escobar, R. I., Carrillo-Mora, P., Valdés-Cristerna, R., Rodríguez-Barragan, M. A., Hernández-Arenas, C., Quinzaños-Fresnedo, J., et al. (2019). Longitudinal analysis of stroke patients' brain rhythms during an intervention with a brain-computer interface. *Neural Plast.* 2019, 7084618–7084618. doi: 10.1155/2019/7084618
- Carter, A. R., Shulman, G. L., and Corbetta, M. (2012). Why use a connectivity-based approach to study stroke and recovery of function? *Neuroimage* 62, 2271–2280. doi: 10.1016/j.neuroimage.2012.02.070
- Cervera, M. A., Soekadar, S. R., Ushiba, J., Millán, J. D. R., Liu, M., Birbaumer, N., et al. (2018). Brain-computer interfaces for post-stroke motor rehabilitation: a meta-analysis. *Ann. Clin. Transl. Neurol.* 5, 651–663. doi: 10.1002/acn3.544
- Chen, X., Lu, B., and Yan, C.-G. (2018). Reproducibility of R-fMRI metrics on the impact of different strategies for multiple comparison correction and sample sizes. *Hum. Brain Mapp.* 39, 300–318. doi: 10.1002/hbm.23843
- Chen, Y.-C., Xia, W., Luo, B., Muthaiah, V. P. K., Xiong, Z., Zhang, J., et al. (2015). Frequency-specific alterations in the amplitude of low-frequency fluctuations in chronic tinnitus. *Front. Neural Circuits* 9:67. doi: 10.3389/fncir.2015.00067
- Cho, W., Heilinger, A., Ortner, R., Murovec, N., Xu, R., Zehetner, M., et al. (2019). “Feasibility of brain-computer interface triggered functional electrical stimulation and avatar for motor improvement in chronic stroke patients,” in: *Converging Clinical and Engineering Research on Neurorehabilitation III*, eds. L. Masia, S. Micera, M. Akay, and J. L. Pons (Pisa: Springer International Publishing), 1097–1100.
- Cincotti, F., Pichiorri, F., Aricò, P., Aloise, F., Leotta, F., Fallani, F. D. V., et al. (2012). “EEG-based brain-computer interface to support post-stroke motor rehabilitation of the upper limb,” in: *2012 Annual International Conference of the IEEE Engineering in Medicine and Biology Society*, 4112–4115.
- Daly, J. J., and Wolpaw, J. R. (2008). Brain-computer interfaces in neurological rehabilitation. *Lancet Neurol.* 7, 1032–1043. doi: 10.1016/S1474-4422(08)70223-0
- Egorova, N., Veldsman, M., Cumming, T., and Brodtmann, A. (2017). Fractional amplitude of low-frequency fluctuations (fALFF) in post-stroke depression. *Neuroimage Clin.* 16, 116–124. doi: 10.1016/j.nicl.2017.07.014
- Friston, K. J., Williams, S., Howard, R., Frackowiak, R. S. J., and Turner, R. (1996). Movement-related effects in fMRI time-series. *Magn. Reson. Med.* 35, 346–355. doi: 10.1002/mrm.1910350312
- Frolov, A. A., Mokienco, O., Lyukmanov, R., Biryukova, E., Kotov, S., Turbina, L., et al. (2017). Post-stroke rehabilitation training with a motor-imagery-based brain-computer interface (BCI)-controlled hand exoskeleton: a randomized controlled multicenter trial. *Front. Neurosci.* 11:400. doi: 10.3389/fnins.2017.00400
- Fugl-Meyer, A. R., Jääskö, L., Leyman, I., Olsson, S., and Steglind, S. (1975). The post-stroke hemiplegic patient. 1. a method for evaluation of physical performance. *Scand. J. Rehabil. Med.* 7, 13–31.
- Grefkes, C., and Fink, G. R. (2014). Connectivity-based approaches in stroke and recovery of function. *Lancet Neurol.* 13, 206–216. doi: 10.1016/S1474-4422(13)70264-3
- Guillot, A., Hoyek, N., Louis, M., and Collet, C. (2012). Understanding the timing of motor imagery: recent findings and future directions. *Int. Rev. Sport Exerc. Psychol.* 5, 3–22. doi: 10.1080/1750984X.2011.623787
- Hanakawa, T., Dimyan, M. A., and Hallett, M. (2008). Motor planning, imagery, and execution in the distributed motor network: a time-course study with functional MRI. *Cerebral Cortex* 18, 2775–2788. doi: 10.1093/cercor/bhn036
- Hsieh, Y.-W., Lin, K.-C., Wu, C.-Y., Shih, T.-Y., Li, M.-W., and Chen, C.-L. (2018). Comparison of proximal versus distal upper-limb robotic rehabilitation on motor performance after stroke: a cluster controlled trial. *Sci. Rep.* 8:2091. doi: 10.1038/s41598-018-20330-3
- Khan, A., Chen, C., Yuan, K., Wang, X., Mehra, P., Liu, Y., et al. (2020). Changes in electroencephalography complexity and functional magnetic resonance imaging connectivity following robotic hand training in chronic stroke. *Top. Stroke Rehabil.* 1–13. doi: 10.1080/10749357.2020.1803584
- Kimberley, T. J., Khandekar, G., and Borich, M. (2008). fMRI reliability in subjects with stroke. *Exp. Brain Res.* 186, 183–190. doi: 10.1007/s00221-007-1221-8
- Kwakkel, G., Kollen, B., and Twisk, J. (2006). Impact of time on improvement of outcome after stroke. *Stroke* 37, 2348–2353. doi: 10.1161/01.STR.0000238594.91938.1e
- La, C., Mossahebi, P., Nair, V. A., Young, B. M., Stamm, J., Birn, R., et al. (2016). Differing patterns of altered slow-5 oscillations in healthy aging and ischemic stroke. *Front. Hum. Neurosci.* 10:156. doi: 10.3389/fnhum.2016.00156
- Loubinoux, I., Carel, C., Pariente, J., Dechaumont, S., Albuher, J.-F., Marque, P., et al. (2003). Correlation between cerebral reorganization and motor recovery after subcortical infarcts. *Neuroimage* 20, 2166–2180. doi: 10.1016/j.neuroimage.2003.08.017
- Lyle, R. C. (1981). A performance test for assessment of upper limb function in physical rehabilitation treatment and research. *Int. J. Rehabil. Res.* 4, 483–492. doi: 10.1097/00004356-198112000-00001
- Mane, R., Chouhan, T., and Guan, C. (2020). BCI for stroke rehabilitation: motor and beyond. *J. Neural Eng.* 17:041001. doi: 10.1088/1741-2552/aba162
- Mrachacz-Kersting, N., Stevenson, A. J. T., Jørgensen, H. R. M., Severinsen, K. E., Aliakbarhosseiniabadi, S., Jiang, N., et al. (2019). Brain state-dependent stimulation boosts functional recovery following stroke. *Ann. Neurol.* 85, 84–95. doi: 10.1002/ana.25375
- Müller-Putz, G., Scherer, R., Brunner, C., Leeb, R., and Pfurtscheller, G. (2008). Better than random? a closer look on BCI results. *Int. Bioelektromagn.* 10, 52–55. Available online at: <http://www.ijbem.org/volume10/number1/52-55.pdf>
- Neuper, C., Scherer, R., Wriessnegger, S., and Pfurtscheller, G. (2009). Motor imagery and action observation: modulation of sensorimotor brain rhythms during mental control of a brain-computer interface. *Clin. Neurophysiol.* 120, 239–247. doi: 10.1016/j.clinph.2008.11.015
- Norouzi-Gheidari, N., Archambault, P. S., and Fung, J. (2012). Effects of robot-assisted therapy on stroke rehabilitation in upper limbs: systematic review and meta-analysis of the literature. *J. Rehabil. Res. Dev.* 49, 479–496. doi: 10.1682/JRRD.2010.10.0210
- Ono, T., Shindo, K., Kawashima, K., Ota, N., Ito, M., Ota, T., et al. (2014). Brain-computer interface with somatosensory feedback improves functional recovery from severe hemiplegia due to chronic stroke. *Front. Neuroeng.* 7:19. doi: 10.3389/fneng.2014.00019
- Page, S. J., Fulk, G. D., and Boyne, P. (2012). Clinically important differences for the upper-extremity Fugl-Meyer scale in people with minimal to moderate impairment due to chronic stroke. *Phys. Ther.* 92, 791–798. doi: 10.2522/ptj.20110009
- Park, C.-H., Chang Won, H., Ohn Suk, H., Kim Sung, T., Bang Oh, Y., Pascual-Leone, A., et al. (2011). Longitudinal changes of resting-state functional connectivity during motor recovery after stroke. *Stroke* 42, 1357–1362. doi: 10.1161/STROKEAHA.110.596155

## FUNDING

This work was supported by the Research Grants Council (Project No. 14204315) in Hong Kong Special Administrative Region Government.

- Perry, A., and Bentin, S. (2009). Mirror activity in the human brain while observing hand movements: a comparison between EEG desynchronization in the  $\mu$ -range and previous fMRI results. *Brain Res.* 1282, 126–132. doi: 10.1016/j.brainres.2009.05.059
- Pichiorri, F., Morone, G., Petti, M., Toppi, J., Pisotta, I., Molinari, M., et al. (2015). Brain–computer interface boosts motor imagery practice during stroke recovery. *Ann. Neurol.* 77, 851–865. doi: 10.1002/ana.24390
- Power, J. D., Barnes, K. A., Snyder, A. Z., Schlaggar, B. L., and Petersen, S. E. (2012). Spurious but systematic correlations in functional connectivity MRI networks arise from subject motion. *Neuroimage* 59, 2142–2154. doi: 10.1016/j.neuroimage.2011.10.018
- Qian, Q., Nam, C., Guo, Z., Huang, Y., Hu, X., Ng, S. C., et al. (2019). Distal versus proximal - an investigation on different supportive strategies by robots for upper limb rehabilitation after stroke: a randomized controlled trial. *J. Neuroeng. Rehabil.* 16:64. doi: 10.1186/s12984-019-0537-5
- Ramos-Murguialday, A., Broetz, D., Rea, M., Läer, L., Yilmaz, Ö., Brasil, F. L., et al. (2013). Brain–machine interface in chronic stroke rehabilitation: a controlled study. *Ann. Neurol.* 74, 100–108. doi: 10.1002/ana.23879
- Ramos-Murguialday, A., Curado, M. R., Broetz, D., Yilmaz, Ö., Brasil, F. L., Liberati, G., et al. (2019). Brain-machine interface in chronic stroke: randomized trial long-term follow-up. *Neurorehabil. Neural Repair* 33, 188–198. doi: 10.1177/1545968319827573
- Remsik, A. B., Williams, L., Gjini, K., Dodd, K., Thoma, J., Jacobson, T., et al. (2019). Ipsilesional Mu rhythm desynchronization and changes in motor behavior following post stroke BCI intervention for motor rehabilitation. *Front. Neurosci.* 13:53. doi: 10.3389/fnins.2019.00053
- Seitz, R. J., Huang, Y., Knorr, U., Tellmann, L., Herzog, H., and Freund, H.-J. (1995). Large-scale plasticity of the human motor cortex. *Neuroreport* 6, 742–744. doi: 10.1097/00001756-199503270-00009
- Sharma, N., Baron, J.-C., and Rowe, J. B. (2009). Motor imagery after stroke: Relating outcome to motor network connectivity. *Ann. Neurol.* 66, 604–616. doi: 10.1002/ana.21810
- Soekadar, S. R., Silvoni, S., Cohen, L. G., and Birbaumer, N. (2015). “Brain–machine interfaces in stroke neurorehabilitation,” in *Clinical Systems Neuroscience*, eds. K. Kansaku, L. G. Cohen, and N. Birbaumer (Tokyo: Springer Japan), 3–14.
- Tombari, D., Loubinoux, I., Pariente, J., Gerdelat, A., Albucher, J.-F., Tardy, J., et al. (2004). A longitudinal fMRI study: in recovering and then in clinically stable sub-cortical stroke patients. *Neuroimage* 23, 827–839. doi: 10.1016/j.neuroimage.2004.07.058
- Tong, K. Y., Pang, P. M. K., Chen, M., Ho, S. K., Zhou, H., and Chan, D. T. W. (2013). Wearable power assistive device for helping a user to move their hand. *United States Patent US12/472,295*. United States Patent and Trademark Office.
- Van Den Heuvel, M. P., and Hulshoff Pol, H. E. (2010). Exploring the brain network: a review on resting-state fMRI functional connectivity. *Eur. Neuropsychopharmacol.* 20, 519–534. doi: 10.1016/j.euroneuro.2010.03.008
- Van Der Lee, J. H., De Groot, V., Beckerman, H., Wagenaar, R. C., Lankhorst, G. J., and Bouter, L. M. (2001). The intra- and interrater reliability of the action research arm test: a practical test of upper extremity function in patients with stroke. *Arch. Phys. Med. Rehabil.* 82, 14–19. doi: 10.1053/apmr.2001.18668
- Van Dokkum, L. E. H., Ward, T., and Laffont, I. (2015). Brain computer interfaces for neurorehabilitation—its current status as a rehabilitation strategy post-stroke. *Ann. Phys. Rehabil. Med.* 58, 3–8. doi: 10.1016/j.rehab.2014.09.016
- Van Essen, D. C., Ugurbil, K., Auerbach, E., Barch, D., Behrens, T. E. J., Bucholz, R., et al. (2012). The human connectome project: a data acquisition perspective. *Neuroimage* 62, 2222–2231. doi: 10.1016/j.neuroimage.2012.02.018
- Várkuti, B., Guan, C., Pan, Y., Phua, K. S., Ang, K. K., Kuah, C. W. K., et al. (2012). Resting state changes in functional connectivity correlate with movement recovery for BCI and robot-assisted upper-extremity training after stroke. *Neurorehabil. Neural Repair* 27, 53–62. doi: 10.1177/1545968312445910
- Wang, X., Wang, H., Xiong, X., Sun, C., Zhu, B., Xu, Y., et al. (2020). Motor imagery training after stroke increases slow-5 oscillations and functional connectivity in the ipsilesional inferior parietal lobule. *Neurorehabil. Neural Repair* 34, 321–332. doi: 10.1177/1545968319899919
- Woodbury, M. L., Velozo, C. A., Richards, L. G., and Duncan, P. W. (2013). Rasch analysis staging methodology to classify upper extremity movement impairment after stroke. *Arch. Phys. Med. Rehabil.* 94, 1527–1533. doi: 10.1016/j.apmr.2013.03.007
- Yan, C.-G., Wang, X.-D., Zuo, X.-N., and Zang, Y.-F. (2016). DPABI: data processing & analysis for (resting-state) brain imaging. *Neuroinformatics* 14, 339–351. doi: 10.1007/s12021-016-9299-4
- Yuan, K., Wang, X., Chen, C., Lau, C. C. Y., Chu, W. C. W., and Tong, R. K. Y. (2020). Interhemispheric functional reorganization and its structural base after BCI-guided upper-limb training in chronic stroke. *IEEE Trans. Neural Syst. Rehabil. Eng.* 28, 2525–2536. doi: 10.1109/TNSRE.2020.3027955
- Zhang, T., Liu, T., Li, F., Li, M., Liu, D., Zhang, R., et al. (2016). Structural and functional correlates of motor imagery BCI performance: insights from the patterns of fronto-parietal attention network. *Neuroimage* 134, 475–485. doi: 10.1016/j.neuroimage.2016.04.030
- Zhu, J., Jin, Y., Wang, K., Zhou, Y., Feng, Y., Yu, M., et al. (2015). Frequency-dependent changes in the regional amplitude and synchronization of resting-state functional MRI in stroke. *PLoS ONE* 10:e0123850. doi: 10.1371/journal.pone.0123850
- Zou, Q.-H., Zhu, C.-Z., Yang, Y., Zuo, X.-N., Long, X.-Y., Cao, Q.-J., et al. (2008). An improved approach to detection of amplitude of low-frequency fluctuation (ALFF) for resting-state fMRI: fractional ALFF. *J. Neurosci. Methods* 172, 137–141. doi: 10.1016/j.jneumeth.2008.04.012
- Zuo, X.-N., Di Martino, A., Kelly, C., Shehzad, Z. E., Gee, D. G., Klein, D. F., et al. (2010). The oscillating brain: complex and reliable. *Neuroimage* 49, 1432–1445. doi: 10.1016/j.neuroimage.2009.09.037

**Conflict of Interest:** RT is one of the inventors of the Hong Kong Polytechnic University-held patent for the hand exoskeleton robot which was used in this study. All authors, however, are of no financial relationship whatsoever for the submitted work with Rehab-Robotics Company Ltd., the company which manufactures the commercial version of the original device under a license agreement with the University.

Copyright © 2021 Lau, Yuan, Wong, Chu, Leung, Wong and Tong. This is an open-access article distributed under the terms of the Creative Commons Attribution License (CC BY). The use, distribution or reproduction in other forums is permitted, provided the original author(s) and the copyright owner(s) are credited and that the original publication in this journal is cited, in accordance with accepted academic practice. No use, distribution or reproduction is permitted which does not comply with these terms.



# Formulation of the Challenges in Brain-Computer Interfaces as Optimization Problems—A Review

Shireen Fathima<sup>1\*</sup> and Sheela Kiran Kore<sup>2</sup>

<sup>1</sup> Department of Electronics and Communication Engineering, HKBK College of Engineering, Bengaluru, India, <sup>2</sup> Department of Electronics and Communication Engineering, KLE Dr. M. S. Sheshagiri College of Engineering and Technology, Belgaum, India

## OPEN ACCESS

### Edited by:

Haider Raza,  
University of Essex, United Kingdom

### Reviewed by:

Veena A. Nair,  
University of Wisconsin-Madison,  
United States  
Yasunari Hashimoto,  
Kitami Institute of Technology, Japan

### \*Correspondence:

Shireen Fathima  
shireen.fathima6@gmail.com

### Specialty section:

This article was submitted to  
Brain Imaging Methods,  
a section of the journal  
Frontiers in Neuroscience

**Received:** 29 March 2020

**Accepted:** 18 December 2020

**Published:** 21 January 2021

### Citation:

Fathima S and Kore SK (2021)  
Formulation of the Challenges in  
Brain-Computer Interfaces as  
Optimization Problems—A Review.  
*Front. Neurosci.* 14:546656.  
doi: 10.3389/fnins.2020.546656

Electroencephalogram (EEG) is one of the common modalities of monitoring the mental activities. Owing to the non-invasive availability of this system, its applicability has seen remarkable developments beyond medical use-cases. One such use case is brain-computer interfaces (BCI). Such systems require the usage of high resolution-based multi-channel EEG devices so that the data collection spans multiple locations of the brain like the occipital, frontal, temporal, and so on. This results in huge data (with high sampling rates) and with multiple EEG channels with inherent artifacts. Several challenges exist in analyzing data of this nature, for instance, selecting the optimal number of EEG channels or deciding what best features to rely on for achieving better performance. The selection of these variables is complicated and requires a lot of domain knowledge and non-invasive EEG monitoring, which is not feasible always. Hence, optimization serves to be an easy to access tool in deriving such parameters. Considerable efforts in formulating these issues as an optimization problem have been laid. As a result, various multi-objective and constrained optimization functions have been developed in BCI that has achieved reliable outcomes in device control like neuro-prosthetic arms, application control, gaming, and so on. This paper makes an attempt to study the usage of optimization techniques in formulating the issues in BCI. The outcomes, challenges, and major observations of these approaches are discussed in detail.

**Keywords:** electroencephalogram, brain-computer interface, optimization, evolutionary algorithms, review of EEG

## 1. INTRODUCTION

Brain computer interfaces (BCI) are an important application of electroencephalogram (EEG) signals (Navalyal and Gavvas, 2014). The usage of EEG signals in such an application other than medical use cases is due to the availability of affordable EEG devices. Also, the effectiveness of the algorithms used in the conventional BCI pipelines play a major role in this regard. In general, BCI system's pipeline consists of the following blocks: pre-processing of the EEG data, event-related potential (ERP) analysis, extraction of features, and classification of data (Sinha et al., 2015b), and so on. The effectiveness of these blocks can be measured as a function of time complexity, computational resources required, and the accuracy of the algorithms. With respect to enhancing the accuracy of the algorithms, various attempts have been laid in making them robust by finding optimal tuning parameters for them. This is however, not a straight forward task as designing of effective objective functions and the choice of optimization problems is a very challenging task. Hence, there is a rich

source of EEG and BCI literature that mainly focuses on using optimization techniques and their enhanced variants in the BCI pipelines. This paper aims at studying the usage of optimization from the view point of the application in BCI, i.e., with respect to the standard BCI pipelines.

Optimization schemes play a major role in most of the engineering problems where direct understanding of the system is not feasible. In case of EEG analysis, it is difficult to ascertain the exact locations of the neuronal firings owing to volume conduction. Invasive EEG can aid in this regard but cannot be applied in day-to-day scenarios for all the participants. In such cases, the domain knowledge can be of great help but in the lack of this knowledge for novel BCI systems, arriving at proper tuning parameters of BCI is very difficult. The system needs to be tested over a large set of parameters available by repeating the experiments for multiple times, which again is not a practical solution. This has motivated the BCI community to adopt optimization schemes in their pipelines.

The usage of optimization techniques in BCI applications requires the proper understanding of the objectives and the domain knowledge plays a vital role here. For instance, in the EEG channel selection problem, the domain knowledge would make the analyst to select the channels which are relevant to the task type. However, it can be seen that optimization tools would recommend some other channels but would enhance the accuracy of the BCI much more than what the domain knowledge-based channel selection might have done. But this set of channels might not be consistent across participants. Hence, it is necessary to have well-defined objective functions while using the optimization algorithms. This study summarizes the BCI applications that have used optimization and also the parameters of BCI are reviewed in detail. This would aid the reader in appreciating the essence of optimization in BCI-based applications.

The rest of the paper is organized as follows. Section 2 of the paper reviews the existing literature that uses optimization in various BCI pipelines. Section 3 discusses the challenges involved in adopting optimization schemes in BCI. Section 4 summarizes the paper and also the possible medical use cases of optimization in EEG analysis. The paper concludes in section 5 with pointers to the guidelines in using optimization techniques in BCI.

## 2. FORMULATION OF OPTIMIZATION PROBLEMS IN BCI

Optimization is a technique that is performed by comparing different solutions to find an optimal solution. Such algorithms aim to maximize or minimize an error function (usually termed as an objective function). The objective function is a representative of the model's tuning parameters. Optimization has seen tremendous applications in various branches of science and engineering. Optimization techniques helps to arrive at optimal parameters in the lack of domain knowledge or when it is not feasible to test the system directly. For instance, in case of EEG feature selection for a novel stimulus, the physical

interpretations of most of the non-linear, time/frequency features is not possible with respect to the task.

The underlying mechanisms of converging toward an optimal solution in case of optimization is very well correlated to various naturally occurring phenomena. Hence, over the past few decades, researches have been motivated from nature in designing such algorithms. Such algorithms are termed as evolutionary algorithms which is a form of stochastic optimization. Most widely used evolutionary algorithms are Particles Swarm Optimization (PSO), Genetic Algorithm (GA), Differential evolution (DE), Ant Colony Optimization (ACO), Artificial Bee Colony (ABC), and so on. We noticed that most of the BCI-based applications have made use of evolutionary algorithms in deriving the optimal tuning parameters for various BCI pipelines.

The following section reviews the formulation of optimization problems around building efficient BCI pipelines. It is to be noted that during this review, we came across various datasets like motor imagery (MI), emotion recognition, visual evoked potential (VEP), sleep apnea detection, mental, or cognitive tasks, ERP analysis, and so on. We also found that the task of EEG classification is mostly carried out using standard machine learning classifiers (having inbuilt optimization mechanisms) and hence, the explicit usage of optimization (by the researchers) is missing in these cases. Hence, we have excluded the EEG classification block in this review.

### 2.1. Optimization of EEG Pre-processing

Noisy signals occurring due to multiple factors during EEG data collection contaminates the signal. The noises inherent in EEG can be classified as follows (Zhang et al., 2016):

#### (i) Technical artifacts

1. Electrode related artifacts: The noise related to electrodes can be due to improper placement, electrode slippage, varying impedance, poor condition of the sensors, and so on. Usually the wet electrodes, if not cleaned properly, gets rusted, and deteriorates the signal.
2. Sweating: The sweating on the scalp can vary the impedance of the electrodes and lead to unwanted artifacts in the signal.
3. Power line interference: strong signals resulting from A/C supplies contaminates the signal which basically adds a sharp peak at around 50/60 Hz.

#### (ii) Physiological Artifacts

1. Electrooculogram (EOG) artifacts: These are mainly caused due to eye blinks or eye movements which adds up as a high amplitude signal upon the EEG signal. This artifact mainly affects the frontal channels due to their vicinity from the eyes (Sinha et al., 2015a). Most of these artifacts falls below 4–5 Hz range (Gavas et al., 2020).
2. Electrocardiogram (ECG) artifacts: This mostly occur on the electrodes placed near to the blood vessels, thereby resulting in an unwanted signal centered around 1.2 Hz due to the contraction and the expansion of the vessels.
3. Electromyographic (EMG) artifacts: These artifacts are a result of various muscle movements from face and neck and

get accumulated on all the EEG channels. The frequency bandwidth of these signals is very large and mostly falls in the frequencies above 30 Hz.

The process of removing these noises from EEG is referred to as the pre-processing stage. Various studies to remove these noise exists, however, the number of studies using optimization schemes in this process is limited. This can be attributed to the nature of solving the EEG pre-processing problem. We pick some of the studies which have used optimization algorithms in this direction and the summary is presented in **Table 1**. The table summarizes the task type i.e., the type of artifact removal and the optimization algorithm used for that task.

The objective functions involved in optimization based EEG noise cleaning can be any of the following:

- *Minimizing the error between the desired and actual EEG* (Pereira et al., 2016).
- *For obtaining optimal tuning parameter weights for the filtering algorithms used.* These weights in turn are derived using the objective of minimizing the error as discussed above. For instance, Alyasseri et al. (2017) used optimization to obtain optimal wavelet parameters for signal denoising. The studies in Priyadharsini and Rajan (2014) and Suja Priyadharsini et al. (2016) showed the usage of optimization algorithms to enhance the capabilities of adaptive network-based fuzzy inference systems in denoising the EEG signals. Similarly, the authors in Quazi and Kahalekar (2017) used Firefly + Levenberg Marquardt optimization algorithms for tuning the neural networks to adaptively filter the artifacts from EEG.
- *Minimizing the mutual information (MI) between the actual EEG and the corrupted EEG.* The works of Gupta and Palaniappan (2011) showed the reduction in power spectral density of eye blink artifacts using genetic algorithms to minimize the MI between the corrupted and the desired EEG signal.

## 2.2. Optimization of ERP Extraction

Event related potential detection in EEG is an important part in the analysis of various mental activities. ERP is a special case of EEG analysis which is indicative of the direct effects of motor, sensory, or cognitive functions. The estimation of ERP is done by averaging the measurements over an ensemble of trials. This approach requires many trials in order to suppress the underlying noise in EEG. Filtering can solve the issue of noise removal to some extent but the filter parameters needs to be tuned based on the statistical properties of the signal. If the parameters are not tuned properly, it may then result in suppressing the ERPs in the EEG. Hence, optimization plays a very important role in this case. Adaptive filtering serves to be beneficial in this regard as noise cancelers (Ahirwal et al., 2012, 2013, 2014). The authors in Ahirwal et al. (2014) show that through ABC optimization, the performance of adaptive filtering can be enhanced as compared to the conventional LMS and RLS filtering. The objective function defined in Ahirwal et al. (2014) is the minimization of the mean squared error by selecting optimal weights in the adaptive filter.

## 2.3. Optimizing the Problem of Feature Selection

Feature vectors usually comprise of high dimensions and this makes the feature selection an important tool for the classification problems. The idea of feature selection can be categorized into three types (Liu et al., 2010), namely,

- *Filter method:* deals with selection of subset of features by analysing the data characteristics without involving the learning algorithm in the process. As a result, the advantage of these methods is that they do not have any bias toward the learning models. Examples of filter methods are Relief, Correlation-based Feature Selection, Consistency, C4.5, minimum redundancy–maximum relevance (mRmR) (Ramos et al., 2016) and so on.
- *Wrapper method:* selects the subset of features based on the performance of the features on the learning algorithm during the evaluation step. Examples involve using optimization techniques like GA with the objective of maximizing the cross validation accuracy (Bhattacharyya et al., 2014; Pal et al., 2014; Xu et al., 2014; Ramos et al., 2016; Baig et al., 2017; Liu et al., 2017; Ramos and Vellasco, 2018; Ghosh et al., 2019), classification error (Wang and Veluvolu, 2017), unsupervised classification (Kimovski et al., 2015), similarity score and clustering validity index (Bhattacharyya et al., 2013; Rakshit et al., 2013), or classifier parsimony Cimpanu et al. (2017).
- *Embedded method:* feature selection is incorporated as a part of the model's training process. The relevance of the features is found by evaluating their utility for optimizing the learning algorithm's objective function. The authors in Yin et al. (2017) used the maximization of geometric distance (margin between the targets) in the learning algorithm.

The design of filter methods is simple, i.e., they are either based on forward selection or backward elimination and feature testing criterion which is based on a certain criterion. Hence, they are easy to understand and to implement and thus they are fast in execution. Since, the wrapper and embedded methods are linked to the learning process, their accuracy is higher in comparison to the filter method. Embedded methods are basically a fusion of filter and wrapper methods. Wrappers typically use cross-validation kind of mechanisms for accuracy computation that prevents overfitting. This makes them slower and leads to lack of generality. However, most of the works are found to use the wrapper approach as it is easier to formulate the objective function as a wrapper when compared to a filter and also the accuracy provided by wrappers are higher. The works of Ramos et al. (2016) showed that wrapper methods are better over filters. These feature selection algorithms either return a subset of features or the weights that signify the relevance of the features. Hence, based on the output, the feature selection algorithms can be classified into subset selection or feature weighting.

The feature extraction stage of EEG analysis deals with extracting frequency and time domain features which can be used as the compact representation of the EEG data. This is then fed as an input to various machine learning-based classification blocks. The features extracted have high dimensionality (Kimovski et al.,

**TABLE 1** | Summary of optimization schemes in EEG artifact removal studies.

References	Task	EEG data	Optimization algorithm
Ahirwal et al. (2012)	Adaptive filtering	Simulated EEG and real VEP	PSO
Ahirwal et al. (2013)	Adaptive noise cancellation	Simulated VEP, real VEP, real sensorimotor evoked potential	PSO, ABC and Cuckoo search
Ahirwal et al. (2014)	Adaptive noise cancellation	MI	Bounded Range ABC
Priyadharsini and Rajan (2014)	EOG component removal from EEG	Simulated data	Variants of memetic algorithm and GA
Wang et al. (2010)	Trial pruning by removing artifacts	MI	GA
Gupta and Palaniappan (2011)	Eye blink artifact removal	BCI MI	Variant of GA
Alyasseri et al. (2017)	Power line and EMG noise removal	Various mental tasks	Hybrid $\beta$ -Hill climbing
Suja Priyadharsini et al. (2016)	EOG and ECG artifacts removal	Simulated data	Artificial immune system algorithm
Pereira et al. (2016)	EOG and EMG artifacts removal	Simulated data	Variant of GA
Quazi and Kahalekar (2017)	EMG, EOG and ECG artifacts removal	EEG added with sleep apnea ECG and EOG	Firefly + Levenberg Marquardt algorithm

**TABLE 2** | Summary of optimization in EEG-based feature selection studies.

References	Algorithm	Task	Accuracy	Number of classes
Rakshit et al. (2013)	Artificial bee colony	MI	64.29	2
Kimovski et al. (2015)	Parallel multi-objective optimization	MI	100	2, 3
Xu et al. (2014)	Particle swarm optimization	MI	78	2
Bhattacharyya et al. (2014)	DE	MI	99.41, 87.99	2
Pal et al. (2014)	Bacterial foraging algorithm	MI	80.29	2
Bhattacharyya et al. (2013)	DE variant	MI	94	3
Yin et al. (2017)	Transfer recursive feature elimination	Emotion classification	75+	2
Cimpanu et al. (2017)	Single and multi-objective Genetic algorithm	Memory load detection	<14% (Error rate)	2
Liu et al. (2017)	Firefly algorithm and learning automata	MI	70.2	4
Eslahi et al. (2019)	Genetic algorithm	MI	84 (max)	4
Fernandez-Fraga et al. (2018)	Ant colony optimization	SSVEP BCI	82.76	–
Wang and Veluvolu (2017)	Evolutionary algorithm	MI	83	4
Ramos et al. (2016)	Genetic algorithm	MI	93.71	2
Baig et al. (2017)	Differential evolution	MI	95	3
Ghosh et al. (2019)	Grey wolf optimization	Silent speech classification	65	5
Ramos and Vellasco (2018)	Quantum- inspired evolutionary algorithm	MI	96.86	2
Selim et al. (2018)	hybrid bio-inspired algorithms	MI	78.55, 86.6,85	4,3,4

2015) that can increase the processing time and can result in the inclusion of outliers as features because of poor signal-to-noise ratio of EEG (Tacchino et al., 2020). These factors culminate in reduced accuracy of the BCI system. Hence, selection of appropriate subset of features is a vital step in the analysis of EEG data. In this stage, the features with enhanced discriminative power are used to carry out the further steps. It is to be noted that most of the times, the conventional feature selection algorithms aim to select features with high variances. This at times does not improve the overall accuracy of the system. The major reason could be the presence of redundant features. However, this problem is not a straight-forward task to solve. Many standard feature selection tools are available (Giorgio, 2020) to solve these issues. In the interest of the current paper's scope, the ones using optimization techniques in case of EEG are summarized in **Table 2**.

## 2.4. Optimization of EEG Channel Selection

For any EEG-based application, the selection of channels that is physiologically significant to the system in hand, is of paramount importance. The EEG data acquired is multichannel in nature. It is advisable to work on a subset of the channels instead of considering the whole. This is because, setting up the EEG system on a participant with many channels is cumbersome and time consuming. It also leads to the inconvenience of the participant which might reflect in lack of attention or distraction during the actual data collection. Apart from these subject-specific issues, this also adds to the increased computational complexity of the overall EEG application. Channel reduction is of great interest in designing portable EEG devices for detecting the onset of epileptic seizures hours before they prevail in order to provide early interventions. Such portable systems would need algorithms which are fast and the hardware smaller in

size. This makes the usage of channel selection an important research problem in the EEG community. The main objectives of EEG channel selection are: (i) Reduction in dimensionality and providing faster processing, (ii) improving the performance of the model created, and (iii) identification and localization of the brain regions that are responsible for the given activity. Many efforts have been laid toward this direction of achieving an optimal subset of channels. It was realized in the EEG research community that these optimal channel sets can be achieved more easily using optimization tools and this benefited more than considering the EEG channels that are known to be responsible for the task. For instance, the brain region corresponding to motor functions is located in the central region. Hence, it is more appealing to consider the central EEG channels for motor imagery-based analysis. However, due to volume conduction, the locations in the vicinity of central channels would also carry some information regarding the motor imagery. The overlap in information among these channels depends on several factors like the subjective nature of the skull shape, the type, and the sensitivity of the EEG used, and so on. Hence, instead of directly selecting the central channels for motor tasks, the selection of channels has to be personalized which can be done using optimization tools. **Table 3** surveys some of the most relevant works in this regard. The accuracy obtained for each of these approaches are also provided. Since, each of these studies used different EEG devices/datasets and subjects, we also report the improvement in accuracy over the state-of-the-art techniques (provided in brackets).

The optimal solution to EEG channel selection refers to a subset of channels that has highest relevance for the given stimulus/experiment. Innovative ways of looking at this problem can be formulated as a multi-objective function as follows,

- *Number of channels*: an obvious expectation is to have the minimum number of selected channels.
- *Region of interest (ROI)-based*: obtaining the candidate channels in the vicinity of the regions in brain that are known to produce the neurophysiological activations
- *Classification accuracy-based*: searching for channels that contributes in obtaining high accuracy of task classification. This can also be related to the case of having minimum error rate for the test set data.

It is important to note that for channel reduction/selection problems, the reduction of raw data plays a vital role in reducing the time and space consumption of the system. Downsampling allows the reduction of computational cost while retaining the vital information in the time-series data. As most relevant EEG activity lies in the range of 0.1–50 Hz, downsampling the signal from higher frequencies to 100 Hz is usually carried out in most of the studies like (Hasan and Gan, 2009; Hasan et al., 2010; He et al., 2013; Gonzalez et al., 2014; Shenoy and Vinod, 2014; Kee et al., 2015; Shan et al., 2015; Zhang and Wei, 2019; Arican and Polat, 2020). Though downsampling seems to be a straightforward approach, some studies reduced the data size by first extracting the features (as features are a compact way of looking at the data) and then the features were subjected to principal component analysis (PCA) to further reduce the

dimension. The studies mentioned in **Table 3** that used this approach are Ghaemi et al. (2017), Hasan and Gan (2009), Jin et al. (2008), and Kim et al. (2013). Few other studies like the ones in Hasan and Gan (2009), Hasan et al. (2010), used both the techniques to reduce the data size. The works by Yang et al. (2012) used time and frequency based feature analysis to reduce the dimension of the data.

## 2.5. EEG Mode Decomposition and Optimization

Mode decomposition of time series signals refers to decomposing a given signal into several realizations which differs in terms of morphological characteristics like frequency response from each other. The summation of all these realizations reproduces the original signal. The realizations are termed as intrinsic mode functions (IMFs). EEG signal mode decomposition becomes important to reconstruct or separate out various neuronal activities (Soler et al., 2020), source localization (Khosropanah et al., 2018), artifact removal (Wang et al., 2015), detection of seizures (Bajaj and Pachori, 2011), and so on.

Various studies have used signal decomposition algorithms like empirical mode decomposition (EMD), ensemble EMD (EEMD), variational mode decomposition (VMD), and so on to decompose physiological signals. Out of these, the VMD algorithm is based on solving an optimization function which in turn makes it robust against the existing mode decomposition algorithms (Gavas and et al., 2018). VMD basically looks at the problem of signal decomposition as an optimization problem by decomposing a 1-dimensional time series into  $K$  number of modes  $u_k(t)$  as,  $x(t) = \sum_{k=1}^K u_k(t)$ , with the criterion that the signal gets reconstructed ideally fully by summing up the  $K$  number of modes while the sum of bandwidths of all modes is kept minimum (Dragomiretskiy and Zosso, 2013). Every mode is compact along the mean frequency  $w_k$ . The method solves a constrained variational function to find optimal  $w_k$  and  $u_k$  given by,

$$\min \left\{ \left\| \sum_k \partial_t \left[ \left( \delta(t) + \frac{j}{\pi t} \right) * u_k(t) \right] e^{-j\omega_k t} \right\|_2^2 \right\} \\ \text{subject to } \sum_k u_k = x \quad (1)$$

The reader is requested to get the detailed explanation of the VMD algorithm from Dragomiretskiy and Zosso (2013). The number of IMFs extracted from the decomposing algorithms is mainly application dependent and is often restricted to a certain number by empirical analysis of the central frequencies of the IMFs. We summarize few of the applications wherein VMD or its variants were used (**Table 4**). Note the number of IMFs extracted in each of the case is different.

**TABLE 3** | Summary of optimization in EEG-based channel selection studies.

References	Algorithm	Task	Accuracy (improvement)	Number of classes	Data reduction
Jin et al. (2008)	Discreet particle swarm	Directional moving	77.54 (7.38)	4	Yes
Hasan and Gan (2009)	Multi-objective PSO	MI	57 (NA)	3	Yes
Hasan et al. (2010)	Multi-objective evolutionary algorithm based on decomposition	MI	58 (NA)	3	Yes
Handiru and Prasad (2016)	Iterative multi-objective optimization	MI	80 (7)	2	No
Yang et al. (2012)	Genetic neural mathematic method	MI	80, 86, 82 (NA)	2	Yes
Yang et al. (2013)	Time-spatial optimization	MI	78 (NA)	2	No
Shan et al. (2015)	A novel algorithm based on Relief	MI	85.2 (31.7), 94.1 (8), 83.2 (19.7)	2 and 4	Yes
Arican and Polat (2020)	Binary particle swarm optimization	Speller systems	90, 89.8(NA)	4	Yes
Lv and Liu (2008)	Common spatial pattern + Particle swarm optimization	MI	83,92(NA)	2	Yes
Kim et al. (2013)	Binary particle swarm optimization and GA	MI	78 (mean) and 67 (mean)	2	Yes
Kee et al. (2015)	Multi-objective genetic algorithm	P300 and MI	85+(5.25–8.60)	2	Yes
He et al. (2013)	Rayleigh coefficient maximization based genetic algorithm	MI	80+(NA)	2	Yes
Joseph and Govindaraju (2019)	Glow swarm optimization	MI	92.59 (6.31, 5.48)	2	No
Zhang and Wei (2019)	PSO	MI	91.94	2	Yes
Ghaemi et al. (2017)	Improved binary gravitation search	MI	76.24 (mean) 80 (max)	4	Yes
Shenoy and Vinod (2014)	Iterative optimization technique	MI	90.77 and 81.21	3 and 4	Yes
Arvaneh et al. (2011)	Sparse common spatial pattern	MI	80+(10)	2 and 2	No
Gonzalez et al. (2014)	Multi-objective hybrid real-binary particle swarm optimization	Auditory ERP	95 (6)	2	Yes
Jin et al. (2019)	Regularized common spatial pattern	MI	81.6 (25.2) 87.4 (10.9) 91.9 (6.8)	2,3,2	Yes

### 3. CHALLENGES INVOLVED IN OPTIMIZATION OF BCI PIPELINES

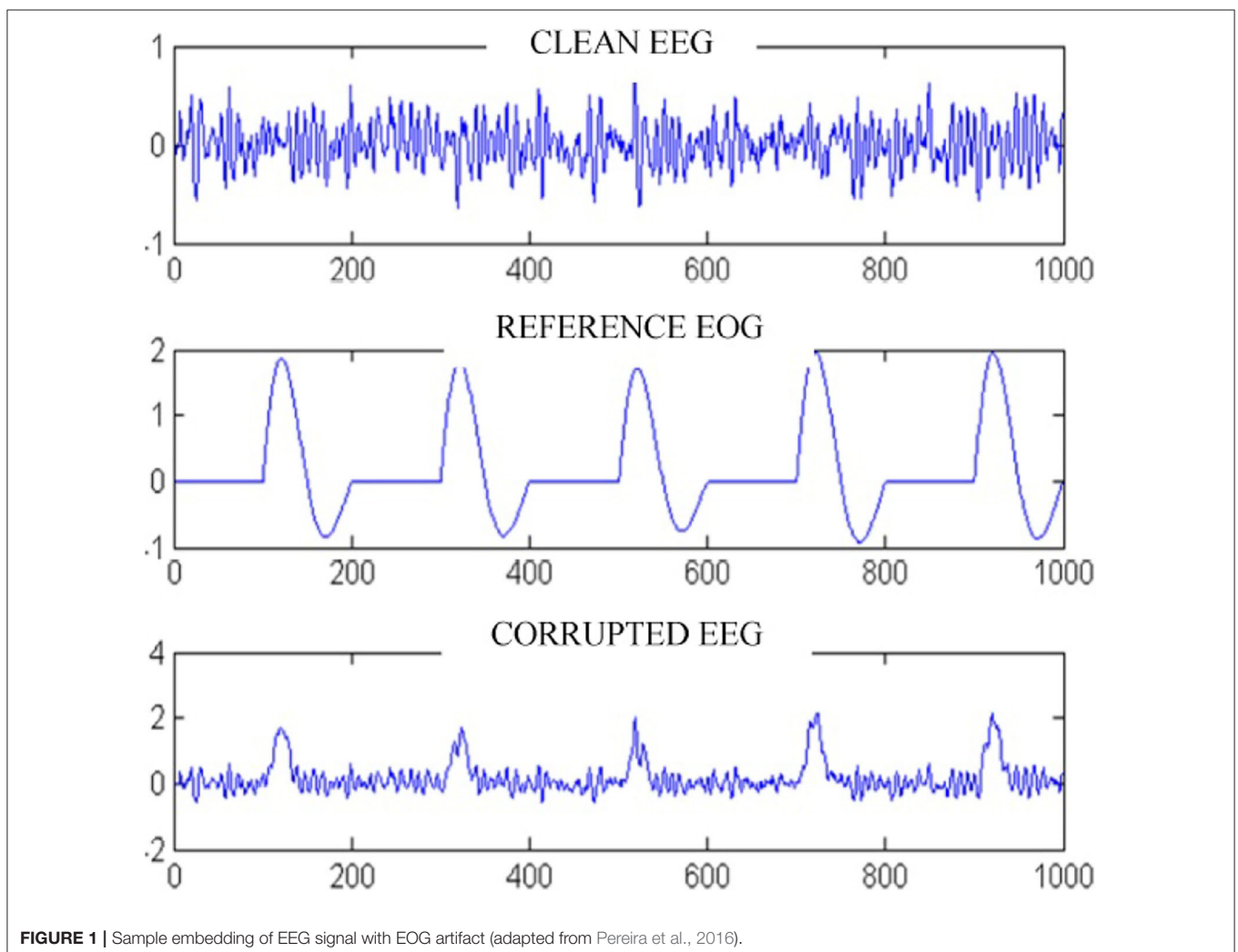
The main issue faced in any EEG-based artifact removal studies, particularly when it comes to the removal of other physiological effects like ECG, EOG from EEG is the absence of exact ground truth (Gavas et al., 2020). Usage of simulated data becomes a straightforward approach of validating the designed noise removal algorithms in such cases. **Figure 1** shows a typical approach of generating an EEG signal with an EOG artifact (Pereira et al., 2016). The simulated data can provide the exact start and stop events of the physiological artifact like blink and also the exact morphology of the artifact embedded onto the raw signal. The test

cases involving the simulated data performs better with the designed algorithms but the results degrade when it comes to real data. In such cases, the usage of conventional signal processing tools or even optimization-based data driven methods perform somewhat similar, as setting up the proper basis functions is difficult in such cases. However, mode decomposition algorithms are seen to be a better alternatives in such cases (Gavas et al., 2020) involving simulated or real EEG data.

Owing to the higher sampling rates and the increased number of channels in EEG, the amount of processing time and resources required for the EEG data is huge. For instance, decomposing a multi-channel EEG data with a high sampling rate using the MVMD (Rehman and Aftab, 2019) can be very

**TABLE 4** | Summary of papers using VMD in EEG signal analysis.

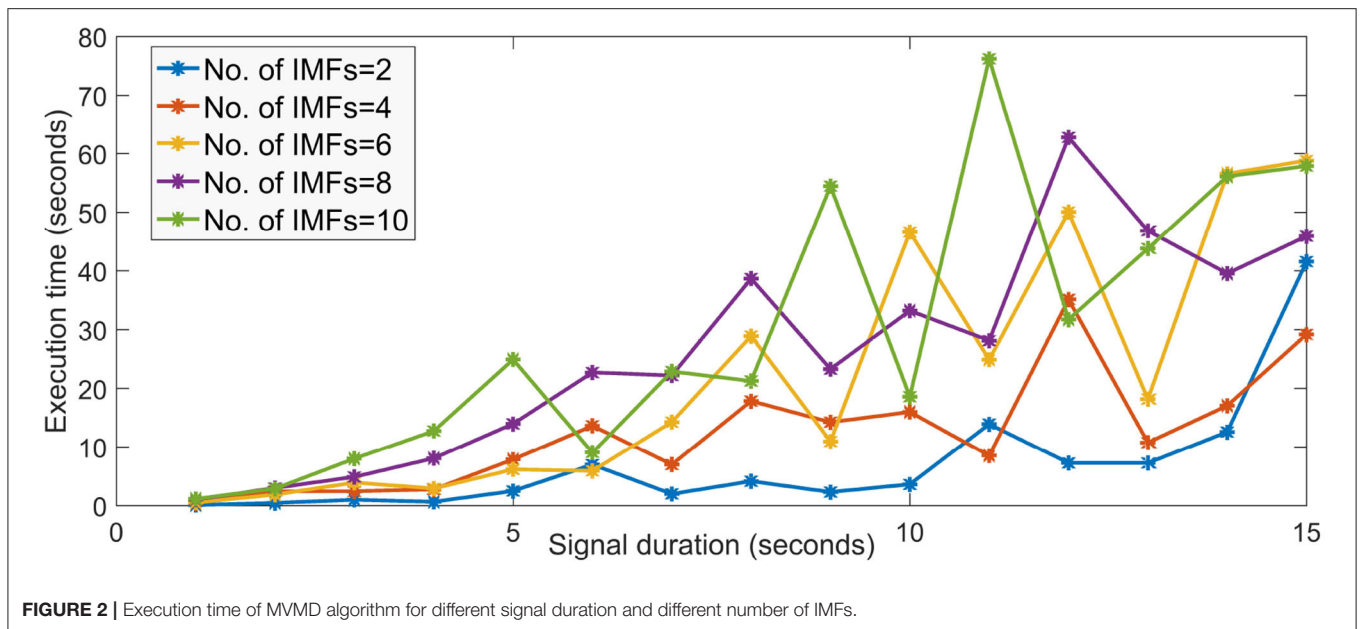
References	Task	No. of EEG channels	VMD type	No. of IMFs
Rehman and Aftab (2019)	Separation of alpha rhythms	4	Multivariate VMD	5
Gavas et al. (2020)	Blink artifact removal	4 and 57	Multivariate VMD	10
Zhang et al. (2017)	Feature extraction for Seizure detection	Single	Univariate VMD	15
Taran and Bajaj (2018)	Identification of focal EEG	Single	Clustering-VMD (univariate)	2
Bhattacharjee et al. (2018)	Sleep Apnea detection	Single	Univariate VMD	5
Dora and Biswal (2020a)	ECG artifact correction from EEG	Single	modified VMD (univariate)	12
Taran and Bajaj (2019)	Emotion recognition	10 out of 24 used	Univariate VMD	–
Dora and Biswal (2020b)	Ocular artifact suppression	5	Univariate VMD	12
Saini et al. (2019)	Ocular artifact removal	Single	Extended Univariate VMD	2 and 3
Saini et al. (2020)	Muscle artifact suppression	Single	Univariate VMD	2
Yücelbaş et al. (2018)	Detection of K-complexes	2	Univariate VMD	–

**FIGURE 1** | Sample embedding of EEG signal with EOG artifact (adapted from Pereira et al., 2016).

slow, computationally very complex and requires huge amount of memory.

To visualize, this, we ran the MATLAB implementation of the MVMD algorithm on a 4 GB RAM, core i5 processor machine

by simulating a 4-channel EEG data of various small duration. The execution time is as seen in **Figure 2**. It is to be noted that the execution time increases drastically as the signal duration and the number of IMFs increases. The number of channels also



plays a major role in determining the run time of the algorithm. For higher number of channels and signal duration, the required system memory and time is very large and cannot run on low configuration devices. Same is the case when dealing with such data using evolutionary algorithms which require atleast a good number of iterations (usually more than 100) to converge to a good solution. Also, the fear of converging lately or getting stuck in local minima can always be a major set back in using such optimization schemes in real time BCI.

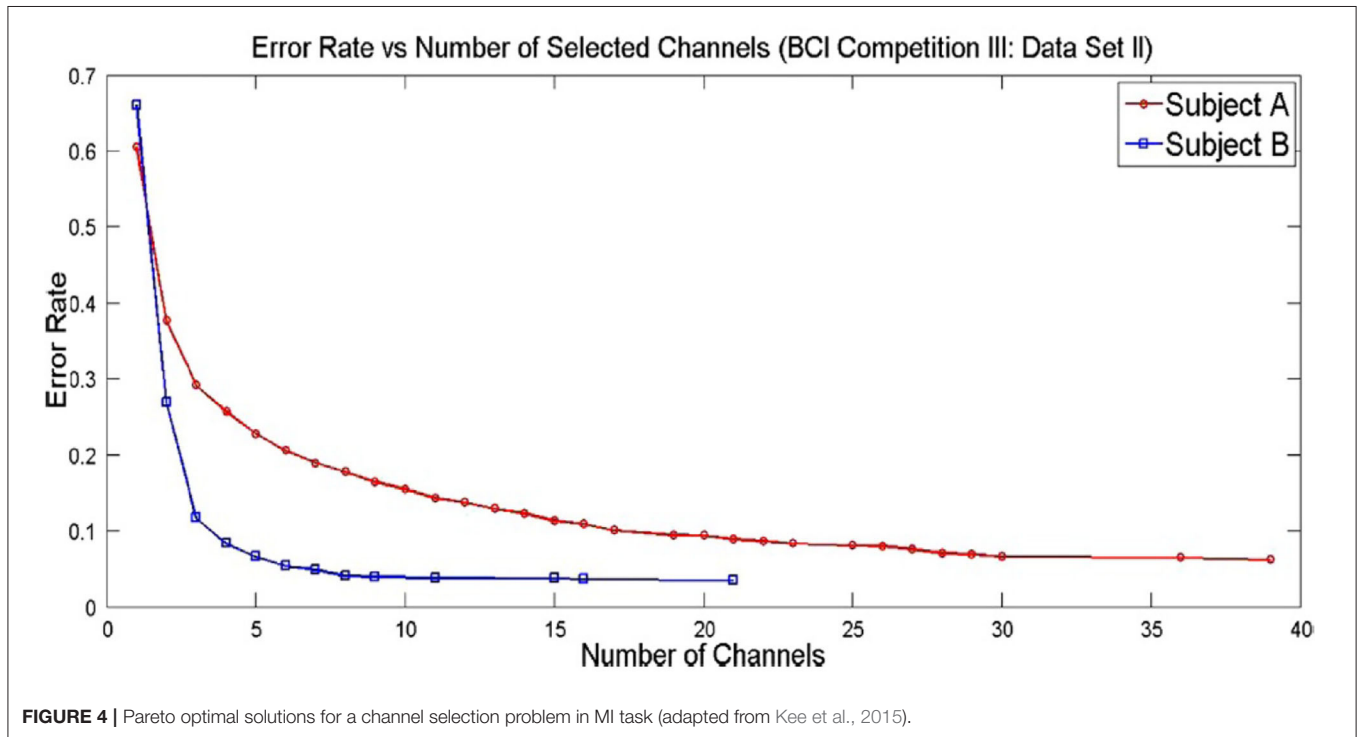
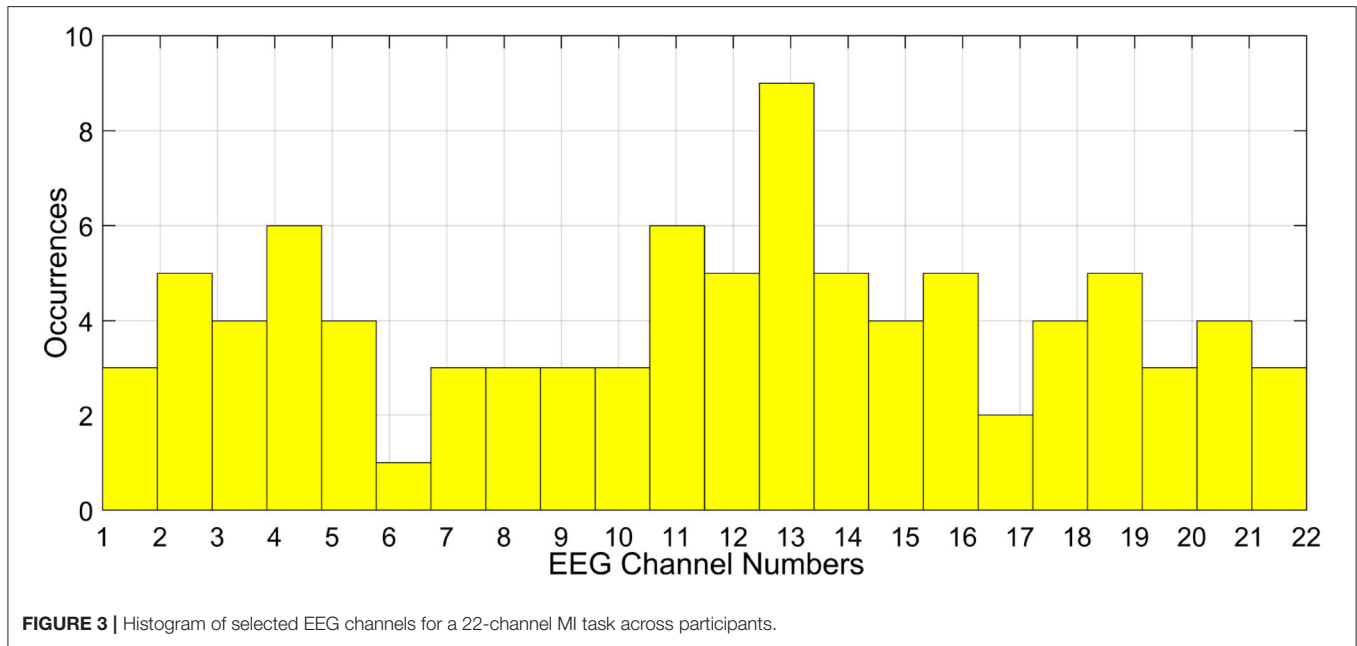
EEG signal mode decomposition is seen to be beneficial for various applications in BCI. However, as seen in **Table 4**, the number of IMFs extracted is not constant across studies even for the same BCI task. This inconsistency is commonly addressed as arising due to the nature of the application but the actual fact lies in the nature or the stochasticity of the EEG signal. If EEG signals were deterministic, then the frequency components across the same IMFs across different EEG data would be similar. This would have helped building new applications that make use of mode decomposition without investing much efforts on experimenting on the optimal number of IMF generation.

Consider the problem of EEG channel selection for MI tasks. By domain knowledge it is known that the central channels like C2, CZ, and C3 are well-suited for motor imagery related activities. However, due to the effect of volume conduction, the idea of relying on only the central channels is questionable. Owing to the subjective aspects like the skull size and the nature of EEG sensor, the channels picking up the motor imagery data faithfully, might vary from person to person. In such cases, the usage of personalized channel selection using optimization schemes seems to be an attractive idea (Shireen Fathima, 2019). The major challenge foreseen in this case is the design of the objective function to select the optimal channels. Even if this problem is tackled, the next major

issue lies in the selection of optimization algorithm and also initializing the tuning parameters of the algorithm. Researchers have mainly used meta-heuristic algorithms in such cases. As EEG signals are highly stochastic and non-linear in nature, different optimization algorithms can lead to the selection of different EEG channels, for the same participant and for the same task.

Even the consistency of channel selection across participants for a given optimization algorithm is not possible. For instance, we used the channel selection method (Khushaba et al., 2011) on a motor imagery BCI as mentioned in Shireen Fathima (2019) on a 22-channel EEG data. The resulting histogram of the selected channels across all the participants for the same task is given in **Figure 3**. The histogram is generated by considering the optimal channel ids for all the participants taken together. It is to be noted that in the figure, the channels are not consistent across all the participants and the generalization of channels is not possible. If same channels were selected as optimal channels, then the histogram would have centered over a small subset of channels. On similar grounds, the results change drastically when different optimization schemes are used for the said purpose. This can really make the task of arriving at a subset of generalized optimal channels to be used during real time BCI challenging, as no algorithm till date yields the same set of optimal channels for the same task and for the same participant.

Solving multi-objective functions of channel selection like least number of channels and least error rate leads to pareto solutions (as shown in **Figure 4**) and selecting a pareto optimal solution depends on the researcher or on the application. **Figure 4** shows the pareto solutions of error rates at the expense of number of channels (Kee et al., 2015). As the number of channels increase, there is a decrease in error rate. In such cases, it is tricky to settle down to a certain count of channels with a satisfactorily lower error rate.



### 4. DISCUSSIONS

Usage of optimization has recently gained wide popularity in EEG analysis, mainly in the field of feature selection and channel selection. This can be attributed to the fact that these two tasks are straightforward, majorly relying on the objective of maximizing accuracy of classification tasks. Though channel selection and feature extraction are means of selecting a subset of the data, however, they both vary considerably in nature.

Channel selection deals with selecting a subset of optimal channels whereas, feature selection deals with selection of a subset of optimal features. A common practice is to apply feature selection on the subset of optimal selected channels. The selected optimal channels can give insights on the source location of the task being performed. However, the selected features can help understand the signal specific characteristics of the underlying effect. Another common practice that we observed in this field is the usage of evolutionary algorithms.

**TABLE 5 |** Summary of optimization strategies employed in EEG analysis.

Task	Objective functions	Advantages	Disadvantages
Noise cleaning	(1) Minimize error	Output signal resembles desired signal	Knowledge of target signal characteristics is a must
	(2) Obtain tuning parameters		
	(3) Minimize mutual information		
ERP extraction	Minimize error in adaptive filters	Data driven	ERP components are prone to get distorted
Feature selection	(1) Filter method	Reduces overall system time complexity	Non repeatable set of features get selected
	(2) Wrapper method	Enhances accuracy	Only subject-specific selection
	(3) Embedded/Hybrid method		
Channel selection	(1) Minimum number of channels	Can lead to usage of low cost devices	Highly subjective
	(2) Region of interest-based	Enhances accuracy	Additional data reduction method required
	(3) Classification accuracy-based	Reduced system complexity	
Mode decomposition	(1) All modes sum up to form the original signal with least error	Decomposition based on frequency information	Increased time complexity
	(2) Sum of bandwidths of all modes is minimum		

Generally, when non-linear optimization schemes are deployed for EEG based problems, the objective function yields multiple local solutions in cases involving high dimensional search space and for lower values of signal-to-noise ratios. This has attracted the researchers to use meta-heuristic algorithms which work very well for such scenarios. Hence, it is obvious to find a rich source of EEG optimization literature involving meta-heuristic algorithms which is also evident in this review.

Selection of proper objective functions is crucial to any optimization-based problem solving. In case of EEG, this becomes more challenging owing to the non-stationary nature of the signal but at the same time, it comes with added advantages. **Table 5** summarizes the objective functions, its advantages and disadvantages in different EEG pipelines. It is evident that optimization when used in any given EEG pipeline comes with its own pros and cons. However, their widespread usage in current times shows the benefits that it has over their conventional counterparts.

As EEG is a very powerful diagnostic tool for detecting abnormal electrical discharges in the brain, its usage in the field

of medicine is inevitable. Optimization has been used in various ways in such EEG-based diagnosis process and hence, this section aims at throwing light on such applications.

One of the early implementations of genetic algorithm in epileptic EEG is found in Marchesi et al. (1997). The authors utilized genetic algorithm to detect the 3 Hz spikes and slow wave complexes in the EEG. The objective function involved the following

$$f = \text{fitness cases} - \text{hits} \tag{2}$$

where *fitness cases* corresponds to the total number of training examples and *hits* refer to the count of the matches. The stopping is thus when the count of the training cases equals to that of the hits or when the maximum number of generations are reached. An overall accuracy of 85% is seen with this setup.

The works in Wen and Zhang (2017) showed the usage of optimization in the frequency domain bin selection and in overall subset of feature selection in the analysis of epileptic EEG. A variant of genetic algorithm is used to first search for the optimal frequency ranges as features and then the features thus obtained are fused with non linear EEG features. The objective function thus aims at minimizing the linear discriminant analysis-based coefficients of the frequency bin summations done over an assortment of bins and traversed using certain constants called the slack variables. For the feature selection process, the objective function aims at minimizing the following,

$$\text{minimize}(FPR - (1 - TPR)) \tag{3}$$

where FPR is the false positive rate and TPR is the true positive rate.

The detection of epileptic seizures is attempted using grid search optimization as in Wang et al. (2019). The usage of optimization in this study was to tune the parameters of the random forest algorithm as it mainly generates a large number of hyperparameters and it is difficult to empirically arrive at the optimal values of these parameters. The targeted hyperparameters were number of decision trees, minimum sample leaf, maximum features, number of split features, and number of estimators. The objective function was to maximize the classification accuracy based on K-fold cross-validation technique. On similar grounds the work in Gomathi et al. (2020) worked toward detecting brain abnormalities arising due to brain stroke, brain tumor, birth defects, genetic mutation, and brain injuries using evolutionary gravitational neocognitron based optimization technique to obtain tuned parameters in a typical neural network classifier. Another attempt in optimizing a standard neural network classifier using genetic algorithm for detecting Alzheimer’s disease is in Kim et al. (2005). This study made use of a single channel EEG and used rest and auditory odd ball stimulus for generating event related potentials. Standard EEG features were derived

and the objective function confined to the NN architecture is used,

$$f = \frac{1}{N \times m} \sum_{i=1}^N \sum_{j=1}^m (NO_{ij} - DO_{ij})^2 \quad (4)$$

where  $NO$  is the network output and  $DO$  is the desired output.  $N$  is the number of training patterns and  $m$  is the number of output nodes of the network. The work in Singh et al. (2019) showed the optimization of parameters in an ensemble of classifier algorithms for the sake of classifying epileptic EEG. Thus, optimization has crucial role to play in the field of medical EEG analysis.

## 5. CONCLUSIONS

This paper summarizes the various optimization approaches in BCI pipelines. It is to be noted that evolutionary optimization techniques have been widely used in the domain of EEG signal analysis. The widely used evolutionary algorithms were GA, ABC, DE, PSO, and so on. It is to be noted that these algorithms were further enhanced so as to adapt to the use-cases in BCI. The usage of evolutionary algorithms for optimizing the parameters in BCI exceeds that of linear programming-based conventional tools of optimization. The reason being that the latter assumes the starting point of the search to be well-defined, whereas in case of evolutionary schemes, the starting point is selected heuristically.

Most of the existing literature on using optimization in BCI focuses mainly on optimal feature or channel selection, and a very few works dealing with EEG preprocessing or ERP detection using optimization are found. The review aims at providing the researches in the field to have a clear understanding of the techniques of optimization applied in BCI domain so far. As a guideline for using optimization in BCI, we observe that,

- Many optimization tools are readily available which can be either used directly for BCI uses-cases or needs to be enhanced so as to obtain better outcomes. The modification or enhancement of existing optimization tools requires a lot of expertise and skill in the field and should not be altered arbitrarily which could end up providing feasible solutions to a limited set of inputs.
- The nature of task and the area of using optimization techniques should be well-studied by using the existing literature. The tables summarizing the techniques and the application area can be used in this regard.
- The optimization problem should be designed carefully so as to match closely with the domain knowledge. In most of the cases, multiobjective optimization method is required and the confusion with pareto optimal solutions should be taken care of, effectively.
- Mode decomposition of EEG signals should be done using high end machines owing to the computational demands of the algorithms. In the absence of such systems, only small portions of EEG with fewer channels can be decomposed into fewer IMFs. The number of IMFs required should be judicious and the center frequencies of each of them should be assessed to avoid unwanted realizations of the signals.

The aim of this review is to help the researchers in knowing the state of existing attempts made in optimizing the BCI pipelines. We further encourage the readers to use the references for each of the pipelines for understanding the methodologies in detail.

## AUTHOR CONTRIBUTIONS

All authors listed have made a substantial, direct and intellectual contribution to the work, and approved it for publication.

## ACKNOWLEDGMENTS

We thank our institute for providing the necessary amenities for carrying out this work.

## REFERENCES

- Ahirwal, M. K., Kumar, A., and Singh, G. K. (2012). Analysis and testing of PSO variants through application in EEG/ERP adaptive filtering approach. *Biomed. Eng. Lett.* 2, 186–197. doi: 10.1007/s13534-012-0071-x
- Ahirwal, M. K., Kumar, A., and Singh, G. K. (2013). EEG/ERP adaptive noise canceller design with controlled search space (CSS) approach in cuckoo and other optimization algorithms. *IEEE/ACM Trans. Comput. Biol. Bioinformatics* 10, 1491–1504. doi: 10.1109/TCBB.2013.119
- Ahirwal, M. K., Kumar, A., and Singh, G. K. (2014). Adaptive filtering of EEG/ERP through bounded range artificial bee colony (BR-ABC) algorithm. *Digital Signal Process.* 25, 164–172. doi: 10.1016/j.dsp.2013.10.019
- Alyasseri, Z. A. A., Khader, A. T., and Al-Betar, M. A. (2017). “Optimal electroencephalogram signals denoising using hybrid  $\beta$ -hill climbing algorithm and wavelet transform,” in *Proceedings of the International Conference on Imaging, Signal Processing and Communication* (Penang), 106–112.
- Arican, M., and Polat, K. (2020). Binary particle swarm optimization (BPSO) based channel selection in the EEG signals and its application to speller systems. *J. Artif. Intell. Syst.* 2, 27–37. doi: 10.33969/AIS.2020.21003

- Arvaneh, M., Guan, C., Ang, K. K., and Quek, C. (2011). Optimizing the channel selection and classification accuracy in EEG-based BCI. *IEEE Trans. Biomed. Eng.* 58, 1865–1873. doi: 10.1109/TBME.2011.2131142
- Baig, M. Z., Aslam, N., Shum, H. P., and Zhang, L. (2017). Differential evolution algorithm as a tool for optimal feature subset selection in motor imagery EEG. *Expert Syst. Appl.* 90, 184–195. doi: 10.1016/j.eswa.2017.07.033
- Bajaj, V., and Pachori, R. B. (2011). Classification of seizure and nonseizure EEG signals using empirical mode decomposition. *IEEE Trans. Inform. Technol. Biomed.* 16, 1135–1142. doi: 10.1109/TITB.2011.2181403
- Bhattacharjee, A., Fattah, S. A., Zhu, W.-P., and Ahmad, M. O. (2018). VMD-RiM: Rician modeling of temporal feature variation extracted from variational mode decomposed EEG signal for automatic sleep apnea detection. *IEEE Access* 6, 77440–77453. doi: 10.1109/ACCESS.2018.2883062
- Bhattacharyya, S., Rakshiti, P., Konar, A., Tibarewala, D., Das, S., and Nagar, A. K. (2013). “Differential evolution with temporal difference Q-learning based feature selection for motor imagery EEG data,” in *2013 IEEE Symposium on Computational Intelligence, Cognitive Algorithms, Mind, and Brain (CCMB)* (Singapore), 138–145. doi: 10.1109/CCMB.2013.6609177

- Bhattacharyya, S., Sengupta, A., Chakraborti, T., Konar, A., and Tibarewala, D. (2014). Automatic feature selection of motor imagery EEG signals using differential evolution and learning automata. *Med. Biol. Eng. Comput.* 52, 131–139. doi: 10.1007/s11517-013-1123-9
- Cimpanu, C., Ferariu, L., Dumitriu, T., and Ungureanu, F. (2017). “Multi-objective optimization of feature selection procedure for EEG signals classification,” in *2017 E-Health and Bioengineering Conference (EHB)* (Sinaia), 434–437. doi: 10.1109/EHB.2017.7995454
- Dora, C., and Biswal, P. K. (2020a). Correlation-based ECG artifact correction from single channel EEG using modified variational mode decomposition. *Comput. Methods Prog. Biomed.* 183:105092. doi: 10.1016/j.cmpb.2019.105092
- Dora, C., and Biswal, P. K. (2020b). An improved algorithm for efficient ocular artifact suppression from frontal EEG electrodes using VMD. *Biocybern. Biomed. Eng.* 40, 148–161. doi: 10.1016/j.bbe.2019.03.002
- Dragomiretskiy and Zosso (2013). Variational mode decomposition. *IEEE Trans. Signal Process.* 531–544. doi: 10.1109/TSP.2013.2288675
- Eslahi, S. V., Dabanloo, N. J., and Maghooli, K. (2019). A GA-based feature selection of the EEG signals by classification evaluation: application in BCI systems. *arXiv preprint arXiv:1903.02081*.
- Fernandez-Fraga, S., Aceves-Fernandez, M., Pedraza-Ortega, J., and Tovar-Arriaga, S. (2018). Feature extraction of EEG signal upon BCI systems based on steady-state visual evoked potentials using the ant colony optimization algorithm. *Discr. Dyn. Nat. Soc.* 2018:2143873. doi: 10.1155/2018/2143873
- Gavas, R., Chatterjee, D., Jaiswal, D., Viraraghavan, V., and Ramakrishnan, R. K. (2020). “Multivariate variational mode decomposition based approach for blink removal from EEG signal,” in *IEEE PerCom Conference* (Austin, TX). doi: 10.1109/PerComWorkshops48775.2020.9156206
- Gavas, R. D., Tripathy, S. R., Chatterjee, D., and Sinha, A. (2018). Cognitive load and metacognitive confidence extraction from pupillary response. *Cogn. Syst. Res.* 52, 325–334. doi: 10.1016/j.cogsys.2018.07.021
- Ghaemi, A., Rashedi, E., Pourrahimi, A. M., Kamandar, M., and Rahdari, F. (2017). Automatic channel selection in EEG signals for classification of left or right hand movement in brain computer interfaces using improved binary gravitation search algorithm. *Biomed. Signal Process. Control* 33, 109–118. doi: 10.1016/j.bspc.2016.11.018
- Ghosh, R., Sinha, N., Biswas, S. K., and Phadikar, S. (2019). A modified grey wolf optimization based feature selection method from EEG for silent speech classification. *J. Inform. Optim. Sci.* 40, 1639–1652. doi: 10.1080/02522667.2019.1703262
- Giorgio (2020). *Feature Selection Library*. Available online at: <https://www.mathworks.com/matlabcentral/fileexchange/68210-feature-selection-library>
- Gomathi, P., Baskar, S., Shakeel, P. M., and Dhulipala, V. S. (2020). Identifying brain abnormalities from electroencephalogram using evolutionary gravitational neocognitron neural network. *Multim. Tools Appl.* 79, 10609–10628. doi: 10.1007/s11042-019-7301-5
- Gonzalez, A., Nambu, I., Hokari, H., and Wada, Y. (2014). EEG channel selection using particle swarm optimization for the classification of auditory event-related potentials. *Sci. World J.* 2014:350270. doi: 10.1155/2014/350270
- Gupta, C. N., and Palaniappan, R. (2011). “Reducing power spectral density of eye blink artifact through improved genetic algorithm,” in *International Conference on Bioinformatics and Biomedical Technology* (Sanya), 25–27.
- Handiru, V. S., and Prasad, V. A. (2016). Optimized bi-objective EEG channel selection and cross-subject generalization with brain-computer interfaces. *IEEE Trans. Hum. Mach. Syst.* 46, 777–786. doi: 10.1109/THMS.2016.2573827
- Hasan, B. A. S., and Gan, J. Q. (2009). Multi-objective particle swarm optimization for channel selection in brain-computer interfaces.
- Hasan, B. A. S., Gan, J. Q., and Zhang, Q. (2010). “Multi-objective evolutionary methods for channel selection in brain-computer interfaces: some preliminary experimental results,” in *IEEE Congress on Evolutionary Computation* (Barcelona), 1–6. doi: 10.1109/CEC.2010.5586411
- He, L., Hu, Y., Li, Y., and Li, D. (2013). Channel selection by Rayleigh coefficient maximization based genetic algorithm for classifying single-trial motor imagery EEG. *Neurocomputing* 121, 423–433. doi: 10.1016/j.neucom.2013.05.005
- Jin, J., Miao, Y., Daly, I., Zuo, C., Hu, D., and Cichocki, A. (2019). Correlation-based channel selection and regularized feature optimization for MI-based BCI. *Neural Netw.* 118, 262–270. doi: 10.1016/j.neunet.2019.07.008
- Jin, J., Wang, X., and Zhang, J. (2008). “Optimal selection of EEG electrodes via DPSO algorithm,” in *2008 7th World Congress on Intelligent Control and Automation* (Chongqing), 5095–5099. doi: 10.1109/WCICA.2008.4593756
- Joseph, A. F. A., and Govindaraju, C. (2019). Channel selection using glow swarm optimization and its application in line of sight secure communication. *Cluster Comput.* 22, 10801–10808. doi: 10.1007/s10586-017-1177-9
- Kee, C.-Y., Ponnambalam, S. G., and Loo, C.-K. (2015). Multi-objective genetic algorithm as channel selection method for P300 and motor imagery data set. *Neurocomputing* 161, 120–131. doi: 10.1016/j.neucom.2015.02.057
- Khosropanah, P., Ramli, A. R., Lim, K. S., Marhaban, M. H., and Ahmedov, A. (2018). Fused multivariate empirical mode decomposition (MEMD) and inverse solution method for EEG source localization. *Biomed. Eng.* 63, 467–479. doi: 10.1515/bmt-2017-0011
- Khushaba, R. N., Al-Ani, A., and Al-Jumaily, A. (2011). Feature subset selection using differential evolution and a statistical repair mechanism. *Expert Syst. Appl.* 38, 11515–11526. doi: 10.1016/j.eswa.2011.03.028
- Kim, H. T., Kim, B. Y., Park, E. H., Kim, J. W., Hwang, E. W., Han, S. K., et al. (2005). Computerized recognition of Alzheimer disease-EEG using genetic algorithms and neural network. *Future Gener. Comput. Syst.* 21, 1124–1130. doi: 10.1016/j.future.2004.03.012
- Kim, J.-Y., Park, S.-M., Ko, K.-E., and Sim, K.-B. (2013). “Optimal EEG channel selection for motor imagery BCI system using BPSO and GA,” in *Robot Intelligence Technology and Applications 2012*, eds J.-H. Kim, E. T. Matson, H. Myung, and P. Xu (Gwangju: Springer), 231–239. doi: 10.1007/978-3-642-37374-9\_23
- Kimovski, D., Ortega, J., Ortiz, A., and Ba nos, R. (2015). Parallel alternatives for evolutionary multi-objective optimization in unsupervised feature selection. *Expert Syst. Appl.* 42, 4239–4252. doi: 10.1016/j.eswa.2015.01.061
- Liu, A., Chen, K., Liu, Q., Ai, Q., Xie, Y., and Chen, A. (2017). Feature selection for motor imagery EEG classification based on firefly algorithm and learning automata. *Sensors* 17:2576. doi: 10.3390/s17112576
- Liu, H., Motoda, H., Setiono, R., and Zhao, Z. (2010). “Feature selection: an ever evolving frontier in data mining,” in *Feature Selection in Data Mining* (Hyderabad), 4–13.
- Lv, J., and Liu, M. (2008). “Common spatial pattern and particle swarm optimization for channel selection in BCI,” in *2008 3rd International Conference on Innovative Computing Information and Control* (Washington, DC), 457. doi: 10.1109/ICICIC.2008.196
- Marchesi, B., Stelle, A., and Lopes, H. (1997). “Detection of epileptic events using genetic programming,” in *Proceedings of the 19th Annual International Conference of the IEEE Engineering in Medicine and Biology Society. Magnificent Milestones and Emerging Opportunities in Medical Engineering* (Cat. No. 97CH36136) (Chicago, IL), Vol. 3, 1198–1201. doi: 10.1109/IEMBS.1997.756577
- Navalyal, G. U., and Gavas, R. D. (2014). A dynamic attention assessment and enhancement tool using computer graphics. *Hum. Centr. Comput. Inform. Sci.* 4:11. doi: 10.1186/s13673-014-0011-0
- Pal, M., Bhattacharyya, S., Roy, S., Konar, A., Tibarewala, D., and Janarthanan, R. (2014). “A bacterial foraging optimization and learning automata based feature selection for motor imagery EEG classification,” in *2014 International Conference on Signal Processing and Communications (SPCOM)* (Bengaluru), 1–5. doi: 10.1109/SPCOM.2014.6983926
- Pereira, L. F., Patil, S. A., and Mahadeshwar, C. D. (2016). “Artifact removal from EEG using ANFIS-GA,” in *2016 Online International Conference on Green Engineering and Technologies (IC-GET)* (Temuco), 1–6. doi: 10.1109/GET.2016.7916726
- Priyadharsini, S. S., and Rajan, S. E. (2014). Evolutionary computing based approach for the removal of ECG artifact from the corrupted EEG signal. *Technol. Health Care* 22, 835–846. doi: 10.3233/THC-140860
- Quazi, M., and Kahalekar, S. (2017). Artifacts removal from EEG signal: FLM optimization-based learning algorithm for neural network-enhanced adaptive filtering. *Biocybern. Biomed. Eng.* 37, 401–411. doi: 10.1016/j.bbe.2017.04.003
- Rakshit, P., Bhattacharyya, S., Konar, A., Khasnobish, A., Tibarewala, D., and Janarthanan, R. (2013). “Artificial bee colony based feature selection for motor imagery EEG data,” in *Proceedings of Seventh International Conference on*

- Bio-Inspired Computing: Theories and Applications (BIC-TA 2012)* (Gwalior), 127–138. doi: 10.1007/978-81-322-1041-2\_11
- Ramos, A. C., Hernández, R. G., and Vellasco, M. (2016). “Feature selection methods applied to motor imagery task classification,” in *2016 IEEE Latin American Conference on Computational Intelligence (LA-CCI)*, 1–6. doi: 10.1109/LA-CCI.2016.7885731
- Ramos, A. C., and Vellasco, M. (2018). “Quantum-inspired evolutionary algorithm for feature selection in motor imagery EEG classification,” in *2018 IEEE Congress on Evolutionary Computation (CEC)*, 1–8. doi: 10.1109/CEC.2018.8477705
- Rehman, N., and Aftab, H. (2019). Multivariate variational mode decomposition. *IEEE Trans. Signal Process.* 67, 6039–6052. doi: 10.1109/TSP.2019.2951223
- Saini, M., and Satija, U. (2019). An effective and robust framework for ocular artifact removal from single-channel EEG signal based on variational mode decomposition. *IEEE Sensors J.* 20, 369–376. doi: 10.1109/JSEN.2019.2942153
- Saini, M., Satija, U., and Upadhyay, M. D. (2020). An effective automated method for detection and suppression of muscle artifacts from single-channel EEG signal. *Healthc. Technol. Lett.* 7, 35–40. doi: 10.1049/htl.2019.0053
- Selim, S., Tantawi, M. M., Shedeed, H. A., and Badr, A. (2018). A CSP\AM-BA-SVM approach for motor imagery BCI system. *IEEE Access* 6, 49192–49208. doi: 10.1109/ACCESS.2018.2868178
- Shan, H., Xu, H., Zhu, S., and He, B. (2015). A novel channel selection method for optimal classification in different motor imagery BCI paradigms. *Biomed. Eng. online*. 14:93. doi: 10.1186/s12938-015-0087-4
- Shenoy, H. V., and Vinod, A. P. (2014). “An iterative optimization technique for robust channel selection in motor imagery based brain computer interface,” in *2014 IEEE International Conference on Systems, Man, and Cybernetics (SMC)* (San Diego, CA), 1858–1863. doi: 10.1109/SMC.2014.6974191
- Shireen Fathima, S. K. (2019). “Enhanced differential evolution-based EEG channel selection,” in *SOMMA* (Trivandrum). doi: 10.1007/978-981-15-4301-2\_14
- Singh, G., Singh, B., and Kaur, M. (2019). Grasshopper optimization algorithm-based approach for the optimization of ensemble classifier and feature selection to classify epileptic EEG signals. *Med. Biol. Eng. Comput.* 57, 1323–1339. doi: 10.1007/s11517-019-01951-w
- Sinha, A., Chatterjee, D., Das, R., Datta, S., Gavas, R., and Saha, S. K. (2015a). “Artifact removal from EEG signals recorded using low resolution Emotiv device,” in *2015 IEEE International Conference on Systems, Man, and Cybernetics (Hongkong)*, 1445–1451. doi: 10.1109/SMC.2015.256
- Sinha, A., Gavas, R., Chatterjee, D., Das, R., and Sinharay, A. (2015b). “Dynamic assessment of learners’ mental state for an improved learning experience,” in *2015 IEEE Frontiers in Education Conference (FIE)*, 1–9. doi: 10.1109/FIE.2015.7344121
- Soler, A., Muñoz-Gutiérrez, P. A., Bueno-López, M., Giraldo, E., and Molinas, M. (2020). Low-density EEG for neural activity reconstruction using multivariate empirical mode decomposition. *Front. Neurosci.* 14:175. doi: 10.3389/fnins.2020.00175
- Suja Priyadharsini, S., Edward Rajan, S., and Femilin Sheniha, S. (2016). A novel approach for the elimination of artefacts from EEG signals employing an improved artificial immune system algorithm. *J. Exp. Theor. Artif. Intell.* 28, 239–259. doi: 10.1080/0952813X.2015.1020571
- Tacchino, G., Coelli, S., Reali, P., Galli, M., and Bianchi, A. M. (2020). Bicoherence interpretation, in EEG, requires signal to noise ratio quantification: an application to sensorimotor rhythms. *IEEE Trans. Biomed. Eng.* 67, 2696–2704. doi: 10.1109/TBME.2020.2969278
- Taran, S., and Bajaj, V. (2018). Clustering variational mode decomposition for identification of focal EEG signals. *IEEE Sensors Lett.* 2, 1–4. doi: 10.1109/LSENS.2018.2872415
- Taran, S., and Bajaj, V. (2019). Emotion recognition from single-channel EEG signals using a two-stage correlation and instantaneous frequency-based filtering method. *Comput. Methods Prog. Biomed.* 173, 157–165. doi: 10.1016/j.cmpb.2019.03.015
- Wang, B., Wong, C., Wan, F., Mak, P. U., Mak, P. I., and Vai, M. I. (2010). “Trial pruning for classification of single-trial EEG data during motor imagery,” in *2010 Annual International Conference of the IEEE Engineering in Medicine and Biology* (Buenos Aires), 4666–4669. doi: 10.1109/IEMBS.2010.5626453
- Wang, G., Teng, C., Li, K., Zhang, Z., and Yan, X. (2015). The removal of EOG artifacts from EEG signals using independent component analysis and multivariate empirical mode decomposition. *IEEE J. Biomed. Health Inform.* 20, 1301–1308. doi: 10.1109/JBHI.2015.2450196
- Wang, X., Gong, G., Li, N., and Qiu, S. (2019). Detection analysis of epileptic EEG using a novel random forest model combined with grid search optimization. *Front. Hum. Neurosci.* 13:52. doi: 10.3389/fnhum.2019.00052
- Wang, Y., and Veluvolu, K. C. (2017). Evolutionary algorithm based feature optimization for multi-channel EEG classification. *Front. Neurosci.* 11:28. doi: 10.3389/fnins.2017.00028
- Wen, T., and Zhang, Z. (2017). Effective and extensible feature extraction method using genetic algorithm-based frequency-domain feature search for epileptic EEG multiclassification. *Medicine* 96, 68–79. doi: 10.1097/MD.0000000000006879
- Xu, P., Liu, T., Zhang, R., Zhang, Y., and Yao, D. (2014). Using particle swarm to select frequency band and time interval for feature extraction of EEG based BCI. *Biomed. Signal Process. Control* 10, 289–295. doi: 10.1016/j.bspc.2013.08.012
- Yang, J., Singh, H., Hines, E. L., Schlaghecken, F., Iliescu, D. D., Leeson, M. S., et al. (2012). Channel selection and classification of electroencephalogram signals: an artificial neural network and genetic algorithm-based approach. *Artif. Intell. Med.* 55, 117–126. doi: 10.1016/j.artmed.2012.02.001
- Yang, Y., Kyrgyzov, O., Wiart, J., and Bloch, I. (2013). “Subject-specific channel selection for classification of motor imagery electroencephalographic data,” in *2013 IEEE International Conference on Acoustics, Speech and Signal Processing* (Vancouver, BC), 1277–1280. doi: 10.1109/ICASSP.2013.6637856
- Yin, Z., Wang, Y., Liu, L., Zhang, W., and Zhang, J. (2017). Cross-subject EEG feature selection for emotion recognition using transfer recursive feature elimination. *Front. Neurobot.* 11:19. doi: 10.3389/fnbot.2017.00019
- Yücelbaş, C., Yücelbaş, Ş., Özşen, S., Tezel, G., Küçüktürk, S., and Yosunkaya, Ş. (2018). A novel system for automatic detection of k-complexes in sleep EEG. *Neural Comput. Appl.* 29, 137–157. doi: 10.1007/s00521-017-2865-3
- Zhang, C. Z., Kareem Abdullah, A., and Abdullabs Abdullah, A. (2016). Electroencephalogram-artifact extraction enhancement based on artificial intelligence technique. *J. Biomimet. Biomater. Biomed. Eng.* 27, 77–91. doi: 10.4028/www.scientific.net/JBBBE.27.77
- Zhang, L., and Wei, Q. (2019). Channel selection in motor imaginary-based brain-computer interfaces: a particle swarm optimization algorithm. *J. Integr. Neurosci.* 18, 141–152. doi: 10.31083/j.jin.2019.02.17
- Zhang, T., Chen, W., and Li, M. (2017). Ar based quadratic feature extraction in the VMD domain for the automated seizure detection of EEG using random forest classifier. *Biomed. Signal Process Control* 31, 550–559. doi: 10.1016/j.bspc.2016.10.001

**Conflict of Interest:** The authors declare that the research was conducted in the absence of any commercial or financial relationships that could be construed as a potential conflict of interest.

Copyright © 2021 Fathima and Kore. This is an open-access article distributed under the terms of the Creative Commons Attribution License (CC BY). The use, distribution or reproduction in other forums is permitted, provided the original author(s) and the copyright owner(s) are credited and that the original publication in this journal is cited, in accordance with accepted academic practice. No use, distribution or reproduction is permitted which does not comply with these terms.



# An Intracortical Implantable Brain-Computer Interface for Telemetric Real-Time Recording and Manipulation of Neuronal Circuits for Closed-Loop Intervention

## OPEN ACCESS

### Edited by:

Saugat Bhattacharyya,  
Ulster University, United Kingdom

### Reviewed by:

Mitsuaki Takemi,  
The University of Tokyo, Japan  
Richard Gault,  
Queen's University Belfast,  
United Kingdom  
Mariana P. Branco,  
University Medical Center Utrecht,  
Netherlands

### \*Correspondence:

Hamed Zaer  
hz@clin.au.dk

† These authors have contributed  
equally to this work and share senior  
authorship

### Specialty section:

This article was submitted to  
Brain-Computer Interfaces,  
a section of the journal  
Frontiers in Human Neuroscience

**Received:** 17 October 2020

**Accepted:** 14 January 2021

**Published:** 03 February 2021

### Citation:

Zaer H, Deshmukh A, Orlowski D,  
Fan W, Prouvot P-H, Glud AN,  
Jensen MB, Worm ES, Lukacova S,  
Mikkelsen TW, Fitting LM, Adler JR Jr,  
Schneider MB, Jensen MS, Fu Q,  
Go V, Morizio J, Sorensen JCH and  
Stroh A (2021) An Intracortical  
Implantable Brain-Computer Interface  
for Telemetric Real-Time Recording  
and Manipulation of Neuronal Circuits  
for Closed-Loop Intervention.  
*Front. Hum. Neurosci.* 15:618626.  
doi: 10.3389/fnhum.2021.618626

**Hamed Zaer<sup>1,2\*</sup>, Ashlesha Deshmukh<sup>3,4</sup>, Dariusz Orlowski<sup>1,2</sup>, Wei Fan<sup>5</sup>,  
Pierre-Hugues Prouvot<sup>5</sup>, Andreas Nørgaard Glud<sup>1,2</sup>, Morten Bjørn Jensen<sup>2,6</sup>,  
Esben Schjødtt Worm<sup>2,6</sup>, Slávka Lukacova<sup>2,6</sup>, Trine Werenberg Mikkelsen<sup>1,2</sup>,  
Lise Moberg Fitting<sup>1,2</sup>, John R. Adler Jr<sup>7,8</sup>, M. Bret Schneider<sup>7,8,9</sup>,  
Martin Snebjerg Jensen<sup>2,10</sup>, Qianhai Fu<sup>3</sup>, Vinson Go<sup>3</sup>, James Morizio<sup>3</sup>,  
Jens Christian Hedemann Sørensen<sup>1,2†</sup> and Albrecht Stroh<sup>5,11†</sup>**

<sup>1</sup> Department of Neurosurgery, Center for Experimental Neuroscience (CENSE), Aarhus University Hospital, Aarhus, Denmark, <sup>2</sup> Department of Clinical Medicine, Aarhus University, Aarhus, Denmark, <sup>3</sup> Department of Electrical and Computer Engineering, Pratt School of Engineering, Duke University, Durham, NC, United States, <sup>4</sup> Department of Biomedical Engineering, Pratt School of Engineering, Duke University, Durham, NC, United States, <sup>5</sup> Leibniz Institute for Resilience Research, Mainz, Germany, <sup>6</sup> Department of Oncology, Radiation Therapy, and Clinical Medicine, Aarhus University Hospital, Aarhus University, Aarhus, Denmark, <sup>7</sup> Zap Surgical Systems, Inc., San Carlos, CA, United States, <sup>8</sup> Department of Neurosurgery, Stanford University School of Medicine, Stanford, CA, United States, <sup>9</sup> Department of Psychiatry and Behavioral Sciences, Stanford University School of Medicine, Stanford, CA, United States, <sup>10</sup> Department of Nuclear Medicine and PET Center, Institute of Clinical Medicine, Aarhus University and Hospital, Aarhus, Denmark, <sup>11</sup> Institute of Pathophysiology, University Medical Center of the Johannes Gutenberg University Mainz, Mainz, Germany

Recording and manipulating neuronal ensemble activity is a key requirement in advanced neuromodulatory and behavior studies. Devices capable of both recording and manipulating neuronal activity brain-computer interfaces (BCIs) should ideally operate un-tethered and allow chronic longitudinal manipulations in the freely moving animal. In this study, we designed a new intracortical BCI feasible of telemetric recording and stimulating local gray and white matter of visual neural circuit after irradiation exposure. To increase the translational reliance, we put forward a Göttingen minipig model. The animal was stereotactically irradiated at the level of the visual cortex upon defining the target by a fused cerebral MRI and CT scan. A fully implantable neural telemetry system consisting of a 64 channel intracortical multielectrode array, a telemetry capsule, and an inductive rechargeable battery was then implanted into the visual cortex to record and manipulate local field potentials, and multi-unit activity. We achieved a 3-month stability of the functionality of the un-tethered BCI in terms of telemetric radio-communication, inductive battery charging, and device biocompatibility for 3 months. Finally, we could reliably record the local signature of sub- and suprathreshold neuronal activity in the visual cortex with high bandwidth without complications. The ability to wireless induction charging combined with the entirely implantable design, the rather

high recording bandwidth, and the ability to record and stimulate simultaneously put forward a wireless BCI capable of long-term un-tethered real-time communication for causal preclinical circuit-based closed-loop interventions.

**Keywords:** brain-machine (computer) interface, electrophysiology, neuromodulation, animal model, EEG, stereotactic radiosurgery, Göttingen minipig, closed-loop

## INTRODUCTION

The recent advances in recording and manipulation techniques, particularly in preclinical animal models, significantly furthered our understanding of the neuronal circuit functions underlying complex behaviors. It becomes now apparent, that complex and multifactorial disorders of the CNS such as depression could be classified as neural circuit disorders (Insel et al., 2010). Yet, for probing the contributory role of distinct components of a neuronal circuitry to a given (dys)-function, a causal, real-time intervention is mandatory. Ideally, a current neuronal activity signature should inform the manipulation schemes in a closed-loop fashion, in an unrestrained, unperturbed subject. Integrated devices capable of interfacing with the external experimenter are termed brain-computer interfaces (BCI) or Brain-machine interfaces (BMI). The first requirement for BCI is a dense recording of the current activity state of the given circuitry. For that, superficial, non-invasive Electroencephalography (EEG) is already well established in the clinical diagnosis of neurological disorders (Lebedev and Nicolelis, 2006). In the framework of BCI, EEG represents the recording module of BCIs enabling the patient to drive an electronic spelling device employing slow cortical potentials (SCPs) (Birbaumer et al., 1999). Also, locked-in amyotrophic lateral sclerosis (ALS) patients can learn to control virtual keyboards via slow cortical potentials or oscillatory EEG components as the input signals for the BCIs (Pfurtscheller et al., 2003; Hinterberger et al., 2005). Until recently, the precision of the non-invasive EEG-based interfaces was limited by a rather low spatial resolution (Srinivasan, 1999), poor signal-to-noise ratio (Bang et al., 2013), and low transfer rate (Wolpaw et al., 2002). Particularly in preclinical animal studies, hard-wired devices restrict the degrees of freedom for behavior studies. However, the newer generation of minimally/non-invasive wearable EEG-based seizure detection devices utilizing closed-loop warning systems, and non-EEG-based devices employing accelerometer (ACM), Electromyography (EMG), etc., have incredibly assisted the clinical management of epileptic disorders (Borujeny et al., 2013; Ramgopal et al., 2014; Van de Vel et al., 2016). Still, long-term monitoring of brain activity via scalp EEG devices has some shortcomings which could be anticipated to be addressed by sub-scalp EEG devices (Duun-Henriksen et al., 2020).

Invasive methods are subclassified into intracranial EEG (ECoG and stereo-EEG) or intracortical and intraparenchymal micro-arrays where penetrating electrodes are employed to target deeper regions including the limbic system (Parvizi and Kastner, 2018). Such methods provide recordings with broader temporal bandwidth up to 500 Hz (Staba et al., 2002; Butterfield et al., 2007), better spatial resolution, and typically

a higher amplitude, as the electrodes are closer to the neural tissue (Lebedev and Nicolelis, 2006; Ball et al., 2009). The iEEG recordings are less affected by electric potentials caused by e.g., the cranial muscles or eye movements (Mak and Wolpaw, 2009). Indeed, ECoG is used for BCIs implemented in neural motor prosthesis devices for paralyzed patients e.g., fully implanted BCI in locked-in ALS patients (Vansteensel et al., 2016). Invasive methods might therefore be more suitable for BCIs due to the higher spatial precision of recording (tenths of millimeters) and lesser need for user training than scalp EEG based systems (Wolpaw et al., 2002; Leuthardt et al., 2004; Lebedev and Nicolelis, 2006; Schalk and Leuthardt, 2011). Long-term clinical usage of invasive BCIs employing micro-arrays is, however, limited by complications related to the implantation surgery and long-term recording instability due to signal degradation of the impedances of the recording sites caused by encapsulation and displacement of electrodes (Shain et al., 2003; Schalk et al., 2007). On the technical side, the low signal transfer rate (below 10 megabits/s) limits the large-scale investigation of brain activity signatures with adequate resolution. A hard-wired interface communication with an extra-corporal remote terminal constrains the movement of the patient/experimental subject (Liu et al., 2018; Zaer et al., 2020). Partly wireless systems allow rather unrestrained movements of the patients, but, still need to be constantly inductively powered when in use (Guenther et al., 2009; Liu et al., 2018).

Another important example of neural interfacing devices as deep brain stimulation (DBS) devices are not classically described as BCI devices. However, the newer generation of DBS units combined with the concept of Bi-directional BCI, for instance in Parkinson's patients, investigates the possibility of stimulation by utilizing the sensing electrodes according to the intermittent nature of the disease symptoms (Angeles et al., 2016).

In terms of achieving the real-time acquisition of the current local neuronal activity state, the use of microelectrode arrays has gained momentum. Recent advances in array design and fabrication allow for the production of ideally tailored multichannel probes according to the geometry of the targeted brain region, in both preclinical and even clinical studies. Depending on the coating, diameter, and distance of the individual electrode sites, not only the local field potential can be assessed, but also the recording of multi- and single-unit (MU and SU) activity is attainable. Spike sorting and mapping enable the identification of the excitatory vs. inhibitory neurons can be identified (Yang et al., 2017). Of particular importance is the high spatial resolution given by the dense array of individual electrode sites. This enables the recording, identification, and replay of complex patterns of local neuronal ensemble activities, due to the ability to use various sites for stimulation. Multielectrode

arrays, therefore, may represent a suitable solution for real-time closed-loop applications.

In this study, we designed a new fully implantable invasive intra-parenchymal BCI for electrophysiological telecommunication in a large animal model using the Göttingen minipig to at least partially overcome the aforementioned current limitations due to hard-wired charging systems and rather low bandwidth. These animals have a sufficiently large brain for testing the human-sized implants, in contrast to the small rodent brain (Gierthmuehlen et al., 2014). The physiology, internal anatomy, and even genome of the Göttingen minipigs are reasonably similar to humans in comparison to rodents (Dolezalova et al., 2014; Sjöstedt et al., 2020). Moreover, Göttingen minipigs are also suited for chronic studies as they grow slowly to a maximum of 35 kg and allow biocompatibility assessment of the implanted materials over long periods providing an accessible large animal model for various preclinical translational study (Sørensen et al., 2011; Bro et al., 2012).

To validate the function and quality of the device we used visual cortical lesions made by ablative radiosurgery. While ablative radiosurgery has been used for decades, relatively recently, studies suggested a neuromodulatory effect of sub-necrotic doses on irradiated neurons (Schneider et al., 2010). For instance, radiosurgery of epileptogenic arteriovenous malformations (AVM) in functional areas has shown cessation or remission of epileptic attacks, unexpectedly prior to fully obliteration of AVM and visible changes in MRI (Steiner et al., 1992). This gap between appearing MRI or histological changes and the clinical effect of irradiation raised the idea of the potential neuromodulatory effect of sublethal radiodoses (Regis et al., 1995, 1999). Irradiating a specifically targeted area within the brain circuits with sublethal doses (“radio-modulation”) is postulated to alter the function of the circuit as a whole (Schneider et al., 2010). The effect of radiation is suggested to be depending on the radiation dose, type, and volume of the targeted brain tissue (Regis, 2014). Below the necrotic radiodoses, there may still be alterations, not visible in anatomical imaging; therefore, evaluation of post-irradiation functional changes in neuronal circuits is mandatory for radiation dose-adjustment to obtain neuromodulatory effects without necrosis. Here, we chose the primary visual cortex as the implantation site. While certainly the primary visual cortex is tasked with the representation and computation of visual afferents, it becomes apparent, that even primary sensory cortical areas go beyond the functions for which they are named. Recent pieces of evidence suggest, that primary cortical networks exhibit complex dysregulations mirroring behavioral states in neuronal disorders originating in distant regions (Iaccarino et al., 2016; Arnoux et al., 2018; Ellwardt et al., 2018). Moreover, the visual cortex (V1) in Göttingen minipigs is surgically easily accessible and big enough to facilitate the process of radiosurgical targeting and implantation of invasive electrodes. By choosing the visual cortex, we could simultaneously achieve different goals. First, verification of the functionality of this BCI. Second, piloting the stereotactic radiosurgical approach on the very thin cortical layer of the visual cortex (2–3 mm). Third, assessing the feasibility of observing radio-neuromodulatory

changes by this system. In this study, as a part of the larger project on evaluation of the neuromodulatory effect of ionizing radiation, we aimed to design a BCI to survey the real-time electrophysiological events after stereotactic radiosurgery in the visual cortex.

## MATERIALS AND METHODS

One female Göttingen minipig, age 6 months, weight 15 kg, was used for this proof of concept study. The Danish Animal Experiments Inspectorate (2016-15-0201-01103) approved this study in compliance with the ARRIVE guidelines and the 2010/63/EU directive for animal experiments. After a month of acclimatization in a standardized research environment facility, the animal underwent Magnetic Resonance Imaging (MRI) of the brain as a baseline and to define the target area for the stereotactic radiosurgery and then implantation of the device as described below in each corresponding subsection.

### Radiotherapy Treatment Planning and Treatment Delivery

Stereotactic radiosurgery treatment planning was based on fused CT and MR image data sets. The planning CTs were acquired with 1.5 mm slice thickness (Brilliance Big Bore CT, Phillips, Amsterdam, Netherlands) (**Figures 1A,B**). The T1 MR scans were acquired with a 1.0 mm slice thickness (**Figures 1C–E**). A point target was defined in the fused CT/MR data sets. Treatment was planned using the Eclipse treatment planning system (Eclipse 13.7, Varian Medical Systems, Palo Alto, CA, United States) and based on a Truebeam linear accelerator equipped with an HD 120 multileaf collimator (MLC) of 2.5 mm leaf widths. The treatment plan consisted of 14 beams (6MV; dose rate 600 MU/min) using a non-coplanar beam arrangement with MLC defined apertures centered at the target. Aperture sizes were quadratic  $5 \times 5$  mm with a calculated target dose of 100 Gy normalized to the defined point target ( $0.03 \text{ cm}^3$  receiving 80 Gy or above). The dose calculated by the Eclipse treatment planning system (Acuros v. 13.7.14 dose calculation algorithm with calculation grid size 0.1 cm) was corrected with small-field dosimetric factors obtained from measurements with a diamond detector [Natural diamond detector, type 600003 (PTW Freiburg GmbH)] in a water phantom. Localization of the irradiation target was obtained by fusing a pre-treatment 1.5 mm slice thickness kV cone-beam CT (CBCT) scan with the planning CT, using the onboard imaging system of the Truebeam accelerator. Couch corrections were performed according to the CBCT with 6 degrees of freedom (translational, rotation, pitch, and roll). A verification CBCT was taken after couch correction (before treatment) to assess if the animal had moved during the correction. An additional CBCT was taken post-treatment to verify intra-fractional positional stability.

### Surgical Procedure

The animal was sedated with an intramuscular injection of Midazolam (0.8 mg/kg)/Ketamine (20 mg/kg) mixture as premedication. An ear vein was catheterized (21G venflon)

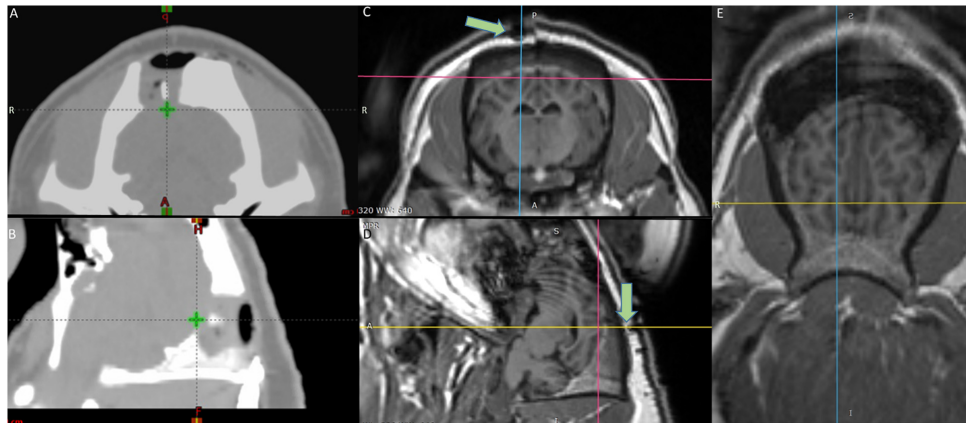


**FIGURE 1 |** Target definition by the fused MRI/CT (A) axial and (B) sagittal view CT scans of the radiotherapy planning system – The green cross shows the target area on the visual cortex (V1) irradiated with 100 Gy. (C) Axial (D) Sagittal (E) Horizontal view MRI images of the brain – the crosshair shows the target area – Green arrows in (C,D) point at the fiducial marker on top of the irradiated area.

and anesthesia was induced with a second IV injection of Midazolam/S-ketamine mixture. Shortly afterward, the minipig was intubated (4.5 mm cuffed tube) and anesthesia was maintained using approximately 2% isoflurane through mechanical ventilation and a mixture of 50% O<sub>2</sub>. Intravenous injection of propofol (20 ml/h) was used during transportation for the imaging procedures. The pig was fixated prone in an MRI-compatible localizer box (Figure 2A; Bjarkam et al., 2004). A mid-sagittal skin incision was made, exposing the skull. The periosteum was removed, and a small drill hole was made posterior to the bregma (Figure 2B). A plastic screw containing copper sulfate was placed in the drill hole, providing a fixed point for the estimation of stereotaxic coordinates (Glud et al., 2017). Three titanium screws were also put in the skull anterior, posterior, and lateral to the fiducial marker as landmarks for more accuracy during the implantation surgery (Figures 2C,D). Preoperative MRI of the animal fixated in the localizer box was carried out using a 3D T1-weighted MRI brain scan (3.0 T Siemens Skyra). The visual cortex was visualized according to the online Brain Atlas of Göttingen minipig (Orlowski et al., 2019). The location of the target (visual cortex) in relation to the fiducial marker was calculated. The cranium was opened by surgical drill and the visual cortex was exposed after opening the dura (Figure 2D). The probe was placed using microsurgical forceps directly into the visual cortex and then the flexible outcoming wire was fixed by fibrin sealant (TISSEEL® Baxter, United States) above the dura (Figure 2E). The Omnetics connector afterward was attached to the skull bone with two titanium screws and an interconnecting plastic bar (Figure 2F). The rest of the flexible wire between the probe and the Omnetics connector then was secured with Bioglue® (CryoLife, United States). Three of the ground wires were put in the muscles and one underneath the titanium screw and thereby fixated to the skull bone. The battery and communicating capsule was placed into the subcutaneous pocket in the posterior neck region and sutured to the muscles with a holding Dacron ribbon (Figure 2F). Then,

the surgical wound was closed. The animal received prophylactic antibiotic [Benzyl Penicillin procaine 30,000 IE/kg (Penovet®, Boehringer Ingelheim, Denmark)] and analgesic [Meloxicam 1.5 mg/kg (Metacam®, Boehringer Ingelheim, Denmark)] both once a day for 5 days.

## Design of the Telemetric Brain-Computer Interface

For achieving the methodological milestone to record and manipulate cortical gray and white matter activity with real-time and closed-loop communication ability, we implemented an integrated telemetric system including a custom-built 8-shank multielectrode probe. The fully implantable array consists of 16 independent electrical stimulation channels and 48 channels for continuous recording (Figures 3A, 4A,D). The implant was designed to record local field potentials (LFP) and multi-unit activity (MUA). The main components of the system entailed an electrode interface, custom application-specific integrated circuits (ASICs) (Figures 4E,G), wireless radiofrequency communication (RF) (Figure 4F), hermetic packaging capsule (size = 70 × 50 × 15 mm, Figure 4D), computer software for bidirectional communication with the implantable device and induction charging pad to be worn around the pig’s neck like a collar (Figures 4D–H).

We have previously reported a former version of this technology (Deshmukh et al., 2020). The interfacing targets had been peripheral neural interfaces which are easier to interface with an implanted capsule. Here, we introduce the technology to be implanted intracerebrally, a decisive new step in terms of technology development. In detail, these were the technical changes and improvements: I. The electrode here represents a multichannel stimulation and recording array. II. In this publication, we developed a 16-stimulation channel and 48-recording channel integrated into the same capsule. III. To provide the power for operating the system we implanted the wireless inductive chargeable system and battery, and IV. to cater

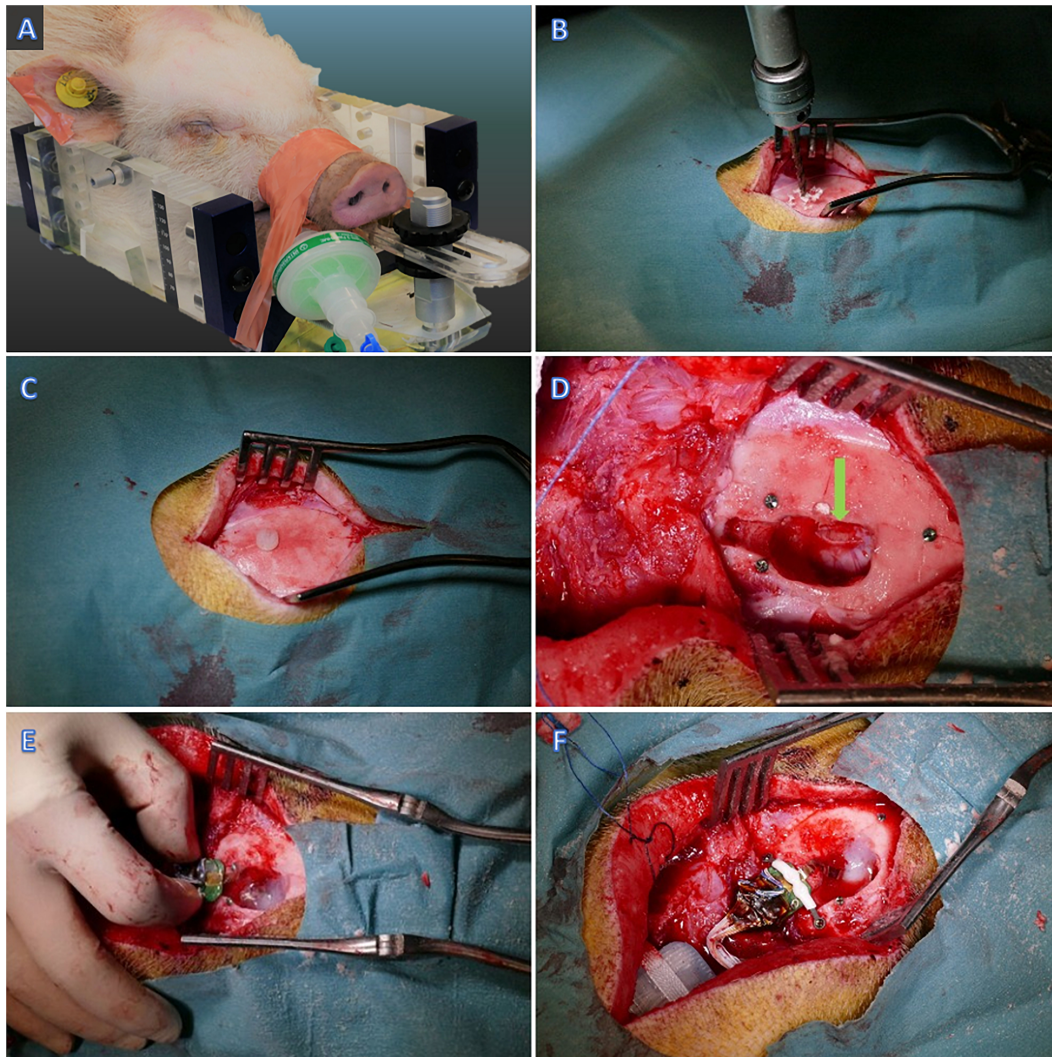


**FIGURE 2 |** Implantation surgery. **(A)** The minipig fixated in the MRI compatible head frame. **(B)** Drilling the skull posterior to Bregma **(C,D)** Plastic and titanium fiducial markers. **(D)** Visual cortex exposure – pointed by green arrow. **(E)** Insertion of the probe in the visual cortex and fixation with Fibrin Sealant. **(F)** Fixation of the Omnetics connector to the skull bone.

to size restrictions, we redesigned our PCBs to lower current requirements. The current draw is reduced from 60 mA to 45 mA.

## Electrode Interface

A custom intracortical electrode array (NeuroNexus, Ann Arbor, MI, United States) consisting of 64 planar silicon electrodes distributed on 8 shanks was designed to study the spatial extent of gray and white matter excitability in the visual cortex. Two electrode types were designed; the stimulatory electrodes to target the white matter and gray matter, respectively, and the recording electrodes (**Figure 4A**). The total length of the array was 10 mm. Each shank has ventral (deeper) and dorsal (closer to the surface) groups of electrodes consisting of stimulation and recording channels for each white matter and the overlying cortex (**Figures 3A, 4A**). The surface area of the stimulatory electrodes was  $1250 \mu\text{m}^2$  while the area of the recording

electrodes was  $177 \mu\text{m}^2$ . The electrodes were separated by  $500 \mu\text{m}$ , except for the 4th and 5th electrodes from the upper side on shanks one and eight which were separated by 4 mm to record deeper in white matter. The electrode was attached to the telemetric device using a 64 channel Omnetics connector and wires coated in silicon.

## Electrophysiology Protocol

Data were recorded at a 27.7 kHz sampling rate. For stimulation, biphasic constant current pulses ( $f = 0.2 \text{ Hz}$ ; pulse duration: 0.1 ms/polarity) were conducted at one of the stimulation electrodes at a given time. To probe local excitability in gray matter, 5–30  $\mu\text{A}$  current was administered at dorsal stimulation electrodes 4, 12, 20, 28, 36, 44, 52, and 60. To probe white matter integrity, 100–400  $\mu\text{A}$  current was administered at ventral stimulation electrodes 2, 16, 24, 32, 40, 48, 56, and 58

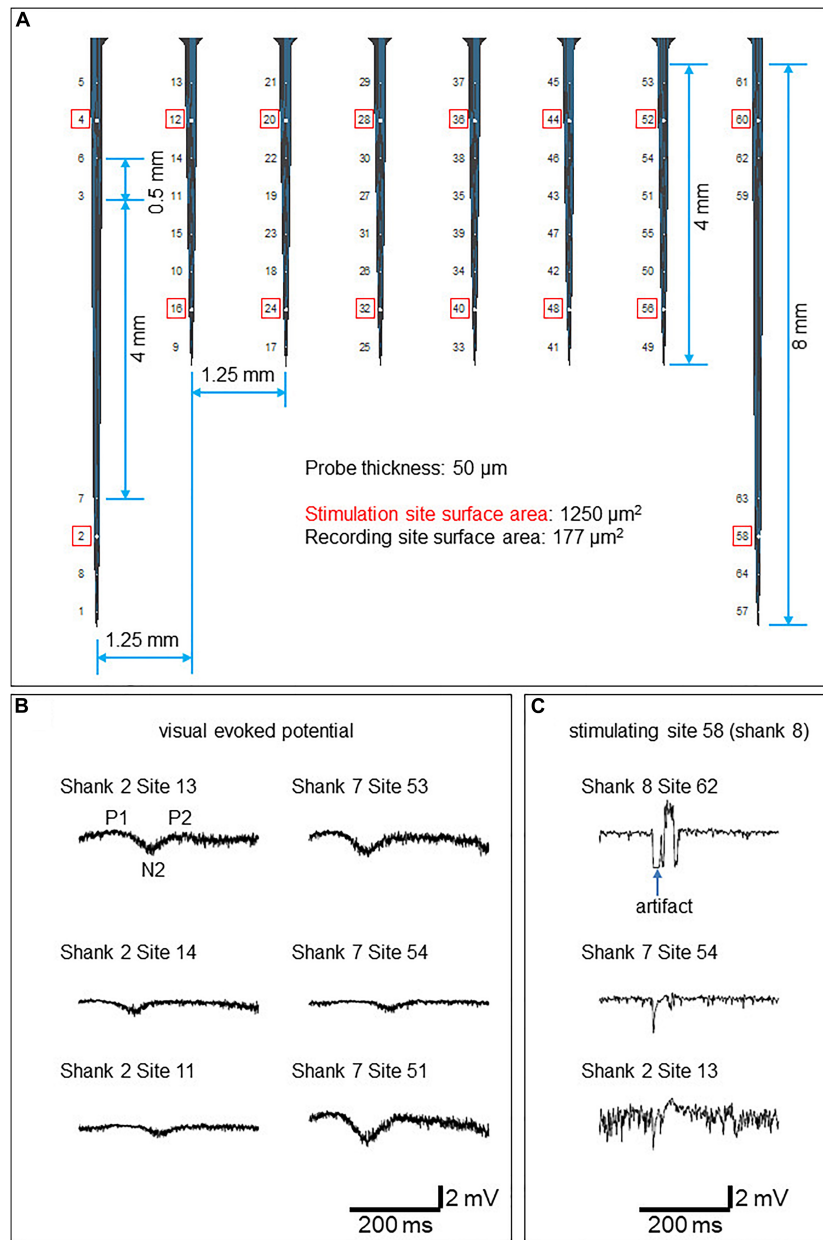


**FIGURE 3 |** Electrophysiology results **(A)** The probe design. Stimulation sites are circled red. **(B)** Example VEPs recorded from the superficial four layers of electrodes in response to LED flashlight. **(C)** Example evoked responses stimulated by 100  $\mu\text{A}$  current conducted at electrode 58 (shank 8).

(Figure 3A). To ensure the physiological origin of the recorded data, visual evoked potentials (VEPs) were recorded in response to a LED flashlight at the right eye in a dimly illuminated room. For electrical stimulation, biphasic constant current pulses ( $f = 0.2$  Hz; pulse duration: 0.1 ms/polarity) were conducted at one of the stimulation electrodes at a given time.

### Histology

Three months after irradiation, the animal was humanly killed by an overdose of Pentobarbital (400 mg/ml) and transcardially perfused with 5 liters of 10% buffered formalin

(Ettrup et al., 2011). The brain was then removed and post-fixed for 5 days in the same fixative and afterward sliced into 1.25 cm thick coronal tissue slabs (Sorensen et al., 2000). The tissue slabs containing areas of interest were cryoprotected in a 30% sucrose solution in buffered saline (PBS) for 10 days, followed by freezing in isopentane cooled by dry ice. The frozen brain slabs were then cryostat sectioned into 40  $\mu\text{m}$  thick sections, which were either directly mounted on the microscopic slides or preserved free-floating in DeOlmos cryoprotecting solution. The response of the brain tissue was visualized using Nissl, anti-MBP, anti-GFAP, and isolectin stainings.

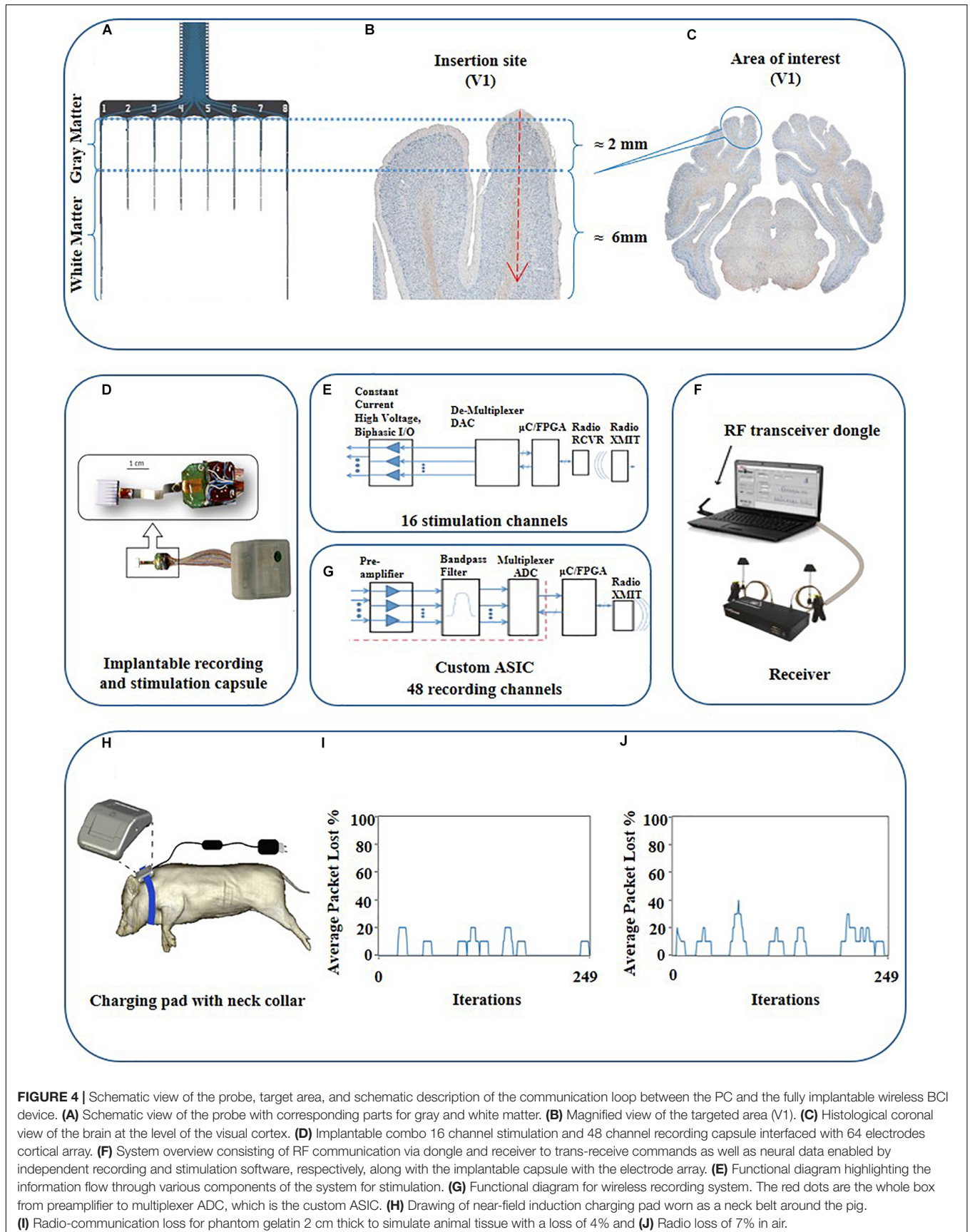


**FIGURE 4 |** Schematic view of the probe, target area, and schematic description of the communication loop between the PC and the fully implantable wireless BCI device. **(A)** Schematic view of the probe with corresponding parts for gray and white matter. **(B)** Magnified view of the targeted area (V1). **(C)** Histological coronal view of the brain at the level of the visual cortex. **(D)** Implantable combo 16 channel stimulation and 48 channel recording capsule interfaced with 64 electrodes cortical array. **(E)** System overview consisting of RF communication via dongle and receiver to trans-receive commands as well as neural data enabled by independent recording and stimulation software, respectively, along with the implantable capsule with the electrode array. **(F)** Functional diagram highlighting the information flow through various components of the system for stimulation. **(G)** Functional diagram for wireless recording system. The red dots are the whole box from preamplifier to multiplexer ADC, which is the custom ASIC. **(H)** Drawing of near-field induction charging pad worn as a neck belt around the pig. **(I)** Radio-communication loss for phantom gelatin 2 cm thick to simulate animal tissue with a loss of 4% and **(J)** Radio loss of 7% in air.

## RESULTS

### Recording System

A low noise, mixed-signal preamplifier, and multiplexing ASICs for 48 input channels was developed for this study. These small printed circuit board (PCB) electronics encapsulate the ASICs for low noise pre-amplifiers and bandpass filters (Won et al., 2002; Obeid et al., 2003) along with the harvester circuits, RF voltage controlled oscillator (VCO), transmitter power amplifier, and antennas. Harvester circuits detect the wireless fluctuating magnetic fields of the charging pads and convert this magnetic energy into an electrical voltage to operate the circuit boards.

The maximum data sampling rate is 50 kHz with a signal bandwidth of 0.8 Hz to 7 kHz. The custom wireless radio has a wideband frequency modulation (FM) architecture for low power and high data rates, consisting of a radiofrequency (RF) voltage controlled oscillator (VCO), RF amplifier, and splitter to two chip antennas. The receiver consists of an RF demodulator and analog demultiplexer which feeds the data into a 16-bit data acquisition (DAQ) system, or to raw analog signal outputs. Input referred noise was  $\sim 5$   $\mu\text{V}/\sqrt{\text{Hz}}$ . The frequency of operation for the wireless recording system was 2.7 GHz. The analog data may be viewed simultaneously for all channels in the custom software (“Neuroware”). The software also marks event timestamps regarding behavioral activity or precise stimulation times with less than 1 ms delay in the recorded data. The software includes filters that can be applied for viewing LFPs and multi-units with highpass, lowpass, or bandpass filtering. The system technically is capable of SU recording with a programmable bandpass filter, however, we did not use this possibility in this experimental setup. The real-time RF signal strengths of the radio communication were remotely monitored before and during the experiment to ensure its smooth running. The recording system was also synchronized with the stimulation system to automatically record stimulation pattern indicator pulses indicating the start and end of the stimulation (Deshmukh et al., 2020).

### Stimulation System

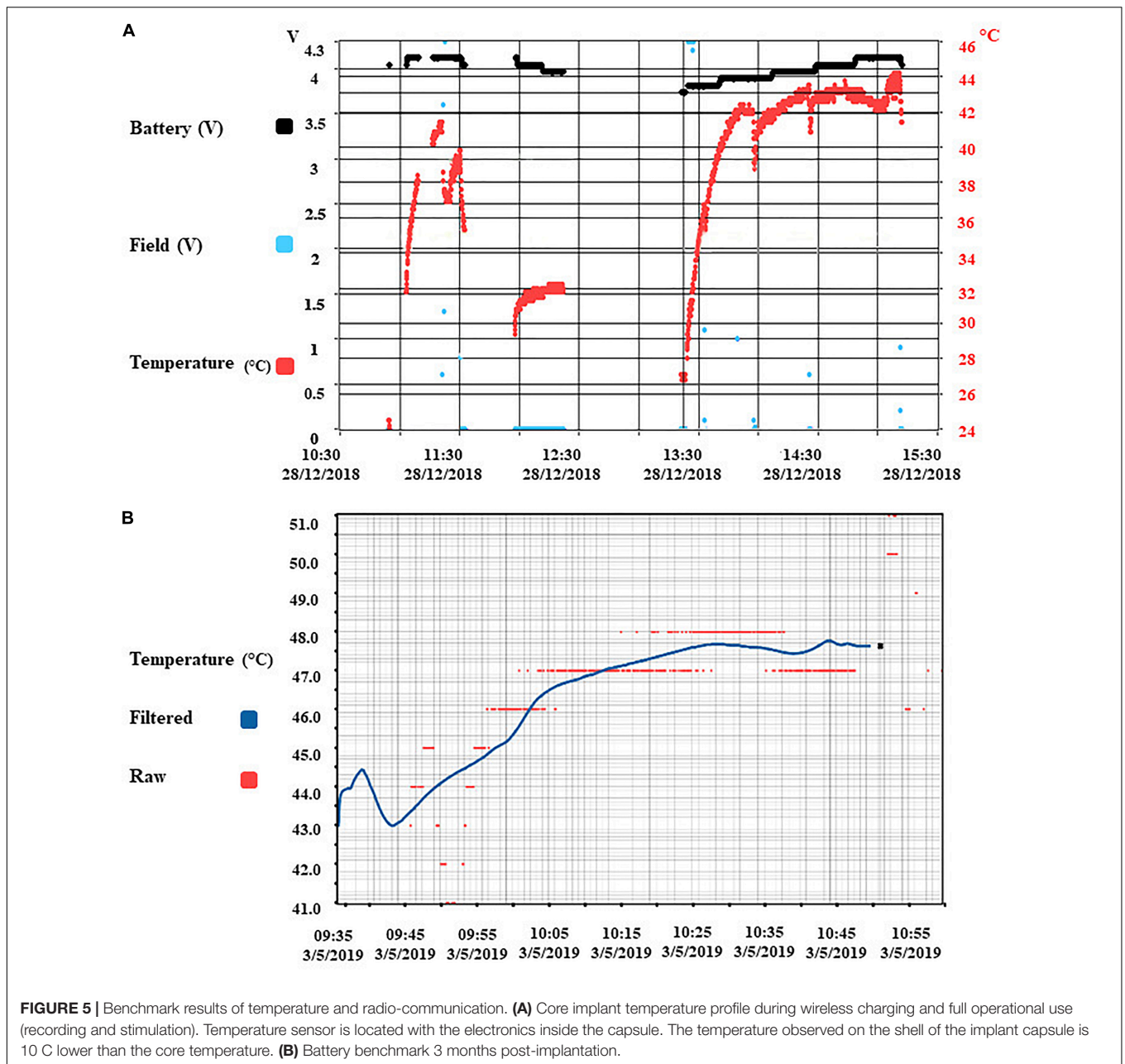
For stimulation, the system consists of 16 independent channels out of which, user can multiplex between any two constant current output channels with a maximum output of  $\pm 4$  mA on each channel. Thus at the given time, the user can simultaneously select any two channels from the available 16 channels for a given stimulation pattern by swapping between the two channels but not all 16 at the same time. The minimum multiplexer switching time delay is 20  $\mu\text{s}$  for stimulation channels, which is the fastest the stimulation driver can switch between two selected channels for stimulation patterns. The stimulator radio system consists of an RF transceiver dongle connected to a PC via a USB cable which sends commands to the WiFi chipset within the capsule. The RF transceiver dongle can monitor and control up to 50 independent implantable stimulator capsules, each with their own unique identifier address for communication, and provides feedback to the stimulation software (“StimWare”) installed on the PC. With a transmission range of up to 3 m, the system provides real-time

feedback to the PC for the implantable capsule consisting of the battery voltage, temperature, and stimulation pattern status as well as the strength of the wireless charging field. The stimulation system is also equipped to run automated diagnostics on the implant like battery life, charging state, radio signal strength, and *in vivo* electrode impedances.

### Induction Charging System

A novel inductive charging system was designed to supply wireless energy to the active and passive electronic components of the implantable capsules for operation and to charge the battery for continuous recording and stimulation (Figures 4D,H). It consists of an efficient power harvester design which is used to capture the energy produced by the induction from the time-varying magnetic field. The interface is designed by following IEC 60601-1 and IEC 60601-1-2 (safety and effectiveness of medical electrical equipment) standards. The wireless induction charging system consists of a loosely coupled transmitter and receiver coils. The receiver coil is placed in the implantable capsule along with the power harvester electronics. The system uses near field charging that places the receiver and transmitter coils 5–7.5 cm apart. The maximum depth inside the animal to achieve efficient implant powering via the charging pad was approx.  $20 \pm 2$  mm. Each of the coil’s electrical parameters entailing coil quality (Q), inductance (L), and resistance (R) are carefully tuned at a resonate frequency to maximize the efficiency of the inductive powering system for energy transfer. We employed a rechargeable LiON 200 mAh battery. The battery is rechargeable; however, the run time of the battery depends on a couple of factors e.g., the current draw on the battery from the application being used via simultaneous recording and stimulation which draws up to 32 mA per hour whereas stimulation alone draws 17–19 mA depending on the stimulation pattern.

Since the heating of electronics has the potential to cause thermal injury in the implantation’s surrounding tissue, the rise in implant temperature was continuously monitored. The temperature changes due to charging were recorded at three different locations in the lab: Inside the capsule, reporting the temperature value to the software every 2500 ms, at the shell of the capsule via heat sensor strips, and via an infrared camera monitoring the capsule shell and its immediate surroundings. Pre-implantation tests were carried out with the capsule immersed in 38°C water inside an insulated container made up of Styrofoam to prevent heat loss, and monitored over time while in operation for multiple battery life charging cycles. The test was also repeated with the capsule encased inside phantom gelatin to represent body tissue. The outside shell temperature of the capsule was observed to be  $8 \pm 2$  C lower than inside the capsule using infrared cameras. Unfortunately, these tests could not be replicated inside the animal due to the lack of visual observable space in the surgical site. The temperature from inside the capsule during benchtop testing in phantom gelatin recorded a maximum of 44°C (Figure 5A). The battery benchmark 3 months post-implantation was done during the full functional operation, and the core temperature rose to 48 C, which may be estimated at around 38 C on the outer shell (Figure 5B).



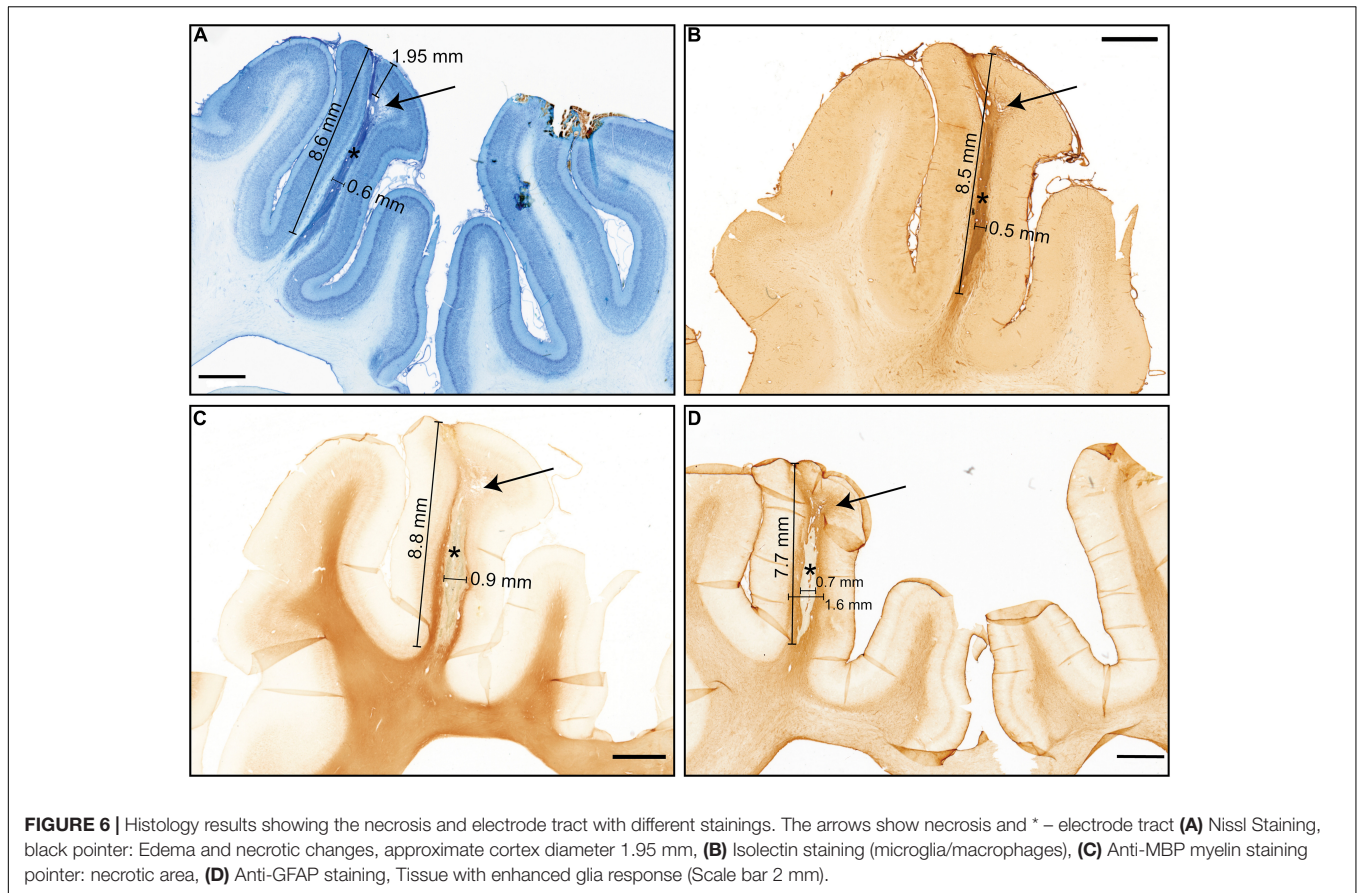
### Software User Interface

The stimulation interface was designed so that the stimulation channel alias names would match the electrode site diagram to ease the experimental planning. Sub-channels 1 to 16 each had a unique alias following the format that equates to “Shank number and Electrode Site number” matching the probe design. This enabled the researcher to know exactly which electrode site has been selected for a two-channel simultaneous stimulation from the entire array. The ability to wirelessly switch between 16 channels in real-time over the entire array gives an advanced ability to cover more targets horizontally and along with the depth of the array catering to better spatial resolution for stimulation. The second spatial control is to choose stimulatory

electrodes on different shanks (irradiated vs. non-irradiated) that helps the user control the protocol in real-time. The recording channels are configured with a similar format to follow an index of 1 through 52 to identify which electrode site on a particular shank is used from the record channel pinout. Within these 52 channels, there were 48 neural recording channels and 4 reference channels.

### Radio Transmission Quality Testing

The implanted transceiver capsule was tested for the quality of its wireless data transmission by measuring the percentage of data packet loss at a maximum distance of 3.6 m through the air and the animal’s tissue. The stimulator radio power loss at



3.6 m distance was validated using 2 cm of phantom gelatin to represent animal tissue with data presented (**Figures 4I,J**). The total loss of packets in lab tests was 7% for in the air and 4% in 2 cm thick phantom gelatin. This means 4% of all data packets were not able to complete the full-duplex data link shown in **Figures 4E,G** between the stimulator to the probe inserted in the animal and then back to the receiving PC transceiver dongle (**Figure 4F**). The wireless radio frequency (RF) communication device was tuned to a specific frequency (2.4 GHz for the stimulation system and 2.7 GHz for the recording system). The impedance of the RF transmitter board and RF receiver were tuned to the said frequency for maximum wireless signal strength which minimizes the data packet loss. Since the efficiency of the frequency changes in different mediums, the minimum power loss of packets reflects the good quality of the wireless data communicated in the intended tissue. The result is supported by the fact that the radio is tuned for better performance in the animal once implanted as opposed to tuning in just air. The recording radio has been optimized to work best once implanted by adjusting the RF antenna strengths to maximum. The tuning was carried out during the assembly of the device by utilizing the attenuation of the RF in phantom gelatin. It was carried out only once and not during the *in vivo* study. This tuning is considered sufficient for long term implantation as it is carried out by fixing the values of the capacitors and impedances to have maximum resonance. This is maintained with the radio and

does not get detuned unless the circuit containing the hardware components somehow gets damaged in the case that the capsule is damaged. The latter is controlled by the percentage packet loss test performed after the device was implanted in the animal (**Figure 4**). This radio tuning method preempts the loss of signal strength due to intervening animal tissue once implanted. The implanted transmitter device also records the presence of radio-signal lock at the receiver, indicating receipt of a strong signal. The effective range of the telemetry system is 3 m.

### Electrophysiology

The visual evoked potentials in response to the LED stimulation are shown in **Figure 3B**. In comparison to flash VEP in humans (Odom et al., 2016), putative components P1, N2, and P2 were observed. N1 was not apparent.

Electrically evoked responses by 100  $\mu$ A stimulation conducted at electrode 58 (shank 8) are shown in **Figure 3C**. A larger artifact was observed at recording sites in the shank where stimulation was conducted.

### Histology

The position of the electrode in V1 (visual cortex) was verified using the online atlas of the Göttingen minipig brain (Orlowski et al., 2019). The inflammatory response of the brain tissue around the probe was observed (**Figure 6A**). The dorsal half, about 2–3 mm, of the visible electrode track, was positioned

in the gray matter, the ventral part of the electrode track was situated in the white matter (**Figures 6A–D**). On the side of the electrode track in the border between cortical gray and white matter, there were visible small irradiation-induced necrotic changes and edema (**Figures 6A,B,D**). The electrode track visible on the sections is around 0.5 mm wide; the length is around 8 mm (the visible tissue reaction stretches a bit longer – up to 10 mm). The glial scar, with a thickness varying from 0.3 to 0.6 mm, surrounded the electrode track (**Figure 6D**). According to the cell-morphology, numerous activated microglia cells and macrophages were observed within the small irradiation-induced necrotic area close to the insertion area (**Figure 6B**).

### Surgical Outcome

One day after BCI implantation surgery, the animal was transported back to the university farm with controlled humidity, temperature, and diet. The wound healed normally during the 10 days after the surgery. While there was no explicit behavior testing, nonetheless, the animal was monitored by the veterinarian nurses on a daily basis, and no signs of obvious behavioral changes, such as increased aggression, or decrease in food intake, had been reported. The animal status was followed for 3 months after the surgery without any sign of infection or failure to thrive.

### DISCUSSION

Assessing neuronal network function while the subject exhibits complex behavioral tasks remains as one of the last methodological frontiers. For a causal understanding of the relevance of the given neuronal ensemble activity for the respective brain function and dysfunction, recording the network signature will not suffice. Therefore, we need to manipulate and modulate the current activity state on the fly, in a closed-loop fashion. BCIs comprising multielectrode arrays would enable bimodal neuromodulatory experimental designs (Grand et al., 2013). Inductive charging and telemetric communication with a fully implanted device will open up new avenues of *in vivo* neuronal activity recordings in a minimally invasive fashion.

We developed this methodological concept that enables us to address the effects of local radiation on the function of neuronal circuits. Even complex and multi-factorial disorders such as depression are thought to be a manifestation of a neuronal circuit disorder, i.e., a dysbalance of the highly interconnected and functionally bound network. It is hypothesized, that the application of stereotactic radiotherapy, even though initially developed for ablation of brain tumors might, at lower doses, lead to neuromodulation (Schneider et al., 2010; Yeh et al., 2020; Zaer, 2020). The study of neuromodulation effects requires identification of the local network signature of spontaneous and sensory-driven activity and the local excitability in a longitudinal fashion to understand the phasic activity of the network and its components. At first, we employed a rather high dose of radiation, known to cause necrosis (Yeh et al., 2020; Zaer, 2020). According to the histology results, the stereotactic radiotherapy was correctly targeted and resulted in irradiation-induced necrosis.

The fully implantable BCI developed here has exhibited stable performance during the study period in terms of the technical specs of the device, such as the battery life, the absence of leakage, quality of radio-communication, and we did not find any significant post mortem inflammatory tissue reaction. The feasibility of inductive charging, wireless recording and stimulation, and the stable signal quality throughout the recording period pioneered a BCI for large animal models. The three-meter-range of the telemetry system permits the experimental subject to behave freely in its environment with minimal interference. Indeed, removing the tethered connections, hypnotic medicine, and the immediate presence of the researcher during the data acquisition should drastically reduce physiological noise and increase data validity. Moreover, the wireless connection will reduce the risk of infection in chronic studies. This fully implantable wireless BCI is capable of providing LFP data, multiunit activities as well as cortical and white matter stimulation on different specified electrodes with simultaneous recording of the real-time responses. Some of the main features of the presented device in comparison to other recently published BCIs are noted in **Table 1** (Rouse et al., 2011; Bagheri et al., 2013; Yin et al., 2014; Musk, 2019; Zhou et al., 2019; NeuroPace, 2020; Zhu et al., 2020). Rather than the possibility

**TABLE 1** | Comparison of different main specifications of recently presented brain-computer interfaces.

Brain-computer interface	Simultaneous Stimulation/recording	Recording channels number	Stimulatory channels number	Wireless induction charging	Sample rate (Hz)	Bandwidth (Hz)	Recording type	ADC resolution (bit)
This study	+	48	16	+	50 kHz	0.7 Hz–8 kHz	LFP-MU	16
WAND (1)	+	128	128	–	1 kHz	500 Hz	LFP	15
Activa PC + S (2)	+	4	8	–	200 Hz	500 Hz	LFP-EEG	10
NeuroPace RNS (3)	+	4	8	–	250 Hz	≥50 kHz	EEG-LFP	10
University of Toronto (4)	+	256	64	–	15 kHz	1 Hz–5 kHz	EEG	8
Neuralink (5)	–	3072	–	–	19.3 kHz	3 Hz–27 kHz	LFP-MU	10
Braingate (6)	–	100	–	–	20 kHz	0.1 Hz–7.8 kHz	LFP-SU	12
WIMAGINE (7)	–	64	–	–	1 kHz	0.5–300 Hz	ECoG	12

LFP, local field potential; MU, multi-unit activity; SU, single-unit activity; EEG, electroencephalogram; ECoG, electrocorticography (1, 3–6, 8).

of wireless inductive charging, other specificities such as high sample rate, ADC resolution, and width bandwidth range can be mentioned as improvements in this study. We perceive it as a strength of our BCI, that it had not been developed as individual components, but in contrast with a comprehensive and unifying goal: the bandwidth, the power of the battery, the software, the impedances of the electrodes for stimulation and recordings had all been tailored for the question at hand, i.e., the recording and stimulation of a neuronal circuit in the visual cortex upon local radio-modulation.

In terms of the closed-loop ability: The system cannot only record but also stimulate, the recorded signals can be displayed and computed in real-time, followed by stimulation. Here, we simply did not showcase an example, which could be, for instance, recording a VEP and stimulating exactly on a determined timestamp after the N1 peak, to probe local excitability.

The wireless communication part of the device can interface with different types of probes according to the study purpose and gives the opportunity of targeting deep brain structures. Other indications of implementing this concept could be probing of deep-brain structures such as the hippocampus, highly relevant for behavioral studies. A large variety of electrode designs from different manufacturers can be connected and integrated into this BCI. Single shank probes with densely spaced recording electrodes for example could even be used for spike sorting, and the identification of putatively inhibitory and excitatory units (Yang et al., 2017). Alternatively, electrode meshes could be used covering large portions of the cortical surface, ideal for studying the propagation of neurophysiological signals, e.g., in the field of epilepsy research. What is more, the capability of simultaneously recording and stimulation opens up closed-loop experimental designs. A key technical advance represents the fully implantable approach and the inductive charging capability, allowing for longitudinal studies. Other examples of the wireless recording of LFP, MU, EOG, EMG together with activity data have also been previously presented, however, lack of closed-loop modulation, inductive wireless charging, and the possibility of full implantation limit their application in neuromodulatory studies (Grand et al., 2013). A major obstacle in the implementation of long-lasting microelectrode-based BCI represents the biological compatibility and degradation of the electrode functionality, mainly due to local gliosis (Lebedev and Nicolelis, 2006; Ball et al., 2009; Orłowski et al., 2017). The second challenging issue is to avoid thermal tissue injury generated by the wireless charging pad. This is intended to be addressed in the future using a variable design of the charging pad belt with variable height adjustments as well as a closed-loop software system. The software system will automatically control the charging duty cycle strength based on data from the temperature and battery life status of the implant, and temperature on the surface of the charging pad.

For BCIs to be implemented in clinical applications in a broader context, it is mandatory to decode network computations from background noise by gaining reproducible, spatially defined signals from specified brain regions (Pfurtscheller et al., 2006). Adequate deciphering is of great importance, providing the necessary input for communication tools, and to at least partially

restore motor function in stroke, Locked-in syndrome, and amyotrophic lateral sclerosis patients (Kennedy and Bakay, 1998). Despite advances in developing robotic limbs for plegic patients (Collinger et al., 2013; Bouton et al., 2016) or communication tools for long-suffering Locked-in individuals (Vansteensel et al., 2016), the clinical implementation of these technologies is still extremely challenging. The shortcomings of these systems rely heavily on the current advances in hardware technology. While there is still a long way to go, our proof-of-concept study at least suggests a few key concepts to improve the integrated framework of a highly sensitive and fully implantable BCIs. For mastering the crucial transition from laboratory to in-home BCI use, research efforts should be directed toward enhancing the stability of BCIs concerning user autonomy, long-lasting functionality in terms of permanent availability of neural interfaces with a minimum neural tissue disturbance and irritation (Huggins et al., 2011; Nijboer, 2015).

## DATA AVAILABILITY STATEMENT

The raw data supporting the conclusions of this article will be made available by the authors, without undue reservation.

## ETHICS STATEMENT

The animal study was reviewed and approved by the Danish Animal Experiments Inspectorate (2016-15-0201-01103) in compliance with the ARRIVE guidelines and the 2010/63/EU directive for animal experiments.

## AUTHOR CONTRIBUTIONS

HZ and AD wrote the first draft of the manuscript. HZ, AD, JM, MSJ, JS, P-HP, VG, QF, and AS collaborated on the designing, and benchmarking of the device prototype. HZ and JS did the implantation surgery with the assistance of LF. MJB, EW, and SL planned and performed the stereotactic radiosurgery together with HZ, JS, DO, and AG. JRA and MBS proposed the concept of the experiment and helped with the study design. DO and TM performed the histology experiment and analysis. P-HP, WF, and AS proposed and performed the electrophysiology protocol and analysis. All authors edited and accepted the final manuscript.

## FUNDING

The authors declare that this study received funding from Zap Surgical Systems Inc., the Boehringer Ingelheim Foundation, and the German Research Foundation. The funders were not involved in the study design, collection, analysis, interpretation of data, the writing of this article, or the decision to submit it for publication.

## ACKNOWLEDGMENTS

We gratefully acknowledge the administration assistance by Ms. Anne Sofie Møller Andersen, the staff at Påskehøjgaard Animal

Facility, and the Department of Radiation Oncology, Aarhus University Hospital. We would also express our gratitude to the ZAP Surgical System Inc., and the Department of Clinical Medicine, Health, Aarhus University for

financial supports. We would like to thank the Boehringer Ingelheim Foundation and the German Research Foundation for support and Dr. Alexis Paez at Neuronexus for convenient collaboration.

## REFERENCES

- Angeles, P., Mace, M., Admiraal, M., Burdet, E., Pavese, N., and Vaidyanathan, R. (2016). *A Wearable Automated System to Quantify Parkinsonian Symptoms Enabling Closed Loop Deep Brain Stimulation*. New York, NY: Springer International Publishing, 8–19.
- Arnoux, I., Willam, M., Griesche, N., Krummeich, J., Watari, H., Offermann, N., et al. (2018). Metformin reverses early cortical network dysfunction and behavior changes in Huntington's disease. *Elife* 7:38744. doi: 10.7554/eLife.38744
- Bagheri, A., Gabran, S. R. I., Salam, M. T., Perez Velazquez, J. L., Mansour, R. R., Salama, M. M. A., et al. (2013). Massively-parallel neuromonitoring and neurostimulation rodent headset with nanotextured flexible microelectrodes. *IEEE Trans. Biomed. Circuits Syst.* 7, 601–609. doi: 10.1109/tbcas.2013.2281772
- Ball, T., Kern, M., Mutschler, I., Aertsen, A., and Schulze-Bonhage, A. (2009). Signal quality of simultaneously recorded invasive and non-invasive EEG. *Neuroimage* 46, 708–716. doi: 10.1016/j.neuroimage.2009.02.028
- Bang, J. W., Choi, J. S., and Park, K. R. (2013). Noise reduction in brainwaves by using both EEG signals and frontal viewing camera images. *Sensors* 13, 6272–6294. doi: 10.3390/s130506272
- Birbaumer, N., Ghanayim, N., Hinterberger, T., Iversen, I., Kotchoubey, B., Kubler, A., et al. (1999). A spelling device for the paralysed. *Nature* 398, 297–298. doi: 10.1038/18581
- Bjarkam, C. R., Cancian, G., Larsen, M., Rosendahl, F., Ettrup, K. S., Zeidler, D., et al. (2004). A MRI-compatible stereotaxic localizer box enables high-precision stereotaxic procedures in pigs. *J. Neurosci. Methods* 139, 293–298. doi: 10.1016/j.jneumeth.2004.05.004
- Borujeny, G. T., Yazdi, M., Keshavarz-Haddad, A., and Borujeny, A. R. (2013). Detection of epileptic seizure using wireless sensor networks. *J. Med. Signals Sens.* 3:63. doi: 10.4103/2228-7477.114373
- Bouton, C. E., Shaikhouni, A., Annetta, N. V., Bockbrader, M. A., Friedenber, D. A., Nielson, D. M., et al. (2016). Restoring cortical control of functional movement in a human with quadriplegia. *Nature* 533, 247–250. doi: 10.1038/nature17435
- Bro, A., Sørensen, J. C. H., Nielsen, M. S., Rosendahl, F., Deding, D., Ettrup, K. S., et al. (2012). The Göttingen minipig in translational neuroscience. *Ellegaard Newsllett.* 38, 8–9.
- Butterfield, D. A., Reed, T. T., Perluigi, M., De Marco, C., Coccia, R., Keller, J. N., et al. (2007). Elevated levels of 3-nitrotyrosine in brain from subjects with amnesic mild cognitive impairment: implications for the role of nitration in the progression of Alzheimer's disease. *Brain Res.* 1148, 243–248. doi: 10.1016/j.brainres.2007.02.084
- Collinger, J. L., Wodlinger, B., Downey, J. E., Wang, W., Tyler-Kabara, E. C., Weber, D. J., et al. (2013). High-performance neuroprosthetic control by an individual with tetraplegia. *Lancet* 381, 557–564. doi: 10.1016/s0140-6736(12)61816-9
- Deshmukh, A., Brown, L., Barbe, M. F., Braverman, A. S., Tiwari, E., Hobson, L., et al. (2020). Fully implantable neural recording and stimulation interfaces: Peripheral nerve interface applications. *J. Neurosci. Methods* 333:108562. doi: 10.1016/j.jneumeth.2019.108562
- Dolezalova, D., Hruska-Plochan, M., Bjarkam, C. R., Sorensen, J. C., Cunningham, M., Weingarten, D., et al. (2014). Pig models of neurodegenerative disorders: Utilization in cell replacement-based preclinical safety and efficacy studies. *J. Comp. Neurol.* 522, 2784–2801. doi: 10.1002/cne.23575
- Duun-Henriksen, J., Baud, M., Richardson, M. P., Cook, M., Kouvas, G., Heasman, J. M., et al. (2020). A new era in electroencephalographic monitoring? Subscalp devices for ultra-long-term recordings. *Epilepsia* 61, 1805–1817. doi: 10.1111/epi.16630
- Ellwardt, E., Pramanik, G., Luchtman, D., Novkovic, T., Jubal, E. R., Vogt, J., et al. (2018). Maladaptive cortical hyperactivity upon recovery from experimental autoimmune encephalomyelitis. *Nat. Neurosci.* 21, 1392–1403. doi: 10.1038/s41593-018-0193-2
- Ettrup, K. S., Glud, A. N., Orlowski, D., Fitting, L. M., Meier, K., Soerensen, J. C., et al. (2011). Basic surgical techniques in the Gottingen minipig: intubation, bladder catheterization, femoral vessel catheterization, and transcardial perfusion. *J. Vis. Exp.* 2011:2652. doi: 10.3791/2652
- Gierthmuehlen, M., Wang, X., Gkogkidis, A., Henle, C., Fischer, J., Fehrenbacher, T., et al. (2014). Mapping of sheep sensory cortex with a novel microelectrocorticography grid. *J. Comp. Neurol.* 522, 3590–3608. doi: 10.1002/cne.23631
- Glud, A. N., Bech, J., Tvilling, L., Zaer, H., Orlowski, D., Fitting, L. M., et al. (2017). A fiducial skull marker for precise MRI-based stereotaxic surgery in large animal models. *J. Neurosci. Methods* 285, 45–48. doi: 10.1016/j.jneumeth.2017.04.017
- Grand, L., Ftomov, S., and Timofeev, I. (2013). Long-term synchronized electrophysiological and behavioral wireless monitoring of freely moving animals. *J. Neurosci. Methods* 212, 237–241. doi: 10.1016/j.jneumeth.2012.10.008
- Guenther, F. H., Brumberg, J. S., Wright, E. J., Nieto-Castanon, A., Tourville, J. A., Panko, M., et al. (2009). A wireless brain-machine interface for real-time speech synthesis. *PLoS One* 4:e8218. doi: 10.1371/journal.pone.0008218
- Hinterberger, T., Veit, R., Wilhelm, B., Weiskopf, N., Vatine, J. J., and Birbaumer, N. (2005). Neuronal mechanisms underlying control of a brain-computer interface. *Eur. J. Neurosci.* 21, 3169–3181. doi: 10.1111/j.1460-9568.2005.04092.x
- Huggins, J. E., Wren, P. A., and Gruis, K. L. (2011). What would brain-computer interface users want? Opinions and priorities of potential users with amyotrophic lateral sclerosis. *Amyotroph. Lateral Sclerosis* 12, 318–324. doi: 10.3109/17482968.2011.572978
- Iaccarino, H. F., Singer, A. C., Martorell, A. J., Rudenko, A., Gao, F., Gillingham, T. Z., et al. (2016). Gamma frequency entrainment attenuates amyloid load and modifies microglia. *Nature* 540, 230–235. doi: 10.1038/nature20587
- Insel, T., Cuthbert, B., Garvey, M., Heinssen, R., Pine, D. S., Quinn, K., et al. (2010). Research domain criteria (RDoC): toward a new classification framework for research on mental disorders. *Am. J. Psychiatry* 167, 748–751. doi: 10.1176/appi.ajp.2010.09091379
- Kennedy, P. R., and Bakay, R. A. E. (1998). Restoration of neural output from a paralyzed patient by a direct brain connection. *NeuroReport* 9, 1707–1711. doi: 10.1097/00001756-199806010-00007
- Lebedev, M. A., and Nicolelis, M. A. (2006). Brain-machine interfaces: past, present and future. *Trends Neurosci.* 29, 536–546. doi: 10.1016/j.tins.2006.07.004
- Leuthardt, E. C., Schalk, G., Wolpaw, J. R., Ojemann, J. G., and Moran, D. W. (2004). A brain-computer interface using electrocorticographic signals in humans. *J. Neural. Eng.* 1, 63–71. doi: 10.1088/1741-2560/1/2/001
- Liu, W. L. A., Chang, M. F., Kuan, Y., Lo, Y., and Zhao, Y. (2018). *Wireless wearable big data brain machine interface*. U. S. Patent Application 10027362. Alexandria, VA: United States Patent and Trademark Office.
- Mak, J. N., and Wolpaw, J. R. (2009). Clinical Applications of Brain-Computer Interfaces: Current State and Future Prospects. *IEEE Rev. Biomed. Eng.* 2, 187–199. doi: 10.1109/RBME.2009.2035356
- Musk, E. (2019). An integrated brain-machine interface platform with thousands of channels. *bioRxiv:703801*. Preprint. doi: 10.1101/703801
- NeuroPace (2020). *RNS System Physician Manual - NeuroPace World-wide-web*. California: NeuroPace.
- Nijboer, F. (2015). Technology transfer of brain-computer interfaces as assistive technology: barriers and opportunities. *Ann. Phys. Rehabil. Med.* 58, 35–38. doi: 10.1016/j.rehab.2014.11.001
- Obeid, I., Morizio, J. C., Moxon, K. A., Nicolelis, M. A., and Wolf, P. D. (2003). Two multichannel integrated circuits for neural recording and signal processing. *IEEE Trans. Biomed. Eng.* 50, 255–258. doi: 10.1109/TBME.2002.807643
- Odom, J. V., Bach, M., Brigell, M., Holder, G. E., McCulloch, D. L., Mizota, A., et al. (2016). ISCEV standard for clinical visual evoked potentials: (2016 update). *Doc. Ophthalmol.* 133, 1–9. doi: 10.1007/s10633-016-9553-y

- Orlowski, D., Glud, A. N., Palomero-Gallagher, N., Sorensen, J. C. H., and Bjarkam, C. R. (2019). Online histological atlas of the Gottingen minipig brain. *Heliyon* 5:e01363. doi: 10.1016/j.heliyon.2019.e01363
- Orlowski, D., Glud, A. N., Palomero-Gallagher, N., Sorensen, J. C. H., and Bjarkam, C. R. (2019). Online histological atlas of the Gottingen minipig brain. *Heliyon* 5:e01363. doi: 10.1016/j.heliyon.2019.e01363
- Orlowski, D., Michalis, A., Glud, A. N., Korshøj, A. R., Fitting, L. M., Mikkelsen, T. W., et al. (2017). Brain tissue reaction to deep brain stimulation—a longitudinal study of DBS in the gottingen minipig. *Neuromodul. Technol. Neural Interf.* 20, 417–423.
- Parvizi, J., and Kastner, S. (2018). Promises and limitations of human intracranial electroencephalography. *Nat. Neurosci.* 21, 474–483. doi: 10.1038/s41593-018-0108-2
- Pfurtscheller, G., Neuper, C., Muller, G. R., Obermaier, B., Krausz, G., Schlogl, A., et al. (2003). Graz-BCI: state of the art and clinical applications. *IEEE Trans. Neural. Syst. Rehabil. Eng.* 11, 177–180. doi: 10.1109/TNSRE.2003.814454
- Pfurtscheller, G., Scherer, R., and Neuper, C. (2006). “EEG-Based Brain Computer Interface,” in *The Brain at Work*, ed. R. Parasuraman (New York, NY: Oxford University Press, Inc), 315–328.
- Ramgopal, S., Thome-Souza, S., Jackson, M., Kadish, N. E., Sánchez Fernández, I., Klehm, J., et al. (2014). Seizure detection, seizure prediction, and closed-loop warning systems in epilepsy. *Epilepsy Behav.* 37, 291–307. doi: 10.1016/j.yebeh.2014.06.023
- Regis, J. (2014). Gamma knife for functional diseases. *Neurotherapeutics* 11, 583–592. doi: 10.1007/s13311-014-0276-z
- Regis, J., Bartolomei, F., Rey, M., Genton, P., Dravet, C., Semah, F., et al. (1999). Gamma knife surgery for mesial temporal lobe epilepsy. *Epilepsia* 40, 1551–1556.
- Regis, J., Peragui, J. C., Rey, M., Samson, Y., Levrier, O., Porcheron, D., et al. (1995). First selective amygdalohippocampal radiosurgery for ‘mesial temporal lobe epilepsy’. *Stereotact. Funct. Neurosurg.* 64(Suppl. 1), 193–201. doi: 10.1159/000098779
- Rouse, A. G., Stanslaski, S. R., Cong, P., Jensen, R. M., Afshar, P., Ullestad, D., et al. (2011). A chronic generalized bi-directional brain-machine interface. *J. Neural. Engin.* 8:036018. doi: 10.1088/1741-2560/8/3/036018
- Schalk, G., and Leuthardt, E. C. (2011). Brain-computer interfaces using electrocorticographic signals. *IEEE Rev. Biomed. Eng.* 4, 140–154. doi: 10.1109/RBME.2011.2172408
- Schalk, G., Kubanek, J., Miller, K. J., Anderson, N. R., Leuthardt, E. C., Ojemann, J. G., et al. (2007). Decoding two-dimensional movement trajectories using electrocorticographic signals in humans. *J. Neural. Eng.* 4, 264–275. doi: 10.1088/1741-2560/4/3/012
- Schneider, B., Borchers, D. J., and Adler, J. R. (2010). Radiation-Based Neuromodulation: Rationale and New Directions. *Cureus* 2:e8. doi: 10.7759/cureus.8
- Shain, W., Spataro, L., Dilgen, J., Haverstick, K., Retterer, S., Isaacson, M., et al. (2003). Controlling cellular reactive responses around neural prosthetic devices using peripheral and local intervention strategies. *IEEE Trans. Neural. Syst. Rehabil. Eng.* 11, 186–188. doi: 10.1109/TNSRE.2003.814800
- Sjöstedt, E., Zhong, W., Fagerberg, L., Karlsson, M., Mitsios, N., Adori, C., et al. (2020). An atlas of the protein-coding genes in the human, pig, and mouse brain. *Science* 367:aay5947. doi: 10.1126/science.aay5947
- Sorensen, J. C., Bjarkam, C. R., Danielsen, E. H., Simonsen, C. Z., and Geneser, F. A. (2000). Oriented sectioning of irregular tissue blocks in relation to computerized scanning modalities: results from the domestic pig brain. *J. Neurosci. Methods* 104, 93–98.
- Sørensen, J. C., Nielsen, M. S., Rosendal, F., Deding, D., Ettrup, K. S., Jensen, K. N., et al. (2011). Development of neuromodulation treatments in a large animal model—do neurosurgeons dream of electric pigs? *Prog. Brain Res.* 194, 97–103. doi: 10.1016/b978-0-444-53815-4.00014-5
- Srinivasan, R. (1999). Methods to improve the spatial resolution of EEG. *Int. J. Bioelectromag.* 1, 102–111.
- Staba, R. J., Wilson, C. L., Bragin, A., Fried, I., and Engel, J. Jr. (2002). Quantitative analysis of high-frequency oscillations (80–500 Hz) recorded in human epileptic hippocampus and entorhinal cortex. *J. Neurophysiol.* 88, 1743–1752. doi: 10.1152/jn.2002.88.4.1743
- Steiner, L., Lindquist, C., Adler, J. R., Torner, J. C., Alves, W., and Steiner, M. (1992). Clinical outcome of radiosurgery for cerebral arteriovenous malformations. *J. Neurosurg.* 77, 1–8. doi: 10.3171/jns.1992.77.1.0001
- Van de Vel, A., Cuppens, K., Bonroy, B., Milosevic, M., Jansen, K., Van Huffel, S., et al. (2016). Non-EEG seizure detection systems and potential SUDEP prevention: State of the art: Review and update. *Seizure* 41, 141–153. doi: 10.1016/j.seizure.2016.07.012
- Vansteensel, M. J., Pels, E. G. M., Bleichner, M. G., Branco, M. P., Denison, T., Freudenburg, Z. V., et al. (2016). Fully Implanted Brain-Computer Interface in a Locked-In Patient with ALS. *N. Engl. J. Med.* 375, 2060–2066. doi: 10.1056/NEJMoa1608085
- Wolpaw, J. R., Birbaumer, N., McFarland, D. J., Pfurtscheller, G., and Vaughan, T. M. (2002). Brain-computer interfaces for communication and control. *Clin. Neurophysiol.* 113, 767–791. doi: 10.1016/s1388-2457(02)00057-3
- Won, D. S., Obeid, L., Morizio, J., Nicoletis, M. A. L., and Wolf, P. (2002). Multichannel CMOS analog front end IC for neural recordings. *Engine. Med. Biol.* 3, 2070–2071. doi: 10.1109/IEMBS.2002.1053172
- Yang, J. W., Prouvot, P. H., Reyes-Puerta, V., Stüttgen, M. C., Stroh, A., and Luhmann, H. J. (2017). Optogenetic Modulation of a Minor Fraction of Parvalbumin-Positive Interneurons Specifically Affects Spatiotemporal Dynamics of Spontaneous and Sensory-Evoked Activity in Mouse Somatosensory Cortex in Vivo. *Cereb. Cortex* 27, 5784–5803. doi: 10.1093/cercor/bhx261
- Yeh, C. I., Cheng, M. F., Xiao, F., Chen, Y. C., Liu, C. C., Chen, H. Y., et al. (2020). Effects of Focal Radiation on [(18)F]-Fluoro-D-Glucose Positron Emission Tomography in the Brains of Miniature Pigs: Preliminary Findings on Local Metabolism. *Neuromodulation* Preprint. doi: 10.1111/ner.13147
- Yin, M., Borton, David, A., Komar, J., Agha, N., Lu, Y., et al. (2014). Wireless Neurosensor for Full-Spectrum Electrophysiology Recordings during Free Behavior. *Neuron* 84, 1170–1182. doi: 10.1016/j.neuron.2014.11.010
- Zaer, H. E. A. (2020). Radionecrosis and cellular changes in small volume stereotactic brain radiosurgery in a porcine model. *Sci. Rep. Nat.* 10:72876–w. doi: 10.1038/s41598-020-72876-w
- Zaer, H., Fan, W., Orlowski, D., Glud, A. N., Andersen, A. S. M., Schneider, M. B., et al. (2020). A Perspective of International Collaboration Through Web-Based Telecommunication—Inspired by COVID-19 Crisis. *Front. Hum. Neurosci.* 14:577465. doi: 10.3389/fnhum.2020.577465
- Zhou, A., Santacruz, S. R., Johnson, B. C., Alexandrov, G., Moin, A., Burghardt, F. L., et al. (2019). A wireless and artefact-free 128-channel neuromodulation device for closed-loop stimulation and recording in non-human primates. *Nat. Biomed. Engin.* 3, 15–26.
- Zhu, B., Shin, U., and Shoaran, M. (2020). Closed-Loop Neural Interfaces with Embedded Machine Learning. *arXiv*. preprint.

**Conflict of Interest:** MBS and JRA are employees of Zap Surgical Systems, Inc., that funded this study, own stock, and have patents in the field of stereotactic radiosurgery without affecting the trial’s outcome. AD, QF, VG, and JM were employees of Triangle BioSystems International as a division of Harvard Bioscience Inc., however, did not have any influence on the result of the experiments.

The remaining authors declare that the research was conducted in the absence of any commercial or financial relationships that could be construed as a potential conflict of interest.

Copyright © 2021 Zaer, Deshmukh, Orlowski, Fan, Prouvot, Glud, Jensen, Worm, Lukacova, Mikkelsen, Fitting, Adler, Schneider, Jensen, Fu, Go, Morizio, Sorensen and Stroh. This is an open-access article distributed under the terms of the Creative Commons Attribution License (CC BY). The use, distribution or reproduction in other forums is permitted, provided the original author(s) and the copyright owner(s) are credited and that the original publication in this journal is cited, in accordance with accepted academic practice. No use, distribution or reproduction is permitted which does not comply with these terms.



# Optimal Approach for Signal Detection in Steady-State Visual Evoked Potentials in Humans Using Single-Channel EEG and Stereoscopic Stimuli

Zoltan Derzsi<sup>1,2\*</sup>

<sup>1</sup> Department of Psychology, New York University Abu Dhabi, Abu Dhabi, United Arab Emirates, <sup>2</sup> Institute of Neuroscience, Newcastle University, Newcastle upon Tyne, United Kingdom

## OPEN ACCESS

### Edited by:

Amit Konar,  
Jadavpur University, India

### Reviewed by:

Benoit R. Cottreau,  
UMR5549 Centre de Recherche  
Cerveau et Cognition (CerCo), France  
Shangen Zhang,  
University of Science and Technology  
Beijing, China

### \*Correspondence:

Zoltan Derzsi  
zd8@nyu.edu

### Specialty section:

This article was submitted to  
Brain Imaging Methods,  
a section of the journal  
Frontiers in Neuroscience

**Received:** 30 August 2020

**Accepted:** 20 January 2021

**Published:** 18 February 2021

### Citation:

Derzsi Z (2021) Optimal Approach for  
Signal Detection in Steady-State  
Visual Evoked Potentials in Humans  
Using Single-Channel EEG and  
Stereoscopic Stimuli.  
*Front. Neurosci.* 15:600543.  
doi: 10.3389/fnins.2021.600543

In EEG studies, one of the most common ways to detect a weak periodic signal in the steady-state visual evoked potential (SSVEP) is spectral evaluation, a process that detects peaks of power present at notable temporal frequencies. However, the presence of noise decreases the signal-to-noise ratio (SNR), which in turn lowers the probability of successful detection of these spectral peaks. In this paper, using a single EEG channel, we compare the detection performance of four different metrics to analyse the SSVEP: two metrics that use spectral power density, and two other metrics that use phase coherency. We employ these metrics find weak signals with a known temporal frequency hidden in the SSVEP, using both simulation and real data from a stereoscopic apparent depth movement perception task. We demonstrate that out of these metrics, the phase coherency analysis is the most sensitive way to find weak signals in the SSVEP, provided that the phase information of the stimulus eliciting the SSVEP is preserved.

**Keywords:** EEG, frequency tagging, SSVEP, phase coherency, stereograms, disparity

## 1. INTRODUCTION

While acquiring an EEG signal is easy, the difficulty of recording decent quality signal cannot be overstated: since the data acquisition equipment is working with very small voltages, it is very susceptible to various external (electrical grid, smartphones, etc.) and internal (eye blinks, vascular pulse, etc.) noise sources, which are often several times more powerful than the signal intended to be measured. Unfortunately, various signal processing techniques can clean up an existing recording only to a certain degree, which may not be sufficient in applications where the signals are exceptionally weak. Despite these problems, EEG remains popular since it has excellent temporal resolution and it is non-invasive: in the clinic it may be used to detect anomalous oscillations in patients with epilepsy or migraine (Camfield et al., 1978; Adeli et al., 2003), it may be used for characterizing a transient or steady-state response in the brain (Ciganek, 1961; Norcia et al., 2015), or may be used in Brain-Computer Interface (BCI) applications (Bayliss and Ballard, 2000; Nakanishi et al., 2018).

One of the oldest applications for EEG is to investigate the response of a brain when exposed to a transient stimulus. In the 1960s, this was done with presenting flashes of light, and the EEG signal was recorded by taking a photograph of the EEG trace displayed on an oscilloscope (Ciganek, 1961).

Since the recorded signals were very noisy, the experiment was repeated several dozen times, and the corresponding films were overlaid on each other. After this operation, the magnitude of the noise is reduced, and a clearer transient response, what we now call a flash-evoked potential or Event-Related Potential (ERP) is revealed. The modern-day equivalent of overlaying exposed and developed films on top of each other is averaging the EEG signal in the time domain: after capturing the response for a flash is presented in each trial, it is possible align each trial's recording to the time of the flash, and averaging the signals to reveal the ERP. This time-averaged signal then can be evaluated against a comparison standard (signal absent, healthy controls, etc.) later-on in the analysis.

Based on the same principle, it is possible to not only investigate the transient response, but the steady-state response of the brain as well: a more sophisticated example is the “frequency tagging” technique, where instead of a single transient stimulus, a continuous periodic stimulus is used. Using the flash example above mentioned earlier, this would mean using flickering light instead of presenting a single flash. Provided that the light conditions are carefully chosen (Herrmann, 2001; Norcia et al., 2015), and are kept constant throughout the trials, the stimulus elicits a detectable neural response, and if there are enough trials recorded, the amplitude of the frequency or frequencies corresponding to the stimulus will be elevated in the spectrum of the SSVEP. The elevated frequencies may not always be the same as the temporal frequency of the stimulus (Hébert-Lalonde et al., 2014): it may be a harmonic (Norcia and Tyler, 1984) or if several temporal frequencies are used at the same time, they may produce intermodulation products (Baith and Levi, 1988): the sum and difference of these frequencies, or an arbitrary combination of these. SSVEPs may be studied with techniques other than EEG as well, such as Magnetoencephalography (MEG) (Srinivasan et al., 1999) or functional Magnetic Resonance Imaging (fMRI) (Boremanse et al., 2013) as well.

To analyse SSVEPs, the signal is converted between the time and frequency domains with a time-frequency transform, which is typically the Fourier transform (Norcia et al., 2015), or alternatively, the continuous wavelet transform (Daubechies, 1990; Adeli et al., 2003; Wu and Yao, 2007) may be used. There is a free and open-source software implementation of both of these, and they are part of a larger package called EEGLAB (Delorme and Makeig, 2004).

With the use of the Fourier transform, if  $S_k(t)$  is the EEG trace recorded at a particular channel on the  $k$ th trial where the stimulus was presented, we can define the Fourier component  $V_k(f)$  at the frequency  $f$  as:

$$V_k(f) = \frac{1}{T_w} \int_0^{T_w} e^{2\pi ift} S_k(t) dt \quad (1)$$

where  $T_w$  is the temporal window which contains the SSVEP and is being used for the Fourier-transform. It is worth noting that Equation (1) is for analogue signals that are continuous in time. In modern computer systems, the signals are sampled at a rate that is at least twice more than the maximum intended temporal frequency to be recorded. In EEG, this sampling frequency ranges

between 250 Hz and 1 kHz. On the sampled signal, which is now discrete in time, it is still possible to execute the Fourier transform, which is typically done by the Fast Fourier Transform (FFT) algorithm (Cooley and Turkey, 1965). The FFT produces a number of components (or “bins”), that are corresponding to discrete temporal frequencies. They contain the spectral power and phase of a small band of these frequencies determined by the ratio of the sampling frequency and the number of samples in the FFT window. To find which component corresponds to a particular temporal frequency in the analogue signal, the following equation may be used:

$$n_c = \left\lceil \frac{f_x}{(f_s/2)/(n_w/2)} \right\rceil + 1; \quad \text{where } n_c \in N \quad (2)$$

$f_x$  is the temporal frequency in question,  $f_s$  is the frequency the EEG signal was sampled at,  $n_w$  is the FFT window size, which is the number of samples the FFT algorithm worked with. The +1 term is there to add the offset for the component corresponding to the temporal frequency of 0 Hz, which is also called the “Direct Current” (DC) component. As the result of the FFT is discrete in frequency,  $n_c$  can only be a natural number and the equation's result should be rounded to the nearest integer. Once the correct Fourier component is identified using this equation, we can use the same signal processing steps as we would for an analogue signal. The Fourier-component is a complex number, and has an amplitude and phase component.

We assume that the SSVEP in the EEG recording in the presence of a periodic stimulus is a linear combination of the “signal” that we want to measure (the neural response to the periodic stimulus), and the “noise” which represents the measurement of every other source contained in the EEG trace. If both the signal and the noise are small enough to not cause non-linear distortion, we can express them as:

$$V_k = [(A_0 + \alpha_k) \exp(i\phi_0 + i\zeta_k)] + [(N_0 + \beta_k) \exp(i\xi_k)] \quad (3)$$

where the first term represents the Fourier component of the signal which is the response to the periodic stimulus; and the second term is the response due to the noise in the EEG trace.  $A_0$  and  $N_0$  are the mean values of the signal and noise amplitudes, respectively across  $k$  trials.  $\alpha_k$  and  $\beta_k$  are trial-dependent.  $\phi_0$  is the phase of the signal that is elicited by the periodic stimulus at the frequency  $f$ . Without loss of generality, we have defined the mean phase in the noise as being zero:  $\langle \zeta_k \rangle = \langle \xi_k \rangle = 0$ , where  $\langle \rangle$  denotes the average over the  $k$  trials. For clarity we have dropped the  $(f)$  throughout, but both terms in this equation depend on the frequency  $f$ . It is applicable for both analog signals by using  $f$  directly, and for digital signals by finding the corresponding Fourier component using Equation (2). Note that the amplitude noise components ( $\alpha_k$ ;  $\beta_k$ ) and the phase noise components ( $\zeta_k$ ;  $\xi_k$ ) are orthogonal. Their effect on the signal  $V_k$  is illustrated in **Figure 1**.

## 1.1. Different Methods for Estimating the SNR

From Equation (3), we have seen that even a single Fourier-component is a consist of several noise terms, and unfortunately

we do not have access to the particular values of these noise terms following a time–frequency transform. Since the definition of noise is very broad and effectively covers any signal or phenomena that is unwanted, different estimation methods exist in the literature. Provided that we have an understanding of the neural mechanism we are investigating, we can select a smaller band in the spectrum. For example, in a study where we have a good understanding of the neural mechanism tested, it is possible to anticipate which temporal frequencies will be present in the SSVEP. In studies where FFT is used to analyse the spectrum of the SSVEP, an acceptable approach is to take the neighboring 10–20 Fourier components surrounding the temporal frequency of interest, and calculate its average value. Then, the SNR may be estimated by calculating the ratio of the values of the of the Fourier component of interest, and the noise level. This was done in several studies (Srinivasan et al., 1999; Cottureau et al., 2011; Alonso-Prieto et al., 2013; Boremanse et al., 2013), and with this method, it is impossible to detect signals that are below the noise.

This method works best if the spectrum used for calculating the noise levels are clear enough, and we know precisely which temporal frequency we are expecting the signal to be present in the SSVEP. Unfortunately, in some cases we may not have such luxury: the noise may not be pure white or pink noise, or perhaps other oscillations may be present in the SSVEP that may not be related to the stimulus at all. In these cases, this SNR estimation method may not be reliable.

Perhaps a better approach is to go back to the original definition: noise is every signal we don't want in our recording. The signal we are investigating is weak, and is buried in the EEG trace in the time domain. If the signal was strong, we would be able to find it just by looking at the EEG signal itself in the time domain. In the time domain, the SNR can simply be calculated by the taking the ratio of the peak levels, in a similar way how the  $A_0$  and  $N_0$  terms play a role in Equation (3). Since the SSVEPs are usually invisible in a single trial, we can assume that they are several times below the noise level. A few example representations of SNRs in the time domain are shown in **Figure 2**. Every subsequent signal processing step, such as filtering or averaging across trials is considered to be part of the detection process. Estimating in the SNR in the frequency domain is not as straightforward as in the time domain, since the noise power depends on the spectral bandwidth, and if discrete time signals are used, the values of the Fourier components will additionally depend on the ratio of the FFT window length and sampling frequency as well.

## 1.2. Detecting Weak Signals in the SSVEP

It is possible to express various metrics that can be used to evaluate the SSVEP and detect the signal.

The spectrum is calculated by taking the scalar means of the amplitudes of the Fourier components for each temporal frequency, across all presentations of the stimulus. Formula A is used in **Table 1** to calculate this metric. Since calculating the spectrum ignores the phase angles altogether, only the amplitude terms  $A_0$  and  $\alpha_k$ ,  $N_0$  and  $\beta_k$  play a role in Equation (3). This is visually represented in the left plot of **Figure 3**: our signal is successfully found, when the 95% of  $k$  vectors are within the shaded annulus. The width of the annulus is proportional to the

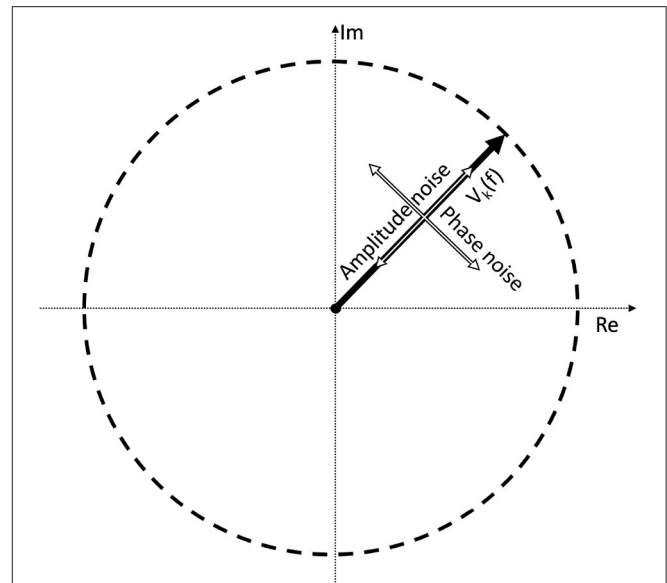


**FIGURE 1** | If we take a complex Fourier component  $V_k(f)$  from a trial, it can be represented as a vector. As this is an EEG signal, it will be naturally noisy. The noise is a vectorial sum of two orthogonal components: the amplitude noise which only affects the length of the vector, and phase noise, which changes the phase angle of the vector, without affecting its amplitude.

trial-dependent terms  $\alpha_k$  and  $\beta_k$  in Equation (3). This formula represents the oldest and most straightforward approach. It is used in many studies, such as Norcia et al. (2015), Hébert-Lalonde et al. (2014), Scherbaum et al. (2011), Gruss et al. (2012), Kamphuisen et al. (2008), Kamphuisen et al. (2008), Skrandies and Jedynak (1999), Baitch and Levi (1988), Alonso-Prieto et al. (2013), Panicker et al. (2011), Rossion et al. (2012), Wu and Yao (2007), Mun et al. (2012), Gruss et al. (2012), and Rideaux et al. (2020). The spectrum can also be used as a control measure or comparison standard, to demonstrate some other technique. A few examples are: Hakvoort (2001) and Lin et al. (2006), where they used spectrum to demonstrate the superiority of multi-channel correlation analysis; and Nakanishi et al. (2018), where they used spectrum to demonstrate the effectiveness of extracting the task-related independent components of the EEG signal.

An other possibility is to take the vector average to calculate the complex spectrum, i.e., to average the complex Fourier components and then calculate the magnitude at the last step to get the result. This is done with formula B in **Table 1**. Assuming each trial consists of an integer number of stimulus cycles, this is equivalent to joining all the trials together in the time domain and computing the Fourier amplitude of the result. This metric takes both the amplitude and the phase ( $A_0$  and  $N_0$ ;  $\phi_0$  in Equation 3, respectively) into account. In the middle plot of **Figure 3**, the complex spectrum is represented as a partial annulus: not only the 95% of the  $k$  vectors have to have a certain length to detect our signal, but they have to be grouped around a certain phase angle  $\phi_0$ . Similarly to the spectrum, the width of the partial annulus is dependent on the amplitude components, but additionally the angle of the partial annulus is proportional to the trial-dependent variations ( $\zeta_k$  and  $\xi_k$  terms in Equation 3) of the

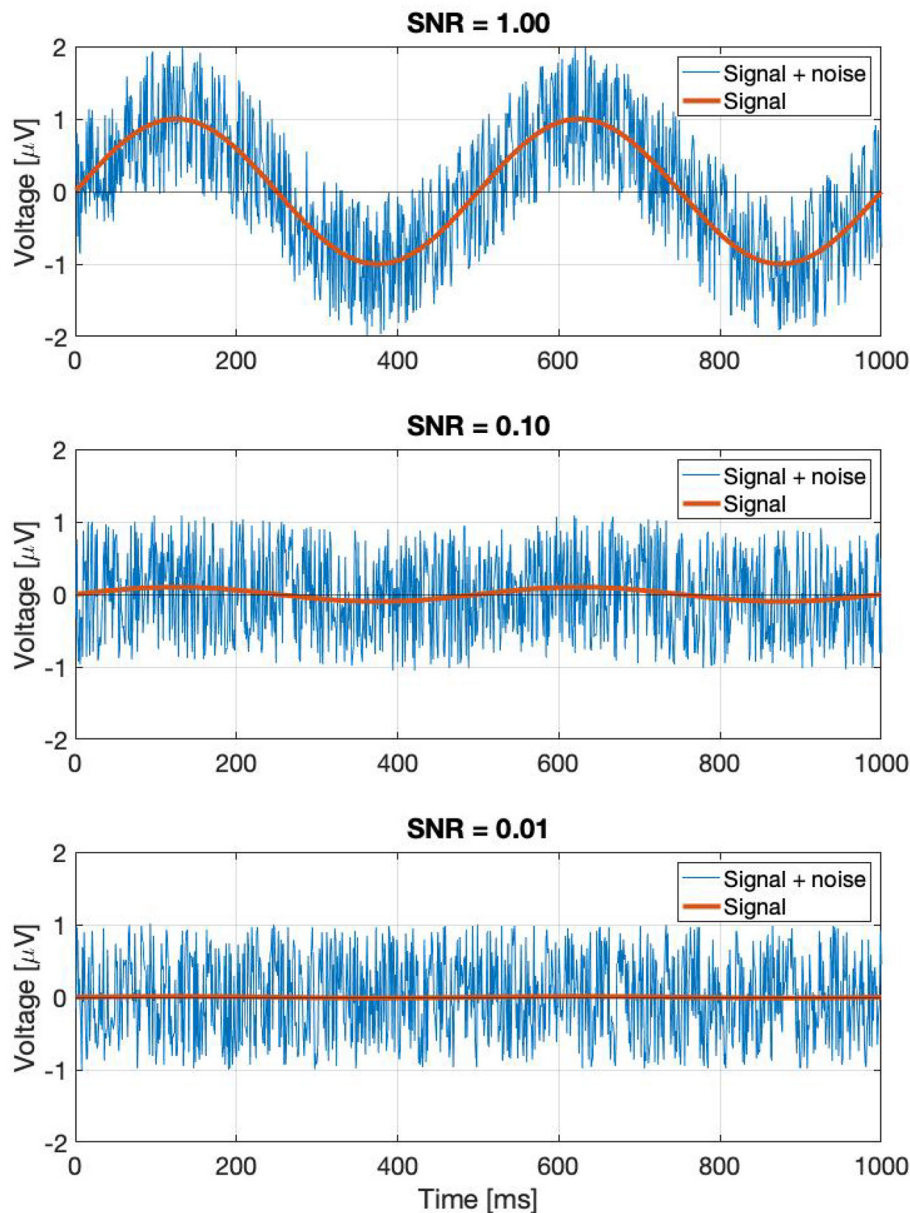


**FIGURE 2** | A demonstration of noisy signals in the time domain. From the top to the bottom, the signal is faded a hundred times.

phase components. With additional filtering in the time domain, formula B was used in the spectral analysis part of Norcia and Tyler (1984). While, Boremanse et al. (2013) used formula A in their study, they averaged the signal in the time domain first, thus effectively used formula B. Except for the missing final step, Cottureau et al. (2011) used formula B, but they kept the final result in vectorial form. Johansson and Jakobsson (2000) purely used formula B.

The third and fourth metrics are the two interpretations of the inter-trial phase coherency (ITC, or simply “Coherency”), and both formula C and D in **Table 1** can be used to calculate it. The coherency metric gets rid of the amplitude component

along with its per-trial variations by normalizing the length of the  $V_k$  vectors in Equation (3) to unity across trials, and only the phase information is preserved. From Equation (3), only the trial-dependent phase angle terms  $\zeta_k$  and  $\xi_k$  play a role in this metric. As the  $\phi_0$  term represents signal propagation time which is treated as a constant, this term is ignored. This metric is visually represented in the right plot of **Figure 3**: as all the vectors are now the same length, successful detection of the signal only occurs when 95% of the  $k$  trials are within the highlighted part of the circle. The subtle difference between formula C and formula D is when the averaging was done: in formula C, the averaging was done as the first step for the vector mean and the second step for

the scalar mean. This formula is used by Norcia and Tyler (1984), and they derived it from first principles. Formula D, on the other hand, executes the averaging at the very last step. This formula is used in EEGLAB (Delorme and Makeig, 2004), in Mitra and Pesaran (1999), Kamphuisen et al. (2008), and Derzsi (2017) as well. The coherency can also be calculated from the variances of the phases across trials:  $1 - \frac{\zeta_k}{\xi_k}$ , but this is often impractical because it is computationally more intensive to get the phase angle variances of  $V_k$  when compared to formula C and D.

We are not aware of any studies which compares the performance of different metrics that can be used for analysing SSVEPs. Norcia and Tyler argue that the vector mean amplitude (B) is preferable to the scalar mean (A), “since noise voltage is proportional to the square root of the bandwidth in Hz” and so “the resulting improvement in signal-to-noise is equal to  $\sqrt{n}$ ” (Norcia and Tyler, 1984). One can see from Equation (3) that if the phase of the original response were entirely random, i.e.,  $\zeta_k$  were uniformly distributed between  $[0^\circ 360^\circ]$ , the first complex component would tend to average to zero across many repetitions, and this metric would asymptote to  $A_0$ , the mean amplitude of the signal. However, in general, which metric is best must depend on the properties of the signal as well as of the noise and thus is hard to derive a priori. In this paper, we find out which of these four metrics provide the most reliable results with the least number of trials to detect weak signals such as the ones used in frequency tagging studies. We compare the performance of the four metrics shown in **Table 1** using a simulation and the SSVEPs from a frequency tagging experiment where human subjects viewed temporally modulated stereoscopic disparity (Norcia and Tyler, 1984; Derzsi, 2017).

## 2. METHODS

We created two simulations in Matlab to evaluate our four metrics in **Table 1**, and we also replicated Norcia and Tyler’s single-carrier frequency tagging study (Norcia and Tyler, 1984).

### 2.1. Simulations

We created two simulations: In the first simulation, we created two different SNR conditions, for the purpose of finding out how many trials are required for our four metrics to successfully detect the signal. The second simulation, we approximated how many trials are needed to reliably detect the signal as a function of the SNR.

The distributions in both simulations are built up from three components: white noise (1); an interfering “birdie” signal (2), which is an 8 Hz sine wave. This signal is unstable, its frequency and its phase angle are both randomized across trials. The purpose of the birdie signal is to imitate an independent separate oscillation in the EEG signal, similarly to alpha waves for example. In both simulations, we use the four metrics to find the frequency tagged carrier (3), which is a weak 13 Hz sine wave, and is always in the same phase across the trials. The detection criterion is always the same: the Fourier component belonging to the frequency tagged signal has to be above the noise threshold, which is the 95<sup>th</sup> percentile of the distribution created

**TABLE 1** | Some metrics that can be extracted from an SSVEP.

Name	Formula	Used in studies
Spectrum	$A(f) = \frac{1}{n} \sum_{k=1}^n  V_k(f) $	Norcia et al. (2015), Hébert-Lalonde et al. (2014), Scherbaum et al. (2011), Gruss et al. (2012), Kamphuisen et al. (2008), Skrandies and Jedynek (1999), Baitch and Levi (1988), Hakvoort (2001) as a control; Lin et al. (2006) as control; Alonso-Prieto et al. (2013), Panicker et al. (2011), Rossion et al. (2012), Wu and Yao (2007), Nakanishi et al. (2018) as control; Mun et al. (2012), Gruss et al. (2012), Rideaux et al. (2020), and many many more...
Complex spectrum	$B(f) = \frac{1}{n} \left  \sum_{k=1}^n V_k(f) \right $	Norcia and Tyler (1984) with additional filtering in the time-domain; Cottureau et al. (2011) and they kept the values in a vectorial form; Boremanse et al. (2013) used formula A, but they averaged in the time domain first; Johansson and Jakobsson (2000)
Coherency 1	$C(f) = \frac{\sum_{k=1}^n V_k(f)}{\sum_{k=1}^n  V_k(f) }$	Norcia and Tyler (1984)
Coherency 2	$D(f) = \frac{1}{n} \left  \sum_{k=1}^n \frac{V_k(f)}{ V_k(f) } \right $	Mitra and Pesaran (1999), Kamphuisen et al. (2008), Derzsi (2017), and the experiment in this paper

$V_k(f)$  is the input Fourier component recorded by a particular channel at frequency  $f$ , in the  $k$ th trial across  $n$  trials.

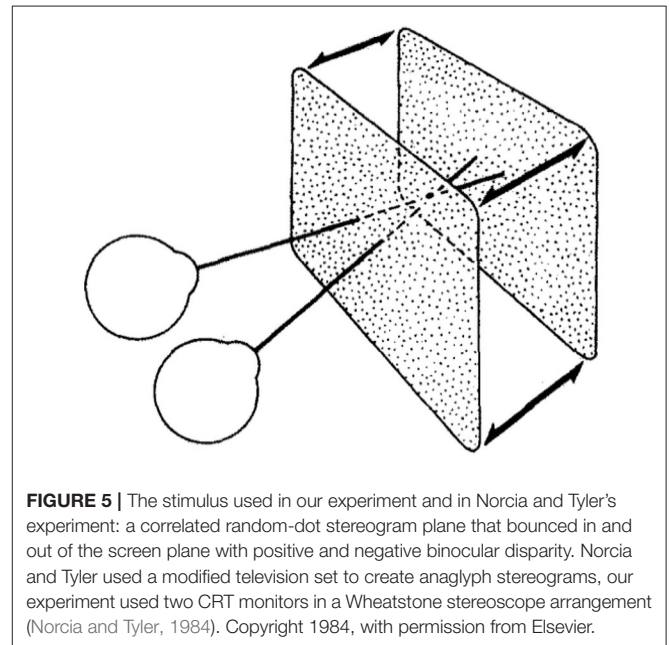
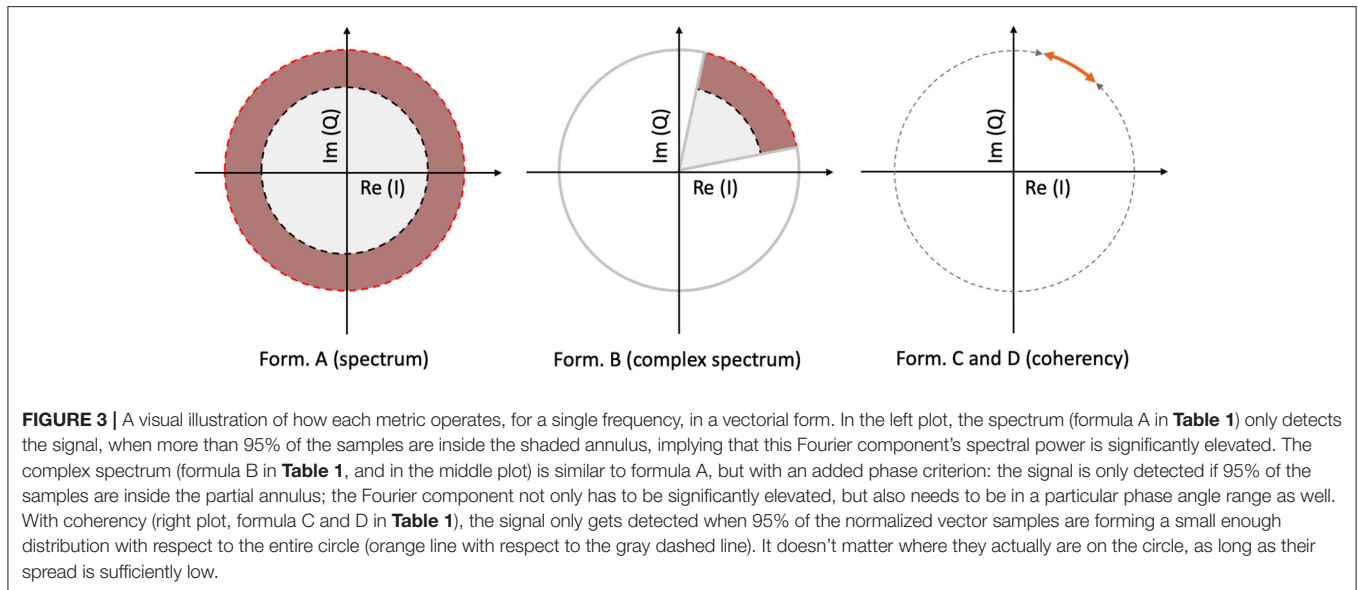
from the birdie signal and the white noise in the frequency band of 0.1–30 Hz.

#### 2.1.1. First Stimulation: Performance of Metrics for a Fixed SNR

In the first simulation, the noise had a peak value of 1, the birdie had the peak value of 8. In the “Strong” condition had the peak value of the frequency-tagged signal was 0.042, which corresponds to an SNR of 0.047. The “Weak” condition had a much smaller frequency-tagged signal, with the peak value of 0.003, which corresponds to an SNR of 0.0003. In each iteration, the simulation code creates a new data set with an increasing number of trials, and calculates the probability of the signal being part of the noise distribution. The signal is deemed to be successfully detected for each metric when this probability is less than or below 0.05.

#### 2.1.2. Second Simulation: Number of Trials Required as a Function of SNR

The second simulation, the noise had a peak value of 0.825, the birdie had a peak value of 0.175, and the SNR was varied between 0.1 and 0.00063 in 10 logarithmic steps. The signal was reliably detected with a metric, when the probability of the signal’s Fourier component was above the noise distribution, with a probability of being part of the noise distribution (consisting of the white noise and the birdie) being  $<0.05$ . Since this simulation involves working with random numbers, the simulation is executed 20 times and the resulting trial numbers were averaged. To shorten the execution time, a maximum trial limit of 3,000 was set. If the number of trials exceeded this number without detecting the signal for a metric, no valid results was returned.



The Matlab code used to create the simulation results are included as **Supplementary Material** to this paper.

## 2.2. EEG Experiment

### 2.2.1. Participants and Ethics

As part of a PhD project (Derzsi, 2017), we measured the spatio-temporal limits of depth perception. As a secondary experiment in the project which is essentially a replication of Norcia and Tyler's study, we collected 537 good trials from the EEG recordings of 4 participants (adults, 2 males, 2 females, age  $23.5 \pm 3.5$  years). The project was approved by the Ethics Committee of the Faculty of Medical Sciences of Newcastle University.

### 2.2.2. Stimulus and Trials

We used two calibrated Dell P992 CRT monitors in a Wheatstone stereoscope configuration to create our stereoscopic stimulus. The participant's head was placed on a chin rest in front of the mirror, and the displays covered  $40 \times 40^\circ$  visual angle. The refresh rate of the monitors was 100 Hz. A photo of the set-up is shown in **Figure 4**.

We wrote a stimulus using Psychtoolbox (Pelli, 1997; Kleiner et al., 2007) which displayed a dynamic random-dot stereogram (Julesz, 1971), consisting of an equal number of black and white dots, presented on a 50% gray background. The mean luminance

of the stimulus was  $57.5 \text{ cd/m}^2$ , and the dot density was 0.06%. The locations of the dots were updated at every frame (10 ms).

The trials were executed by the participants, and they were short, between 6 and 8 s. Each trial featured a “dot onset” preamble of between 1 and 1.5 s where the dots were displayed with zero disparity. Then once this time had elapsed, the applied binocular disparity (“disparity onset”) alternated between  $\pm 0.05^\circ$ , at a rate of 2.1 Hz, or 48 frames, as depicted in **Figure 5**. This alternation continued for a random time between 5 and 6 s. The EEG traces were then temporally aligned such that the onset of the disparity alternation occurred at  $t = 0$  as per **Figure 6** corresponded.

### 2.2.3. EEG Recordings and Preprocessing

We used Electrical Geodesics’ (“EGI,” Eugene, Oregon, USA) 128 channel HydroCel Geodesic Sensor Net (GSN) system to record our EEG data. The electrode cap is connected to the participant using silver chloride electrodes, with sponges soaked in an electrolyte, which is made of saline solution with baby shampoo mixed in. For each channel, the impedances were kept below 50 k $\Omega$ . The signal was sampled at 1 kHz, and the “disparity onset” event was presented as a TTL signal that was directly coupled from the CRT monitor using a photodiode and a peak detector circuit.

In Net Station (EGI’s proprietary EEG software) we filtered the continuous recordings between 0.1 and 70 Hz, and a narrow band-stop (notch) filter was also in place to reduce the effect of the 50 Hz mains hum. The recordings then were segmented to the “disparity onset” event within the trials, and further processing was done in Matlab. Trials containing cardiovascular artifacts, or eye blinks and other muscle movements were rejected. If a trial had more than 10% noisy channels that showed signs of electrode detachment, or the drying of electrolyte for example in the EEG signal, it was also rejected. For further analysis, we only used a single channel (no. 72 of the GSN), which was located just above the inion.

### 2.2.4. Analysis

We analyzed the trials using our own code in Matlab, and some analysis was done using EEGLAB (Delorme and Makeig, 2004). We analyzed the simulation results and the EEG data the same way, with the exception that we investigated only the first harmonic of tagged frequency in the simulation.

In the spectral analysis, the neural response to the stimulus is detected by identifying a peak at the known temporal frequency of the stimulus, or a harmonic. In both spectral metrics (formula A and B in **Table 1**), we compared the sample’s Fourier component value at these signal harmonics to every other frequency (i.e., the noise) in the analysis. We counted successful signal detection as occurring when the value at the harmonic is larger than the 95th percentile of the noise. The probability of false detection is calculated by the ratio of how many other peaks in the noise are above the 95th percentile, and how many Fourier

components are included at distinct temporal frequencies in the analysis:

$$p = \left( \sum_{f=f_{min}}^{f_{max}} S_{signal}(f) > [95th \text{ percentile}(N_{noise}(f))] \right) / \left( \sum (f_{max} - f_{min}) \right) \quad (4)$$

where  $S(f)$  is the value of the signal sample,  $N_{noise}$  noise distribution at the frequency  $f$ .

$S_{signal}(f)$  is always a single component in the simulation. In the experimental data analysis, we used the first six harmonics of the temporal frequency of the periodic stimulus.

### 2.2.5. Analysis and Statistics on our EEG Data

In the trials, we looked at the  $(1/\sqrt{f})$ -compensated spectrum and the calculated coherency of the SSVEPs of one single channel at the central occipital area. Since the waveform of the temporal modulation of the stereogram’s depth plane is a symmetrical square wave which only contains odd harmonics, and we know that the neural mechanism triggered is sensitive to changes in disparity, we expect the first derivative of this signal to be present in our EEG recordings. Therefore, we only consider the presence of the even harmonics to be linked to processing, and the odd harmonics to be the original signal passing through the human visual system.

The coherency values are compared against a large number (1,000) synthesized, phase-scrambled noise data sets. Unlike the bootstrapping operation, where the data would be re-sampled at a trial level, we generated our data sets with identical number of trials to the real data we analyzed. This allows us to calculate the 95th percentile of the noise distribution not just across the spectrum, but across data sets, and create a reliable measure of upper noise floor or “noise threshold.” If a coherency value is above this noise threshold, we know immediately that it is statistically significant. The exact probability can be worked out using formula 4 as well.

## 3. RESULTS

### 3.1. Simulations

#### 3.1.1. First Simulation: Performance of Metrics for a Fixed SNR

In the high SNR (0.047) condition, the signals are shown in three sets of plots in **Figure 7**. In this condition, the frequency-tagged signal is so powerful that the coherency analysis (formula C and D in **Table 1**) is capable of detecting it with only three trials. This is shown in the top middle and top right plot. The complex spectrum (formula B in **Table 1**) is on the edge of detecting the signal too, but its  $p$ -value is slightly below the significance threshold of 0.05. However, just by adding an extra trial in the middle plot, it also successfully detects the frequency tagged signal. While there is a distinct peak at the spectrum (formula A in **Table 1**) at the tagged frequency of 13 Hz as well, it takes far

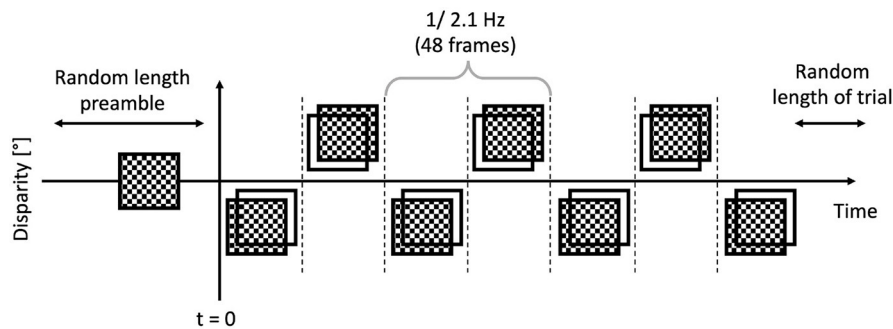


**FIGURE 6** | Anatomy of a trial: the preamble was displayed for a random time between 1 and 1.5 s, then the modulated bouncing disparity appeared on the screen, for a random time between 5 and 6 s. The timing of the “disparity onset” event was recorded with millisecond precision.

more, 11 trials for the spectral analysis to detect it reliably. This is shown in the bottom left plot.

For the low SNR (0.0003) condition, the performance of each metric (see **Figure 15**) under the conditions set in the included supplementary code show the probability of erroneous detection (i.e., significance level,  $p$ -value) as a function of how many trials are included in a data set. The coherency analysis (formula C and D in **Table 1**) requires around 200 trials for a  $p$ -value of 0.05, with formula C showing to be a little more sensitive than formula D. The complex spectrum metric (formula B in **Table 1**) requires about 800 trials to achieve the same significance level. For the same signal and same conditions, the spectral analysis (formula A in **Table 1**) does not provide meaningful results. For the purpose of illustration, **Figure 15**'s scatter of  $p$ -values are fitted with a simple exponential model ( $y = a \times \exp(bx)$ ), with good quality fitting  $r^2 \geq 0.85$ , with the exception of the spectral analysis, as the  $p$ -values hover around 0.4–0.5.

In the low SNR condition, the signals are shown in the top plots of **Figure 6** at 350 trials, and in the top plots at 900 trials. The spectral analysis shows in the far left plots how powerful the birdie signal is with respect to the tagged carrier signal: under these circumstances, detecting the tagged signal in the spectrum is impossible. In top middle left plot, the complex spectrum (formula B in **Table 1**) does show a peak at the tagged frequency, but its  $p$ -value is too high to be deemed reliable. The coherency analysis (formula C and D in **Table 1**, middle and far right plots) show confidence levels below 0.05, implying that the signal was reliably detected. Formula D's coherency value is lower (0.15) than Formula C's (0.2), but -similarly to the complex spectrum- formula C shows a false positive at the birdie signal's frequency of 8 Hz.

Adding more trials to the experiment shows two additional benefits: from **Figures 7, 8**, the noise floor is noticeably lower, particularly with the coherency analysis at the right plots; and adding more trials to the data set allows the complex spectrum to detect the frequency tagged signal as well. The effect of the birdie is still visible in all metrics, but with formula D in the bottom far right plot of **Figure 7** it is considerably diminished.

### 3.1.2. Second Simulation: Number of Trials Required as a Function of SNR

In **Figure 14**, the straight lines are estimations from information theory. At high SNRs, up to about 0.06 and above, only a

single trial is enough to find the frequency tagged signal with the spectrum and the complex spectrum techniques (formula A and B in **Table 1**). Below these SNRs, the required trial numbers increase rapidly, requiring about a hundred trials at the SNR of 0.03. The traces split noticeably at around the SNR of 0.02, where the spectrum requires about 4–5 times more trials than the coherency (formula C and D in **Table 1**) and the complex spectrum to detect the signal (B in **Table 1**). By the time the SNR gets to as small as 0.01, more than 3,000 trials are needed to be detected with the spectrum, at which point the simulation terminated. Going further to weaker and weaker SNRs, the complex spectrum and the coherency lines split: at around the SNR of 0.0035, approximately the complex spectrum requires double the number of trials than the coherency to detect the signal. This ratio diminishes somewhat as the SNR approaches even smaller values. At the SNR of 0.002, more than 3,000 trials are required for the complex spectrum to detect the signal, at which point the simulation terminates. Interestingly, the required number of trials seem to peak at the SNR of 0.002, and fewer trials are needed for worse SNRs. At the SNR of 0.0005, the complex spectrum required about 1,000 trials, whereas the coherency only needed 4–500.

## 3.2. EEG Experiment

**Figures 9, 10** show the results of all four metrics (see **Table 1**), for two participants. The plots were generated from 111 and 139 trials, respectively. In the two left (spectrum and complex spectrum) plots, the blue lines are the 95<sup>th</sup> percentile of the noise spectrum with the harmonics of the stimulus signal excluded.

The spectrum (formula A in **Table 1**, far left plots), besides a peak around the alpha (8–12 Hz) band with one participant, is unremarkable. The near left plots show the results of the complex spectrum calculated with formula B in **Table 1**, which does seem to show peaks at the first harmonic of the temporal modulation frequency with both participants, and the second and fourth harmonics with one participant. There are other peaks present above the 95<sup>th</sup> percentile in unrelated frequencies between the first and the second harmonics in a similar fashion to the response to the birdie signal presented in the simulation results in **Figures 8, 7**, respectively.

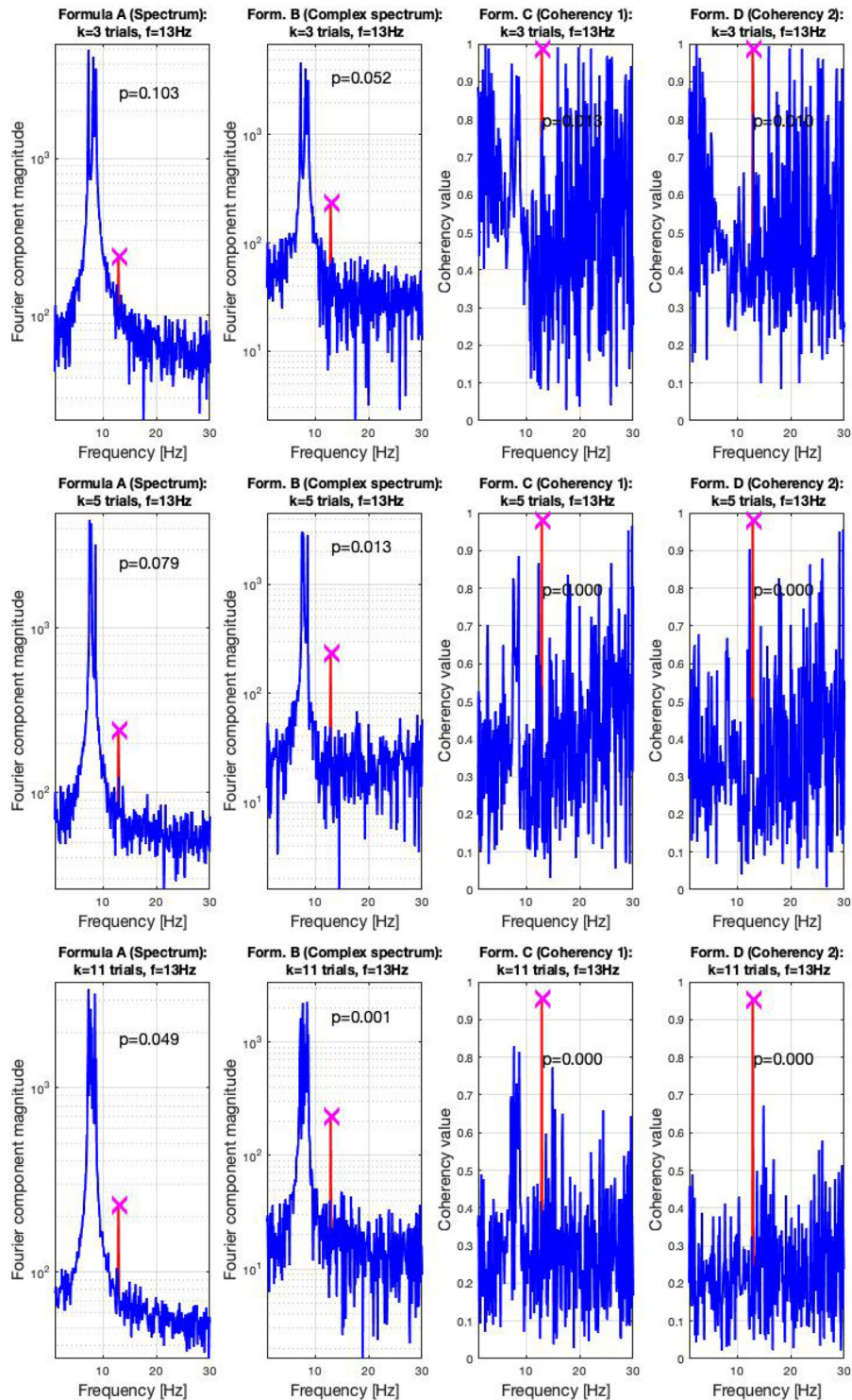


**FIGURE 7 |** In the high SNR (0.0047) condition tested by the simulation, only a handful of trials were enough to detect the hidden signal: in the top right plots, formula C and D only required three trials to achieve reliable detection. In the middle plots, in the middle left, the complex spectrum detected the signal at 4 trials. For the spectrum to do the same, 11 trials were necessary, as visible in the bottom plot. These plots are generated using the code in the **Supplementary Material**, using the same signal. The frequency tagged signal is at 13 Hz, and the unstable birdie signal originating from an independent oscillation is at  $8 \pm 0.8$  Hz.

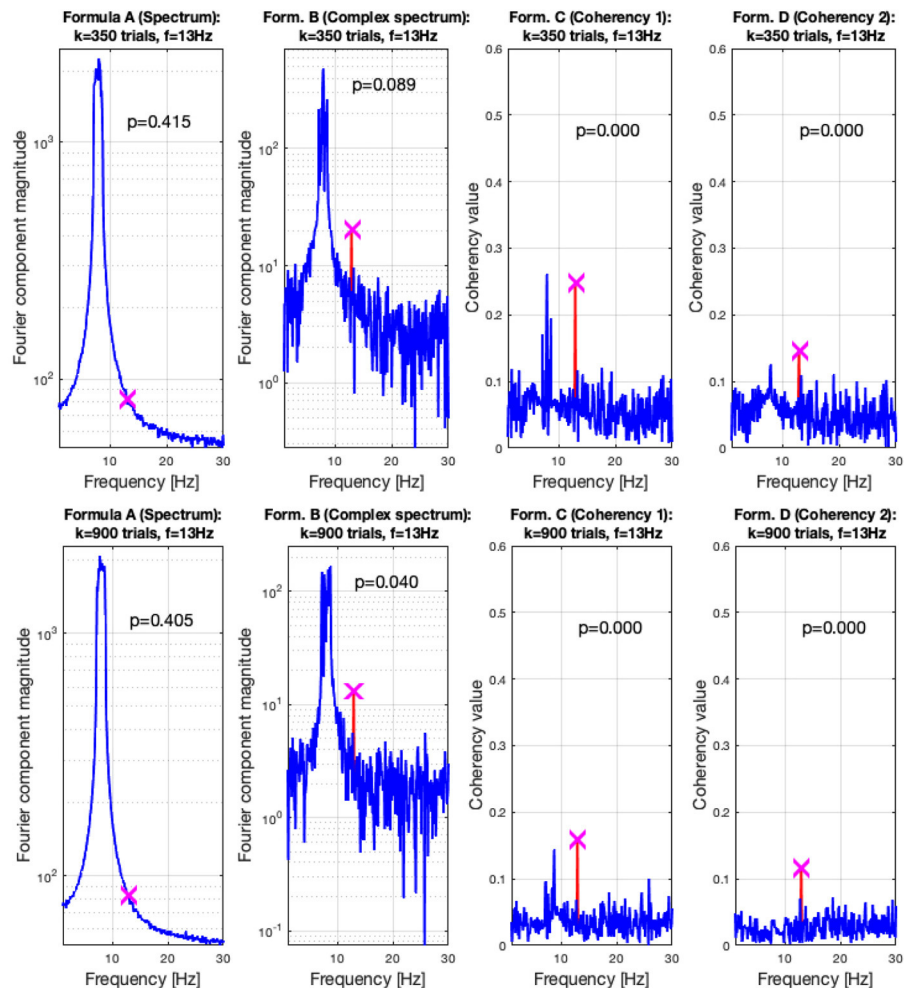
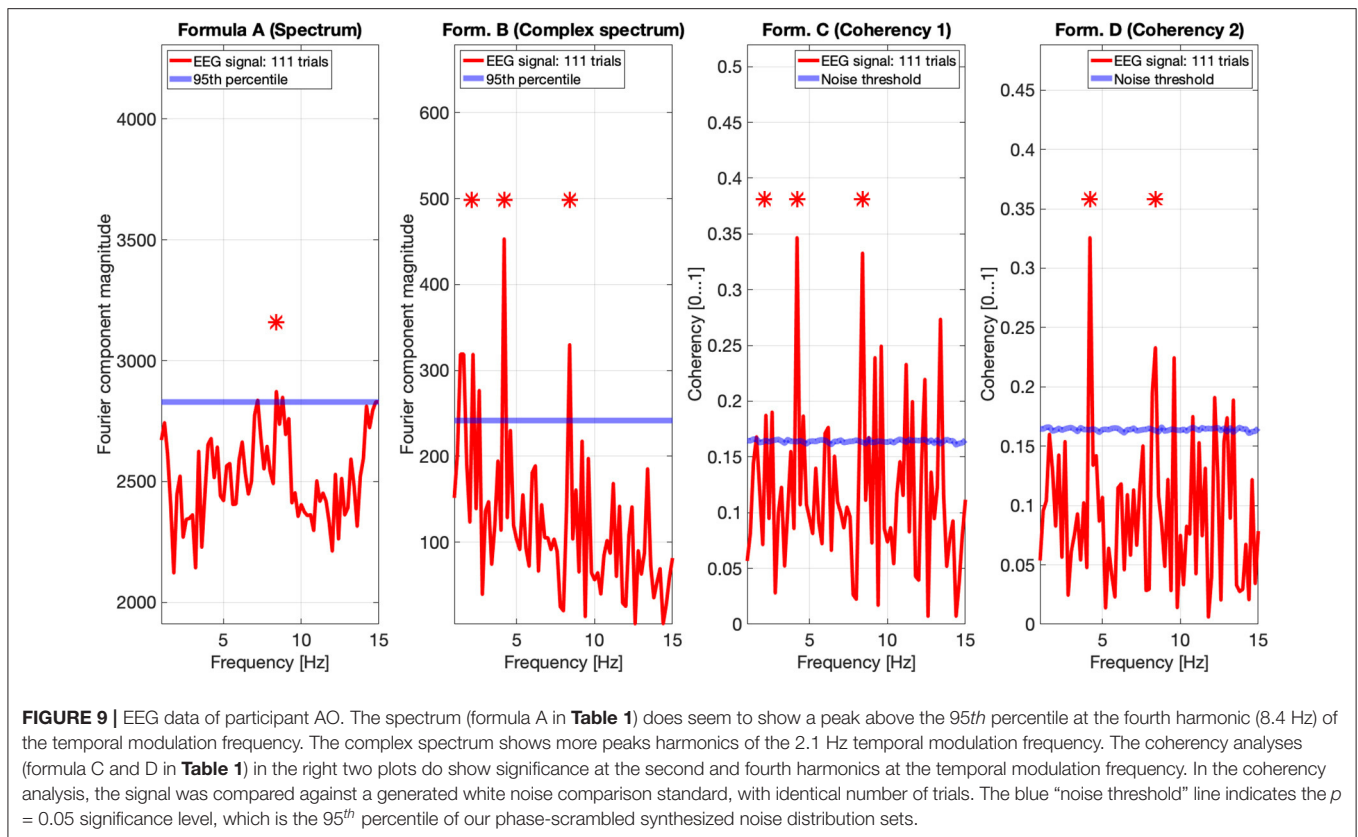


**FIGURE 8** | In the low SNR (0.0003) condition tested by the simulation, at 350 trials in the top plots, the hidden signal was detected successfully with the coherency (formula C and D in **Table 1**) method. The complex spectrum (formula B in **Table 1**) provided reliable results only at the bottom at 900 trials. The spectrum failed to detect the signal at all. These plots are generated using the code in the **Supplementary Material**, using the same signal. The frequency tagged signal is at 13 Hz, and the birdie signal originating from an independent oscillation is at  $8 \pm 0.8$  Hz. The birdie signal's interference is visible in all plots except formula D's in the far right of the bottom plots.

The two right plots show the coherency of the signal (formula C and D in **Table 1**), with the peaks on the red traces highlighting the harmonics of the temporal modulation frequency. The blue lines in the right plots are noise thresholds, which is calculated as the mean 95<sup>th</sup> percentile of 1,000 phase-scrambled noise data sets, with matching number of trials to the EEG data. This “noise threshold” is used as an indicator for significance: if a signal is above the noise threshold, it is deemed to be significant, and thus the signal is detected. The star above the peak indicates that the first, second, and fourth harmonics are distinct from the noise, with a detection error probability of  $<0.05$ . The exact probabilities are calculated with formula 4. Furthermore, the coherency peaks are smaller with formula D than formula C, but at the same time there are fewer coherency peaks above the noise threshold at unrelated temporal frequencies.

In **Figure 11**, we pooled together the trials of our four participants, and plotted the results from all four metrics: the spectrum (formula A in **Table 1**) is in the far plot, the complex spectrum (formula B in **Table 1**), and the coherency (formula D in **Table 1**) are in the right plots. The spectrum of the EEG recordings show the alpha band of 10...12 Hz increased. Apart from this, the spectrum's plot is unremarkable, there are no visible peaks at any of the harmonics of the depth alternation frequency. The complex spectrum in the near right plot did detect the second harmonics of the stimulus frequency, and there are other distinct peaks at further harmonics, but below the significance threshold.

However, the two left plot's coherency analysis shows distinct peaks at the second (4.2 Hz), fourth (8.4 Hz), and sixth (12.6 Hz) harmonics, which are phase-locked to the stimulus stereograms's depth alternation. Additionally, formula



C also detected the base harmonic (2.1 Hz) of the stimulus as well.

## 4. DISCUSSION

### 4.1. EEG Experiment: Successful Replication of Norcia and Tyler’s 1984 Study

While we aimed to replicate the original (Norcia and Tyler, 1984) study as closely as we could in our experiment, since some hardware could not be obtained easily over 30 years after the original study. We have implemented some changes: we doubled the number of participants to 4 and they were naïve to the subject, we rejected trials based on detected artifacts in the EEG signal instead of letting the participants report bad trials themselves, and a single temporal frequency was chosen for the depth alternation which provided us with the strongest neural response. Our display covered a larger visual angle and did not require the wearing of anaglyph glasses. Unlike our study with constant stimulus frequency, Norcia and Tyler used the frequency sweeping technique for the depth alternation. Their frequency response of a single participant is shown in the top plot of **Figure 12**, with a peak at around 3.5 Hz. The second harmonic of our temporal modulation frequency was reasonably close to this value, 4.2 Hz.

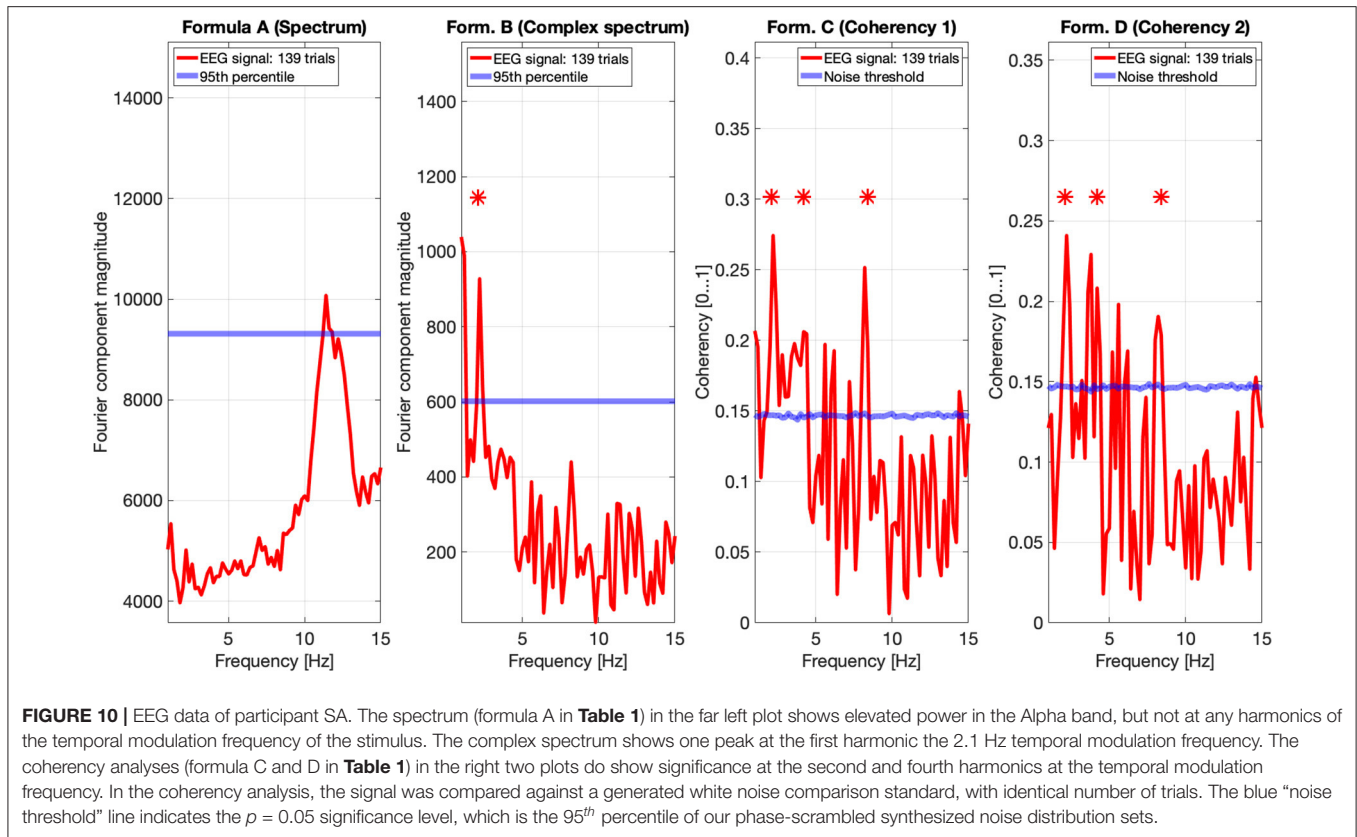
Apart from the above, our dot density and the peak disparity values were close to identical to the original study. Norcia and

Tyler concentrated only at analysing the second harmonic of the depth alternation frequency, because they used discrete tunable filters on the recorded EEG waveform and they calculated the coherency value manually.

Our signal acquisition and processing was done using computers, and so were the time-frequency transforms, which allowed us to not only investigate coherency at the second harmonic of the temporal modulation frequency, but to do so over the entire spectrum until the 500 Hz Nyquist-limit. However, we only analyzed and plotted a smaller sensible part of this band, from 0.1 to 15 Hz. Perhaps a notable drawback of using discrete time signals is when analysing short bursts of it: in our case, only 5 s after the disparity onset event mean that the window of the Fast Fourier Transform is rather small, which lead to a relatively poor, but yet still acceptable frequency resolution of 0.2 Hz per Fourier component. Without increasing the sampling frequency or using longer trials, this is unavoidable. We also believe that this is one of the reasons why our coherency values are smaller than what Norcia and Tyler reported. However, with our statistics, the frequency tagged signal is reliably detected, and thus we have successfully replicated Norcia and Tyler’s study.

### 4.2. Control Measures

The data presented here is a subset of a larger PhD project (Derzsi, 2017), where we used this technique to characterize depth perception in the human visual system: we have found the corresponding coherency peaks for conditions with different



temporal and spatial frequencies, but for the purpose of this paper that compares various metrics in a frequency tagging experiment, only a small fraction of results are included here. In **Figure 13**, we demonstrate that the coherency peak follows the temporal modulation frequency, and that the signal is detectable with fewer trials.

### 4.3. Can Pooling Across Participants Ever Be a Sensible Choice?

A good practice in studies is to collect a number of trials from a participant, generate a per-individual result, and then pool across them to come up with the grand average that is used in the final analysis.

Pooling across participants at a trial level when analysing the spectrum does not produce meaningful results, because of the risk of data being driven by a small number of powerful outliers, which can lead to improper conclusions.

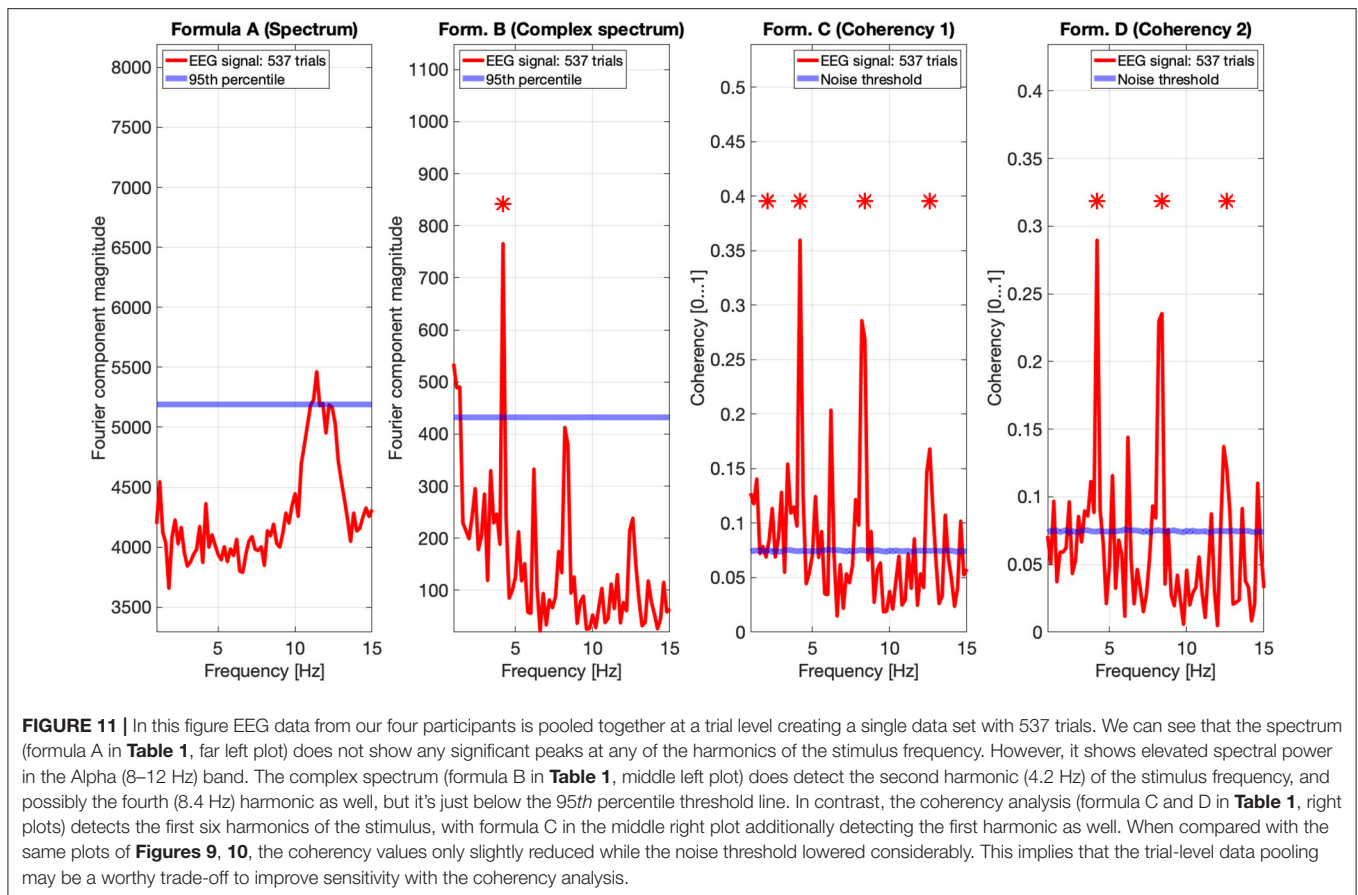
However, since the coherency analysis rejects the amplitude component of the EEG data by principle, the risk described above is eliminated. As each participant will have a different signal propagation time in their brains, the phase angles of the frequency-tagged signals will be different as well.

Pooling across participants at a trial level will result in a reduced coherency value because of the increased spread of the phase angle distribution of the signal (different  $\phi_0$  and different  $\zeta_k$  in Equation 3 for each participant). Since in the coherency analysis, we are evaluating the coherency data against synthesized

phase-scrambled control data sets, the actual coherency value itself does not matter: as long as it's significantly elevated from the noise, it is detected successfully. In our case, this is shown in **Figures 9–11**: the coherency value for a single participant at 4.2 Hz is 0.33, which reduces to 0.28 after pooling four participants together. However, the noise level in the single participant's data reduces to around 0.08 in **Figure 11**, which means that our chances of detecting the signal has increased despite the overall reduction of the coherency values, making pooling across participants at a trial level a worthwhile trade-off for low temporal frequencies. Provided that the variance of signal propagation times of individuals is less than half a period of the temporal frequency of the stimulus, the overall reduction of coherency values will not be considerable, and this minimizes the risk of losing the signal.

### 4.4. Noise Model Choice

In nature, the electrical noise is fundamentally pink noise: the noise power follows a  $1/f$  pattern in the spectrum, and the EEG signals are no exception. Since the EEG equipment measures voltage and not power, the noise follows a  $1/\sqrt{f}$  pattern. This has to be compensated for when evaluating the spectrum and the complex spectrum (formula A and B in **Table 1**). However, irrespective of what type of “noise” we are dealing with—whether external electrical noise or the electrical signal of some unrelated biological function—the noise will not be phase-locked to the temporal modulation frequency of the stimulus.



Thus, following a Fourier transform, the distribution of the arguments of the vectorial representations of the complex Fourier components are completely stochastic within the interval of 0 and  $360^\circ$ . Additionally, since in a frequency tagging experiment we consider every irrelevant signal component as noise, it is difficult to create a model that accurately imitates the signals created by the brain. In the simulation, the presence of white noise and the birdie signal was an attempt to replicate this, but it is fundamentally insufficient. In reality, there may be a large number of birdies present, mixed with transients and other artifacts from various sources. For instance, at 111 (see **Figure 9**) and at 139 trials (see **Figure 10**), we should see some relevant peaks at the spectrum, even if they are below the significance threshold. The lack of peaks in the spectra of real data show that the noise model used in the spectrum simulations is too forgiving, and this leads to a rather optimistic prediction of the performance of the spectrum in the simulations. This, however, only applies to the spectrum, and not for the coherency analysis.

Since the coherency analysis effectively removes the amplitude component along with its noise component of the signal completely, the resulting phase noise distribution will always be a uniform distribution, irrespective of what type of noise the acquired signal contained. This property enables it to be compared against artificially generated controls with very good accuracy.

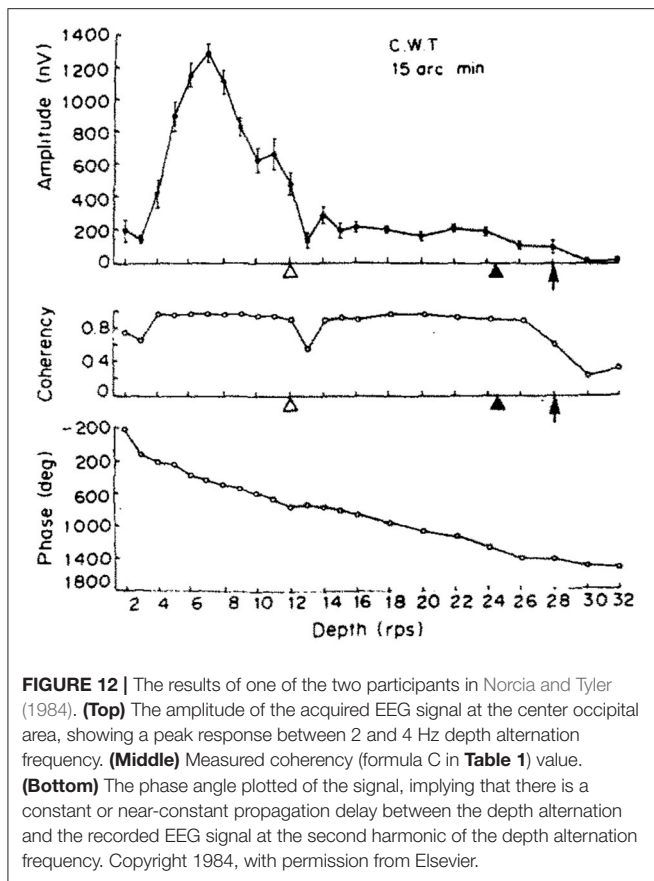
When comparing the coherency plot of the EEG signal in **Figure 11** in between harmonics (for example 10 and 12 Hz, or 15 Hz and above in **Derzsi (2017)** with the coherency plots on either **Figure 7** or **Figure 6**, we can see that the coherency values are indeed uniformly distributed with respect to temporal frequency.

We could have implemented any other noise types in the simulation, but for the sake of simplicity and to due to the fact that the coherency analysis is insensitive by principle to the type of noise used, we decided to use only white noise.

#### 4.5. Comparing the Performance of Spectrum and Coherency With Weak Signals

The metric that performs the worst is the spectrum (formula A in **Table 1**). At very low SNRs the signal is undetectable with conventional spectral analysis. Findings from information theory (Proakis, 2000; Proakis and Salehi, 2008; Derzsi, 2017) suggest that techniques using or exclusively relying on the phase information perform more reliably at low SNRs. We have verified this with both our simulation results in **Figure 15** and even with real data in **Figure 11**. This further reinforces that spectral evaluation in a weak-signal frequency-tagging study is one of the worst things to do.

The best performer is the coherency analysis, formula C and D in **Table 1**: since it effectively rejects the amplitude component of



a vector along with its noise component, it increases the SNR, and this property makes it less prone to external interfering signals. Since the coherency is a measure of how consistent the phase angles are across the trials, the actual phase angles themselves are not being taken into account. Rather, their distribution with respect to the whole circle is the property that carries information (see Figure 3, middle and right plots), and this makes the coherency analysis is far more resistant against noise than any other approach presented in this paper. The only extra information required in the stimulus is the annotation of the phase as well as the frequency: without it, the coherency analysis is useless.

Based on findings from information theory, we can derive the error performance (Proakis and Salehi, 2008) of various information enclosure (modulation) methods as a function of the SNR. This way, we can approximate how many trials are required as a minimum for successfully detecting a frequency-tagged signal (Derzsi, 2017) that has the phase information annotated with the error probability of  $p = 0.05$ . These are:

$$L_{\text{spectrum}} = \frac{[erfc^{-1}(2 \times 0.05)]^2}{\text{SNR}} \tag{5}$$

$$L_{\text{coherency}} \approx \frac{\frac{1}{4} \times [erfc^{-1}(2 \times 0.05)]^2}{\text{SNR}} \tag{6}$$

where  $L$  is the number of trials required,  $erfc$  is the complementary error function, and  $\text{SNR}$  is the signal-to-noise ratio. It is worth noting that these functions provide a strictly monotonically decreasing number of trials as a function of the SNR. These estimated performances are plotted in Figure 14, and provide similar results to the simulated performance in Figure 15: for example, at the SNR of  $10^{-3}$ , about 400 trials are required for coherency analysis and about 1,100 trials are required for the spectral analysis to provide meaningful results. When comparing this theoretical finding with the simulation results, it shows that these estimations show in Equations (5) and (6) are pessimistic at low SNRs, and optimistic at high SNRs. With a similar SNR in the simulation code that is included as Supplementary Material in this paper, these are about 4–500 and more than 3,000 trials, respectively.

Based on this information, provided that there are no external interfering signals and that the phase of the stimulus was known, we can improve a frequency tagged signal's detection probability by at least a factor of 4, just by analysing its coherency and not its spectrum. Of course, with real-world data this improvement is not as marked, but still considerable.

These equations that estimate the performance do not make a difference between the spectrum formula A and B and the coherency formula C and D. Spectral analysis either fails to detect a weak signal completely, or requires an unrealistically large number of trials to provide acceptable results. The spectral analysis method also is prone to show external interfering signals as false positive results. The coherency analysis, in all cases is a more sensitive approach for weak signals, with the capability of either greatly diminish or completely reject external interfering signals.

#### 4.6. What SNR Is Reasonable in Real Data?

The actual observed SNR depends on the modality and the conditions of the stimulus. Bright flashes produce a very strong response, and relatively few trials are required to produce meaningful results. For example, Hébert-Lalonde et al. (2014) were able to find spatial visual deficits with a blinking spot on the screen from about just a minute of EEG recording. Binocular vision, on the other hand, produces a more subtle response: In Baitch and Levi (1988), over 100 trials were required to detect the lack of binocular visual processing in stereoblind participants. Binocular disparity processing produces even weaker signals: in the EEG study presented in this paper, more than 100 trials were required to detect the disparity-defined visual stimulus with the coherency analysis. Not even 500 trials were enough to detect the signal in the spectrum. Increasing the binocular disparity does not necessarily increase the strength of the neural response: too large, or too quickly changing disparities can not be fused properly. If the visual system does not have enough time to solve the stereo correspondence problem (Ip et al., 2014) or the participant is no longer able to follow it in depth (Alvarez et al., 2005), the depth perception from binocular disparity falls apart. This has been verified experimentally with psychophysics (Kane et al., 2014), and with frequency tagging (Derzsi, 2017) as well.

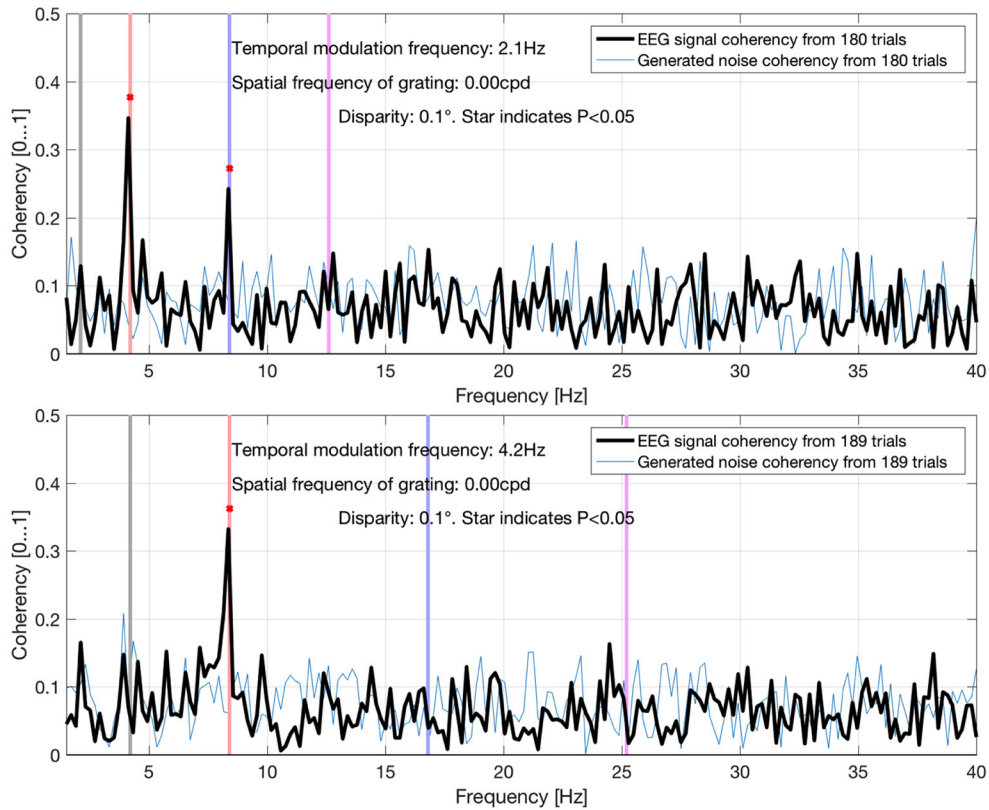


**FIGURE 13 |** Coherency values at different uniform plane (0 cycles-per-degree grating) conditions in Derzsi (2017): the gray line is the temporal modulation frequency of the grating, and the colored (red, blue, magenta) lines are the (second, fourth, and sixth, respectively) harmonics. As the temporal modulation frequency increases, the second harmonics' coherency value follows. The "generated noise coherency" is used as the comparison standard to detect the presence of the signal.

**Number of trials required to achieve p=0.05 significance as a function of signal to noise ratio**

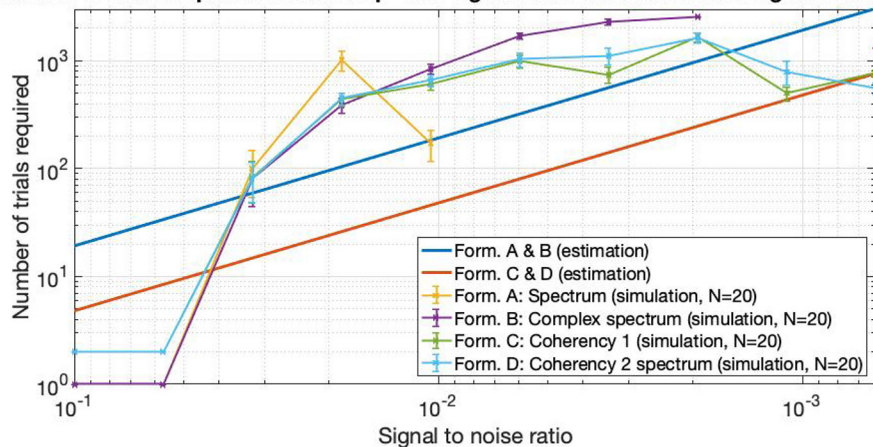


**FIGURE 14 |** As the SNR gets worse and worse, more and more trials are needed to detect the signal. The estimations are from Equations (5) and (6), they are approximated from information theory. The simulated performance is shown for each formula. For SNR 0.06 and above, only 2 trials are enough to detect the frequency tagged signal for the coherency analysis and a single trial for the spectral analysis. Where the lines are incomplete, more than 3,000 trials were not enough to detect the signal, at which point the simulation was terminated. Having the simulation executed 20 times, we see that the coherency analysis requires the least number of trials to reliably detect the signal.

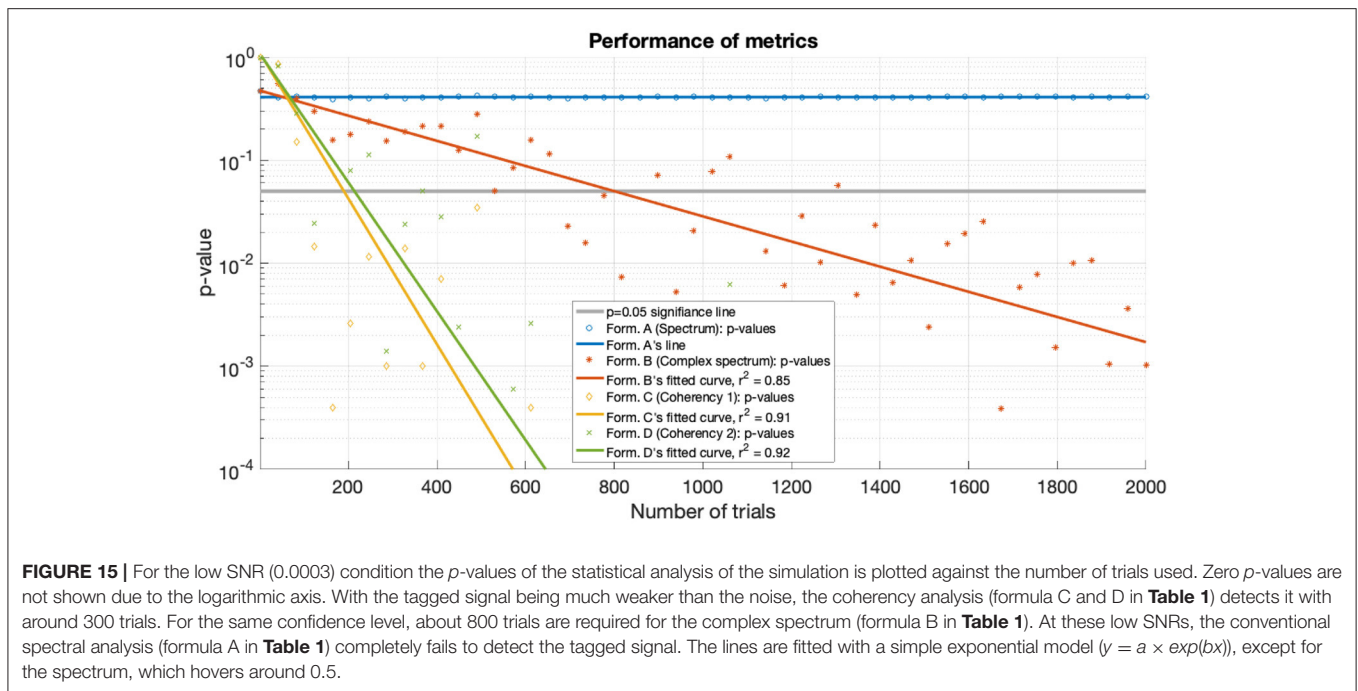


**FIGURE 15 |** For the low SNR (0.0003) condition the  $p$ -values of the statistical analysis of the simulation is plotted against the number of trials used. Zero  $p$ -values are not shown due to the logarithmic axis. With the tagged signal being much weaker than the noise, the coherency analysis (formula C and D in **Table 1**) detects it with around 300 trials. For the same confidence level, about 800 trials are required for the complex spectrum (formula B in **Table 1**). At these low SNRs, the conventional spectral analysis (formula A in **Table 1**) completely fails to detect the tagged signal. The lines are fitted with a simple exponential model ( $y = a \times \exp(bx)$ ), except for the spectrum, which hovers around 0.5.

For spectral analysis, Equation (5) may be modified to provide an approximation of SNR from the number of trials used:

$$SNR \approx \frac{[erfc^{-1}(2 \times 0.05)]^2}{L_{spectrum}} \quad (7)$$

This equation is approximate in nature, because many studies collect more data than what is absolutely minimally required for statistical significance. A visualization of this equation is shown with the dark blue straight line in **Figure 14**. In practice, this means that the estimation is somewhat pessimistic, so the SNRs reported by this formula are somewhat lower than in reality.

From the examples with flashing stimuli above, we estimate that the time-domain SNR are varying between 0.04 and 0.003: for 30 trials used in Hébert-Lalonde et al. (2014)'s flashing spot study is 0.04; for 100 trials used in Baitch and Levi (1988)'s binocular flash study is 0.02; 480 trials used in the control part of Nakanishi et al. (2018)'s flashing of characters is 0.003; 192 trials used in Gruss et al. (2012)'s flashing faces study is 0.015.

For the random-dot stereogram examples from above the SNR is worse, varying from approximately 0.01 to <0.002: for 100 trials used in Cottureau et al. (2012)'s disparity-defined annulus study is 0.015, but with the aid of fMRI; for 384 trials in Rideaux et al. (2020)'s moving circle defined by random-dot stereograms, it is 0.0025; in the study presented in this paper 537 trials were not enough to detect the frequency-tagged signal, therefore the SNR is estimated to be <0.004.

Therefore, the added sensitivity for the coherency analysis may be beneficial in these low SNR conditions, as it decreases the probability of erroneous detection. Additionally, since the coherency analysis is capable of detecting the signals in even lower SNRs, it will be an ideal analysis candidate for future or

unpublished studies, where conventional analysis methods have failed provide convincing results.

### 4.7. Simulations

Both simulations demonstrate that the coherency analysis is the most sensitive method for detecting a weak signal in the SSVEP. In the first stimulation, where we used two conditions to imitate the presence of a strong (see **Figure 7**) and a weak (see **Figure 6**) signal, and in both cases, the coherency analysis required the lowest number of trials to detect the signal. This is further reinforced by the plot of performance in the low SNR condition in **Figure 15**, where the coherency analysis detected the signal at around 200 trials, the complex spectrum analysis detected the signal at around 800 trials, and the spectral analysis did not gain any confidence after 2,000 trials.

In the second simulation, where the required number of trials to achieve  $p = 0.05$  significance are plotted against the SNR (see **Figure 14**), we see a similar picture: as the signal gets weaker and weaker, the sensitivity of the coherency analysis is more and more apparent. However, we must note that when the tagged signal is strong, and only a single trial is enough to detect it with the spectral analysis, it is pointless to do the coherency analysis, as it requires at least two trials to provide meaningful results.

From Equations (5) and (6), we know that the number of trials required is strictly monotonically increasing as the SNR decreases, but interestingly the behavior of the simulation results do not clearly show this. For example, prior to losing formula A's performance at the SNR of 0.01, it required only a fraction of trials to detect the signal than in the iteration before. The same is observed with the with the coherency results below the SNR of 0.002. We believe that this phenomenon is an artifact, due to the limit of double precision numbers, and the fact that we are rapidly

approaching Shannon's theoretical limit of information capacity (Shannon, 2001) in these conditions. Realistically, considering that it is very difficult to collect more than 2–300 trials in a frequency tagging experiment from a single participant without fatigue, the practical limit of SNR at which the coherency analysis performs best is around  $x * 10^{-3}$ . For the spectrum, this is considerably higher,  $x * 10^{-2}$ . Therefore, the best use of the coherency analysis is when the signals are very weak, and could not be detected with any other method.

#### 4.8. Does the Interfering Birdie Signal Matter at All in Coherency Analysis?

In a frequency-tagging study where the mechanism tested is well isolated, the straightforward approach to rely on the tagged frequencies themselves. Human stereopsis is a great example for such a mechanism, as it can do both intermodulation (Baitch and Levi, 1988) and frequency multiplication (Norcia and Tyler, 1984; Norcia et al., 2015) very cleanly, so the temporal frequencies in the analysis can be calculated easily. In these cases, a powerful unrelated signal can safely be ignored, and the more sensitive formula C may be used to find even the weakest signals.

However, when the operation of the mechanism studied is not so straightforward, such as the case with muscle movements (Nazarpour et al., 2012) or face perception (Boremanse et al., 2013), the experimenter may not have the luxury of ignoring any signal by labeling it as a birdie. In these cases, where finding and eliminating birdies is vital to avoid erroneous conclusions, formula D is the safer option as it's the most robust against external interference. We also suggest the use of a time-frequency analysis method in addition to the coherency analysis in such cases.

### 5. CONCLUSION

When employing the EEG frequency tagging technique in an experiment and analysing the SSVEP, spectrum may be the obvious choice at first glance. Due to its simplicity, it is easy to write reliable analysis software. The apparent ease of use, however comes at a price: as it preserves both the amplitude and phase noise components, spectral analysis is a very insensitive analysis method. Provided that the frequency and the phase information of the stimulus is known either by starting the stimulus in the same phase or recording the phase angle of it in each trial, it is possible to analyse the inter-trial coherency of the recordings, which can detect signals that are too weak to be seen in the spectrum. An added benefit is that the coherency may reliably be compared against artificially generated controls. Therefore, based on our simulation results and experimental verification, we found that the coherency analysis offers the detection of weaker signals, or requires fewer trials in an experiment.

### REFERENCES

Adeli, H., Zhou, Z., and Dadmehr, N. (2003). Analysis of eeg records in an epileptic patient using wavelet transform. *J. Neurosci. Methods* 123, 69–87. doi: 10.1016/S0165-0270(02)00340-0

Based on our analysis, we suggest the annotation of the phase angle of the stimulus and the use of coherency analysis instead of spectral analysis in future frequency tagging studies.

### DATA AVAILABILITY STATEMENT

The original contributions presented in the study are included in the article/**Supplementary Material**, further inquiries can be directed to the corresponding author/s.

### ETHICS STATEMENT

The studies involving human participants were reviewed and approved by Ethics Committee, Faculty of Medical Sciences, Newcastle University. The patients/participants provided their written informed consent to participate in this study. Written informed consent was obtained from the individual(s) for the publication of any potentially identifiable images or data included in this article.

### AUTHOR CONTRIBUTIONS

ZD designed and constructed the experimental hardware, collected data, wrote the signal processing script, and wrote the paper. The author confirms being the sole contributor of this work and has approved it for publication.

### FUNDING

Funding for the Ph.D. project was provided by the Wellcome Trust (grant number 099756/Z/12/Z), and we also have received a high-performance graphics card from Nvidia. This publication is made possible by the generous support of the NYU Abu Dhabi Grants for Publication Program.

### ACKNOWLEDGMENTS

We would like to thank Ayaka Tsutsumi for helping with data collection, Jenny Read for the helpful discussions and adding a mathematical representation for the theory, and comments on the manuscript, and Nvidia for providing the graphics card in a hardware grant which helped reducing computational time by a factor of 200. We would also like to thank New York University Abu Dhabi for funding the publication cost of this paper.

### SUPPLEMENTARY MATERIAL

The Supplementary Material for this article can be found online at: <https://www.frontiersin.org/articles/10.3389/fnins.2021.600543/full#supplementary-material>

Alonso-Prieto, E., Belle, G. V., Liu-Shuang, J., Norcia, A. M., and Rossion, B. (2013). The 6 Hz fundamental stimulation frequency rate for individual face discrimination in the right occipito-temporal cortex. *Neuropsychologia* 51, 2863–2875. doi: 10.1016/j.neuropsychologia.2013.08.018

- Alvarez, T. L., Semmlow, J. L., and Pedrono, C. (2005). Divergence eye movements are dependent on initial stimulus position. *Vis. Res.* 45, 1847–1855. doi: 10.1016/j.visres.2005.01.017
- Baitch, L. W., and Levi, D. M. (1988). Evidence for nonlinear binocular interactions in human visual cortex. *Vis. Res.* 28, 1139–1143. doi: 10.1016/0042-6989(88)90140-X
- Bayliss, J., and Ballard, D. (2000). A virtual reality testbed for brain-computer interface research. *IEEE Trans. Rehabil. Eng.* 8, 188–190. doi: 10.1109/86.847811
- Boremanse, A., Norcia, A. M., and Rossion, B. (2013). An objective signature for visual binding of face parts in the human brain. *J. Vis.* 13:6. doi: 10.1167/13.11.6
- Camfield, P. R., Metrakos, K., and Andermann, F. (1978). Basilar migraine, seizures, and severe epileptiform EEG abnormalities a relatively benign syndrome in adolescents. *Neurology* 28:584. doi: 10.1212/WNL.28.6.584
- Ciganek, L. (1961). The EEG response (evoked potential) to light stimulus in man. *Electroencephalogr. Clin. Neurophysiol.* 13, 165–172. doi: 10.1016/0013-4694(61)90132-8
- Cooley, J., and Turkey, J. (1965). *An Algorithm for Machine Calculation of Complex Fourier Series*, Vol. 19. New York, NY. doi: 10.1090/S0025-5718-1965-0178586-1
- Cottareau, B. R., McKee, S. P., Ales, J. M., and Norcia, A. M. (2011). Disparity-tuned population responses from human visual cortex. *J. Neurosci.* 31, 954–965. doi: 10.1523/JNEUROSCI.3795-10.2011
- Cottareau, B. R., McKee, S. P., Ales, J. M., and Norcia, A. M. (2012). Disparity-specific spatial interactions: evidence from EEG source imaging. *J. Neurosci.* 32, 826–840. doi: 10.1523/JNEUROSCI.2709-11.2012
- Daubechies, I. (1990). The wavelet transform, time-frequency localization and signal analysis. *IEEE Trans. Inform. Theory* 36, 961–1005. doi: 10.1109/18.57199
- Delorme, A., and Makeig, S. (2004). EEGLab: an open source toolbox for analysis of single-trial EEG dynamics including independent component analysis. *J. Neurosci. Methods* 134, 9–21. doi: 10.1016/j.jneumeth.2003.10.009
- Derzsi, Z. (2017). *Measuring the spatio-temporal resolution of stereopsis in humans using EEG*. (Ph.D. thesis). Newcastle University, Newcastle upon Tyne, England.
- Gruss, L. F., Wieser, M. J., Schweinberger, S. R., and Keil, A. (2012). Face-evoked steady-state visual potentials: effects of presentation rate and face inversion. *Front. Hum. Neurosci.* 6:316. doi: 10.3389/fnhum.2012.00316
- Hakvoort, G. (2001). *Comparison of PSDA and CCA Detection Methods in a SSVEP-Based BCI-System*. Technical report.
- Hébert-Lalonde, N., Carmant, L., Safi, D., Roy, M.-S., Lassonde, M., and Saint-Amour, D. (2014). A frequency-tagging electrophysiological method to identify central and peripheral visual field deficits. *Doc. Ophthalmol.* 129, 17–26. doi: 10.1007/s10633-014-9439-9
- Herrmann, C. S. (2001). Human EEG responses to 1-100 hz flicker: resonance phenomena in visual cortex and their potential correlation to cognitive phenomena. *Exp. Brain Res.* 137, 346–353. doi: 10.1007/s002210100682
- Ip, I. B., Minini, L., Dow, J., Parker, A. J., and Bridge, H. (2014). Responses to interocular disparity correlation in the human cerebral cortex. *Ophthalm. Physiol. Opt.* 34, 186–198. doi: 10.1111/opo.12121
- Johansson, B., and Jakobsson, P. (2000). Fourier analysis of steady-state visual evoked potentials in subjects with normal and defective stereo vision. *Doc. Ophthalmol.* 101, 233–246. doi: 10.1023/A:1002876804178
- Julesz, B. (Eds.). (1971). *Foundations of Cyclopean Perception*. University of Chicago Press.
- Kamphuisen, A., Bauer, M., and van Ee, R. (2008). No evidence for widespread synchronized networks in binocular rivalry: MEG frequency tagging entrains primarily early visual cortex. *J. Vis.* 8:4. doi: 10.1167/8.5.4
- Kane, D., Guan, P., and Banks, M. S. (2014). The limits of human stereopsis in space and time. *J. Neurosci.* 34, 1397–1408. doi: 10.1523/JNEUROSCI.1652-13.2014
- Kleiner, M., Brainard, D., Pelli, D., Ingling, A., Murray, R., Broussard, C., et al. (2007). What's new in psychtoolbox-3. *Perception* 36:1. doi: 10.1177/03010066070360S101
- Lin, Z., Zhang, C., Wu, W., and Gao, X. (2006). Frequency recognition based on canonical correlation analysis for SSVEP-based BCIs. *IEEE Trans. Biomed. Eng.* 53, 2610–2614. doi: 10.1109/TBME.2006.886577
- Mitra, P. P., and Pesaran, B. (1999). Analysis of dynamic brain imaging data. *Biophys. J.* 76, 691–708. doi: 10.1016/S0006-3495(99)77236-X
- Mun, S., Park, M.-C., Park, S., and Whang, M. (2012). SSVEP and ERP measurement of cognitive fatigue caused by stereoscopic 3D. *Neurosci. Lett.* 525, 89–94. doi: 10.1016/j.neulet.2012.07.049
- Nakanishi, M., Wang, Y., Chen, X., Wang, Y.-T., Gao, X., and Jung, T.-P. (2018). Enhancing detection of SSVEPs for a high-speed brain speller using task-related component analysis. *IEEE Trans. Biomed. Eng.* 65, 104–112. doi: 10.1109/TBME.2017.2694818
- Nazarpour, K., Barnard, A., and Jackson, A. (2012). Flexible cortical control of task-specific muscle synergies. *J. Neurosci.* 32, 12349–12360. doi: 10.1523/JNEUROSCI.5481-11.2012
- Norcia, A. M., Appelbaum, L. G., Ales, J. M., Cottareau, B. R., and Rossion, B. (2015). The steady-state visual evoked potential in vision research: a review. *J. Vis.* 15:4. doi: 10.1167/15.6.4
- Norcia, A. M., and Tyler, C. W. (1984). Temporal frequency limits for stereoscopic apparent motion processes. *Vis. Res.* 24, 395–401. doi: 10.1016/0042-6989(84)90037-3
- Panicker, R. C., Puthusserypady, S., and Sun, Y. (2011). An asynchronous P300 BCI with SSVEP-based control state detection. *IEEE Trans. Biomed. Eng.* 58, 1781–1788. doi: 10.1109/TBME.2011.2116018
- Pelli, D. G. (1997). The videotoolbox software for visual psychophysics: transforming numbers into movies. *Spatial Vis.* 10, 437–442. doi: 10.1163/156856897X00366
- Proakis, J. G. (2000). *Digital Communications, 4th Edn*. New York, NY: McGraw-Hill Companies.
- Proakis, J. G., and Salehi, M. (2008). *Digital Communications, 5th Edn*. New York, NY: McGraw-Hill Companies.
- Rideaux, R., Michael, E., and Welchman, A. E. (2020). Adaptation to binocular anticorrelation results in increased neural excitability. *J. Cogn. Neurosci.* 32, 100–110. doi: 10.1162/jocn\_a\_01471
- Rossion, B., Prieto, E. A., Boremanse, A., Kuefner, D., and Van Belle, G. (2012). A steady-state visual evoked potential approach to individual face perception: effect of inversion, contrast-reversal and temporal dynamics. *NeuroImage* 63, 1585–1600. doi: 10.1016/j.neuroimage.2012.08.033
- Scherbaum, S., Fischer, R., Dshemuchadse, M., and Goschke, T. (2011). The dynamics of cognitive control: evidence for within-trial conflict adaptation from frequency-tagged EEG. *Psychophysiology* 48, 591–600. doi: 10.1111/j.1469-8986.2010.01137.x
- Shannon, C. E. (2001). A mathematical theory of communication. *ACM SIGMOBILE Mobile Comput. Commun. Rev.* 5, 3–55. doi: 10.1145/584091.584093
- Skrandies, W., and Jedynek, A. (1999). Learning to see 3-D: psychophysics and brain electrical activity. *Neuroreport* 10, 249–253. doi: 10.1097/00001756-199902050-00009
- Srinivasan, R., Russell, D. P., Edelman, G. M., and Tononi, G. (1999). Increased synchronization of neuromagnetic responses during conscious perception. *J. Neurosci.* 19, 5435–5448. doi: 10.1523/JNEUROSCI.19-13-0543.5.1999
- Wu, Z., and Yao, D. (2007). Frequency detection with stability coefficient for steady-state visual evoked potential (SSVEP)-based BCIs. *J. Neural Eng.* 5, 36–43. doi: 10.1088/1741-2560/5/1/004

**Conflict of Interest:** The author declares that the research was conducted in the absence of any commercial or financial relationships that could be construed as a potential conflict of interest.

Copyright © 2021 Derzsi. This is an open-access article distributed under the terms of the Creative Commons Attribution License (CC BY). The use, distribution or reproduction in other forums is permitted, provided the original author(s) and the copyright owner(s) are credited and that the original publication in this journal is cited, in accordance with accepted academic practice. No use, distribution or reproduction is permitted which does not comply with these terms.



# Effects of Emotional Stimulations on the Online Operation of a P300-Based Brain–Computer Interface

Minju Kim, Jongsu Kim, Dojin Heo, Yunjoo Choi, Taejun Lee and Sung-Phil Kim\*

Department of Biomedical Engineering, Ulsan National Institute of Science and Technology, Ulsan, South Korea

## OPEN ACCESS

### Edited by:

Haider Raza,  
University of Essex, United Kingdom

### Reviewed by:

Rupert Ortner,  
g.tec Medical Engineering Spain S.L.,  
Spain  
Isao Nambu,  
Nagaoka University of Technology,  
Japan

### \*Correspondence:

Sung-Phil Kim  
spkim@unist.ac.kr

### Specialty section:

This article was submitted to  
Brain–Computer Interfaces,  
a section of the journal  
Frontiers in Human Neuroscience

**Received:** 30 September 2020

**Accepted:** 05 February 2021

**Published:** 26 February 2021

### Citation:

Kim M, Kim J, Heo D, Choi Y,  
Lee T and Kim S-P (2021) Effects  
of Emotional Stimulations on  
the Online Operation of a P300-Based  
Brain–Computer Interface.  
*Front. Hum. Neurosci.* 15:612777.  
doi: 10.3389/fnhum.2021.612777

Using P300-based brain–computer interfaces (BCIs) in daily life should take into account the user's emotional state because various emotional conditions are likely to influence event-related potentials (ERPs) and consequently the performance of P300-based BCIs. This study aimed at investigating whether external emotional stimuli affect the performance of a P300-based BCI, particularly built for controlling home appliances. We presented a set of emotional auditory stimuli to subjects, which had been selected for each subject based on individual valence scores evaluated *a priori*, while they were controlling an electric light device using a P300-based BCI. There were four conditions regarding the auditory stimuli, including high valence, low valence, noise, and no sound. As a result, subjects controlled the electric light device using the BCI in real time with a mean accuracy of 88.14%. The overall accuracy and P300 features over most EEG channels did not show a significant difference between the four auditory conditions ( $p > 0.05$ ). When we measured emotional states using frontal alpha asymmetry (FAA) and compared FAA across the auditory conditions, we also found no significant difference ( $p > 0.05$ ). Our results suggest that there is no clear evidence to support a hypothesis that external emotional stimuli influence the P300-based BCI performance or the P300 features while people are controlling devices using the BCI in real time. This study may provide useful information for those who are concerned with the implementation of a P300-based BCI in practice.

**Keywords:** emotional stimulation, brain-computer interface, P300, ERP, auditory stimulus

## INTRODUCTION

A brain–computer interface (BCI) provides a direct communication channel between people and external environments without any involvement of muscles by translating brain signals directly into the commands (Wolpaw et al., 2000, 2002). Due to this capacity, BCIs can provide an alternative means of communication with the external world for those who are suffering from severe neurological disorders, such as amyotrophic lateral sclerosis, spinal cord injury, or brainstem stroke (Birbaumer and Cohen, 2007). Not only as a means for communication with the external world, BCIs can also be used to restore, enhance, supplement, and improve lost central nervous system (CNS) functions as well as to provide a decent research tool (Brunner et al., 2015). In

particular, non-invasive BCIs based on electroencephalography (EEG) have been widely used due to their high temporal resolution and relatively low cost (Nicolas-Alonso and Gomez-Gil, 2012).

Brain-computer interfaces can be classified into several categories such as active, reactive, and passive BCIs (Zander and Kothe, 2011). Active BCIs elicit brain signals such as sensorimotor rhythms by self-paced and voluntary mental activity. Reactive BCIs induce brain signals such as event-related potentials (ERPs) or steady-state visually evoked potentials (SSVEPs) by providing external stimuli in a synchronous manner. Passive BCIs detect brain signals to infer various mental states. Among reactive BCIs relying on ERPs, P300-based BCIs have been the most widely investigated, where P300 refers to one of the ERP components induced by the oddball task paradigm (Sara et al., 1994). For instance, a P300-based BCI implements an oddball task with the visual arrangement of letters in a matrix form and enables one to select and type a letter using brain activity only (Farwell and Donchin, 1988). It has been further expanded for device control by selecting a target function amid available control functions using brain activity (Aloise et al., 2010; Carabalona et al., 2010; Corralajo et al., 2014; Halder et al., 2015; Miralles et al., 2015; Schettini et al., 2015; Pinegger et al., 2016; Zhang et al., 2017). This type of BCI, potentially combined with the Internet of things (IoT), is especially useful for those with severe neurological disorders to operate living goods such as home appliances (Aydin et al., 2016; Zhong et al., 2019).

To bring BCIs to one's daily life for efficient communications and control of devices (Wolpaw et al., 2000), however, a number of issues need to be resolved. One of them is the fact that the BCI users are likely to be exposed to virtually all kinds of stimulations from environments, which can contribute unexpected and undefined sources of noise to EEG. In particular, the BCI users would undergo dynamically changing states of emotions driven by external and internal events, which would increase a chance to temporarily distort or alternate EEG patterns, affecting the performance of BCIs. This is particularly crucial for P300-based BCIs, because a number of ERP components (e.g., late positive potentials) are known to be related to emotional states and possibly overlapped with P300 (Schupp et al., 2000; Olofsson et al., 2008; Hajcak et al., 2010). For instance, Mehmood and Lee (2015) investigated ERPs during the perception of emotional visual stimuli (happy, scared, calm, and sad) and observed the occurrence of P300 at occipital and parietal regions. Also, Conroy and Polich (2007) reported that the frontal P300 amplitude varied with valence using emotional stimuli provided in an oddball paradigm.

Recently, a number of studies investigated the effect of using emotional stimuli as targets for P300-based BCIs. Zhao et al. (2013) demonstrated that P300-based BCIs using emotional faces as target stimuli showed higher performance than using non-face objects or neutral faces, due to the addition of ERP components of human face encoding and emotion processing to those of target recognition, which enhanced the discrimination of ERPs for targets. Onishi and colleagues (Onishi et al., 2017; Onishi and Nakagawa, 2019) used emotional auditory

stimuli in a certain range of valence for P300-based BCIs and suggested that auditory stimuli of positive valence improved BCI performance. In addition, Fernandez-Rodríguez et al. (2019) reported that using emotional or neutral pictures resulted in better performance than using letters as a BCI stimulus, which was supported by more preferable evaluations by the users on neutral and positive emotional pictures. Lu et al. (2019) developed an audiovisual P300 speller equipped with emotional visual and auditory stimuli, which resulted in an improvement of performance. All of these studies, however, used emotional stimuli as targets for the oddball paradigm, which users attended to all the time. However, when we take the scenario of daily use of BCIs into consideration, external emotional stimuli would be more likely irrelevant to BCI control of devices, which the BCI users need to ignore but can be affected—e.g., the sound of a laugh or a crash. In this context, little is known about the effect of external emotional stimuli on P300-based BCIs, not as target stimuli used as a part of BCIs, but as ambient stimuli irrelevant to BCIs.

Therefore, this study aims to investigate whether external emotional stimuli irrelevant to the oddball paradigm influence the performance of a P300-based BCI used for controlling home appliances. To modulate one's emotional states, we used external emotional auditory stimuli concurrently with the oddball task in which visual device control icons were used as target or non-target stimuli. Thus, the BCI user selected a visual target while receiving auditory emotional stimuli irrelevant to visual stimuli. The emotional auditory stimuli used in this study were selected from the International Affective Digitized Sounds (IADS) (Bradley and Lang, 2007). To address individual differences in emotional responses to a given emotional auditory stimulus, we sorted a particular set of auditory stimuli for each user through a precedential behavioral experiment. To examine the effect of emotional changes on practical use of BCIs, we built an online P300-based BCI system that controlled an electric light device and examined the real-time effect of emotional stimuli on the users' performances of controlling the electric light via the BCI system.

## MATERIALS AND METHODS

### Participants

Seventeen healthy subjects participated in the study (7 Female, ages 22–28 with mean  $24.61 \pm 1.58$ ). For a fair comparison of BCI outcomes, the age range in this study was selected similar to the previous BCI studies (Zhao et al., 2013; Lian et al., 2017; Onishi et al., 2017; Voznenko et al., 2018; Fernandez-Rodríguez et al., 2019). All subjects had normal or were corrected to normal vision and had no history of neurological or psychiatric disorders. All subjects gave informed consent for this study, approved by the Ulsan National Institutes of Science and Technology, Institutional Review Board (UNIST-IRB-18-08-A).

### Data Acquisition and Preprocessing

The scalp EEG data of subjects were acquired from 31 active wet electrodes (FP1, FPz, FP2, F7, F3, Fz, F4, F8, FC5, FC1,

FC2, FC6, T7, C3, Cz, C4, CP5, T8, CP1, CP2, CP6, P7, P3, Pz, P4, P8, O1, Oz, and O2), using a standard EEG cap placed on the head following the 10–20 system of American Clinical Neurophysiology Society Guideline 2. Reference and ground electrodes were placed on mastoids of the left and right ears, respectively. The impedance of all electrodes was kept below 5 k $\Omega$ . EEG signals were amplified by a commercial EEG amplifier (anti-CHamp, Brain Product GmbH, Germany) and sampled at 500 Hz.

In our study, EEG signals were preprocessed as follows. First, a raw EEG signal was high-pass filtered above 0.5 Hz. Then, a bad EEG channel was detected and removed if more than 70% of all other channels showed a cross-correlation lower than 0.4 with that channel after being band-pass filtered through 0.5 to 1 Hz (Bigdely-Shamlo et al., 2015). This process removed four channels on average across subjects. Potential noise components from the reference were removed by using the common average reference (CAR) technique. The re-referenced EEG signal was low-pass filtered below 50 Hz. Then, artifacts were eliminated by the artifact subspace reconstruction (ASR) method (Mullen et al., 2015; Chang et al., 2018). Finally, the signal was low-pass filtered again below 12 Hz for the ERP analysis.

## Experimental Setup

The experiment was conducted twice on two different days in each subject, with an interval of 6–8 days between the experiments. In the first experiment, a pre-survey was taken for selecting emotion-induced sounds used as individual auditory stimuli for each subject. In the second experiment, subjects performed an online P300-based BCI session to control an electric light device while listening to the set of sounds selected in the first experiment. Afterward, they took a post-survey again for the emotion-induced sounds used in the BCI session.

## Sound Samples Selection

We selected sound stimuli for individual subjects, used for inducing positive and negative emotions in them during the operation of the P300-based BCI; 100 emotional sound samples were prepared initially from the International Affective Digitized Sounds, the 2nd edition (IADS-2) (Bradley and Lang, 2007) based on the reported mean valence rating: 50 highest mean valence rating (**Supplementary Table 1**) and 50 lowest mean valence rating (**Supplementary Table 2**). These samples included natural sounds made by people, animals, and objects that are commonly experienced in daily life (**Supplementary Table 1** and **Supplementary Table 2**). For each of the sound samples, the survey in the first experiment asked each subject to report how strongly they felt an emotion by scoring emotional response in each of the two emotional dimensions: valence and arousal. The score was scaled between  $-100$  and  $100$  in each dimension. We informed subjects to score valence toward  $-100$  if they felt strongly negative by the sound and toward  $+100$  if they felt strongly positive. Also, we informed subjects to score arousal toward  $-100$  if they were weakly aware of an emotion and toward  $+100$  means if they were strongly aware of an emotion. The survey questions were provided to subjects in the text form.

In each subject, after the first experiment, we selected the 15 sound samples from each high valence (HV) and low valence

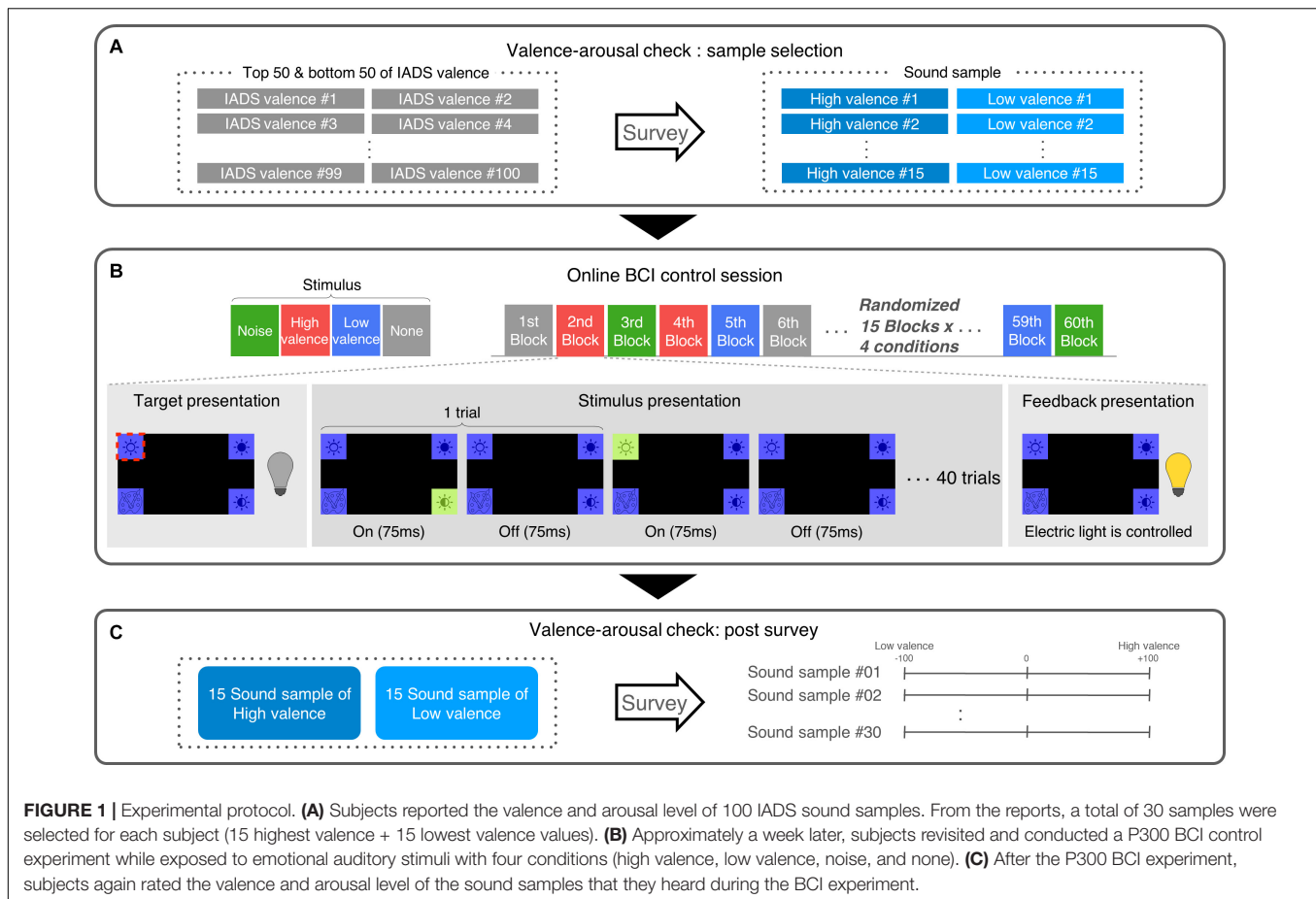
(LV) group showing the largest absolute valence scores along with positive arousal scores (**Figure 1A**).

## Online BCI Operation

In the second experiment, before the online P300-based BCI session, subjects performed a training session. The training session consisted of 40 blocks. Each block started with a fixation period for 500 ms where a fixation cross appeared at the center of the screen, followed by the random presentation of four visual stimuli located at each of the four corners of the screen. The stimuli were designed as a purple square with an icon indicating a control function of the electric light device. When highlighted, the color of square was changed to light green (**Figure 1B**). Subjects were given the information about which of the four stimuli was a target and asked to gaze at it through the block. Then, a trial began by highlighting one of the stimuli randomly for 75 ms followed by an inter-trial interval of 75 ms. There were 40 trials per block—four stimuli were highlighted exactly 10 times each in a random order, which led to 6 s of stimuli presentation. Including a fixation period, 4 s of target presentation and 4 s of feedback presentation and 1 s of inter-block interval, one block lasts 15.5 s resulting in 10.3 min of the training session. Note that no auditory stimulus was given to subjects during training.

After the training session was over, we epoched the acquired EEG data according to the stimulus information by distinguishing each stimulus as a target or non-target. Note that there was an overlap between successive epochs because the length of an epoch was set to  $-200$  to  $600$  ms in this study which was longer than the length of a trial. This was originally designed for the development of online P300-based BCIs in our previous studies and shown to work properly (Kim et al., 2019). Then, we obtained ERPs in response to the target or the non-target in each block by taking average of EEG in the corresponding epoch over trials. From these ERPs, we extracted features from the P300 component as well as other potential components by taking out ERP amplitude values between 150 and 600 ms after stimulus onset. The features were then used to train a classifier based on support vector machine (SVM) with a linear kernel and penalty parameter  $C$  as 1, which discriminated between target and non-target. Note that there were 40 training samples in the target class and 120 samples in the non-target class, respectively. These data were imbalanced, possibly posing a problem for classification. Our previous study (Lee et al., 2020) showed that adjusting the penalty parameter  $C$  could resolve the problem of imbalance slightly, but the resulting improvement in accuracy was only marginal. According to this study, we did not adjust  $C$  in the online BCI experiment. In addition, during online BCI operation, one of the four stimuli that was closest to the target class based on SVM score was decided as a target.

With a P300-based BCI containing the trained classifier, subjects performed the online session to control an electric light device (Phillips hue 2.0, Phillips, Netherlands). The online session consisted of 60 blocks with four auditory conditions: HV sound presentation (HV), LV sound presentation (LV), noise sound presentation (Noise), and no sound (None). As a noise sound, we used a recording of ambient daily sounds mixed with human voices, dishes, and objects clattering. All sound samples were



6 s long so that it could be played in the same duration as the 6-s visual stimulation length. Subjects listened to the auditory stimulus through earphone at a sound level of 61 dB on average. There were 15 blocks in each of the four conditions. The order of the blocks was randomized. The composition of a block was same as that in training session, except for feedback presentation. In each block, subjects were given the information of which control command (out of four) they should operate and selected it using the BCI through 40 trials of the stimulus presentation in a block. The four commands included light on, light off, color change, and brightness change. After the block, subjects received feedback immediately from the real-time operation of the electric light device located in front of them according to the functional command generated by the BCI, regardless of the correctness of the operation (Figure 1B). Unlike automatic progress of the experiment in training session, the progress to the next block was done manually, one block lasted 20 s to 35 s, and the entire online session took approximately 20 min.

After the online session, subjects conducted a *post hoc* survey for the selected sound stimuli used in the session with the same scoring scheme as in the first experiment (i.e., -100 to 100 for valence and arousal each) (Figure 1C). This post survey was designed to examine how much emotional responses to the selected sound samples changed before and after the online BCI session.

## Data Analysis

### ERP Analysis

We analyzed ERPs for the target stimuli obtained from the online test session across different auditory conditions. Specifically, we focused on the amplitude of a positive peak that was defined as the highest amplitude within a time window from 250 to 500 ms after stimulus onset. We also measured the latency of this peak in each ERP. To examine whether these ERP features were different across the four conditions, we applied repeated measures ANOVA (rmANOVA) for each ERP feature at each channel. Note that the number of subjects (i.e., samples) tested varied across channels due to individual differences of bad channel removal results (see Table 1). Also, the channel FT10 was completely excluded in this ERP analysis because this channel was removed in every subject except for one subject, which was due to problem of the corresponding electrode cap used in the experiment.

### BCI Performance Analysis

Using the BCI control results from the online test session, we calculated accuracy given by the ratio of the number of blocks with correct target selection to the number of all blocks (i.e., 60). After obtaining accuracy of all subjects for each condition, we divided subjects into two groups according to the extent to which the presence of emotional stimuli affected subjects' BCI

**TABLE 1** | The statistical test results of differences in the P300 peak amplitude and latency between emotional conditions (rmANOVA). The values that showed significance ( $p < 0.05$ ) were highlighted in bold.

Channel	Amplitude		Latency		The number of subject
	<i>F</i>	<i>p</i> -value	<i>F</i>	<i>p</i> -value	
F3	<b>2.9188</b>	<b>0.0442</b>	0.9812	0.4101	16
Fz	1.1825	0.3263	0.7303	0.5390	17
F4	0.4108	0.7460	0.0348	0.9912	17
FC1	1.4411	0.2425	0.6397	0.5932	17
FC2	1.8931	0.14543	1.6373	0.1951	15
C3	2.1072	0.1116	2.4873	0.0717	17
Cz	0.1228	0.9462	0.3986	0.7546	17
C4	0.3269	0.8059	0.2995	0.8256	16
CP1	0.4269	0.7346	1.6363	0.1934	17
CP2	0.2813	0.8386	0.1964	0.8983	17
P3	0.2955	0.8285	1.0302	0.3876	17
Pz	0.6687	0.5754	0.0560	0.9823	17
P4	1.609	0.1996	1.0347	0.3857	17
O1	2.2360	0.0980	1.0720	0.3712	15
Oz	0.5893	0.6254	0.2911	0.8316	15
O2	1.1	0.3590	1.7083	0.1788	16

control: a large difference (LD) and small difference (SD) groups. The LD group consisted of subjects who showed an increase or decrease of accuracy in either the HV or LV conditions by more than 10% compared to the None condition. The SD group consisted of the rest subjects. Since 15 blocks were conducted for each condition, one correct (or wrong) selection would cause the change of accuracy as much as 6.67%. Compared to None, more than one correct or wrong selection in either HV or LV was deemed to be a large difference in this study, as one or less correct or wrong selection in both HV and LV than in None would not sufficiently pronounce a difference of accuracy. Therefore, we set 10% of accuracy as a criterion to discriminate subject groups into the LD and SD groups. This division was intended to observe whether those who were influenced more by emotional stimuli regardless of the valence of emotion (HV or LV) showed different tendency compared to others. There were nine subjects in the LD group, and 8 in the SD group, respectively. Then, we compared BCI control accuracy as well as ERP features (see section “ERP Analysis”) and emotional EEG features (see section “Emotional EEG Analysis”) between the four conditions within each group. This further analysis was conducted to examine whether we could observe any influence of emotional stimuli on the BCI operation if we sharpened our focus on a certain group of individuals.

### Emotional EEG Analysis

We analyzed EEG characteristics reflecting overt emotional responses to auditory stimuli during the operation of the BCI. Specifically, we examined frontal alpha asymmetry (FAA) that has been well known to represent valence (Coan and Allen, 2003). FAA was calculated by asymmetry between left and right hemisphere alpha-band power of EEG. In this study, FAA was determined as follows:

$$FAA = 10(\ln(\text{Power}_{\text{right}}) - \ln(\text{Power}_{\text{left}})) \quad (1)$$

where  $\text{Power}_{\text{left}}$  was the average power of alpha band (8–14 Hz) at channel FP1, F3 and F7; and  $\text{Power}_{\text{right}}$  was the average power of the same frequency band at channel FP2, F4, and F8. We measured FAA from EEG data in each condition in each subject. Then, we compared FAA across the four conditions using rmANOVA.

## RESULTS

### Survey Results

We compared the valence scores from the survey of a set of 30 sound samples selected for each subject taken before and after the online BCI session (Figure 2). There was no instance that the sign of the valence scores was altered for any of the samples. However, the absolute values of the valence scores significantly decreased after the online BCI session (HV:  $p = 0.0012$ ; LV:  $p < 0.001$ ).

### ERP Differences

We visually inspected the ERPs from the training data to examine whether the P300 component was induced by the target stimulus (Figure 3A). As expected, the P300 component appeared to be present in response to the target but not to the non-target over many channels (e.g., Pz, Oz, and others). Next, we compared the ERPs of different auditory conditions from the test data (Figure 3B, Supplementary Table 3 and Supplementary Table 4). We observed no conspicuous difference between the conditions in the ERP patterns in response to the target stimulus. The rmANOVA was conducted on those channels in which P300 was observed: F3, Fz, F4, FC1, FC2, C3, Cz, C4, CP1, CP2, P3, Pz, P4, O1, Oz, and O2. The rmANOVA revealed no significant difference in the peak ERP amplitude and latency among the conditions except for F3 (Table 1). In order to examine the peak amplitude level at F3, the peak amplitude was compared

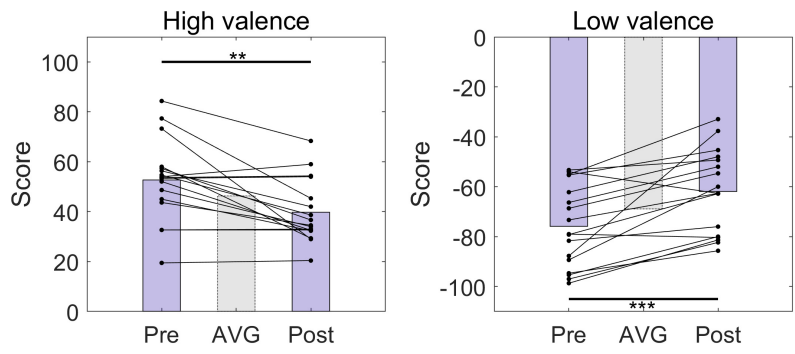


**FIGURE 2 |** The distributions of the valence scores of high-, and low-valence stimuli used in the experiment before (Pre) and after (Post) the online BCI session. The bars indicate the average valence scores. AVG, average over all pre- and post-session scores. There were 15 high-valence and 15 low-valence stimuli, respectively. There was an approximately 1-week interval between pre- and post-session. \*\* $p < 0.01$ , \*\*\* $p < 0.001$ , paired  $t$ -test.

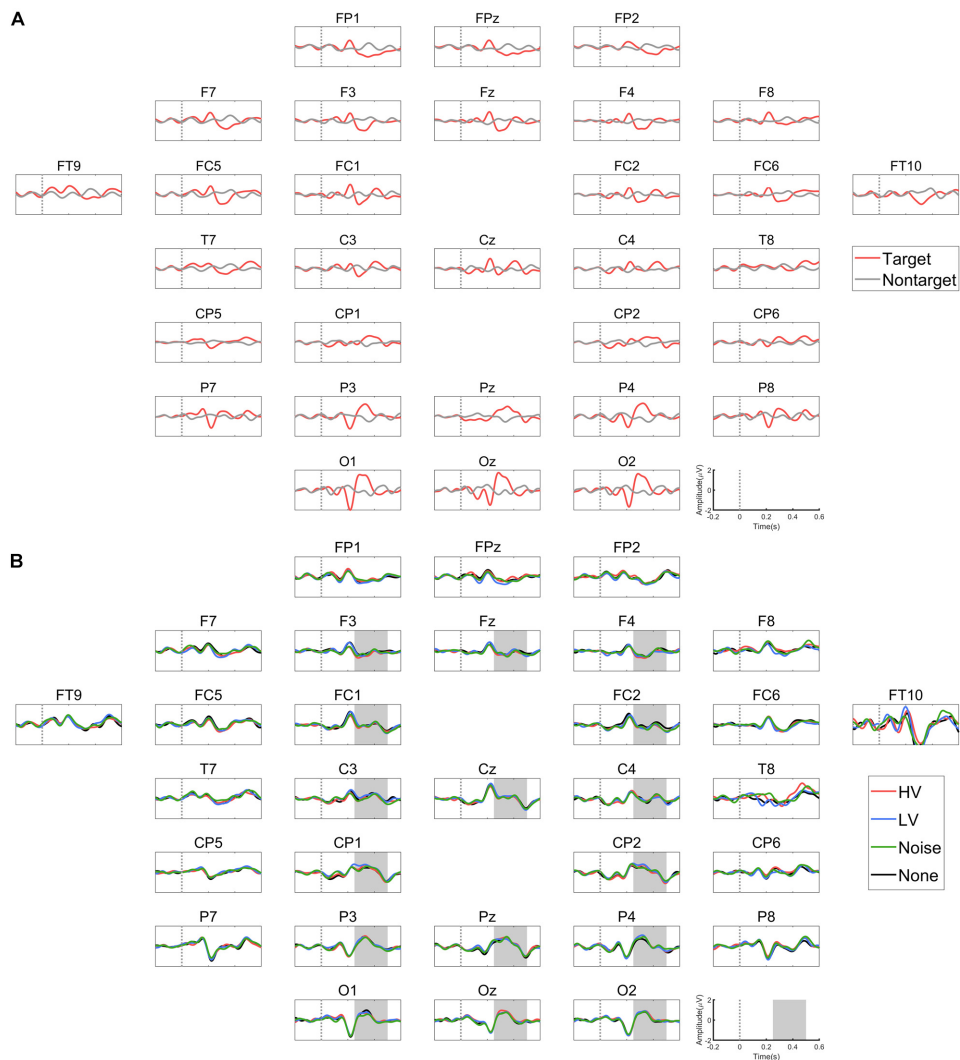


**FIGURE 3 |** ERP graphs. **(A)** Grand average ERP graphs obtained from the training set. The red line represents ERP of target and black line does that of non-target stimuli. **(B)** Grand average ERP graphs obtained from the test set for each of the four emotional auditory stimulation conditions. The shaded area indicates where the analysis for P300 component was conducted.

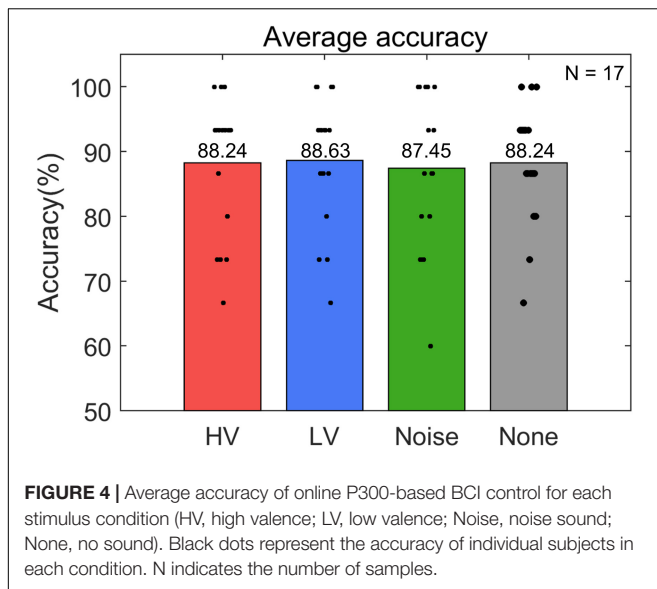


**FIGURE 4 |** Average accuracy of online P300-based BCI control for each stimulus condition (HV, high valence; LV, low valence; Noise, noise sound; None, no sound). Black dots represent the accuracy of individual subjects in each condition. N indicates the number of samples.

between the target and non-target stimuli, and a paired *t*-test showed no significant difference for all conditions (HV:  $p = 0.35$ , LV:  $p = 0.27$ , Noise:  $p = 0.21$ , None:  $p = 0.26$ ). In addition, we repeated the comparison of the ERP peak amplitude and latency in each group of subjects: the LD and SD groups. For this analysis, we used the Friedman test followed by the Tukey's-HSD *post hoc* test. The LD group showed a significant difference in the peak amplitude only at channel O1 between the HV and None conditions (HV < None,  $p = 0.02$ ), while it showed no difference in the peak latency. The SD group showed a significant difference between the conditions in neither the peak amplitude nor peak latency ( $p > 0.05$ ).

### Online BCI Performance

Subjects operated the P300-based BCI to control the electric light device with an average accuracy of  $88.14 \pm 7.26\%$  (Figure 4). The

maximum and minimum accuracy among subjects was 98.33% and 73.33%, respectively. The rmANOVA showed no significant difference in accuracy between the conditions [ $F(3,48) = 0.086$ ,  $p = 0.98$ ]. The accuracy was also compared in two groups. The average accuracy of the LD group was  $85.93 \pm 5.15\%$  and that of the SD group was  $90.63 \pm 8.77\%$ . Wilcoxon rank sum test showed no significant difference between these groups ( $p = 0.118$ ). In addition, The Friedman test did not show any significance between the conditions in either the LD [ $\chi^2(3, N = 8) = 0.89$ ,  $p = 0.828$ ] or SD group [ $\chi^2(3, N = 9) = 0.49$ ,  $p = 0.922$ ] (Figure 5).

Additionally, subjects were grouped again according to their accuracy in the None condition. Subjects who showed higher accuracy than the average belonged to the high accuracy group and those with lower accuracy than the average belonged to the low accuracy group. The average accuracy of the high accuracy group was  $92.29 \pm 5.77\%$  and that of the low accuracy group was  $84.44 \pm 6.61\%$ . Wilcoxon rank sum test showed a significant difference between these groups ( $p = 0.0216$ ). Among eight subjects in the SD group, only one subject was included in the low accuracy group. Similarly, 8 out of 9 subjects in the LD group belonged to the low accuracy group (Figure 6).

### Frontal Alpha Asymmetry

Overall, the rmANOVA revealed no significant difference in FAA between the conditions [ $F(3,48) = 2.496$ ,  $p = 0.071$ ] (Figure 7). In the group-wise analysis, the Wilcoxon signed rank test did not show any significant change of FAA from the None condition to each of the other auditory conditions (HV, LV, and Noise), in either the LD or SD group ( $p > 0.05$ ) (Figure 8 and Table 2).

## DISCUSSION

In the present study, we investigated the effect of externally induced emotions on the performance of a P300-based BCI. Subjects participating in this study received emotional auditory stimuli designed to induce positive (HV) and negative (LV)

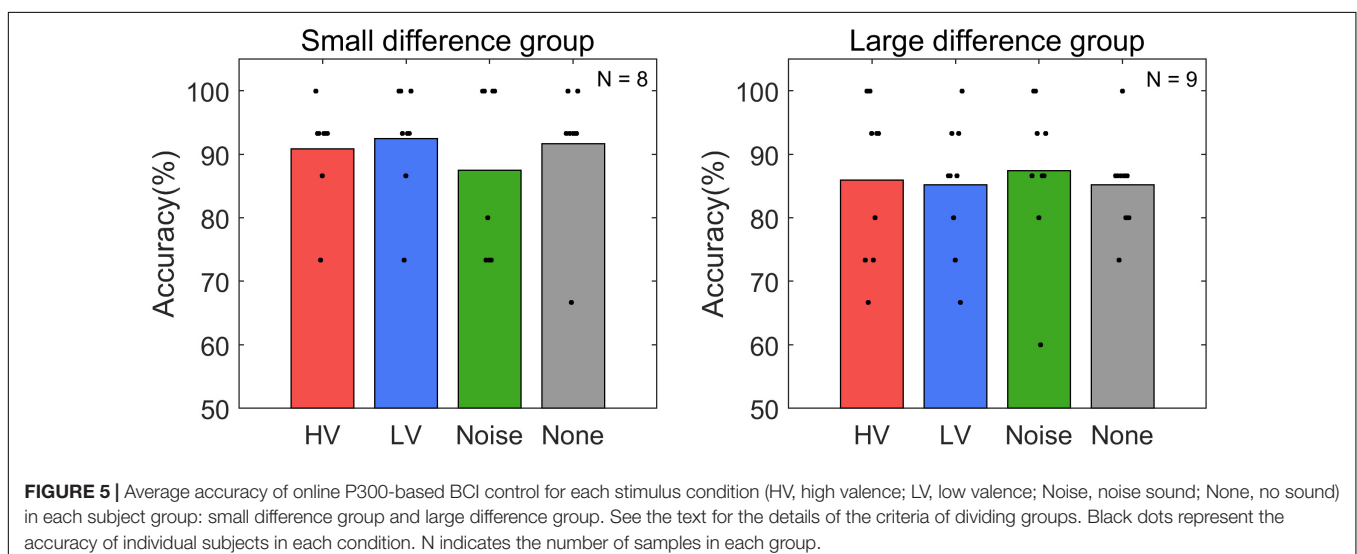
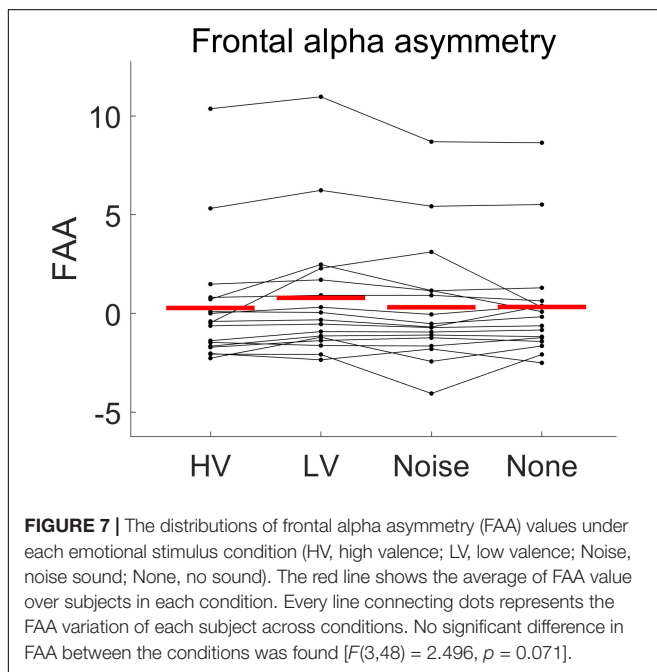
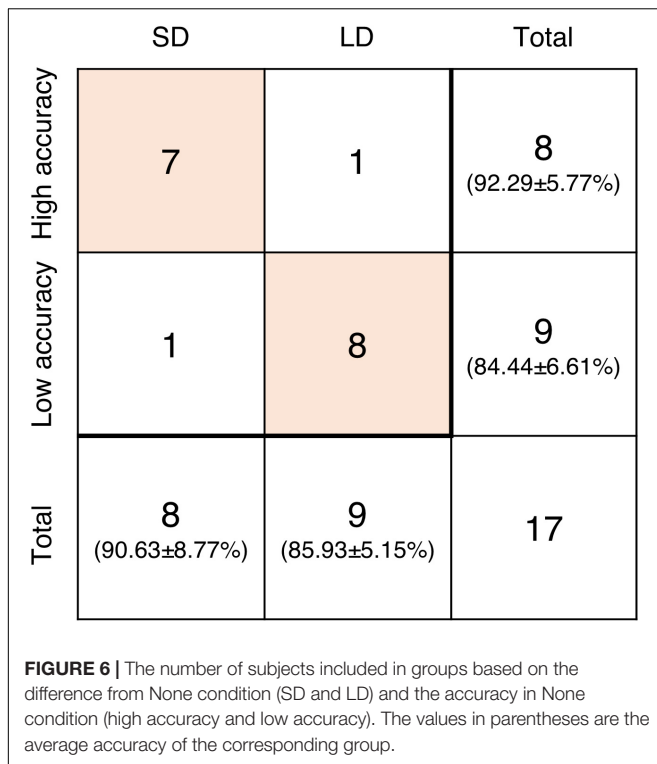


**FIGURE 5 |** Average accuracy of online P300-based BCI control for each stimulus condition (HV, high valence; LV, low valence; Noise, noise sound; None, no sound) in each subject group: small difference group and large difference group. See the text for the details of the criteria of dividing groups. Black dots represent the accuracy of individual subjects in each condition. N indicates the number of samples in each group.



emotions while controlling an electric light device through the P300-based BCI. In addition to these emotional stimuli, noise (neutral valence) as well as no sound was presented. We compared the ERP properties, online BCI performance and FAA between the four conditions (HV, LV, Noise, and None). We found no significant difference in the ERP peak amplitude and peak latency over most EEG channels except for

F3 (although a difference in the peak amplitude was found at F3, the amplitude level was relatively small and thus hard to extract meaningful results). Also, BCI control accuracy and FAA were not different between the conditions. Subjects controlled the electric light using the BCI fairly well under all conditions (online control accuracy of 88.14% on average). Furthermore, we examined whether the extent to which individuals were influenced by emotional stimuli contributed to individual differences in accuracy. To this end, we divided subjects into two groups based on the difference of accuracy between the emotional and None conditions. We observed no significant difference in BCI control accuracy, ERP peak amplitude and FAA across the conditions within each of the large difference (LD) group and small difference (SD) group. From the results of the present study, there was no clear evidence that emotional stimulations would affect the P300-based BCI performance.

Previous studies have suggested that visual or auditory emotional stimuli can influence P300-based BCIs when the stimuli are used as targets to select (Onishi et al., 2017; Fernandez-Rodríguez et al., 2019; Onishi and Nakagawa, 2019). In these studies, P300-based BCIs included emotional stimuli—such as sounds or images with different valence levels—as task-relevant stimuli, so that the user was attending to those emotional stimuli. This paradigm is different from our study in which emotional stimuli are irrelevant to the task. In our paradigm, the user is attending to emotionless stimuli relevant to the task, while receiving a separate set of task-irrelevant emotional stimuli. Our task paradigm is closer to real-life situations because the user would be exposed to a variety of emotional stimuli from uncontrolled environments when controlling home appliances using BCIs.

In previous studies where background stimuli were present during the use of BCI, the BCI accuracy was not improved, but in most cases decreased (Lian et al., 2017; Voznenko et al., 2018; Cherepanova et al., 2019; Xu et al., 2020). Especially, the visual BCI performance deteriorated when background stimuli, whether auditory or visual, attracted attention. Also, the more mental workload was required, the more the accuracy decreased (Cherepanova et al., 2019; Xu et al., 2020). In addition, the presence of background stimuli without any requirement of attention often showed reduced performance in BCI (Lian et al., 2017; Voznenko et al., 2018). According to Voznenko et al. (2018), music listening while using a BCI influenced each individual differently. Some subjects were negatively affected by music stimuli regardless of the genre of music, whereas others showed the decreased accuracy in specific genre of music. The authors discussed that subjects reported different levels of interference with music depending on their preference, which could cause distraction to the music. Hence, it can be deduced that when background stimuli do not demand mental workload, the effect of them depends on the extent to which people are distracted to them. In our study, the auditory emotional stimuli, which did not demand any attention, did not show significant influence on the BCI performance. It might be because the emotional stimuli did not evoke distraction enough to decrease the BCI performance on average in subjects of this study.

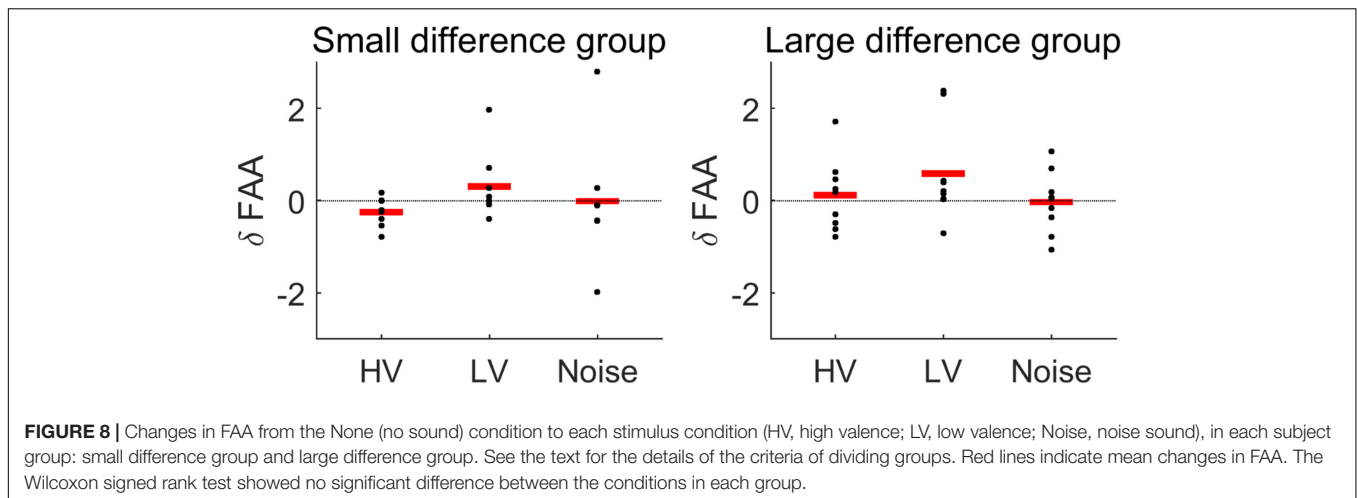


**TABLE 2 |** The statistical test results of changes in frontal alpha asymmetry (FAA) in a given stimulation condition compared to the condition of no sound (Wilcoxon signed rank test).

Subject group	Stimulation condition	Signed-rank statistic	<i>p</i> -value
SD	HV	6	0.1094
SD	LV	24	0.4609
SD	Noise	12	0.4609
LD	HV	23	1
LD	LV	38	0.0742
LD	Noise	22	1

SD, small difference group; LD, large difference group; HV, high valence; LV, low valence.

When we narrowed our focus on a subset of subjects showing differences in BCI control accuracy with emotional stimuli, overall BCI control accuracy in the LD group was not different between emotional conditions. This may be because the effect of emotional stimuli on BCI performance could vary over subjects in the LD group. Also, average accuracy in the SD group tended to be higher than in the LD group. SD group, those whose accuracy under emotional conditions did not change from the control condition, tended to be good at operating P300 BCIs. Therefore, good BCI performers might be relatively less influenced by emotional conditions. However, it is still premature to draw any conclusion from this analysis due to the lack of a sufficient number of samples. Therefore, a more in-depth study is necessary to investigate influences of emotional state changes on the use of the BCI specifically for those who are more susceptible to external emotional events.

Even though we asked subjects to rate valence and arousal scores of emotional auditory stimuli independently of BCI control, we additionally computed FAA in each condition to estimate their emotional states during the online BCI control task. FAA has been widely used as a metric to represent emotional valence (Davidson et al., 1979; Harmon-Jones et al., 2010). It was confirmed in our experiment that the valence score of HV stimuli remained positive and that of LV stimuli remained negative

before and after the task. We also found no difference between the SD and LD groups in the valence scores for HV and LV stimuli, respectively ( $p > 0.05$ ). In contrast, FAA showed no difference between the HV, LV, Noise, and None conditions. This result of FAA may be associated with no significant difference in ERPs and BCI performance, implying that external emotional stimuli given during BCI control did not induce emotional changes much in the brain. We conjecture that no clear effect of the valence of emotional stimuli on FAA might be due to the fact that subjects were likely to concentrate on selecting targets during the online BCI control session with real-time feedback from the device, which could weaken the effect of auditory emotional stimuli. However, this conjecture would not be made possible if we only look into the survey results as self-reporting on HV or LV stimuli remained positive or negative. In addition, we observed decreases in the absolute valence scores after the BCI control session. This reduced emotional recognition of stimuli intensity may be potentially due to repeated experiences because people tend to habituate to emotional stimuli when those stimuli are repeated and evaluate the repeated emotional stimuli to a smaller degree (Dijksterhuis and Smith, 2002; Leventhal et al., 2007).

In this study, we found no evidence to support a hypothesis that emotional stimuli would influence the performance of P300-based BCIs. However, there are some limitations in this study, which needs further investigations. First, the number of subjects in each group was too small for statistical test results within each group to be considered significant. Future studies with a larger sample size should follow up to confirm our preliminary results. Second, FAA in the HV or LV condition was not increased compared to that in the None condition, which might indicate that the HV or LV auditory stimuli did not successfully evoke positive emotions. If the auditory stimuli had been selected based on FAA combined with self-reports, the effect of emotional stimuli on FAA might be more clearly manifested. This may indicate a need to simultaneously measure FAA during self-reporting on emotional stimuli in future studies. Third, it was plausible that our BCI control task was so intense that subjects' attention might be mostly attracted to the task and visual processing, leaving little room for the perception of auditory

stimuli. To verify this plausibility, we should have a brief session in which we simply provided the prepared set of auditory stimuli to subjects and analyzed ERPs and FAA to confirm that subjects' emotional state changed. The follow-up studies may need to consider such an addition to experimental design. Lastly, the age range of subjects in our study was below 29 years. Subjects had to attend to the BCI task while the irrelevant auditory stimuli were presenting in the experiment. Since younger people are better at ignoring irrelevant stimuli (McDowd and Filion, 1992), which would work as one of the strategies to successfully complete the required task, those who are older than subjects in this study may produce different results. To clarify this important inquiry, further studies need to investigate the effect of emotions on P300-based BCIs for elder populations.

Nonetheless, to the best of our knowledge, the present study investigates the effect of emotional stimuli on the online performance of a P300-based BCI for the first time and reveals that there is no significant effect by neither positive nor negative stimuli. We envision that the present study's results may provide useful information to those who are concerned with potential effects of ambient stimuli when they build a P300-based BCI in practice.

## DATA AVAILABILITY STATEMENT

The raw data supporting the conclusions of this article are available on request to the corresponding author.

## ETHICS STATEMENT

The studies involving human participants were reviewed and approved by the Ulsan National Institutes of

Science and Technology, Institutional Review Board. The patients/participants provided their written informed consent to participate in this study.

## AUTHOR CONTRIBUTIONS

MK conducted the experiments, analyzed the data, and wrote the manuscript. DH and JK conducted the experiments, analyzed the data, and wrote the manuscript. YC participated in writing the manuscript. TL designed the experiments and conducted the experiments. S-PK oversaw the study and managed every part of the research. All authors read and approved the final manuscript.

## FUNDING

This work was partly supported by the Institute of Information and Communications Technology Planning and Evaluation (IITP) grant funded by the Korea government (MSIT) (No. 2017-0-00432, Development of non-invasive integrated BCI SW platform to control home appliances and external devices by user's thought via AR/VR interface) and the 2019 Research Fund (1.190047.01) of Ulsan National Institute of Science and Technology (UNIST).

## SUPPLEMENTARY MATERIAL

The Supplementary Material for this article can be found online at: <https://www.frontiersin.org/articles/10.3389/fnhum.2021.612777/full#supplementary-material>

## REFERENCES

- Aloise, F., Schettini, F., Aricò, P., Bianchi, L., Riccio, A., Mecella, M., et al. (2010). "Advanced brain computer interface for communication and control," in *Proceedings of the International Conference on Advanced Visual Interfaces*, ed. G. Santucci (New York, NY: Association for Computing Machinery), 399–400. doi: 10.1145/1842993.1843076
- Aydin, E. A., Bay, Ö.F., and Güler, I. (2016). Implementation of an embedded web server application for wireless control of brain computer interface based home environments. *J. Med. Syst.* 40:27. doi: 10.1007/s10916-015-0386-0
- Bigdely-Shamlo, N., Mullen, T., Kothe, C., Su, K. M., and Robbins, K. A. (2015). The PREP pipeline: standardized preprocessing for large-scale EEG analysis. *Front. Neuroinform.* 9:16. doi: 10.3389/fninf.2015.00016
- Birbaumer, N., and Cohen, L. G. (2007). Brain-computer interfaces: communication and restoration of movement in paralysis. *J. Physiol.* 579, 621–636. doi: 10.1113/jphysiol.2006.125633
- Bradley, M. M., and Lang, P. J. (2007). *The International Affective Digitized Sounds (2nd Edition; IADS-2): Affective Ratings of Sounds and Instruction Manual. Technical Report B-3*. Gainesville: University of Florida.
- Brunner, C., Birbaumer, N., Blankertz, B., Guger, C., Kübler, A., Mattia, D., et al. (2015). BNCI horizon 2020: towards a roadmap for the BCI community. *Brain Comput. Interfaces* 2, 1–10. doi: 10.1080/2326263X.2015.1008956
- Carabalona, R., Grossi, F., Tessadri, A., Caracciolo, A., Castiglioni, P., and De Munari, I. (2010). "Home smart home: brain-computer interface control for real smart home environments," in *Proceedings of the 4th International Convention on Rehabilitation Engineering and Assistive Technology (iCREATE'10)*, eds Z. Gao and P. Thajchayapong (Midview City: Singapore Therapeutic Assistive & Rehabilitative Technologies (START) Centre), 51.
- Chang, C. Y., Hsu, S. H., Pion-Tonachini, L., and Jung, T. P. (2018). "Evaluation of artifact subspace reconstruction for automatic EEG artifact removal," in *Proceedings of the 40th Annual International Conference of the IEEE Engineering in Medicine and Biology Society (EMBC)* (Honolulu, HI: IEEE), 1242–1245.
- Cherepanova, A. D., Petrova, A. I., Voznenko, T. I., Dyumin, A. A., Gridnev, A. A., and Chepin, E. V. (2019). "The research of distracting factors influence on quality of brain-computer interface usage," in *Biologically Inspired Cognitive Architectures Meeting*, ed. A. Samsonovich (Cham: Springer), 44–49.
- Coan, J. A., and Allen, J. J. (2003). Frontal EEG asymmetry and the behavioral activation and inhibition systems. *Psychophysiology* 40, 106–114. doi: 10.1111/1469-8986.00011
- Conroy, M. A., and Polich, J. (2007). Affective valence and P300 when stimulus arousal level is controlled. *Cogn. Emot.* 21, 891–901. doi: 10.1080/02699930600926752
- Corrallejo, R., Nicolás-Alonso, L. F., Álvarez, D., and Hornero, R. (2014). A P300-based brain-computer interface aimed at operating electronic devices at home for severely disabled people. *Med. Biol. Eng. Comput.* 52, 861–872. doi: 10.1007/s11517-014-1191-5
- Davidson, R. J., Schwartz, G. E., Saron, C., Bennett, J., and Goleman, D. J. (1979). Frontal versus parietal EEG asymmetry during positive and negative affect. *Psychophysiology* 16, 202–203.

- Dijksterhuis, A., and Smith, P. K. (2002). Affective habituation: subliminal exposure to extreme stimuli decreases their extremity. *Emotion* 2, 203–214. doi: 10.1037/1528-3542.2.3.203
- Farwell, L. A., and Donchin, E. (1988). Talking off the top of your head: toward a mental prosthesis utilizing event-related brain potentials. *Electroencephalogr. Clin. Neurophysiol.* 70, 510–523. doi: 10.1016/0013-4694(88)90149-6
- Fernandez-Rodríguez, L., Velasco-Ivarez, F., Medina-Juliá, M. T., and Ron-Angevin, R. (2019). Evaluation of emotional and neutral pictures as flashing stimuli using a P300 brain-computer interface speller. *J. Neural Eng.* 16:056024. doi: 10.1088/1741-2552/ab386d
- Hajcak, G., MacNamara, A., and Olvet, D. M. (2010). Event-related potentials, emotion, and emotion regulation: an integrative review. *Dev. Neuropsychol.* 35, 129–155. doi: 10.1080/87565640903526504
- Halder, S., Pinedger, A., Käthner, I., Wriessnegger, S. C., Faller, J., Pires Antunes, J. B., et al. (2015). Brain-controlled applications using dynamic P300 speller matrices. *Artif. Intell. Med.* 63, 7–17. doi: 10.1016/J.ARTMED.2014.12.001
- Harmon-Jones, E., Gable, P. A., and Peterson, C. K. (2010). The role of asymmetric frontal cortical activity in emotion-related phenomena: a review and update. *Biol. Psychol.* 84, 451–462. doi: 10.1016/j.biopsycho.2009.08.010
- Kim, M., Kim, M. K., Hwang, M., Kim, H. Y., Cho, J., and Kim, S. P. (2019). Online home appliance control using EEG-Based brain-computer interfaces. *Electronics* 8, doi: 10.3390/electronics8101101
- Lee, T., Kim, M., and Kim, S. P. (2020). Improvement of P300-based brain-computer interfaces for home appliances control by data balancing techniques. *Sensors* 20:5576. doi: 10.3390/s20195576
- Leventhal, A. M., Martin, R. L., Seals, R. W., Tapia, E., and Rehm, L. P. (2007). Investigating the dynamics of affect: psychological mechanisms of affective habituation to pleasurable stimuli. *Motiv. Emot.* 31, 145–157. doi: 10.1007/s11031-007-9059-8
- Lian, J., Bi, L., and Fan, X. A. (2017). “Effects of illumination and noise on the performance of a P300 brain-computer interface for assistive vehicles,” in *Proceedings of the 2017 8th International IEEE/EMBS Conference on Neural Engineering* (Shanghai: IEEE), 337–340. doi: 10.1109/NER.2017.8008359
- Lu, Z., Li, Q., Gao, N., Yang, J., and Bai, O. (2019). Happy emotion cognition of bimodal audiovisual stimuli optimizes the performance of the P300 speller. *Brain Behav.* 9:e01479.
- McDowd, J. M., and Filion, D. L. (1992). Aging, selective attention, and inhibitory processes: a psychophysiological approach. *Psychol. Aging* 7, 65–71. doi: 10.1037/0882-7974.7.1.65
- Mehmood, R. M., and Lee, H. J. (2015). “ERP analysis of emotional stimuli from brain EEG signal,” in *Proceedings of the International Conference on Biomedical Engineering and Science*, eds M. F. Secca, J. Schier, A. Fred, H. Gamboa, and D. Elias (Setubal: Science and Technology Publications), 44–48.
- Miralles, F., Vargiu, E., Dauwalder, S., Solà, M., Müller-Putz, G., Wriessnegger, S. C., et al. (2015). Brain computer interface on track to home. *Sci. World J.* 2015:623896. doi: 10.1155/2015/623896
- Mullen, T. R., Kothe, C. A., Chi, Y. M., Ojeda, A., Kerth, T., Makeig, S., et al. (2015). Real-time neuroimaging and cognitive monitoring using wearable dry EEG. *IEEE Trans. Biomed. Eng.* 62, 2553–2567. doi: 10.1109/TBME.2015.2481482
- Nicolas-Alonso, L. F., and Gomez-Gil, J. (2012). Brain computer interfaces, a review. *Sensors* 12, 1211–1279. doi: 10.3390/s120201211
- Olofsson, J. K., Nordin, S., Sequeira, H., and Polich, J. (2008). Affective picture processing: an integrative review of ERP findings. *Biol. Psychol.* 77, 247–265. doi: 10.1016/j.biopsycho.2007.11.006
- Onishi, A., and Nakagawa, S. (2019). How does the degree of valence influence affective auditory P300-based BCIs? *Front. Neurosci.* 13:45. doi: 10.3389/fnins.2019.00045
- Onishi, A., Takano, K., Kawase, T., Ora, H., and Kansaku, K. (2017). Affective stimuli for an auditory P300 brain-computer interface. *Front. Neurosci.* 11:522. doi: 10.3389/fnins.2017.00522
- Pinedger, A., Wriessnegger, S. C., Faller, J., and Müller-Putz, G. R. (2016). Evaluation of different EEG acquisition systems concerning their suitability for building a brain-computer interface: case studies. *Front. Neurosci.* 10:441. doi: 10.3389/fnins.2016.00441
- Sara, G., Gordon, E., Kraiuhin, C., Coyle, S., Howson, A., and Meares, R. (1994). The P300 ERP component: an index of cognitive dysfunction in depression? *J. Affect. Disord.* 31, 29–38. doi: 10.1016/0165-0327(94)90124-4
- Schettini, F., Riccio, A., Simone, L., Liberati, G., Caruso, M., Frasca, V., et al. (2015). Assistive device with conventional, alternative, and brain-computer interface inputs to enhance interaction with the environment for people with amyotrophic lateral sclerosis: a feasibility and usability study. *Arch. Phys. Med. Rehabil.* 96, S46–S53. doi: 10.1016/j.apmr.2014.05.027
- Schupp, H. T., Cuthbert, B. N., Bradley, M. M., Cacioppo, J. T., Ito, T., and Lang, P. J. (2000). Affective picture processing: the late positive potential is modulated by motivational relevance. *Psychophysiology* 37, 257–261. doi: 10.1111/1469-8986.3720257
- Voznenko, T. I., Dyumin, A. A., Aksnova, E. V., Gridnev, A. A., and Delov, V. A. (2018). The experimental study of “Unwanted Music” noise pollution influence on command recognition by brain-computer interface. *Procedia Comput. Sci.* 123, 528–533. doi: 10.1016/j.procs.2018.01.080
- Wolpaw, J. R., Birbaumer, N., Heetderks, W. J., McFarland, D. J., Peckham, P. H., Schalk, G., et al. (2000). Brain-computer interface technology: a review of the first international meeting. *IEEE Trans. Rehabil. Eng.* 8, 164–173. doi: 10.1109/TRE.2000.847807
- Wolpaw, J. R., Birbaumer, N., McFarland, D. J., Pfurtscheller, G., and Vaughan, T. M. (2002). Brain-computer interfaces for communication and control. *Clin. Neurophysiol.* 113, 767–791. doi: 10.1016/s1388-2457(02)00057-3
- Xu, G., Wu, Y., and Li, M. (2020). The study of influence of sound on visual ERP-based brain computer interface. *Sensors* 20:1203. doi: 10.3390/s20041203
- Zander, T. O., and Kothe, C. (2011). Towards passive brain-computer interfaces: applying brain-computer interface technology to human-machine systems in general. *J. Neural Eng.* 8:025005. doi: 10.1088/1741-2560/8/2/025005
- Zhang, R., Wang, Q., Li, K., He, S., Qin, S., Feng, Z., et al. (2017). A BCI-based environmental control system for patients with severe spinal cord injuries. *IEEE Trans. Biomed. Eng.* 64, 1959–1971. doi: 10.1109/TBME.2016.2628861
- Zhao, Q., Zhang, Y., Onishi, A., and Cichocki, A. (2013). “An affective BCI using multiple ERP components associated to facial emotion processing,” in *Brain-Computer Interface Research*, eds C. Guger, B. Allison, and G. Edlinger (Berlin: Springer).
- Zhong, S., Liu, Y., Yu, Y., Tang, J., Zhou, Z., and Hu, D. (2019). A dynamic user interface based BCI environmental control system. *Int. J. Hum. Comput. Interact.* 36, 55–66. doi: 10.1080/10447318.2019.1604473

**Conflict of Interest:** The authors declare that the research was conducted in the absence of any commercial or financial relationships that could be construed as a potential conflict of interest.

Copyright © 2021 Kim, Kim, Heo, Choi, Lee and Kim. This is an open-access article distributed under the terms of the Creative Commons Attribution License (CC BY). The use, distribution or reproduction in other forums is permitted, provided the original author(s) and the copyright owner(s) are credited and that the original publication in this journal is cited, in accordance with accepted academic practice. No use, distribution or reproduction is permitted which does not comply with these terms.



# A New Subject-Specific Discriminative and Multi-Scale Filter Bank Tangent Space Mapping Method for Recognition of Multiclass Motor Imagery

Fan Wu<sup>1,2</sup>, Anmin Gong<sup>3</sup>, Hongyun Li<sup>1,2</sup>, Lei Zhao<sup>2,4</sup>, Wei Zhang<sup>5</sup> and Yunfa Fu<sup>1,2,6,7\*</sup>

<sup>1</sup> Faculty of Information Engineering and Automation, Kunming University of Science and Technology, Kunming, China, <sup>2</sup> Brain Cognition and Brain-Computer Intelligence Fusion Innovation Group, Kunming University of Science and Technology, Kunming, China, <sup>3</sup> Department of Information Engineering, Engineering University of PAP, Xi'an, China, <sup>4</sup> College of Science, Kunming University of Science and Technology, Kunming, China, <sup>5</sup> Kunming Medical University, Kunming, China, <sup>6</sup> Yunnan Provincial Key Laboratory of Computer Technology Application, Kunming, China, <sup>7</sup> School of Medicine, Kunming University of Science and Technology, Kunming, China

## OPEN ACCESS

### Edited by:

Haider Raza,  
University of Essex, United Kingdom

### Reviewed by:

Rosa So,  
Institute for Infocomm Research  
(A\*STAR), Singapore  
Yu Zhang,  
Lehigh University, United States

### \*Correspondence:

Yunfa Fu  
fyf@ynu.edu.cn

### Specialty section:

This article was submitted to  
Brain-Computer Interfaces,  
a section of the journal  
Frontiers in Human Neuroscience

**Received:** 17 August 2020

**Accepted:** 15 February 2021

**Published:** 08 March 2021

### Citation:

Wu F, Gong A, Li H, Zhao L,  
Zhang W and Fu Y (2021) A New  
Subject-Specific Discriminative  
and Multi-Scale Filter Bank Tangent  
Space Mapping Method  
for Recognition of Multiclass Motor  
Imagery.  
*Front. Hum. Neurosci.* 15:595723.  
doi: 10.3389/fnhum.2021.595723

**Objective:** Tangent Space Mapping (TSM) using the geometric structure of the covariance matrices is an effective method to recognize multiclass motor imagery (MI). Compared with the traditional CSP method, the Riemann geometric method based on TSM takes into account the nonlinear information contained in the covariance matrix, and can extract more abundant and effective features. Moreover, the method is an unsupervised operation, which can reduce the time of feature extraction. However, EEG features induced by MI mental activities of different subjects are not the same, so selection of subject-specific discriminative EEG frequency components play a vital role in the recognition of multiclass MI. In order to solve the problem, a discriminative and multi-scale filter bank tangent space mapping (DMFBTSM) algorithm is proposed in this article to design the subject-specific Filter Bank (FB) so as to effectively recognize multiclass MI tasks.

**Methods:** On the 4-class BCI competition IV-2a dataset, first, a non-parametric method of multivariate analysis of variance (MANOVA) based on the sum of squared distances is used to select discriminative frequency bands for a subject; next, a multi-scale FB is generated according to the range of these frequency bands, and then decompose multi-channel EEG of the subject into multiple sub-bands combined with several time windows. Then TSM algorithm is used to estimate Riemannian tangent space features in each sub-band and finally a linear Support Vector Machines (SVM) is used for classification.

**Main Results:** The analysis results show that the proposed discriminative FB enhances the multi-scale TSM algorithm, improves the classification accuracy and reduces the

execution time during training and testing. On the 4-class BCI competition IV-2a dataset, the average session to session classification accuracy of nine subjects reached  $77.33 \pm 12.3\%$ . When the training time and the test time are similar, the average classification accuracy is 2.56% higher than the latest TSM method based on multi-scale filter bank analysis technology. When the classification accuracy is similar, the training speed is increased by more than three times, and the test speed is increased two times more. Compared with Supervised Fisher Geodesic Minimum Distance to the Mean (Supervised FGMDRM), another new variant based on Riemann geometry classifier, the average accuracy is 3.36% higher, we also compared with the latest Deep Learning method, and the average accuracy of 10-fold cross validation improved by 2.58%.

**Conclusion:** Research shows that the proposed DMFBTSM algorithm can improve the classification accuracy of MI tasks.

**Significance:** Compared with the MFBTSM algorithm, the algorithm proposed in this article is expected to select frequency bands with good separability for specific subject to improve the classification accuracy of multiclass MI tasks and reduce the feature dimension to reduce training time and testing time.

**Keywords:** tangent space mapping, discriminative and multiscale filter bank, multiclass motor-imagery, Riemannian geometry based classifier, electroencephalogram

## INTRODUCTION

Brain-computer interface (BCI) is a revolutionizing human-computer interaction (Grimann et al., 2010), and BCI based on motor imagery (MI-BCI) is an important type of BCI which is expected to provide communication and control with the outside world for patients with severe motor disabilities (Wolpaw and Wolpaw, 2012), especially in motor dysfunction rehabilitation training (Soares et al., 2013). However, at present, MI-BCI can classify few MI tasks, and it can provide few effective instructions, which limits the communication capability and control freedom of this type of BCI, making it difficult to enter practical applications. In order to add instructions, it is necessary to study the recognition of multiclass MI tasks. At present, the recognition accuracy of multi-class MI needs to be improved, which is a challenging work. This article intends to explore effective methods to improve the recognition accuracy of multi-class MI.

Neuroscience research has shown that brain activities related to MI and motor execution (ME) can cause similar sensorimotor rhythm changes (Pfurtscheller and Neuper, 1997), and the EEG amplitude of certain frequency bands will decrease event-related desynchronization (ERD) or increase event related synchronization (ERS). This ERD/ERS phenomenon or pattern is most prominent in mu rhythm (8–12 Hz) and beta rhythm (13–30 Hz), and can also be observed in gamma rhythm close to 40 Hz (Rao, 2013). In MI-BCI, these patterns are mainly extracted. However, due to the non-stationarity of EEG, low signal-to-noise ratio and limited available calibration data, it is difficult to extract MI feature patterns with good separability (Lotte et al., 2018). In MI-BCI, the classical processing method

is to extract sources from the pre-processed EEG data using a spatial filter such as CSP, then extract the feature vectors from the source signal, and finally classify the feature vectors using a vector-based classifier (such as LDA) (Yger et al., 2017). Studies have shown that Common Spatial Pattern (CSP) has significant advantages in extracting MI features (Lotte et al., 2018) CSP maximizes the variance of the EEG signal of one class of MI while minimizing the variance of the other class. After band-pass filtering, the variance of the EEG signal is the power of the corresponding frequency band. Therefore, CSP is a more suitable method to extract the features of the two classes of MI (Ramoser et al., 2000). Deep Learning is a specific machine learning algorithm in which features and the classifier are jointly learned directly from data (Lotte et al., 2018). Advantages of Deep Learning include that they are well suited for end-to-end learning, that is, learning from the raw data without any *a priori* feature selection, that they scale well to large datasets, and that they can exploit hierarchical structure in natural signals (Schirrneister et al., 2017). Disadvantages of Deep Learning methods include that they may output false predictions with high confidence may require a large amount of training data, may take longer to train than simpler models, and involve a large number of hyperparameters such as the number of layers or the type of activation function (Nguyen et al., 2015). Convolutional neural networks (ConvNets) are the most popular Deep Learning approaches for BCI (Lotte et al., 2018). In order to adapt the existing ConvNets architectures from the field of computer vision to EEG input, the authors created three ConvNets with different architectures, with the number of convolutional layers ranging from 2 layers in a “shallow” ConvNet over a 5-layer deep ConvNet up to a 31-layer residual network (ResNet) (Schirrneister et al., 2017). In

Sakhavi et al. (2018), according to the features generated by filter bank CSP (FBCSP), the authors design and optimize a ConvNet for classification.

In addition to CSP and its various improvement methods (Ang et al., 2008, 2012; Zhang et al., 2015, 2016), the researchers used the Riemannian method based on the covariance matrix in the Riemannian manifold in MI-BCI and achieved better performance, and this new processing method does not require source extraction. At present, Riemannian manifold of symmetric positive definite (SPD) matrices has attracted more and more attention due to their rich framework for manipulating the covariance structure of the data. The concept of the covariance matrices in the manifold has been successfully used in radar signal processing (Barbaresco, 2008), diffusion tensor Imaging (Fletcher and Joshi, 2004) and computer vision (Tuzel et al., 2008). A similar method is combined with K nearest neighbors and recognizes different sleep states based on EEG (Li et al., 2009). Barachant et al. (2010) first used the Riemannian method to classify two-class MI-EEG data and achieved an average classification accuracy of 85.2%. The Minimum Distance to Riemannian Mean (MDRM) introduced in their works is the most basic Riemannian method (Congedo et al., 2017). In this method, the Riemannian mean of each class is calculated first based on the training data, and then classify incoming trials by comparing the Riemannian distances between the covariance matrices corresponding to the incoming trials and the Riemannian mean of each class during the test session (Barachant et al., 2010). Another more sophisticated and effective Riemannian classifiers is based on tangent space mapping (TSM), and its classification performance is significantly better than CSP and other methods (Congedo et al., 2017). Barachant et al. mapped the covariance matrices onto the tangent space, and then selected features in it and used LDA, the results showed that compared with MDRM, it can significantly improve the accuracy of multi-class (4-class) MI recognition (Barachant et al., 2012). Barachant et al. (2013) derived a new kernel by establishing a connection with the Riemannian geometry of symmetric positive definite matrices, and combined with a support vector machine to test different kernels, and demonstrated that this new approach outperformed significantly state of the art results, effectively replacing the traditional spatial filtering approach.

In order to further improve the classification performance of MI-BCI, Ang et al. (2008) proposed the filter bank CSP (FBCSP) method, a four-stage procedure in which CSP is applied at several fixed frequency bands, and where the most relevant sub-band CSP features are automatically pair-wise selected based upon mutual information criteria. Recently, Zhang et al. (2015) proposed the sparse filter bank CSP (SFBCSP) in which a small number of sub-band CSP features are automatically selected based on LASSO (least absolute shrinkage and selection operator) regression. According to some recent achievements, we know that a breakthrough has been made in the research of MI task recognition based on Deep Learning (Li et al., 2019; Olivas Padilla and Chacon Murguía, 2019; Xu et al., 2020). In Xu et al. (2020), a new deep multi-view feature learning method for the classification task of motor imagery electroencephalogram

(EEG) signals is proposed in order to obtain more representative motor imagery features in EEG signals. In Li et al. (2019), the researchers proposes a variant of Discriminative Filter Bank Common Spatial Pattern (DFBCSP) for extracting MI features, and then sets the resulting samples into a matrix, which is then fed to one or many ConvNets previously optimized by using a Bayesian optimization for classification. In Olivas Padilla and Chacon Murguía (2019), a densely feature fusion convolutional neural networks (DFFN) is proposed. DFFN takes into account the correlation between adjacent layers and cross-layer features, thus reducing information loss in the process of convolutional operation. It also takes into account the local and global characteristics of the network, and improves the identification accuracy of the ordinary ConvNets framework in multi-class MI. In the improvement of the method based on Riemannian geometry, Barachant et al. proposed Fisher Geodesic Discriminant Analysis for performing Geodesic filtering to make the classes more separable along the geodesics, which improves the drawback of MDRM not taking into account intra-class distribution (Barachant et al., 2010). More recently, Satyam et al., combined the two adaptive strategies of RETRAIN and REBIAS (Shenoy et al., 2006) with MRDM and Fisher Geodesic Minimum Distance to Riemannian Mean (FgMDRM), and the result achieved an average classification accuracy of approximately 74% on the test set (Session 2) of the 2a data set of BCI Competition IV (Kumar et al., 2019). Islam et al. (2017) proposed a multi-band TSM method, which takes into account multiple frequency bands and helps to extract effective noise robust features for narrow-band signals, but the study did not consider the question of the subject-specific frequency band. However, MI-BCI is an active BCI. The EEG features induced by MI mental activity of different subjects are often different. It is necessary to customize the feature extraction method for specific subjects. Islam et al. proposed a multiband tangent space mapping with sub-band selection (MTSMS). The sub-band selection method adopted can be based on the mutual information between features and class labels, thereby effectively extract the frequency band of a specific subject, and further improve the performance of MI-BCI (Islam et al., 2018). In addition, in order to overcome the limitation of using fixed band window analysis in MI-BCI, Hersche et al. (2018) proposed a multi-scale filter bank TSM (MFBTSM), in which FB contains the frequency bands are multi-scale and overlapping. At the same time, multi-scale and overlapping time windows are divided, so that multiple time windows are used to analyze EEG trials and perform FB analysis in each time window. This greatly increases the number of tangent spatial features, but induce redundant information. The disadvantages of MFBTSM is that the filter bank used by each subject is the same, and the test time and training time increase due to the large feature dimension.

In order to make up for the disadvantages of MFBTSM, this article intends to use a non-parametric method of multivariate analysis of variance based on the sum of squared distances to select the subject-specific discriminative EEG frequency components, and these component is vital for identifying multiple types of MI tasks. It is important to use multi-scale filter bank TSM at the same time, and finally use SVM for classification.

## MATERIALS AND METHODS

### Riemann Geometry Associated With the Proposed Method

#### EEG Signals Are Represented as Covariance Matrices

To use Riemannian geometry to process EEG signals, it is necessary to represent the EEG signals as covariance matrices, which are SPD matrices. Let  $X_i \in \mathbb{R}^{N_c \times N_s}$  be the MI EEG signal of the  $i$ -th trial, where  $N_c$  is the number of channels and  $N_s$  is the number of samples. The sample covariance matrix (SCM) of the  $i$ -th trial is denoted by  $P_i \in \mathbb{R}^{N_c \times N_c}$ , which is estimated by eq. (1) (Barachant et al., 2012):

$$P_i = 1/(N_s - 1)X_iX_i^T \quad (1)$$

Let  $S(n)$  denote the set of  $n \times n$  symmetric matrices, and  $P(n)$  denote the set of  $n \times n$  SPD matrices.

#### Riemannian Manifold and Tangent Space

The space of SPD matrices  $P(n)$  is a differentiable Riemannian manifold  $\mathcal{M}$  (Förstner and Moonen, 2003). The derivatives at a matrix  $\mathbf{P}$  on the manifold lies in a vector space  $T_{\mathbf{P}}$ , which is the tangent space at that point. The tangent space is lying in the space  $S(n)$ . The manifold and the tangent space are  $m = n(n+1)/2$  dimensional.

Each tangent space has an inner product  $\langle \cdot, \cdot \rangle_{\mathbf{P}}$  that varies smoothly from point to point over the manifold. The natural metric on the manifold of SPD matrices is defined by the local inner product:

$$\langle S_1, S_2 \rangle_{\mathbf{P}} = \text{Tr}(S_1\mathbf{P}^{-1}S_2\mathbf{P}^{-1}) \quad (2)$$

The inner product induces a norm for the tangent vectors on the tangent space, such that,  $\|S\|_{\mathbf{P}}^2 = \langle S, S \rangle_{\mathbf{P}} = \text{Tr}(S\mathbf{P}^{-1}S\mathbf{P}^{-1})$ . We note that, at Identity matrix, such norm simplifies into the Frobenius norm, i.e.,  $\langle S, S \rangle_I = \|S\|_F^2$ .

#### Riemannian Geodesic Distance and Riemannian Distance

Let  $\Gamma(t) : [0, 1] \rightarrow P(n)$  be any (differentiable) path from  $\Gamma(0) = P_1$  to  $\Gamma(1) = P_2$ . The length of  $\Gamma(t)$  is given by:

$$L(\Gamma(t)) = \int_0^1 \|\dot{\Gamma}(t)\|_{\Gamma(t)} dt \quad (3)$$

With the norm defined previously. The minimum length curve connecting two points on the manifold is called the geodesic, and the Riemannian distance between the two points is given by the length of this curve. The natural metric (2) induces the geodesic distance (Moakher, 2005):

$$\delta_R(P_1, P_2) = \|\log(P_1^{-1}P_2)\|_F = \left[ \sum_{i=1}^n \log^2 \lambda_i \right]^{1/2} \quad (4)$$

Where,  $\lambda_i, i = 1 \dots n$  are the real eigenvalues of  $P_1^{-1}P_2$ .

#### Exponential Map

For each point  $\mathbf{P} \in P(n)$ , we can thus define a tangent space composed by the set of tangent vectors at  $\mathbf{P}$ . Each tangent vector  $S_i$  can be seen as the derivative at  $t = 0$  of the geodesic  $\Gamma_i(t)$  between  $\mathbf{P}$  and the exponential mapping  $P_i = \text{Exp}_{\mathbf{P}}(S_i)$ , defined as:

$$\text{Exp}_{\mathbf{P}}(S_i) = P_i = \mathbf{P}^{\frac{1}{2}} \exp(\mathbf{P}^{-\frac{1}{2}} S_i \mathbf{P}^{-\frac{1}{2}}) \mathbf{P}^{\frac{1}{2}} \quad (5)$$

The inverse mapping is given by the logarithmic mapping defined as:

$$\log_{\mathbf{P}}(P_i) = S_i = \mathbf{P}^{\frac{1}{2}} \log(\mathbf{P}^{-\frac{1}{2}} P_i \mathbf{P}^{-\frac{1}{2}}) \mathbf{P}^{\frac{1}{2}} \quad (6)$$

#### Euclidean Mean

Using the Euclidean distance on  $\mathcal{M}(n)$ ,  $\delta_E(P_1, P_2) = \|P_1 - P_2\|_F$ , it is possible to define the Euclidean mean of  $I \geq 1$  SPD matrices by:

$$\mathfrak{A}(P_1, \dots, P_I) = \arg \min_{P \in P(n)} \sum_{i=1}^I \delta_E^2(P, P_i) = \frac{1}{I} \sum_{i=1}^I P_i \quad (7)$$

#### Riemannian Mean

Similar to Euclidean mean, Karcher/Fréchet means extends the notion of mean/center of mass to  $P(n)$  by estimating the SPD matrix which minimizes the sum of squared AIRM distances to all the SPD matrices in the set. Mathematically the Riemannian mean of  $I \geq 1$  SPD matrices is given by:

$$\mathfrak{G}(P_1, \dots, P_I) = \arg \min_{P \in P(n)} \sum_{i=1}^I \delta_R^2(P, P_i) \quad (8)$$

Eq. (8) has a unique minimum, and there is no closed solution for  $I > 2$ , but many iterative algorithms solve this problem through numerical analysis (Moakher, 2005).

### Discriminative and Multi-Scale Filter Bank Tangent Space Mapping

The structure of Discriminative and Multi-scale Filter Bank Tangent Space Mapping (DMFBTSM) proposed in this article is shown in **Figure 1**. First, a set of filters is used to decompose the multi-channel EEG signal into multiple frequency band components. These filters are called the parent filter bank (Filter Bank, FB), and the parent FB covers all frequency components in the range of 2–40 Hz. Then use the one-way multivariate analysis of variance (MANOVA) based on the sum of squared distances to calculate the F statistic for each sub-band component decomposed. According to the F statistic, select EEG frequency bands that are separable for MI of the specific subject, and then generate discriminative and multi-scale filter bank (DMFB).

#### The One-Way MANOVA Based on the Sum of Squared Distances

In this article, a non-parametric method of MANOVA based on the sum of squared distances (Anderson, 2001) is used to select the EEG frequency bands that are separable for MI of the specific subject. The test statistic is a multivariate analog to Fisher's F-ratio and is calculated directly from any symmetric distance or dissimilarity matrix.

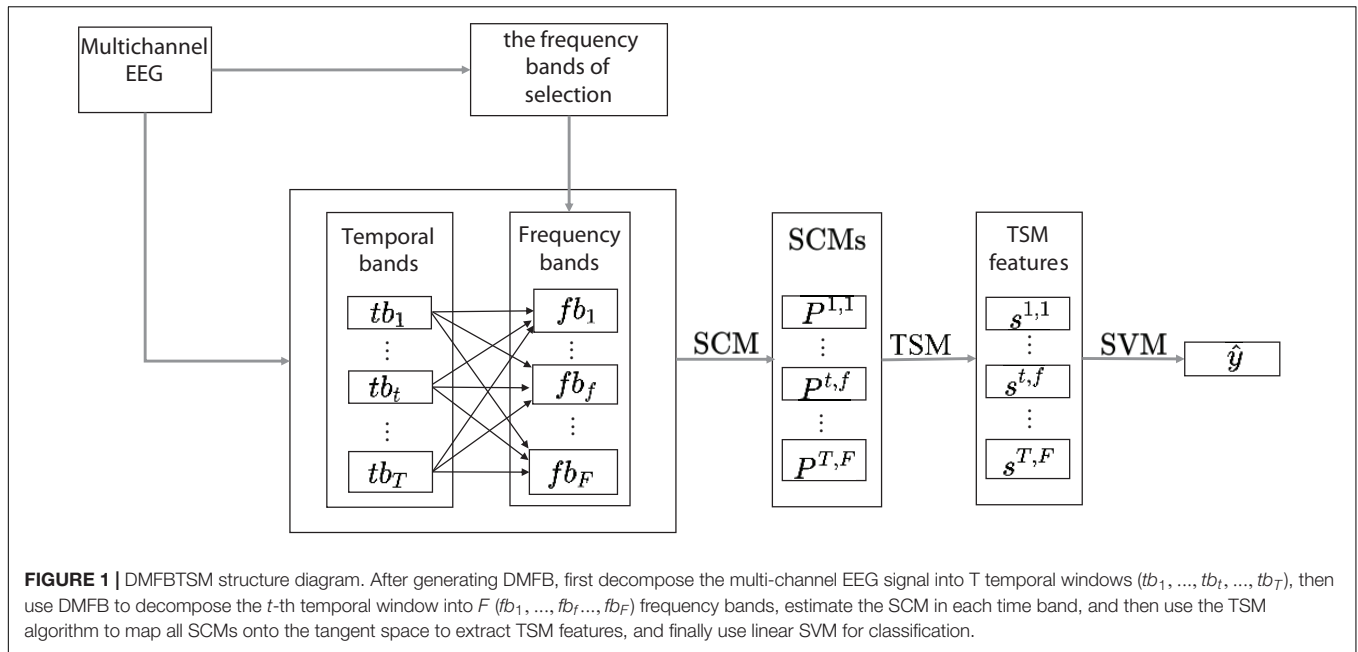


**FIGURE 1 |** DMFBTSM structure diagram. After generating DMFB, first decompose the multi-channel EEG signal into T temporal windows (tb<sub>1</sub>, ..., tb<sub>t</sub>, ..., tb<sub>T</sub>), then use DMFB to decompose the t-th temporal window into F (fb<sub>1</sub>, ..., fb<sub>f</sub>, ..., fb<sub>F</sub>) frequency bands, estimate the SCM in each time band, and then use the TSM algorithm to map all SCMs onto the tangent space to extract TSM features, and finally use linear SVM for classification.

First, the EEG signals of a specific subject’s frequency range of 2–40 Hz are decomposed into 2 Hz width, a total of 19 sub-bands. Then estimate the SCMs of all trials in each sub-band and calculate the distance matrix between each pair of SCMs, as shown in **Figure 2**. Finally, the F statistic of each sub-band is calculated by MANOVA based on the square of the distance. The calculation process is as follows.

Assuming that the test data of the subject has a classes, each class has n trials, the total number of trials is N = a\*n, and the total sum of squares is:

$$SS_T = \frac{1}{N} \sum_{i=1}^{N-1} \sum_{j=i+1}^N d_{ij}^2 \tag{9}$$

where, d<sub>ij</sub> is the distance between the SCM of the i-th trial and the SCM of the j-th trial. In a similar fashion, the within-group or residual sum of squares is:

$$SS_W = \frac{1}{n} \sum_{i=1}^{N-1} \sum_{j=i+1}^N d_{ij}^2 \epsilon_{ij} \tag{10}$$

where, if the i-th trial and the j-th trial are in the same class, the value of ε<sub>ij</sub> is 1, otherwise it is 0, as shown in **Figure 2B**. The sum of squares between classes, SS<sub>A</sub> and F statistics are calculated by eqs. (11, 12):

$$SS_A = SS_T - SS_W \tag{11}$$

$$F = \frac{SS_A / (a - 1)}{SS_W / (N - a)} \tag{12}$$

In this article, the aforementioned Riemannian distance and Euclidean distance are applied to eqs. (9–12), respectively. If the sample points of different classes have different center positions

in the multivariate space (centroid in the case of Euclidean distance), the ratio of the inter-class distance to the intra-class distance will be large, and the generated F-statistic will be relatively large. After calculating the F statistics of all sub-bands, arrange the sub-bands in descending order of F scores, take the first several separable sub-bands, and merge the adjacent separable sub-bands to obtain the EEG frequency bands that are separable for MI of the specific subject.

### Divide Multi-Channel EEG Using Multi-Scale Time and Frequency Windows

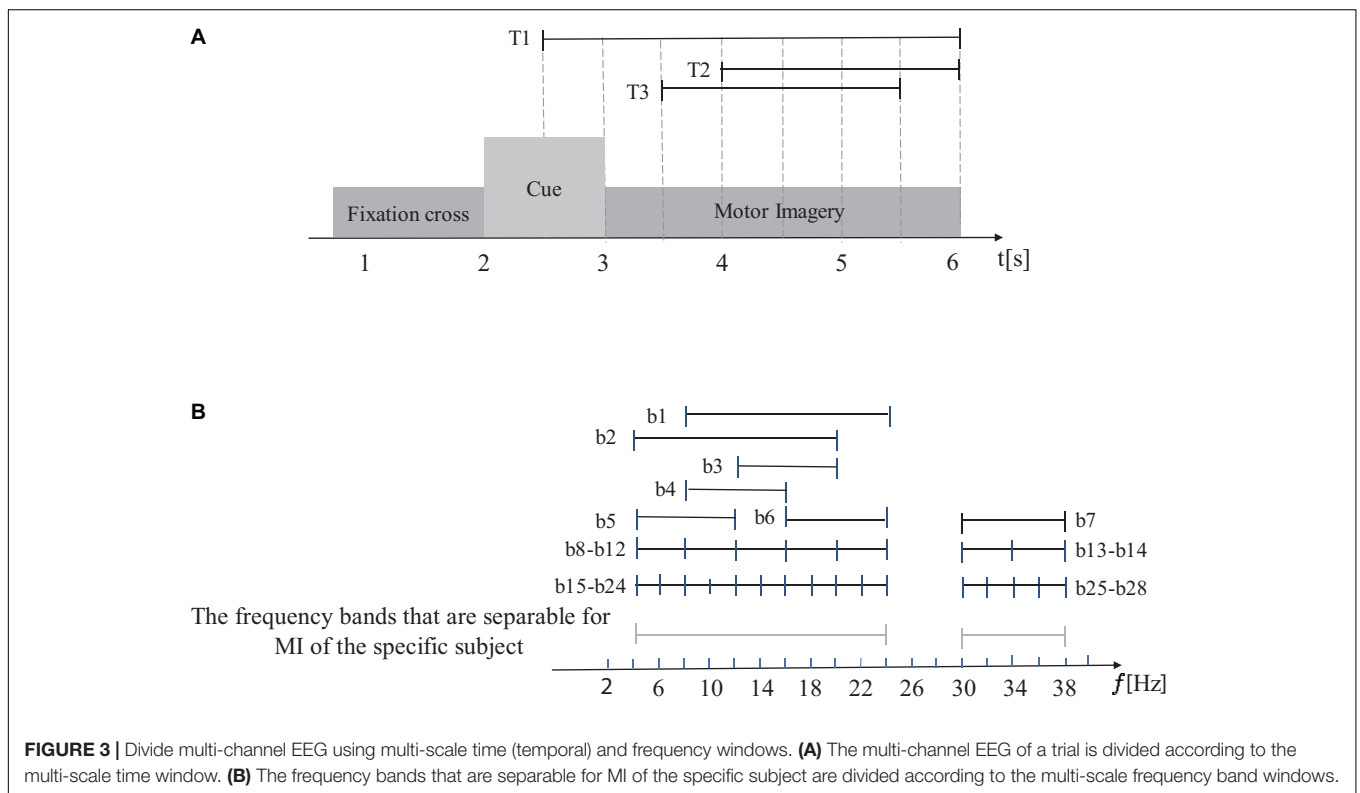
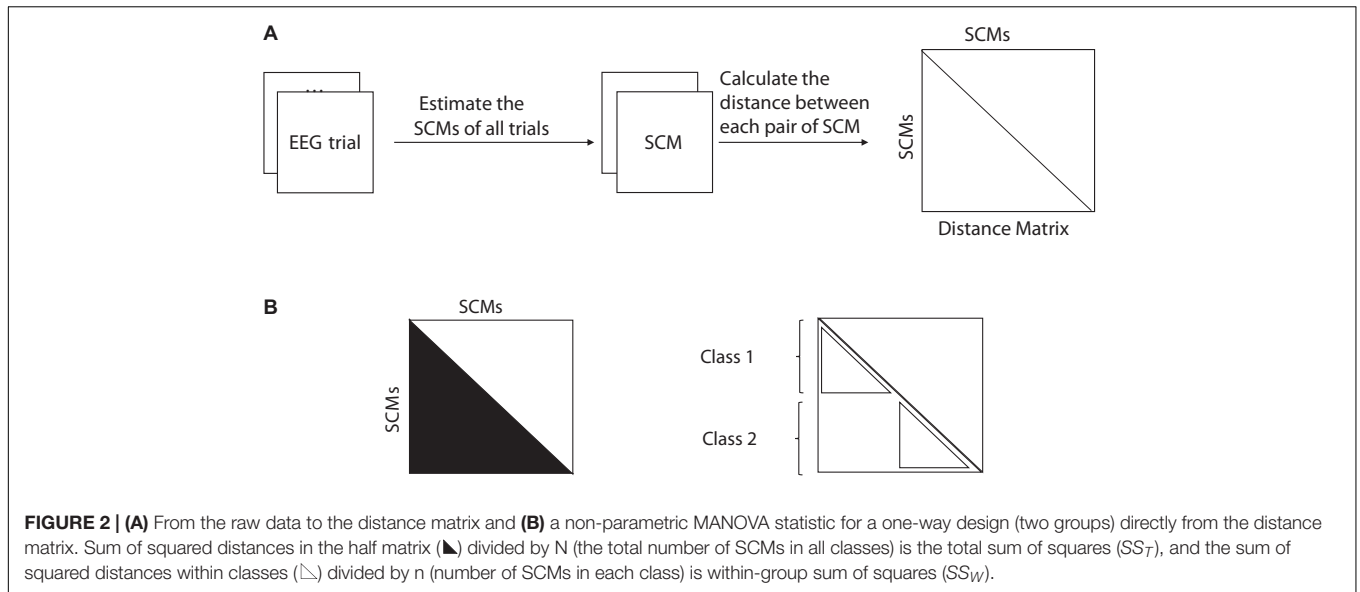
First, the multi-channel EEG of a trial is divided according to the multi-scale time window shown in **Figure 3A**, and then according to the multi-scale frequency band window division shown in **Figure 3B**, the frequency bands that are separable for MI of the specific subject are divided according to the multi-scale frequency band windows shown in **Figure 3B** to generate DMFB, and then the DMFB band-pass filters the signal of each time window.

### Tangent Space Mapping

This article uses the TSM algorithm proposed by Barachant et al. (2010), as shown in **Figure 4**. The algorithm first needs to find a reference point P<sub>ϕ</sub>, which is the Riemann average of all EEG trials on manifold M: P<sub>ϕ</sub> = ϕ(P<sub>i</sub>, i 1...I). Then map the SCM corresponding to each trial onto the tangent space T<sub>P</sub> to generate a set of m = N<sub>C</sub>(N<sub>C</sub> + 1)/2-dimensional tangent vectors S [s<sub>1</sub>...s<sub>I</sub>] ∈ R<sup>m</sup> × I, The tangent vector s<sub>i</sub> is calculated as eq. (13):

$$s_i = \text{upper}(P_{\phi}^{-\frac{1}{2}} \log_{P_{\phi}}(P_i) P_{\phi}^{-\frac{1}{2}}) \tag{13}$$

where, P<sub>i</sub> is the SCM corresponding to the i-th trial, upper means to vectorize the upper triangular part of a SPD matrix, with appropriate weighting.



## RESULTS

### Description of Data

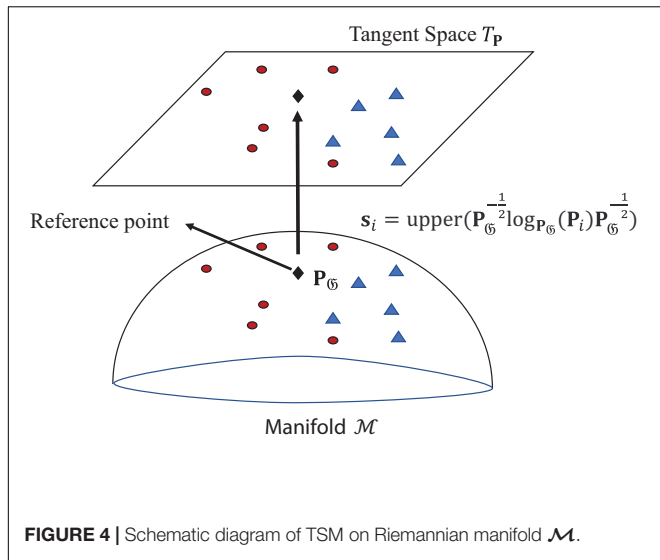
First, analyze the justifiability of selecting frequency bands for specific subjects based on F statistics, using BCI Competition III dataset IVa and BCI competition IV dataset 2a<sup>1</sup>, and finally using

<sup>1</sup><http://bbci.de/competition/>

BCI Competition IV 2a data set evaluation the performance of the proposed method.

### BCI Competition IV Dataset 2a

Dataset 2a (Naeem et al., 2006) contains EEG data from 9 subjects who perform four kinds of motor imagery (right hand, left hand, foot, and tongue imagined movements). This dataset is provided by the Knowledge Discovery Institute (BCI Laboratory) of Graz University of Technology, Austria. EEG signals are recorded



using 22 electrodes. For each subject, a training set (session 1) and a test set (sessions 2) are available. The same number of trials for all the MI tasks were provided for testing and training session. Each of the session had 72 trials for each of the four motor imagery classes.

### BCI Competition III Dataset IVa

Dataset IVa (Dornhege et al., 2004) contains 2-class of MI EEG. This dataset is provided by the Knowledge Discovery Institute (BCI Laboratory) of Graz University of Technology, Austria. It records the EEG of 5 healthy subjects who perform two classes of MI (right hand and foot), Each subject recorded 280 trials, of which the first 168, 224, 84, 56, and 28 trials constituted the training set of subjects A1, A2, A3, A4, and A5, and the remaining trials constituted their test set.

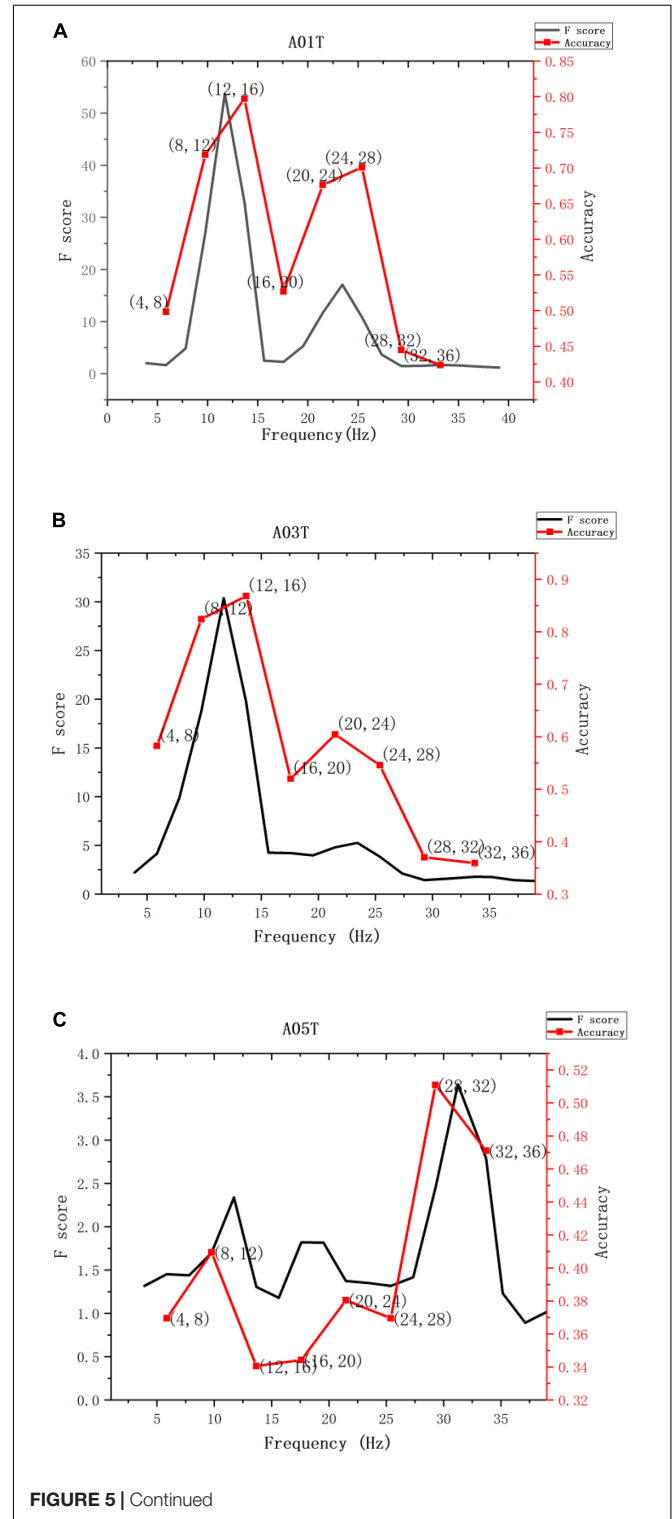
## Experimental Results

### F Statistic Selects the Frequency Bands That Are Separable for MI of the Specific Subject

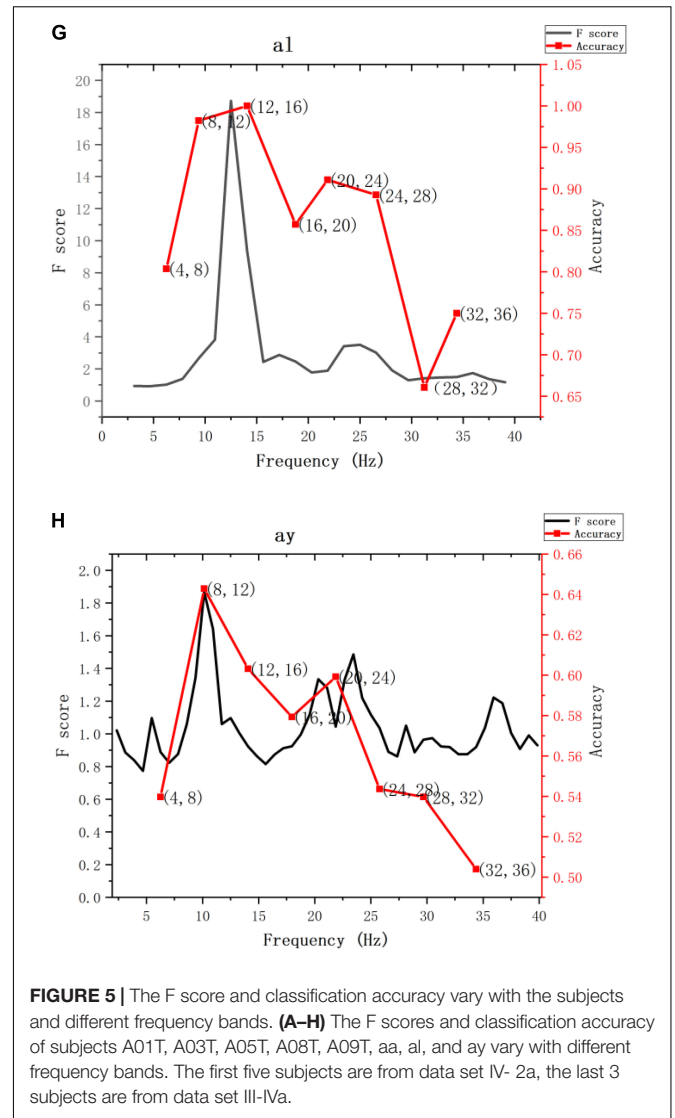
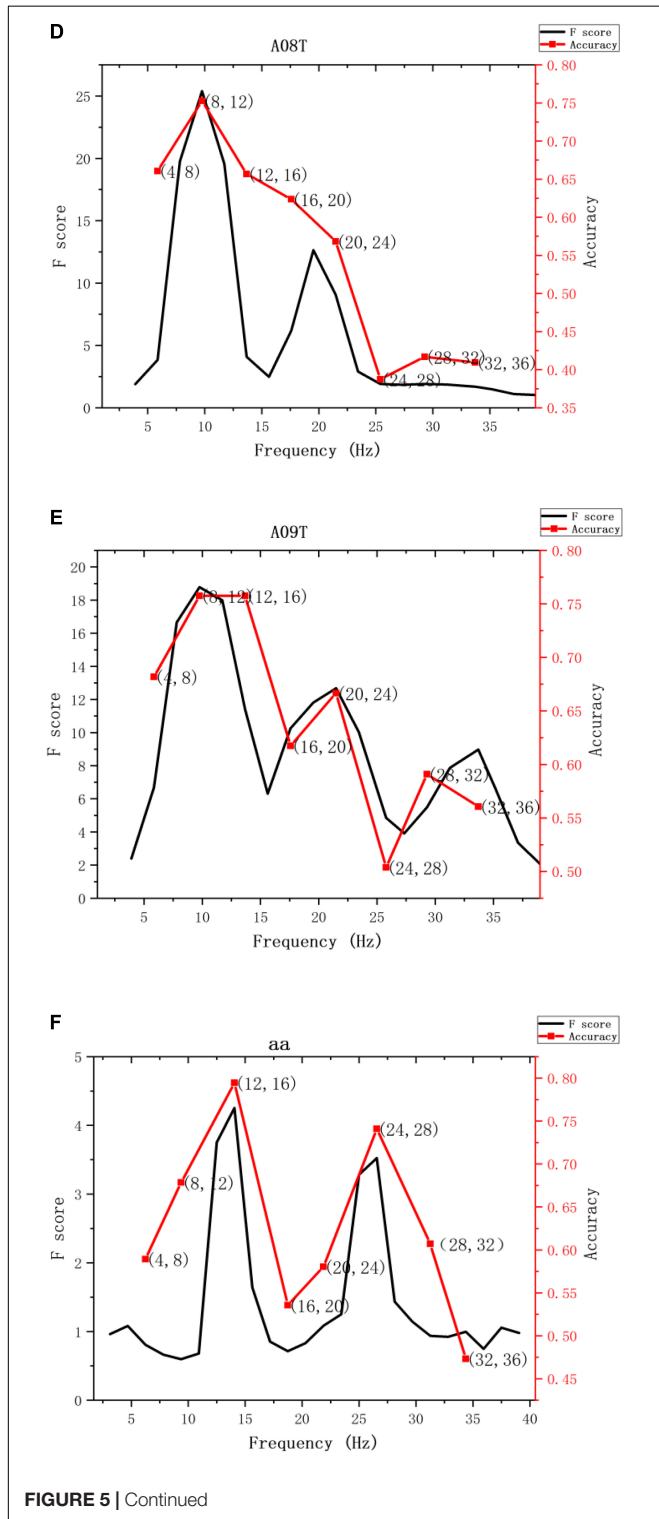
Using the parent FB in the frequency range of 2 to 40 Hz, the EEG signal of each subject was decomposed into 19 sub-bands, and then the Riemannian distance was selected as the distance metric to calculate the F score of each sub-band. In order to show the justifiability of using the F score of each sub-band as the criterion for selecting a separable frequency band, the classification accuracy of different sub-bands of the test data of different subjects on the BCI competition public data set is calculated, as shown in **Figure 5**, where the sub-band width for calculating the classification accuracy is 4 Hz, and the range is from 4 to 36 Hz. It can be seen from **Figure 5** that the classification accuracy of the sub-band with a higher F score is better than that of the sub-band with a lower F score. Therefore, it is justified to use one-way MANOVA based on the square of the distance to select the separable sub-bands. Then, the sub-bands are sorted in descending order of F score, and the top G sub-bands are used for MI classification.

### Multi-Class MI (4-Class) Classification Results

In this study, nine subjects in the BCI competition IV data set 2a (four types of MI) were selected for separable frequency bands, and multi-scale time-frequency TSM features were extracted and classified. In order to better evaluate the performance



of DMFBTSM, first compare with MFBTSM, the results are shown in **Table 1**, and then test other three related methods on the same data set. The first method is the combination of FgMDRM and RETAIN Adaptive strategy, called Supervised Adaptive FgMDRM (Supervised FgMDRM). In this method, the



FgMDRM classifier is first trained on training/calibration session data, then during the testing session, the classifier is retrained after each prediction (Kumar et al., 2019). The second method is the combination of TSM and adaptive Riemannian kernel SVM, known as adaptive Riemannian kernel SVM (ARK-SVM) (Barachant et al., 2013), and the third method is FBCSP (Ang et al., 2012). Comparison results of these three methods with DMFBTSM are shown in **Table 2**.

In addition, this article is compared with the latest three Deep Learning-based methods. In Deep Multi-view feature learning method (Xu et al., 2020), the author uses the improved, the deep restricted Boltzmann machine (RBM) network to learn the multi-view features of EEG signals, and finally uses SVM to classify deep multi-view features. The DFFN algorithm is a dense feature fusion convolutional neural network using CSP and ConvNet technology (Li et al., 2019). In the Monolithic Network method (Olivas Padilla and Chacon Murguia, 2019), the authors used a variant of discriminative FBCSP to extract signal features,

**TABLE 1** | Under different distance measures [N/A (no distance metric), Euclidian distance and Riemannian distance], multi-scale time-frequency TSM features were extracted, and average classification accuracy (%) and standard deviation (std), average training time and average test time were obtained from the 4 MI classes on the test data (session 2) of 9 subjects in BCI Competition IV data-set 2a.

Method	MFBTSM			DMFBTSM		
	N/A	N/A	Euclidian distance	Euclidian distance	Riemannian distance	Riemannian distance
Distance metric	N/A	N/A	Euclidian distance	Euclidian distance	Riemannian distance	Riemannian distance
Time window selection	T1	T1, T2, T5	T1	T1, T2, T5	T1	T1, T2, T5
A1	91.81	90.04	91.81	92.53	92.53	93.24
A2	51.59	55.48	56.54	61.13	55.48	60.78
A3	83.52	81.32	82.42	83.15	87.18	87.18
<b>A4</b>	73.25	71.92	69.74	70.18	70.18	71.49
A5	63.41	69.57	67.75	68.12	68.12	66.67
A6	58.60	56.74	61.4	59.53	60.0	61.4
A7	86.64	85.56	83.03	85.92	87.0	86.28
A8	81.55	83.76	80.81	83.39	83.39	85.61
A9	82.58	84.85	82.2	84.85	85.23	83.33
Mean	74.77	75.47	75.08	76.53	76.57	77.33
Std	13.9	12.8	11.7	12.0	13.4	12.3
Avg. training time [s]	34.32	55.39	10.43	29.78	11.04	32.68
Avg. testing time [s]	10.91	20.92	4.47	12.56	4.70	12.24

**TABLE 2** | Mean classification accuracy (%) and standard deviation (std) obtained across nine subjects in data-set 2a.

Method	DMFBTSM	Supervised FgMDRM	FgMDRM	ARK-SVM	FBCSP
Mean	77.33	73.97	68.31	65.29	67.21
Std	12.3	13.1	14.2	14.4	19.2

and then developed a Bayes-optimized ConvNet network for classification. The Shallow-ConvNet algorithm inspired by the FBCSP pipeline, specifically tailored to decode band power features (Schirrmmeister et al., 2017). After extracting the FBCSP features, the CW-ConvNets algorithm inputs them into the ConvNets for classification (Sakhavi et al., 2018). Comparison results of the method proposed in this article and the three Deep Learning methods are shown in **Table 3**.

**Tables 1, 2** present the mean and standard deviation of the classification accuracy (averaged across all the subjects) on a session to session transfer evaluation for these methods. The results presented in **Table 3** are obtained by combining and randomly arranging the training data (Session 1) and test data (Session 2) of each subject's data set according to the data organization method in Xu et al. (2020), and then performing 10 fold cross-validation.

In order to calculate the sub-band F score, Riemannian distance and Euclidean distance are selected and compared in this study. In addition, due to the differences in MI of different subjects, in order to ensure the accuracy of MI classification, the number of sub-bands G selected by each specific subject may not be the same. In addition, in order to ensure the accuracy of MI classification, the number of sub-bands G selected by each specific subject may not be the same. At the same time, in order to reduce the number of features to reduce training time and test time, the value of G ranges from 11 to 14. Specifically, subject 1 and 9 chose G as 13, subject 2, subject 3, subject 6, and subject 8 chose G as 11, subject 4 and 7 chose G as 14, and subject 5 chose G as 12. Choose one (T1) or three (T1, T2, and T3) time windows

for decomposing EEG signals for comparison. In the case of one time window, the feature dimension of the subjects is 10879, and the feature dimension varies from 5060 to 7840 after frequency band selection. In addition, 10-fold cross-validation was used for the selection of time window and frequency band, as well as the determination of the SVM's hyperparameter C.

In order to evaluate the computational cost of the proposed method, the average training and testing time of all trials for each subject is measured. The training time includes the preprocessing and training time of the classifier, and the testing time includes the feature extraction and classification time. The experiments were conducted on an Intel Core i5-7200U 2.71 GHz processor with 8 GB RAM.

**Table 1** shows that the proposed discriminative FB enhances the multi-scale TSM algorithm. The best classification accuracy obtained by using Euclidean distance as the distance metric is  $76.53 \pm 12.0\%$ , the shortest training time is 10.43 s, and the shortest test time is 4.47 s; The best classification accuracy obtained by using Riemannian distance as the distance metric is  $77.33 \pm 12.3\%$ , the shortest training time is 11.04 s, and the shortest test time is 4.70 s.

## DISCUSSION

Existing studies have shown that, compared with the conventional CSP method, Riemannian geometry based methods can bypass the spatial filtering of electrodes to make the calibration phase easier, and significantly improve the

**TABLE 3** | Mean classification accuracy (%) and standard deviation (std) on test data by 10 fold cross-validation achieved by DMFBTSM, Deep Multi-View Feature Learning, Shallow-ConvNet, CW-ConvNet, Monolithic Network, and DFFN, for dataset 2a.

Method	DMFBTSM	Deep Multi-View Feature Learning	Shallow-ConvNet	CW-ConvNet	Monolithic Network	DFFN
Mean	81.0876	78.5074	71.86	73.07	78.41	76.44
Std	11.2	12.0	12.4	15.1	6.3	11.6

recognition accuracy of MI tasks (Barachant et al., 2012, 2013). In fact, the improvement brought by Riemannian geometry is due to the consideration of the non-linear information contained in the covariance matrices, thus better extracting features, which are usually discarded by the linear space filtering methods. On the basis, the multi-band Riemannian method can use a small amount of calibration data to extract the noise robust features, and achieve better results (Islam et al., 2017, 2018; Hersche et al., 2018). In order to further improve the multi-band Riemannian method, this article uses a non-parametric method of MANOVA based on the sum of squared distances (Anderson, 2001) to select frequency bands that are separable for specific subjects, and multi-scale division is performed on the multi-channel EEG signals in these frequency bands. Finally, use TSM to extract tangent space features.

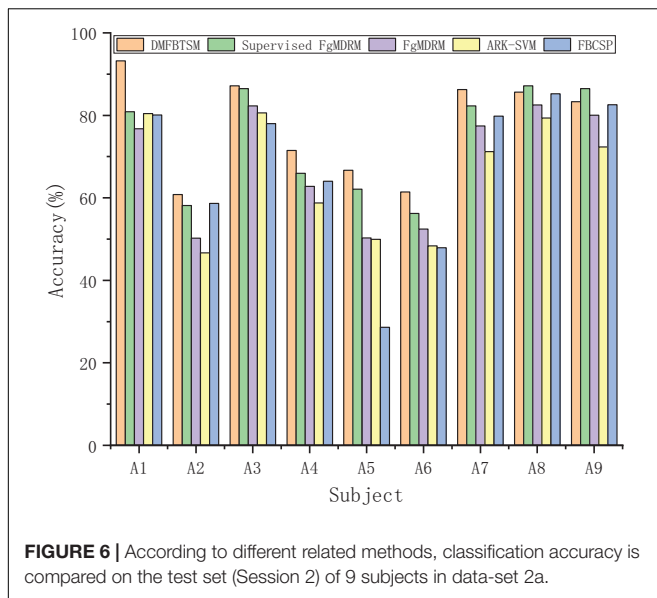
It can be seen from **Table 1** that when a time window (T1) is used, the classification accuracy of DMFBTSM using Euclidean distance is 0.31% higher than that of MFBTSM, the training time is shortened by more than three times, and the test time is shortened by more than two times; the classification accuracy of DMFBTSM using Riemannian distance is 1.8% higher than that of MFBTSM, the training time is shortened by more than three times, and the test time is shortened by more than two times. In the case of using three time windows (T1, T2, and T3), the classification accuracy of DMFBTSM using Euclidean distance is 1.06% higher than that of MFBTSM, training time is shortened by 1.9 times, and test time is shortened by 1.7 times; the classification accuracy of DMFBTSM using Riemannian distance is 1.1% higher than that of MFBTSM, the training time is shortened by 1.7 times, and the test time is shortened by 1.7 times. The test time and training time of DMFBTSM with three time windows are approximately equal to those of MFBTSM with one time window, but the classification accuracy is improved by 2.56%. The performance is improved, mainly because DMFBTSM eliminates the poorly separable frequency bands in the MI task of the subject, making the extracted features more effective and reducing the dimensionality of the feature vector. As a result, the probability of overfitting of the classifier due to much high dimension of the feature vectors in the case of limited samples will decrease.

In addition, the average classification accuracy of DMFBTSM using Riemannian distance is higher than that of DMFBTSM using Euclidean distance, and the test time is close to the training time. In the case of three time windows (T1, T2, and T3) and one time window (T1), the classification accuracy of DMFBTSM using Riemannian distance is 0.8 and 1.49% higher than that of DMFBTSM using Euclidean distance. It should be noted that not every subject's MI classification accuracy will be improved due to the choice of frequency band. For subject A4, the classification

accuracy of DMFBTSM is lower than that of MFBTSM. The performance is improved, mainly because DMFBTSM eliminates the poorly separable frequency bands in the MI task of the subject, making the extracted features more effective and reducing the dimensionality of the feature vectors, so that the classifier would not overfit due to the too high dimension of the feature vectors in the case of limited samples.

It can be seen from **Table 2** that the average classification accuracy of Supervised FgMDRM is 5.66% higher than that of FgMDRM. This is because the combination of FgMDRM and the RETRAIN adaptive strategy allows the classifier to add new samples during the testing session and continuously retrain. However, the retraining process is supervised and requires the real labels of the new samples. In addition, the role of this adaptive technology is related to the subjects' proficiency in BCI, because the more proficient the subjects, the more stable EEG patterns are produced., So that more effective samples can be used for retraining. The average accuracy of DMFBTSM is approximately 12% higher than that of ARK-SVM, which shows that DMFBTSM can extract more sufficient, more robust and more robust Riemann covariance features than single-time band TSM. The average classification accuracy of DMFBTSM with the best result is 3.36% higher than that of the supervised FgMDRM with the second best result, and it can be seen from **Figure 6** that except for the two subjects A8 and A9, PMFBTSM achieved the best results among other subjects. This result is also reasonable. The TSM-based Riemann method can use techniques such as filter bank analysis and band selection to extract more effective features and combine the advantages of the chosen classifier to generate more complex decision functions. Although TSM-based Riemann methods have better overall function than MDRM methods, they are not suitable for online operation because of the increased algorithmic complexity and possible need of intense learning inherited by the classifier. The average accuracy of DMFBTSM is approximately 10% higher than that of FBCSP, which is the classical method of frequency domain feature extraction using filter bank analysis and spatial filtering. The results are compared to better evaluate the proposed method.

As can be seen from **Table 3**, the average accuracy of the proposed method through 10-fold cross-validation on the test set is 9.23% and 8.02% higher than the two classical deep learning methods Shallow-ConvNet and CW-ConvNet, respectively, 2.58% higher than the latest deep learning method the Deep multi-view feature learning, and 2.68 and 4.65% higher than that of the Monolithic Network and DFFN methods, respectively. The first Deep Learning method proposes a new deep multi-view feature learning method in order to obtain more representative moving image features from EEG signals. The last three Deep Learning algorithms adopted ConvNet to



learn the spatial characteristics extracted by CSP (Xu et al., 2020). Compared with the traditional CSP method, the Riemann geometric method based on TSM takes into account the nonlinear information contained in the covariance matrix, and can extract more abundant and effective features. Moreover, the method is an unsupervised operation, which can reduce the time of feature extraction (Congedo et al., 2017). These Deep Learning-based methods mentioned above are very useful, and have their own advantages and disadvantages and their respective suitable occasions compared with the methods mentioned in this article. As highlighted in Yger et al. (2017), the processing procedures of Riemannian approaches such as MDRM is simpler and involves fewer stages than more classic approaches. Also, Riemannian classifiers apply equally well to all BCI paradigms (e.g., BCIs based on mental imagery, ERPs and SSVEP); only the manner in which data points are mapped in the SPD manifold differs (Congedo et al., 2017). Another disadvantage of the Riemann method is that the TSM-based method seems to increase the number of sensors (so the greater the dimension of the covariance matrix), the worse the classification accuracy will become (Yger et al., 2017). This may be due to the fact that the increase in the transformation dimension requires more attention. When almost singular covariance matrices are generated, they cannot be effectively processed by Riemannian geometry (Yger et al., 2015).

In our future work, we will try to combine some new Deep Learning classifiers with DMFBTSM method to further improve the classification accuracy of multi-class MI-BCI. In addition, the methods proposed in this article will extract a large number of real-valued Riemannian covariance features, thus increasing the number of weights and the complexity of classifiers, which makes them unsuitable for real-time execution on devices with limited resources. Therefore, it is considered to combine regularization, sparse feature selection and other techniques with linear classification to deal with a large number of Riemannian

covariance features, so that the model obtained by training will have less memory footprint and better classification performance.

## CONCLUSION

A Discriminative and multi-scale Filter Bank Tangent Space Mapping (DMFBTSM) algorithm is proposed in this article to design the FB of a specific subject. On the 4-class BCI competition IV-2a data set, the average classification accuracy of nine subjects reached  $77.33 \pm 12.3\%$ . When the training time and the test time are similar, the classification accuracy is increased by 2.56% compared to MFBTSM. When the classification accuracy is similar, the training speed is increased by more than three times, and the test speed is increased two times more. Compared with Supervised Fisher Geodesic Minimum Distance to the Mean (Supervised FGMDRM), another new variant based on Riemann geometry classifier, the average accuracy is 3.36% higher. The results show that the proposed DMFBTSM algorithm can be expected to select a frequency band with good separability for specific subjects to improve the classification accuracy of multiclass MI tasks.

Our future work is to apply the proposed method to neurofeedback to further improve the classification accuracy of multi-class MI-BCI.

## DATA AVAILABILITY STATEMENT

Publicly available datasets were analyzed in this study. This data can be found here: <http://bbci.de/competition/>.

## ETHICS STATEMENT

The studies involving human participants were reviewed and approved by the Medical Ethics Committee of Kunming University of Science and Technology School of Medicine. The patients/participants provided their written informed consent to participate in this study.

## AUTHOR CONTRIBUTIONS

FW: conceptualization, methodology, programming, and writing and editing. AG: methodology, writing – reviewing and editing. LZ: designing the experiment. WZ: investigation and validation. HL: investigation and checking language. YF: perfecting the model and revising the manuscript, project administration, funding acquisition, and supervision. All authors contributed to the article and approved the submitted version.

## FUNDING

This research was supported by grants from the National Natural Science Foundation of China projects (NSFC, Nos. 81771926, 61763022, 81470084, 61463024, and 62006246).

## REFERENCES

- Anderson, M. J. (2001). A new method for non-parametric multivariate analysis of variance. *Austral Ecol.* 26, 32–46. doi: 10.1111/j.1442-9993.2001.01070.pp.x
- Ang, K. K., Chin, Z. Y., Wang, C., Guan, C. T., and Zhang, H. (2012). Filter bank common spatial pattern algorithm on BCI competition IV datasets 2a and 2b. *Front. Neurosci.* 6:39. doi: 10.3389/fnins.2012.00039
- Ang, K. K., Chin, Z. Y., Zhang, H. H., and Guan, C. T. (2008). “Filter bank common spatial pattern (fbcsp) on brain-computer interface,” in *Proceedings of the International Joint Conference on Neural Networks*, Hong Kong.
- Barachant, A., Bonnet, S., Congedo, M., and Jutten, C. (2010). “Riemannian geometry applied to BCI classification,” in *Latent Variable Analysis and Signal Separation*, Vol. 6365, eds V. Vigneron, V. Zarzoso, E. Moreau, R. Gribonval, and E. Vincent (Berlin: Springer), 629–636. doi: 10.1007/978-3-642-15995-4\_78
- Barachant, A., Bonnet, S., Congedo, M., and Jutten, C. (2012). Multiclass brain-computer interface classification by Riemannian geometry. *IEEE Trans. Biomed. Eng.* 59, 920–928. doi: 10.1109/tbme.2011.2172210
- Barachant, A., Bonnet, S., Congedo, M., and Jutten, C. (2013). Classification of covariance matrices using a Riemannian-based kernel for BCI applications. *Neurocomputing* 112, 172–178. doi: 10.1016/j.neucom.2012.12.039
- Barbareco, F. (2008). “Innovative tools for radar signal processing Based on Cartan’s geometry of SPD matrices & Information Geometry,” in *Proceedings of the 2008 IEEE Radar Conference*, Rome.
- Congedo, M., Barachant, A., and Bhatia, R. (2017). Riemannian geometry for EEG-based brain-computer interfaces; a primer and a review. *Brain Comput. Interfaces* 4, 155–174. doi: 10.1080/2326263x.2017.1297192
- Dornhege, G., Blankertz, B., Curio, G., and Müller, K.-R. (2004). Boosting bit rates in non-invasive EEG single-trial classifications by feature combination and multi-class paradigms. *IEEE Trans. Biomed. Eng.* 10, 993–1002. doi: 10.1109/tbme.2004.827088
- Fletcher, P. T., and Joshi, S. (2004). “Principal geodesic analysis on symmetric spaces: statistics of diffusion tensors,” in *Computer Vision and Mathematical Methods in Medical and Biomedical Image Analysis*, Vol. 3117, eds M. Sonka, I.A. Kakadiaris, and J. Kybic (Berlin: Springer), 87–98. doi: 10.1007/978-3-540-27816-0\_8
- Förstner, W., and Moonen, B. (2003). “A Metric for Covariance Matrices,” in *Geodesy-The Challenge of the 3rd Millennium*, eds E. W. Grafarend, F. W. Krumm, and V. S. Schwarze (Berlin: Springer), 299–309. doi: 10.1007/978-3-662-05296-9\_31
- Graimann, B., Allison, B. Z., and Pfurtscheller, G. (2010). *Brain-Computer Interfaces: Revolutionizing Human-Computer Interaction*. Berlin: Springer.
- Hersche, M., Rellstab, T., Schiavone, P. D., Cavigelli, L., Benini, L., and Rahimi, A. (2018). “Fast and accurate multiclass inference for MI-BCIs using large multiscale temporal and spectral features,” in *Proceedings of the Conference 26th European Signal Processing conference (EUSIPCO)*, Rome, 1704–1708.
- Islam, M. R., Tanaka, T., Akter, M. S., and Molla, M. K. I. (2017). “Classification of Motor Imagery BCI Using Multiband Tangent Space Mapping,” in *Proceedings of the 2017 22nd International Conference on Digital Signal Processing (DSP)*, London.
- Islam, M. R., Tanaka, T., and Molla, M. K. I. (2018). Multiband tangent space mapping and feature selection for classification of EEG during motor imagery. *J. Neural Eng.* 15:046021. doi: 10.1088/1741-2552/aac313
- Kumar, S., Yger, F., and Lotte, F. (2019). “Towards adaptive classification using Riemannian geometry approaches in brain-computer interfaces,” in *Proceedings of the 2019 7th International Winter Conference on Brain-Computer Interface (BCI)*, Gangwon.
- Li, D., Wang, J., Xu, J., and Fang, X. (2019). Densely Feature Fusion Based on Convolutional Neural Networks for Motor Imagery EEG Classification. *IEEE Access* 7, 132720–132730. doi: 10.1109/access.2019.2941867
- Li, Y., Wong, K. M., and deBruin, H. (2009). “EEG signal classification based on a Riemannian distance measure,” in *Proceedings of the IEEE Toronto International Conference on Science and Technology for Humanity*, Toronto, ON.
- Lotte, F., Bougrain, L., Cichocki, A., Clerc, M., Congedo, M., Rakotomamonjy, A., et al. (2018). A review of classification algorithms for EEG-based brain-computer interfaces: a 10 year update. *J. Neural Eng.* 15:031005. doi: 10.1088/1741-2552/aab2f2
- Moakher, M. (2005). A differential geometric approach to the geometric mean of symmetric positive-definite matrices. *SIAM J. Matrix Anal. Appl.* 26, 735–747. doi: 10.1137/s0895479803436937
- Naem, M., Brunner, C., Leeb, R., Graimann, B., and Pfurtscheller, G. (2006). Separability of four-class motor imagery data using independent components analysis. *J. Neural Eng.* 3, 208–216. doi: 10.1088/1741-2560/3/3/003
- Nguyen, A., Yosinski, J., and Clune, J. (2015). “Deep neural networks are easily fooled: high confidence predictions for unrecognizable images,” in *Proceedings of the IEEE Computer Society Conference on Computer Vision and Pattern Recognition*, Vol. 7, Boston, MA, 427–436.
- Olivas Padilla, B. E., and Chacon Murguia, M. I. (2019). Classification of multiple motor imagery using deep convolutional neural networks and spatial filters. *Appl. Soft Comput. J.* 75, 461–472. doi: 10.1016/j.asoc.2018.11.031
- Pfurtscheller, G., and Neuper, C. (1997). Motor imagery activates primary sensorimotor area in humans. *Neurosci. Lett.* 239, 65–68. doi: 10.1016/s0304-3940(97)00889-6
- Ramoser, H., Müller-Gerking, J., and Pfurtscheller, G. (2000). Optimal spatial filtering of single trial EEG during imagined hand movement. *IEEE Trans. Rehabil. Eng.* 8, 441–446. doi: 10.1109/86.895946
- Rao, R. P. (2013). *Brain-Computer Interfacing: An Introduction*. Cambridge: Cambridge University Press.
- Sakhavi, S., Guan, C., and Yan, S. (2018). Learning temporal information for brain-computer interface using convolutional neural networks. *IEEE Trans. Neural Netw. Learn. Syst.* 29, 5619–5629. doi: 10.1109/tnnls.2018.2789927
- Schirrmeyer, R. T., Springenberg, J. T., Fiederer, L. D. J., Glasstetter, M., Eggenberger, K., Tangermann, M., et al. (2017). Deep learning with convolutional neural networks for EEG decoding and visualization. *Hum. Brain Mapp.* 38, 5391–5420. doi: 10.1002/hbm.23730
- Shenoy, P., Blankertz, B., Rao, R. P., Krauledat, M., and Müller, K. R. (2006). Towards adaptive classification for BCI. *J. Neural Eng.* 3, R13–R23.
- Soares, E., Curado, M. R., Liberati, G., Ramos-Murguialday, A., Broetz, D., Rea, M., et al. (2013). Brain-machine interface in chronic stroke rehabilitation: a controlled study. *Ann. Neurol.* 74, 100–108. doi: 10.1002/ana.23879
- Tuzel, O., Porikli, F., and Meer, P. (2008). Pedestrian detection via classification on Riemannian manifolds. *IEEE Trans. Pattern Anal. Mach. Intell.* 30, 1713–1727. doi: 10.1109/tpami.2008.75
- Wolpaw, J., and Wolpaw, E. W. (2012). *Brain-Computer Interfaces: Principles and Practice*. Oxford: Oxford University Press.
- Xu, J., Zheng, H., Wang, J., Li, D., and Fang, X. (2020). Recognition of EEG signal motor imagery intention based on deep multi-view feature learning. *Sensors* 20:3496. doi: 10.3390/s20123496
- Yger, F., Berar, M., and Lotte, F. (2017). Riemannian approaches in brain-computer interfaces: a review. *IEEE Trans. Neural Syst. Rehabil. Eng.* 25, 1753–1762. doi: 10.1109/tnsre.2016.2627016
- Yger, F., Lotte, F., and Sugiyama, M. (2015). “Averaging covariance matrices for EEG signal classification based on the CSP: an empirical study,” in *Proceedings of the 2015 23rd European Signal Processing Conference (Eusipco)*, Nice, 2721–2725.
- Zhang, Y., Wang, Y., Jin, J., and Wang, X. (2016). “Sparse support vector machine for simultaneous feature selection and classification in motor-imagery-based BCI,” in *Advances In Cognitive Neurodynamics (V)*, eds R. Wang and X. Pan (Singapore: Springer), 363–369. doi: 10.1007/978-981-10-0207-6\_50
- Zhang, Y., Zhou, G., Jin, J., Wang, X., and Cichocki, A. (2015). Optimizing spatial patterns with sparse filter bands for motor-imagery based brain-computer interface. *J. Neurosci. Methods* 255, 85–91. doi: 10.1016/j.jneumeth.2015.08.004

**Conflict of Interest:** The authors declare that the research was conducted in the absence of any commercial or financial relationships that could be construed as a potential conflict of interest.

Copyright © 2021 Wu, Gong, Li, Zhao, Zhang and Fu. This is an open-access article distributed under the terms of the Creative Commons Attribution License (CC BY). The use, distribution or reproduction in other forums is permitted, provided the original author(s) and the copyright owner(s) are credited and that the original publication in this journal is cited, in accordance with accepted academic practice. No use, distribution or reproduction is permitted which does not comply with these terms.



# Enhancement of Event-Related Desynchronization in Motor Imagery Based on Transcranial Electrical Stimulation

Jiaxin Xie<sup>1†</sup>, Maoqin Peng<sup>2†</sup>, Jingqing Lu<sup>1</sup>, Chao Xiao<sup>1</sup>, Xin Zong<sup>1</sup>, Manqing Wang<sup>3</sup>, Dongrui Gao<sup>1,3</sup>, Yun Qin<sup>1\*</sup> and Tiejun Liu<sup>1\*</sup>

<sup>1</sup>MOE Key Lab for Neuroinformation, School of Life Science and Technology, University of Electronic Science and Technology of China, Chengdu, China, <sup>2</sup>College of Electronic Engineering, Chengdu University of Information Technology, Chengdu, China, <sup>3</sup>School of Computer Science, Chengdu University of Information Technology, Chengdu, China

## OPEN ACCESS

### Edited by:

Saugat Bhattacharyya,  
Ulster University, United Kingdom

### Reviewed by:

Madiha Tariq,  
RMIT University, Australia  
Bradley Jay Edelman,  
Max Planck Institute of Neurobiology  
(MPIN), Germany

### \*Correspondence:

Yun Qin  
yunqin@uestc.edu.cn  
Tiejun Liu  
liutiejun@uestc.edu.cn

<sup>†</sup>These authors have contributed  
equally to this work and share first  
authorship

### Specialty section:

This article was submitted to  
Brain-Computer Interfaces,  
a section of the journal  
Frontiers in Human Neuroscience

**Received:** 30 November 2020

**Accepted:** 26 February 2021

**Published:** 18 March 2021

### Citation:

Xie J, Peng M, Lu J, Xiao C, Zong X,  
Wang M, Gao D, Qin Y and Liu T  
(2021) Enhancement of  
Event-Related Desynchronization in  
Motor Imagery Based on Transcranial  
Electrical Stimulation.  
*Front. Hum. Neurosci.* 15:635351.  
doi: 10.3389/fnhum.2021.635351

Due to the individual differences controlling brain-computer interfaces (BCIs), the applicability and accuracy of BCIs based on motor imagery (MI-BCIs) are limited. To improve the performance of BCIs, this article examined the effect of transcranial electrical stimulation (tES) on brain activity during MI. This article designed an experimental paradigm that combines tES and MI and examined the effects of tES based on the measurements of electroencephalogram (EEG) features in MI processing, including the power spectral density (PSD) and dynamic event-related desynchronization (ERD). Finally, we investigated the effect of tES on the accuracy of MI classification using linear discriminant analysis (LDA). The results showed that the ERD of the  $\mu$  and  $\beta$  rhythms in the left-hand MI task was enhanced after electrical stimulation with a significant effect in the tDCS group. The average classification accuracy of the transcranial alternating current stimulation (tACS) group and transcranial direct current stimulation (tDCS) group (88.19% and 89.93% respectively) were improved significantly compared to the pre-and pseudo stimulation groups. These findings indicated that tES can improve the performance and applicability of BCI and that tDCS was a potential approach in regulating brain activity and enhancing valid features during noninvasive MI-BCI processing.

**Keywords:** brain-computer interfaces, motor imagery, transcranial alternating current stimulation, transcranial direct current stimulation, event-related desynchronization

## INTRODUCTION

Brain-computer interface technology based on motor imagery (MI-BCI) has played an important role in improving and restoring human motor function by activating brain plasticity to induce patients to recover motor control function (Decety and Boisson, 1990). However, studies have shown that individuals differ in their ability to control the BCI. Approximately 15–30% of people could not operate the BCI system effectively, which indicated that their accuracy is lower than that of the majority of people and that they need more training time (Guger et al., 2003). Therefore, it is very important to find methods to improve the applicability of the MI-BCI system and the classification accuracy of electroencephalogram (EEG).

Previous studies have used invasive or noninvasive neural regulation technology to reversibly regulate the activity state of the central nervous system, peripheral nervous system, or autonomic nervous system *via* electrical stimulation or drug regulation to enhance the decoding accuracy and applicability of BCI (He et al., 2015; Cho et al., 2016). Among them, transcranial electrical stimulation (tES; Kuo and Nitsche, 2012; Bestmann and Walsh, 2017), as a non-invasive neuromodulation technique, has attracted considerable attention in recent years. At present, tES mainly adopts transcranial direct current stimulation (tDCS; Unal and Bikson, 2018) and transcranial alternating current stimulation (tACS; Paulus, 2011). According to the polarity of stimulation, an anode is placed on or inside the cortex for tDCS and subthreshold direct current stimulation is introduced to regulate neural activity (Wei et al., 2013; Flöel, 2014). Studies have found that the application of a weak direct current through a scalp electrode could affect the action potential threshold of neurons, increase the activity of spontaneous neurons and then noninvasively regulate the excitability of the cerebral cortex (Bindman et al., 1964; Nitsche and Paulus, 2000; Tsuiki et al., 2019). tACS applies a low-intensity alternating current to the cerebral cortex to regulate the activity of the intracranial central nerve (Kasten and Herrmann, 2017). Ten Hertz tACS stimulation in the primary motor cortex could promote the excitability of the motor cortex, although other frequencies had difficulty evoking excitability changes (Wach et al., 2013).

Studies have shown that tES could effectively regulate brain activities in working memory (Talsma et al., 2017), perception, motor learning, motor control, and other cognitive functions (Nitsche and Paulus, 2000; Angelakis and Liouta, 2011). Therefore, researchers proposed using tES in the BCI system to enhance the excitability of the cerebral cortex and improve the performance of the BCI system (Thomas and Roi, 2018). Baxter et al. (2016) used tDCS in an MI-BCI system and found that although tDCS can improve motor learning ability, cathode stimulation can reduce the power of the  $\alpha$  and  $\beta$  bands in the process of right-hand imagery tasks. However, anode tDCS could induce a significant change in the  $\mu$  rhythm ERD mode, which can conditionally improve the performance of BCI (Wei et al., 2013). Also, several articles have studied the modulation of tACS on motor learning ability (Pollok et al., 2015; Sugata et al., 2018) and showed that the capacity for motor learning was significantly increased for 70 Hz tACS (response time was 270 ms) compared to sham stimulation (response time was 340 ms; Sugata et al., 2018). The application of alpha frequency (7–13 Hz) tACS induced a leftward bias in visuospatial attention relative to the sham ( $P < 0.001$ ; Schuhmann et al., 2019). In addition, applying tACS in the mental rotation task experiment significantly decreased the subject's alpha and beta rhythm stimulation shortened response time (before\_alpha = 0.37 s, before\_beta = 0.39 s, after\_alpha = 0.3 s, after\_beta = 0.34 s; Zhang et al., 2016).

In conclusion, tES could promote motor learning, motor control, MI behavior, and other cognitive functions by regulating the excitability of the cerebral cortex. As a noninvasive stimulation technology, BCIs may be easily accepted. However,

previous studies only discussed the effectiveness of a single stimulus mode in BCI systems and did not compare and analyze the stimulus modes that can improve the applicability and effectiveness of BCI systems in the same task. In this article, we designed an experimental paradigm that combines two different modes of stimuli within the same framework and quantified the changes in EEG *via* three measurements from spatial, temporal, and classification dimensions to detect the type of stimulus that can effectively enhance ERD and BCI performance during MI. Here, tDCS and tACS were applied to the Cz position of the subjects' brains to regulate brain activity and feature extraction was combined with power spectral density (PSD; Liu et al., 2013) and common spatial pattern (CSP; Tariq et al., 2019). Finally, the two features with the largest power difference were extracted by CSP, and the feature vectors were classified by linear discriminant analysis (LDA; Tariq et al., 2020).

## EXPERIMENT PREPARATION

### Subjects

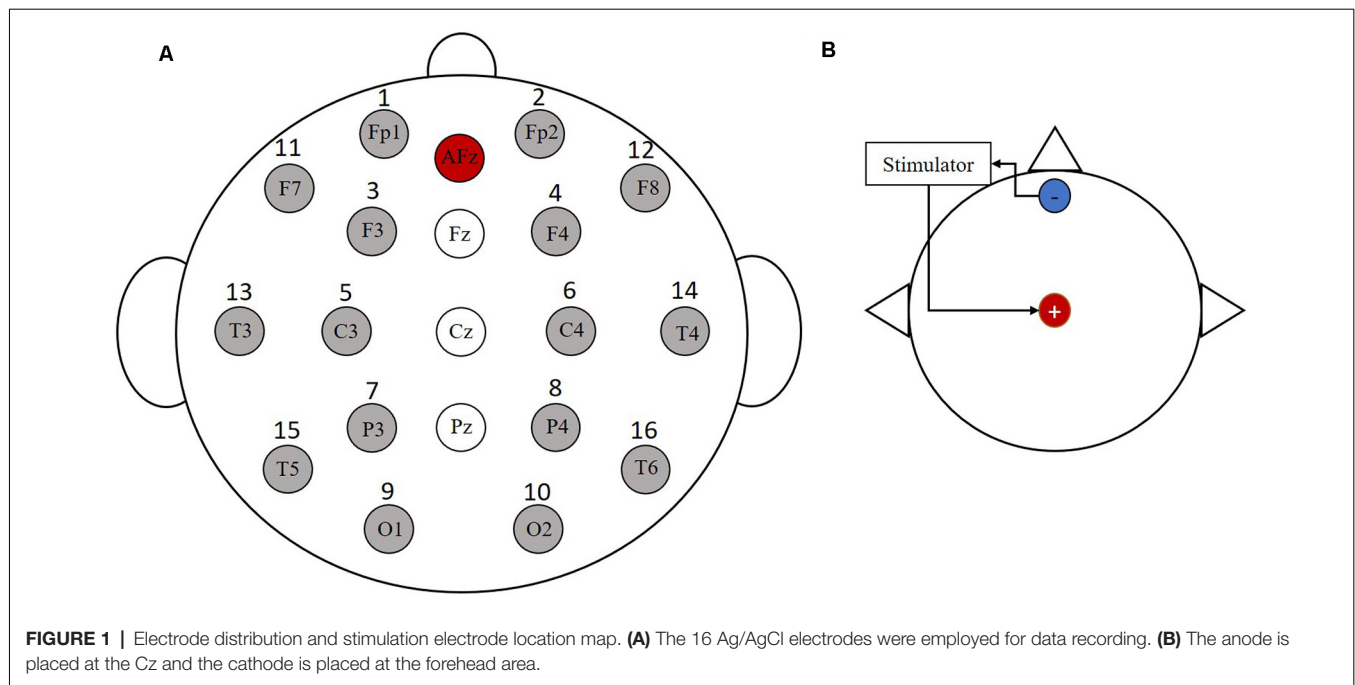
This experiment recruited 15 male college students (23–25 years old, average  $24.4 \pm 0.44$ ). All the participants were right-handed. None of them had any history of nervous system disease or received any acute or chronic drugs that affected the central nervous system. Written informed consent according to the Declaration of Helsinki was obtained from all participants. This study was approved by the Ethics Committee of the University of Electronic Science and Technology of China (UESTC).

### Signal Acquisition

In this experiment, 16 Ag/AgCl electrodes (i.e., Fp1, Fp2, F3, F4, C3, C4, P3, P4, O1, O2, F7, F8, T3, T4, T5, T6) were employed for data recording using a Syntop amplifier (Syntop Instrument, Beijing, China). The placement of each electrode was determined by the international 10-20 system electrode position method. The electrode distribution diagram is shown in **Figure 1A**. The reference electrode in this experiment was at the AFz location. Also, the sampling frequency was 1,000 Hz and the impedance was kept below 5 K $\Omega$ .

### Electrical Stimulation

Before the subjects performed the MI task, they all randomly underwent three stimulation experiments: tDCS, tACS, and pseudo stimulation, with each stimulation lasting for 10 min. Pseudo stimulation was used as the control to eliminate the placebo effect. The electrode placement position for electrical stimulation is shown in **Figure 1B**, where the anode was placed at Cz and the cathode was placed at the forehead area. The current intensity of tDCS was 1 mA, the stimulation frequency of tACS was 10 Hz, and the stimulation intensity was determined by the specificity of the subjects (increasing the current intensity gradually in a step size of 0.05 mA from 0 to the intensity at which the subject indicated a stinging sensation or eye pressure flashing). Then, the current intensity at that moment was recorded as the stimulation threshold in the formal experiment (the intensity was not higher than 2 mA).



## Experimental Paradigm

In this article, we designed an experimental paradigm that combines electrical stimulations with MI-BCIs. The MI experiment was conducted in an exclusive room with soft luminance light and a comfortable temperature. One day before the MI experiment, the experimenter asked the subjects to pay attention to certain tasks, including having good rest at night, refusing psychotropic drugs, and maintaining a healthy life. Before the start of the formal experiment, the subjects were sat down in front of the lab computer and explained the procedure of the experiment, and then they signed relevant consent.

To familiarize the subjects with the experimental process, they were asked to practice the MI experiment with 40 trials before the formal experiment. During the experiment, participants performed a total of four 30-min MI task experiments and received one kind of stimulation, namely, pseudo stimulation, tDCS, or tACS. The entire experimental flow chart and single-trial design are shown in **Figure 2**. First, the subjects performed a set of motor imagery EEG experiments before tES, which consisted of 80 trials. The EEG data obtained in this group were used to determine the baseline level of all subjects. Second, the subjects randomly received electrical stimulation lasting for 10 min. During the period of stimulation, there was no EEG acquisition. After stimulation, the subjects were asked to perform another group of MI EEG experiments (all MI EEG experiments' conditions were the same, including the MI tasks, experimental trials, and duration time). To avoid the post effect of tES, the time interval between each stimulation experiment was at least 24 h.

In one trial, a prompt “+” first appeared on the screen to remind the subjects that the task was about to start. Second, pictures of a left- or right-hand fist appeared on the screen

randomly, prompting the subjects to carry out the corresponding left- or right-hand MI, which lasted 6 s. Finally, the screen turned black for 3 s, reminding the subjects to take a break. Each experiment performed a total of 80 trials, including 40 trials for the left-hand task and 40 trials for the right-hand task.

## MATERIALS AND METHODS

To study the effect of tES on ERD based on MI, EEG data in four different conditions (prestimulation, pseudo stimulation, tACS, and tDCS) were collected. After EEG preprocessing, the power spectrum of the EEG was calculated and used to extract the specific frequency band, which could represent the greatest difference between the left- and right-hand MI tasks. Then, dynamic ERD based on sliding time windows was obtained. The EEG features in individual EEG frequency bands were extracted using the CSP algorithm and applied in the following pattern recognition classification. The classification accuracy of the left- and right-hand MI of the subjects in each condition was obtained, and the effect of tES on the performance of the MI-BCI was evaluated. The overall implementation steps are shown in **Figure 3**.

## Signal Preprocessing

Preprocessing aims to obtain effective and reliable EEG trials. The specific steps are as follows: convert the raw data to average reference; filter the data with a 5–40 Hz bandpass filter to obtain the relevant frequency band information; set the threshold to  $\pm 100 \mu\text{V}$  (according to the EEG amplitude range, the trial with more than  $100 \mu\text{V}$  is considered as a bad trial; Goh et al., 2017); reject data with extreme values; process

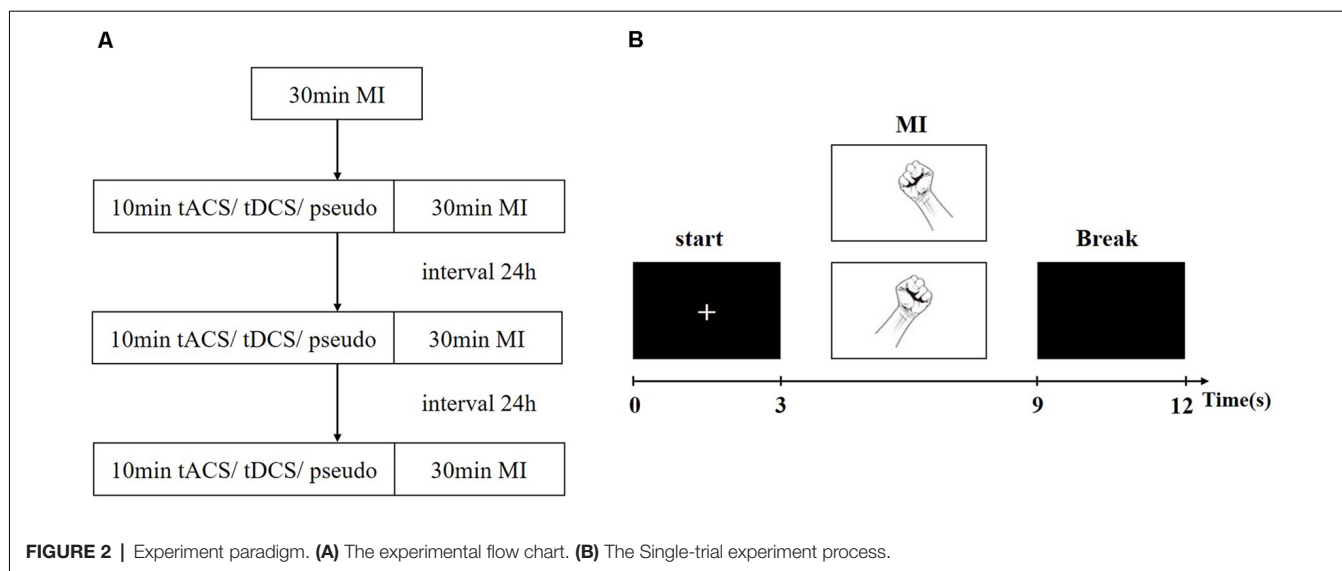


**FIGURE 2 |** Experiment paradigm. **(A)** The experimental flow chart. **(B)** The Single-trial experiment process.

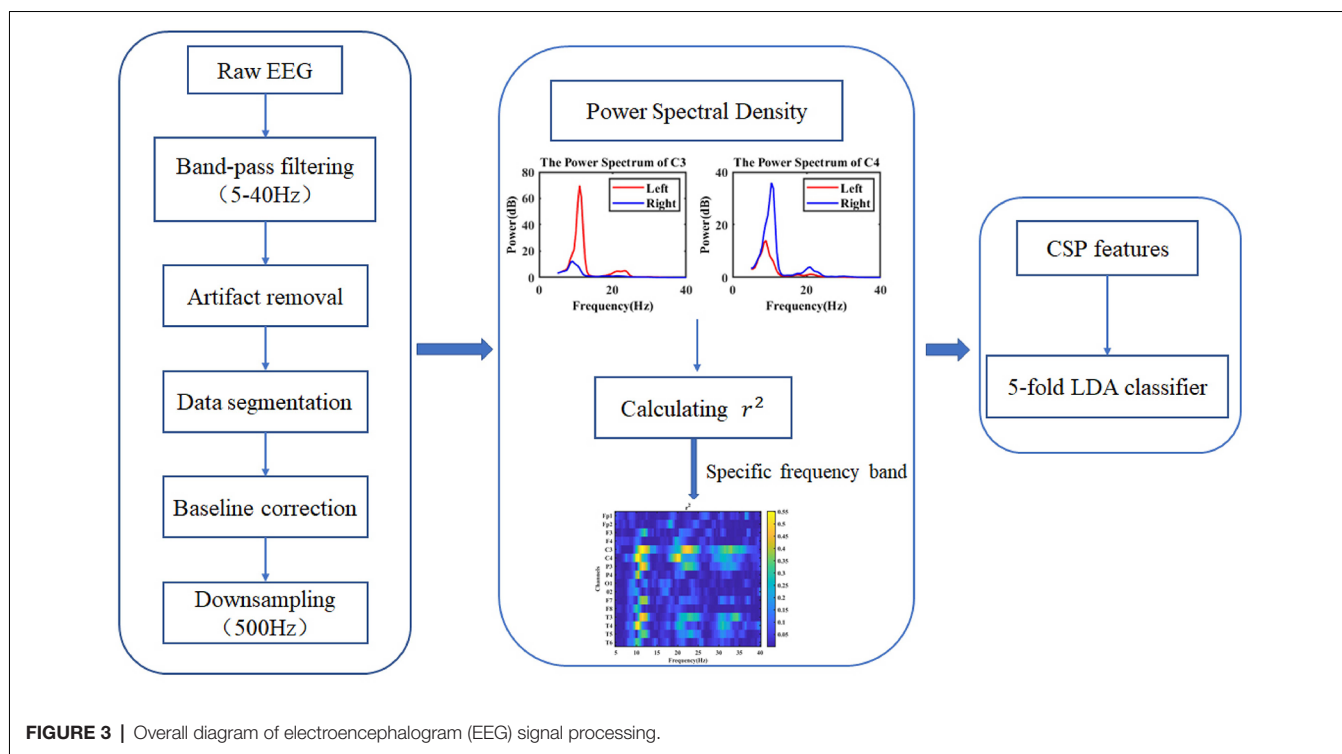


**FIGURE 3 |** Overall diagram of electroencephalogram (EEG) signal processing.

the remaining data by FastICA to avoid interference by the electrooculogram (EOG) and electromyogram (EMG) artifacts; segment data within the period of  $[-1, 9\text{ s}]$ , in which  $[-1, 0\text{ s}]$  was considered the baseline for data correction; and downsample the signal to 500 Hz. During the processing of FastICA, the typical characteristics of EOG and EMG were considered. As for EOG (Nguyen et al., 2012), the low frequency-dominated power distribution was always observed in the prefrontal electrodes, while EMG was distributed above 20 Hz, and can be found in most electrodes (Goncharova et al., 2003). After the EOG and

EMG components were identified and removed, the pure EEG data was reconstructed.

### Calculation of $\Delta$ Power

When imagining the movement of different parts of the body, differences are observed in the spatial distribution of the ERD obtained from the EEG signal. For example, when imagining the movement of the left hand, the ERD phenomenon in the right motor cortex was more significant, in which the electrode with maximum discriminatory power was C4, while

when imagining the movement of the right hand, the ERD phenomenon prominent area was in the left-brain area, and the electrode was C3. Therefore, in this article, the  $\mu$  and  $\beta$  rhythm power were extracted from the C3 and C4 power spectra for each trial of each subject and stimulation condition. First, the PSD of all trials (6 s for each trial) was calculated based on the Pwelch method (Blankertz et al., 2010). For  $\mu$  rhythm power, the frequency range is 8–13 Hz, and for  $\beta$  rhythm power, the frequency range is 17–25 Hz. Then, we obtained the power difference of C3 and C4 under the same conditions (tasks, rhythms, and stimulation were the same), and the calculation was as follows:

$$\Delta\text{Power} = \text{OSP} - \text{SSP} \tag{1}$$

where OSP is the PSD of the contralateral electrode during the MI tasks, SSP is the PSD of the ipsilateral electrode, and  $\Delta\text{Power}$  is the difference between the contralateral and ipsilateral sides. For example, to obtain  $\Delta\text{Power}$  during the left-hand MI task, C4 is on the contralateral side and C3 is on the ipsilateral side. Then, normalized  $\Delta\text{Power}$  was obtained:

$$\text{normalized } \Delta \text{ Power} = \frac{\Delta\text{Power}}{\text{OSP} + \text{SSP}} \tag{2}$$

This step aims to eliminate individual differences.

### Feature Extraction

The CSP method is currently considered the most suitable algorithm for processing the two-category feature extraction of EEG signals (Lu et al., 2010). It is very suitable for processing multidimensional signals and data. By using the spatial correlation of the EEG signal synchronously, the noise of the signal can be eliminated and localization of local cortical nerve activity can be achieved.

From the PSD results, the power spectra of all channels of the subjects in the MI task were estimated. Then, to determine the individual-specific bandpass filter, we calculated the  $r^2$  relative to the two-hand MI tasks for each subject (Xu et al., 2011).  $r^2$  was described as follows:

$$r^2 = \left( \frac{\sqrt{N_1 N_2} \text{MEAN}(P_1) - \text{MEAN}(P_2)}{N_1 + N_2 \text{STD}(P_1 \cup P_2)} \right)^2 \tag{3}$$

where  $N_1$  and  $N_2$  represent the number of trials (both  $N_1$  and  $N_2$  are 40);  $P_1$  and  $P_2$  are the power spectra of EEG data of left and right hand MI tasks, respectively. In the equation above, a larger value of  $r^2$  corresponds to a greater power difference between the EEG data of left- and right-hand MI tasks in this frequency band. In **Figure 4**, according to the value of  $r^2$ , we can select the appropriate bandpass filter frequency band and apply a specific bandpass filter to the MI EEG data.

The CSP algorithm was used to extract features from the processed EEG signals. By designing the parameters of the spatial filter, the best projection matrix  $W$  was obtained. The EEG signal passed through the spatial filter to obtain the feature vectors that represent the characteristics of left and right signals, one of which has the largest variance and the other has the smallest variance. Finally, the two types of signals were classified by

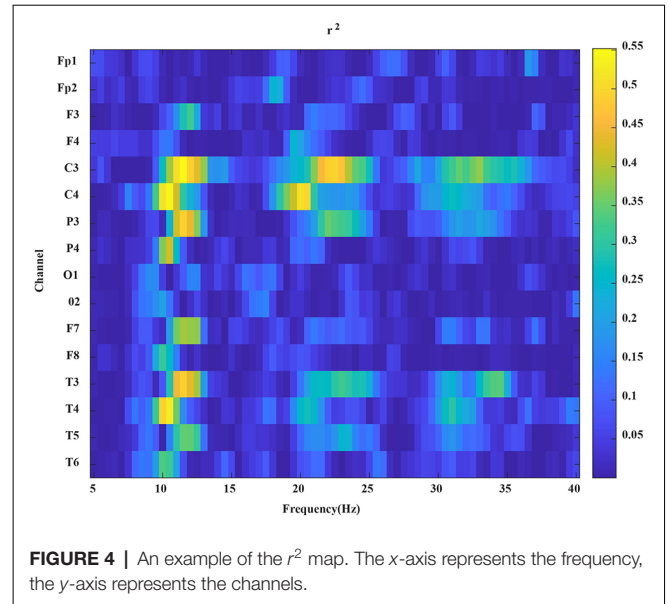


**FIGURE 4 |** An example of the  $r^2$  map. The  $x$ -axis represents the frequency, the  $y$ -axis represents the channels.

classification algorithms. The specific algorithm processes are as follows (Muller-Gerking et al., 1999):

Note: in the following expressions,  $i$  represents the MI task category,  $i = 1, 2$ . It is stipulated that  $i = 1$  is left-hand movement, and  $i = 2$  is right-hand movement.

Assume that  $X_1$  and  $X_2$  are the single-trial EEG matrices for the left and right hand MI tasks under the same experimental conditions. The matrix dimension is  $N * T$ , where  $N$  is the number of EEG channels, and  $T$  is the number of sampling points ( $N \leq T$ ).  $Y_1$  and  $Y_2$  are two types of MI tasks. In the case of ignoring noise interference,  $X_1$  and  $X_2$  are expressed as follows:

$$X_i = [A_i A_m] \begin{bmatrix} Y_i \\ Y_M \end{bmatrix}, \tag{4}$$

where  $Y_M$  is the common source signal of two tasks. The left-hand movement  $Y_1$  and right-hand movement  $Y_2$  source signals of these two tasks are assumed to be linearly independent of each other, and  $Y_1$  and  $Y_2$  are composed of  $m_1$  and  $m_2$ , respectively.

The covariance matrix of  $X_1$  and  $X_2$  is calculated as follows:

$$R_i = \frac{X_i X_i^T}{\text{tr}(X_i X_i^T)}, \tag{5}$$

where  $\text{tr}$  represents the trace of the matrix, which is the sum of the diagonal elements of the matrix  $XX^T$ , and  $R_i$  is the covariance matrix of a single trial. According to the total trial  $n_i$ , the average covariance matrix  $\bar{R}$  is as follows:

$$\bar{R}_i = \frac{1}{n_i} \sum_{j=1}^{n_i} R_{ij}. \tag{6}$$

The mixed space covariance matrix  $R$  is as follows:

$$R = \bar{R}_1 + \bar{R}_2, \tag{7}$$

where  $R$  is a positive definite matrix, and eigenvalue decomposition is performed on  $R$  according to the singular value theorem:

$$R = U\lambda U^T, \tag{8}$$

where  $\lambda$  is a diagonal matrix composed of the eigenvalues arranged in descending order and  $U$  is the matrix composed of the eigenvectors corresponding to the eigenvalues after decomposition. The whitened matrix  $P$  is obtained as follows:

$$P = \frac{1}{\sqrt{\lambda}}U^T, \tag{9}$$

$$Y_i = P\bar{R}_iP^T. \tag{10}$$

Then, decomposing the principal component of the whitened matrix obtains the following:

$$Y_i = Q_i\lambda_iQ_i^T, \tag{11}$$

where  $Y_1, Y_2$  have the same eigenvector. The sum of the diagonal matrix of two eigenvalues  $\lambda_1$  and  $\lambda_2$  is the identity matrix:

$$\lambda_1 + \lambda_2 = E. \tag{12}$$

The projection matrix  $W$  can be obtained through the eigenmatrix  $Q$  and the whitened matrix:

$$W = Q^TP, \tag{13}$$

where the projection matrix  $W$  is the required spatial filter. The EEG matrix  $X_i$  is projected through the spatial filter  $W$ , and the characteristics can be obtained:

$$Z_i = WX_i. \tag{14}$$

To avoid the instantaneous change caused by body motion, the variance of the feature signal obtained through the spatial filter is calculated and normalized, and then the feature vector  $f_i$  is extracted as follows:

$$\begin{cases} Z_i = WX_i \\ f_i = \frac{\text{var}(Z_i)}{\sum \text{var}(Z_i)} \end{cases}. \tag{15}$$

### Quantification of ERD

To compare changes in the C3 and C4 amplitudes elicited by different motor imagery tasks, dynamic ERD was quantified as the relative amplitude (RA) to reveal the power decrease and increase in sliding time windows based on the reference baseline (Jeon et al., 2011); and, we segmented the EEG epochs into 1 s time windows.

The calculation of ERD in each time window was as follows:

$$Act_{(j)} = \frac{1}{N} \sum_{i=1}^N y_{ij}^2, \tag{16}$$

where,  $y_{ij}$  is the  $j$ th sample of the  $i$ th trial,  $N$  is the number of trials and  $Act_{(j)}$  is the average power at  $j$ th sample squared.

$$R = \frac{1}{k+1} \sum_{j=r_0}^{r_0+k} Act_{(j)}, \tag{17}$$

where  $R$  is the average power in the reference interval  $[r_0, r_0 + k]$ . Due to the great individual difference, in this study, the reference interval adopted the whole time course during MI tasks, i.e.,  $[-1\ 9\ s]$ .

$$RA_{(j)} (\%) = \left( \frac{Act_{(j)} - R}{R} \right) \times 100\%. \tag{18}$$

### Pattern Recognition Classification

Suppose that the dataset  $D = \{(X_1, Y_1), (X_2, Y_2), \dots, (X_m, Y_m)\}$ , where  $X_i$  is an  $n$ -dimensional vector,  $y_i \in \{0, 1\}$ . Here,  $N_j(j = 0, 1)$  is the number of samples of type  $j$ ,  $X_j(j = 0, 1)$  is the set,  $\mu_j(j = 0, 1)$  is the mean value, and  $\Sigma_j(j = 0, 1)$  is the covariance matrix.

The expression of  $\mu_j$  is as follows:

$$\mu_j = \frac{1}{N_j} \sum_{x \in X_j} x, \dots, j = 0, 1. \tag{19}$$

The expression of  $\Sigma_j$  is as follows:

$$\Sigma_j = \sum_{x \in X_j} (x - \mu_j)(x - \mu_j)^T, \dots, j = 0, 1. \tag{20}$$

Since there are two types of data, we only need to project the data onto a straight line. Assuming that the projection line is a vector  $w$ , the projection of any sample on  $w$  is  $w^T x_i$ ; the center points  $\mu_0$  and  $\mu_1$  of the two categories, projected on  $w$  are  $w^T \mu_0$  and  $w^T \mu_1$ , respectively. The main purpose of LDA is to maximize the distance between the centers of different categories of data to maximize  $\|w^T \mu_0 - w^T \mu_1\|_2^2$ . At the same time, we need to make the projection points of the same kind of data as small as possible; that is, the covariance  $w^T \Sigma_0 w$  and  $w^T \Sigma_1 w$  of projection points between similar samples should be as small as possible. Therefore, we need to minimize  $w^T \Sigma_0 w + w^T \Sigma_1 w$ .

The optimization objective of the LDA algorithm is as follows:

$$\begin{aligned} W^* &= \underset{w}{\operatorname{argmax}} \frac{\|w^T \mu_0 - w^T \mu_1\|_2^2}{w^T \Sigma_0 w + w^T \Sigma_1 w} \\ &= \frac{w^T (\mu_0 - \mu_1)(\mu_0 - \mu_1)^T w}{w^T (\Sigma_0 + \Sigma_1) w}. \end{aligned} \tag{21}$$

The between-class scatter matrix  $S_B$  is as follows:

$$S_B = (\mu_0 - \mu_1)(\mu_1 - \mu_0)^T. \tag{22}$$

The within-class scatter matrix  $S_W$  is as follows:

$$S_W = \Sigma_0 + \Sigma_1, \tag{23}$$

Therefore, the  $W^*$  is rewritten as follows:

$$W^* = \underset{w}{\operatorname{argmax}} \frac{w^T S_B w}{w^T S_W w}. \tag{24}$$

Since both the numerator and denominator contain the quadratic term of  $w$ , the objective function is independent of the module length of  $w$ . Let:

$$w^T S_W w = 1. \quad (25)$$

The optimization problem is as follows:

$$\begin{cases} \min_{(w)} -w^T S_B w \\ \text{s.t. } w^T S_W w = 1 \end{cases}. \quad (26)$$

The Lagrangian function of the optimization problem is as follows:

$$L(w, \lambda) = -w^T S_B w + \lambda (w^T S_W w - 1), \quad (27)$$

Then, by finding the first partial derivative of  $w$  for equation (20) and setting it to zero, we can obtain the following:

$$S_W^{-1} S_B w = \lambda w. \quad (28)$$

By finding the eigenvector of the matrix, we can obtain  $w$ .

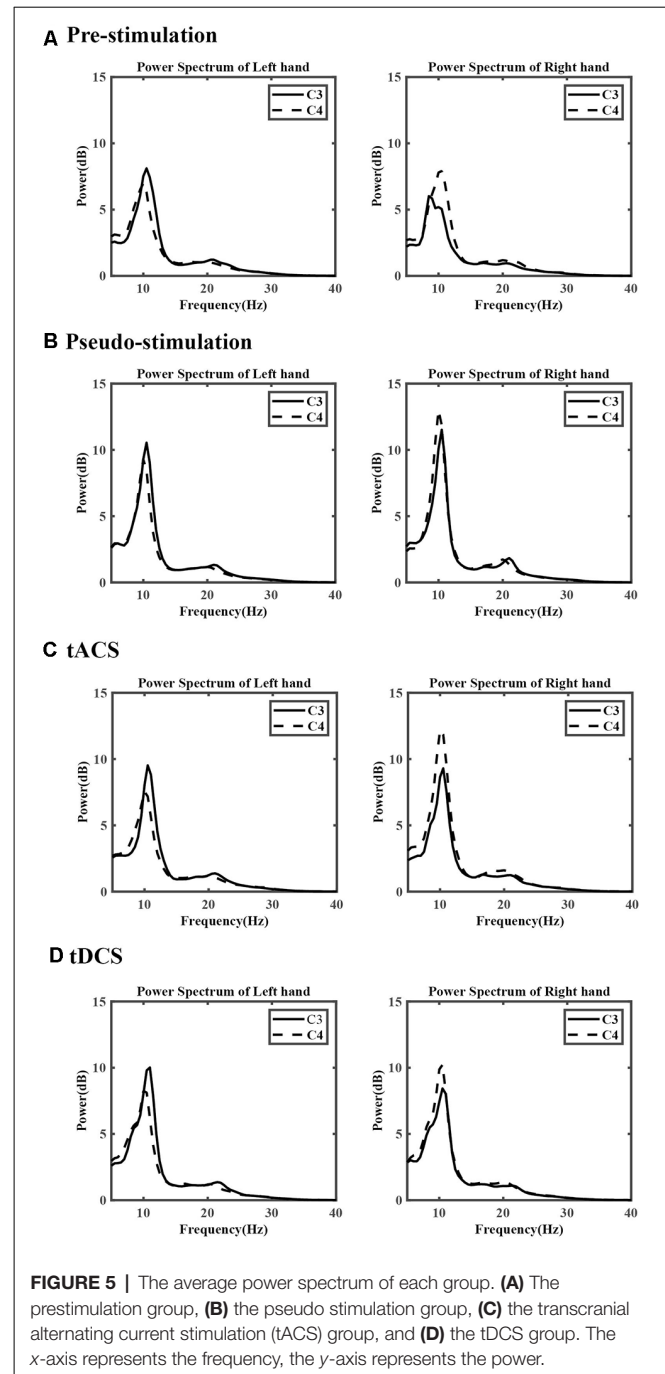
## Statistical Analysis

Group-level statistical tests were conducted for different EEG measurements, including the normalized  $\Delta$ Power, dynamic ERD, and classification accuracy. Before the statistical tests, the data distribution was first examined based on Mauchly's test of sphericity. Then, a repeated measurement variance analysis of the general linear model was performed for each group to test the significance among the subjects in different experimental conditions. For the normalized  $\Delta$ Power, one-way repeated-measures analysis of variance (ANOVA) and *post hoc t*-tests were performed on the power for the  $\mu$  and  $\beta$  rhythms of the left- and right-hand MI tasks in four conditions. To obtain the optimal time range, the values of ERD difference between the contralateral and ipsilateral sides of all the time windows were compared between pre- and poststimulation in left- and right-hand sides (paired *t*-test). For the classification accuracy the significance of differences among experimental conditions was also tested *via* ANOVA. All statistic thresholds were set to  $P < 0.05$  without correction.

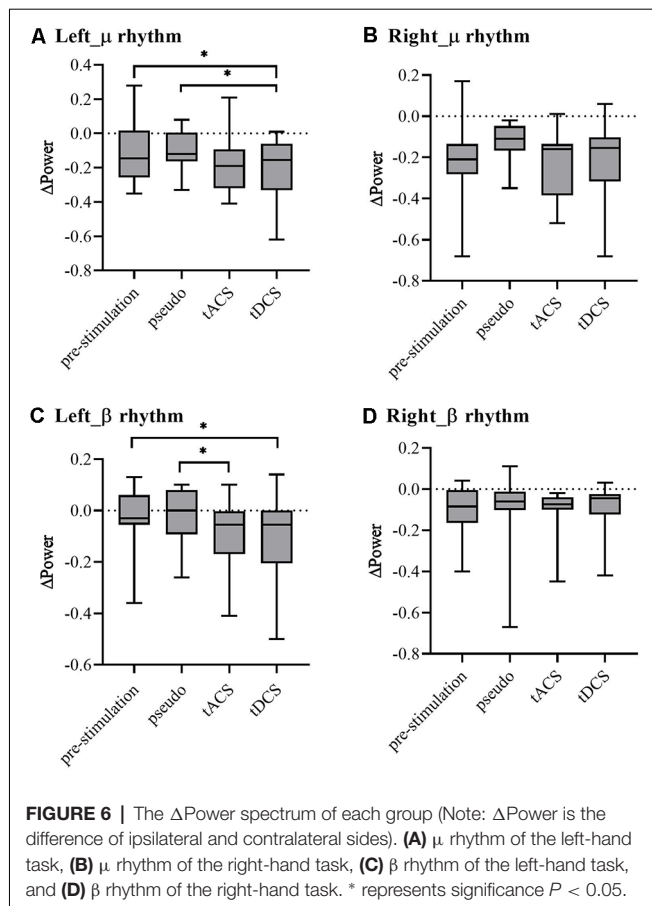
## RESULTS AND ANALYSIS

### Analysis of the Power Spectrum Characteristics

The power change of the  $\mu$  and  $\beta$  rhythms among the sensory-motor rhythms (SMRs) during the left- and right-hand MI tasks was calculated according to the average power spectrum collected by the C3 and C4 channels for all subjects in the four experimental conditions. The results are shown in **Figure 5**. For the power change of the  $\mu$  rhythm at 8–13 Hz, during the right-hand MI tasks, the power of C3 was lower than that of C4 both in pre- and poststimulation. When subjects performed left-hand MI tasks, obvious power differences were not observed between C3 and C4 in the prestimulation and pseudo stimulation groups. However, after tACS and tDCS, the phenomenon could be observed obviously. For the  $\beta$  rhythm of 17–25 Hz, the power change in the C3 and C4 regions was slight.



To compare the power change statistically, in **Figure 6**, the  $\mu$  and  $\beta$  rhythm power were extracted from the C3 and C4 power spectra for each trial of each subject and stimulation condition. ANOVAs were performed on the  $\Delta$ Power for  $\mu$  and  $\beta$  rhythm power of left- and right-hand MI tasks in four experiments to evaluate the reference effects. Significant differences revealed by ANOVA were further analyzed for multiple comparisons using Tukey's *post hoc* test. For left-hand tasks, the  $\mu$  and  $\beta$  rhythms were in line with the Mauchly sphere test hypothesis ( $P = 0.05$ ). For the  $\mu$  rhythm,



compared with the pre- and pseudo stimulation groups, the tDCS group showed significant differences but the tACS group showed almost no significant change (tDCS-pre:  $P = 0.03 < 0.05$ ; tDCS-Pseudo:  $P = 0.01 < 0.05$ ). For the  $\beta$  rhythm, tDCS showed significant differences compared with prestimulation and tACS showed significant differences compared with pseudo stimulation, while tDCS showed marginal significance (tDCS-Pre:  $P = 0.01 < 0.05$ ; tACS-Pseudo:  $P = 0.01 < 0.05$ ; tDCS-Pseudo:  $P = 0.05$ ). For right-hand tasks, the  $\mu$  and  $\beta$  rhythms were in line with the Mauchly sphere test hypothesis ( $P = 0.05$ ). Neither tDCS and tACS were significantly different.

## Analysis of Event-Related Desynchronization Features

Figures 7, 8 show the ERD relative amplitude (RA) time courses of all subjects from  $[-1, 9$  s] [from 1 s before the MI task (6 s) to 3 s after the task] for the two MI tasks. A smaller RA of the contralateral side corresponded to greater desynchronized ERD movement. In this study, different ERD phenomena were observed. In Figure 7, the duration of C4 ERD in the tACS and tDCS groups was longer than that in the pre- and pseudo stimulation groups. Also, the RA in the tACS and tDCS groups was smaller than that in pre- and pseudo stimulation groups. In Figure 8, the duration of C3 ERD in the tACS and tDCS groups was longer than that

in pre- and pseudo stimulation groups. The RA in the tACS and tDCS groups was smaller than that in pre- and pseudo stimulation groups.

Also, the optimal time range of ERD was verified. For the left-hand tasks, we used one-way ANOVA to test the significance of the RA difference between the contralateral and ipsilateral sides in different experimental conditions, and the optimal time window [3, 5 s] was found (tACS-Pre:  $P = 0.03 < 0.05$ ; tDCS-Pre:  $P = 0.03 < 0.05$ ). However, in the right-hand tasks, the optimal time range was [3–5 s], with statistical significance (tACS-Pre:  $P = 0.13 > 0.05$ ; tDCS-Pre:  $P = 0.07 > 0.05$ ). Compared with prestimulation, tDCS presented marginal significance; however, tACS was not significant.

## Analysis of Classification Accuracy

In this article, the LDA classifier was used to train and test the MI classification of subjects under four different conditions: prestimulation, pseudo stimulation, tACS, and tDCS. After preprocessing the data, we determined the individual specific bandpass filter of the two tasks, and the results showed that nine subjective specific frequency bands were from 8–15 Hz, four subjective specific frequency bands were from 17–25 Hz, and two subjective specific frequency bands were from 8–30 Hz. Then, the filtered data were extracted by CSP and the two types of extracted feature vectors  $f_1$  and  $f_2$  were input into the LDA classifier as training data for classification. According to the relatively small distance between similar data points and the relatively large distance between data points of different classifications, the best separation plane was obtained. Then the 5-fold cross-validation method was implemented for training and testing. The final classification accuracy results of all subjects are shown in Table 1. The average classification accuracy of the four groups of experiments is shown in Figure 9.

From the data in the table, the average accuracy of MI was effectively improved after the subjects received tDCS. For tACS, the accuracy of subjects 5, 8, and 11 after tACS decreased compared with that before stimulation. Subjects 1, 3, and 6 had better accuracy improvement with tACS than those with tDCS. Among all subjects in the experimental group, the highest accuracy of 98.75% was found for subject 1 after tACS, and the lowest accuracy of 75.11% was observed in subjects 8 after tACS. Figure 9 shows that the overall classification accuracy of the tACS group and the tDCS group was significantly improved compared to that of the pre- and pseudo stimulation groups, although the improvement effect of the tDCS group was higher than that of the tACS group.

To investigate the effect of the tACS and tDCS proposed in this article for improving the accuracy of MI classification tasks, we used one-way ANOVA to test the significance of the MI classification accuracy of the subjects under different experimental conditions ( $P = 0.05$ ). First, we confirmed the homogeneity of the sample's variance, which is consistent with the Mauchly sphere test hypothesis ( $P = 0.134 > 0.05$ ), thus demonstrating that the main effect is significant. Second, the results of tACS and tDCS were

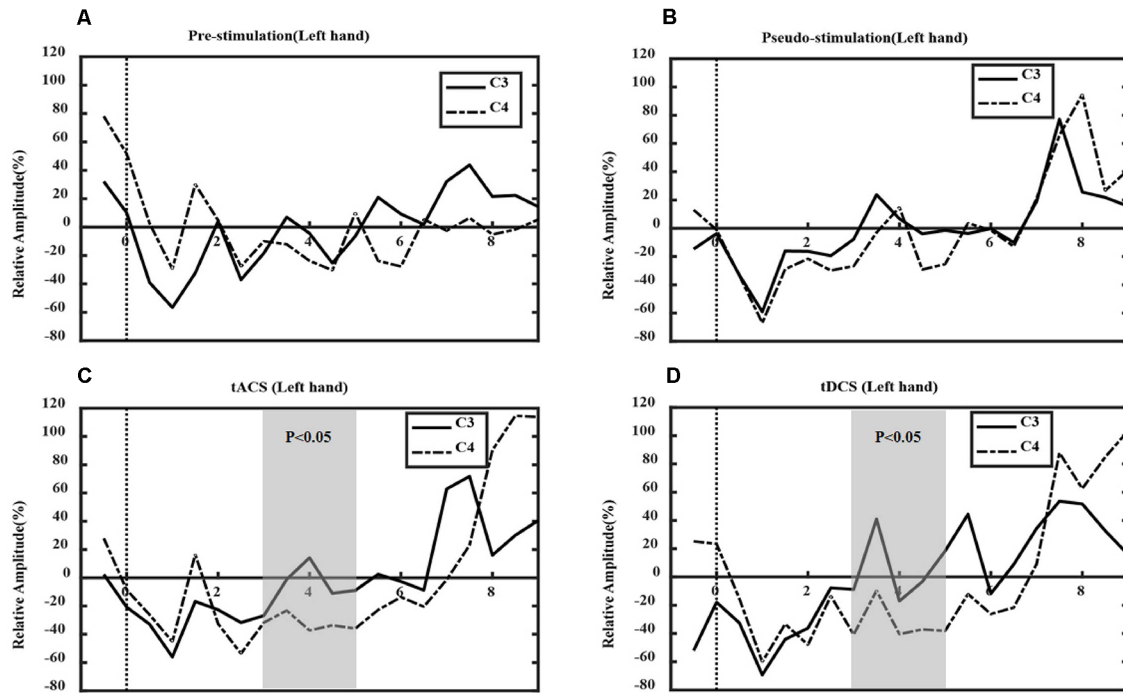


**FIGURE 7 |** Event-related desynchronization (ERD) in left-hand tasks. Where the x-axis represents time and the y-axis represents relative amplitude (RA). **(A)** The prestimulation group, **(B)** the pseudo stimulation group, **(C)** the tACS group, and **(D)** the tDCS group. The RA in tACS and tDCS groups are smaller than in prestimulation and pseudo stimulation groups. The optimal time window is [3, 5 s] (tACS:  $P = 0.03 < 0.05$ ; tDCS:  $P = 0.03 < 0.05$ ).

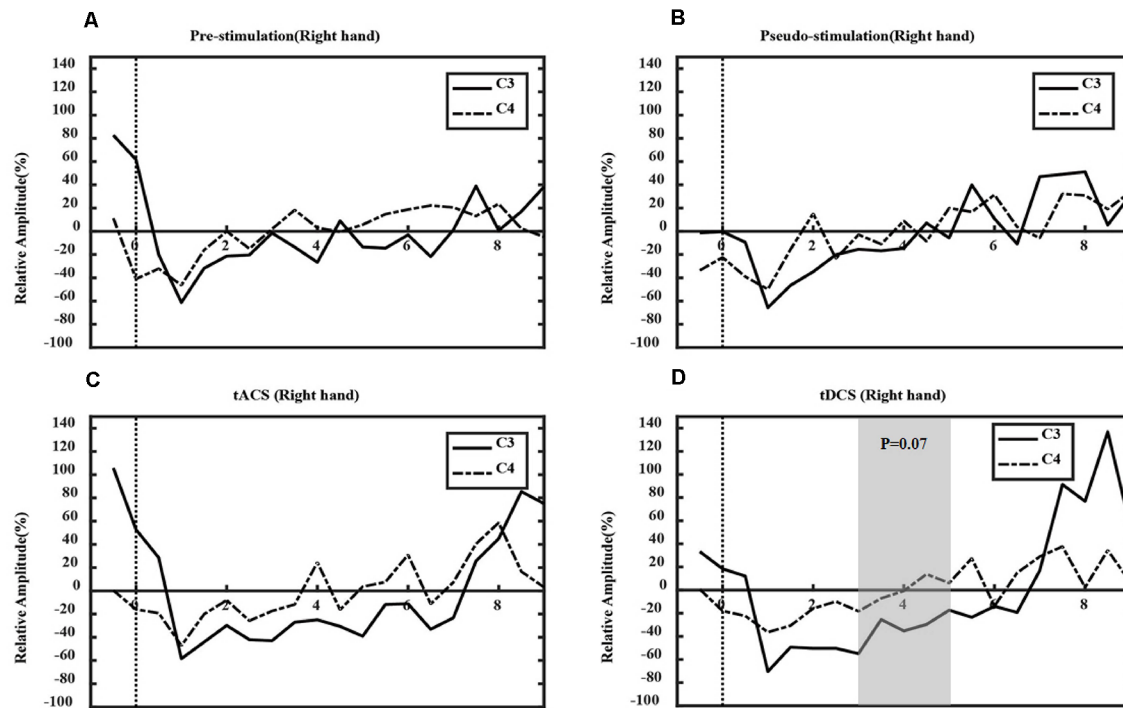
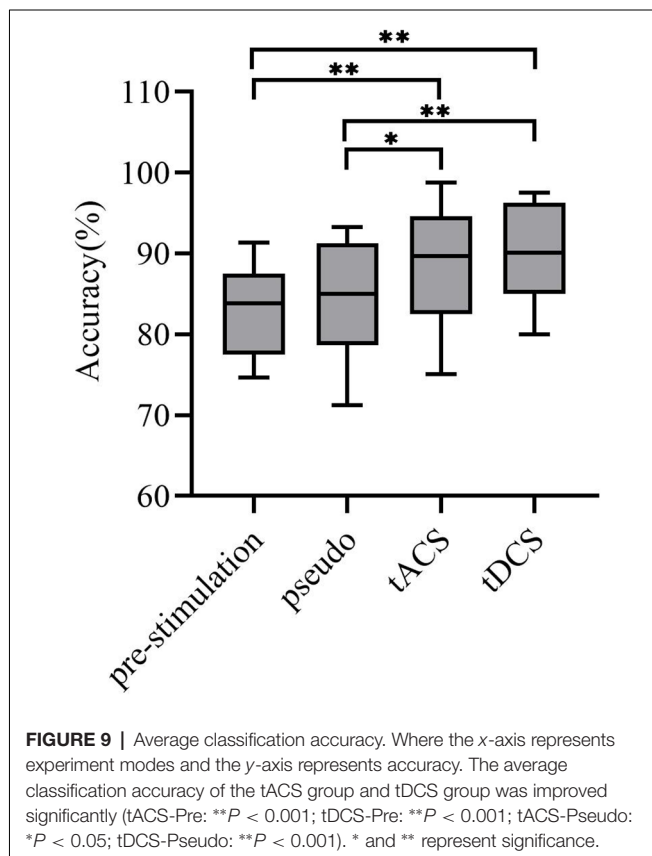


**FIGURE 8 |** ERD in right-hand tasks. Where the x-axis represents time and the y-axis represents RA. **(A)** The prestimulation group, **(B)** the pseudo stimulation group, **(C)** the tACS group, and **(D)** the tDCS group. The RA in tACS and tDCS groups are smaller than in pre-stimulation and pseudo-stimulation groups. The optimal time range is [3, 5 s] (tDCS:  $P = 0.07 > 0.05$ ).

**TABLE 1** | The classification accuracy of subjects' motor imagery.

Subjects	Pre-stimulation (%)	Pseudo-stimulation (%)	tACS (%)	tDCS (%)
Subject 1	91.25	93.21	98.75	96.88
Subject 2	83.83	85.84	92.50	97.50
Subject 3	74.68	76.25	86.25	80.00
Subject 4	85.00	85.00	89.74	90.06
Subject 5	82.49	85.00	80.00	86.25
Subject 6	77.50	78.64	85.05	82.68
Subject 7	77.61	71.25	81.27	87.49
Subject 8	77.49	77.50	75.11	81.27
Subject 9	88.77	91.28	94.93	96.31
Subject 10	87.5	92.5	94.64	97.5
Subject 11	91.32	92.78	89.64	92.7
Subject 12	84.29	80.2	95	95
Subject 13	83.55	87.34	87.5	90
Subject 14	74.78	82.06	82.5	85
Subject 15	85.12	87.98	90	90.28
Mean $\pm$ Standard	83.01 $\pm$ 1.43	84.46 $\pm$ 1.73	88.19 $\pm$ 1.70	89.93 $\pm$ 1.56



compared with the results of the pre-and pseudo stimulation groups, respectively. These statistics revealed significant differences for all accuracies compared with the pre-and pseudo stimulation groups (tACS-Pre:  $P < 0.001$ ; tDCS-Pre:  $P < 0.001$ ; tACS-Pseudo:  $P < 0.05$ ; tDCS-Pseudo:  $P < 0.05$ ). Therefore, we concluded that the accuracy of the subjects in the tACS and tDCS groups was significantly improved compared with that of the pre-stimulation and pseudo stimulation groups.

## DISCUSSION

The main purpose of this article was to study the effect of tES on ERD based on MI-BCI. Subjects performed the MI classification experiment under four conditions: prestimulation, pseudo stimulation, tDCS, and tACS. The effects of tACS and tDCS on ERD were analyzed from three aspects: power spectral density, dynamic ERD, and classification accuracy. Also, the average classification accuracy was used to verify the improvement of BCI task ability.

Motor imagery was described as imagining a movement rather than executing a real movement, and this method is promising for patients with tetraplegia, spinal cord injury, and amyotrophic lateral sclerosis (ALS; Abiri et al., 2019). However, the main drawback of the MI was that the training time could take weeks or months. tACS and tDCS as noninvasive neuromodulation techniques could provide alternative ways to enhance the valid metrics by modifying ERD patterns (Kuo and Nitsche, 2012). Whether for motor execution or MI, ERD changes in SMRs are always produced (Jeon et al., 2011; Bauer et al., 2015). Among them, the  $\mu$  rhythm and  $\beta$  rhythm among SMRs were considered to be related to motor ability and motor control (Pfurtscheller et al., 1994). In the process of the unilateral MI task, the power of the  $\mu$  rhythm and  $\beta$  rhythm decreased in the contralateral motor-sensory area, namely, the ERD (Pfurtscheller and Neuper, 1994, 1997). Many articles have indicated that tES could modulate ERD during MI. In this study, some interesting findings were obtained: (1) tES could induce both  $\mu$  rhythm and  $\beta$  rhythm ERD increases in the left-hand MI task; (2) tES can prolong the ERD duration and decrease the relative power; and (3) tES can enhance the MI accuracy effectively.

These findings could provide a reference for related fields. Studies have indicated that there is differential lateralization of hand movement neural representation in right- and left-handed individuals, and handedness is closely linked to the ability to control an SMR-BCI (Zapala et al., 2020). In the current study, all the subjects recruited were right-handed, power

suppression of the  $\mu$  rhythm occurred during right-hand MI of all conditions, but there was no significance between pre- and poststimulation. However, in the left-hand MI task, the power of the  $\mu$  rhythm declined obviously after tDCS, and the  $\Delta$ Power of the  $\mu$  rhythm decreased significantly compared with pre- and pseudo stimulation (tDCS-pre:  $P = 0.03 < 0.05$ ; tDCS-Pseudo:  $P = 0.01 < 0.05$ ). These results implied that tES may evoke a much higher effect on the neural representation of the non-dominant hand MI task. Also, as one important motor rhythm, the power of the  $\beta$  rhythm was not significant in this study. Interestingly, the  $\Delta$ Power of the  $\beta$  rhythm in the left-hand MI showed a significant decrease after tDCS compared with pre-stimulation ( $P < 0.05$ ), indicating that this power difference between bilateral electrodes may create the potential control signal that drives a BCI. Moreover, the relative amplitude of ERD during MI was enhanced after tACS and tDCS, indicating that transcranial electrical stimulation can enhance the excitability of the cerebral cortex and regulate brain activity (Pellicciari et al., 2013). Although the duration of ERD in tACS and tDCS seemed to have been prolonged, not all the whole period of MI in each trial was usable. The effective response time of MI was different among individuals, due to the pattern of neural activation (Williams et al., 2012), and a previous study indicated that the overall optimal time segment was [4, 6 s] (Gong et al., 2013). In this article, the optimal time range was [3, 5 s], where the left-hand relative amplitudes of ERD in tACS and tDCS were significant ( $P < 0.05$ ), but the right-hand relative amplitudes of ERD, which were also the range of [3, 5 s], were not significant after tACS.

To verify the influence of tES on MI-BCI task ability, we compared the classification accuracy of the four conditions. tACS enhanced motor imagery ability in terms of the  $\mu$  and  $\beta$  rhythm. A possible mechanism was that beta rhythm stimulation was related to the excitability of the primary motor cortex and the alpha rhythm stimulation was associated with motor educability (Zhang et al., 2016). tDCS could enhance ERD patterns and conditionally improve BCI performance in both the online and offline BCI classification results (Wei et al., 2013). In this study, we used CSPs to extract the signal features and LDA to classify the feature vectors (Wang et al., 2005; Sharma and Paliwal, 2015). The results showed that the average classification accuracy of the tACS group and tDCS group was improved significantly ( $P < 0.001$ ). However, individual differences impacted tACS, possibly because of the difference of endogenous oscillations among individuals with tACS frequencies.

In this study, we designed an experimental paradigm that combines two different modes of stimuli and compared them with the stimuli to determine the most effective at enhancing event-related desynchronization during the MI period. In the same processing framework, the comparison analysis of the quantified EEG metrics was conducted from three dimensions including the PSD difference between contralateral and ipsilateral electrodes (spatial effect), the time-varying ERD calculation using sliding windows (temporal effect), and the classification accuracy based on the classical LDA method in MI-BCI (classification performance). From the results of EEG

metrics and classification accuracy, we speculated that tDCS has potential in regulating brain activity and enhancing valid features in noninvasive MI-BCI processing. Moreover, the time range of [3, 5 s] after MI start-up led to the optimal ERD combined with tDCS, which may be helpful for the actual BCI performance improvement. However, this study also has many limitations in the experimental and analytical methods. For example, for the experimental design, the duration of electrical stimulation was 10 min and the anode of the stimulation position was located in Cz. In subsequent experiments, different experimental groups could set the stimulation duration to 5, 15, and 20 min, and implement different placement of the anode of tES (Kasashima et al., 2012; Mordillo-Mateos et al., 2012; Wei et al., 2013; Koo et al., 2016). Additionally, the effect of tACS may change due to differences in the endogenous oscillation among individuals. Even if the deviation from the internal frequency of individuals is very small, it may cause other effects or reduce the modulation effect of tACS (Herrmann et al., 2013). The preliminary conclusion based on the findings was that tES may make subjects start MI tasks faster; however, this point requires further investigation. Moreover, the number of subjects should be increased in subsequent experiments to verify the results of the statistical test.

## CONCLUSION

In this article, tDCS and tACS were conducted and evaluated based on the same motor imagery (MI) tasks and subjects. The two tES methods can effectively enhance the activation of the cerebral motor cortex, which makes ERD more obvious during the MI period. Then, we quantified ERD by dynamic time windows, which can provide the optimal time range of [3, 5 s] for future MI-BCIs. Moreover, in the case of using the basic feature extraction and classification algorithm for EEG signal processing, both kinds of stimulation methods can improve the performance of MI-BCI using a lower difficulty algorithm and tDCS showed superiority in regulating activity and evoking effective features in MI-BCI.

## DATA AVAILABILITY STATEMENT

The raw data supporting the conclusions of this article will be made available by the authors, without undue reservation.

## ETHICS STATEMENT

The studies involving human participants were reviewed and approved by Ethics Committee of the University of Electronic Science and Technology of China. The patients/participants provided their written informed consent to participate in this study.

## AUTHOR CONTRIBUTIONS

JX, MP, DG, and CX conceived and designed the work. JL, XZ, MW, and DG acquired the data. MP, XZ, MW, and CX analyzed

the data. JX, MP, MW, and JL wrote the article. All authors revised the work for important intellectual content. All authors contributed to the article and approved the submitted version.

## FUNDING

This work was partly supported by the grant from the National Key R&D Program of China 81771925 and the foundation of

National Key Laboratory of Human Factor Engineering Grant, SYFD061902K.

## SUPPLEMENTARY MATERIAL

The Supplementary Material for this article can be found online at: <https://www.frontiersin.org/articles/10.3389/fnhum.2021.635351/full#supplementary-material>.

## REFERENCES

- Abiri, R., Borhani, S., Sellers, E. W., Jiang, Y., and Zhao, X. (2019). A comprehensive review of EEG-based brain-computer interface paradigms. *J. Neural Eng.* 16:011001. doi: 10.1088/1741-2552/aaf12e
- Angelakis, E., and Liouta, E. (2011). Transcranial electrical stimulation: methodology and applications. *J. Neurother.* 15, 337–357. doi: 10.1080/10874208.2011.623092
- Bauer, R., Fels, M., Vukelić, M., Ziemann, U., and Gharabaghi, A. (2015). Bridging the gap between motor imagery and motor execution with a brain-robot interface. *NeuroImage* 108, 319–327. doi: 10.1016/j.neuroimage.2014.12.026
- Baxter, B. S., Edelman, B. J., Nesbitt, N., and He, B. (2016). Sensorimotor Rhythm BCI with simultaneous high definition-transcranial direct current stimulation alters task performance. *Brain Stimul.* 9, 834–841. doi: 10.1016/j.brs.2016.07.003
- Bestmann, S., and Walsh, V. (2017). Transcranial electrical stimulation. *Curr. Biol.* 27, R1258–R1262. doi: 10.1016/j.cub.2017.11.001
- Bindman, L. J., Lippold, O. C. J., and Redfearn, J. W. T. (1964). The action of brief polarizing currents on the cerebral cortex of the rat (1) during current flow and (2) in the production of long-lasting after-effects. *J. Physiol.* 172, 369–382. doi: 10.1113/jphysiol.1964.sp007425
- Blankertz, B., Sannelli, C., Halder, S., Hammer, E. M., Kübler, A., Müller, K.-R., et al. (2010). Neurophysiological predictor of SMR-based BCI performance. *NeuroImage* 51, 1303–1309. doi: 10.1016/j.neuroimage.2010.03.022
- Cho, Y. K., Kim, S., Jung, H. H., Chang, J. W., Kim, Y. J., Shin, H. C., et al. (2016). Neuromodulation methods for animal locomotion control. *Biomed. Eng. Lett.* 6, 134–147. doi: 10.1007/s13534-016-0234-2
- Decety, J., and Boisson, D. (1990). Effect of brain and spinal cord injuries on motor imagery. *Eur. Arch. Psychiatry Clin. Neurosci.* 240, 39–43. doi: 10.1007/BF02190091
- Flöel, A. (2014). tDCS-enhanced motor and cognitive function in neurological diseases. *NeuroImage* 85, 934–947. doi: 10.1016/j.neuroimage.2013.05.098
- Goh, S. K., Abbass, H. A., Tan, K. C., Al-Mamun, A., Wang, C., and Guan, C. (2017). “Automatic EEG artifact removal techniques by detecting influential independent components,” in *IEEE Transactions on Emerging Topics in Computational Intelligence*, Vol. 1, ed Yew-Soon Ong (Singapore: IEEE), 270–279.
- Goncharova, I. I., McFarland, D. J., Vaughan, T. M., and Wolpaw, J. R. (2003). EMG contamination of EEG: spectral and topographical characteristics. *Clin. Neurophysiol.* 114, 1580–1593. doi: 10.1016/s1388-2457(03)00093-2
- Gong, P., Chen, M. Y., Zhang, L., and Jian, W. J. (2013). Hht-based selection of optimal time-frequency patterns for motor imagery. *Appl. Mech. Mat.* 380–384, 2724–2727. doi: 10.1109/NCES.2012.6544071
- Guger, C., Edlinger, G., Harkam, W., Niedermayer, I., and Pfurtscheller, G. (2003). How many people are able to operate an EEG-based brain-computer interface (BCI)? *IEEE Trans. Neural Syst. Rehabil. Eng.* 11, 145–147. doi: 10.1109/TNSRE.2003.814481
- He, B., Baxter, B., Edelman, B. J., Cline, C. C., and Ye, W. W. (2015). Noninvasive brain-computer interfaces based on sensorimotor rhythms. *Proc. IEEE* 103, 907–925. doi: 10.1109/JPROC.2015.2407272
- Herrmann, C. S., Stefan, R., Toralf, N., and Daniel, S. (2013). Transcranial alternating current stimulation: a review of the underlying mechanisms and modulation of cognitive processes. *Front. Hum. Neurosci.* 7:279. doi: 10.3389/fnhum.2013.00279
- Jeon, Y., Nam, C. S., Kim, Y. J., and Whang, M. C. (2011). Event-related (de)synchronization (ERD/ERS) during motor imagery tasks: implications for brain-computer interfaces. *Int. J. Indust. Ergon.* 41, 428–436. doi: 10.1016/j.ergon.2011.03.005
- Kasashima, Y., Fujiwara, T., Matsushika, Y., Ushiba, J., Kimura, A., and Meigen, L. (2012). Modulation of event-related desynchronization during motor imagery with transcranial direct current stimulation (tDCS) in patients with chronic hemiparetic stroke. *Clin. Neurophysiol.* 221, 263–268. doi: 10.1007/s00221-012-3166-9
- Kasten, F. H., and Herrmann, C. S. (2017). Transcranial alternating current stimulation (tACS) enhances mental rotation performance during and after stimulation. *Front. Hum. Neurosci.* 11:2. doi: 10.3389/fnhum.2017.00002
- Koo, H., Kim, M. S., Han, S. W., Kim, Y. H., Ko, S. H., and Shin, Y. I. (2016). P152 After-effects of anodal transcranial direct current stimulation on the excitability of the motor cortex in rats. *Restor. Neurol. Neurosci.* 34, 859–868. doi: 10.3233/RNN-160664
- Kuo, M.-F., and Nitsche, M. A. (2012). Effects of transcranial electrical stimulation on cognition. *Clin. EEG Neurosci.* 43, 192–199. doi: 10.1177/1550059412444975
- Liu, Y., Li, N. Q., and Li, Y. X. (2013). EEG-based motor imagery feature extraction. *Adv. Mat. Res.* 846, 944–947.
- Lu, H., Eng, H.-L., Guan, C., Plataniotis, K. N., and Venetsanopoulos, A. N. (2010). Regularized common spatial pattern with aggregation for EEG classification in small-sample setting. *IEEE Trans. Biomed. Eng.* 57, 2936–2946. doi: 10.1109/TBME.2010.2082540
- Mordillo-Mateos, L., Turpin-Fenoll, L., Millán-Pascual, J., Núñez-Pérez, N., Panyavin, I., Gómez-Argüelles, J. M., et al. (2012). Effects of simultaneous bilateral tDCS of the human motor cortex. *Brain Stimul.* 5, 214–222. doi: 10.1016/j.brs.2011.05.001
- Muller-Gerking, J., Pfurtscheller, G., and Flyvbjerg, H. (1999). Designing optimal spatial filters for single-trial EEG classification in a movement task. *Clin. Neurophysiol.* 110, 787–798. doi: 10.1016/s1388-2457(98)00038-8
- Nguyen, H.-A. T., Musson, J., Li, F., Wang, W., Zhang, G., Xu, R., et al. (2012). EOG artifact removal using a wavelet neural network. *Neurocomputing* 97, 374–389. doi: 10.1016/j.neucom.2012.04.016
- Nitsche, M. A., and Paulus, W. (2000). Excitability changes induced in the human motor cortex by weak transcranial direct current stimulation. *J. Physiol.* 527, 633–639. doi: 10.1111/j.1469-7793.2000.t01-1-00633.x
- Paulus, W. (2011). Transcranial electrical stimulation (tES - tDCS; tRNS, tACS) methods. *Neuropsychol. Rehabil.* 21, 602–617. doi: 10.1080/09602011.2011.557292
- Pellicciari, M. C., Brignani, D., and Miniussi, C. (2013). Excitability modulation of the motor system induced by transcranial direct current stimulation: a multimodal approach. *NeuroImage* 83, 569–580. doi: 10.1016/j.neuroimage.2013.06.076
- Pfurtscheller, G., and Neuper, C. (1997). Motor imagery activates primary sensorimotor area in humans. *Neurosci. Lett.* 239, 65–68. doi: 10.1016/S0304-3940(97)00889-6
- Pfurtscheller, G., and Neuper, C. (1994). Event-related synchronization of mu rhythm in the EEG over the cortical hand area in man. *Neurosci. Lett.* 174, 93–96. doi: 10.1016/0304-3940(94)90127-9
- Pfurtscheller, G., Pregenzer, M., and Neuper, C. (1994). Visualization of sensorimotor areas involved in preparation for hand movement based on classification of  $\mu$  and central  $\beta$  rhythms in single EEG trials in man. *Neurosci. Lett.* 181, 43–46. doi: 10.1016/0304-3940(94)90556-8
- Pollok, B., Boysen, A. C., and Krause, V. (2015). The effect of transcranial alternating current stimulation (tACS) at alpha and beta frequency on motor learning. *Behav. Brain Res.* 293, 234–240. doi: 10.1016/j.bbr.2015.07.049

- Schuhmann, T., Kemmerer, S. K., Duecker, F., De Graaf, T. A., Ten Oever, S., De Weerd, P., et al. (2019). Left parietal tACS at alpha frequency induces a shift of visuospatial attention. *PLoS One* 14:e0217729. doi: 10.1371/journal.pone.0217729
- Sharma, A., and Paliwal, K. K. (2015). A deterministic approach to regularized linear discriminant analysis. *Neurocomputing* 151, 207–214. doi: 10.1016/j.neucom.2014.09.051
- Sugata, H., Yagi, K., Yazawa, S., Nagase, Y., Tsuruta, K., Ikeda, T., et al. (2018). Modulation of motor learning capacity by transcranial alternating current stimulation. *Neuroscience* 391, 131–139. doi: 10.1016/j.neuroscience.2018.09.013
- Talsma, L. J., Kroese, H. A., and Slagter, H. A. (2017). *Boosting Cognition: Effects of Multiple-Session Transcranial Direct Current Stimulation on Working Memory*. Cambridge, MA: MIT Press.
- Tariq, M., Trivailo, P. M., and Simic, M. (2019). Classification of left and right foot kinaesthetic motor imagery using common spatial pattern. *Biomed. Phys. Eng. Express* 6:015008. doi: 10.1088/2057-1976/ab54ad
- Tariq, M., Trivailo, P. M., and Simic, M. (2020). Mu- $\beta$  event-related (de) synchronization and EEG classification of left-right foot dorsiflexion kinaesthetic motor imagery for BCI. *PLoS One* 15:e0230184. doi: 10.1371/journal.pone.0230184
- Thomas, R., and Roi, C. K. (2018). Transcranial electrical stimulation (tES) mechanisms and its effects on cortical excitability and connectivity. *J. Inherit. Metab. Dis.* 41, 1123–1130. doi: 10.1007/s10545-018-0181-4
- Tsuiki, S., Sasaki, R., Miyaguchi, S., Kojima, S., Saito, K., Inukai, Y., et al. (2019). The effect of combined transcranial direct current stimulation and peripheral nerve electrical stimulation on corticospinal excitability. *PLoS One* 14:e0214592. doi: 10.1371/journal.pone.0214592
- Unal, G., and Bikson, M. (2018). “Transcranial direct current stimulation (tDCS),” in *Neuromodulation*, eds Elliot S. Krames, P. Hunter Peckham and Ali R. Rezai (United Kingdom: Academic Press), 1589–1610.
- Wach, C., Krause, V., Moliadze, V., Paulus, W., Schnitzler, A., and Pollok, B. (2013). Effects of 10 Hz and 20 Hz transcranial alternating current stimulation (tACS) on motor functions and motor cortical excitability. *Behav. Brain Res.* 241, 1–6. doi: 10.1016/j.bbr.2012.11.038
- Wang, Y., Gao, S., and Gao, X. (2005). Common spatial pattern method for channel selection in motor imagery based brain-computer interface. *Conf. Proc. IEEE Eng. Med. Biol. Soc.* 5, 5392–5395. doi: 10.1109/IEMBS.2005.1615701
- Wei, P., He, W., Zhou, Y., and Wang, L. (2013). Performance of motor imagery brain-computer interface based on anodal transcranial direct current stimulation modulation. *IEEE Trans. Neural Syst. Rehabil. Eng.* 21, 404–415. doi: 10.1109/TNSRE.2013.2249111
- Williams, J., Pearce, A. J., Loporto, M., Morris, T., and Holmes, P. S. (2012). The relationship between corticospinal excitability during motor imagery and motor imagery ability. *Behav. Brain Res.* 226, 369–375. doi: 10.1016/j.bbr.2011.09.014
- Xu, P., Yang, P., Lei, X., and Yao, D. (2011). An enhanced probabilistic LDA for multi-class brain computer interface. *PLoS One* 6:e14634. doi: 10.1371/journal.pone.0014634
- Zapala, D., Zabielska-Mendyk, E., Augustynowicz, P., Cudo, A., Jaśkiewicz, M., Szewczyk, M., et al. (2020). The effects of handedness on sensorimotor rhythm desynchronization and motor-imagery BCI control. *Sci. Rep.* 10:2087. doi: 10.1038/s41598-020-59222-w
- Zhang, L., Wu, Z., Zhang, X., and Tang, J. (2016). “Performance in motor imagery tasks can be improved by transcranial alternating current stimulation,” in *2016 9th International Congress on Image and Signal Processing, BioMedical Engineering and Informatics (CISP-BMEI)*, Datong, China.

**Conflict of Interest:** The authors declare that the research was conducted in the absence of any commercial or financial relationships that could be construed as a potential conflict of interest.

Copyright © 2021 Xie, Peng, Lu, Xiao, Zong, Wang, Gao, Qin and Liu. This is an open-access article distributed under the terms of the Creative Commons Attribution License (CC BY). The use, distribution or reproduction in other forums is permitted, provided the original author(s) and the copyright owner(s) are credited and that the original publication in this journal is cited, in accordance with accepted academic practice. No use, distribution or reproduction is permitted which does not comply with these terms.



# Adaptive Filtering for Improved EEG-Based Mental Workload Assessment of Ambulant Users

Olivier Rosanne<sup>1\*</sup>, Isabela Albuquerque<sup>1</sup>, Raymundo Cassani<sup>1</sup>, Jean-François Gagnon<sup>2</sup>, Sébastien Tremblay<sup>3</sup> and Tiago H. Falk<sup>1</sup>

<sup>1</sup> Institut National de la Recherche Scientifique - Centre Énergie, Matériaux et Télécommunication, Université du Québec, Montréal, QC, Canada, <sup>2</sup> Thales Research and Technology, Quebec City, QC, Canada, <sup>3</sup> École de Psychologie, Université Laval, Quebec City, QC, Canada

## OPEN ACCESS

### Edited by:

Amit Konar,  
Jadavpur University, India

### Reviewed by:

Rubita Sudirman,  
University of Technology Malaysia,  
Malaysia  
Liang Zou,  
China University of Mining and  
Technology, China

### \*Correspondence:

Olivier Rosanne  
olivier.rosanne@inrs.ca

### Specialty section:

This article was submitted to  
Brain Imaging Methods,  
a section of the journal  
Frontiers in Neuroscience

**Received:** 29 September 2020

**Accepted:** 08 March 2021

**Published:** 07 April 2021

### Citation:

Rosanne O, Albuquerque I, Cassani R,  
Gagnon J-F, Tremblay S and Falk TH  
(2021) Adaptive Filtering for Improved  
EEG-Based Mental Workload  
Assessment of Ambulant Users.  
*Front. Neurosci.* 15:611962.  
doi: 10.3389/fnins.2021.611962

Recently, due to the emergence of mobile electroencephalography (EEG) devices, assessment of mental workload in highly ecological settings has gained popularity. In such settings, however, motion and other common artifacts have been shown to severely hamper signal quality and to degrade mental workload assessment performance. Here, we show that classical EEG enhancement algorithms, conventionally developed to remove ocular and muscle artifacts, are not optimal in settings where participant movement (e.g., walking or running) is expected. As such, an adaptive filter is proposed that relies on an accelerometer-based referential signal. We show that when combined with classical algorithms, accurate mental workload assessment is achieved. To test the proposed algorithm, data from 48 participants was collected as they performed the Revised Multi-Attribute Task Battery-II (MATB-II) under a low and a high workload setting, either while walking/jogging on a treadmill, or using a stationary exercise bicycle. Accuracy as high as 95% could be achieved with a random forest based mental workload classifier with ambulant users. Moreover, an increase in gamma activity was found in the parietal cortex, suggesting a connection between sensorimotor integration, attention, and workload in ambulant users.

**Keywords:** EEG, physical activity, amplitude modulation features, wearable sensors, adaptive filtering, mental workload assessment

## 1. INTRODUCTION

Many professions, such as first responders (firemen, policemen, paramedics) and pilots are often faced with cognitive challenges including information overload, multitasking, interruptions, and fatigue. All these factors increase stress and reduce the efficiency with which this complex set of tasks is performed (Grtner et al., 2019). In many cases, these individuals are also exposed to a combination of physical and mental factors that further contribute to a high mental workload (MW), thus resulting in increased chances for errors, which could be life threatening. As such, MW monitoring has gained popularity in recent years.

Mental workload assessment can follow three methods: subjective, behavioral, or instrumental/objective. Subjective assessment relies on users reporting their perceived levels of mental workload and the NASA task load index (TLX) (Hart and Staveland, 1988; Cao et al., 2009) has been widely used. Behavioral methods, in turn, rely on task performance metrics (e.g., accuracy, response times, error rate) to characterize MW states. As can be seen, it is difficult for subjective and behavioral assessment methods to provide real-time measures of MW, thus

have limited applications in closed-loop systems to improve task performance. This is where instrumental or objective methods have filled a gap. With such systems, real-time correlates of MW are obtained and unobtrusive neuronal and physiological measures have been explored, such as electroencephalography (EEG), electrocardiography (ECG), and galvanic skin response, amongst others.

With the popularization of wearable devices and improved dry electrode technologies, EEGs have emerged as a potential candidate for automated instrumental MW assessment (Lean and Shan, 2012; Mullen et al., 2015). Successful applications have been shown in aircraft pilots and car drivers (Borghini et al., 2014), and air traffic controllers (Aricò et al., 2016), to name a few. Numerous different features have been explored and shown useful, including power spectral, magnitude, and phase coherence (Aghajani and Omurtag, 2016; Dimitrakopoulos et al., 2017; So et al., 2017). For example, increases in theta and decreases in alpha band powers have been shown in prefrontal and parietal brain regions when task difficulty increases (Borghini et al., 2014). Temporal complexity measures have also shown some robustness against ocular and muscular artifacts (Tiwari et al., 2019) and spectro-temporal measures have been shown to provide complementary information to conventional power spectral ones (Albuquerque et al., 2019). Most available works, however, have relied on stationary users, such as sitting pilots and drivers (Borghini et al., 2014; Johnson et al., 2015), or have controlled for body movements (Hogervorst et al., 2014).

Practical applications, however, have users that are highly ambulatory (e.g., first responders). It is known that dry electrodes are very sensitive to movement artifacts, which could severely hamper MW monitoring performance (Morikawa et al., 2013). In our previous work, we explored the use of several conventional EEG enhancement algorithms to gauge their benefits in instrumental measurement of MW in highly ecological settings (Rosanne et al., 2019). We found that while some improvements were seen relative to using noisy raw data, overall MW measurement performance levels remained lower than what has typically been reported for stationary users. This is due to the fact that existing enhancement algorithms have been developed and optimized to remove muscle and eye blink/movement artifacts, and not necessarily movement artifacts seen with, e.g., running.

To overcome this limitation, here we propose the use of an adaptive filter to remove movement-specific motion artifacts from mobile EEG data. Accelerometry signals measured from the participant's torsos are used as reference signals for the adaptive filter. The algorithm was tested on a database collected in-house from 48 participants while they performed the Multi-Attribute Task Battery-II (Santiago-Espada et al., 2011) under two workload conditions (low and high) and two physical activity (PA) types (stationary bike and treadmill), each at three activity levels (none, medium, and high). Experimental results show the proposed algorithm accurately removing body movement artifacts and resulting in MW monitoring performance as high as 97% and independent of activity type and level.

Lastly, with the enhanced signals available, we conducted an in-depth analysis of the top features selected for MW assessment,

thus obtaining insights into the cognitive processes involved during the workload task under physical activity. We found typical patterns related to visuo-motor control, attention, and fronto-parietal communication; patterns that would otherwise have been lost due to movement artifacts.

The remainder of this paper is organized as follows: section II describes the materials and methods used in the experiment. Section III presents and discusses the obtained results, and section IV presents the study conclusions.

## 2. MATERIALS AND METHODS

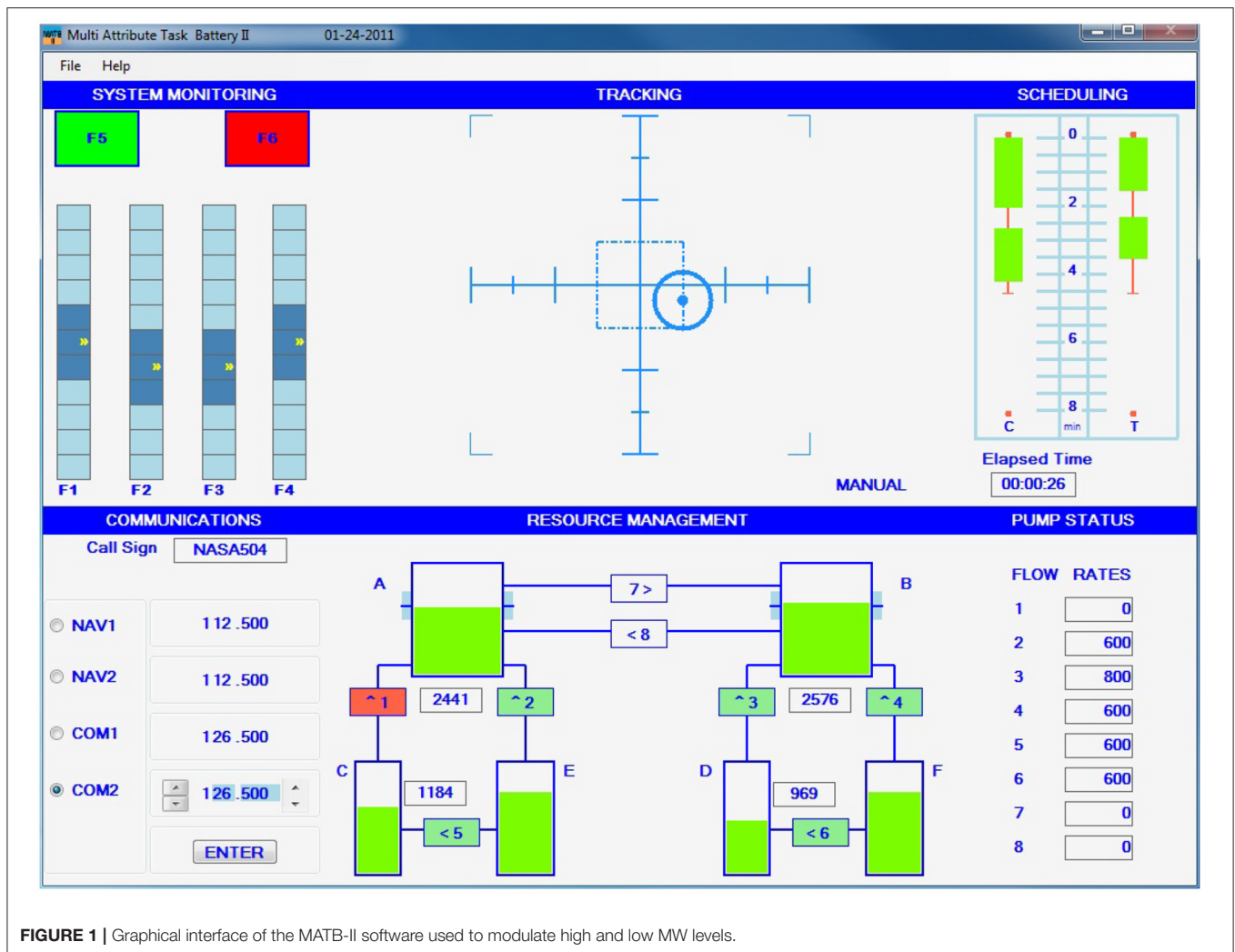
### 2.1. Data Collection

Data was collected from 48 participants (23 females,  $27.4 \pm 6.6$  year old), of which 22 utilized a treadmill during the experiment and 26 a stationary bike. Participants using the treadmill were asked to wear a safety harness around their chest in order to avoid falls. The experimental protocol was approved by the Ethics Boards at INRS and Université Laval, participants provided written consent, and were monetarily compensated for their time.

The experimental protocol comprised two MW levels (low/high) elicited through the MATB-II software, which has participants executing three simultaneous tasks: system monitoring, tracking, and resource management, as presented in **Figure 1**. Low and high MW settings were implemented based on changing the difficulty levels for each of the three tasks. As an example, a low MW task was composed by “easy” versions of the three tasks. Participants used an Xbox 360 joystick to interact with the MATB-II interface.

While executing MATB-II, subjects were asked to either bike or walk/jog on a treadmill at three levels of physical activity (PA): no movement, medium (treadmill: 3 km/h, bike: 50 rpm), and high (treadmill: 5 km/h, bike: 70 rpm). In total, six combinations of MW and physical activity were tested. The experiment was then split into six sessions, each one corresponding to one of the six combinations described above, counterbalanced to avoid ordering effects. Each session took 10 min to run and was systematically followed by a 5-min break. Before every session, two baseline periods were recorded. The first corresponded to 1 min without task nor physical activity. The second, in turn, corresponded to 1 min with only physical activity at the same level to be executed in the upcoming session. At the end of the experiment, each subject was asked to fill the NASA-TLX questionnaire (Hart and Staveland, 1988) to subjectively evaluate their perceived workload levels, as well as the reported their fatigue levels using the Borg scale (Borg, 1998).

EEG data was acquired from the participants using the Neurolectics Enobio 8-channel portable headset with the following channel locations according to the international 10–20 system: Fp1, Fp2, AF7, AF8, T9, T10, P3, P4 (see **Figure 2**). Signals were collected at a sampling rate 500 Hz and were later downsampled to 250 Hz. Two virtual inter-hemispheric bipolar signals were also computed, namely Fp1-Fp2 and P3-P4. Movement activity was also recorded with a sampling rate of 50 Hz using the embedded accelerometer available in the Zephyr Bioharness wearable device, which was placed on the chest of each subject. Accelerometry data was upsampled to 250 Hz to



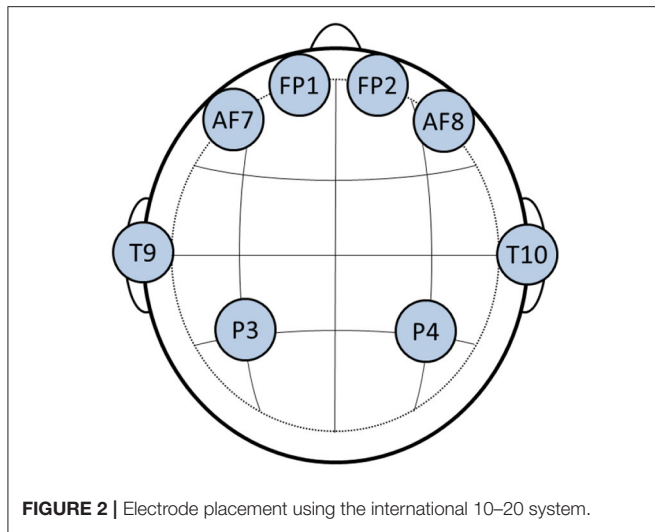
coincide with the EEG data. The interested reader is referred to Albuquerque et al. (2020) for more details about the database.

## 2.2. Movement Artifacts

To illustrate the effects of movement, particularly in the walking/jogging conditions, **Figure 3** depicts the average spectral representation of each of the eight EEG channels, as well as that of the accelerometer signals (bottom plot) during 10 s of the high physical activity condition. Here, the accelerometer signal corresponds to a L2-normalization of the accelerometer x, y, and z axes. As can be seen, particularly for the frequency range below 10 Hz, there is a significant effect from gait/movement on the EEG spectra, something previously reported in the literature (Zhang et al., 2014; Nathan and Contreras-Vidal, 2016). As movement artifacts are known to be detrimental to EEG quality (Gao et al., 2010; McMenamin et al., 2011), this has motivated the proposal of an adaptive filter using the accelerometer signal as a reference signal.

Movement artifacts observed in EEG signals can be caused either by a relative movement between the skin and the electrode (Burbank and Webster, 1978) or by a change in electrical

potential when the skin stretches and contracts during movement (de Talhouet and Webster, 1996; Kearney et al., 2007). Movement artifacts have been reported to span spectral content between 0.11 and 20 Hz (Bouten et al., 1997), thus overlap with frequency bands relevant for mental workload monitoring (Mak et al., 2013). Conventional EEG enhancement algorithms, traditionally developed for ocular and muscle artifacts (Urigüen and Garcia-Zapirain, 2015; Mucarquer et al., 2019; Zou et al., 2019), have been shown to help with ambulatory users. For example, in Gwin et al. (2010), independent component analysis (ICA) and component-based template regression was used to remove gait movement artifacts from EEG event related potentials. ICA-based decomposition was also used to remove head movements in Onikura and Iramina (2015). Notwithstanding, these conventional solutions have been shown to interfere with MW assessment (Rosanne et al., 2019). Moreover, ICA-based enhancement methods typically rely on human intervention to remove artifactual components, thus have limited use in real-time applications. Adaptive filtering, in turn, has been used to reduce head movement artifacts (Mihajlović et al., 2014) and simulated random noise in EEGs (Raya and Sison, 2002). To the best of



our knowledge, however, the use of adaptive filtering, with or without combined “blind” filtering approaches (i.e., that do not rely on human intervention), has yet to be quantified for EEG-based mental workload monitoring of ambulant users. We aim to fill this gap.

### 2.3. Adaptive Filtering

Figure 4 depicts a block diagram of the adaptive filtering scheme explored herein. Signal  $x(n)$  corresponds to the accelerometer signal, whereas  $s(n)$  corresponds to the neuronal activity signal. From the accelerometer signal, movement artifacts are modeled and represent  $y(n)$ . When added to the neuronal activity signal  $s(n)$ , the output represents the noisy EEG signal  $d(n) = s(n) + y(n)$  recorded during physical activity. The goal of the adaptive filter is to find the optimal distortion weights  $\hat{W}(n)$  from the accelerometer signal  $x(n)$  to best estimate the movement artifacts via  $\hat{y}(n)$  and remove their effects from the noisy EEG signal via  $e(n) = d(n) - \hat{y}(n)$ .

More specifically:

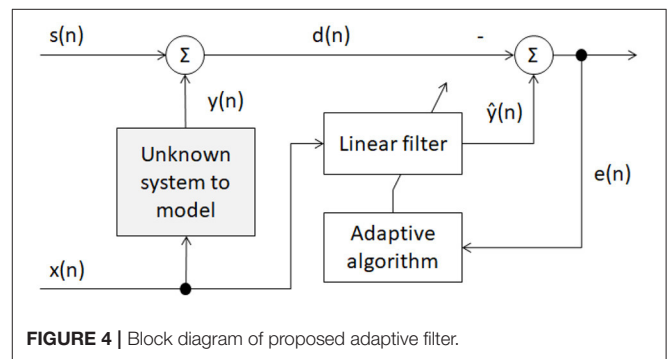
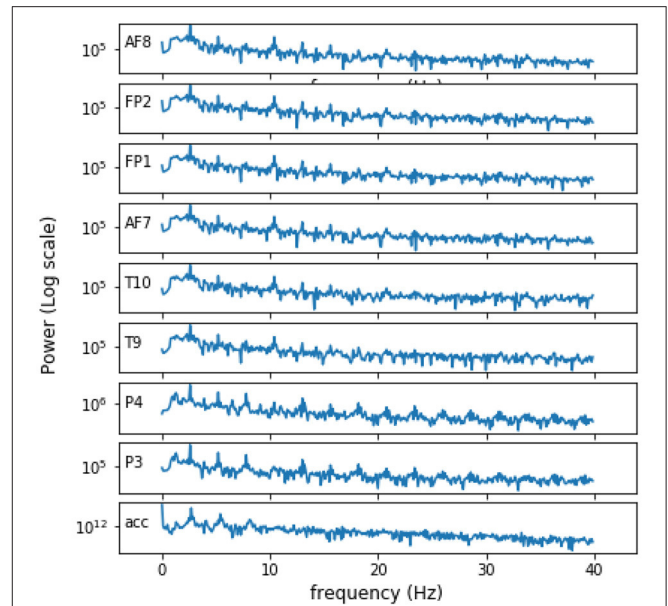
$$\hat{y}(n) = \hat{W}(n) * x(n), \tag{1}$$

and

$$\begin{aligned} e(n) &= d(n) - \hat{y}(n), \\ e(n) &= y(n) + s(n) - \hat{y}(n). \end{aligned} \tag{2}$$

The filter weights are found using the normalized least mean squares (NLMS) procedure (Diniz, 1997) for loss function  $C(n)$  using the steepest descent algorithm, i.e.:

$$\begin{aligned} \nabla_{\hat{w}^H} C(n) &= \nabla_{\hat{w}^H} \mathbb{E} [e(n)^2] \\ &= \mathbb{E} [2e(n) \nabla_{\hat{w}^H} e(n)] \\ &= -2 \mathbb{E} [x(n)e(n)], \end{aligned} \tag{3}$$



where  $\nabla$  is the gradient operator and  $\mathbb{E}[\cdot]$  the expected value. This leads to the following update rule:

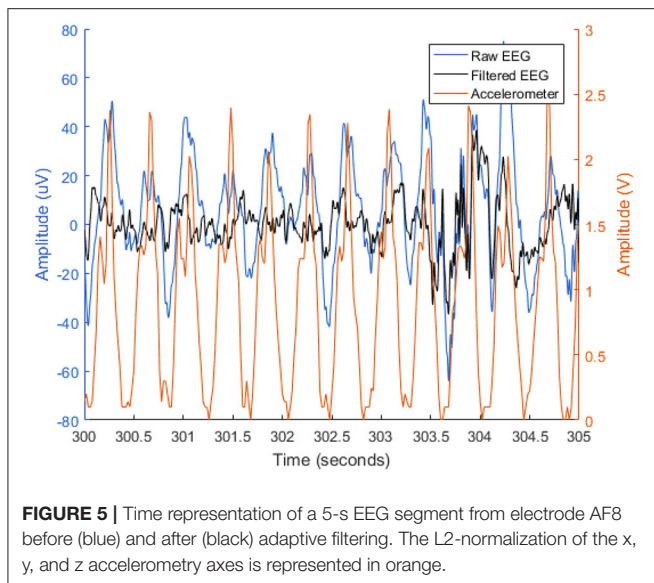
$$\hat{w}(n + 1) = \hat{w}(n) + \mu \mathbb{E}[x(n)e(n)], \tag{4}$$

where  $\mu/2$  is the step size.

We approximate the last term using the single-sample unbiased estimator  $\mathbb{E}[x(n)e(n)] = \frac{x(n)e(n)}{|x(n)|^2}$ , thus simplifying (4) to:

$$\hat{w}(n + 1) = \hat{w}(n) + \frac{\mu x(n)e(n)}{|x(n)|^2}. \tag{5}$$

Here, a filter length of 500 samples was used, corresponding to a signal duration of 2 s. Figure 5 depicts the noisy and enhanced EEG signals, as well as the accelerometry signal, to visually showcase the movement effects on the EEG signal and the effectiveness of the adaptive filter.



## 2.4. Benchmark Enhancement Algorithms

As mentioned previously, numerous EEG enhancement algorithms exist. Most have been developed to remove eye and muscular artifacts. Some are completely autonomous, whereas others rely on expert supervision. Here, four algorithms widely used for automatic (i.e., not relying on human intervention) EEG enhancement are used as benchmarks. They are used alone or in combination with each other. The following configurations are applied to the entire signals prior to epoching:

- **ASR:** artifact subspace reconstruction (ASR) is a method developed to remove transient and large-amplitude artifacts from noisy EEG. It relies on principal components analysis to reject large-variance components prior to reconstruction. The method relies on automatically identifying clean portions of the EEG signal and using these segments to determine thresholds for rejecting components. As stated in Chang et al. (2019), ASR has become the standard benchmark for EEG enhancement. The interested reader is referred to Mullen et al. (2015) for more details on the ASR method.
- **ADJUST:** Automatic EEG artifact Detection based on the Joint Use of Spatial and Temporal features (ADJUST) is an automatic artifact removal method that relies on “templates” of the effects of stereotyped artifacts (e.g., due to eye movements, blinks, and heart beats) on independent components. Components related to stereotyped artifacts are then removed and the signal is reconstructed. It has been reported that non-stereotyped artifacts, such as those due to movement, are not accurately removed with ADJUST and multiple methods are needed. More details about ADJUST can be found in Mognon et al. (2011).
- **Wavelet-ICA:** Wavelet-enhanced independent component analysis (ICA) relies on wavelet coefficient thresholding of independent components to reject artifactual components. The method has been shown to outperform conventional ICA

and to better preserve EEG spectral and phase coherence properties (Castellanos and Makarov, 2006), especially for low-density EEG configurations (Cassani et al., 2014).

- **HAPPE:** The Harvard Automated Processing Pipeline for Electroencephalography (HAPPE) is a pipeline suitable for low density EEG channels and limited data samples. It relies on wICA and multiple artifact rejection algorithm (MARA) to detect artifactual components for rejection. The interested reader is referred to Gabard-Durnam et al. (2018) for complete details on the HAPPE method.
- **Algorithm Combinations:** In addition to the combined methods approach in HAPPE, the following additional benchmark algorithmic combinations were also explored: ASR + wICA and ASR + ADJUST. Moreover, the proposed adaptive filter was also used in combination with the benchmark algorithms to explore their combined effectiveness. Henceforth, results represented as “Raw” assume no enhancement, “AF” when only the adaptive filter has been applied, and methods combined with AF will be preceded by the prefix “AF\_.”

## 2.5. Feature Extraction

Prior to feature extraction, EEG signals were first filtered with a FIR band-pass filter in the range 1–45 Hz. The following feature sets were extracted from the raw and enhanced signals:

### 2.5.1. Power Spectral Density

Power Spectral Density (PSD) features measure signal power across different subband frequencies. In this study, nine frequency bands were considered, namely:  $\delta$  (1–4 Hz),  $\theta$  (4–8 Hz),  $\alpha$  (8–12 Hz),  $\beta$  (12–30 Hz), low  $\gamma$  (30–45 Hz),  $\delta$  to  $\beta$  (1–30 Hz),  $\theta$  to  $\beta$  (4–30 Hz), low  $\alpha$  (8–10 Hz), and high  $\alpha$  (10–12 Hz). The relative power of each of these bands was calculated by normalizing per-band values by the full-band power. A total of 90 PSD features were extracted. Numerous studies have reported the usefulness of such features for mental workload assessment (Liu et al., 2017; Craik et al., 2019; Zhang et al., 2019).

### 2.5.2. Phase and Magnitude Spectral Coherence

Phase and Magnitude Spectral Coherence (PMSC) features are useful for measuring connectivity between cortical regions as these techniques measure co-variance of the phase and magnitude between two signals. The interested reader is referred to Aoki et al. (1999) for more details on PMSC computation. PMSC is computed for two pairs of electrodes, namely FP1-FP2 and P3-P4 for each 5 sub-bands ( $\delta$ ,  $\theta$ ,  $\alpha$ ,  $\beta$ ,  $\gamma$ ). A total of 20 PMSC features were extracted. These features are motivated from Zhang et al. (2014) and Zarjam et al. (2015) that have shown their usefulness in mental workload assessment.

### 2.5.3. Amplitude Modulation Rate-of-Change

Amplitude Modulation (AM) rate-of-change features quantify the rate-of-change of specific frequency sub-bands and provides insight into cross-frequency magnitude-magnitude coupling/interactions and reveals interactions between different brain processes (Tort et al., 2010; Voytek et al., 2010; Seeber et al., 2014), as well as long-range communication (Zanto et al.,

2011; Clayton et al., 2015). The interested reader is referred to Trambaioli et al. (2011) and Fraga et al. (2013) for more complete details on the measure. A total of 140 features were extracted that provide robustness against movement artifacts, as described in Albuquerque et al. (2018).

#### 2.5.4. Phase and Magnitude Spectral Coherence of Amplitude Modulation Features (PMSC-AM)

PMSC-AM extends the capacity of PMSC features to amplitude modulations. These features were recently proposed for affective state monitoring and showed useful for arousal and valence prediction (Clerico et al., 2015, 2018). They are explored here for the first time as correlates of mental workload. These features are based on the modulated signals of each band which make a total of fourteen signals per channels (see Clerico et al., 2018 for more details). After splitting the signals into epochs, the magnitude spectral coherence and phase coherence is then computed for the FP1-FP2 and P3-P4 channel pairs only. A total of 56 features were extracted.

### 2.6. Feature Selection and Ranking

Feature selection is a common step in classification tasks to remove redundant (Peng et al., 2005) or irrelevant features (Blum and Langley, 1997) and for dimensionality reduction (Fan and Fan, 2008) to improve classification performance. In this study, we rely on the so-called minimum Redundancy Maximum Relevance (mRMR) filter method (Peng et al., 2005) which not only finds the most relevant features for the task at hand, but removes features with high mutual information, thus minimizing redundancy. The algorithm has been shown to be extremely useful for EEG-based affective state assessment (e.g., Cassani et al., 2014; Clerico et al., 2018). In addition to feature selection, we further rank the importance of the top-features using a wrapper-based method. It is important to emphasize that feature selection/ranking is not crucial here, given the number of features explored. Nonetheless, we use it to obtain insights into the neuronal patterns related to mental workload during activity and how such patterns may be affected by movement artifacts.

### 2.7. Classification and Hyperparameter Tuning

We are interested in exploring the effects of movement artifacts and, consequently, EEG enhancement on mental workload assessment. Here, we assume the binary problem of classifying low vs. high mental workload levels. Two conventional classifiers are explored, namely random forest (RF) (Qi, 2012) and support vector machine (SVM). A repeated (10 times) 10-fold cross validation testing setup is used.

For hyperparameter tuning, the cross-validation grid search available in the scikit-learn library (Pedregosa et al., 2011) was explored. This approach, however, yielded a high number of trees (around 500) for the RF classifier, as compared to the amount of available data (Oshiro et al., 2012). As an alternative, we empirically fixed tree depth to 8 and stopped adding trees once the evolution of the area under the curve—receiver operating characteristics (AUC-ROC) became constant across out-of-bag conditions. Next, a similar strategy was used to optimize tree

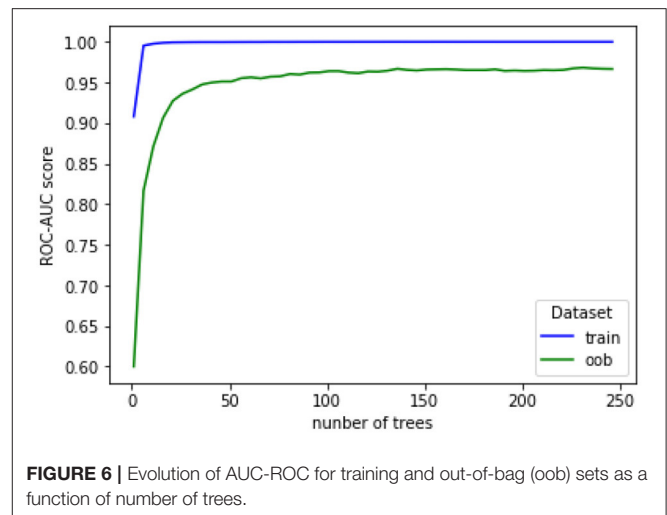


**FIGURE 6** | Evolution of AUC-ROC for training and out-of-bag (oob) sets as a function of number of trees.

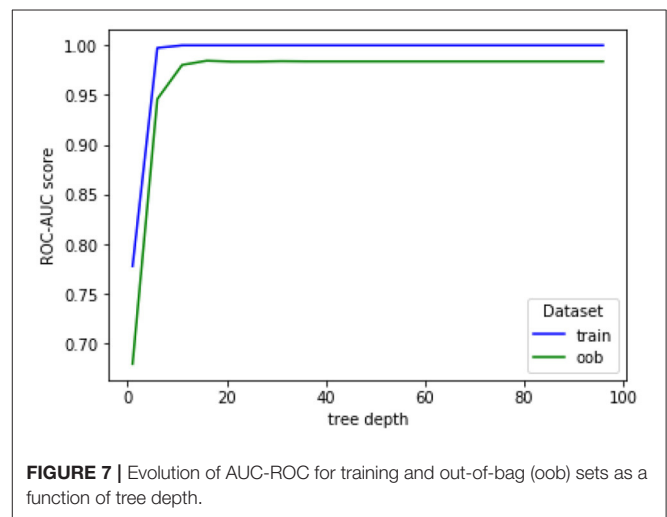
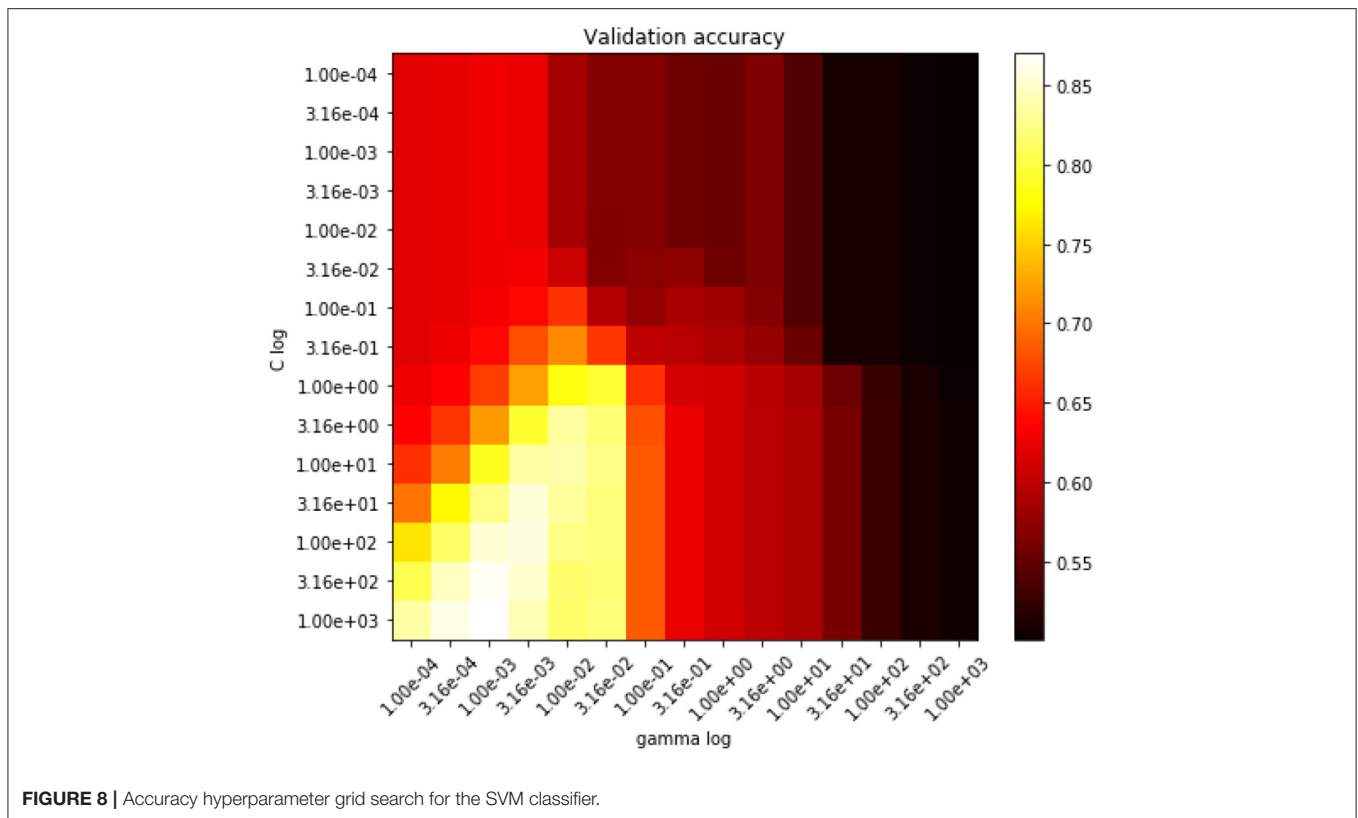


**FIGURE 7** | Evolution of AUC-ROC for training and out-of-bag (oob) sets as a function of tree depth.

depth and we fixed the number of trees to the value found in the previous analysis. In both cases, a stratified 5-fold cross-validation procedure was used with all subjects to ensure reliable generalization performance.

**Figure 6** shows the evolution of AUC-ROC scores for the training and out-of-bag (oob) sets as a function of number of trees. When building each random tree in the forest, not all features and samples of the dataset are used. Instead, a small randomly-selected set called the bootstrap bag is used to build a single tree; this bag is different for each tree. The oob set, thus, corresponds to the remaining unused samples. The accuracy with the oob set is shown to stabilize at around 100 trees. Moreover, **Figure 7** depicts accuracy as a function of tree depth. As can be seen, for the out-of-bag set the accuracy plateaus at around a depth of 10. Henceforth, these values are used in our experiments.

**Figure 8** presents accuracy values obtained during a grid search to find the optimal  $C$  and  $\gamma$  values of the support vector classifier. It can be seen that the best accuracy is reached with  $C = 310$  and  $\gamma = 0.001$  with a Radial Basis Function kernel; these values are used henceforth.



### 3. RESULTS AND DISCUSSION

#### 3.1. Classification Performance

##### 3.1.1. Ablation Study

In order to estimate the impact of the adaptive filter on EEG enhancement, mental workload classification accuracy is reported with and without its use. **Tables 1, 2** present classification accuracy values for the RF and SVM classifiers, respectively. While each column corresponds to a tested benchmark enhancement algorithm, with or without (termed “Base”) adaptive filtering, each row corresponds to a specific feature set used for classification in the low and high physical activity (PA) conditions. Row labeled “All” indicates fusion of all features. Results reported are the average of a 10-fold cross-validation test setup repeated ten times by shuffling the partitions each time. Whenever the achieved results with the adaptive filter were significantly different (based on a paired *t*-test) than without, results are indicated with superscripts “†” and “‡” for  $p \leq 0.05$  and  $p \leq 0.01$ , respectively.

As can be seen from the **Tables 1, 2**, the adaptive filter significantly improved accuracy for most tested configurations, particularly for features derived from the amplitude modulation analysis, as well as for the high physical activity conditions in which movement artifacts are most pronounced. Overall, the RF classifier consistently outperformed the SVM.

For PSD based features, the best results were achieved with a combination of ASR and ADJUST methods (93.68%), followed closely by HAPPE and AF (92.96%) for low physical activity

conditions and the ASR-wICA-AF combination for high PA conditions. Similar accuracy values were achieved for the AM and PMSC feature sets. The PMSC-AM features, on the other hand, resulted in the lowest values, thus suggesting that they may not be useful for mental workload assessment when used alone. Overall, fusion of the different feature sets showed to result in the highest accuracy for both RF and SVM classifiers, thus suggesting their complementarity. The highest accuracy achieved was of 97.90% with the HAPPE-AF combination for both the high and low PA conditions. Such findings show that by combining all feature sets with the proposed adaptive filtering and HAPPE enhancement methods, the same mental workload measurement accuracy can be achieved despite physical activity levels.

##### 3.1.2. Effect of Number of Features

The results reported in **Tables 1, 2** relied on all extracted features. In order to investigate the impact of feature dimensionality on overall accuracy, **Figure 9** depicts the achieved accuracy as a function of number of features used, in decreasing importance, as ranked by mRMR. Here, the AF-HAPPE enhancement combination is used with the RF classifier and the average accuracy over a single 10-fold cross-validation setup is used. For this comparison, default classifier parameters are used in order to gauge the effectiveness of the features *per se*, and not the classifier. As can be seen, sharp increases in accuracy are achieved with the first 60 features and then slight increases occur after 100 and then 200 features are considered. A small gap is seen for both low and

**TABLE 1 |** RF mental workload classification accuracy for different feature and enhancement algorithm configurations.

Random forest		Raw		ASR		ADJUST		HAPPE		ASR_ADJUST		ASR_wICA		wICA	
		Base	AF	Base	AF	Base	AF	Base	AF	Base	AF	Base	AF	Base	AF
PSD	low PA	86.27	85.59 <sup>‡</sup>	88.60	89.71 <sup>‡</sup>	89.23	88.89	86.25	92.96 <sup>‡</sup>	93.68	90.37 <sup>‡</sup>	92.34	92.73	88.66	90.87 <sup>‡</sup>
	high PA	87.15	85.05 <sup>‡</sup>	89.55	89.89	89.92	89.76	89.57	90.91 <sup>‡</sup>	89.14	91.80 <sup>‡</sup>	94.13	94.61 <sup>‡</sup>	89.14	91.69 <sup>‡</sup>
AM	low PA	83.91	84.28 <sup>‡</sup>	84.78	86.48 <sup>‡</sup>	88.12	88.26	83.90	91.93 <sup>‡</sup>	91.94	87.28 <sup>‡</sup>	87.26	89.47 <sup>‡</sup>	84.83	87.88 <sup>‡</sup>
	high PA	83.83	84.77 <sup>‡</sup>	86.84	89.21 <sup>‡</sup>	88.27	89.08 <sup>‡</sup>	87.33	89.36 <sup>‡</sup>	87.62	89.13 <sup>‡</sup>	90.91	92.60 <sup>‡</sup>	85.59	89.27 <sup>‡</sup>
PMSC	low PA	84.23	85.76 <sup>‡</sup>	82.67	82.66	90.05	92.26 <sup>‡</sup>	87.85	95.15 <sup>‡</sup>	89.38	87.08 <sup>‡</sup>	84.33	82.44 <sup>‡</sup>	84.66	86.03 <sup>‡</sup>
	high PA	82.07	82.78 <sup>‡</sup>	80.74	79.95 <sup>‡</sup>	86.79	88.08 <sup>‡</sup>	89.80	90.51 <sup>‡</sup>	89.90	84.84 <sup>‡</sup>	82.44	80.46 <sup>‡</sup>	81.31	83.81 <sup>‡</sup>
PMSC-AM	low PA	65.79	70.81 <sup>‡</sup>	67.89	68.32	66.62	71.92 <sup>‡</sup>	73.84	78.34 <sup>‡</sup>	67.77	64.99 <sup>‡</sup>	70.18	67.48 <sup>‡</sup>	65.56	70.19 <sup>‡</sup>
	high PA	67.90	74.10 <sup>‡</sup>	67.57	67.66	69.59	70.56 <sup>‡</sup>	71.46	75.71 <sup>‡</sup>	68.46	64.78 <sup>‡</sup>	67.75	67.05 <sup>‡</sup>	68.59	72.09 <sup>‡</sup>
All	low PA	89.17	95.03 <sup>‡</sup>	90.23	94.32 <sup>‡</sup>	92.55	95.65 <sup>‡</sup>	93.24	97.90 <sup>‡</sup>	96.21	93.56 <sup>‡</sup>	93.61	95.86 <sup>‡</sup>	90.49	96.22 <sup>‡</sup>
	high PA	88.89	91.20 <sup>‡</sup>	90.77	93.39 <sup>‡</sup>	94.22	95.36 <sup>‡</sup>	94.54	97.89 <sup>‡</sup>	93.36	93.54	94.95	95.19	90.20	93.97 <sup>‡</sup>

**TABLE 2 |** SVM mental workload classification accuracy for different feature and enhancement algorithm configurations.

SVM		Raw		ASR		ADJUST		HAPPE		ASR_ADJUST		ASR_wICA		wICA	
		Base	AF	Base	AF	Base	AF	Base	AF	Base	AF	Base	AF	Base	AF
PSD	low PA	59.31	59.35	61.72	60.16 <sup>‡</sup>	64.08	67.16 <sup>‡</sup>	67.98	73.57 <sup>‡</sup>	70.72	71.37	66.66	63.13 <sup>‡</sup>	59.99	59.82
	high PA	64.22	66.56 <sup>‡</sup>	65.78	67.81 <sup>‡</sup>	68.40	70.00 <sup>‡</sup>	67.56	73.58 <sup>‡</sup>	67.61	71.91 <sup>‡</sup>	69.29	70.96 <sup>‡</sup>	64.79	70.07 <sup>‡</sup>
AM	low PA	56.75	59.03 <sup>‡</sup>	58.37	61.05 <sup>‡</sup>	61.63	69.18 <sup>‡</sup>	62.69	73.39 <sup>‡</sup>	69.48	68.65 <sup>‡</sup>	60.74	62.74 <sup>‡</sup>	56.15	59.63 <sup>‡</sup>
	high PA	62.49	65.35 <sup>‡</sup>	66.67	64.64 <sup>‡</sup>	68.88	69.66 <sup>‡</sup>	66.16	70.94 <sup>‡</sup>	68.45	70.36 <sup>‡</sup>	68.80	66.77 <sup>‡</sup>	63.27	67.22 <sup>‡</sup>
PMSC	low PA	60.25	72.25 <sup>‡</sup>	60.70	69.61 <sup>‡</sup>	61.59	68.45 <sup>‡</sup>	63.94	75.11 <sup>‡</sup>	70.45	68.22 <sup>‡</sup>	61.06	69.71 <sup>‡</sup>	61.07	73.27 <sup>‡</sup>
	high PA	60.43	71.86 <sup>‡</sup>	65.79	68.48 <sup>‡</sup>	67.97	69.62 <sup>‡</sup>	70.80	72.98 <sup>‡</sup>	72.09	67.64 <sup>‡</sup>	66.35	69.04 <sup>‡</sup>	60.05	71.34 <sup>‡</sup>
PMSC-AM	low PA	56.05	62.53 <sup>‡</sup>	56.57	58.89 <sup>‡</sup>	56.03	62.04 <sup>‡</sup>	59.83	65.23 <sup>‡</sup>	59.37	58.68 <sup>‡</sup>	56.60	58.04 <sup>‡</sup>	55.36	59.79 <sup>‡</sup>
	high PA	59.35	65.37 <sup>‡</sup>	59.63	60.29	61.36	61.69	59.11	63.43 <sup>‡</sup>	58.49	58.61	59.96	62.62 <sup>‡</sup>	60.10	64.21 <sup>‡</sup>
All	low PA	64.94	78.34 <sup>‡</sup>	66.59	73.54 <sup>‡</sup>	73.28	80.25 <sup>‡</sup>	78.88	87.49 <sup>‡</sup>	76.60	79.58 <sup>‡</sup>	68.22	75.37 <sup>‡</sup>	66.87	77.39 <sup>‡</sup>
	high PA	71.37	81.09 <sup>‡</sup>	73.31	76.26 <sup>‡</sup>	78.33	81.03 <sup>‡</sup>	79.38	86.93 <sup>‡</sup>	78.94	77.88 <sup>‡</sup>	74.42	77.72 <sup>‡</sup>	71.22	81.86 <sup>‡</sup>

high physical activity conditions once all 306 features are used. If feature dimensionality is of concern, the achieved results and the small gap between low and high PA conditions suggest that 236 features can be a good compromise (94 and 90%, low and high PA, respectively), followed by 111 features (91 and 87%, low and high PA, respectively). For comparison, with the top-60 features, accuracy of 84 and 88% are achieved, respectively.

### 3.2. Top-Ranking Features

To obtain insights from top-selected features, we performed an in-depth analysis of the top-60 features selected from the combined “All” feature set in the low and high physical activity conditions using both the raw data and the top-performing AF\_HAPPE enhanced data; **Table 3** lists these features.

As can be seen, for all conditions tested, modulation spectral features resulted in the majority of the top 60 features. For example, for the high PA conditions without and with AF\_HAPPE processing, they corresponded to 50 and 70% of the top features, respectively. This corroborates findings from Albuquerque et al. (2018, 2019) and Clerico et al. (2018) that show the importance of such features for mental workload and affective state assessment, as well as their robustness to movement artifacts.

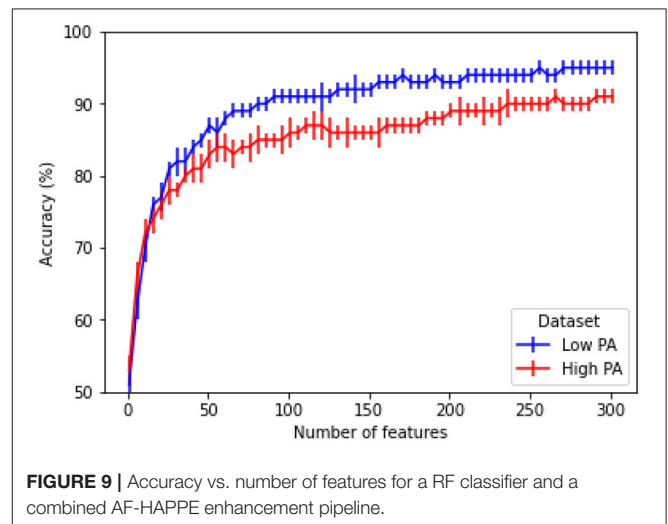


**FIGURE 9 |** Accuracy vs. number of features for a RF classifier and a combined AF-HAPPE enhancement pipeline.

Coherence based measures, in turn, were the second top-performing features and appeared mostly in high PA conditions. They represented ~17 and 18% of the top features for the raw and enhanced conditions, respectively. Coherence measures

**TABLE 3 |** Top-60 features for different physical activity (PA) and signal processing conditions.

Raw		AF_HAPPE	
Low PA	High PA	Low PA	High PA
$\beta$ -m $\alpha$ -P4	msc- $\beta$ -m $\theta$ -FP1-FP2	$\gamma$ -m $\gamma$ -FP1-FP2	phc- $\beta$ -m $\delta$ -FP1-FP2
$\alpha$ -m $\delta$ -AF8	msc- $\delta$ -P3-P4	$\delta$ -P3-P4	$\gamma$ -m $\delta$ -P4
tab-FP1	$\gamma$ -m $\delta$ -T10	$\gamma$ -m $\beta$ -P4	$\beta$ -m $\delta$ -T9
$\alpha$ -AF8	$\alpha$ -m $\theta$ -T10	$\alpha$ 1-T9	$\gamma$ -m $\theta$ -AF8
$\theta$ -m $\theta$ -FP1	$\alpha$ -m $\delta$ -FP1	$\beta$ -m $\alpha$ -AF7	$\beta$ -m $\theta$ -AF8
$\gamma$ -m $\delta$ -P4	$\gamma$ -m $\theta$ -FP2	$\theta$ -m $\theta$ -T9	$\beta$ -m $\theta$ -P4
$\gamma$ -m $\theta$ -T10	$\beta$ -m $\delta$ -AF7	$\gamma$ -m $\delta$ -P4	$\gamma$ -m $\delta$ -AF8
$\theta$ -m $\theta$ -T9	$\beta$ -m $\theta$ -P4	dtab-T10	$\theta$ -m $\theta$ -P3-P4
$\theta$ -m $\theta$ -FP1-FP2	$\beta$ -m $\delta$ -FP1-FP2	$\beta$ -m $\theta$ -AF7	tab-FP2
$\theta$ -m $\theta$ -T10	$\beta$ -m $\delta$ -T10	$\theta$ -P3-P4	$\gamma$ -m $\alpha$ -FP1-FP2
$\alpha$ 1-FP1-FP2	$\alpha$ -m $\theta$ -AF8	$\delta$ -m $\delta$ -FP1	$\alpha$ -T9
$\alpha$ -m $\theta$ -P3	$\alpha$ -m $\delta$ -P3	$\gamma$ -m $\theta$ -FP2	$\gamma$ -m $\delta$ -FP2
$\gamma$ -m $\theta$ -FP2	msc- $\alpha$ -m $\delta$ -FP1-FP2	$\gamma$ -m $\delta$ -P3	$\beta$ -T9
$\gamma$ -m $\beta$ -FP2	$\alpha$ -FP2	tab-T9	msc- $\gamma$ -m $\delta$ -FP1-FP2
$\theta$ -m $\delta$ -FP1-FP2	$\beta$ -m $\alpha$ -P4	$\beta$ -m $\delta$ -P3	$\beta$ -m $\delta$ -FP2
$\alpha$ -m $\theta$ -P3-P4	$\alpha$ -AF8	$\gamma$ -m $\delta$ -FP2	$\alpha$ 2-P4
$\gamma$ -m $\alpha$ -P3	$\theta$ -m $\delta$ -FP1-FP2	dtab-T9	dtab-P3
dtab-T9	$\alpha$ 2-T10	$\theta$ -m $\theta$ -FP1-FP2	$\gamma$ -m $\theta$ -T10
$\beta$ -m $\beta$ -P3-P4	$\theta$ -FP2	$\gamma$ -m $\beta$ -AF8	$\beta$ -m $\theta$ -FP2
tab-T9	tab-FP2	$\gamma$ -m $\delta$ -FP1	$\gamma$ -P3
$\delta$ -m $\delta$ -AF7	$\alpha$ 2-T9	$\beta$ -P3	$\beta$ -m $\theta$ -T9
phc- $\delta$ -m $\delta$ -P3-P4	$\beta$ -m $\theta$ -P3	$\gamma$ -m $\gamma$ -FP2	$\gamma$ -m $\theta$ -FP2
$\gamma$ -m $\beta$ -P4	$\gamma$ -m $\alpha$ -P3-P4	$\theta$ -m $\delta$ -FP1	$\gamma$ -m $\beta$ -P3
$\beta$ -m $\beta$ -T9	$\gamma$ -m $\alpha$ -FP2	phc- $\beta$ -m $\theta$ -P3-P4	$\gamma$ -FP1
$\beta$ -m $\beta$ -P3	$\theta$ -T10	$\gamma$ -m $\gamma$ -P3	$\delta$ -AF8
dtab-AF7	$\beta$ -m $\delta$ -P3-P4	$\theta$ -m $\theta$ -P3	$\beta$ -m $\alpha$ -FP1-FP2
$\gamma$ -m $\alpha$ -FP2	dtab-T9	$\gamma$ -m $\gamma$ -FP1	$\gamma$ -m $\theta$ -FP1-FP2
$\theta$ -T10	$\beta$ -T10	$\beta$ -m $\theta$ -FP1	$\gamma$ -m $\theta$ -P4
$\gamma$ -m $\alpha$ -T9	tab-T10	$\gamma$ -m $\gamma$ -P3-P4	$\delta$ -m $\delta$ -FP1
$\theta$ -m $\theta$ -AF8	$\gamma$ -T9	$\gamma$ -m $\beta$ -FP1-FP2	$\beta$ -m $\alpha$ -AF7
$\gamma$ -m $\theta$ -P3	$\theta$ -m $\theta$ -P3	$\beta$ -m $\alpha$ -P3	$\theta$ -m $\delta$ -P4
$\gamma$ -T10	dtab-FP1	$\gamma$ -m $\theta$ -FP1	msc- $\beta$ -m $\theta$ -FP1-FP2
$\delta$ -AF7	$\beta$ -P3	$\alpha$ 2-T9	$\delta$ -m $\delta$ -AF8
$\delta$ -m $\delta$ -P3-P4	msc- $\gamma$ -FP1-FP2	$\beta$ -m $\delta$ -P4	tab-FP1-FP2
$\alpha$ -m $\theta$ -T10	msc- $\alpha$ -m $\theta$ -FP1-FP2	$\delta$ -m $\delta$ -P4	$\beta$ -AF8
$\beta$ -m $\delta$ -P3-P4	$\alpha$ -m $\theta$ -FP2	$\delta$ -P4	$\beta$ -m $\theta$ -P3
$\gamma$ -m $\theta$ -P3-P4	$\alpha$ 1-P3-P4	phc- $\theta$ -P3-P4	$\beta$ -P3-P4
$\beta$ -m $\delta$ -P3	$\gamma$ -m $\delta$ -P3-P4	$\gamma$ -m $\beta$ -FP1	$\gamma$ -m $\delta$ -T9
$\alpha$ -T10	$\delta$ -m $\delta$ -P4	$\gamma$ -m $\alpha$ -FP1-FP2	$\alpha$ 1-T10
$\alpha$ 2-P3-P4	$\gamma$ -P3	$\theta$ -m $\delta$ -P3	$\delta$ -m $\delta$ -FP2
$\theta$ -m $\delta$ -P4	$\alpha$ 1-T9	$\beta$ -m $\alpha$ -P4	msc- $\beta$ -m $\beta$ -FP1-FP2
$\beta$ -m $\theta$ -P3-P4	$\beta$ -m $\theta$ -P3-P4	$\beta$ -m $\theta$ -P3-P4	$\beta$ -m $\delta$ -P4
$\theta$ -m $\delta$ -T10	$\alpha$ -m $\delta$ -FP2	$\beta$ -m $\beta$ -P4	$\alpha$ -T10
msc- $\beta$ -m $\delta$ -P3-P4	$\gamma$ -T10	$\gamma$ -m $\theta$ -FP1-FP2	$\gamma$ -m $\gamma$ -T9

(Continued)

**TABLE 3 |** Continued

Raw		AF_HAPPE	
Low PA	High PA	Low PA	High PA
phc- $\beta$ -P3-P4	$\beta$ -P3-P4	$\beta$ -m $\beta$ -FP2	msc- $\delta$ -P3-P4
$\alpha$ -m $\delta$ -P4	msc- $\beta$ -m $\delta$ -FP1-FP2	$\gamma$ -m $\alpha$ -FP1	msc- $\beta$ -m $\alpha$ -FP1-FP2
$\gamma$ -FP1-FP2	$\delta$ -FP1-FP2	$\delta$ -m $\delta$ -P3-P4	msc- $\gamma$ -m $\theta$ -FP1-FP2
$\theta$ -P3-P4	msc- $\gamma$ -m $\theta$ -FP1-FP2	$\gamma$ -m $\beta$ -FP2	$\gamma$ -m $\alpha$ -P3-P4
phc- $\delta$ -P3-P4	$\beta$ -P4	$\delta$ -FP1-FP2	$\gamma$ -m $\alpha$ -T9
$\alpha$ 1-P3-P4	tab-P4	$\gamma$ -m $\beta$ -P3-P4	$\delta$ -m $\delta$ -P4
$\beta$ -m $\delta$ -T9	$\delta$ -T9	$\beta$ -m $\beta$ -FP1-FP2	msc- $\delta$ -FP1-FP2
$\alpha$ 1-T9	dtab-T10	$\gamma$ -T10	$\beta$ -m $\delta$ -AF7
$\gamma$ -m $\delta$ -P3-P4	$\alpha$ -m $\delta$ -T10	$\gamma$ -m $\gamma$ -T10	$\beta$ -m $\beta$ -P3-P4
$\theta$ -P4	msc- $\beta$ -FP1-FP2	$\gamma$ -m $\beta$ -T10	$\gamma$ -m $\theta$ -AF7
$\alpha$ 2-P4	msc- $\theta$ -FP1-FP2	$\gamma$ -m $\alpha$ -P3-P4	$\gamma$ -m $\theta$ -P3-P4
dtab-P3	dtab-P4	$\beta$ -m $\delta$ -P3-P4	$\gamma$ -m $\beta$ -P3-P4
$\theta$ -FP2	$\delta$ -P3-P4	$\theta$ -m $\delta$ -P3-P4	msc- $\theta$ -FP1-FP2
$\beta$ -FP2	tab-T9	$\alpha$ -m $\delta$ -T9	$\beta$ -m $\theta$ -AF7
$\alpha$ 2-T9	msc- $\delta$ -FP1-FP2	dtab-FP1	msc- $\alpha$ -FP1-FP2
$\alpha$ -P3	$\beta$ -FP2	$\gamma$ -m $\alpha$ -T10	phc- $\gamma$ -FP1-FP2

Feature names are self explanatory and follow the feature-electrode notation; "tab" corresponds to 4–30 Hz spectral subband power; "dtab" to 1–30 Hz; "phc" to phase coherence; and "msc" to magnitude square coherence.

have been linked movement and visual-motion discrimination and are indicative of the additional mental resources involved during physical activity (Händel and Haarmeier, 2009; Cheron et al., 2016). The important coherence features were mostly extracted from the pre-frontal regions, which have been linked to mental workload and attention (Mandrick et al., 2013), while a few were extracted from parietal regions, thus suggesting some contribution of balance control also involved (Hülsdünker et al., 2015).

Regarding brain hemispheres, features from the right regions were selected slightly more often than the left hemisphere, particularly in high PA conditions. This corroborates previous work (Perennou et al., 1999) that has shown the existence of a right hemispheric dominance for postural control. Inter-hemispheric signals, in turn, corresponded to roughly 33% of the top features for all PA conditions. Within the top features, inter-hemispheric parietal features typically appeared in low PA conditions, whereas inter-hemispheric pre-frontal features appeared during high PA conditions. This suggests a shift in visuo-motor (Iacoboni and Zaidel, 2004) and attention (Vossel et al., 2016) aspects during low PA, to more complex motor behaviors and sensorimotor integration aspects with high PA (Geschwind and Iacoboni, 1999). Overall, in the enhancement scenario, the parietal regions were responsible for the majority of the top features, followed closely by the pre-frontal cortex, for both low and high PA conditions. These results are in line with the classical mental workload literature with non-ambulant users (Aoki et al., 1999; Holm et al., 2009; Borghini et al., 2012;

Mandrick et al., 2013; Käthner et al., 2014; Al-Shargie, 2019), thus further showing the promise of the proposed adaptive filtering scheme.

Lastly, regarding EEG subband frequencies, as expected, adaptive filtering combined with HAPPE reduced the importance of features extracted from  $\theta$  and  $\alpha$  bands, as these have the highest overlap with the accelerometry data. It did, on the other hand, boost the importance of features extracted from the  $\beta$  and  $\gamma$  bands. It is well-known that  $\gamma$  is highly sensitive to muscle activity (Muthukumaraswamy, 2013) and HAPPE is known to remove such artifacts. With the proposed enhancement scheme,  $\gamma$  features (and  $\gamma - m\delta$ ) remained consistent between low and high PA conditions and covered aspects related to sensory motor integration (Aoki et al., 1999; Sauseng et al., 2015), attention (Sammer et al., 2007; Wang et al., 2017), and balance control (Gwin et al., 2011; Sipp et al., 2013). The importance of the  $\beta$  band, in turn, has been observed in other studies during intense physical exercises (Rahman et al., 2019), anticipation in a decision making game (Cohen et al., 2009) and increment of cognitive control and attention (Kakkos et al., 2019).

## 4. CONCLUSIONS

This paper has proposed the use of an adaptive filtering scheme to remove movement artifacts from EEG signals for robust mental workload assessment. Experimental results have shown that the proposed adaptive filtering scheme is best combined with HAPPE and can result in 97% mental workload prediction accuracy for both low and high physical activity conditions. Moreover, an in-depth analysis of the top-selected features have shown the

importance of modulation spectral features for the task at hand, as well as the potential of the proposed enhancement solution at maintaining important discriminant information from the EEG for mental workload measurement, in particular those captured by  $\gamma$  frequency band-based features.

## DATA AVAILABILITY STATEMENT

The raw data supporting the conclusions of this article will be made available by the authors, without undue reservation.

## ETHICS STATEMENT

The studies involving human participants were reviewed and approved by Ethics Review Boards of INRS, Université Laval, and the PERFORM Centre (Concordia University). The patients/participants provided their written informed consent to participate in this study.

## AUTHOR CONTRIBUTIONS

OR, IA, RC, and J-FG: statistical analysis and programming. OR, IA, and RC: data collection. ST and TF: funding and supervision. All authors experimental design, writing, and reviewing.

## ACKNOWLEDGMENTS

The authors wish to acknowledge funding from NSERC, MITACS, PROMPT, and Thales Digital Solutions Inc. The grant number for NSERC is CRDPJ 485455-15.

## REFERENCES

- Aghajani, H., and Omurtag, A. (2016). "Assessment of mental workload by EEG+fNIRS," in *2016 38th Annual International Conference of the IEEE Engineering in Medicine and Biology Society (EMBC)* (Orlando, FL: IEEE), 3773–3776. doi: 10.1109/EMBC.2016.7591549
- Albuquerque, I., Rosanne, O., Gagnon, J. F., Tremblay, S., and Falk, T. H. (2019). "Fusion of spectral and spectro-temporal eeg features for mental workload assessment under different levels of physical activity," in *2019 9th International IEEE/EMBS Conference on Neural Engineering (NER)* (San Francisco, CA: IEEE), 311–314. doi: 10.1109/NER.2019.8717092
- Albuquerque, I., Tiwari, A., Gagnon, J. F., Lafond, D., Parent, M., Tremblay, S., et al. (2018). "On the analysis of EEG features for mental workload assessment during physical activity," in *2018 IEEE International Conference on Systems, Man, and Cybernetics (SMC)* (Miyazaki: IEEE), 538–543. doi: 10.1109/SMC.2018.00101
- Albuquerque, I., Tiwari, A., Parent, M., Cassani, R., Gagnon, J.-F., Lafond, D., et al. (2020). WAUC: a multi-modal database for mental workload assessment under physical activity. *Front. Neurosci.* 14:549524. doi: 10.3389/fnins.2020.549524
- Al-Shargie, F. (2019). *Multilevel Assessment of Mental Stress Using SVM With EEOC: An EEG Approach*. engrXiv.
- Aoki, F., Fetz, E., Shupe, L., Lettich, E., and Ojemann, G. (1999). Increased gamma-range activity in human sensorimotor cortex during performance of visuomotor tasks. *Clin. Neurophysiol.* 110, 524–537. doi: 10.1016/S1388-2457(98)00064-9
- Aricò, P., Borghini, G., Di Flumeri, G., Colosimo, A., Bonelli, S., Golfetti, A., et al. (2016). Adaptive automation triggered by eeg-based mental workload index: a passive brain-computer interface application in realistic air traffic control environment. *Front. Hum. Neurosci.* 10:539. doi: 10.3389/fnhum.2016.00539
- Blum, A. L., and Langley, P. (1997). Selection of relevant features and examples in machine learning. *Artif. Intell.* 97, 245–271. doi: 10.1016/S0004-3702(97)00063-5
- Borg, G. (1998). *Borg's Perceived Exertion and Pain Scales*. Human Kinetics.
- Borghini, G., Astolfi, L., Vecchiato, G., Mattia, D., and Babiloni, F. (2014). Measuring neurophysiological signals in aircraft pilots and car drivers for the assessment of mental workload, fatigue and drowsiness. *Neurosci. Biobehav. Rev.* 44, 58–75. doi: 10.1016/j.neubiorev.2012.10.003
- Borghini, G., Vecchiato, G., Toppi, J., Astolfi, L., Maglione, A., Isabella, R., et al. (2012). "Assessment of mental fatigue during car driving by using high resolution EEG activity and neurophysiologic indices," in *2012 Annual International Conference of the IEEE Engineering in Medicine and Biology Society* (San Diego, CA: IEEE), 6442–6445. doi: 10.1109/EMBC.2012.6347469
- Bouten, C. V., Koekkoek, K. T., Verduin, M., Kodde, R., and Janssen, J. D. (1997). A triaxial accelerometer and portable data processing unit for the assessment of daily physical activity. *IEEE Trans. Biomed. Eng.* 44, 136–147. doi: 10.1109/10.554760
- Burbank, D. P., and Webster, J. G. (1978). Reducing skin potential motion artefact by skin abrasion. *Med. Biol. Eng. Comput.* 16, 31–38. doi: 10.1007/BF02442929
- Cao, A., Chintamani, K. K., Pandya, A. K., and Ellis, R. D. (2009). NASA TLX: software for assessing subjective mental workload. *Behav. Res. Methods* 41, 113–117. doi: 10.3758/BRM.41.1.113
- Cassani, R., Falk, T. H., Fraga, F. J., Kanda, P. A., and Anghinah, R. (2014). The effects of automated artifact removal algorithms on electroencephalography-based Alzheimer's disease diagnosis. *Front. Aging Neurosci.* 6:55. doi: 10.3389/fnagi.2014.00055
- Castellanos, N. P., and Makarov, V. A. (2006). Recovering EEG brain signals: artifact suppression with wavelet enhanced independent component analysis. *J. Neurosci. Methods* 158, 300–312. doi: 10.1016/j.jneumeth.2006.05.033

- Chang, C. Y., Hsu, S. H., Pion-Tonachini, L., and Jung, T. P. (2019). Evaluation of artifact subspace reconstruction for automatic artifact components removal in multi-channel EEG recordings. *IEEE Trans. Biomed. Eng.* 67, 1114–1121. doi: 10.1109/TBME.2019.2930186
- Cheron, G., Petit, G., Cheron, J., Leroy, A., Cebolla, A., Cevallos, C., et al. (2016). Brain oscillations in sport: toward EEG biomarkers of performance. *Front. Psychol.* 7:246. doi: 10.3389/fpsyg.2016.00246
- Clayton, M. S., Yeung, N., and Kadosh, R. C. (2015). The roles of cortical oscillations in sustained attention. *Trends Cogn. Sci.* 19, 188–195. doi: 10.1016/j.tics.2015.02.004
- Clerico, A., Gupta, R., and Falk, T. H. (2015). “Mutual information between inter-hemispheric eeg spectro-temporal patterns: a new feature for automated affect recognition,” in *2015 7th International IEEE/EMBS Conference on Neural Engineering (NER)* (Montpellier: IEEE), 914–917. doi: 10.1109/NER.2015.7146774
- Clerico, A., Tiwari, A., Gupta, R., Jayaraman, S., and Falk, T. H. (2018). Electroencephalography amplitude modulation analysis for automated affective tagging of music video clips. *Front. Comput. Neurosci.* 11:115. doi: 10.3389/fncom.2017.00115
- Cohen, M. X., Elger, C. E., and Fell, J. (2009). Oscillatory activity and phase-amplitude coupling in the human medial frontal cortex during decision making. *J. Cogn. Neurosci.* 21, 390–402. doi: 10.1162/jocn.2008.21020
- Craik, A., He, Y., and Contreras-Vidal, J. L. (2019). Deep learning for electroencephalogram (EEG) classification tasks: a review. *J. Neural Eng.* 16:031001. doi: 10.1088/1741-2552/ab0ab5
- de Talhouet, H., and Webster, J. G. (1996). The origin of skin-stretch-caused motion artifacts under electrodes. *Physiol. Meas.* 17, 81. doi: 10.1088/0967-3334/17/2/003
- Dimitrakopoulos, G. N., Kakkos, I., Dai, Z., Lim, J., deSouza, J. J., Bezerianos, A., et al. (2017). Task-independent mental workload classification based upon common multiband EEG cortical connectivity. *IEEE Trans. Neural Syst. Rehabil. Eng.* 25, 1940–1949. doi: 10.1109/TNSRE.2017.2701002
- Diniz, P. S. (1997). *Adaptive Filtering*. Berlin: Springer.
- Fan, J., and Fan, Y. (2008). High dimensional classification using features annealed independence rules. *Ann. Stat.* 36:2605. doi: 10.1214/07-AOS504
- Fraga, F. J., Falk, T. H., Kanda, P. A., and Anghinah, R. (2013). Characterizing Alzheimer's disease severity via resting-awake EEG amplitude modulation analysis. *PLoS ONE* 8:e72240. doi: 10.1371/journal.pone.0072240
- Gabard-Durnam, L. J., Mendez Leal, A. S., Wilkinson, C. L., and Levin, A. R. (2018). The harvard automated processing pipeline for electroencephalography (HAPPE): standardized processing software for developmental and high-artifact data. *Front. Neurosci.* 12:97. doi: 10.3389/fnins.2018.00097
- Gao, J., Zheng, C., and Wang, P. (2010). Online removal of muscle artifact from electroencephalogram signals based on canonical correlation analysis. *Clin. EEG Neurosci.* 41, 53–59. doi: 10.1177/155005941004100111
- Geschwind, D. H., and Iacoboni, M. (1999). “Structural and functional asymmetries of the human frontal lobes,” in *The Human Frontal Lobes: Functions and Disorders*, eds B. L. Miller, and J. L. Cummings (New York, NY: Guilford Press), 45–70.
- Grtner, A., Behnke, A., Conrad, D., Kolassa, I.-T., and Rojas, R. (2019). Emotion regulation in rescue workers: differential relationship with perceived work-related stress and stress-related symptoms. *Front. Psychol.* 9:2744. doi: 10.3389/fpsyg.2018.02744
- Gwin, J. T., Gramann, K., Makeig, S., and Ferris, D. P. (2010). Removal of movement artifact from high-density EEG recorded during walking and running. *J. Neurophysiol.* 103, 3526–3534. doi: 10.1152/jn.00105.2010
- Gwin, J. T., Gramann, K., Makeig, S., and Ferris, D. P. (2011). Electrocortical activity is coupled to gait cycle phase during treadmill walking. *Neuroimage* 54, 1289–1296. doi: 10.1016/j.neuroimage.2010.08.066
- Händel, B., and Haarmeier, T. (2009). Cross-frequency coupling of brain oscillations indicates the success in visual motion discrimination. *Neuroimage* 45, 1040–1046. doi: 10.1016/j.neuroimage.2008.12.013
- Hart, S. G., and Staveland, L. E. (1988). Development of nasa-tlx (task load index): results of empirical and theoretical research. *Adv. Psychol.* 52, 139–183. doi: 10.1016/S0166-4115(08)62386-9
- Hogervorst, M. A., Brouwer, A. M., and Van Erp, J. B. (2014). Combining and comparing EEG, peripheral physiology and eye-related measures for the assessment of mental workload. *Front. Neurosci.* 8:322. doi: 10.3389/fnins.2014.00322
- Holm, A., Lukander, K., Korpela, J., Sallinen, M., and Müller, K. M. (2009). Estimating brain load from the EEG. *Sci. World J.* 9, 639–651. doi: 10.1100/tsw.2009.83
- Hülsdünker, T., Mierau, A., Neeb, C., Kleinöder, H., and Strüder, H. (2015). Cortical processes associated with continuous balance control as revealed by EEG spectral power. *Neurosci. Lett.* 592, 1–5. doi: 10.1016/j.neulet.2015.02.049
- Iacoboni, M., and Zaidel, E. (2004). Interhemispheric visuo-motor integration in humans: the role of the superior parietal cortex. *Neuropsychologia* 42, 419–425. doi: 10.1016/j.neuropsychologia.2003.10.007
- Johnson, M. K., Blanco, J. A., Gentili, R. J., Jaquess, K. J., Oh, H., and Hatfield, B. D. (2015). “Probe-independent eeg assessment of mental workload in pilots,” in *2015 7th International IEEE/EMBS Conference on Neural Engineering (NER)* (Montpellier: IEEE), 581–584. doi: 10.1109/NER.2015.7146689
- Kakkos, I., Dimitrakopoulos, G. N., Gao, L., Zhang, Y., Qi, P., Matsopoulos, G. K., et al. (2019). Mental workload drives different reorganizations of functional cortical connectivity between 2d and 3d simulated flight experiments. *IEEE Trans. Neural Syst. Rehabil. Eng.* 27, 1704–1713. doi: 10.1109/TNSRE.2019.2930082
- Käthner, I., Wriessnegger, S. C., Müller-Putz, G. R., Kübler, A., and Halder, S. (2014). Effects of mental workload and fatigue on the P300, alpha and theta band power during operation of an ERP (P300) brain-computer interface. *Biol. Psychol.* 102, 118–129. doi: 10.1016/j.biopsycho.2014.07.014
- Kearney, K., Thomas, C., and McAdams, E. (2007). “Quantification of motion artifact in ECG electrode design,” in *2007 29th Annual International Conference of the IEEE Engineering in Medicine and Biology Society* (Lyon: IEEE), 1533–1536. doi: 10.1109/IEMBS.2007.4352594
- Lean, Y., and Shan, F. (2012). Brief review on physiological and biochemical evaluations of human mental workload. *Hum. Fact. Ergon. Manuf. Serv. Ind.* 22, 177–187. doi: 10.1002/hfm.20269
- Liu, Y., Ayaz, H., and Shewokis, P. A. (2017). Mental workload classification with concurrent electroencephalography and functional near-infrared spectroscopy. *Brain Comput. Interfaces* 4, 175–185. doi: 10.1080/2326263X.2017.1304020
- Mak, J. N., Chan, R. H., and Wong, S. W. (2013). “Evaluation of mental workload in visual-motor task: spectral analysis of single-channel frontal EEG,” in *IECON 2013–39th Annual Conference of the IEEE Industrial Electronics Society* (Vienna: IEEE), 8426–8430. doi: 10.1109/IECON.2013.6700546
- Mandrick, K., Derosiere, G., Dray, G., Coulon, D., Micallef, J.-P., and Perrey, S. (2013). Prefrontal cortex activity during motor tasks with additional mental load requiring attentional demand: a near-infrared spectroscopy study. *Neurosci. Res.* 76, 156–162. doi: 10.1016/j.neures.2013.04.006
- McMenamin, B. W., Shackman, A. J., Greischar, L. L., and Davidson, R. J. (2011). Electromyogenic artifacts and electroencephalographic inferences revisited. *NeuroImage* 54, 4–9. doi: 10.1016/j.neuroimage.2010.07.057
- Mihajlović, V., Patki, S., and Grundlehner, B. (2014). “The impact of head movements on EEG and contact impedance: an adaptive filtering solution for motion artifact reduction,” in *2014 36th Annual International Conference of the IEEE Engineering in Medicine and Biology Society* (Chicago, IL: IEEE), 5064–5067. doi: 10.1109/EMBC.2014.6944763
- Mogron, A., Jovicich, J., Bruzzone, L., and Buiatti, M. (2011). Adjust: an automatic EEG artifact detector based on the joint use of spatial and temporal features. *Psychophysiology* 48, 229–240. doi: 10.1111/j.1469-8986.2010.01061.x
- Morikawa, K., Matsumoto, A., Patki, S., Grundlehner, B., Verwegen, A., Xu, J., et al. (2013). “Compact wireless eeg system with active electrodes for daily healthcare monitoring,” in *2013 IEEE International Conference on Consumer Electronics (ICCE)* (Berlin), 204–205. doi: 10.1109/ICCE.2013.6486859
- Mucarquer, J. A., Prado, P., Escobar, M. J., El-Deredy, W., and Zaňartu, M. (2019). Improving eeg muscle artifact removal with an EMG array. *IEEE Trans. Instr. Meas.* 69, 815–824. doi: 10.1109/TIM.2019.2906967
- Mullen, T. R., Kothe, C. A. E., Chi, Y. M., Ojeda, A., Kerth, T., Makeig, S., et al. (2015). Real-time neuroimaging and cognitive monitoring using wearable dry eeg. *IEEE Trans. Biomed. Eng.* 62, 2553–2567. doi: 10.1109/TBME.2015.2481482
- Muthukumaraswamy, S. (2013). High-frequency brain activity and muscle artifacts in MEG/EEG: a review and recommendations. *Front. Hum. Neurosci.* 7:138. doi: 10.3389/fnhum.2013.00138
- Nathan, K., and Contreras-Vidal, J. L. (2016). Negligible motion artifacts in scalp Electroencephalography (EEG) during treadmill walking. *Front. Hum. Neurosci.* 9:708. doi: 10.3389/fnhum.2015.00708

- Onikura, K., and Iramina, K. (2015). "Evaluation of a head movement artifact removal method for EEG considering real-time processing," in *2015 8th Biomedical Engineering International Conference (BMEiCON)* (Pattaya: IEEE), 1–4. doi: 10.1109/BMEiCON.2015.7399577
- Oshiro, T. M., Perez, P. S., and Baranauskas, J. A. (2012). "How many trees in a random forest?" in *Machine Learning and Data Mining in Pattern Recognition*, ed P. Perner (Berlin; Heidelberg: Springer Berlin Heidelberg), 154–168. doi: 10.1007/978-3-642-31537-4\_13
- Pedregosa, F., Varoquaux, G., Gramfort, A., Michel, V., Thirion, B., Grisel, O., et al. (2011). Scikit-learn: machine learning in Python. *J. Mach. Learn. Res.* 12, 2825–2830.
- Peng, H., Long, F., and Ding, C. (2005). Feature selection based on mutual information: criteria of max-dependency, max-relevance, and min-redundancy. *IEEE Trans. Pattern Anal. Mach. Intell.* 27, 1226–1238. doi: 10.1109/TPAMI.2005.159
- Perennou, D., Benaim, C., Rouget, E., Rousseaux, M., Blard, J., and Pelissier, J. (1999). Postural balance following stroke: towards a disadvantage of the right brain-damaged hemisphere. *Rev. Neurol.* 155, 281–290.
- Qi, Y. (2012). "Random forest for bioinformatics," in *Ensemble Machine Learning*, eds C. Zhang, Y. Ma and (Princeton, NJ: Springer), 307–323. doi: 10.1007/978-1-4419-9326-7\_11
- Rahman, M., Karwowski, W., Fafrowicz, M., and Hancock, P. A. (2019). Neuroergonomics applications of electroencephalography in physical activities: a systematic review. *Front. Hum. Neurosci.* 13:182. doi: 10.3389/fnhum.2019.00277
- Raya, M. A. D., and Sison, L. G. (2002). "Adaptive noise cancelling of motion artifact in stress ECG signals using accelerometer," in *Proceedings of the Second Joint 24th Annual Conference and the Annual Fall Meeting of the Biomedical Engineering Society (Engineering in Medicine and Biology)*, Vol. 2 (Houston, TX: IEEE), 1756–1757. doi: 10.1109/IEMBS.2002.1106637
- Rosanne, O., Albuquerque, I., Gagnon, J. F., Tremblay, S., and Falk, T. H. (2019). "Performance comparison of automated eeg enhancement algorithms for mental workload assessment of ambulant users," in *2019 9th International IEEE/EMBS Conference on Neural Engineering (NER)* (IEEE), 61–64. doi: 10.1109/NER.2019.8716977
- Sammer, G., Blecker, C., Gebhardt, H., Bischoff, M., Stark, R., Morgen, K., et al. (2007). Relationship between regional hemodynamic activity and simultaneously recorded EEG-theta associated with mental arithmetic-induced workload. *Hum. Brain Mapp.* 28, 793–803. doi: 10.1002/hbm.20309
- Santiago-Espada, Y., Myer, R., Latorella, K., and Comstock, J. (2011). *The Multi-Attribute Task Battery II (Matb-II) Software for Human Performance and Workload Research: A User's Guide (NASA/TM-2011-217164)*. Hampton, VA: NASA Langley Research Center.
- Sauseng, P., Conci, M., Wild, B., and Geyer, T. (2015). Predictive coding in visual search as revealed by cross-frequency EEG phase synchronization. *Front. Psychol.* 6:1655. doi: 10.3389/fpsyg.2015.01655
- Seeber, M., Scherer, R., Wagner, J., Solis-Escalante, T., and Müller-Putz, G. R. (2014). EEG beta suppression and low gamma modulation are different elements of human upright walking. *Front. Hum. Neurosci.* 8:485. doi: 10.3389/fnhum.2014.00485
- Sipp, A. R., Gwin, J. T., Makeig, S., and Ferris, D. P. (2013). Loss of balance during balance beam walking elicits a multifocal theta band electrocortical response. *J. Neurophysiol.* 110, 2050–2060. doi: 10.1152/jn.00744.2012
- So, W. K., Wong, S. W., Mak, J. N., and Chan, R. H. (2017). An evaluation of mental workload with frontal EEG. *PLoS ONE* 12:e0174949. doi: 10.1371/journal.pone.0174949
- Tiwari, A., Albuquerque, I., Gagnon, J. F., Lafond, D., Parent, M., Tremblay, S., et al. (2019). "Mental workload assessment during physical activity using non-linear movement artefact robust electroencephalography features," in *2019 IEEE International Conference on Systems, Man and Cybernetics (SMC)* (Bari: IEEE), 4149–4154. doi: 10.1109/SMC.2019.8914038
- Tort, A. B., Komorowski, R., Eichenbaum, H., and Kopell, N. (2010). Measuring phase-amplitude coupling between neuronal oscillations of different frequencies. *J. Neurophysiol.* 104, 1195–1210. doi: 10.1152/jn.00106.2010
- Trambaiolli, L. R., Falk, T. H., Fraga, F. J., Anghinah, R., and Lorena, A. C. (2011). "EEG spectro-temporal modulation energy: a new feature for automated diagnosis of Alzheimer's disease," in *2011 Annual International Conference of the IEEE Engineering in Medicine and Biology Society* (Boston, MA: IEEE), 3828–3831. doi: 10.1109/IEMBS.2011.6090951
- Urigüen, J. A., and Garcia-Zapirain, B. (2015). EEG artifact removal—state-of-the-art and guidelines. *J. Neural Eng.* 12:031001. doi: 10.1088/1741-2560/12/3/031001
- Vossel, S., Weidner, R., Moos, K., and Fink, G. R. (2016). Individual attentional selection capacities are reflected in interhemispheric connectivity of the parietal cortex. *Neuroimage* 129, 148–158. doi: 10.1016/j.neuroimage.2016.01.054
- Voytek, B., Canolty, R. T., Sheshyuk, A., Crone, N., Parvizi, J., and Knight, R. T. (2010). Shifts in gamma phase-amplitude coupling frequency from theta to alpha over posterior cortex during visual tasks. *Front. Hum. Neurosci.* 4:191. doi: 10.3389/fnhum.2010.00191
- Wang, D., Chen, J., Zhao, D., Dai, F., Zheng, C., and Wu, X. (2017). Monitoring workers' attention and vigilance in construction activities through a wireless and wearable electroencephalography system. *Autom. Constr.* 82, 122–137. doi: 10.1016/j.autcon.2017.02.001
- Zanto, T. P., Rubens, M. T., Thangavel, A., and Gazzaley, A. (2011). Causal role of the prefrontal cortex in top-down modulation of visual processing and working memory. *Nat. Neurosci.* 14:656. doi: 10.1038/nn.2773
- Zarjam, P., Epps, J., and Lovell, N. H. (2015). Beyond subjective self-rating: EEG signal classification of cognitive workload. *IEEE Trans. Auton. Mental Dev.* 7, 301–310. doi: 10.1109/TAMD.2015.2441960
- Zhang, C., Yu, X., Yang, Y., and Xu, L. (2014). Phase synchronization and spectral coherence analysis of EEG activity during mental fatigue. *Clin. EEG Neurosci.* 45, 249–256. doi: 10.1177/1550059413503961
- Zhang, P., Wang, X., Chen, J., You, W., and Zhang, W. (2019). Spectral and temporal feature learning with two-stream neural networks for mental workload assessment. *IEEE Trans. Neural Syst. Rehabil. Eng.* 27, 1149–1159. doi: 10.1109/TNSRE.2019.2913400
- Zou, L., Chen, X., Dang, G., Guo, Y., and Wang, Z. J. (2019). Removing muscle artifacts from EEG data via underdetermined joint blind source separation: a simulation study. *IEEE Trans. Circuits Syst. II Express Briefs* 67, 187–191. doi: 10.1109/TCSII.2019.2903648

**Conflict of Interest:** J-FG was employed by the company Thales Research and Technology. The remaining authors declare that the research was conducted in the absence of any commercial or financial relationships that could be construed as a potential conflict of interest.

The remaining authors declare that this study received funding from Thales Digital Solutions Inc. The funder was not involved in the study design, collection, analysis, interpretation of data, the writing of this article or the decision to submit it for publication.

Copyright © 2021 Rosanne, Albuquerque, Cassani, Gagnon, Tremblay and Falk. This is an open-access article distributed under the terms of the Creative Commons Attribution License (CC BY). The use, distribution or reproduction in other forums is permitted, provided the original author(s) and the copyright owner(s) are credited and that the original publication in this journal is cited, in accordance with accepted academic practice. No use, distribution or reproduction is permitted which does not comply with these terms.



# Cross-Subject EEG Emotion Recognition With Self-Organized Graph Neural Network

Jingcong Li<sup>1,2</sup>, Shuqi Li<sup>3\*</sup>, Jiahui Pan<sup>1,2</sup> and Fei Wang<sup>1,2</sup>

<sup>1</sup> School of Software, South China Normal University, Guangzhou, China, <sup>2</sup> Pazhou Lab, Guangzhou, China, <sup>3</sup> School of Computer Science, South China Normal University, Guangzhou, China

As a physiological process and high-level cognitive behavior, emotion is an important subarea in neuroscience research. Emotion recognition across subjects based on brain signals has attracted much attention. Due to individual differences across subjects and the low signal-to-noise ratio of EEG signals, the performance of conventional emotion recognition methods is relatively poor. In this paper, we propose a self-organized graph neural network (SOGNN) for cross-subject EEG emotion recognition. Unlike the previous studies based on pre-constructed and fixed graph structure, the graph structure of SOGNN are dynamically constructed by self-organized module for each signal. To evaluate the cross-subject EEG emotion recognition performance of our model, leave-one-subject-out experiments are conducted on two public emotion recognition datasets, SEED and SEED-IV. The SOGNN is able to achieve state-of-the-art emotion recognition performance. Moreover, we investigated the performance variances of the models with different graph construction techniques or features in different frequency bands. Furthermore, we visualized the graph structure learned by the proposed model and found that part of the structure coincided with previous neuroscience research. The experiments demonstrated the effectiveness of the proposed model for cross-subject EEG emotion recognition.

## OPEN ACCESS

### Edited by:

Haider Raza,  
University of Essex, United Kingdom

### Reviewed by:

Archana Venkataraman,  
Johns Hopkins University,  
United States  
Di Wang,  
Nanyang Technological University,  
Singapore

### \*Correspondence:

Shuqi Li  
surkyli@m.scnu.edu.cn

### Specialty section:

This article was submitted to  
Brain Imaging Methods,  
a section of the journal  
Frontiers in Neuroscience

**Received:** 29 September 2020

**Accepted:** 17 May 2021

**Published:** 09 June 2021

### Citation:

Li J, Li S, Pan J and Wang F (2021)  
Cross-Subject EEG Emotion  
Recognition With Self-Organized  
Graph Neural Network.  
*Front. Neurosci.* 15:611653.  
doi: 10.3389/fnins.2021.611653

**Keywords:** SEED dataset, graph neural network, cross-subject, emotion recognition, graph construction

## 1. INTRODUCTION

Human emotion is a complex psychophysiological process that plays an important role in daily communications. Emotion recognition is a significant and fundamental research topic in affective computing and neuroscience (Cowie et al., 2001). In general, human emotions can be recognized using data from different modalities, such as facial expression images, body language, textual information and physiological signals such as electromyogram (EMG), electrocardiogram (ECG), and electroencephalogram (EEG) (Busso et al., 2004; Shu et al., 2018). EEG is a widely used technique in neuroscience research that is able to directly capture brain signals that could reflect neural activities in real time. Therefore, EEG-based emotion recognition has received considerable attention in the areas of affective computing and neuroscience (Coan and Allen, 2004; Lin et al., 2010; Alarcao and Fonseca, 2017; Li et al., 2019).

In order to facilitate EEG-based emotion recognition research, the SJTU emotion EEG dataset (SEED) was released (Duan et al., 2013). In addition, its evolutionary dataset termed SEED-IV was also available (Zheng et al., 2018). Before the experiments on SEED and SEED-IV datasets, a

series of film clips with different emotional tendencies were chosen as stimulation materials. In the SEED dataset, happy, sad and neutral emotions were included, while the SEED-IV dataset consisted of happy, sad, fear and neutral emotions. During the experiments, each participant watched the film clips while his/her EEG signals were recorded with a 62-channel ESI NeuroScan System. Consequently, the recorded EEG signals and the corresponding emotion labels of film clips can be used to train an emotion recognition model. If the trained emotion recognition model is effective, we will be able to decode the emotions of a new participant when he/she watched a film. Therefore, based on the SEED and SEED-IV datasets, different emotion recognition methods can be evaluated on common benchmarks.

In the past few years, many feature extraction and machine learning approaches have been proposed for EEG-based emotion recognition. In an original research on SEED dataset, the features of the energy spectrum (ES), differential entropy (DE), rational asymmetry (RASM), and differential asymmetry (DASM) were proven to be effective features for EEG-based emotion recognition (Duan et al., 2013). To explore different EEG features for cross-subject emotion recognition, 18 kinds of linear and non-linear EEG features were evaluated (Li et al., 2018b). Moreover, a machine learning technique was used to investigate stable EEG patterns for emotion recognition and achieved high performance on SEED and DEAP emotion recognition datasets (Zheng et al., 2017). To eliminate the individual differences in EEG signals, a deep adaption network (DAN) was proposed and applied on the SEED and SEED-IV datasets to conduct cross-subject emotion recognition (Li et al., 2018a). A novel group sparse canonical correlation analysis (GSCCA) method was proposed for simultaneous EEG channel selection and emotion recognition (Zheng, 2016).

Recently, deep learning and graph representation methodology were proven to be powerful tools to model structured data and achieved significant performance in many applications (Linial et al., 1995; Even, 2011). A deep belief network (DBN) was applied to process differential entropy features extracted from multichannel EEG signals (Zheng et al., 2014). To investigate critical frequency bands and channels for EEG-based emotion recognition, a deep neural network was proposed (Zheng and Lu, 2015). Long-short term memory (LSTM) was used to learn features from EEG signals, and these features were discriminative for emotion recognition on the DEAP dataset (Alhagry et al., 2017). EEG signals were recorded by EEG caps placed on the scalp, and these data can be considered to be a typical kind of structured data (Micheloyannis et al., 2006). Accordingly, graph representation approaches also achieved impressive performance in handling EEG signals in emotion recognition experiments. For example, a dynamic graph convolutional neural network (DGCNN) was proposed for emotion recognition, and its graph structure was determined by a dynamic adjacency matrix that reflected the intrinsic relationships between different EEG electrodes (Song et al., 2019b). In order to explore the deeper-level information of graph-structured EEG data, a graph convolutional broad network (GCB-net) was proposed and achieved high performance on the

SEED and DREAMER datasets (Zhang et al., 2019). To capture both local and global interchannel relations, a regularized graph neural network (RGNN) was proposed and achieved state-of-the-art performance on the SEED and SEED-IV datasets (Zhong et al., 2020).

In this paper, we proposed a novel model for cross-subject EEG emotion recognition and evaluated the model on two common datasets. The main contributions of this paper can be summarized as follows:

1. A novel cross-subject emotion recognition model, termed the self-organized graph neural network (SOGNN), was proposed.
2. The SOGNN is able to achieve state-of-the-art emotion recognition performance with cross-subject accuracy of 86.81% on the SEED dataset and 75.27% on the SEED-IV dataset.
3. Interchannel connections and time-frequency features are aggregated by the self-organized graph construction module, graph convolution and hierarchical structure of the SOGNN to improve the cross-subject emotion recognition performance.

The remainder of this paper is organized as follows. The EEG emotion recognition datasets (SEED and SEED-IV) and the proposed SOGNN model are presented in section 2. In section 3, numerical emotion recognition experiments are conducted. In addition, the performance of the current methods and the proposed methods are presented and compared. Some discussions and analysis of the proposed model are presented in section 4. The conclusions of this paper are given in section 5.

## 2. MATERIALS AND METHODS

### 2.1. EEG Emotion Recognition Datasets

In order to facilitate EEG-based emotion recognition research, the SJTU emotion EEG dataset (SEED) was released on <http://bcmi.sjtu.edu.cn/~seed/> (Duan et al., 2013). In addition, its evolutionary dataset termed SEED-IV was also available (Zheng et al., 2018). Before the experiments on the SEED and SEED-IV datasets, a series of film clips with different emotional tendencies were chosen as stimulation materials. The SEED dataset includes happy, sad and neutral film clips while the SEED-IV dataset consists of happy, sad, fear and neutral film clips. During the experiments, each participant watched film clips while his/her EEG signals were recorded with a 62-channel ESI NeuroScan System.

In the SEED and SEED-IV datasets, 15 subjects (7 males and 8 females) participated in the experiments. During the experiments, 62-channel EEG signals of each subject were recorded when he/she was watching film clips with different emotion labels. There are 675 EEG samples (45 samples \* 15 subjects) in SEED datasets. For each subject, there are 15 samples of happy, 15 samples of sad, and 15 samples of neutral emotion. There are 1,080 samples (72 samples \* 15 subjects) in SEED-IV dataset. For each subject, there are 4 different kinds of emotion including happy, sad, fear and neutral emotion that the number

of each emotion class is 18. So the number of samples per subject/class are balanced.

The signals were synchronously recorded at a 1,000 Hz sampling rate. Bandpass frequency filters of 0–75 and 1–75 Hz were applied to filter the unrelated artifacts for the SEED and SEED-IV datasets, respectively. To accelerate the computation, the signals were downsampled with sampling frequency of 200 Hz. In addition, the dataset provider applied the linear dynamic system approach to filter out noise and artifacts that were unrelated to the EEG features (Shi and Lu, 2010; Zheng et al., 2018). In the two datasets, the EEG features of the differential entropy (DE), power spectral density (PSD), asymmetry(ASM), differential asymmetry (DASM), differential caudality (DCAU), and radial asymmetry (RASM) were provided. The DE feature and PSD feature extract contents about the frequency and energy spectrum, respectively; the DASM feature and RASM feature obtain asymmetrical information of EEG channels, and DCAU feature computes the differences between channel pairs. Compared with the other features, the DE feature is more discriminative for emotion recognition according to the previous research (Duan et al., 2013; Song et al., 2019b; Zhong et al., 2020).

Therefore, we used DE features as the input data for our model. The DE features are frequency domain features that are calculated by a 512-point short-time Fourier transform with a non-overlapped Hanning window of 1 s and averaged in 5 frequency bands, e.g.,  $\delta$  band (1–3 Hz),  $\theta$  band (4–7 Hz),  $\alpha$  band (8–13 Hz),  $\beta$  band (14–30 Hz), and  $\gamma$  band (31–50 Hz). As a result, the output DE feature can be represented as a  $5 \times T$  matrix in which  $T$  denotes the time window which is dependent on the stimulated film clip. The time window  $T$  of the SEED dataset ranges from 185 to 265 while the window of SEED-IV ranges from 12 to 64. For normalization, the features with a short time window will be zero-padded to a length of 265 for SEED dataset and a length of 64 for the SEED-IV dataset.

Based on the benchmark SEED and SEED IV datasets, different EEG emotion recognition models can be evaluated and compared with each other.

## 2.2. Self-Organized Graph Neural Network

Generally, EEG signal can be considered to be a typical kind of structured data and defined on a graph (Micheloyannis et al., 2006). Graph representation techniques and graph neural networks were proven to be effective in processing brain signals (Petrosian et al., 2000; de Haan et al., 2009; Varatharajah et al., 2017; Zhang et al., 2020). Here, the EEG signal is defined on a graph model as follows:

$$\begin{aligned} \mathcal{G} &= (\mathcal{V}, \mathcal{E}, A) \\ \mathcal{V} &= \{v_i | i = 1, \dots, N\} \\ \mathcal{E} &= \{e_{ij} | v_i, v_j \in \mathcal{V}\} \\ A &= \{a_{ij}\} \end{aligned} \tag{1}$$

where  $\mathcal{V}$  denotes the nodes (a total of  $N$  nodes) in graph  $\mathcal{G}$ ,  $\mathcal{E}$  are the connected edges between different nodes, each node denotes one EEG electrode,  $A \in \mathbb{R}^{N \times N}$  is the adjacency matrix, and its element  $a_{ij}$  denotes the adjacent connection weight between nodes  $v_i$  and  $v_j$ . Consequently, the structure of a graph is determined by its adjacency matrix.

As shown in **Figure 1**, the brain graph structure is predefined by a distance function  $f$  between different channels in many previous studies (Micheloyannis et al., 2006; Ktena et al., 2018; Wang et al., 2018; Zhang et al., 2019; Zhong et al., 2020). However, the predefined and fixed graph structures could not properly model the dynamic brain signals of different subjects in different emotion states.

Here, we propose a self-organized graph construction module for modeling EEG emotion features. The proposed self-organized graph is determined by the input brain signals rather than based on a predefined graph structure as in many previous researches. The adjacent weight  $a_{ij}$  of the self-organized graph is defined by function  $f(v_i, v_j)$  as

$$a_{ij} = f(v_i, v_j) = \frac{\exp(\theta(v_i W)\theta(v_j W)^T)}{\sum_{i=1}^N \exp(\theta(v_i W)\theta(v_j W)^T)} \tag{2}$$

where  $v \in \mathbb{R}^{1 \times F}$  is a feature vector of one node (i.e., EEG electrode) in  $\mathcal{V} \in \mathbb{R}^{N \times F}$ , there are a total of  $N$  nodes (EEG electrodes),  $W \in \mathbb{R}^{F \times L}$  and  $\theta$  are the weight and tanh activation function of a linear layer, respectively; and the exponential function is part of the softmax activation function for normalization and obtains a positive and bounded adjacent weight. The linear layer work as a bottleneck to reduce computational cost.

To clarify the details of the self-organized graph construction module, we also presented its matrix operation form in **Figure 2**. The self-organized adjacent matrix can be calculated as follows:

$$G = \text{Tanh}(\mathcal{V}W) \tag{3}$$

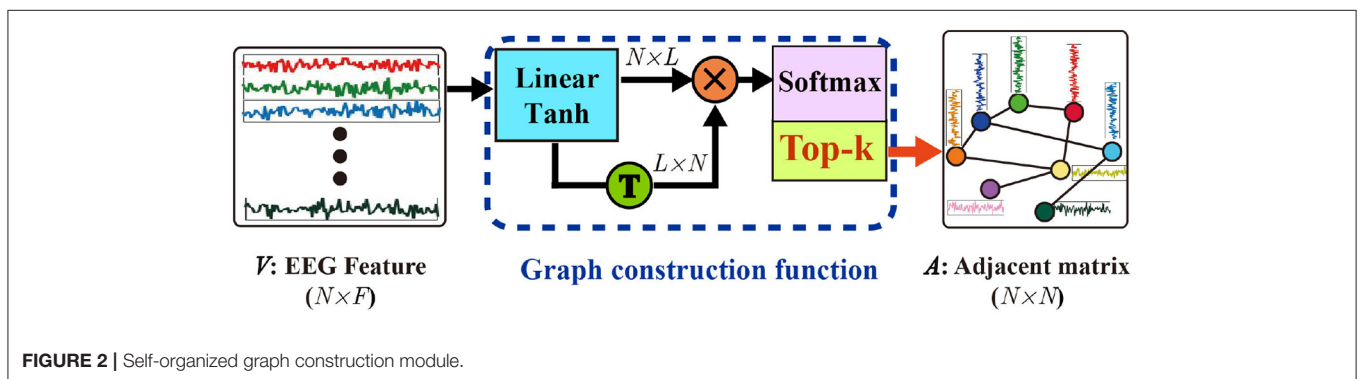
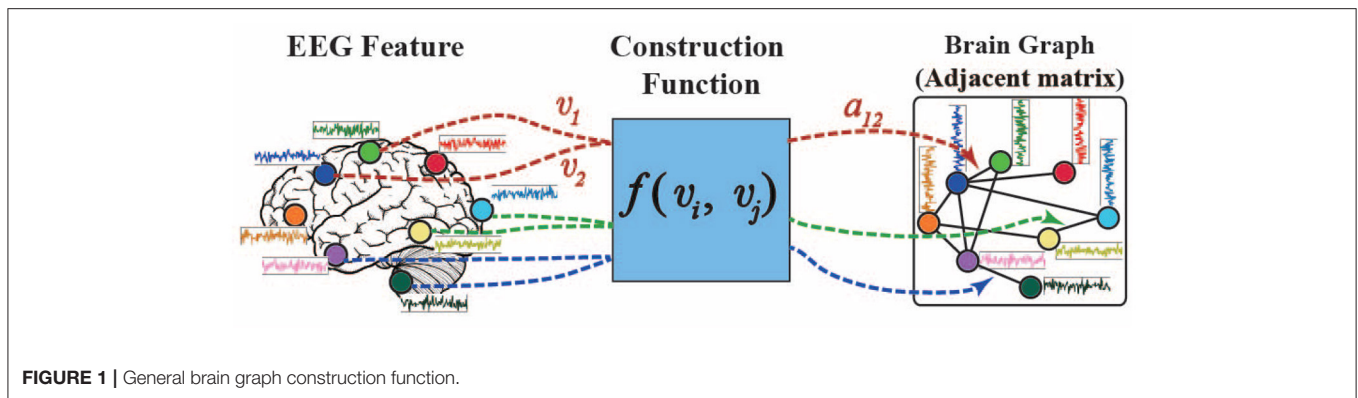
$$A = \text{Softmax}(GG^T) \tag{4}$$

where  $\mathcal{V} \in \mathbb{R}^{N \times F}$  is the input EEG features whose row vectors are node features of the graph to build, the  $W \in \mathbb{R}^{F \times L}$  denote the weight of a linear layer, we adopted tanh activation function,  $G \in \mathbb{R}^{N \times L}$  is the output of the linear layer, softmax activation function is applied to obtain a positive and bounded adjacent matrix  $A$ . With the self-organized graph construction module, the graph structure, is dynamically constructed by the corresponding input features.

Generally, the computational costs of sparse graphs are much lower than those of dense graphs. To construct a sparse graph, we adopt a top-k technique in which only the k largest weights of the adjacent matrix will be maintained while the small connection weights will be set to zero. The top-k operation is applied as follow

$$\begin{cases} \text{for } i = 1, 2, \dots, N \\ \text{index} = \text{argtopk}(A[i, :]) \\ A[i, \text{index}] = 0 \end{cases} \tag{5}$$

where  $\text{argtopk}(\cdot)$  is a function to obtain the index of the top-k largest values of each vector  $A[i, :]$  in adjacent matrix  $A$ , and  $\text{index}$  denotes the index of those values that do not belong to the top-k largest values in  $A[i, :]$ . As a result, only the k largest values in each row vector of adjacent matrix  $A$  are maintained while the



remaining values will be set to zero. Actually, the top-k strategy can be considered as a modified max-pooling layer. Therefore, the parameters of the network can be updated as the network with max-pooling layers with backpropagation.

With the self-organized graph construction module, the graph structure is dynamically constructed by the corresponding input EEG features. Then, the newly built graphs can be processed by the graph convolutional layers to extract the local/global connection features for emotion recognition.

Based on the self-organized graph construction module, we propose SOGNN as shown in **Figure 3**. The SOGNN is composed of three conv-pool blocks, three self-organized graph layers, three graph convolution layers, one fully-connected layer and an output layer.

For the proposed SOGNN model, its input EEG feature is sized  $Electrodes \times Bands \times TimeFrames$ . To simplify the illustration of the model, we take the SEED dataset with a  $62 \times 5 \times 265$  input feature as an example in **Figure 3**. \*Maps indicates the number of output feature maps of each layer. In each conv-pool block, standard convolution and max-pooling layers were applied to extract features for each EEG electrode independently. Therefore, the features of different EEG electrodes will not mix with each other so that the corresponding graph structure can be maintained. In the conv-pool 1 block, the  $5 \times 5$  convolutional kernel extracts features in a window of 5 frequency bands and 5 time frames. Therefore, the output features are sized  $62 \times 1 \times 261$  in the SEED dataset. A  $1 \times 4$  max-pooling layer is applied to downsample the features of the SEED dataset. Then the output

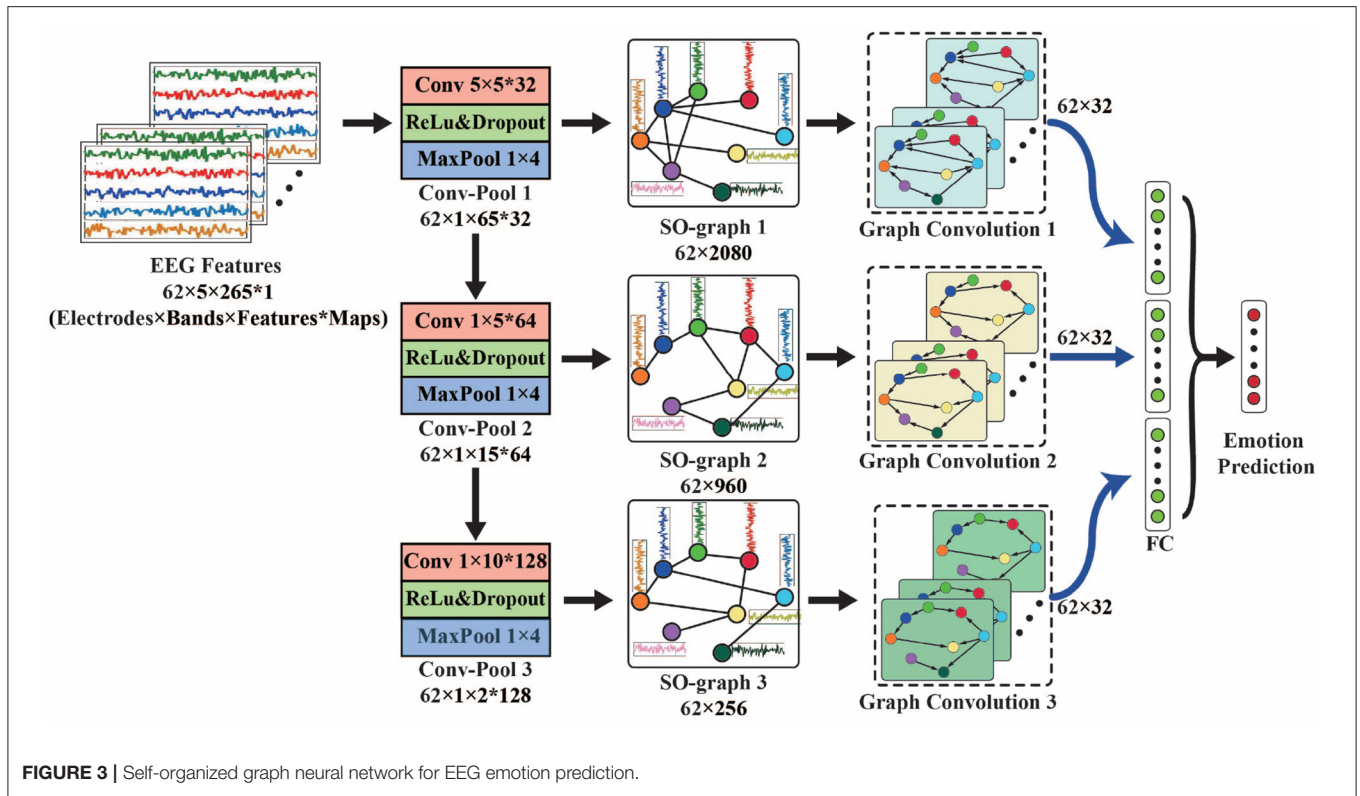
feature map of conv-pool 1 block is sized  $62 \times 1 \times 65$  for the input feature of SEED. For the SEED-IV dataset,  $1 \times 2$  max-pooling layers are used. A convolutional kernel  $1 \times 5$  was applied in conv-pool 2 and 3. There are 32, 64, and 128 convolutional kernels in conv-pool 1-3 blocks that will obtain 32, 64, and 128 output feature maps, respectively.

The output of each conv-pool block was reshaped as a matrix with the shape of electrodes  $\times$  features and fed into self-organized graph layers (SO-graphs 1-3). In the SO-graph layer, the feature of each EEG electrode remains unchanged, and only the adjacent weights between different EEG electrodes are calculated according to (2)–(5). For each SO-graph layer, there are 64 linear units, 32 output units and top-10 adjacent weights. With different input features, the graph features of the SO-graph 1-3 layers are different. Next, we applied graph convolution layers to process these graph features.

According to previous research (Bruna et al., 2013; Song et al., 2019b), spectral graph convolution multiplied a signal  $x \in \mathbb{R}^n$  with a graph convolution kernel  $\Theta$  by a graph convolution operator  $*_G$  as,

$$\Theta *_G x = \Theta(L)x = \Theta(U\Lambda U^T)x = U\Theta(\Lambda)U^T x \quad (6)$$

where graph Fourier basis  $U \in \mathbb{R}^{N \times N}$  is the matrix of eigenvectors for the normalized graph Laplacian  $L = I_n - D^{-1/2}AD^{-1/2} = ULU^T \in \mathbb{R}^{N \times N}$  ( $I_n$  is an identity matrix,  $D \in \mathbb{R}^{N \times N}$  is the diagonal degree matrix with  $D_{ii} = \sum_j A_{ij}$ ,  $A \in \mathbb{R}^{N \times N}$  is the adjacency matrix mentioned in Equation



1);  $\Lambda \in \mathbb{R}^{N \times N}$  is the diagonal matrix of the eigenvalues of  $L$ , and filter  $\Theta(\Lambda)$  is also a diagonal matrix. According to this definition, a graph signal  $x$  is filtered by a kernel  $\Theta$  with multiplication between  $\Theta$  and graph Fourier transform  $U^T x$  (Shuman et al., 2013).

The outputs of the graph convolution layers were flattened and concatenated as a feature vector. This feature vector will be fed into fully-connected (FC) layer with a softmax activation function to predict emotional states. The proposed SOGNN model can be trained by minimizing the cross-entropy error of its prediction and ground truth. As a result, the loss function is defined as

$$L = - \sum_{i \in \Omega} \sum_c y_{ic} \log(p_{ic}) + (1 - y_{ic}) \log(1 - p_{ic}) \quad (7)$$

where  $p_{ic}$  is the output value of the  $c$ -th output unit of the SOGNN model with the input of the  $i$ -th training sample,  $p_{ic}$  can be considered as the model's predicted probability of the  $c$ -th class,  $y_{ic}$  is the ground truth, and  $\Omega$  denotes all of the training samples.

### 3. RESULTS

In this section, a series of experiments will be conducted to evaluate the proposed model. In addition, the corresponding experimental results of our method will be presented and compared with the results of the other methods. The model implementation will be publicly available at <https://github.com/>

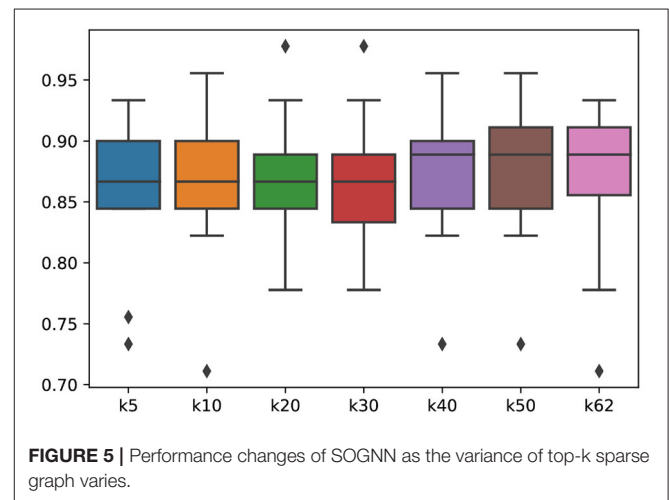
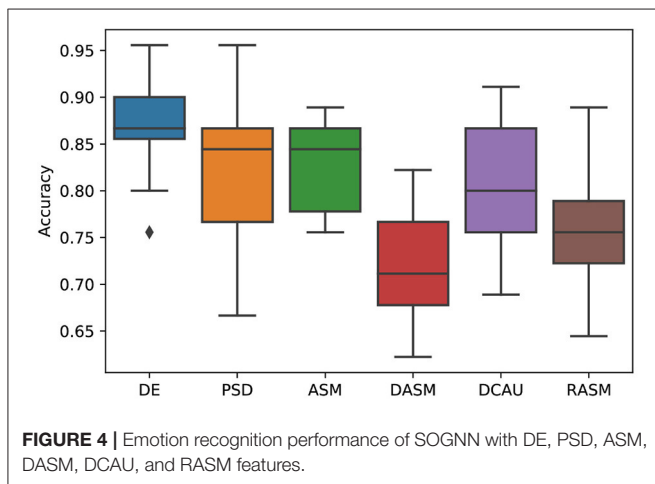
tailofcat/SOGNN. In our experiments, the hardware and software configuration of our system is a platform with an Nvidia Titan Xp, Ubuntu 16.04, PyTorch 1.5.1, and PyTorch-geometric 1.5.0 (Fey and Lenssen, 2019).

In order to investigate the cross-subject emotion recognition performance, a leave-one-subject-out (LOSO) cross-validation strategy was applied in the experiments. In each run of the LOSO experiment, the DE features of 14 subjects in SEED/SEED-IV are used as the training dataset while the data of the remaining subject is the validation dataset. Regarding normalization, the features of each subject will be normalized by subtracting its mean and then dividing by its standard deviation.

In order to train the proposed SOGNN model, the Adam optimizer is applied to minimize the model's loss. The proposed model was trained by the Adam optimizer with a learning rate of 0.00001, a weight-decay rate of 0.0001 and mini-batch size of 16. A drop-out operation with a dropout rate of 0.1 was applied in the training procedure to randomly block the output units of the internal layers. During the training procedure, we monitored the model's mean area under the curve (AUC) from the receiver operating characteristic curve for all emotion classes. Once the training averaged AUC score reached 0.99, the training procedure was stopped. Finally, the trained SOGNN model could be applied for emotion prediction. Once the proposed SOGNN model was trained, it could be applied to the validation dataset. For the SEED/SEED-IV database with 15 subjects, the LOSO experiment will be conducted in 15 runs. Then, the average validation accuracy can be considered as the model's performance, which can

**TABLE 1** | Leave-one-subject-out emotion recognition accuracy (mean/standard deviation) on SEED and SEED-IV.

Model	SEED						SEED-IV
	Delta band	Theta band	Alpha band	Beta band	Gamma band	All bands	All bands
SVM (Zhong et al., 2020)	43.06/8.27	40.07/6.50	43.97/10.89	48.64/10.29	51.59/11.83	56.73/16.29	37.99/12.52
TCA (Pan et al., 2011)	44.10/8.22	41.26/9.21	42.93/14.33	43.93/10.06	48.43/9.73	63.64/14.88	56.56/13.77
SA (Fernando et al., 2013)	54.23/7.47	50.60/8.31	55.06/10.60	56.72/10.78	64.47/14.96	69.00/10.89	64.44/9.46
T-SVM (Collobert et al., 2006)	-	-	-	-	-	72.53/14.00	-
TPT (Sanginetto et al., 2014)	-	-	-	-	-	76.31/15.89	-
DGCNN (Song et al., 2019b)	49.79/10.94	46.36/12.06	48.29/12.28	56.15/14.01	54.87/17.53	79.95/9.02	52.82/9.23
A-LSTM (Song et al., 2019a)	-	-	-	-	-	-	55.03/9.28
DAN (Li et al., 2018a)	-	-	-	-	-	83.81/8.56	58.87/8.13
BiDANN-S (Li et al., 2018c)	63.01/7.49	63.22/7.52	63.50/9.50	73.59/9.12	73.72/8.67	84.14/6.87	65.59/10.39
BiHDM (Li et al., 2020)	-	-	-	-	-	85.40/7.53	69.03/8.66
RGNN (Zhong et al., 2020)	64.88/6.87	60.69/5.79	60.84/7.57	<b>74.96/8.94</b>	<b>77.50/8.10</b>	85.30/6.72	73.84/8.02
SOGNN (Ours)	<b>70.37/7.68</b>	<b>76.00/6.92</b>	<b>66.22/11.52</b>	72.54/8.97	71.70/8.03	<b>86.81/5.79</b>	<b>75.27/8.19</b>



be compared with the results of other EEG-based emotion recognition models.

As shown in **Table 1**, the experimental results of the proposed SOGNN and many other methods on the SEED and SEED-IV databases are presented. The bold values indicated the largest values in all methods. In the experiments of the model for one-band features, we changed the input features from 5 bands to 1 band, changed the input size of the model to fit the inputs, and retrained the model for evaluation of sub-band features. The proposed SOGNN with delta or theta band features achieved higher accuracies than the other methods with the same features. Regarding the features of the other bands, the proposed SOGNN achieved relatively high performance which was quite close to the best performing methods.

With the features of all bands, the SOGNN achieved averaged accuracy of 86.81% on the SEED dataset and 75.27% on the SEED-IV dataset, which are higher than the performances of the state-of-the-art methods, i. e. the BiHDM (Li et al., 2020) and RGNN (Zhong et al., 2020) models. The proposed SOGNN

achieved a macro-F1 score of 0.8669 and an AUC score of 0.9685 on the SEED dataset. The F1 scores of happy, sad and neutral emotion class are 0.8556, 0.8577, and 0.8874. For SEED-IV dataset, it achieved a macro-F1 score of 0.7547 and an AUC score of 0.9162. The F1 scores of happy, sad, fear and neutral class are 0.7517, 0.7419, 0.7441, and 0.7810. As a typical kind of neural network, the performance of the SOGNN may be different when the model is randomly initialized by different random seeds. According to our experiments, the averaged accuracy on SEED dataset is from 0.83 to 0.88 while the averaged accuracy on SEED-IV dataset is between 0.70 and 0.78. In **Table 1**, we presented the medium results of the two datasets. The performance of the proposed SOGNN demonstrated its effectiveness in cross-subject emotion recognition.

Many previous graph models like DGCNN and BiDANN were based on predefined graph structure according to prior knowledge of EEG emotion signals. However, the predefined and fixed graph structures could not properly model the dynamic brain signals of different subjects in different emotion states. The

strength of the proposed SOGNN is that it could automatically extract graph structure from EEG features. The graph structure of SOGNN is dynamic and independent for different EEG features. As a result, the proposed SOGNN obtained more accurate and robust emotion recognition performance. In the next section, we will discuss and analyze the proposed model.

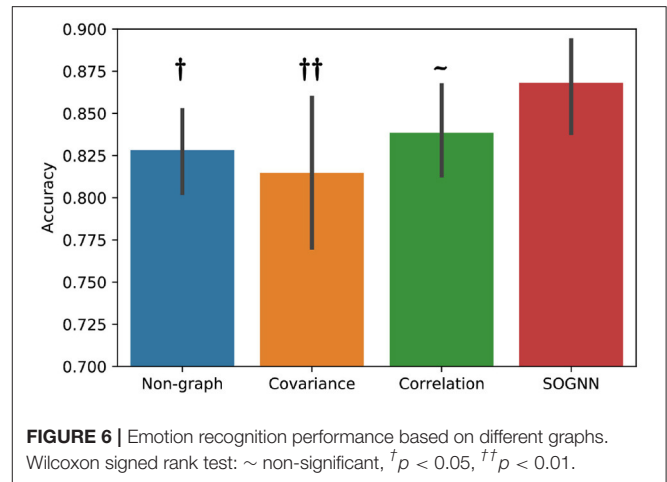
## 4. DISCUSSION

In this section, we analyze the proposed method and its internal properties in detail. We will discuss the performance differences of the SOGNN model with different features, self-organized graphs with different top-k rates, different graph construction methods, interchannel connections, etc.

**Figure 4** shows the emotion recognition accuracies of the proposed SOGNN model with different features including DE, PSD, ASM, DASM, DCAU, and RASM features. We found that the DE feature is the most discriminate feature while the performances of the other features are much lower. This finding is consistent with previous researches (Song et al., 2019b; Zhong et al., 2020).

Accordingly, dense graph convolution usually has high computational costs. Therefore, it is significant to construct a sparse and effective graph in practice. To obtain a sparse adjacent matrix of graph, we applied the top-k technique in which only the k-largest connection weights of each EEG electrode in the adjacent matrix were maintained while the remaining small weights were set to zero. As shown in **Figure 5**, the performance of the SOGNN with different top-k sparse graphs is presented. In the figure, k-10 denotes that only the 10 largest connection weights were maintained while the remaining weights were set to zeros. Likewise, k-62 indicates that the total connections between all 62 electrodes were reserved. We can find that the model with k-10 connections achieved similar performances as those models with more connections. This finding indicates the effectiveness of the model with sparse adjacent matrix.

In the proposed SOGNN model, a self-organized graph construction module is applied to dynamically learn the interchannel relationships of EEG signals across subjects. Here, we investigate different graph construction technique and their performance. **Figure 6** presents the emotion recognition accuracies on SEED dataset of the models with different graphs. To compare the performance of the models with different graphs, we would like to conduct statistical analyses. Evaluated on a dataset with only 15 subjects, the results of each model may not follow normal distribution. Wilcoxon signed-rank test is a non-parametric statistical hypothesis test which is suitable for the analysis on non-normally distributed data. With Wilcoxon signed-rank test result, we are able to determine whether the proposed model could achieve statistically significant better performance than the other models. As shown in **Figure 6**, the SOGNN achieved significantly better performance than non-graph model and the model with covariance graph. Regarding the covariance graph, the values of the elements in its adjacent matrix are usually too large that the graph convolutional layers will be easily saturated. This might be the reason for the low



performance of the model with the covariance graph. The correlation graph can be considered as a normalized version of the covariance graph in which its adjacent matrix is normalized to be in  $[0, 1]$ . As a result, its performance is improved a little. Here, we propose a straightforward method termed self-organized graph construction in (5). The proposed SOGNN could achieve state-of-the-art emotion recognition performance on the SEED and SEED-IV datasets. Our experiments demonstrated the effectiveness of the proposed model and the self-organized graph construction method.

To analyze the interchannel relationships learned by the proposed model, we obtained the average adjacent matrix of its self-organized graph (SO-graphs 1-3 as indicated in **Figure 3**) for SEED samples. Then, the average adjacent matrixes of SO-graphs 1-3 are normalized to  $[0, 1]$  for ease of analysis and presented in **Figure 7A**. These graphs reflect the common connections of EEG electrodes for emotion recognition. The SO-graph 1 is diagonally dominant that only few diagonal elements are relatively large while most of the rest elements are close to zero. That is only the features of a few EEG channels are discriminative for first graph convolution layer. Moreover, the off-diagonal elements of SO-graph 2 and 3 indicated that interchannel relationships also play important roles in classifying different emotion EEG signals.

Furthermore, we analyze the interchannel connections of the learned graphs for emotion recognition. We extracted the diagonal elements of the adjacent matrixes for SO-graph 1-3 and transformed into topographic maps. The topographic maps for SO-graphs 1-3 are presented in **Figure 7B**. According to the topographic maps, the prefrontal, and centro-parietal electrodes (e.g., F7, CPZ, FP2) had the largest weights in the topographic maps. The five electrodes with the largest weights connected with CPZ and FP2 are also presented. According to a previous study (Davidson et al., 1999), the activation in the regions of prefrontal cortex is related to blunted positive and negative emotions. A positive waveform will be enhanced over the centro-parietal electrode (CPZ) for emotional pictures (Lang and Bradley, 2010). In many related studies (Tyng et al., 2017; Alia-Klein et al., 2018; Pan et al., 2018), the prefrontal-parietal network is activated by

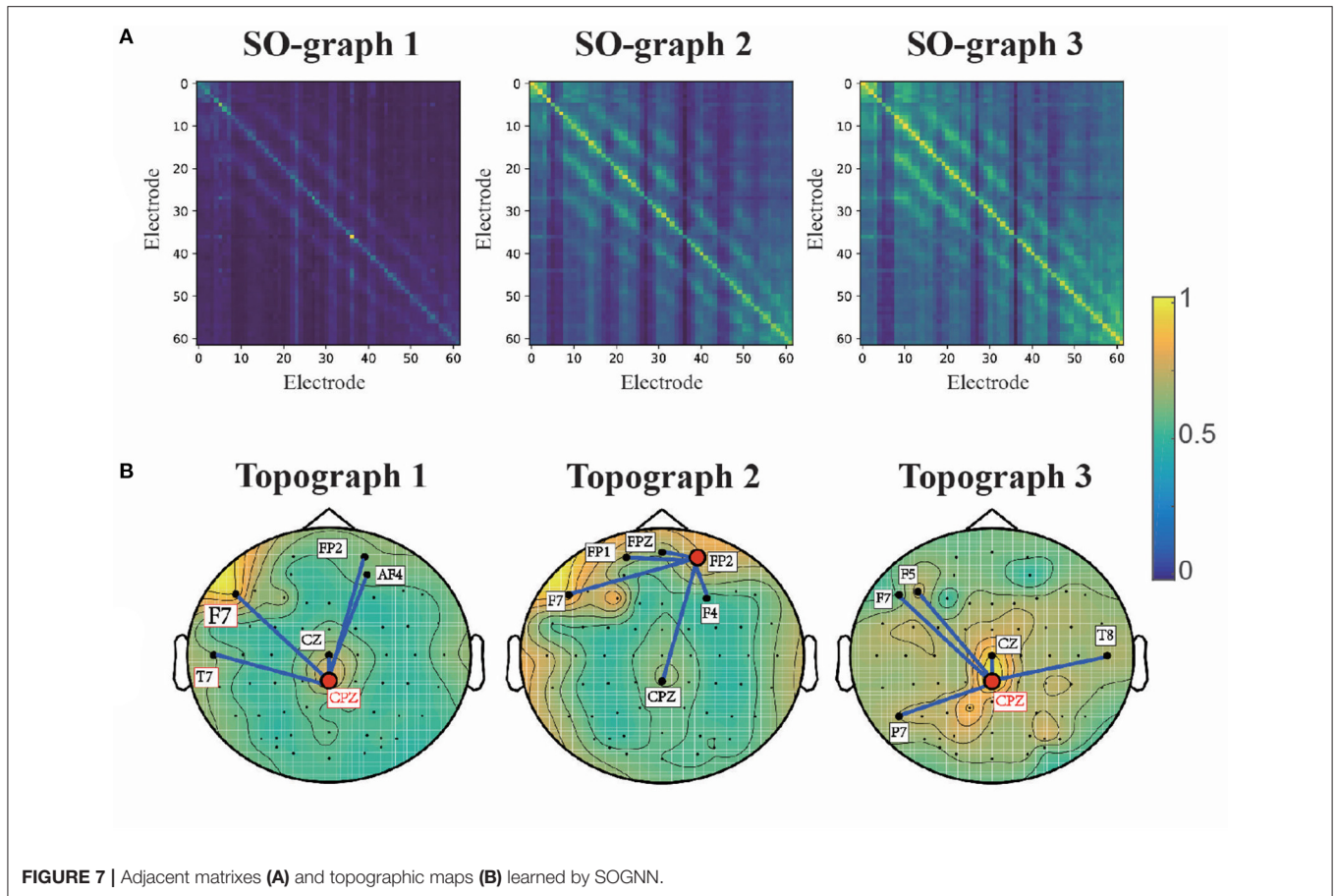


**FIGURE 7** | Adjacent matrixes (A) and topographic maps (B) learned by SOGNN.

emotion-related stimulus such as facial feelings, negative emotion processing, anger, etc. The interchannel relations between prefrontal, parietal and occipital channels are discriminative for emotion recognition EEG signals. Our findings coincide with the spatial distribution for emotion, as suggested by prior studies.

The above experiments and analysis of the proposed SOGNN model are significant for EEG-based emotion recognition. As a novel graph processing method for brain signals, it may bring some inspiration for neuroscience research, such as graph-based functional magnetic resonance imaging data processing.

## 5. CONCLUSION

In this paper, a novel model termed SOGNN was proposed for cross-subject emotion recognition. The SOGNN model was able to dynamically learn the interchannel relationships of EEG emotion signals using a self-organized graph construction module. The proposed model achieved state-of-the-art performance on two open EEG emotion recognition databases, i.e., SEED and SEED-IV. In addition, a series of analyses demonstrated the effectiveness of the proposed model on graph construction and emotion recognition. The experimental

results indicated that the SOGNN model is not only an effective model for recognizing emotions, but it is also a potential technique for other EEG-based applications. In the future, we would like to build more efficient networks to model brain signals and effectively decode high-level cognitive behaviors. Moreover, some new emerging machine learning techniques can also inspire the methodology for emotion recognition and affective computing.

## DATA AVAILABILITY STATEMENT

Publicly available datasets were analyzed in this study. This data can be found here: <https://bcmi.sjtu.edu.cn/resource.html>.

## ETHICS STATEMENT

The studies involving human participants were reviewed and approved by Ethics Committee of South China Normal University. The patients/participants provided their written informed consent to participate in this study. Written informed consent was obtained from the individual(s) for the publication of any potentially identifiable images or data included in this article.

## AUTHOR CONTRIBUTIONS

JL proposed the idea, conducted the experiments, and wrote the manuscript. SL and FW provided advice on the research approaches, signal processing, and checked and revised the manuscript. JP offered important help that guided the experiments and analysis methods. All authors contributed to the article and approved the submitted version.

## FUNDING

This work was supported by the National Natural Science Foundation of China (Grant Nos. 62006082, 61836003, and 61906019), the Key Realm R and D Program of Guangzhou

(Grant No. 202007030005), the Guangdong Natural Science Foundation (Grant Nos. 2021A1515011600, 2020A1515110294, and 2021A1515011853), and Guangzhou Science and Technology Plan Project (Grant No. 202102020877).

## ACKNOWLEDGMENTS

We thank Prof. Zhu Liang Yu and his group at South China University of Technology for providing the computation platform. We thank Dr. Zhenfu Wen at New York University for taking care of our research work. Finally, we would also like to thank the editors, reviewers, and editorial staff who participated in the publication process of this paper.

## REFERENCES

- Alarcao, S. M., and Fonseca, M. J. (2017). Emotions recognition using EEG signals: a survey. *IEEE Trans. Affect. Comput.* 10, 374–393. doi: 10.1109/TAFFC.2017.2714671
- Alhagry, S., Fahmy, A. A., and El-Khoribi, R. A. (2017). Emotion recognition based on EEG using LSTM recurrent neural network. *Emotion* 8, 355–358. doi: 10.14569/IJACSA.2017.081046
- Alia-Klein, N., Preston-Campbell, R. N., Moeller, S. J., Parvaz, M. A., Bachi, K., Gan, G., et al. (2018). Trait anger modulates neural activity in the fronto-parietal attention network. *PLOS ONE* 13:e0194444. doi: 10.1371/journal.pone.0194444
- Bruna, J., Zaremba, W., Szlam, A., and LeCun, Y. (2013). Spectral networks and locally connected networks on graphs. *arXiv [Preprint]. arXiv:1312.6203*.
- Busso, C., Deng, Z., Yildirim, S., Bulut, M., Lee, C. M., Kazemzadeh, A., et al. (2004). “Analysis of emotion recognition using facial expressions, speech and multimodal information,” in *Proceedings of the 6th International Conference on Multimodal Interfaces*, 205–211. doi: 10.1145/1027933.1027968
- Coan, J. A., and Allen, J. J. (2004). Frontal EEG asymmetry as a moderator and mediator of emotion. *Biol. Psychol.* 67, 7–50. doi: 10.1016/j.biopsycho.2004.03.002
- Collobert, R., Sinz, F. H., Weston, J., and Bottou, L. (2006). Large scale transductive SVMs. *J. Mach. Learn. Res.* 7, 1687–1712.
- Cowie, R., Douglas-Cowie, E., Tsapatsoulis, N., Votsis, G., Kollias, S., Fellenz, W., et al. (2001). Emotion recognition in human-computer interaction. *IEEE Signal Process. Mag.* 18, 32–80. doi: 10.1109/79.911197
- Davidson, R. J., Abercrombie, H., Nitschke, J. B., and Putnam, K. (1999). Regional brain function, emotion and disorders of emotion. *Curr. Opin. Neurobiol.* 9, 228–234. doi: 10.1016/S0959-4388(99)80032-4
- de Haan, W., Pijnenburg, Y. A., Strijers, R. L., van der Made, Y., van der Flier, W. M., Scheltens, P., et al. (2009). Functional neural network analysis in frontotemporal dementia and Alzheimer’s disease using EEG and graph theory. *BMC Neurosci.* 10:101. doi: 10.1186/1471-2202-10-101
- Duan, R.-N., Zhu, J.-Y., and Lu, B.-L. (2013). “Differential entropy feature for EEG-based emotion classification,” in *2013 6th International IEEE/EMBS Conference on Neural Engineering (NER)* (San Diego, CA: IEEE), 81–84. doi: 10.1109/NER.2013.6695876
- Even, S. (2011). *Graph Algorithms*. Cambridge University Press. doi: 10.1017/CBO9781139015165
- Fernando, B., Habrard, A., Sebban, M., and Tuytelaars, T. (2013). “Unsupervised visual domain adaptation using subspace alignment,” in *2013 IEEE International Conference on Computer Vision (Sydney, NSW)*, 2960–2967. doi: 10.1109/ICCV.2013.368
- Fey, M., and Lenssen, J. E. (2019). “Fast graph representation learning with PyTorch Geometric,” in *ICLR Workshop on Representation Learning on Graphs and Manifolds* (New Orleans, LA).
- (Grant No. 202007030005), the Guangdong Natural Science Foundation (Grant Nos. 2021A1515011600, 2020A1515110294, and 2021A1515011853), and Guangzhou Science and Technology Plan Project (Grant No. 202102020877).
- Ktena, S. I., Parisot, S., Ferrante, E., Rajchl, M., Lee, M., Glocker, B., et al. (2018). Metric learning with spectral graph convolutions on brain connectivity networks. *Neuroimage* 169, 431–442. doi: 10.1016/j.neuroimage.2017.12.052
- Lang, P. J., and Bradley, M. M. (2010). Emotion and the motivational brain. *Biol. Psychol.* 84, 437–450. doi: 10.1016/j.biopsycho.2009.10.007
- Li, H., Jin, Y.-M., Zheng, W.-L., and Lu, B.-L. (2018a). “Cross-subject emotion recognition using deep adaptation networks,” in *International Conference on Neural Information Processing* (Siem Reap: Springer), 403–413. doi: 10.1007/978-3-030-04221-9\_36
- Li, J., Qiu, S., Shen, Y.-Y., Liu, C.-L., and He, H. (2019). Multisource transfer learning for cross-subject EEG emotion recognition. *IEEE Trans. Cybernet.* 50, 3281–3293. doi: 10.1109/TCYB.2019.2904052
- Li, X., Song, D., Zhang, P., Zhang, Y., Hou, Y., and Hu, B. (2018b). Exploring EEG features in cross-subject emotion recognition. *Front. Neurosci.* 12:162. doi: 10.3389/fnins.2018.00162
- Li, Y., Wang, L., Zheng, W., Zong, Y., Qi, L., Cui, Z., et al. (2020). A novel bi-hemispheric discrepancy model for EEG emotion recognition. *IEEE Trans. Cogn. Dev. Syst.* doi: 10.1109/TCDS.2020.2999337
- Li, Y., Zheng, W., Zong, Y., Cui, Z., Zhang, T., and Zhou, X. (2018c). A bi-hemisphere domain adversarial neural network model for EEG emotion recognition. *IEEE Trans. Affect. Comput.* doi: 10.1109/TAFFC.2018.2885474
- Lin, Y.-P., Wang, C.-H., Jung, T.-P., Wu, T.-L., Jeng, S.-K., Duann, J.-R., et al. (2010). EEG-based emotion recognition in music listening. *IEEE Trans. Biomed. Eng.* 57, 1798–1806. doi: 10.1109/TBME.2010.2048568
- Linal, N., London, E., and Rabinovich, Y. (1995). The geometry of graphs and some of its algorithmic applications. *Combinatorica.* 15, 215–245. doi: 10.1007/BF01200757
- Micheloyannis, S., Pachou, E., Stam, C. J., Vourkas, M., Erimaki, S., and Tsirka, V. (2006). Using graph theoretical analysis of multi channel EEG to evaluate the neural efficiency hypothesis. *Neurosci. Lett.* 402, 273–277. doi: 10.1016/j.neulet.2006.04.006
- Pan, J., Zhan, L., Hu, C., Yang, J., Wang, C., Gu, L., et al. (2018). Emotion regulation and complex brain networks: association between expressive suppression and efficiency in the fronto-parietal network and default-mode network. *Front. Hum. Neurosci.* 12:70. doi: 10.3389/fnhum.2018.00070
- Pan, S. J., Tsang, I. W., Kwok, J. T., and Yang, Q. (2011). Domain adaptation via transfer component analysis. *IEEE Trans. Neural Netw.* 22, 199–210. doi: 10.1109/TNN.2010.2091281
- Petrosian, A., Prokhorov, D., Homan, R., Dasheiff, R., and Wunsch, I. I., D. (2000). Recurrent neural network based prediction of epileptic seizures in intra- and extracranial EEG. *Neurocomputing* 30, 201–218. doi: 10.1016/S0925-2312(99)00126-5
- Sanginetto, E., Zen, G., Ricci, E., and Sebe, N. (2014). “We are not all equal: personalizing models for facial expression analysis with transductive parameter transfer,” in *Proceedings of the 22nd ACM International Conference on Multimedia* (Orlando, FL), 357–366. doi: 10.1145/2647868.2654916

- Shi, L.-C. and Lu, B.-L. (2010). "Off-line and on-line vigilance estimation based on linear dynamical system and manifold learning," in *2010 Annual International Conference of the IEEE Engineering in Medicine and Biology (IEEE)*, 6587–6590
- Shu, L., Xie, J., Yang, M., Li, Z., Li, Z., Liao, D., et al. (2018). A review of emotion recognition using physiological signals. *Sensors* 18:2074. doi: 10.3390/s18072074
- Shuman, D. I., Narang, S. K., Frossard, P., Ortega, A., and Vandergheynst, P. (2013). The emerging field of signal processing on graphs: extending high-dimensional data analysis to networks and other irregular domains. *IEEE Signal Process. Mag.* 30, 83–98. doi: 10.1109/MSP.2012.2235192
- Song, T., Zheng, W., Lu, C., Zong, Y., Zhang, X., and Cui, Z. (2019a). MPED: a multi-modal physiological emotion database for discrete emotion recognition. *IEEE Access* 7, 12177–12191. doi: 10.1109/ACCESS.2019.2891579
- Song, T., Zheng, W., Song, P., and Cui, Z. (2019b). EEG emotion recognition using dynamical graph convolutional neural networks. *IEEE Trans. Affect. Comput.* 11, 532–541. doi: 10.1109/TAFFC.2018.2817622
- Tyng, C. M., Amin, H. U., Saad, M. N., and Malik, A. S. (2017). The influences of emotion on learning and memory. *Front. Psychol.* 8:1454. doi: 10.3389/fpsyg.2017.01454
- Varatharajah, Y., Chong, M. J., Saboo, K., Berry, B., Brinkmann, B., Worrell, G., et al. (2017). "EEG-GRAPH: a factor-graph-based model for capturing spatial, temporal, and observational relationships in electroencephalograms," in *Advances in Neural Information Processing Systems*, eds I. Guyon, U. V. Luxburg, S. Bengio, H. Wallach, R. Fergus, S. Vishwanathan, and R. Garnett (Long Beach, CA: NeurIPS Proceedings), 5371–5380.
- Wang, X. H., Zhang, T., Xu, X. M., Chen, L., Xing, X. F., and Chen, C. L. P. (2018). "EEG emotion recognition using dynamical graph convolutional neural networks and broad learning system," in *2018 IEEE International Conference on Bioinformatics and Biomedicine (BIBM)* (Madrid: IEEE), 1240–1244. doi: 10.1109/BIBM.2018.8621147
- Zhang, D., Chen, K., Jian, D., and Yao, L. (2020). Motor imagery classification via temporal attention cues of graph embedded EEG signals. *IEEE J. Biomed. Health Inform.* 24, 2570–2579. doi: 10.1109/JBHI.2020.2967128
- Zhang, T., Wang, X., Xu, X., and Chen, C. P. (2019). GCB-net: graph convolutional broad network and its application in emotion recognition. *IEEE Trans. Affect. Comput.* doi: 10.1109/TAFFC.2019.2937768
- Zheng, W. (2016). Multichannel EEG-based emotion recognition via group sparse canonical correlation analysis. *IEEE Trans. Cogn. Dev. Syst.* 9, 281–290. doi: 10.1109/TCDS.2016.2587290
- Zheng, W.-L., Liu, W., Lu, Y., Lu, B.-L., and Cichocki, A. (2018). Emotionmeter: a multimodal framework for recognizing human emotions. *IEEE Trans. Cybernet.* 49, 1110–1122. doi: 10.1109/TCYB.2018.2797176
- Zheng, W.-L., and Lu, B.-L. (2015). Investigating critical frequency bands and channels for EEG-based emotion recognition with deep neural networks. *IEEE Trans. Auton. Mental Dev.* 7, 162–175. doi: 10.1109/TAMD.2015.2431497
- Zheng, W.-L., Zhu, J.-Y., and Lu, B.-L. (2017). Identifying stable patterns over time for emotion recognition from EEG. *IEEE Trans. Affect. Comput.* 10, 417–429. doi: 10.1109/TAFFC.2017.2712143
- Zheng, W.-L., Zhu, J.-Y., Peng, Y., and Lu, B.-L. (2014). "EEG-based emotion classification using deep belief networks," in *2014 IEEE International Conference on Multimedia and Expo (ICME)* (Chengdu: IEEE), 1–6. doi: 10.1109/ICME.2014.6890166
- Zhong, P., Wang, D., and Miao, C. (2020). EEG-based emotion recognition using regularized graph neural networks. *IEEE Trans. Affect. Comput.* doi: 10.1109/TAFFC.2020.2994159

**Conflict of Interest:** The authors declare that the research was conducted in the absence of any commercial or financial relationships that could be construed as a potential conflict of interest.

Copyright © 2021 Li, Li, Pan and Wang. This is an open-access article distributed under the terms of the Creative Commons Attribution License (CC BY). The use, distribution or reproduction in other forums is permitted, provided the original author(s) and the copyright owner(s) are credited and that the original publication in this journal is cited, in accordance with accepted academic practice. No use, distribution or reproduction is permitted which does not comply with these terms.



# Changes in EEG Brain Connectivity Caused by Short-Term BCI Neurofeedback-Rehabilitation Training: A Case Study

Yuhao Wang<sup>1</sup>, Jingjing Luo<sup>1,2\*</sup>, Yuzhu Guo<sup>3</sup>, Qiang Du<sup>1</sup>, Qiying Cheng<sup>1</sup> and Hongbo Wang<sup>1\*</sup>

<sup>1</sup> Academy for Engineering and Technology, Fudan University (FAET), Shanghai, China, <sup>2</sup> Jihua Laboratory, Foshan, China, <sup>3</sup> School of Automation Science and Electrical Engineering, Beihang University, Beijing, China

## OPEN ACCESS

### Edited by:

Saugat Bhattacharyya,  
Ulster University, United Kingdom

### Reviewed by:

Andrej Savic,  
University of Belgrade, Serbia  
Rodrigo Ezequiel Ramele,  
Instituto Tecnológico de Buenos  
Aires, Argentina  
Chen Liu,  
Sun Yat-sen University, China

### \*Correspondence:

Hongbo Wang  
wanghongbo@fudan.edu.cn  
Jingjing Luo  
luojingjing@fudan.edu.cn

### Specialty section:

This article was submitted to  
Brain-Computer Interfaces,  
a section of the journal  
Frontiers in Human Neuroscience

**Received:** 08 November 2020

**Accepted:** 31 May 2021

**Published:** 24 June 2021

### Citation:

Wang Y, Luo J, Guo Y, Du Q, Cheng Q and Wang H (2021) Changes in EEG Brain Connectivity Caused by Short-Term BCI Neurofeedback-Rehabilitation Training: A Case Study. *Front. Hum. Neurosci.* 15:627100. doi: 10.3389/fnhum.2021.627100

**Background:** In combined with neurofeedback, Motor Imagery (MI) based Brain-Computer Interface (BCI) has been an effective long-term treatment therapy for motor dysfunction caused by neurological injury in the brain (e.g., post-stroke hemiplegia). However, individual neurological differences have led to variability in the single sessions of rehabilitation training. Research on the impact of short training sessions on brain functioning patterns can help evaluate and standardize the short duration of rehabilitation training. In this paper, we use the electroencephalogram (EEG) signals to explore the brain patterns' changes after a short-term rehabilitation training.

**Materials and Methods:** Using an EEG-BCI system, we analyzed the changes in short-term (about 1-h) MI training data with and without visual feedback, respectively. We first examined the EEG signal's Mu band power's attenuation caused by Event-Related Desynchronization (ERD). Then we use the EEG's Event-Related Potentials (ERP) features to construct brain networks and evaluate the training from multiple perspectives: small-scale based on single nodes, medium-scale based on hemispheres, and large-scale based on all-brain.

**Results:** Results showed no significant difference in the ERD power attenuation estimation in both groups. But the neurofeedback group's ERP brain network parameters had substantial changes and trend properties compared to the group without feedback. The neurofeedback group's Mu band power's attenuation increased but not significantly (fitting line slope = 0.2,  $t$ -test value  $p > 0.05$ ) after the short-term MI training, while the non-feedback group occurred an insignificant decrease (fitting line slope = -0.4,  $t$ -test value  $p > 0.05$ ). In the ERP-based brain network analysis, the neurofeedback group's network parameters were attenuated in all scales significantly ( $t$ -test value:  $p < 0.01$ ); while the non-feedback group's most network parameters didn't change significantly ( $t$ -test value:  $p > 0.05$ ).

**Conclusion:** The MI-BCI training's short-term effects does not show up in the ERD analysis significantly but can be detected by ERP-based network analysis significantly. Results inspire the efficient evaluation of short-term rehabilitation training and provide a useful reference for subsequent studies.

**Keywords:** brain-computer interface, electroencephalogram, motor imagery, neurofeedback-rehabilitation, short-term training, event-related potentials, brain-network analysis

## INTRODUCTION

Electroencephalograph (EEG)-based BCI systems is often applied in combination with motor imagery (MI) paradigm (Alkadhi et al., 2005) for neurorehabilitation training (Kumar et al., 2016; Baig et al., 2017; Oikonomou et al., 2017; Cheng et al., 2018), especially for enhancing motor recovery from brain injuries such as stroke hemiplegia (Buch et al., 2008; Zimmermann-Schlatter et al., 2008; Daly et al., 2009; Langhorne et al., 2009; Barclay et al., 2020). Neurofeedback (NF) is also commonly applied in the BCI system. Thus cortical movement intention can be transferred to physical activity or stimulation that feeds back to the patient as a consequent response, forming a closed-loop neural circuit (Yu et al., 2015; Zich et al., 2015; Sitaram et al., 2017). Clinical studies have shown improvement in neurorehabilitation using MI-BCI system with NF (Prasad et al., 2009; Caria et al., 2011; Shindo et al., 2011; Ramos-Murguialday et al., 2013; Mukaino et al., 2014), and results are supported by the underlying mechanisms of neural plasticity and brain reorganization (Rozelle and Budzynski, 1995; Ang et al., 2014).

Neurorehabilitation assessment is essential for both patients as well as BCI system evaluation. Clinical assessments of physical function restoration such as functional upper extremity test (FMA), wolf motor function test (WMFT) are used as typical methods (Rozelle and Budzynski, 1995; Mihara et al., 2013; Ang et al., 2014; Li et al., 2014; Kim et al., 2016; Leeb et al., 2016). However, most physical assessments are only applicable after substantial functional recovery with a long training period and are the indirect measure of brain injury recovery. Researchers have been studying brain imaging techniques such as functional Magnetic Resonance Imaging (fMRI) (Song et al., 2014; Young et al., 2014), EEG (Daly and Wolpaw, 2008; Ono et al., 2015), and electromyogram (EMG) (Rozelle and Budzynski, 1995; Daly and Wolpaw, 2008). The goal is to find new assessment methods to analyze the brain directly and observe subtle changes in neural reorganization. For BCI rehabilitation, the challenge is to establish an EEG quantitative standard to evaluate the rehabilitation effect. MI as a typical BCI rehabilitation paradigm varies in its performance when applying different feedback strategies (Ahn and Jun, 2015; Marzbani et al., 2016; Renton et al., 2017). There are other factors such as induction paradigm or training engagement, may affect potential brain recovery, thus make it more important to find direct and rapid measurements for BCI rehabilitation using EEG.

For BCI EEG analysis, sensorimotor rhythm (SMR) of neurophysiological oscillations and event-related potentials (ERPs) are commonly used as neurophysiological features. As a particular example of SMR, desynchronization/synchronization

(ERD/ERS) modulation during MI or movement execution (Pfurtscheller and Da Silva, 1999; Graitmann et al., 2009; Nicolas-Alonso and Gomez-Gil, 2012) is proportional to the motor function's impaired level of patients (Matsumoto et al., 2010; Rossiter et al., 2014; Naros and Gharabaghi, 2015; Soekadar et al., 2015). And it was found to be improved in the prolonged MI-BCI rehabilitation (Rozelle and Budzynski, 1995; Pfurtscheller and Da Silva, 1999; Yoshida et al., 2016). The ERPs as EEG averages are direct amplitude changes in response to exhibited events (Kok, 1997). Both signals characterize as potential recovery measures, given that they may carry information about underlying mechanisms of brain recovery. What's more, the functional connectivity of brain networks is another strategy to reveal changes in neural activity. For example, brain network analysis based on fMRI has been used in clinical-pathological studies (Van Den Heuvel and Pol, 2010). Compared to the fMRI, the convenience and high temporal resolution of the EEG signal has led to an increasing number of scholars using it to analyze the brain networks (Varela et al., 2001; Wang et al., 2010; Faith et al., 2011; Sakkalis, 2011; Carter et al., 2012; Stam and Van Straaten, 2012; Belardinelli et al., 2017). Further studies use the EEG to apply graph theory on the cortical network (Bullmore and Sporns, 2009; Fallani et al., 2013; Cheng et al., 2015) to measure brain changes by rehabilitation training (Brown, 1970; de Vico Fallani et al., 2014; Philips et al., 2017).

Studies mentioned above show that neural functional changes reflected by EEG signals are reliably correlated with changes in physical function. Still, the results are observed only after prolonged training, which may not be comprehensive enough. Thus, we consider the short-term effects of BCI on brain activity. BCI training with feedback could alternately enhance and suppress spontaneous rhythmic activity for short periods (Nowlis and Kamiya, 1970; Beatty et al., 1974; Serman, 1974) and leads to sustained changes in neural activity (Kaplan, 1975; Wyler et al., 1976). Lin et al. found that short-term training leading to significant neural activity changes in brain network by using functional connectivity of fMRI (Lin et al., 2017). In neurorehabilitation, Tsuchimoto et al. (2019) found that BCI training with neurofeedback can effect on patients' EEG synchrony in the short term. We can infer that the short-term MI-BCI rehabilitation training variations based on EEG signals may also have the ability to interpret the rehabilitation process. Evaluating those variations can help to portray the recovery process more accurately. Yet, the variations are still unclear, and an efficient and rapid recovery assessment method of short-term MI-BCI rehabilitation training has not been proposed. Using the EEG to study the state of neural signal expression in a short

time may provide a new approach to measuring the effects of rehabilitation training.

Our study investigated how the short-term MI-BCI training affects the human brain and uses EEG signals to evaluate it. We used EEG's Mu band power attenuation to analyze the impact of short-term rehabilitation training and use network methods to analyze the effectiveness of exercise on various network scales. In section II, the experimental data are presented, and the analysis methods are described. Section III presents the experimental results of the short-term ERD modulation and the ERP-based cortical network, respectively. Discussion and conclusions are presented at the end.

## MATERIALS AND METHODS

### Data Acquisition

We used left- and right-handed motor imagery data from a publicly available dataset (Kaya et al., 2018). All 5 subjects underwent 3 days of MI-BCI training were selected, of which four subjects with no visual feedback and one subject with visual feedback. In all experiments, an EEG distribution with 19 electrodes in the International Standard 10–20 system was used. Data was acquired using a medical-grade EEG-1200 recording system with a JE-921A acquisition cassette (Nihon Kohden, Japan) and band-filtered at 0.53~70 Hz at the recording phase. Participants were seated in a chair and observed a computer screen about 200 cm in front of the BCI system. A typical rehabilitation training of left/right hand MI was applied as the experiment paradigm. Two formats of experiments were conducted, a “non-feedback” mode as well as a “feedback” mode, introduced as follows.

### Non-feedback Data

The whole process lasted 51.5 min, assembled from three 15-min sessions, with a 2.5-min break to initialize the system before the session start, followed by a 2-min break between the two sessions for the subject to relax (Figure 1C). Each session contained 300 trials in total, each consisting of pause and action phases. The

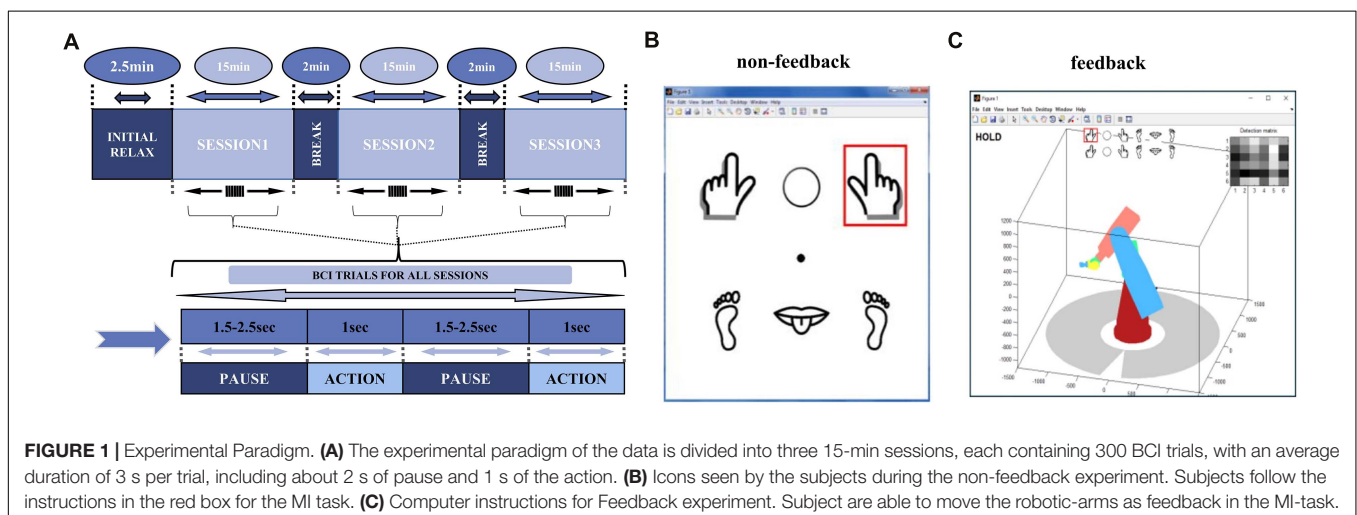
pause phase had a duration of 1.5–2.5 s randomly, with an average of 2 s. During the action phase, the screen showed a GUI interface with a red square, to instruct the participant to perform the corresponding task for 1 s (Figure 1A). The red square upon the left- or right-handed cartoon image indicated the grasping MI task, and upon the middle circle indicated a “hold” task with no imagery (Figure 1A). The experiment was carried out on 3 days at irregular intervals. The four subjects of non-feedback paradigm were labeled as A, C, D, E in this article.

### Feedback Data

The feedback paradigm had the same overall steps as the non-feedback paradigm, however subjects were asked to control actions of a 3D virtual robotic arm. During the action phase, the screen showed a virtual robotic-arm bellow the task icons. Depending on the real-time decoding analysis of Mu-suppression, robotic arm appeared to move left/right or stay “hold” (Figure 1B). The robotic-arm moved as the feedback of an imagery success. The first session followed the same steps as in the non-feedback paradigm. In second and third sessions, subject's imagery was actively performed, and the movement of the virtual robotic arm was determined by subjects themselves initially. It was then set as specific task sequences, e.g., to “move two units to the left” or to “move 1 unit to the left and then three units to the right.” We labeled the feedback subject as subject B later in the article. We arranged EEG data of 3 days in parallel for statistical analysis for each subject. In each day, left- or right-hand imagery task trials were used with all “hold” trials removed for EEG analysis in this article.

### Mu Suppression Score

ERD/ERS in MI task is calculated by the power spectral density (PSD) of EEG signals in the personalized frequency range, typically at 8–13 Hz known as the Mu band (Kuhlman, 1978; Pfurtscheller and Da Silva, 1999). In the ERD phenomenon, the corresponding region of primary motor cortex (M1) in the hemisphere contralateral to the movement is attenuated. In this study, the C3 and C4 electrode positions from the 10



to 20 international system are located close to the M1 region. Therefore, for the right-hand MI, we used the C3 channel as the contralateral side, and its symmetric electrode C4 as the ipsilateral side. The same applies to the left-hand MI.

The quantification of ERD/ERS can be calculated using the classical approach called Mu-suppression. The obtained EEG signal is first converted to the frequency domain by Fourier transform. Then, we used multi-taper method (Thomson, 1982) to calculate the PSD, selected frequency range with Mu-suppression for individual experiment to derive the band power. Change of contralateral Mu-band energy between the task state and the resting state was evaluated, using the most recent 1-s before task initiation representing resting state (Thomson, 1982; Oberman et al., 2008; Braadbaart et al., 2013). The following formula gives the Mu-suppression score (MuSC):

$$MuSC = -\frac{MuP_{bo} - MuP_{nbo}}{MuP_{nbo}} * 100 \quad (1)$$

where  $MuP_{bo}$  is the band power of the task state, and  $MuP_{nbo}$  is the band power of the resting state.

As human brain is characterized by inter-individual variability and rapid dynamic changes, we applied a sliding frequency window with a size of 3 Hz (0.67 overlaps) to precisely select the subject-specific Mu-band boundaries. The most suppressed window comparing the MI state (0~1 s) against the corresponding resting state (-1~0 s) was chosen as MI-related EEG oscillations for each subject each day. The screening results for subject-specific Mu-band boundaries are presented in **Supplementary Table 1**.

## Network Analysis

### Functional Connectivity Estimation

Neuronal oscillations are implicit in the underlying coordination mechanisms of the brain (Singer, 1999; Varela et al., 2001). The channels with EEG signal contain a collection of oscillations of regional neurons. The synchronization of oscillations between channels may indicate that the brain has information flow between regions (Womelsdorf et al., 2007). Functional Connectivity is a method for assessing the synchronization of oscillating signals from channel to channel. The degree between channels indicates how much information is exchanged.

ERPs is any stereotyped electrophysiological response to a stimulus, which have excellent temporal resolution. Considering the immediacy of the short-term changes targeted in this study, we chose ERPs as the basis for brain network calculations. In the scenario of MI, ERPs are generally obtained by trial averaging. Band-pass filtering is commonly used in some EEG studies for data preprocessing and to investigate the extraction and amplification of signals of interest by different band-pass filter bands, such as Movement-related cortical potentials (MRCP, 0.05–6 Hz). In this study, We made preliminary band-pass pre-process for different frequency bands that may be triggered by MI, then the EEG signal was averaged over every 20 trials as “trial-block” to obtain a pronounced ERP curve. Pearson’s correlation coefficient was used for the functional connectivity estimation, directly expressing the correlation of

amplitude characteristics. The Pearson correlation coefficient was calculated as follows:

$$\rho = \frac{E[(X - \mu_X)(Y - \mu_Y)]}{\sigma_X \sigma_Y} = \frac{E[(X - \mu_X)(Y - \mu_Y)]}{\sqrt{\sum_{i=1}^n (X_i - \mu_X)^2} \sqrt{\sum_{i=1}^n (Y_i - \mu_Y)^2}} \quad (2)$$

where  $X$  and  $Y$  represent the calculated signal values for trial-block ERPs of two channels.  $\mu_X$  and  $\mu_Y$  represent the mean of  $X$  and  $Y$ .  $\sigma_X$  and  $\sigma_Y$  represent the standard deviation of  $X$  and  $Y$ . The formula calculates the covariance ratio between the two channels to the product of two standard deviations.

### Network Indicators

Graph theory plays a crucial role in network analysis. Each EEG channel represents a single node in graph. Degrees derived from Functional Connectivity estimates between nodes then form a graph. Since MI-action focuses on C3 and C4 nodes’ expression, we consider the direct calculation of the change in C3 and C4 nodes’ degree as the task proceeds.

$$E_i(G) = \sum_{j \neq i \in G} d_{ij} \quad (3)$$

where  $i$  is the node of interest,  $G$  is the whole brain connectivity map.  $J$  is other nodes and  $E_i(G)$  is the sum of the connection weights of the node of the claim. All other nodes within the region were calculated. We also performed the same calculation to O1 and P1 nodes’ degrees far away from the M1 region, used as a comparison study. Also, the summation of degrees for all nodes in the region provides a complete picture of the corresponding brain regions’ overall neural activity:

$$E_{region}(R) = \sum_{j \neq i \in R} d_{ij} \quad (4)$$

Where  $E_{region}$  refers to the region of interest, which can be the left or right hemisphere.  $R$  is the set of nodes within the brain hemisphere, and  $j$  is the other nodes. This equation calculates the sum of the weights of all weighted edges in the region. This calculation allows us to estimate the overall activity of the nodes in the region.

The clustering coefficient (Gonzalez-Lima and McIntosh, 1994; Latora and Marchiori, 2001) is used in this analysis, aiming to explore the whole brain’s variation. Clustering coefficients are divided into three calculation methods: global, local, and average. The global clustering coefficient is used to explore the variation of the whole brain. The clustering coefficient calculation requires that the graph be binary and coherent. Thresholds should be properly chosen to binarize the calculated connectivity in the brain network analysis. To ensure the connectivity of the graph, we use the threshold value of 0.6 in this experiment. The coefficient is obtained by dividing the number of closed-loop ternary groups by the number of all ternary groups in the graph, calculated as follows:

$$C_{total}(G) = \frac{3 \times G_{\Delta}}{3 \times G_{\Delta} + G_{\Lambda}} \quad (5)$$

where  $G_{\Delta}$  represents the number of closed-loop triads in the graph (three nodes connected), and  $G_{\wedge}$  means that there are only two edges with weight one between the three nodes. In this experiment, we calculate the changes of the clustering coefficients of the whole brain and the hemispheres overtime to get a global picture of the brain network's changes in the short-term for the MI task.

## RESULTS

### Change of ERD MuSC

We applied Mu-band boundary selection for each individual and results were within alpha and lower-beta band (5–20 Hz, filtering results listed in the **Supplementary Material** for reference). MuSC was calculated from the 636 non-feedback subject A and 616 feedback subject B trials then averaged for each consecutive 20 trials constructing “trial blocks” results. The MuSC of the non-feedback subject A tends to be downwards with the fitting line slope of  $-0.4$  (**Figure 2A**), by contrast, the feedback B's MuSC rises with the fitting line slope of  $0.2$  (**Figure 2B**), similar to the result in previous studies (Shindo et al., 2011; Yoshida et al., 2016). However, there is no significant difference between the two experiments due to the large variance. Changes in ERD's MuSC can be observed in short-term MI experiments with feedback, but the trend of the data is subtle and difficult to use to measure the effect of short-term training. Four non-feedback subjects showed consistent result of ERD/ERS, thus we took non-feedback subject A as the typical subject to show the comparisons and analysis in the following.

### Change of ERP Network

We used different frequency bands (0.53–4 Hz, 3–6 Hz, 5–10 Hz, 8–16 Hz, and 15–30 Hz) to apply an initial inspection of degree-of-nodes for four non-feedback subjects (A,C,D,E) and 3-day data separately of the feedback subject B. This

was to design an appropriate EEG preprocessing filter before construction the ERP functional network. We study the three sequential sessions with MI training of both paradigms and label the first to third sessions in the experimental sequence as super-trial 1–3, respectively. Results showed that both the 2nd and 3rd super-trial of the 3-day data of the feedback group in 3–6 Hz had significant decrease compared to the 1st super-trial ( $p = 2e-3, 7e-3$  for day 1 respectively,  $p = 2e-3$ , for day 2,  $p = 6.5e-4, 5e-5$  for day 3, respectively) (see **Table 1**). Some other frequency band above 5 Hz also showed a partially significant trend. However, signal in the 0.53~4 Hz band of the low frequency component did not show differences during on-going training sessions. In contrast, non-feedback subjects showed subtle increase at 0.53~4 Hz, while no trend showing in other frequency ranges. Results indicated a consistent change along the short-term training for the feedback group.

To investigate the detailed dynamic change along the short-term training, we compared 1st and 3rd super-trial ERPs of the feedback subject B, at both 0.3–30 Hz and 3–30 Hz frequency bands. In the case of 0.3–30 Hz filtering (**Figure 3A**), the ERP dynamic processes did not show significant changes, with topographic maps appearing similarly patterns at the MI task. However, ERP dynamic changes were revealed under the 3–30 Hz filtering (**Figure 3B**), such as a strengthening of the negative potential at 0.35 s, of the following positive potential at 0.55 s, and the negative potential at 0.65 s. ERP features at 3~30 Hz presented strengthened deflections from the beginning of the training session to the end. By combining results in **Table 1**, result indicated the EEG low frequency component containing MI brain activities, as consistent with (Ramos-Murguialday and Birbaumer, 2015; Schwarz et al., 2019), and it contained information of short-term variations at the feedback paradigm. We choose a 3~30 Hz band-pass filter to capture EEG characteristics as interested before average and further analysis.

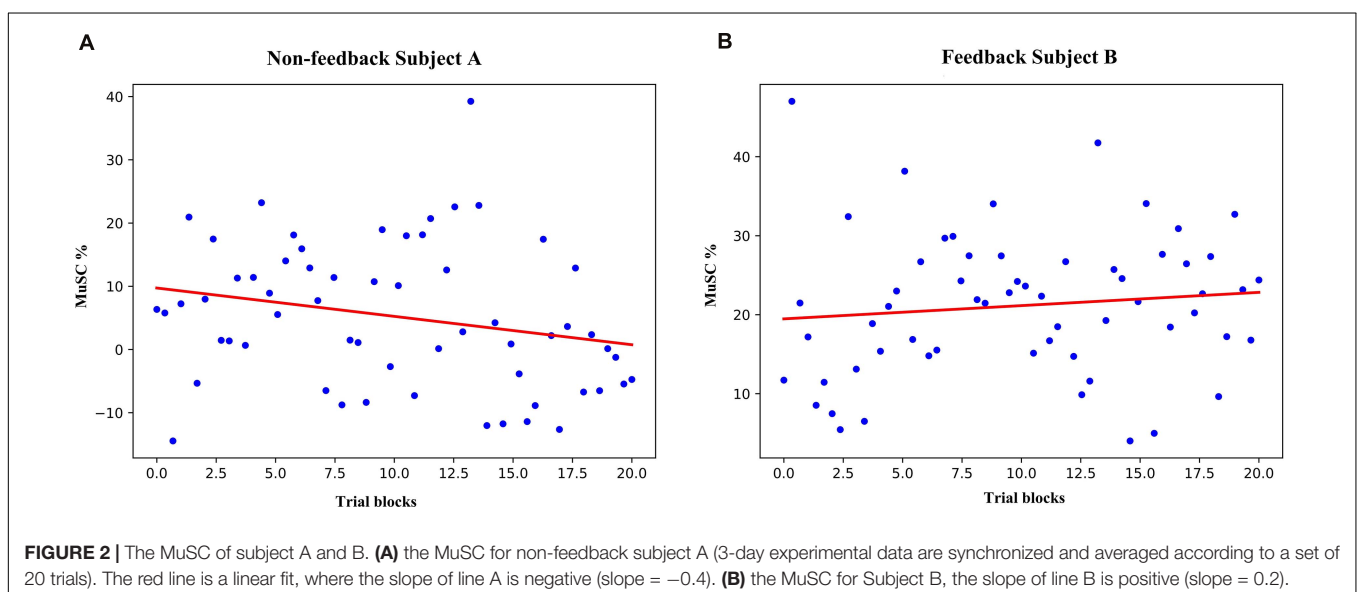


**TABLE 1 |** Degree-of-nodes for all subjects in different frequency bands.

Freq	0.5~3~4 Hz			3~6 Hz			5~10 Hz			8~16 Hz			15~30 Hz			
	Subj	Sess1	2	3	Sess1	2	3	Sess1	2	3	Sess1	2	3	Sess1	2	3
B1	29.3 ± 0.8	28.3 ± 2.6	28.5 ± 1.9	<b>30.4 ± 0.6</b>	<b>28.1 ± 1.4**</b>	<b>27.1 ± 3.0**</b>	23.6 ± 2.8	24.3 ± 1.9	21.9 ± 4.1	19.5 ± 2.7	22.1 ± 1.9*	20.3 ± 3.1	20.2 ± 2.2	18.6 ± 2.1	19.6 ± 2.2	19.6 ± 2.2
B2	<b>29.7 ± 0.9</b>	<b>30.3 ± 0.6</b>	<b>29.2 ± 1.0**</b>	<b>27.6 ± 1.4*</b>	<b>25.7 ± 2.6</b>	<b>25.7 ± 2.6</b>	21.4 ± 3.4	21.7 ± 3.4	20.2 ± 3.0	19.5 ± 4.2	19.2 ± 2.3	20.6 ± 2.4	16.3 ± 2.7	16.8 ± 2.8	17.4 ± 1.6	17.4 ± 1.6
B3	30.6 ± 0.6	29.6 ± 1.9	29.7 ± 1.7	<b>30.5 ± 0.9</b>	<b>27.1 ± 1.4**</b>	<b>25.8 ± 1.5**</b>	18.8 ± 2.3	17.7 ± 1.2	18.5 ± 1.7	<b>25.0 ± 2.3</b>	<b>23.2 ± 2.2</b>	<b>22.2 ± 2.2*</b>	23.7 ± 2.2	<b>18.5 ± 1.6</b>	<b>20.9 ± 1.1**</b>	<b>19.0 ± 2.6</b>
A	18.8 ± 3.1	16.3 ± 2.5	17.4 ± 3.6	20.0 ± 1.9	17.5 ± 2.8	18.8 ± 2.3	17.7 ± 1.2	18.5 ± 1.7	18.7 ± 2.5	15.0 ± 1.7	16.0 ± 1.9	16.6 ± 1.5	14.8 ± 1.7	14.8 ± 1.1	15.3 ± 1.1	15.3 ± 1.1
C	<b>27.1 ± 1.2</b>	<b>27.0 ± 1.3</b>	<b>28.2 ± 1.2*</b>	25.9 ± 1.7	25.2 ± 2.1	25.4 ± 1.1	26.1 ± 1.0	25.7 ± 1.4	26.1 ± 1.0	21.9 ± 1.4	21.4 ± 1.9	20.8 ± 0.8	16.7 ± 1.3	16.0 ± 1.6	15.7 ± 1.4	15.7 ± 1.4
D	<b>26.9 ± 1.7</b>	<b>28.5 ± 1.1</b>	<b>28.1 ± 0.9*</b>	24.4 ± 1.6	23.3 ± 1.3	22.7 ± 2.0	21.6 ± 1.5	20.0 ± 1.8	20.6 ± 1.1	17.7 ± 1.8	16.7 ± 2.3	17.1 ± 1.5	14.3 ± 0.9	14.4 ± 1.3	14.9 ± 2.1	14.9 ± 2.1
E	<b>20.7 ± 2.6</b>	<b>21.6 ± 4.1</b>	<b>22.4 ± 1.5*</b>	22.1 ± 2.3	23.7 ± 2.1	22.5 ± 1.1	16.0 ± 1.8	14.5 ± 1.5	15.7 ± 2.1	17.7 ± 1.2	16.7 ± 1.6	17.5 ± 1.2	16.3 ± 1.1	17.1 ± 1.3	16.1 ± 1.4	16.1 ± 1.4

\*Decreasing with  $p < 0.05$ ; \*\*decreasing with  $p < 0.01$ ; +, increasing with  $p < 0.05$ ; ++, increasing with  $p < 0.01$ . The bold values means the significant change of the data ( $p < 0.05$  or  $p < 0.01$ ).

As event-related responses apart from Mu-suppression, we analyzed ERPs of left or right MI task for non-feedback subject A and feedback subject B. It was derived from averaging 20 trials at  $-0.5 \sim 1$  s filtered at 3–30 Hz for of all EEG channels. The ERP responses initiated after the start of the MI task. The overall ERP performance of the feedback (**Figure 4A**) and non-feedback subject (**Figure 4B**) were stable for left- and right-handed MI, with slightly different ERP performance for different side-channels for left- and right-handed MI.

### Degree of Nodes

Single node degrees were analyzed for non-feedback subject A and feedback subject B, respectively. **Figure 5A** shows the analyzed nodes. The contralateral analysis target nodes for left-handed motion include C4, O2, Fp2, and right-handed C3, O1, Fp1, and the opposite nodes for ipsilateral motion. The subject experiments were divided into three groups according to the order in which the sessions were performed. The trials for MI task execution were selected from each group, averaging the 20 original trials to containing ERP features to calculate the network's connectivity. In **Figure 5B**, the connectivity histogram of subject A's ipsilateral and contralateral sides Fp node's contralateral side is significantly different ( $t$ -test value  $p = 0.01$ ) between the first and third super-trials, while the other nodes not significantly different. In **Figure 5C** for subject B, the second and third super-trials of the C and Fp nodes are significantly different from the first in both ipsilateral and contralateral ( $t$ -test value  $p = 2.3e-5, 1.2e-5$  for C;  $p = 2.1e-5, 3.7e-6$  for Fp in contralateral and  $p = 1.5e-8, 2.5e-6$  for C;  $p = 3.2e-6, 1.2e-6$  for Fp in ipsilateral); in addition, the O nodes' contralateral experiments were significantly different between the first and third super-trials ( $t$ -test value  $p = 0.6e-2$  and  $0.3e-3$  in contralateral and ipsilateral). Different significant downward trends can be observed in subject A and subject B. Thus, we hypothesize that feedback BCI training leads to decreased node degrees in the ERP brain network.

### Degree of Region

In this part, we calculated the sum of the connectivity in the left and right hemispheres as LnL and LnR, and connectivity between two sides (excluding the medial node) as EX (**Figure 6A**). Then used linear regression to fit a straight line of scatter. In **Figure 6B** for subject A, The slopes of the three fitted lines all approach 0 in both left-handed and right-handed MI. In Subject B's feedback experiment (**Figure 6C**), the slopes of all fitted lines were negative, indicating a decrease in regional connectivity. During left-handed MI, the slope of LnR on the opposite side was smaller than that of LnL on the same side (Ex fitting line slope =  $-0.67$ , LnL fitting line slope =  $-0.32$ , LnR fitting line slope =  $-0.66$ ), whereas this phenomenon does not appear, the fitted lines for right-handed MI are (Ex fitting line slope =  $-0.53$ , LnL fitting line slope =  $-0.31$ , LnR fitting line slope =  $-0.42$ ). **Figure 5** gives a clear contrast between the regional degree summation. The feedback experiments will have an overall downward trend, and its contralateral downward trend is more pronounced in left MI. The slopes of LnR in their leftMI are smaller than LnL both in subjects A and B, which is presumed to be related to the ERD/ERS features of the EEG.

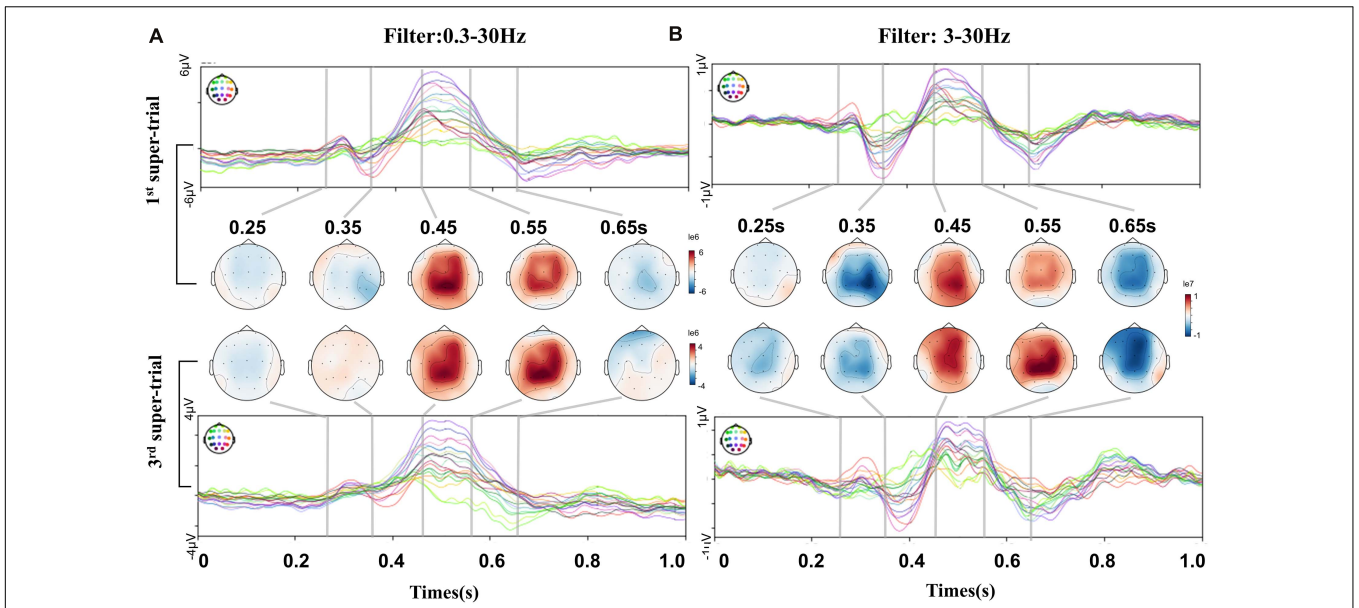


**FIGURE 3 |** ERP and topographic comparisons between the 1st and 3rd super-trials of the short-term BCI training process. This comparison was for feedback subject B. Each super-trials containing consecutive 100 non-hold trials. **(A)** Filter with 0.3–30 Hz. No significant change between the 1st and 3rd super-trials. Some drift changes were present in the prefrontal channels. **(B)** Filter with 3–30 Hz. The 1st and 3rd topographic maps show dynamic differences. N-potential attenuation at 0.35 s, P-potential enhanced at 0.55 s, then N-potential enhanced at 0.65 s.

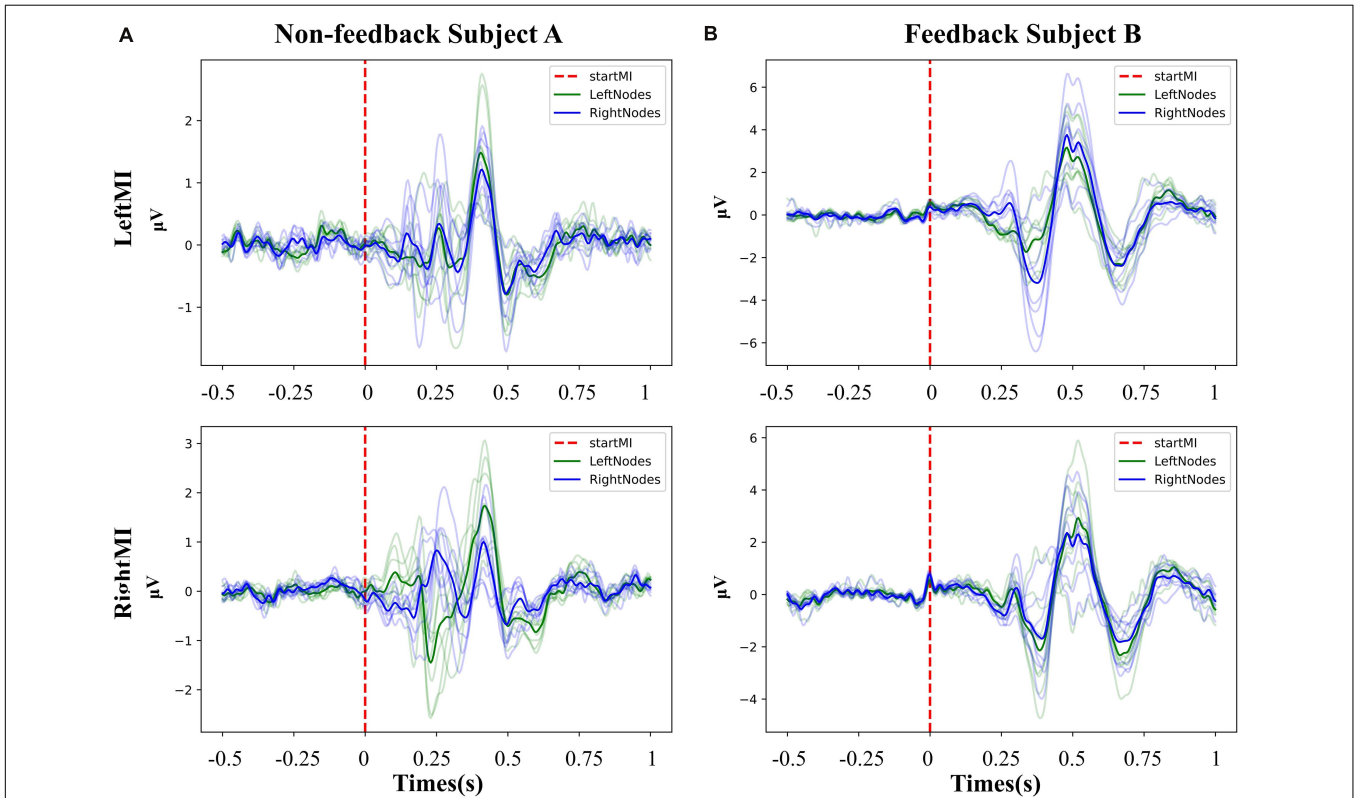
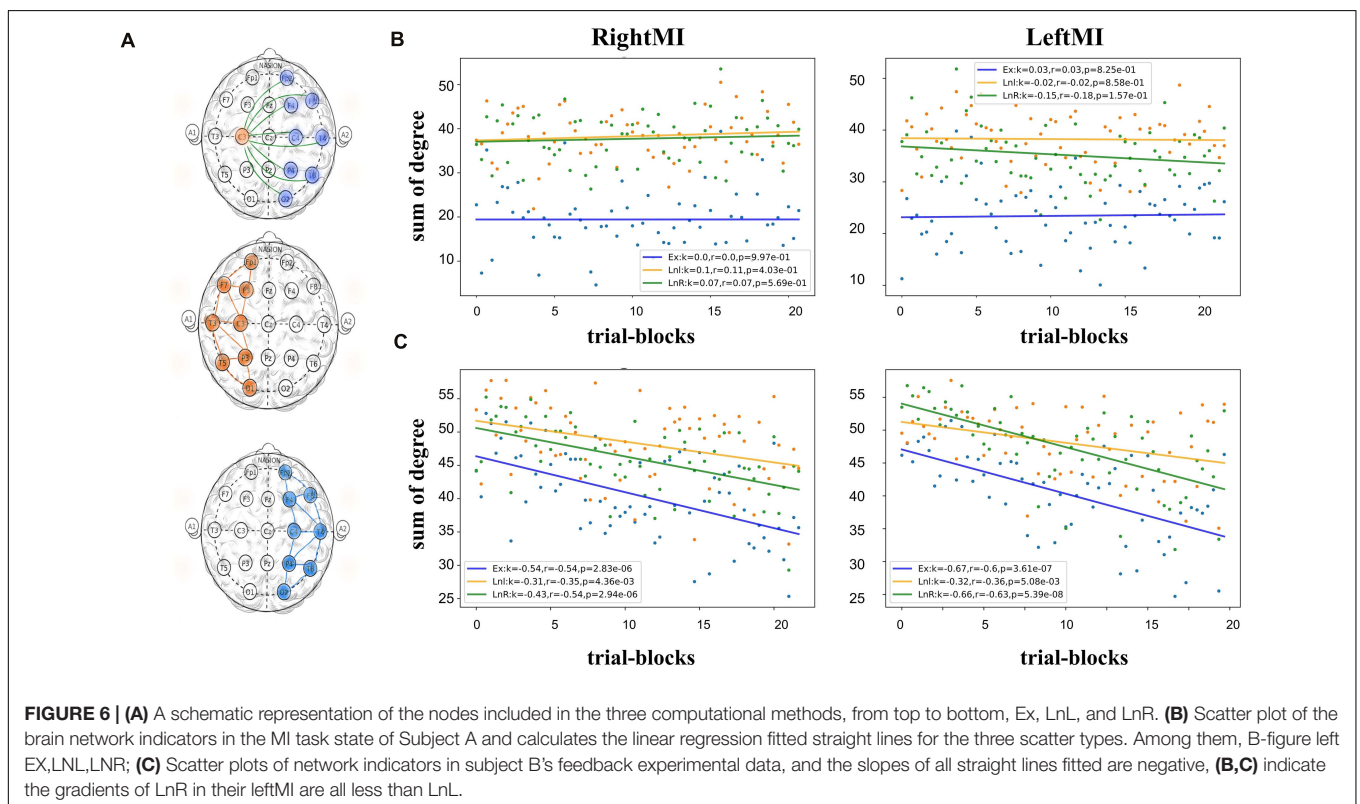
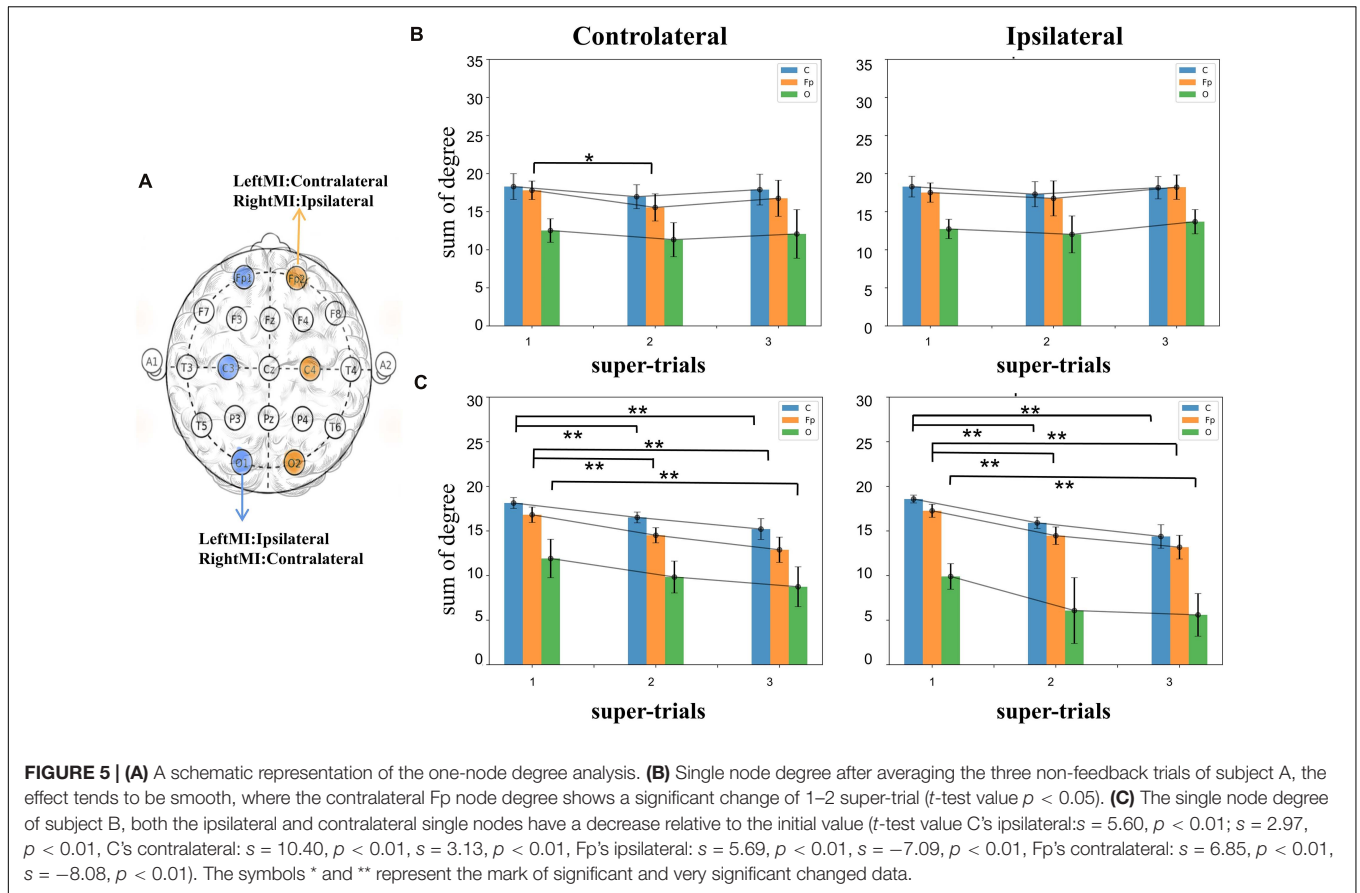


**FIGURE 4 |** The overall ERP performance of the feedback and non-feedback subject. **(A)** Non-feedback subject A, the potential graph of each channel during left- and right- handed MI training (–0.5~1 s). **(B)** Feedback subject B, the potential graph of each channel during left- and right- handed MI training (–0.5~1 s). Both subjects present clear ERP curves, and the ERP curves of the left channels and the right channels show slight differences at different MI task.



## Clustering of Network

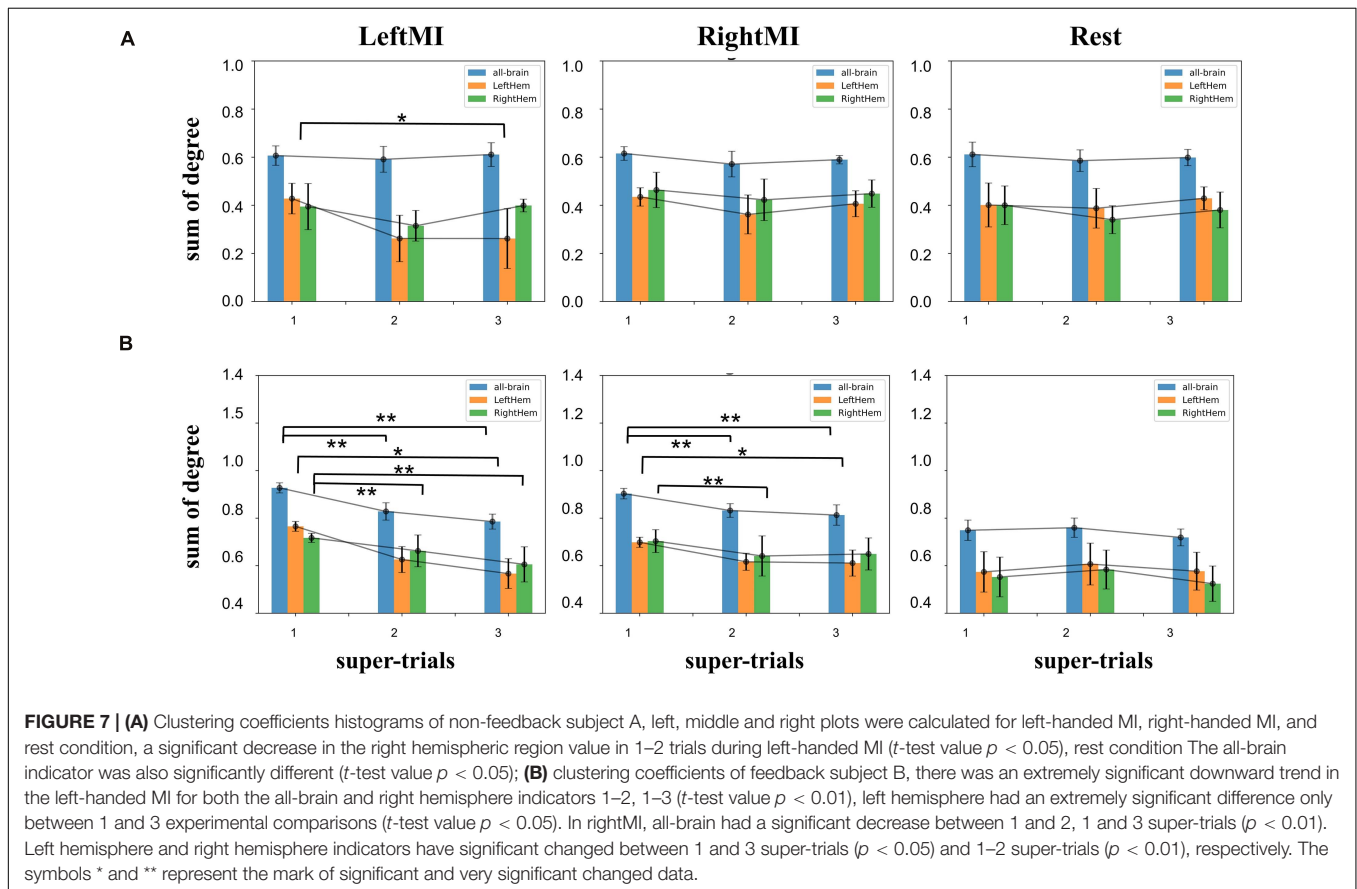
Clustering coefficients were calculated for the whole brain, left hemisphere, and right hemisphere. The differences between the task and resting states were calculated separately. Among the three calculations of subject A (**Figure 7A**), there was a downward trend and significant difference ( $t$ -test value  $p = 0.04$ ) between the 1–3 super-trials of left-handed MI in the right hemisphere. **Figure 7B** for Subject B shows a significant downward trend for left-handed MI's both all-brain and right hemisphere ( $p = 1.3e-3$  and  $0.2e-3$  for all-brain), and the left hemisphere was significantly different only in first-to-third experimental comparisons ( $t$ -test value  $p = 0.04$ ); in right-handed MI, all-brain, left and right hemisphere had significant decreases (all: $t$ -test value  $p = 4.3e-3$ ,  $6.9e-3$ , left:  $t$ -test value  $p = 0.04$ , right:  $p = 4.3e-3$ ) while there are no significant changes in the rest state. The results show that feedback experiments altered the task-state clustering coefficient to decay and more extensive in the contralateral sides. Training did not affect the resting state significantly.

## DISCUSSION

In the present study, we focused on using EEG signals to investigate what impact MI-BCI training can have on the brain in short-term. We applied controlled research using MI-BCI training with/without visual feedback.

Firstly we analyzed the Mu band's energy attenuation on the contralateral side. The result showed ERD changed with an increasing trend at the feedback group. This was consistent with studies of rehabilitation in Shindo et al. (2011) and Yoshida et al. (2016), suggesting ERD strengthened for successful BCI training. On the other hand, the non-feedback group presented little change, and the change from 1-h feedback training was of no statistical significance, which was different from the long-term rehabilitation training. Therefore, characteristics of cortical motor activities need to be further investigated, to introduce new assessment tools to quantify changes with MI-BCI training of short-terms.

We then studied ERPs of MI tasks in this study. In the MI analysis of ERP, MRCP is often used. the ERP analyzed in this paper intersects with MRCP but is not identical in definition. The low frequency (below 6 Hz or so) negative shifts in the EEG signal representing brain activity changes related to movement. In our investigation, the negative deflection of MRCP appeared relatively obvious only after filtering above 3 Hz. The corresponding ERP dynamic presented visible changes along the MI training process as well. The EEG signal band-pass filtered at 3–6 Hz contains information of significant changes in relation to short-term training. On the other hand, signals below 3 Hz had relatively large amplitude but the response was dynamically consistent during the training process. This may obscure functional changes of great interest to us. Previous studies have mentioned



that there are discriminable information for MI decoding in Bands at 1~6 Hz of ERP (Ramos-Murguialday and Birbaumer, 2015; Korik et al., 2018; Schwarz et al., 2019). For example, Ramos et al. used filtering in the 3~45 Hz for a BCI motor task analysis. Korik et al. studied ERP at 4~8 Hz for decoding imagined 3D hand movement in EEG (Korik et al., 2018). Marshall et al. investigated ERP with 3 Hz high-pass filter for infants' auditory (Marshall et al., 2009). Thus we applied preprocess filtering with low cut-off frequency at 3 Hz to satisfy our analysis requirements. As we choose 3–30 Hz of EEG containing MI brain activities for investigation functional changes during short-term training, it contains ERD range as well.

Different behavioral patterns have different brain network activations (Gonzalez-Lima and McIntosh, 1994; Büchel and Friston, 1997; Büchel and Friston, 2000; Horwitz et al., 2000; Taylor et al., 2000). Functional connectivity has been defined as 'neural context' (McIntosh, 1999, 2000; McIntosh et al., 2001). By calculating functional connectivity, we can further apply graph theory to analyze brain networks. Graph theory, which describes the brain as a single interconnected network (Bullmore and Sporns, 2009; Fallani et al., 2013; Cheng et al., 2015), provides a theoretical framework with the potential ability to characterize the behavior of complex brain systems and can reveal important information about the local and global organization of functional brain networks. Applying the methodology described above, this paper validates the changes in brain networks brought about by short-term MI training of these two neural contexts with and without feedback and their differences. For example, in **Figure 5**, we see that the feedback experimental set of individual nodes of this brain network (i.e., with visual feedback) shows a significant downward trend in degree summation. We speculate that this trend stems from the fact that MI training with visual feedback leads to decreased connectivity of the blocks represented by the nodes due to stronger inhibitory action generation, mentioned in previous literature (Waldvogel et al., 2000; Attwell and Iadecola, 2002). In **Figure 7**, we analyzed network connectivity changes from the perspective of the cerebral hemispheres' internal and external interactions. We speculated that the decreasing trend of the feedback group might be caused by the concentration of neural clusters in the brain area and the concentration of ERP changes in specific relevant areas, which led to a decrease in the overall correlation within the region. The reduction in the contralateral MI of the left hand indicated certain ERD characteristics. Feedback MI training more significantly affects brain networks in the task state than in the resting state. In conclusion, this ERP-based constructed network change showed a significant decrease in the short-time task state, contralateral effectiveness, etc., intuitively reflecting the immediate effect of short-term BCI training on the brain.

In the current research on BCI rehabilitation training, we see that many studies have been devoted to finding indicators of long-term rehabilitation. In contrast, the indicators proposed in this paper found that brain network activity changes over a short period. Feedback training results are more significant than those of no-feedback training indicators, which are expected

to be applied to short-term training value assessment. Unlike other classical brain network analysis methods such as fMRI (Van Den Heuvel and Pol, 2010), EEG signals have unique advantages—high temporal and spatial resolution, which can be analyzed more quickly and easily. It makes a good pavement for the short-term MI-BCI rehabilitation assessment. This paper differs from the conventional brain network construction of EEG (Friston, 2011). It adopts an EEG signal combination processing method with ERP characteristics, which can reduce EEG signals' instability and reflect signals' event characteristics more effectively.

However, there are many limitations for improvement in this study. For example, the experimental sample data is insufficient. The ERP construction method used for network construction has not been tried in non-MI rehabilitation training. The present analysis is based on the visual feedback training of healthy subjects. The sample data can be improved in many aspects: for example, changing healthy subjects to patients or using different feedback methods; it is also possible to make a comparison between short-term training and long-term training indicators and integrate the processes of existing indicators proposed in this paper to form a perfect evaluation method to quantify the goals of rehabilitation training better.

## CONCLUSION

In summary, this paper is a preliminary attempt in the field of EEG brain network-based rehabilitation assessment. We applied Mu band power's attenuation and ERP-based brain network to analyze the EEG changes during short-term MI task. We found significant changes in brain connectivity, that the functional network topology coefficients of feedback subject showed a significant decrease after about 1 h of MI-BCI training, while the non-feedback group's most network parameters didn't change significantly. The experimental results showed the necessity of neurofeedback. This study has laid a good foundation for subsequent BCI closed-loop neurological rehabilitation studies. The analytical approach for measuring the effectiveness of short-term rehabilitation training proposed in this study is expected to facilitate the establishment of a more personalized rehabilitation assessment system, which, when correlated with long-term clinical indicators, can lead to more credible and regulated individual treatment schedules and help patients to undergo more efficient rehabilitation.

The next step of the study is to collect more data or try to apply generative methods to deal with the data scarcity. Furthermore, we also consider different feedback strategies to link the short-term indicators to the specific neurological mechanisms, so as to provide a more underlying and reliable basis for experimental results.

## DATA AVAILABILITY STATEMENT

The original contributions presented in the study are included in the article/**Supplementary Material**, further inquiries can be directed to the corresponding author/s.

## AUTHOR CONTRIBUTIONS

YW: conceptualization. YW and JL: validation and writing—original draft preparation. JL, YW, and QC: formal analysis. QC and HW: resources. JL, QC, and HW: writing—review and editing. All authors have read and agreed to the published version of the manuscript.

## FUNDING

This research was supported by the Independent Deployment of Scientific Research Projects of Jihua Laboratory (X190051TB190), the National Natural Science Foundation of China (U1913216), the Shanghai Municipal Science and Technology Major Project (2017SHZDZX01), the National Natural Science Foundation of China (Grant No. 61876015),

## REFERENCES

- Ahn, M., and Jun, S. C. (2015). Performance variation in motor imagery brain-computer interface: a brief review. *J. Neurosci. Methods* 243, 103–110. doi: 10.1016/j.jneumeth.2015.01.033
- Alkadhi, H., Brugger, P., Boendermaker, S. H., Crelier, G., Curt, A., HeppReymond, M.-C., et al. (2005). What disconnection tells about motor imagery: evidence from paraplegic patients. *Cereb. Cortex* 15, 131–140. doi: 10.1093/cercor/bhh116
- Ang, K. K., Guan, C., Phua, K. S., Wang, C., Zhou, L., Tang, K. Y., et al. (2014). Brain-computer interface-based robotic end effector system for wrist and hand rehabilitation: results of a three-armed randomized controlled trial for chronic stroke. *Front. Neuroeng.* 7:30. doi: 10.3389/fneng.2014.00030
- Attwell, D., and Iadecola, C. (2002). The neural basis of functional brain imaging signals. *Trends Neurosci.* 25, 621–625. doi: 10.1016/s0166-2236(02)02264-6
- Baig, M. Z., Aslam, N., Shum, H. P., and Zhang, L. (2017). Differential evolution algorithm as a tool for optimal feature subset selection in motor imagery EEG. *Expert Syst. Appl.* 90, 184–195. doi: 10.1016/j.eswa.2017.07.033
- Barclay, R. E., Stevenson, T. J., Poluha, W., Semenko, B., and Schubert, J. (2020). Mental practice for treating upper extremity deficits in individuals with hemiparesis after stroke. *Cochrane Database Syst. Rev.* 2011:CD005950.
- Beatty, J., Greenberg, A., Deibler, W. P., and O'Hanlon, J. F. (1974). Operant control of occipital theta rhythm affects performance in a radar monitoring task. *Science* 183, 871–873. doi: 10.1126/science.183.4127.871
- Belardinelli, P., Laer, L., Ortiz, E., Braun, C., and Gharabaghi, A. (2017). Plasticity of premotor cortico-muscular coherence in severely impaired stroke patients with hand paralysis. *NeuroImage* 14, 726–733. doi: 10.1016/j.nicl.2017.03.005
- Braadbaart, L., Williams, J. H., and Waiter, G. D. (2013). Do mirror neuron areas mediate mu rhythm suppression during imitation and action observation? *Int. J. Psychophysiol.* 89, 99–105. doi: 10.1016/j.ijpsycho.2013.05.019
- Brown, B. B. (1970). Recognition of aspects of consciousness through association with EEG alpha activity represented by a light signal. *Psychophysiology* 6, 442–452. doi: 10.1111/j.1469-8986.1970.tb01754.x
- Buch, E., Weber, C., Cohen, L. G., Braun, C., Dimyan, M. A., Ard, T., et al. (2008). Think to move: a neuromagnetic brain-computer interface (BCI) system for chronic stroke. *Stroke* 39, 910–917. doi: 10.1161/strokeaha.107.505313
- Büchel, C., and Friston, K. (2000). Assessing interactions among neuronal systems using functional neuroimaging. *Neural Netw.* 13, 871–882. doi: 10.1016/s0893-6080(00)00066-6
- Büchel, C., and Friston, K. J. (1997). Modulation of connectivity in visual pathways by attention: cortical interactions evaluated with structural equation modelling and fMRI. *Cereb. Cortex (New York, NY: 1991)* 7, 768–778. doi: 10.1093/cercor/7.8.768
- Bullmore, E., and Sporns, O. (2009). Complex brain networks: graph theoretical analysis of structural and functional systems. *Nat. Rev. Neurosci.* 10, 186–198. doi: 10.1038/nrn2575

the Natural Science Foundation of Beijing Municipality, China (Grant No. 4202040), and Shanghai Science and Technology Innovation Action Plan (19441908200).

## ACKNOWLEDGMENTS

We would like to thank editor and reviewers for helpful comments to improve this manuscript.

## SUPPLEMENTARY MATERIAL

The Supplementary Material for this article can be found online at: <https://www.frontiersin.org/articles/10.3389/fnhum.2021.627100/full#supplementary-material>

- Caria, A., Weber, C., Brötz, D., Ramos, A., Ticini, L. F., Gharabaghi, A., et al. (2011). Chronic stroke recovery after combined BCI training and physiotherapy: a case report. *Psychophysiology* 48, 578–582. doi: 10.1111/j.1469-8986.2010.01117.x
- Carter, A. R., Shulman, G. L., and Corbetta, M. (2012). Why use a connectivity-based approach to study stroke and recovery of function? *Neuroimage* 62, 2271–2280. doi: 10.1016/j.neuroimage.2012.02.070
- Cheng, D., Liu, Y., and Zhang, L. (2018). “Exploring motor imagery EEG patterns for stroke patients with deep neural networks,” in *Proceedings of the 2018 IEEE International Conference on Acoustics, Speech and Signal Processing (ICASSP)* (Piscataway, NJ: IEEE), 2561–2565.
- Cheng, L., Wu, Z., Sun, J., Fu, Y., Wang, X., Yang, G. Y., et al. (2015). Reorganization of motor execution networks during sub-acute phase after stroke. *IEEE Trans. Neural Syst. Rehabil. Eng.* 23, 713–723. doi: 10.1109/tnsre.2015.2401978
- Daly, J. J., Cheng, R., Rogers, J., Litinas, K., Hrovat, K., and Dohring, M. (2009). Feasibility of a new application of noninvasive brain computer interface (BCI): a case study of training for recovery of volitional motor control after stroke. *J. Neurol. Phys. Ther.* 33, 203–211. doi: 10.1097/npt.0b013e3181c1fc0b
- Daly, J. J., and Wolpaw, J. R. (2008). Brain-computer interfaces in neurological rehabilitation. *Lancet Neurol.* 7, 1032–1043. doi: 10.1016/s1474-4422(08)70223-0
- de Vico Fallani, F., Richiardi, J., Chavez, M., and Achard, S. (2014). Graph analysis of functional brain networks: practical issues in translational neuroscience. *Philos. Trans. R. Soc. B Biol. Sci.* 369:20130521. doi: 10.1098/rstb.2013.0521
- Faith, A., Chen, Y., Rikakis, T., and Iasemidis, L. (2011). “Interactive rehabilitation and dynamical analysis of scalp EEG,” in *Proceedings of the 2011 Annual International Conference of the IEEE Engineering in Medicine and Biology Society* (Piscataway, NJ: IEEE), 1387–1390.
- Fallani, F. D. V., Pichiorri, F., Morone, G., Molinari, M., Babiloni, F., Cincotti, F., et al. (2013). Multiscale topological properties of functional brain networks during motor imagery after stroke. *Neuroimage* 83, 438–449. doi: 10.1016/j.neuroimage.2013.06.039
- Friston, K. J. (2011). Functional and effective connectivity: a review. *Brain Connect.* 1, 13–36. doi: 10.1089/brain.2011.0008
- Gonzalez-Lima, F., and McIntosh, A. R. (1994). Neural network interactions related to auditory learning analyzed with structural equation modeling. *Hum. Brain Mapping* 2, 23–44. doi: 10.1002/hbm.460020105
- Graimann, B., Allison, B., and Pfurtscheller, G. (2009). “Brain-computer interfaces: a gentle introduction,” in *Brain-Computer Interfaces*, eds B. Graimann, G. Pfurtscheller, and B. Allison (Berlin: Springer), 1–27. doi: 10.1007/978-3-642-02091-9\_1
- Horwitz, B., Friston, K. J., and Taylor, J. G. (2000). Neural modeling and functional brain imaging: an overview. *Neural Netw.* 13, 829–846. doi: 10.1016/s0893-6080(00)00062-9
- Kaplan, B. J. (1975). Biofeedback in epileptics: equivocal relationship of reinforced EEG frequency to seizure reduction. *Epilepsia* 16, 477–485. doi: 10.1111/j.1528-1157.1975.tb06076.x

- Kaya, M., Binli, M. K., Ozbay, E., Yanar, H., and Mishchenko, Y. (2018). A large electroencephalographic motor imagery dataset for electroencephalographic brain computer interfaces. *Sci. Data* 5, 180211.
- Kim, T., Kim, S., and Lee, B. (2016). Effects of action observational training plus brain-computer interface-based functional electrical stimulation on paretic arm motor recovery in patient with stroke: a randomized controlled trial. *Occup. Ther. Int.* 23, 39–47. doi: 10.1002/oti.1403
- Kok, A. (1997). Event-related-potential (ERP) reflections of mental resources: a review and synthesis. *Biol. Psychol.* 45, 19–56. doi: 10.1016/s0301-0511(96)05221-0
- Korik, A., Sosnik, R., Siddique, N., and Coyle, D. (2018). Decoding imagined 3D hand movement trajectories from EEG: evidence to support the use of mu, beta, and low gamma oscillations. *Front. Neurosci.* 12:130. doi: 10.3389/fnins.2018.00130
- Kuhlman, W. N. (1978). Functional topography of the human mu rhythm. *Electroencephalogr. Clin. Neurophysiol.* 44, 83–93. doi: 10.1016/0013-4694(78)90107-4
- Kumar, S., Sharma, R., Sharma, A., and Tsunoda, T. (2016). “Decimation filter with common spatial pattern and fishers discriminant analysis for motor imagery classification,” in *Proceedings of the 2016 International Joint Conference on Neural Networks (IJCNN)* (Piscataway, NJ: IEEE), 2090–2095.
- Langhorne, P., Coupar, F., and Pollock, A. (2009). Motor recovery after stroke: a systematic review. *Lancet Neurol* 8, 741–754. doi: 10.1016/s1474-4422(09)70150-4
- Latora, V., and Marchiori, M. (2001). Efficient behavior of small-world networks. *Phys. Rev. Lett.* 87:198701.
- Leeb, R., Biasucci, A., Schmidlin, T., Corbet, T., Vuadens, P., and Millán, J. D. R. (2016). “BCI controlled neuromuscular electrical stimulation enables sustained motor recovery in chronic stroke victims,” in *Proceedings of the 6th International Brain-Computer Interface Meeting (No. CONF)* (Asilomar, CA).
- Li, M., Liu, Y., Wu, Y., Liu, S., Jia, J., and Zhang, L. (2014). Neurophysiological substrates of stroke patients with motor imagery-based brain-computer interface training. *Int. J. Neurosci.* 124, 403–415. doi: 10.3109/00207454.2013.850082
- Lin, P., Yang, Y., Gao, J., De Pisapia, N., Ge, S., Wang, X., et al. (2017). Dynamic default mode network across different brain states. *Sci. Rep.* 7:46088.
- Marshall, P. J., Reeb, B. C., and Fox, N. A. (2009). Electrophysiological responses to auditory novelty in temperamentally different 9-month-old infants. *Dev. Sci.* 12, 568–582. doi: 10.1111/j.1467-7687.2008.00808.x
- Marzbani, H., Marateb, H. R., and Mansourian, M. (2016). Neurofeedback: a comprehensive review on system design, methodology and clinical applications. *Basic Clin. Neurosci.* 7:143.
- Matsumoto, J., Fujiwara, T., Takahashi, O., Liu, M., Kimura, A., and Ushiba, J. (2010). Modulation of mu rhythm desynchronization during motor imagery by transcranial direct current stimulation. *J. NeuroEng. Rehabil.* 7:27. doi: 10.1186/1743-0003-7-27
- McIntosh, A. R. (1999). Mapping cognition to the brain through neural interactions. *Memory* 7, 523–548. doi: 10.1080/096582199387733
- McIntosh, A. R. (2000). Towards a network theory of cognition. *Neural Netw.* 13, 861–870. doi: 10.1016/s0893-6080(00)00059-9
- McIntosh, A. R., Fitzpatrick, S. M., and Friston, K. J. (2001). On the marriage of cognition and neuroscience. *Neuroimage* 14, 1231–1237. doi: 10.1006/nimg.2001.0941
- Mihara, M., Hattori, N., Hatakenaka, M., Yagura, H., Kawano, T., Hino, T., et al. (2013). Near-infrared spectroscopy-mediated neurofeedback enhances efficacy of motor imagery-based training in poststroke victims: a pilot study. *Stroke* 44, 1091–1098. doi: 10.1161/strokeaha.111.674507
- Mukaino, M., Ono, T., Shindo, K., Fujiwara, T., Ota, T., Kimura, A., et al. (2014). Efficacy of brain-computer interface-driven neuromuscular electrical stimulation for chronic paresis after stroke. *J. Rehabil. Med.* 46, 378–382. doi: 10.2340/16501977-1785
- Naros, G., and Gharabaghi, A. (2015). Reinforcement learning of self-regulated  $\beta$ -oscillations for motor restoration in chronic stroke. *Front. Hum. Neurosci.* 9:391. doi: 10.3389/fnhum.2015.00391
- Nicolas-Alonso, L. F., and Gomez-Gil, J. (2012). Brain computer interfaces, a review. *Sensors* 12, 1211–1279.
- Nowlis, D. P., and Kamiya, J. (1970). The control of electroencephalographic alpha rhythms through auditory feedback and the associated mental activity. *Psychophysiology* 6, 476–484. doi: 10.1111/j.1469-8986.1970.tb01756.x
- Oberman, L. M., Ramachandran, V. S., and Pineda, J. A. (2008). Modulation of mu suppression in children with autism spectrum disorders in response to familiar or unfamiliar stimuli: the mirror neuron hypothesis. *Neuropsychologia* 46, 1558–1565. doi: 10.1016/j.neuropsychologia.2008.01.010
- Oikonomou, V. P., Georgiadis, K., Liaros, G., Nikolopoulos, S., and Kompatsiaris, I. (2017). “A comparison study on EEG signal processing techniques using motor imagery EEG data,” in *Proceedings of the 2017 IEEE 30th international symposium on computer-based medical systems (CBMS)* (Piscataway, NJ: IEEE), 781–786.
- Ono, T., Tomita, Y., Inose, M., Ota, T., Kimura, A., Liu, M., et al. (2015). Multimodal sensory feedback associated with motor attempts alters BOLD responses to paralyzed hand movement in chronic stroke patients. *Brain Topogr.* 28, 340–351. doi: 10.1007/s10548-014-0382-6
- Pfurtscheller, G., and Da Silva, F. L. (1999). Event-related EEG/MEG synchronization and desynchronization: basic principles. *Clin. Neurophysiol.* 110, 1842–1857. doi: 10.1016/s1388-2457(99)00141-8
- Philips, G. R., Daly, J. J., and Principe, J. C. (2017). Topographical measures of functional connectivity as biomarkers for post-stroke motor recovery. *J. Neuroeng. Rehabil.* 14:67.
- Prasad, G., Herman, P., Coyle, D., McDonough, S., and Crosbie, J. (2009). “Using motor imagery based brain-computer interface for post-stroke rehabilitation,” in *Proceedings of the 2009 4th International IEEE/EMBS Conference on Neural Engineering* (Piscataway, NJ: IEEE), 258–262.
- Ramos-Murguialday, A., and Birbaumer, N. (2015). Brain oscillatory signatures of motor tasks. *J. Neurophysiol.* 113, 3663–3682. doi: 10.1152/jn.00467.2013
- Ramos-Murguialday, A., Broetz, D., Rea, M., L  er, L., Yilmaz,   , Brasil, F. L., et al. (2013). Brain-machine interface in chronic stroke rehabilitation: a controlled study. *Ann. Neurol.* 74, 100–108. doi: 10.1002/ana.23879
- Renton, T., Tibbles, A., and Topolovec-Vranic, J. (2017). Neurofeedback as a form of cognitive rehabilitation therapy following stroke: a systematic review. *PLoS One* 12:e0177290. doi: 10.1371/journal.pone.0177290
- Rossiter, H. E., Boudrias, M. H., and Ward, N. S. (2014). Do movement-related beta oscillations change after stroke? *J. Neurophysiol.* 112, 2053–2058. doi: 10.1152/jn.00345.2014
- Rozelle, G. R., and Budzynski, T. H. (1995). Neurotherapy for stroke rehabilitation: a single case study. *Biofeedback Self Regul.* 20, 211–228. doi: 10.1007/bf01474514
- Sakkalis, V. (2011). Review of advanced techniques for the estimation of brain connectivity measured with EEG/MEG. *Comput. Biol. Med.* 41, 1110–1117. doi: 10.1016/j.compbiomed.2011.06.020
- Schwarz, A., Pereira, J., Kobler, R., and M  ller-Putz, G. R. (2019). Unimanual and bimanual reach-and-grasp actions can be decoded from human EEG. *IEEE Trans. Biomed. Eng.* 67, 1684–1695. doi: 10.1109/tbme.2019.2942974
- Shindo, K., Kawashima, K., Ushiba, J., Ota, N., Ito, M., Ota, T., et al. (2011). Effects of neurofeedback training with an electroencephalogram-based brain-computer interface for hand paralysis in patients with chronic stroke: a preliminary case series study. *J. Rehabil. Med.* 43, 951–957. doi: 10.2340/16501977-0859
- Singer, W. (1999). Neuronal synchrony: a versatile code for the definition of relations? *Neuron* 24, 49–65. doi: 10.1016/s0896-6273(00)80821-1
- Sitaram, R., Ros, T., Stoeckel, L., Haller, S., Scharnowski, F., Lewis-Peacock, J., et al. (2017). Closed-loop brain training: the science of neurofeedback. *Nat. Rev. Neurosci.* 18, 86–100. doi: 10.1038/nrn.2016.164
- Soekadar, S. R., Witkowski, M., Birbaumer, N., and Cohen, L. G. (2015). Enhancing Hebbian learning to control brain oscillatory activity. *Cereb. Cortex* 25, 2409–2415. doi: 10.1093/cercor/bhu043
- Song, J., Young, B. M., Nigogosyan, Z., Walton, L. M., Nair, V. A., Grogan, S. W., et al. (2014). Characterizing relationships of DTI, fMRI, and motor recovery in stroke rehabilitation utilizing brain-computer interface technology. *Front. Neuroeng.* 7:31. doi: 10.3389/fneng.2014.00031
- Stam, C. V., and Van Straaten, E. C. W. (2012). The organization of physiological brain networks. *Clin. Neurophysiol.* 123, 1067–1087. doi: 10.1016/j.clinph.2012.01.011

- Sterman, M. B. (1974). MacDonald, Jr, and Stone, rK Biofeedback training of sensorimotor EEG in man and its effect on epilepsy. *Epilepsia* 15, 395–416. doi: 10.1111/j.1528-1157.1974.tb04016.x
- Taylor, J. G., Krause, B., Shah, N. J., Horwitz, B., and Mueller-Gaertner, H. W. (2000). On the relation between brain images and brain neural networks. *Hum. Brain Mapping* 9, 165–182. doi: 10.1002/(sici)1097-0193(200003)9:3<165::aid-hbm5>3.0.co;2-p
- Thomson, D. J. (1982). Spectrum estimation and harmonic analysis. *Proc. IEEE* 70, 1055–1096. doi: 10.1109/proc.1982.12433
- Tsuchimoto, S., Shindo, K., Hotta, F., Hanakawa, T., Liu, M., and Ushiba, J. (2019). Sensorimotor connectivity after motor exercise with neurofeedback in post-stroke patients with hemiplegia. *Neuroscience* 416, 109–125. doi: 10.1016/j.neuroscience.2019.07.037
- Van Den Heuvel, M. P., and Pol, H. E. H. (2010). Exploring the brain network: a review on resting-state fMRI functional connectivity. *Eur. Neuropsychopharmacol.* 20, 519–534. doi: 10.1016/j.euroneuro.2010.03.008
- Varela, F., Lachaux, J. P., Rodriguez, E., and Martinerie, J. (2001). The brainweb: phase synchronization and large-scale integration. *Nat. Rev. Neurosci.* 2, 229–239. doi: 10.1038/35067550
- Waldvogel, D., van Gelderen, P., Muellbacher, W., Ziemann, U., Immisch, I., and Hallett, M. (2000). The relative metabolic demand of inhibition and excitation. *Nature* 406, 995–998. doi: 10.1038/35023171
- Wang, L., Yu, C., Chen, H., Qin, W., He, Y., Fan, F., et al. (2010). Dynamic functional reorganization of the motor execution network after stroke. *Brain* 133, 1224–1238. doi: 10.1093/brain/awq043
- Womelsdorf, T., Schoffelen, J. M., Oostenveld, R., Singer, W., Desimone, R., Engel, A. K., et al. (2007). Modulation of neuronal interactions through neuronal synchronization. *Science* 316, 1609–1612. doi: 10.1126/science.1139597
- Wyler, A. R., Lockard, J. S., Ward, A. A. Jr., and Finch, C. A. (1976). Conditioned EEG desynchronization and seizure occurrence in patients. *Electroencephalogr. Clin. Neurophysiol.* 41, 501–512. doi: 10.1016/0013-4694(76)90062-6
- Yoshida, N., Hashimoto, Y., Shikota, M., and Ota, T. (2016). Relief of neuropathic pain after spinal cord injury by brain–computer interface training. *Spin. Cord Ser. Cases* 2:16021.
- Young, B. M., Nigogosyan, Z., Reimsik, A., Walton, L. M., Song, J., Nair, V. A., et al. (2014). Changes in functional connectivity correlate with behavioral gains in stroke patients after therapy using a brain–computer interface device. *Front. Neuroeng.* 7:25. doi: 10.3389/fneng.2014.00025
- Yu, T., Xiao, J., Wang, F., Zhang, R., Gu, Z., Cichocki, A., et al. (2015). Enhanced motor imagery training using a hybrid BCI with feedback. *IEEE Trans. Biomed. Eng.* 62, 1706–1717. doi: 10.1109/tbme.2015.2402283
- Zich, C., Debener, S., Kranczioch, C., Bleichner, M. G., Gutberlet, I., and De Vos, M. (2015). Real-time EEG feedback during simultaneous EEG–fMRI identifies the cortical signature of motor imagery. *Neuroimage* 114, 438–447. doi: 10.1016/j.neuroimage.2015.04.020
- Zimmermann-Schlatter, A., Schuster, C., Puhan, M. A., Siekierka, E., and Steurer, J. (2008). Efficacy of motor imagery in post-stroke rehabilitation: a systematic review. *J. Neuroeng. Rehabil.* 5:8.

**Conflict of Interest:** The authors declare that the research was conducted in the absence of any commercial or financial relationships that could be construed as a potential conflict of interest.

Copyright © 2021 Wang, Luo, Guo, Du, Cheng and Wang. This is an open-access article distributed under the terms of the Creative Commons Attribution License (CC BY). The use, distribution or reproduction in other forums is permitted, provided the original author(s) and the copyright owner(s) are credited and that the original publication in this journal is cited, in accordance with accepted academic practice. No use, distribution or reproduction is permitted which does not comply with these terms.

# Advantages of publishing in Frontiers



## OPEN ACCESS

Articles are free to read for greatest visibility and readership



## FAST PUBLICATION

Around 90 days from submission to decision



## HIGH QUALITY PEER-REVIEW

Rigorous, collaborative, and constructive peer-review



## TRANSPARENT PEER-REVIEW

Editors and reviewers acknowledged by name on published articles

## Frontiers

Avenue du Tribunal-Fédéral 34  
1005 Lausanne | Switzerland

Visit us: [www.frontiersin.org](http://www.frontiersin.org)

Contact us: [frontiersin.org/about/contact](http://frontiersin.org/about/contact)



## REPRODUCIBILITY OF RESEARCH

Support open data and methods to enhance research reproducibility



## DIGITAL PUBLISHING

Articles designed for optimal readership across devices



## FOLLOW US

@frontiersin



## IMPACT METRICS

Advanced article metrics track visibility across digital media



## EXTENSIVE PROMOTION

Marketing and promotion of impactful research



## LOOP RESEARCH NETWORK

Our network increases your article's readership